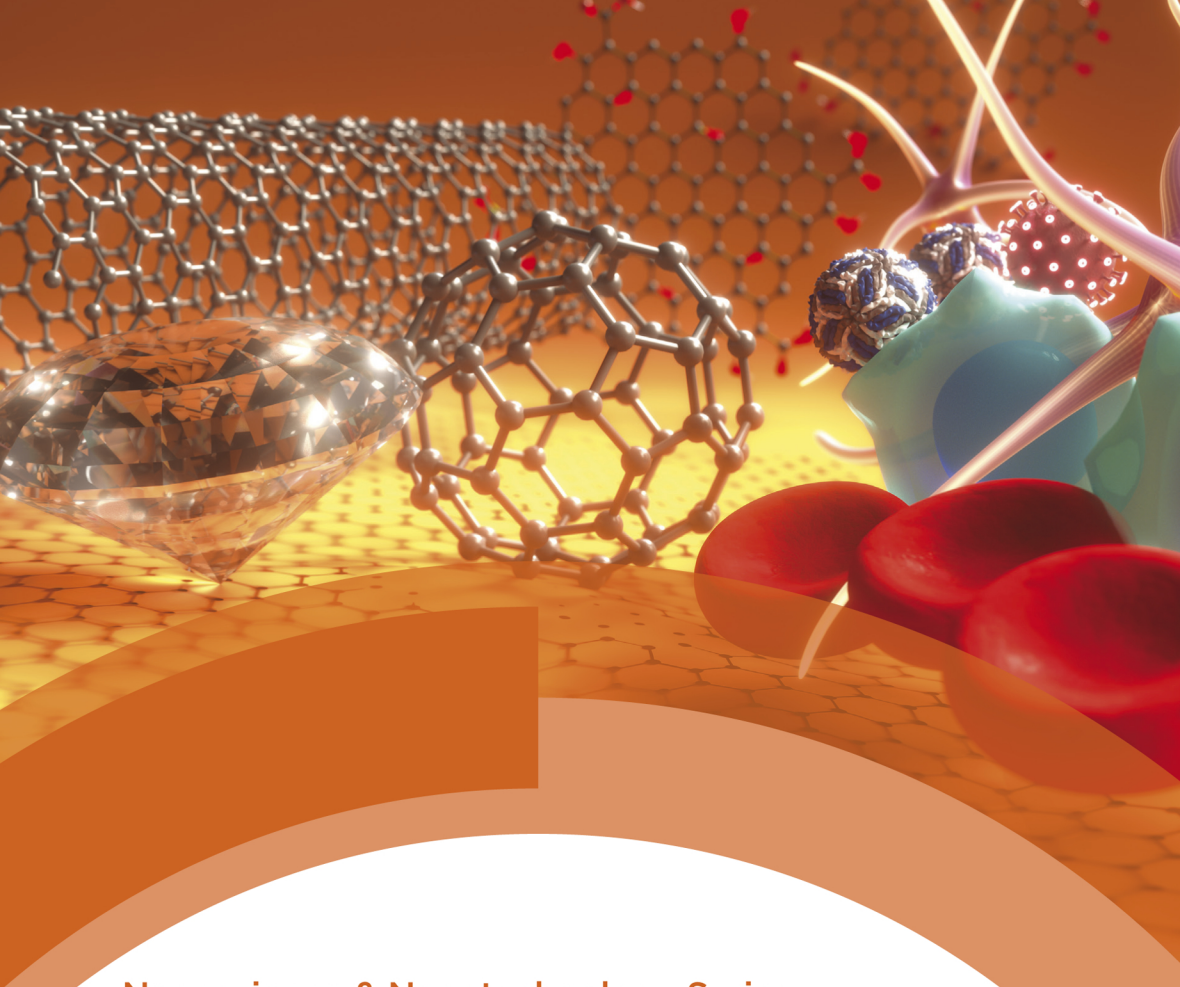

Nanoscience & Nanotechnology Series

Carbon Nanostructures for Biomedical Applications

Edited by Tatiana Da Ros, Nazario Martín and Jean-Francois Nierengarten

ROYAL SOCIETY OF CHEMISTRY

Carbon Nanostructures for Biomedical Applications

Nanoscience & Nanotechnology Series

Editor-in-chief:
Nguyễn T. K. Thanh, *University College London, UK*

Series editors:
Gabriel Caruntu, *Central Michigan University, USA*
Shinya Maenosono, *Japan Advanced Institute of Science and Technology, Japan*
Neerish Revaprasadu, *University of Zululand, South Africa*

Titles in the series:
1: Nanotubes and Nanowires
2: Fullerenes: Principles and Applications
3: Nanocharacterisation
4: Atom Resolved Surface Reactions: Nanocatalysis
5: Biomimetic Nanoceramics in Clinical Use: From Materials to Applications
6: Nanofluidics: Nanoscience and Nanotechnology
7: Bionanodesign: Following Nature's Touch
8: Nano-Society: Pushing the Boundaries of Technology
9: Polymer-based Nanostructures: Medical Applications
10: Metallic and Molecular Interactions in Nanometer Layers, Pores and Particles: New Findings at the Yoctolitre Level
11: Nanocasting: A Versatile Strategy for Creating Nanostructured Porous Materials
12: Titanate and Titania Nanotubes: Synthesis, Properties and Applications
13: Raman Spectroscopy, Fullerenes and Nanotechnology
14: Nanotechnologies in Food
15: Unravelling Single Cell Genomics: Micro and Nanotools
16: Polymer Nanocomposites by Emulsion and Suspension
17: Phage Nanobiotechnology
18: Nanotubes and Nanowires, 2nd Edition
19: Nanostructured Catalysts: Transition Metal Oxides
20: Fullerenes: Principles and Applications, 2nd Edition
21: Biological Interactions with Surface Charge Biomaterials
22: Nanoporous Gold: From an Ancient Technology to a High-Tech Material
23: Nanoparticles in Anti-Microbial Materials: Use and Characterisation
24: Manipulation of Nanoscale Materials: An Introduction to Nanoarchitectonics
25: Towards Efficient Designing of Safe Nanomaterials: Innovative Merge of Computational Approaches and Experimental Techniques
26: Polymer–Graphene Nanocomposites
27: Carbon Nanotube-Polymer Composites
28: Nanoscience for the Conservation of Works of Art
29: Polymer Nanofibers: Building Blocks for Nanotechnology

30: Artificial Cilia
31: Nanodiamond
32: Nanofabrication and its Application in Renewable Energy
33: Semiconductor Quantum Dots: Organometallic and Inorganic Synthesis
34: Soft Nanoparticles for Biomedical Applications
35: Hierarchical Nanostructures for Energy Devices
36: Microfluidics for Medical Applications
37: Nanocharacterisation, 2nd Edition
38: Thermometry at the Nanoscale: Techniques and Selected Applications
39: Nanoceramics in Clinical Use: From Materials to Applications, 2nd Edition
40: Near-infrared Nanomaterials: Preparation, Bioimaging and Therapy Applications
41: Nanofluidics, 2nd Edition
42: Nanotechnologies in Food, 2nd Edition
43: ZnO Nanostructures: Fabrication and Applications
44: Diatom Nanotechnology: Progress and Emerging Applications
45: Nanostructured Materials for Type III Photovoltaics
46: Chemically Derived Graphene: Functionalization, Properties and Applications
47: Graphene-based Membranes for Mass Transport Applications
48: Carbon Nanostructures for Biomedical Applications

How to obtain future titles on publication:
A standing order plan is available for this series. A standing order will bring delivery of each new volume immediately on publication.

For further information please contact:
Book Sales Department, Royal Society of Chemistry, Thomas Graham House, Science Park, Milton Road, Cambridge, CB4 0WF, UK
Telephone: +44 (0)1223 420066, Fax: +44 (0)1223 420247
Email: booksales@rsc.org
Visit our website at www.rsc.org/books

Carbon Nanostructures for Biomedical Applications

Edited by

Tatiana Da Ros
Trieste University, Italy
Email: daros@units.it

Nazario Martín
Universidad Complutense Madrid, Spain
Email: nazmar@quim.ucm.es

and

Jean-Francois Nierengarten
University of Strasbourg, France
Email: nierengarten@unistra.fr

ROYAL SOCIETY OF CHEMISTRY

Nanoscience & Nanotechnology Series No. 48

Print ISBN: 978-1-78801-567-7
PDF ISBN: 978-1-83916-107-0
EPUB ISBN: 978-1-83916-124-7
Print ISSN: 1757-7136
Electonic ISSN: 1757-7144

A catalogue record for this book is available from the British Library

The Royal Society of Chemistry is a charity, registered in England and Wales, Number 207890, and a company incorporated in England by Royal Charter (Registered No. RC000524), registered office: Burlington House, Piccadilly, London W1J 0BA, UK, Telephone: +44 (0) 20 7437 8656.

For further information see our web site at www.rsc.org

Printed in the United Kingdom by CPI Group (UK) Ltd, Croydon, CR0 4YY, UK

Preface

With the advent of 2D graphene in 2004, two-dimensional carbon-based materials became a reality, and currently represent one of the most studied topics in science involving many other elements of the Periodic Table. However, the seminal discovery that started the revolution of carbon nanoforms was the discovery of 0D fullerenes in 1985, which was followed by a variety of other new forms of carbon, namely 1D carbon nanotubes (single and multi-walled), endohedral fullerenes (having a chemical species in the inner cavity), carbon nanohorns, carbon nanoonions and other less-common, and now emerging nanocarbons which, altogether, drew a new scenario of carbon nanostructures that has strongly attracted the interest of the scientific community.

The aforementioned carbon nanoforms have played a central role in the development of groundbreaking advanced materials for application in a variety of fields such as optoelectronic devices, spintronics and solar cells, just to name a few. Actually, around these carbon-based materials a huge synthetic work has been developed by the chemical community in order to efficiently optimize the search for potential applications, namely in the multidisciplinary field of nanotechnology. In contrast, carbon nanostructures have been significantly less used for bio-medical applications. A plausible reason for this could be due to their scarcity or total lack of solubility in the biological aqueous media. However, as nicely shown in this book, solubility of carbon nanostructures in water has been fully achieved by means of the many successful chemical strategies developed for chemical functionalization. Remarkable examples can be found in the following chapters with amazingly huge carbon nanostructures soluble in water.

Nanoscience & Nanotechnology Series No. 48
Carbon Nanostructures for Biomedical Applications
Edited by Tatiana Da Ros, Nazario Martín and Jean-Francois Nierengarten

Published by the Royal Society of Chemistry, www.rsc.org

The great effort devoted to employ chemically modified fullerenes for biological applications has allowed one to address the wide variety of emergent nanoforms of carbon. The resulting innovative materials have been judiciously used for a variety of applications in the fields of biology and medicine. Carbon nanomaterials are quite unique biocompatible platforms for the development of multifunctional systems for a wide variety of applications whose potential is shown in the different chapters collected in this book, ranging from drug delivery systems to cell growth bioactive substrates.

The origin of this book is based on the previous great experience of the three editors of this book of editing a special issue in the *Journal of Materials Chemistry B* entitled "Carbon nanostructures in biology and medicine" in 2017. The success of this special issue (*J. Mater. Chem. B*, **2017**, *5*, 6425) containing 25 original works (and some authors of which have now participated in this book), encouraged us to embark on this new and pleasant venture.

As the editors of this book, we are fully convinced that it should be of interest for the specialists in the field as well as an encouraging updated reference for those non-specialists. The variety of topics contained in these chapters written by specialists represents a useful source of information on a top scientific field. We also strongly believe that this book will stimulate the imagination and inspiration of those scientists engaged in the fields of carbon nanostructures and biomedical applications.

We would like to thank all the contributors to this book, which gather two apparently orthogonal fields, who enthusiastically accepted to participate in this appealing venture. We would also like to extend our gratitude to all those colleagues cited in the book for their inspiring works. This gratitude is also for the Royal Society of Chemistry and, in particular, for the staff of the RSC involved in this venture. Their continuous support, dedication and enthusiasm have been essential in making this book a wonderful reality.

Nazario Martín
Tatiana Da Ros
Jean-François Nierengarten

Contents

Nanoscience & Nanotechnology Series No. 48
Carbon Nanostructures for Biomedical Applications
Edited by Tatiana Da Ros, Nazario Martín and Jean-Francois Nierengarten

Published by the Royal Society of Chemistry, www.rsc.org

CHAPTER 1

Carbon Nanostructures: Drug Delivery and Beyond

AGNIESZKA GAJEWSKA[a], AKCAN ISTIF[a], JASRA GUL[a,b], MICHELE CHIRONI[a], ANDREA FAIDIGA[a], MARCO ROCCO[a], KETTY SLAVEC[a], TERESA GIANFERRARA[a] AND TATIANA DA ROS*[a]

[a]Department of Chemical and Pharmaceutical Sciences, University of Trieste, Trieste, Italy; [b]International Center for Chemical and Biological Sciences (ICCBS), University of Karachi, Karachi, Pakistan
*E-mail: daros@units.it

1.1 Introduction

Since the discovery of fullerenes in 1985, the family of carbon nanostructures has widened a lot and nowadays it includes nanotubes, nanodiamonds, nanoonions, nanoribbons, nanocones, nanohorns, graphene and its direct derivatives, as graphene quantum dots, and carbon dots. Despite the fact that they all present interesting characteristics, in the last few years the most studied, from a biological point of view, are carbon nanotubes (CNTs), graphene oxide (GO), graphene quantum dots (GQDs), carbon quantum dots (CQDs) and carbon nanodiamonds (NDs). In fact, lately the interest for fullerenes has dramatically decreased, affecting the number of studies on their properties, but there are still brilliant examples of their biological potential as reported by various authors.[1]

One of the most explored bio-applications of carbon nanostructures is related to their capability to load different payloads and to cross the cellular

Nanoscience & Nanotechnology Series No. 48
Carbon Nanostructures for Biomedical Applications
Edited by Tatiana Da Ros, Nazario Martín and Jean-Francois Nierengarten

Published by the Royal Society of Chemistry, www.rsc.org

membrane, allowing the intracellular delivery of drugs into cells. Here we will discuss some of the most recent developments in this field, except for fullerenes, which have been recently widely reviewed.[2]

1.2 Carbon Nanotubes

CNTs consist of one or several concentric graphene sheets rolled up in a cylindrical shape with a range in diameter from 0.4 nm up to 100 nm. They have been studied from many different aspects.

The biological applications of CNTs are strongly dependent on all of the health hazards that this new material can cause. For several years, the effects of CNTs in cells and tissues have been explored by *in vivo* and toxicological studies. However, it turned out that many parameters of CNTs, (as contaminants, surface chemistry, processing methods, agglomerate states, length, diameter and more) can have various toxic effects.

As was reported, the toxic effect of CNTs can arise not directly from them, but from the residues produced during the synthetic process as nickel, cobalt or iron nanoparticles, which can remain in the CNTs and generate reactive oxygen species (ROS) in a biological environment. It turns out that ROS cause inflammatory symptoms and induce mitochondrial membrane degradation, depletion of antioxidant agents, rise in inflammatory biomarkers, and decreases cell viability. It has been demonstrated that 30% of iron in SWCNTs is able to generate free radicals within 15 min of exposure to epidermal keratinocytes in the presence of DMPO (5,5-dimethyl-1-pyrroline-1-oxide).[3] In a later study it was shown that higher amounts of catalyst generate higher concentrations of free radicals and increase inflammatory responses.[4] Additionally, nickel alters the expression of the gene encoding the protein HIF1A, a factor of transcript involved in the regulation of inflammatory genes and apoptosis.[5] All studies on the toxicity of CNTs must than take into account the nature of the metallic catalyst and its percentage/quantity. It is difficult to obtain pure CNTs by removing all traces of catalysts and several methods can be employed to decrease residual catalysts including centrifugation, high-temperature annealing[6] and oxidation treatment by acid reflux.[7]

Toxicity can be also influenced by the modification on the CNTs' surface. Only with acid-treatment on the CNTs' surface is it possible to introduce a number of defect sites along the CNTs' surface (as mentioned earlier). Muller *et al.* changed the number of defect sites on MWCNTs by mechanical grinding and annealing at high temperature and demonstrated that acute pulmonary toxicity and genotoxicity increased after intratracheal administration of MWCNTs with a larger number of defect sites.[8] However, another study by Kagan *et al.* showed that oxidized SWCNTs can be biodegraded more easily by myeloperoxidase enzyme, found in neutrophils and macrophages. The enzyme interacts with carboxylic sites on the nanotubes' surface[9] and oxidized CNTs may be more biocompatible than pristine CNTs from this point of view. Following this pathway, Sayes and co-workers examined cell viability in the presence of oxidized and phenylated tubes. They discovered that the phenylated tubes exhibit lower toxicity, and this can be due to the hindering of the defect sides of the tubes.[10] Dumortier *at al.* have examined the toxicity of CNTs functionalized by

1,3-dipolar cycloaddition. They concluded that CNTs, fully soluble in aqueous culture media, did not modify primary immune cells viability *in vitro*.[11] Also, the CNTs' surface area and their hydrophobic nature have an impact on the toxicity. The tubes, in fact, can potentially interact with several molecules like proteins, RNA, DNA and enzymes with toxic effects on the biological environment.[12] Dutta and co-workers found that the bovine or human serum albumin adsorption onto the CNT surface resulted in inflammatory responses after uptake by macrophage cells. Normally that effect occurs only when albumin adopts structural changes or becomes damaged.[13] The effect of functionalization of the tubes highlights the importance of assessing the toxicity profile for every type of new CNT modification.

Finally, the CNTs' length cannot be ignored. CNT sizes have an important effect on clearance. The length can range from nanometers up to millimeters. The exposure to long fiber-like material can induce dangerous damages in DNA and genetic mutations over a period of exposure, causing an extremely malignant form of cancer, mesothelioma. Symptoms of these biopersistent fibers are the granulomas, which are the signs of oxidative stress, causing excessive fibrous tissue.[14]

Macrophage are the cells responsible for the removal of foreign material like CNTs from living organisms. Fibers with a length exceeding 20 μm are extremely resistant to phagocytosis[15] and Poland *et al.* have shown that CNTs as spherical or stellate shaped agglomerates with less than 20 μm have no significant damaging reactions compared to samples with individualized MWCNTs, agglomerates, and ropes of MWCNTs with lengths exceeding 20 μm.[14] CNTs can be toxic, but many solutions exist, to moderate or eliminate adverse effects arising from the mentioned problems. In conclusion, CNTs should be used without the presence of metal catalysts, have an appropriate functionalization for the planned purpose with low surface oxidation, present a covered surface to effectively escape bio-interactions and be short to avoid long retention times.

To approach their potential application and effect on humans, pharmacokinetics and biodistribution in animal models have been and are currently being explored, and they depend on numerous factors such as chemical-physical characteristics, solubility, surface functionalization, aggregation of the derivatives themselves,[16] while CNT excretion is mainly renal.[17]

The possible biomedical applications of CNTs span many fields. One example is regenerative medicines due to their biocompatibility, resistance, and possible functionalization of their surface with biomolecules as collagen fibers to form a nanomaterial capable of acting as a scaffold in tissue regeneration, as already reported many years ago.[18] Another potentiality, not properly unraveled up to now, is their supposed antioxidant activity. If this function could be confirmed, they could also be used in the prevention of aging and preservation of food.[19] However, the most promising and studied application for CNTs is delivery systems. In fact, they can be loaded with different pharmaceutical ingredients and be delivered at specific sites, with prolonged accumulation into targeted tissues and reduced prospective systemic toxic effects.[20] The latter aspect is of particular importance in the case of anticancer drugs, the mechanism of action of which is mainly related to their toxic effects

(*i.e.* alkylation, DNA intercalation, tubulin aggregation/disaggregation equilibrium unbalance among others). In this context, CNTs propose an opportunity to capsulate anticancer drugs, thus reducing their toxicity for an organism and enhancing local accumulation in the targeted site.[21] Moreover, it is important to remember that, with the proper modification, it is possible to stimulate the drug release from the drug-CNT complex only in a tumor environment, for example, by lowering the pH under the physiological value (Figure 1.1).[22]

Their capability to act as efficient vehicles for the transport of many molecules is related to their ability to enter into cells, mainly with two mechanisms,[23] one of which–the so-called nano-needle process-is not invasive for biological membranes, considering that the tubes pierce through the phospholipidic double layer without disrupting the surface.[23b] This internalization method could also play a role in the application of CNTs in vaccines.[24] The uptake mechanism, however, depends on various factors such as length, size, nature of functional groups and hydrophobicity (Figure 1.2).[25]

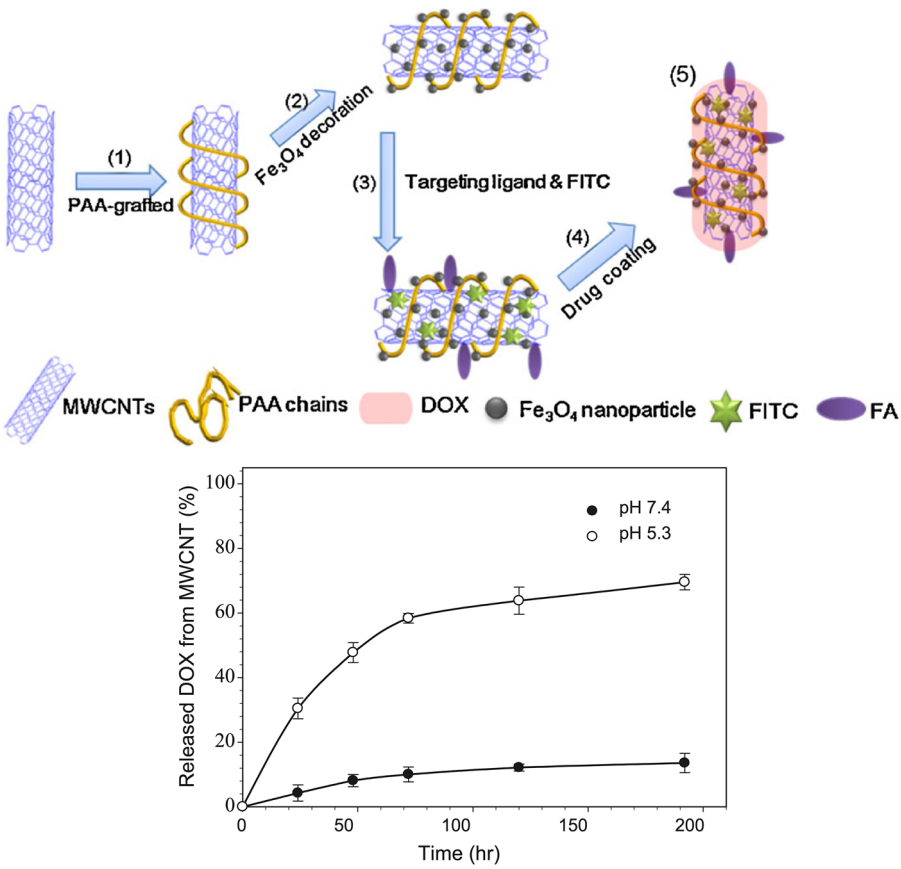

Figure 1.1 *Top*: Preparation of Fe_3O_4 magnetic nanoparticles decorated poly(acrylic acid)-grafted MWCNTs, covalently linked to folic acid and fluorescein (steps 1–3) and embedding doxorubicin by non-covalent interactions. *Bottom*: doxorubicin release profile at acid and neutral pH at 37 °C. Adapted from ref. 22 with permission from Elsevier, Copyright 2012.

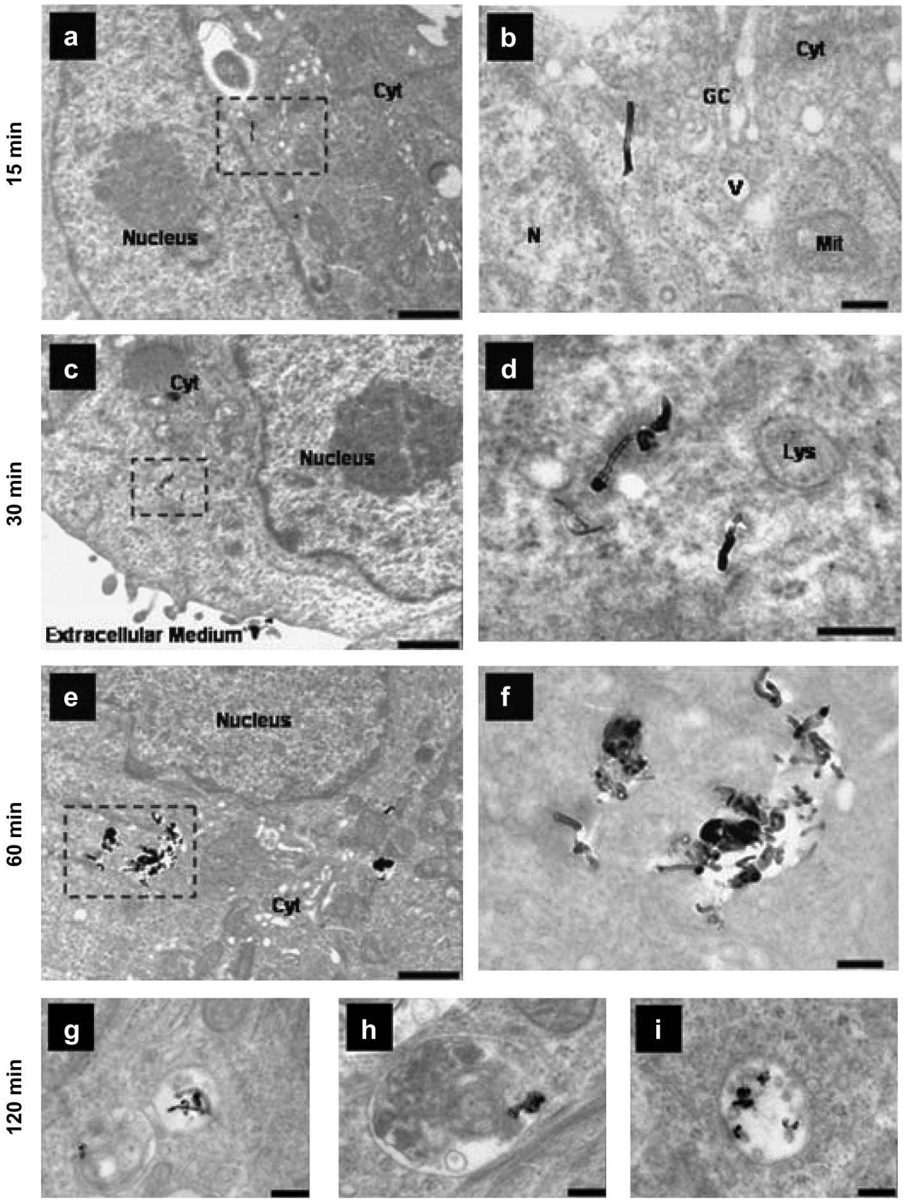

Figure 1.2 Distribution of functionalized MWCNTs into A549 cells at different time of incubation. Scale bars: 1 mm in a, c and e; 200 nm in b, d, f, g, h and i. Cyt, cytoplasm; N, nucleus; GC, Golgi complex; V, vesicle; Mit, mitochondria; Lys, lysosome. Reproduced from ref. 25 with permission from Elsevier, Copyright 2012.

1.2.1 CNTs as Cellular Substrates

One of the very promising and important implementations of CNTs is connected with their topological and chemical structure. It is well established that topographies and patterns can influence cellular behaviors. By controlling the nanoscale topography of cellular substrates, the implantation of medical devices facilitates new biological processes, including embryogenesis, angiogenesis and pathological conditions.

CNTs as nanoparticles are inherently appropriate for surface modifications by simple incorporation or deposition on their surface. They have a fibrillar shape and versatile optical, electrical and mechanical characteristics for applications as a cellular substrate. Many groups have successfully utilized CNTs for cellular growth surfaces to provide structural support or present novel properties.[26] For instance, a range of cell phenotypes have shown high binding affinities for CNT surfaces, demonstrating that CNTs may be used for a variety of tissue implantation devices or novel substrates.[27]

Several papers have presented CNTs as conducive to neuronal adhesion and safe for neural processes outgrowth, suggesting that CNTs are biocompatible with neurons. Cellot *et al.* reported that CNTs provide a shortcut for the electrical signaling connecting tight junctions adhered onto the nanotube surface at proximal and distal portions of the neuron.[28] Mature neuronal cells have also been derived directly from human embryonic stem cells (hESCs) using polymer-grafted CNT thin film scaffolds.[29] Malarkey and co-workers, by modulating the thickness and the conductivity of a CNT film, were able to change neuron morphology, neurite outgrowth and the number of growth cones.[30] Even if, until now, neuronal interfacing has no direct clinical benefits, research developments in this area may help to explain biological mechanisms and neural interactions relevant to injury and disease. Preferential interactions of neural cells and CNTs permit the study of axonal outgrowth and connection between neural clusters and patterned CNTs. Also, the directed growth and migration along CNT surface architectures allowed the study of their role to prevent and repair nerve injuries, such as spinal cord injury or stroke.[31]

Lee *et al.* pretreated rats with amine-modified SWCNTs, and they found a protection effect on neurons as well as an improvement in the recovery of behavioral functions in rats with induced stroke. Authors suggest that CNTs with positive charges may have contributed to a favorable environment for neurons.[32] Roman *et al.* investigated the administration of PEGylated SWCNTs after traumatic neural cord injury, which could promote regeneration of axons into the lesion cavity and functional recovery of the hindlimbs.[33] They found that, after a spinal cord injury (SPI), neurofilament-positive fibers of SWCNT-PEG induced a modest improvement in hindlimb locomotor recovery without causing hyperalgesia. These data suggest that SWCNT-PEG may be an effective material to promote axonal repair and regeneration after SPI.

By functionalization, CNTs can be conjugated with imaging agents, such as metallic nanoparticles, quantum dots, or isotopes to make imaging possible *via* conventional techniques. Chen *et al.* studied the conjugation of

CNTs with super paramagnetic iron oxide nanoparticles (SPIO) and NIR fluorescent quantum dots CdTe.[34] The CNTs-SPIO-CdTe nanohybrids exhibited the superparamagnetic behavior of SPIO with a saturation magnetization of about 65 $emug^{-1}$ at room temperature and strong emission band located at a near-infrared wavelength of 734 nm. Different authors used magnetic resonance imaging (MRI) for visualizing CNTs in cells[35] or living organisms[36] taking advantage of the presence of iron oxide impurities.

Recent studies on the application of CNTs for radiotherapy reported several examples of CNTs as a radioisotope carrier. In the case of encapsulation of the radionuclides, Hong *et al.* presented single-walled CNTs filled with sodium iodide-125 (Auger and γ-emitter) for *in vitro* and *in vivo* study.[37] The material had a specific tissue accumulation (lung) and the leakage of the radionuclide was not observed. More recent studies proposed the use of nanocapsules bearing radioactive samarium salt, that can be used both in diagnostics and in therapy, as a new tool for theranostic applications.[38]

1.2.2 CNTs as Drug Delivery Systems

As already mentioned, CNTs can be internalized by cells and, by presenting a high surface area, they are ideal to transport a number of compounds on their surface. Their potentiality as drug delivery systems have been explored in depth,[39] with special attention paid to vehiculation for anticancer drugs, a case in which selectivity is a major necessity.

Internalization selectivity can be achieved by exploiting different specific transporters and receptors. A successful approach has been reported by using CNTs decorated with fructose, exploiting glucose transporter (GLUT) receptor-mediated pathways, in particular GLUT5, which is a membrane protein transporting fructose into the cytoplasm.[40] The authors reported a functionalization of CNTs using block copolymer, in which doxorubicin was also introduced. Both covalent and supramolecular approaches were used to decorate the tubes and in the same case also folic acid was introduced to exploit FA receptors for cellular internalization in breast cancer. Tumor breast cancers, in fact, overexpress FA receptors and GLUT5.

The combination of nanotubes, functionalized with folic acid and doxorubicin, with silk protein leads to an injectable hybrid silk hydrogel with enhanced strength resistance due to the presence of carbon nanomaterials. This construct was also able to selectively target the cells overexpressing FA receptors and deliver anthracycline due to the degradation of the silk, with enhancement of the release using NIR pulsed irradiation to trigger the local increase of temperature that helps the detachment of the drug.[41]

In drug delivery studies with CNTs, anthracyclines, such as doxorubicin, are probably the most used drugs[39] because they have very attractive anticancer compounds but they present important cardiotoxic side-effects. Consequently, the idea of decreasing this toxicity by means of a proper vehiculation is very appealing. Moreover, these compounds present aromatic structures, permitting an efficient loading on the tubes also with

strategies that are not covalent, and their fluorescence allowed one to follow directly the fate of the drugs. These studies have been recently summarized in a review.[42]

Pemetrexed, a folic acid analog anti-metabolite anticancer, and/or quercetin, endowed also with proapoptotic activity, were allowed to interact with MWCNTs to obtain three different complexes, bearing one of the two compounds or both at the same time, respectively. The release of pemetrexed and quercetin was investigated at acidic and neutral pH, with better results at pH 7.4, as well as the antitumoral activity on human breast adenocarcinoma cells (MDA-MB-231) and pancreatic cells (PANC-1), demonstrating that there is a synergic effect of pemetrexed and quercetin in PANC-1 cells.[43] With an analogous supramolecular approach, also a complex with tamoxifen was prepared. In this case, however, the drug was entrapped on the nanotubes' surface by a subsequent wrapping of the MWCNTs with lentinan, a biocompatible polysaccharide, that confers water solubility to the complex. This complex was efficiently taken up into cells, inducing enhanced cytotoxicity in human breast adenocarcinoma MCF-7 cells, when combined with the hyperthermia obtained by photoirradiation of the tubes.[44]

Theoretical calculation of the interaction of 5-Fluorouracil (5-FU) with carbon nanotubes was performed finding a good stability.[45] Analogously, the interactions between gemcitabine and pyrrolidine functionalized SWCNTs were explored finding a favorable binding of the drug to the tubes also due to the presence of H bonds with the pyrrolidine nitrogen.[46]

PEGylated MWCNTs were loaded also with another anti-metabolite compound, gemcitabine, and hyaluronic acid, to test the *in vitro* drug release of the anticancer drug, with a good profile. The complex showed a lower hemolytic effect than the drug itself and *in vivo* experiments demonstrated a significative reduction of the tumor and an ameliorated survival with respect to the free drug treatment.[47] Gemcitabine was also combined with MWCNTs and lentinan, a polysaccharide derived from mushrooms, with the aim of associating the chemotherapeutic approach with photothermal treatment, due to the presence of the tubes. These can be irradiated in the NIR and release energy as heat, with local increase of temperature that can kill the cells. The ternary complex CNT-gemcitabine-lentinan was demonstrated to be more effective than the CNTs, the free drug or the CNT-drug construct. Moreover, combination with the local irradiation allows one to obtain a specific enhanced effect only into tumor cells.[48]

Another classical anticancer drug, paclitaxel, was linked to SWCNTs through the interposition of a pH sensitive linker, with the ability to release paclitaxel in the tumor environment. Selective targeting was possible due to the presence of a specific antibody, CD44. The *in vitro* and *in vivo* studies were conducted also in combination with salinomycin, that is known to eradicate cancer stem cells, conjugated to the nanotubes with a PEG chain as well. The results showed an increased efficacy in suppressing the tumor when both the constructs were simultaneously used (Figure 1.3).[49]

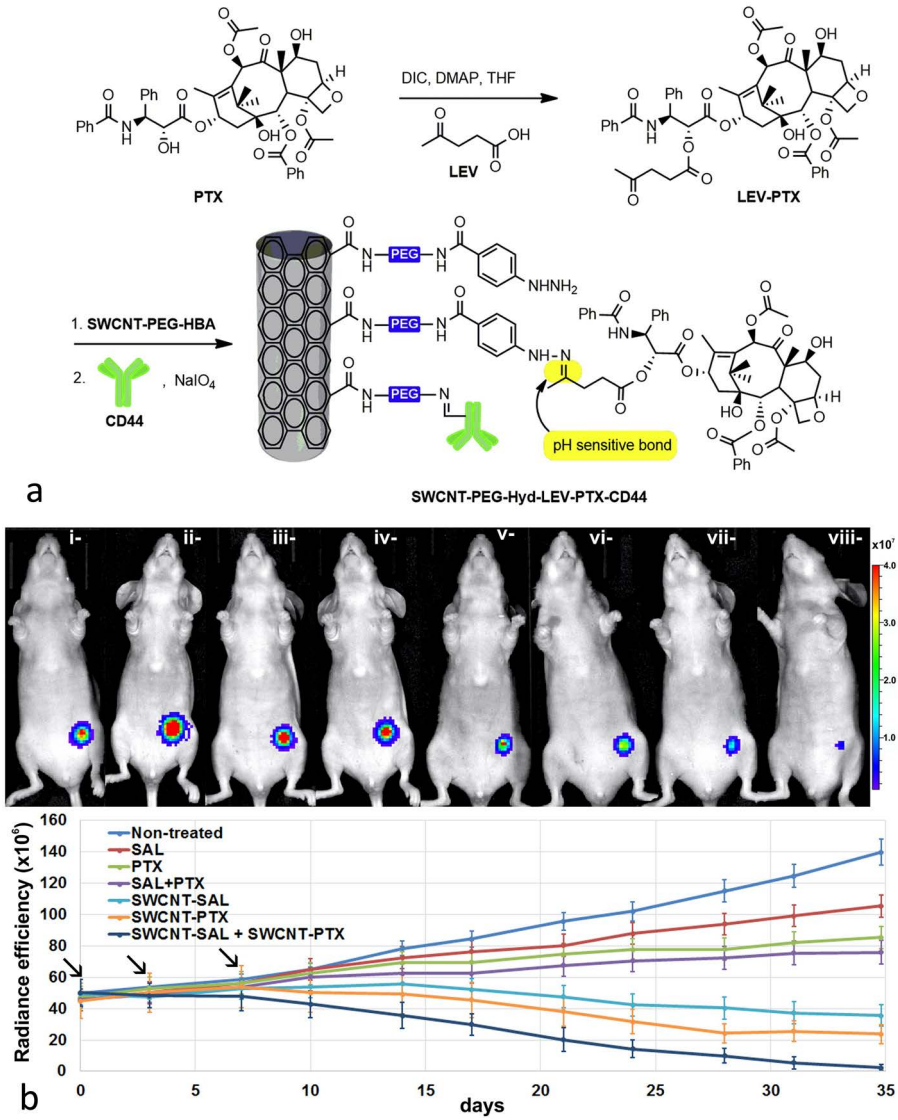

Figure 1.3 *Panel a*: Preparation of MWCNTs decorated with paclitaxel using a pH sensitive bond (hydrazone) and CD44 antibodies, as selective targeting agent. *Panel b, top*: bioluminescence intensity in *in vivo* experiment in MDA-MB-231 tumor-bearing mice. *Panel b, bottom*: radiance efficiency, corresponding to the tumor volume, at different times. The arrows indicate the injections of the materials. The evaluated mice groups are non-treated mice (Non-treated); treated with salinomycin (SAL); treated with paclitaxel (PTX); treated with a combination of salinomycin and paclitaxel (SAL + PTX); treated with salinomycin-conjugated SWCNTs (SWCNT-SAL); treated with paclitaxel-conjugated SWCNTs (SWCNT-PTX); treated with a combination of salinomycin-conjugated and paclitaxel-conjugated SWCNTs (SWCNT-SAL + SWCNT-PTX). Data expressed as mean ± SD, $n = 3$ per group. Adapted from ref. 49 with permission from Elsevier, Copyright 2016.

With the same aim of killing cancer stem cells, Berber *et al.* explored the synergistic effect of polybenzimidazole-decorated MWCNTs in combination with Pt nanoparticles. The latter release cytotoxic Pt ions in acidic conditions and the proposed scaffold was demonstrated to be very efficient as anticancer.[50]

Another antitumor platinum-based drug, oxaliplatin, was used to design a double functionalized MWCNTs-based drug delivery system, in which also the *trans*-activating transcriptional activator (TAT) was introduced, obtaining a copolymeric structure using polyethylenimine. The presence of the TAT was finalized to the enhancement of the permeability of brain endothelial cells, ameliorating the blood–brain barrier (BBB) penetration, and the construct was able to induce a higher production of ROS, with consequent high efficacy in killing tumor cells in *in vivo* glioma models.[51]

As mentioned, BBB is an important obstacle in delivering drugs to CNS, and the studies to overcome it are of the utmost interest. Recently a nanotube-based construct has been proposed, conjugating on the carbon surface ribavirin, as an antiviral compound, and an opportunely selected nanobody against nervous necrosis virus. The experiments on cells demonstrated that there is a much higher cellular uptake when the nanobody is present with respect to the control system without it and *in vivo* experiments on zebrafish highlighted that the antibody portion allowed concentration of the preparation into the brain (Figure 1.4), with a decrease of infected larvae mortality.[52]

In another study, three different bisphosphonates were covalently conjugated to oxidized MWCNTs to obtain an efficient vehiculation of the antitumor compounds, the use of which usually requires high dosages to reach an efficient effect, but these doses, at the same time, trigger toxic mechanisms. With the aim of finding a better delivery system, drug release from the decorated CNTs was studied at three pH (1.2, 5.5, 7.4) obtaining different kinetics profiles. However, the activities of the CNT-bisphosphonates conjugates on MCF7 cells were not conclusive, in fact the behaviors of the three derivatives were very different from each other (from an increase to a dramatic loss of activity).[53]

As mentioned, studies in the field of drug delivery have been very active[42] for many years. After exploring the combination of CNTs with the most classical anticancer drugs, a lot of work has been done recently on alternative or novel molecules with potentiality in tumor therapy.

Mangiferin, a polyphenolic C-glycoside, is a new anticancer drug with a poor bioavailability that limits its use. In order to improve this aspect, MWCNTs were used to conjugate this compound through the interposition of PEG chains. The proposed system demonstrated better bioavailability and at the same time an ameliorated cytotoxic effect *versus* U-87 glioma cells.[54]

As recently reviewed,[55] formononetin, a chromen-4-one richly present in legumes, clovers and herbs, shows a significant cytotoxicity potentially useful for the treatment of cancers because it induces apoptosis triggering the loss of the mitochondrial membrane potential. This molecule has been

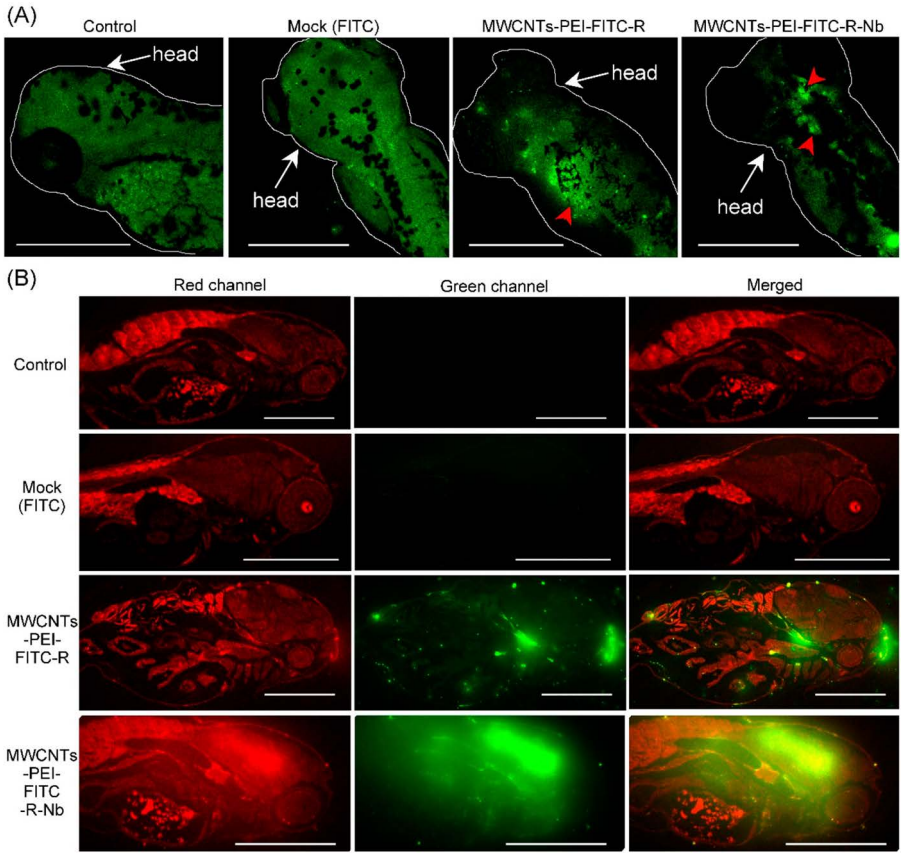

Figure 1.4 *Panel a*: Zebrafish confocal microscopy figures: control; after incubation with FITC as mock treatment; after incubation with ribavirin-MWCNTs complex; after incubation with ribavirin-Antibody-MWCNTs. *Panel b*: confocal microscopy figures of tissues samples from different groups (control; after incubation with FITC as mock treatment; after incubation with ribavirin-MWCNTs complex; after incubation with ribavirin-Antibody-MWCNTs). Red channel corresponds to indocarbocyanine dye (DiI) fluorescence while the green channel is the FITC fluorescence. Scale bars: 500 μm. Reproduced from ref. 52 with permission from American Chemical Society, Copyright 2019.

loaded, with a supramolecular approach, on oxidized CNTs. The formononetin release gave good results and its effect was evaluated on murine fibroblasts 3T3 and cervical carcinoma HeLa cells as healthy and tumor lines, respectively. While no strong effect was evident in 3T3 treated cells, a cell viability decrease to 40% was reported in the case of HeLa both in the case of the free drug and the formononetin-loaded CNTs. However, the CNT construct was more active in increasing ROS intracellular concentration and in decreasing the mitochondrial membrane potential.[56]

Combretastatin A4 is a compound able to destabilize the tubulin equilibrium, hampering its polymerization and inducing apoptosis but the drawbacks of its use are its aspecificity and low solubility in a biological environment. The conjugation with SWCNTs, through the interposition of glycol chains, allowed a good dispersibility of the construct, that releases 90% of the loaded drug in 50 h. The activity was then evaluated demonstrating much better performances than the free drug.[57]

Metformin is emerging as a new candidate for anticancer drugs, but one of the already clear limitations of its use is the high dosage necessary to exert the activity. With the aim to decrease the quantity of metformin to be administrated, the use of CNTs as a delivery system was explored, employing oxidized CNTs forming salts with the metformin itself. The oxidized CNTs showed a dose-dependent cytotoxicity on HT29R and MCF7. In the case of PC3 the vector showed no toxicity at all. Moreover, due to the presence of the CNTs, the vehiculation of metformin at a concentration of 2.4 μg mL^{-1} induced a reduction of cell viability comparable to that obtained with 64.5 μg mL^{-1} of the free drug, with a very significant increment of activity. Peculiarly, these constructs are scarcely internalized into cells, probably because of the presence of the guanidine unit, which acts as a possible inhibitor of micropinocytosis.[58]

Curcumin as model of an anticancer drug was used to explore the capability of microemulsions of MWCNTs in polymethacrylate to act as drug delivery systems. The authors reported a high content of entrapped curcumin as well as a sustained and prolonged release of the drug at pH 7.4.[59]

To the best of our knowledge, the first report on an oral preparation, specifically tablets, to administrate carbon nanotubes with a drug targeted to the colon was reported in 2019. Oral drug delivery systems targeted to the colon can use different approaches to obtain a selective responsive system, one of those is the enzymatic responsive release adopted in this case. Using wet granulation, the tablets were prepared using MWCNTs and pectin at different percentages. The idea is that peptidase in the colon environment triggers the degradation of pectin with the subsequent release of the entrapped drug. Celecoxib was used as chemoprevention therapy for colorectal cancer. The CNTs presence increased the friability of the tablets but the overall resistance of the preparation was quite good, and the swelling experiments demonstrated that no MWCNTs were released in the solution. The *in vitro* experiments in the presence of peptidases result in a proper degradation of the tablets and the release studies showed a low concentration of the drug in a solution at acidic pH with a substantial release at neutral pH, mimicking the colon.[60]

The delivery of RNA, DNA and their derivatives is also a potential application of MWCNTs.[61] For example, MWCNTs were functionalized with small interfering RNA (siRNA), which is a promising gene silencing compound for directed immunogenetic cancer therapy, in order to stabilize siRNA and deliver it to the targeted cell more efficiently. As *in vivo* delivery of siRNAs to the target cell is limited by the scarce stability, low uptake efficiency and

pharmacokinetics of siRNA, this approach could facilitate the release of the drug or gene into the cell and thus the loaded compound reaches the targeted tissue, escaping lysosomal degradation, enzymatic cleavage and interference of proteins. The result is a greater biostability of nucleic acids with an increase in the ability to reach the target by DNA compared to free DNA. Moreover, Kateb *et al.* suggested that MWCNTs could be used as non-toxic and biodegradable nanocarriers for targeted therapy in brain cancer, a challenging tissue to be reached.[62]

1.3 Nanodiamonds

NDs were first produced by a research group from the USSR in July 1963 through the detonation of a 40/60 blend of 2-methyl-1,3,5-trinitrobenzene (TNT) and 1,3,5-trinitroperhydro-1,3,5-triazine (RDX).[63] The first public disclosure of NDs took place with the discovery of 50 Å sized diamonds in meteorites in 1987,[64] and, one year later, the detonation-based production of NDs was reported.[65] Despite the fact that NDs can be produced by different approaches, the most common method is still detonation, being one of the more suitable techniques for large-scale production. In this case, the so-called detonation nanodiamonds present a small primary particle size and a feasible surface functionalization. Another important method of production is milling of diamonds obtained with the high-pressure high temperature process (HPHT),[66] in which presses are used to obtain shock compression of graphite in the presence of metal catalysts. Depending on the chosen catalyst, pressure and temperature vary, usually ranging between 5 and 7 GPa and from 1300 to 1800 °C, respectively. With this process it is possible to obtain particles of irregular shape with a diameter of 10–20 nm, and with a high nitrogen content (100–300 ppm), which confers a very important characteristic to this type of ND. The typical diameter of NDs is in the range of 2 to 100 nm and they are the most stable carbon derivatives with such small dimensions,[67] based on which it is possible to classify NDs into three main groups: nanocrystalline diamond particulates (10–100 nm), ultra-nanocrystalline diamond particulates (0–10 nm, a range that includes detonation nanodiamonds), and diamondoids (~1 to ~2 nm).[68]

NDs are characterized by a core of sp^3 carbon atoms and the possible surface groups are ketone, aldehyde, carboxylic acid, ester, anhydride, cyclic ketone, lactone, amine, epoxide, *etc.*;[69] but in some cases the core can be coated with a graphitic shell composed of sp^2 carbon whose amount is strongly dependent on synthetic methods and purification procedure.[69]

NDs present stability and chemical inertia of the core, high hardness, rigidity, high surface area (20% of the carbon atoms are at the surface),[70] thermal resistivity and conductivity,[71] optical transparency in a wide range of the electromagnetic spectrum, and tendency to aggregate. The optical properties are of particular interest, in particular fluorescence, which was observed especially for HPHT diamonds.[72] This property is due to the presence of

impurities and defects in the lattice, such as vacant nitrogen centers. The centers are able to absorb strongly around 500 nm and to emit at 700 nm. Other advantages are the continuous emission and the photostability.[69,73] Furthermore, since the emission derives from defects inside the reticle, it is not inhibited by surface functionalizations, thus providing an additional advantage in the chemical modifications of this material.

Since cellular uptake can occur through pinocytosis or clathrin-mediated endocytosis, the mode of internalization of the nanoparticles in the cells does not cause any damage to the integrity of the membranes (Figure 1.5).[74] Several factors can play a role in the uptake processes such as the cell type,[75] incubation time, surface characteristics, size, shape and aggregation of the nanodiamonds.[76]

NDs seem to be excellent candidates for biomedical applications, generally showing less cytotoxicity than other nanocarbonaceous materials, such as graphite, graphene and carbon nanotubes.[77] They appear to be well tolerated and show no serious toxic effects *in vivo*.[78] The biocompatibility of NDs has been studied by evaluating both cell death, morphological changes, changes in metabolic activity, alterations in the proliferation and expression of genes and proteins and oxidative stress.[79] The effects of both short-term and long-term nanodiamond treatment have been assessed *in vitro* on different cell cultures, such as macrophages, and several cancer and healthy

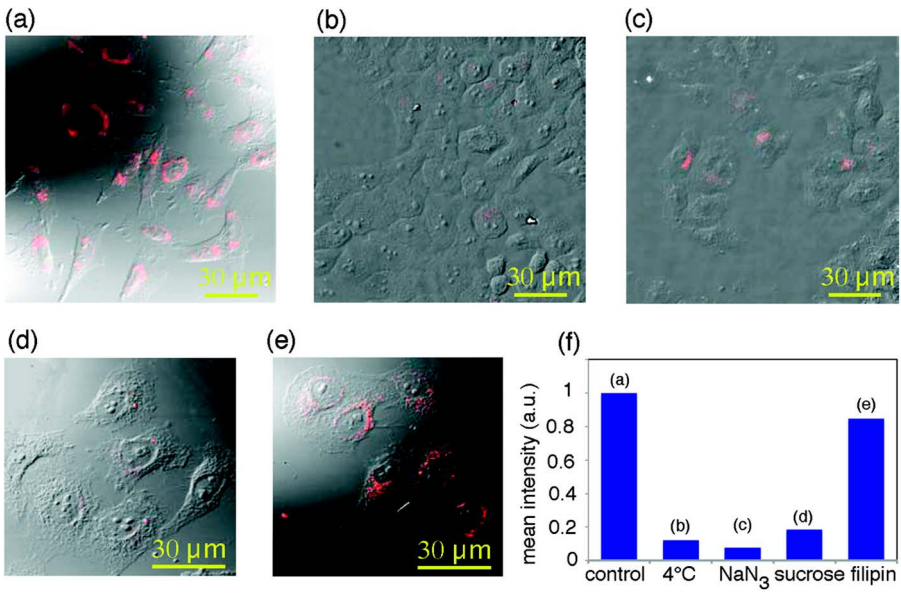

Figure 1.5 Differential interference contrast (DIC) images of NDs treated HeLa cells at (a) 37 °C; (b) 4 °C; (c) 37 °C in the presence of NaN_3; (d) 37 °C in the presence of sucrose; (e) 37 °C in the presence of filipin as potential inhibitors of the NDs' cellular uptake. (f) Histogram of mean photoluminescence intensity per cell. Reproduced from ref. 74 with permission, from American Chemical Society, Copyright 2009.

cells. These studies pointed out that NDs are highly biocompatible and highly absorbed inside the cells. Furthermore, these materials do not cause any morphological and metabolic alteration in the cells, they do not affect cell vitality and do not stimulate changes in inflammatory marker levels.[79] *In vivo* tests allowed one to understand that NDs tend to accumulate in lungs, liver, spleen, kidneys and bladder without however altering organ functions. Slight morphological changes in the liver can be observed, but without modification of metabolic activity so as to be considered reversible damage, while some evidence of oxidative stress was found at the lung level.[80] The administration was carried out through different pathways (sub-cutaneous, intravenous, inhalation and oral) and a good tolerability in organisms emerged with no changes in the systemic inflammatory response.[80*b*]

The evaluation of the possible pro-coagulant effect is important for a possible intravenous administration and the NDs do not seem to alter the prothrombin time, the fibrinogen levels or the platelet count.[81] *In vivo* studies on primates, treated with 15 mg Kg^{-1} or 25 mg Kg^{-1} of NDs, were performed for six months and the results showed no metabolic alterations, cytotoxicity, inflammatory response or alteration in organ function. Only few alterations of cardiomyocytes, capillaries of the hepatic parenchyma (less pronounced alterations in the group treated with lower dosages) and pulmonary alveoli were detected (Figure 1.6).[81]

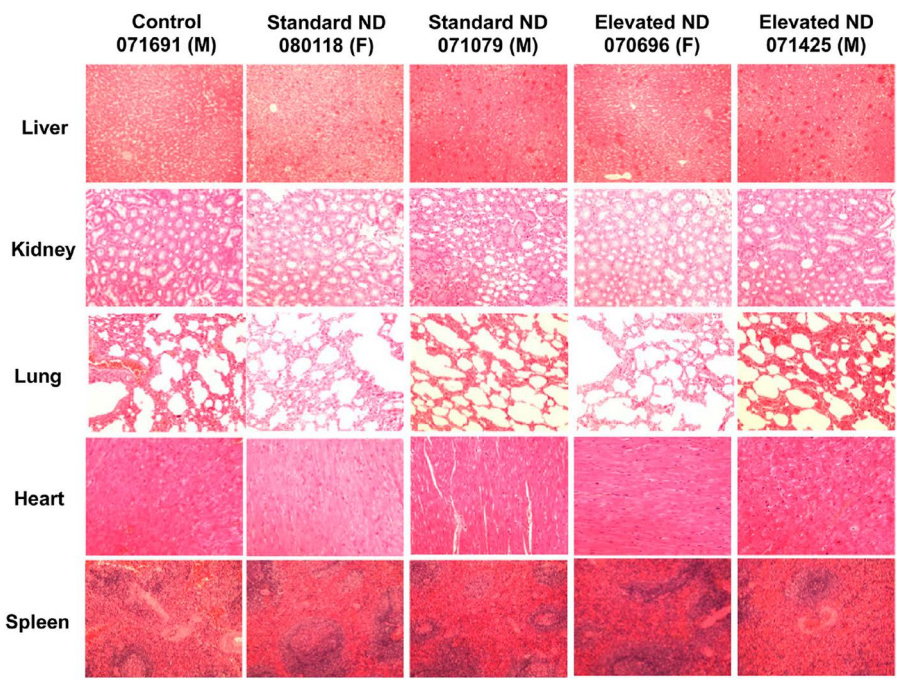

Figure 1.6 Tissue samples from monkeys treated with different kinds of NDs at 15 or 25 mg kg^{-1}, six months after administration. Reproduced from ref. 81 with permission from American Chemical Society, Copyright 2016.

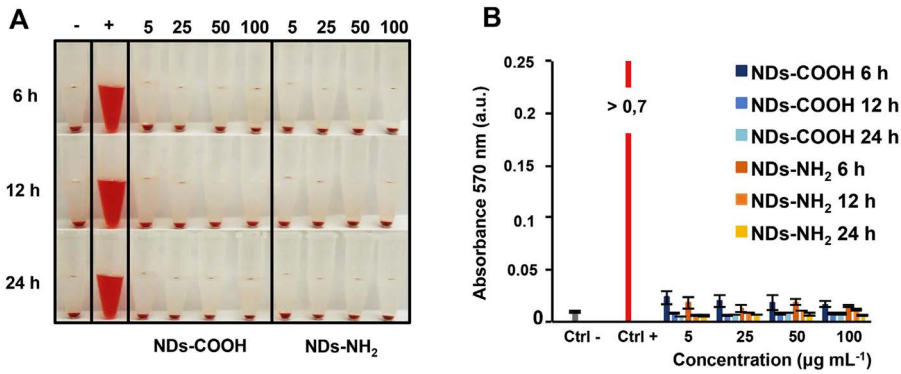

Figure 1.7 *Panel (A)*. Hemolysis tests at different times and different concentrations of variously functionalized NDs (namely presenting carboxylic or amine groups on the surface). *Panel (B)*. Histogram of the absorbance related to the release of hemoglobin from red blood cells after the ND treatment. Reproduced from ref. 83 with permission from Elsevier, Copyright 2020.

Tsai and collaborators demonstrated the absence of an immune response when NDs were administered by intravenous injection in mice, due to the non-activation of the proinflammatory cytokine TNF–α[82] and recently the absence of hemolytic effect was confirmed (Figure 1.7).[83] In the latter work, the effect of oxidized and amine functionalized nanodiamonds was explored, finding a different behavior of the two materials on the peripheral blood mononuclear cells, with an impact stronger for the one oxidized. Other studies pointed out that oxidized NDs can cause malformations in embryonic cells with a correlation with the concentration and with the presence of carboxylic groups.[78]

1.3.1 NDs as Drug Delivery Systems

The application of NDs in drug delivery is one of the most interesting and studied biological applications of these nanoparticles. In fact, they are excellent candidates for drug delivery due to their biocompatibility, dimensional homogeneity and chemical inertia of the core together with a wide variety of functional groups on the surface and large surface area, which allows the adsorption of a considerable amount of molecules. To date, most of the efforts have been devoted to the functionalization of NDs with anticancer drugs using a non-covalent method, in order to leave the drug molecules unaltered.[77] Unfortunately, this approach does not allow one to control the drug release in a proper way. As in the case of CNTs, one of the most studied drugs are anthracyclines.[84] Both in the presence of covalent and non-covalent bonds, these derivatives show an increase in half-life, and decrease in side effects and in drug efflux when delivered using NDs. The chemoresistance

inhibition seems to be related to the cell efflux pumps (ABC, ATP-Binding Cassette) being overcome, with a consequent accumulation of the molecules into the cells.[77] For example, treatment with doxorubicin functionalized nanodiamonds ensured longer retention in 4T1 tumors than the free drug and markedly reduced tumor sizes.[84a] Analogous behavior has been reported in canine kidney cells MDCK, liver cancer LT2-MYC and Huh7 cells and breast cancer cells MDA-MB-231.[85] Wang *et al.* in fact studied the mechanism of action of the NDs-epirubicin complexes, observing that epirubicin is released at acid/neutral pH and, therefore, the release at the blood level is minimal while it is maximized for tumor cells, with a consequent decrease in myelosuppression. This mechanism seems to be related to the internalization into cells by macropinocytosis, considering that macropinosomes merge with lysosomes presenting an acid pH. Once again it has been demonstrated that the retention of the drug into hepatoblastoma LT2-MYC is prolonged compared to the free drug. The efficacy of NDs-Daunorubicin complexes on human erythroleukemia cell line (K562 cells) was also studied, evidencing a constant release of the drug into the cells at pH 4 and the prevention of the drug outflow, with an increase of the drug presence into the cytoplasm.[86]

1.3.2 Other Applications of NDs

The so-called nitrogen vacancies (NVs) are defects of the NDs core created within the NDs grid by high energy irradiation (with electrons, protons or helium ions) that induces interruptions in the lattice, while the annealing process (600–800 °C) allows these defects to be filled with nitrogen atoms.[87] These materials emit a red luminescence with a wavelength of about 700 nm if radiated at 560 nm, thus allowing one to trace cellular processes by fluorescence microscopy. NDs containing NV could replace commonly used bioimaging agents due to their longer emission capacity, not being photobleached.[88] HPHT NDs are the most studied as bioimaging agents due to the higher presence of nitrogen in the lattice (300 ppm) in comparison to other kinds of NDs. However, this synthetic method does not produce particles with sizes below 20 nm and this could be an obstacle for biomedical applications. Anyhow, Fu *et al.* used these materials to treat HeLa cells and they observed the translocation of NDs into the cells, with the presence of both aggregates and single particles in the cytoplasm. Since, as already mentioned, the NDs photoluminescence is not influenced by surface modifications, their functionalization is possible without hampering this characteristic as demonstrated with the covalent functionalization of NDs using poly-lysine, which allowed the complexation with DNA by means of electrostatic interactions.[89] This characteristic is very peculiar for these materials and the absence of photobleaching allows the use of NDs in theranostics.

Among the heterogeneous studies of NDs, in one of the early-stage reports, it was demonstrated that the stabilization of protein antigens on the surface of the NDs led to a prolonged and intense immune response, offering the possibility to use NDs in disease prevention.[90]

The incorporation of NDs into polymers, through covalent or non-covalent bonding, can also find application in the biomedical field; for example, NDs functionalized with octadecylamine dispersed in L-polylactic acid allowed an increase in resistance, hardness and Young's modulus of the final material, applicable as a biocompatible and biodegradable/resorbable implantable device in the case of bone damage.[91] NDs are also promising materials in tissue engineering and regenerative medicine. It was shown that they can be an effective neuronal growth platform similar to protein-coated materials when assembled as monolayers.[92]

Wehling *et al.* reported the potential antibacterial activity of NDs and, in particular, of the oxidized ones, able to decrease the viability of *E. coli*, a Gram-negative bacterium, at a concentration of 5 mg L^{-1}. NDs presenting a less oxygenated surface did not exert the same effect, suggesting that the mechanism of action is related to the reactivity of these oxygen-containing groups. However, there is a strong influence of the presence of proteins in the environment: the higher the content, the lesser the antibacterial effect (Figure 1.8).[93] This characteristic can be exploited with the use of NDs as excipients in different pharmaceutical formulations. In fact, thanks to their antibacterial properties, they could be used to avoid bacterial contamination.[94] Moreover, thanks to their ability to partially shield UV rays they could be used for the preparation of sun creams and as protective agents with photosensitive drugs[95] and, lastly, they also have a certain antioxidant activity that could be exploited biologically.[80b]

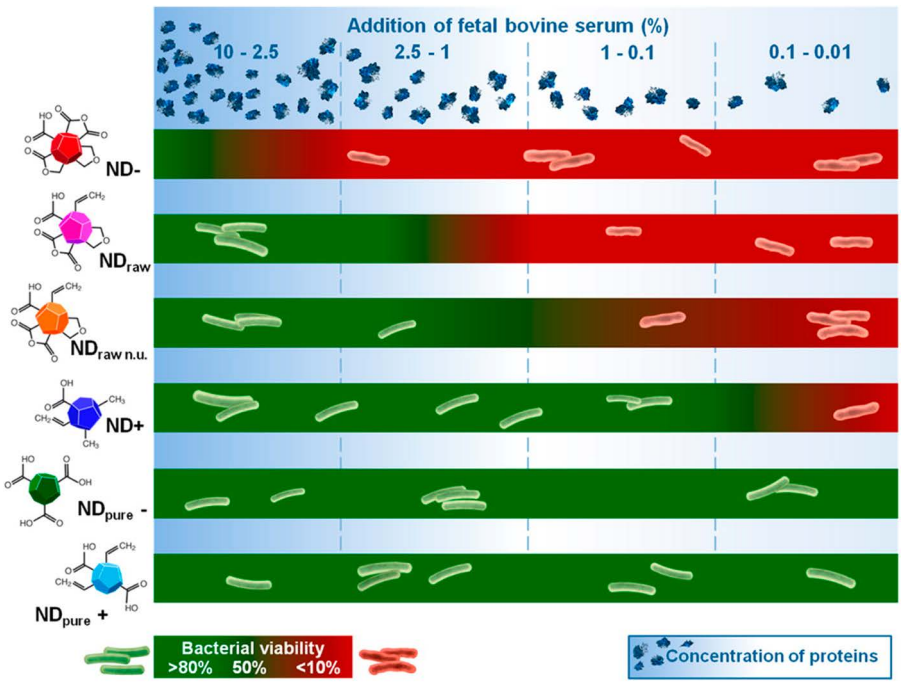

Figure 1.8 Activity of different NDs *vs.* bacteria in function of the protein concentration (ranging from 2.5% to 10%) in the used media. Reproduced from ref. 93 with permission from American Chemical Society, Copyright 2014.

1.4 Graphene and Carbon Quantum Dots

1.4.1 GQDs

Graphene quantum dots (GQDs) basically combine the structure of graphene with the quantum confinement and edge effects of CDs and possess unique properties, which are important for the applications in medicine, electronic, photoluminescence, electrochemical and electrochemiluminescence.[96]

GQDs mostly consist of 1–3 layers of graphene flakes with a diameter of less than 20 nm.[97] The surface groups of GQDs may vary due to the synthetic methodology and the photoluminescence peak may shift depending on the surface functionalization.[98]

Due to the edge effects,[99] the quantum confinement[100] and the unique bulk properties of graphene and the possible functionalization,[101] GQDs have very advantageous properties for a wide range of applications. The synthesis of GQDs may already add different functional groups on the graphene-like surface depending on the chosen preparation. GQDs can be functionalized to adjust biocompatibility, photoluminescence, electronic properties, or optical properties. The intended modifications can be performed with GDQ production using pre-treated starting materials or proper conditions, or as post-production modifications.

The synthesis of nitrogen-doped graphene quantum dots was performed by cutting nitrogen-doped graphene with a hydrothermal method.[102] The so-obtained N-doped GQDs have a N/C atomic ratio of *ca.* 5.6% and diameter of 1–7 nm and show strong blue photoluminescence and upconversion photoluminescence properties. Analogously, fluorinated GQDs, with a F/C atomic ratio of *ca.* 23.7% and diameter of 1–7 nm, can be produced from fluorinated graphene as a modified starting material by using a hydrothermal cutting method.[103] It was shown that fluorination changes the optoelectronic properties of GQDs, upconverts photoluminescence and alters electronic properties similar to the effect of GQD nitrogen doping. The optical properties of solvothermally synthesized GQDs are tunable by the degree of surface oxidation, which brings fine solubility, high stability and upconversion photoluminescence,[98b] and photoluminescence quantum yields can increase from 4.1% to 12.2% with the increase of surface oxidation.

With a simple electrochemical approach, it is possible to produce luminescent and electrocatalytically active nitrogen-doped GQDs with oxygen-rich functional groups from reduced graphene oxide by using tetrabutyl ammonium perchlorate (TBAP) in acetonitrile as electrolyte to introduce N atoms on the surface of GQDs.[98a] The so-produced GQDs present a N/C atomic ratio of *ca.* 4.3%, have blue luminescence and possess electrocatalytic activity.

After the production of GQDs, the usual functionalization is performed through the generation of an amide bond *via* covalent conjugation of amines to the carboxyl groups of graphene quantum dots.[104] Wolk *et al.* activated the carboxylic function with oxalyl chloride treatment, followed by the addition of dodecyl amine. These modified GQDs showed excellent solubility in various organic solvents. Li *et al.* synthesized folic acid functionalized graphene quantum dots loaded with IR780, a lipophilic NIR fluorescent cyanine dye.[105] The preparation took place by mixing folic acid, EDC, NHS

and GQDs in aqueous solution saturated with $NaHCO_3$. Thus, folic acid was covalently attached to the surface of the GQD. The next step was the mixture with IR780 at different concentrations and the latter was linked *via* strong π–π stacking interactions. The obtained complex presented improved photostability, enhanced tumor targeting ability and very high photothermal conversion efficiency (87.9%) (Figure 1.9).

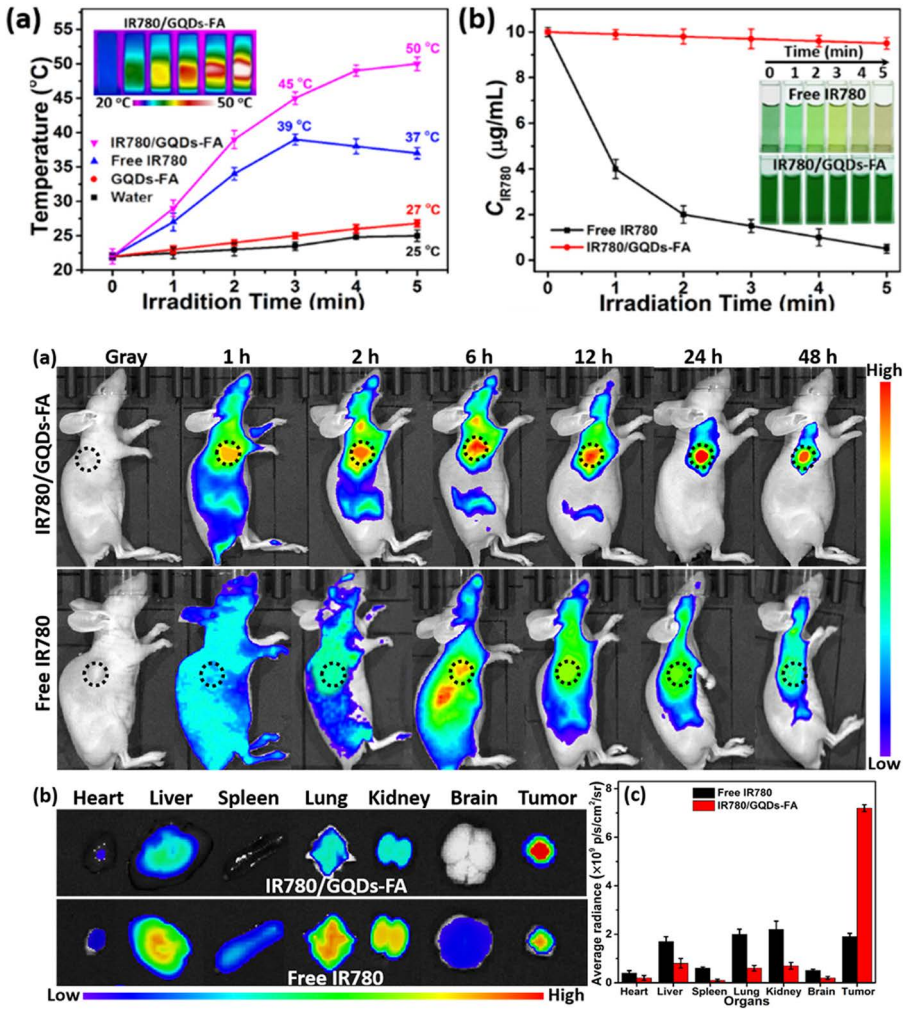

Figure 1.9 *Top: panel (a)*. Photothermal profiles of water, free IR780, GQDs-FA and IR780/GQDs-FA laser irradiated at 808 nm at 1 W cm^{-2}. *Panel (b)*. Effect of the irradiation time of IR780 and IR780/GQDs-FA on IR780 concentration in aqueous solution. *Bottom: panel (a)* NIR fluorescence intensities of free IR780 and IR780/GQDs-FA in the tumor region. *Panel (b)*. *Ex vivo* evaluation of the dissected organs at 24 h post injection. *Panel (c)*. Fluorescence intensity of the excised organs after treatment with IR780 and IR780/GQDs-FA. Reproduced from ref. 105 with permission from American Chemical Society, Copyright 2017.

1.4.1.1 GQD Applications

GQDs have potential applications in biomedical, optoelectronic, and energy-related fields mainly due to properties such as water solubility and luminescence, which make them excellent candidates for bioimaging and drug delivery.

Kuo *et al.* synthesized GQDs with sizes of approximately 7.1 nm to use them in two-photon photodynamic therapy and simultaneous three-dimensional two-photon bioimaging, especially on multidrug-resistant bacteria. The GQDs were demonstrated to be photosensitizing, with high two-photon absorption in the near IR region, a large absolute cross section of two-photon excitation, strong two-photon luminescence, and impressive two-photon stability. They were coated with two different antibodies, Ab_{LPS} and $Ab_{protein\ A}$, in order to enhance the specificity and efficiency against Gram-negative *E. coli* and Gram-positive MRSA, respectively. The relative maximum at 800 nm was chosen to obtain maximum bactericidal activity. It was shown that GQDs have highly effective photodynamic activity both against Gram-positive and Gram-negative bacteria, due to their capacity to generate reactive oxygen species, which occur with two-photon excitation with ultra-low energy in short photoexcitation time (Figure 1.10).[106]

With the aim of producing novel agents for cancer cell imaging and optical detection of Hg^{2+}, Li *et al.* were able to synthesized GQDs with a size range of 2–8 nm from the pyrolysis of maleic acid and folic acid.[107] The resulting folic acid functionalized GQDs display a strong and tunable fluorescence emission under visible light excitation. The authors could tune the fluorescence properties by changing the folic acid ratio in the pyrolysis process. Due

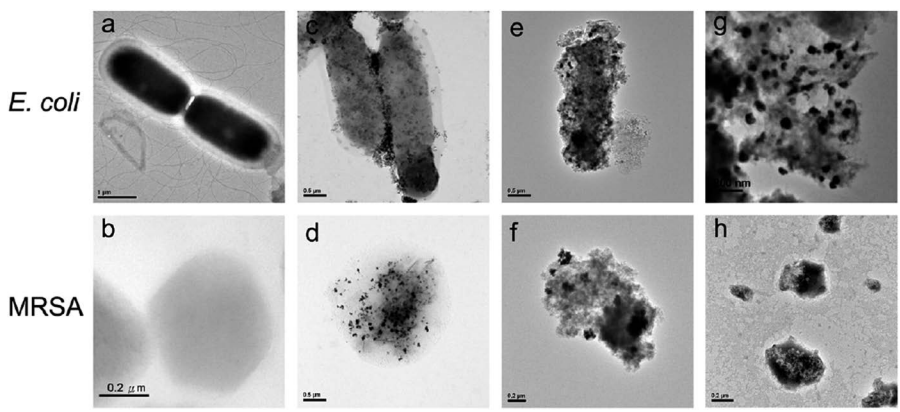

Figure 1.10 TEM images showing: no treated (a) *E. coli* and (b) MRSA; the effect of the treatment with GQD-Ab_{LPS} and GQDs-$Ab_{protein\ A}$ on *E. coli* and MRSA after (c, d) 3 h and (e, f) 5 days of incubation, respectively. (g) Photoexcited GQDs-Ab_{LPS} treated *E. coli* and (h) GQDs-$Ab_{protein\ A}$ treated MRSA, respectively, after 3 h of incubation (2.64 mW of TPE for 15 s, excitation at 800 nm, delivered dose OD_{600} ~ 0.05 of bacteria and 0.5 μg mL^{-1} GQDs). Adapted from ref. 106 with permission from American Chemical Society, Copyright 2016.

to the high number of folic acid units, their good lipid-solubility and their red fluorescence emission, these GQDs as turn-on fluorescent probes are more suitable for cancer cell imaging compared with the previously reported graphene quantum dots. The resolution of cell imaging was considerably improved since the red light has better biological tissue penetration and less back spectrum interference compared with blue light. Folic acid functionalized GQDs could be easily internalized by the human cervical epithelioid carcinoma cells (HepG2), with an over-expressing folate receptor on the cell membranes. The same study showed that the graphene quantum dots can react with Hg^{2+} and therefore a sensitive fluorescence quenching occurs, providing sensitivity and selectivity among all tested metal and nonmetallic ions (Figure 1.11).

1.4.2 Carbon Dots

Carbon dots (known as carbon nanodots, C-dots, CDs), one of the newest members of fluorescent carbon nanomaterials,[108] were first reported in 2006 by Sun *et al.*[109] Their shape is described as quasi-spherical, with a diameter below 10 nm. Generally, they have a sp^2-conjugated core and present several oxygen-containing species such as carboxyl, hydroxyl and aldehyde groups.[110] In some rare cases, they can contain a diamond-like structure with sp^3 carbons.[111] They possess excellent water-solubility and the presence of carboxylic functions enable their functionalization with a wide range of organic, polymeric, inorganic, or biological species. The production of carbon dots is achieved by a large variety of simple, fast and cheap synthetic routes. Their photoluminescence, high photostability, and low toxicity make them potential candidates to replace toxic metal-based quantum dots, which pose health concerns and well known environmental and biological hazards.

The structural and physicochemical properties of CDs may remarkably depend on the synthetic routes, which may add various defects, heteroatoms

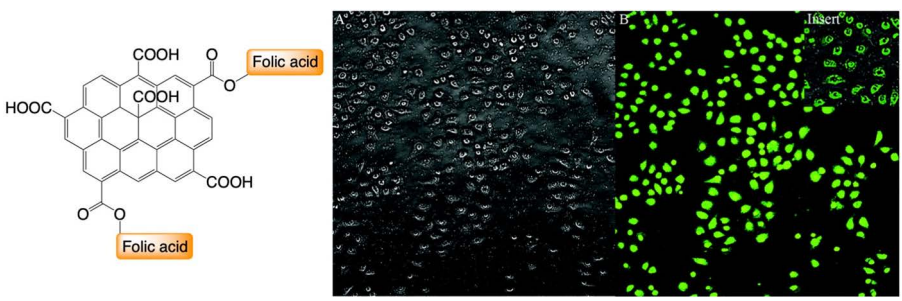

Figure 1.11 *Left*: Schematic structure of FA-GQDs. *Right*: Bright field (A) and confocal fluorescence microscopy image of HepG2 cells treated with FA-GQDs (B) and GQDs (insert) at 37 °C for 10 min. Reproduced from ref. 107 with permission from Royal Society of Chemistry.

and functional groups to their structure. Their surface groups contribute to their optical properties and make them water dispersible.[112] Depending on production and purification methodologies, the chemical composition of carbon dots may vary widely. It has been reported that the carbon dots from purified candle soot contain 36.8% carbon, 5.9% hydrogen, 9.6% nitrogen and 44.7% oxygen, and that of raw candle soot contains 91.7% carbon, 1.8% hydrogen, 1.8% nitrogen and 4.4% oxygen.[113] In the same study, solid-state ^{13}C NMR measurements showed that carbon dots do not have saturated sp^3 carbon atoms and they contain three types of carbon signals: external C=C bonds, internal C=C bonds and C=O bonds.

As GQDs, carbon nanodots also possess tunable photoluminescence properties arising from quantum confinement effects. Their photoluminescence quantum yield is usually lower than GQDs due to the emissive traps on the surface. Therefore, a surface passivation layer is necessary to improve their brightness.

Synthesis and functionalization of carbon dots cannot be separated since most of the surface decorations occur during their production depending on the starting material or solvent. The synthesis of carbon dots can be generally classified into "top-down" and "bottom-up" methods. The process includes cleaving or breaking down of carbonaceous materials *via* chemical, electrochemical, or physical approaches. A variety of small organic molecules can be pyrolyzed or carbonized to obtain carbon nanodots. Top-down approaches are focused on breaking off the bulk carbon material through laser ablation, arc-discharge and electrochemical soaking. In 2006, Sun *et al.* prepared CDs of around 5 nm in diameter *via* laser ablation of a carbon target in the presence of water vapor with argon as the carrier gas.[109] The carbon target was prepared by hot-pressing a mixture of graphite powder and cement, and followed by stepwise baking, curing and annealing in argon flow. The as-produced carbon dots and acid-treated sample have no detectable photoluminescence. However, after surface passivation by attaching PEG_{1500N} to the acid-treated carbon structures, bright luminescence emissions were observed. After excitation at 400 nm, the photoluminescence quantum yields ranged from 4% to 10%, supposedly depending on the degree of surface passivation.[109] Hu *et al.* synthesized carbon dots in a one-step procedure, by laser irradiation of a suspension of graphite powders dispersed in organic solvents, achieving at the same time the surface modifications with PEG_{200N}. The luminescence was attributed to carboxylate ligands on the surface of carbon dots and the measured quantum yields of the three samples ranged from 3% to 8%. From HR-TEM images it seemed that carbon dots mostly contain defects and the lattice spacing was between 0.20 and 0.23 nm, while the size distribution was 1–8 nm.[111] As already mentioned, in 2007 Liu *et al.* developed a new methodology to synthesize carbon dots from candle soot[113] and the same methodology was studied by Bottini *et al.*[114] The resulting products were purified using polyacrylamide gel electrophoresis (PAGE) to remove relatively big particles, attributed to an incomplete combustion. Oxidative acid treatment was performed to break down inherent interactions and to obtain

well-dispersed carbon dots, which become negatively charged and hydrophilic, due to the introduction of –OH and –COOH groups on their surface. Their diameter was approximately 1 nm and their quantum yields were quite low (<1%), in comparison with those produced through laser ablation.

Sahu *et al.* prepared highly photoluminescent carbon dots in one step from hydrothermal treatment of a renewable bioprecursor, orange juice *(Citrus nobilis deliciosa)*. The mechanism for the formation of carbon dots is described as the hydrothermal carbonization of the main constituents of orange juice such as sucrose, glucose, fructose, citric acid and ascorbic acid, at relatively low temperature (120 °C). XPS and FTIR data indicate that the carbon dots are functionalized with hydroxyl, epoxy, carbonyl and carboxylic acid groups and their calculated photoluminescence quantum yield is 26%.[110b] In another study, carbon dots with an average diameter 3.4 ± 0.8 nm were synthesized by Hsu *et al.* from used green tea through grinding, calcination and centrifugation. The obtained carbon dots were highly water-soluble, biocompatible, with photoluminescence at 420 nm when excited at 345 nm (quantum yield 4.3%).[115] In the last few years, a more engineered approach has been proposed, using amino acids and amines as sources for the production of CDs by means of microwaves.[116]

The photoluminescence and optical properties of carbon dots are an intriguing research topic from many aspects. The storage and transport of electrons impacted by light is another attractive research field for carbon dots. Since their discovery, their potential applications in bioimaging, sensing, catalysis, optoelectronics and energy conversion have widely been studied. Cao *et al.*[117] synthesized carbon dots following the procedure reported by Sun *et al.*[109] and passivated their surface with poly-(propionylethylenimine-*co*-ethylenimine) (PPEI-EI, with EI fraction ~20%). The prepared carbon dots were investigated in MCF-7 cells as a bioimaging agent with two-photon fluorescence microscopy by exciting at 800 nm. It was reported that after 2 h of incubation at 37 °C they emitted strong photoluminescence both on the cell membrane and in the cytoplasm and their internalization was found to be temperature dependent as at 4 °C no cellular uptake was observed.

1.4.2.1 CD Applications

Carbon dots are frequently studied in biological areas because of their low toxicity, good biocompatibility and water solubility. These properties make them good candidates as bioimaging agents and drug nanocarriers.[110b,118] Their *in vitro* cytotoxicity was evaluated by MTT assay on murine fibroblasts L929 and no significant toxicity was reported, indeed they showed to be tolerable at high dose (200 mg mL^{-1}).[110b] Yang *et al.* evaluated the *in vitro* and *in vivo* toxicity on MCF-7 and HT-29 cell lines of PEG-functionalized carbon dots. They obtained comparable data for PEG-CDs and oligomeric PEG molecules, thus suggesting that these fluorescent dots do not show any toxic effect, like the biocompatible oligomer. Moreover, they do not cause any significant toxic effects on mice at dosages beyond those commonly used for *in vivo* optical imaging.[119] Hsu *et al.* studied the cells growth inhibition of MCF-7,

MDA-MB-231, and HeLa cells, and their bioimaging with carbon dots prepared from calcination of green tea. These materials are effective cell growth inhibitors for MCF-7, MDA-MB-231 and HeLa cells, and cause low toxicity to normal cells such as MCF-10A and LLC-PK1 lines.[115]

Salinas-Castillo *et al.* developed a fluorescent carbon dot nanosensor for selective and sensitive detection of Cu^{2+}.[120] The particles had an average size of 12 nm and they were synthesized with a one-step method by pyrolysis of citric acid in the presence of polyethylenimine (PEI) in a microwave oven. The photoluminescence quantum yield was calculated as 30%. The selectivity of the carbon dots for Cu^{2+} was studied through the variation of CD fluorescence intensities in the presence of different metal cations. It was observed that fluorescent carbon dots were highly selective for Cu^{2+} detection, and Fe^{3+} ions caused a quenching effect only when excited at 850 nm, due to the shifting of the maximum emission.

Like the other carbon nanostructures, carbon dots have great potential for bioapplications, especially in drug delivery as they can be tailored to target different tissues, both by using different preparation methods and different surface decorations.

Zhou *et al.* combined and compared three different materials, the so-called black CDs, the gel-like and the yellow carbon dots (respectively, B-CDs, G-CDs and Y-CDs), studying the differences in doxorubicin loading and obtaining a huge increase (>50%) in loading using a combination of CDs. Moreover, these new materials demonstrated their ability to cross the BBB and their affinity for bones in Zebrafish, as in the *in vivo* model.[121] CDs showed efficient uptake in microglial cells as demonstrated by fluorescence measurements of the intrinsic luminescence of QDs. The most interesting findings reported by these authors is the capability of the construct to reduce the secretion of nitric oxide induced by lipopolysaccharide treatment,[122] which can be of utmost interest in neuroprotective approaches.

Another approach to obtain selective affinity for specific tissues, in particular tumor tissues, implied the presence of carboxylic and amino groups on the CDs surface, that allowed the interactions with amino acid transporter 1, with a consequent preferential uptake in human tumor xenografts in mice and in glioma *in vivo* models.[123]

The preparation of the dots using tryptophan as a carbon source has been reported. The choice of the starting material was related to its capability to cross the BBB *via* transporter-mediated endocytosis. In principle, the eventual presence of tryptophan on the CDs' surface after the preparation could allow this material to overcome the BBB, as demonstrated by the presence of dots in the central nervous system in experiments on zebrafish, thus confirming the efficacy of these structures to cross the barrier.[124] A more traditional approach for the selective delivering of molecules into cells by exploiting the overexpression of folate receptors followed decorating CDs with folic acid.[125] In order to obtain structures endowed with selective mitochondrial targeting, some authors proposed triphenylphosphine derivatives in a quite complex construct presenting TPP-D-α-tocopheryl polyethylene glycol succinate derivative linked to the CDs, to form micelle-like structures.[126]

Moreover, the intracellular selectivity was obtained by exploiting a specific decoration of the CDs' surface, as recently reviewed.[127] For example, the Golgi apparatus can be selectively targeted by decorating the CDs' surface with cysteine, thus obtaining the *in situ* image of the apparatus.[128] The introduction of the ricin A-chain also allowed delivery of the latter into the cells escaping the lysosome degradation, due to the presence of CDs (Figure 1.12).[129] Experiments on carcinoma HEp-2 cells enabled the following of different steps of internalizations by colocalizations first with lysosomes, then with Golgi and later on with the endoplasmic reticulum (ER) (Figure 1.12).

A plethora of CDs were prepared starting from different sources, from milk[130] to a combination of citric acid and PEI,[131] but the proper preparation of CDs using chitosan, ethylenediamine and mercaptosuccinic acid leads to materials able to target mitochondria without any further specific functionalization and to be used as markers for these organelles considering their photostability.[132] Analogously, CDs were prepared by hydrothermal treatment of D-glucosamine and *p*-styrenesulfonate to mimic the sulfonate glucosaminoglycane. The so-obtained nanoparticles demonstrated uptake and diffusion into the cellular cytoplasm of rat bone mesenchymal stem cells and promotion of cellular osteogenic and chondrogenic differentiation without influencing the pluripotency of stem cells.[133]

In order to target bone tissue, CDs were prepared using alendronate. The presence of bisphosphonate units on the surface of the dots allowed good interactions with hydroxyapatite when the content of amines on the surface was low. The presence of the CDs was immediately detectable due to their intrinsic fluorescence in *in vivo* experiments on zebrafish.[134] This tropism permits one to envision a future in the treatment of bone diseases for CDs and it was corroborated also by another research in which the dots were decorated with specific peptide sequences able to induce osteoblast adhesion, proliferation and differentiation, and combined with hyperbranched polyurethane. These complexes enhanced osteoconductivity and bone differentiation.[135]

In the frame of drug delivery, antitumor applications are always the major covered topic and CDs are no exception, with a rich literature corpus focused on anthracycline delivery. So far, CDs from many different sources and in varied constructs have been explored. Complex systems have been prepared, as doxorubicin bearing CDs embedded into liposomes,[136] or CDs prepared directly in the presence of amino-functionalized mesoporous silica nanoparticles.[137] The free drug capability to enter into and to kill the cells of three-dimensional multicellular spheroids, used as a tumor model, was outclassed by micelles of CDs loaded with doxorubicin, which proved to be effective also for MCF-7 anthracycline resistant cells.[127]

In order to exploit also the formation of electrostatic bonds between the polyamine units and doxorubicin, carbon dots were coupled to polyamine-containing organosilane derivatives. This construct presented very high drug loading. The cellular uptake in MCF-7 was followed by fluorescence, confirming the presence of the CDs into the cytoplasm. The *in vivo* experiments showed that the efficacy of doxorubicin was higher when associated with CDs than when administered as a free drug.[138]

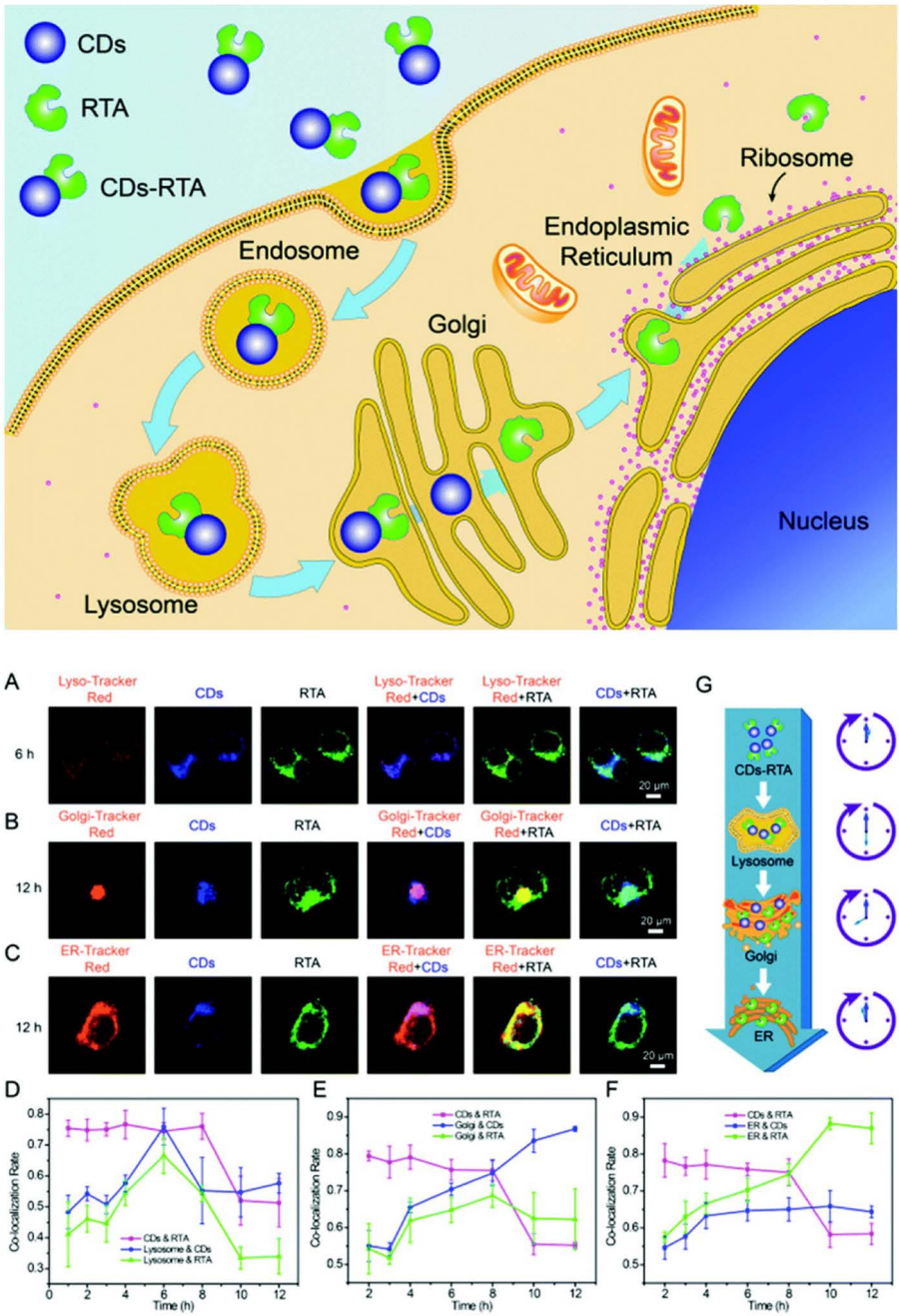

Figure 1.12 *Left*: Delivery route of the ricin A-chain by Golgi targeting CDs. *Right*: Fluorescence colocalization assay of CDs–RTA conjugates with (A) lysosome, (B) Golgi apparatus and (C) ER after 6 h and 12 h of incubation. Colocalization rate between CDs and RTA with lysosome (D), Golgi apparatus (E) and ER (F), treated with CDs–RTA conjugates at 2, 3, 4, 6, 8, 10 and 12 h. (G) Intracellular transport pathways of CDs–RTA conjugates. Adapted from ref. 129 with permission from Royal Society of Chemistry.

Acid-triggered release of doxorubicin was also achieved using hydrazone linkers[139] or imine-based conjugation of the drug on CDs, with 50% of the release at acidic pH while only 7% was undesirably removed from the vehicle at neutral pH.[140] Also, the carbon dots-mesoporous silica structures loaded with doxorubicin present a pH-sensitive release of the drug but in this case also a thermo-responsive release of the drug upon NIR irradiation was observed.[138] With the same aim, heparin and doxorubicin functionalized carbon dots were prepared obtaining a system responding to acid pH and a better effect than the free drug on cells, while the heparin presence ameliorates hemocompatibility.[141] Good hemocompatibility was also reported for hyaluronic modified CDs used to release doxorubicin.[132] Doxorubicin-conjugated CDs were also able to enter the cellular nuclei and to exert their cytotoxic activity also on cancer stem cells.[142]

CDs decorated with PEG and biotin units at the extremity of the glycolic chains were able to incorporate irinotecan and to release the latter if irradiated in the NIR. The consequent temperature rise not only helps the detachment of the drug but also leads to local hyperthermia, that increases the cell death also in a spheroid tumor model.[143]

Blue- and green-emitting cationic carbon dots were complexed, by means of electrostatic interactions, with 17β-estradiol hemisuccinate, able to interact with and be selectively taken up by estrogen receptor-rich cancer cells. In such a way it was possible to stain the responsive cells and to deliver doxorubicin, inducing apoptosis more efficiently than in estrogen receptor negative cells.[144]

The delivery of epirubicin and temozolomide conjugated to CDs on various glioblastoma brain tumor cell lines was achieved by linking transferrin to the CDs at the same time. The complex bearing the targeting agent and the two drugs proved to be very effective also due to the synergistic effect of the two drugs together.[145]

Decoration of carbon dots with a derivatized polyethylenimine provided an amphiphilic construct able to transfer gene and drugs into cells, as demonstrated by Wang *et al.* This material forms micelle structures endowed with a transfection capability higher than Lipofectamine 2000. The encapsulation of apoptosis-inducing siRNA resulted in cell death and the use of the construct in tumor spheroid models corroborates the results.[146] Analogous results of efficient gene knockdown by siRNA delivered by CDs were reported *in vitro* and *in vivo.*[147]

The delivery of inhibitors of miRNAs encoded by various oncogenic viruses is a strategy to avoid the insurgence of related cancers such as Kaposi's sarcoma. Among the silencing agents, locked nucleic acids (LNAs) are very effective antisense molecules and their intracellular delivery by means of CDs leads to the decrease of cell proliferation of KSHV-positive lymphoma cells and to a significant reduction of the tumor size in a primary effusion lymphoma mice model.[148]

These materials were studied also to deliver other drugs. Antibacterial activity of an amoxicillin-CDs preparation was shown and good results were achieved in inhibiting both Gram-positive and Gram-negative bacteria, *S. aureus* and *E. coli*, respectively.[149] Also, the combination with metronidazole

was evaluated against *Porphyromonas gingivalis*, with an efficacy increase of 72% with respect to the free drug.[150] Poly(lactic-*co*-glycolic acid) combined with CDs provided a good platform for antibiotic release upon irradiation, with a sustained delivery of azithromycin and tobramycin, macrolide and aminoglycoside antibiotics, respectively, with good performances against bacterial biofilm.[151] The combination of bacterial cellulose with titanium dioxide and CDs was demonstrated to be active against *S. aureus*, being at the same time well tolerated by human L929 fibroblast cells, with wound healing effects. These findings suggest the possibility of using such a system for specific bandages, with enhanced cure capability.[152]

Carbon dots deposited on β-cyclodextrin grafted with poly(*N*-vinyl caprolactam) diethylene glycol dimethacrylate copolymer were studied on NIH 3T3 fibroblast cell lines as a thermoresponsive film and no cytotoxicity was found. The local anesthetic lidocaine was loaded on to the film and the *in vitro* and *ex vivo* drug release profiles at body temperatures resulted in a very effective system for transdermal drug administration.[153]

1.5 Conclusions

Growing interest in the family of carbon nanostructures has led to the exploration of their potential application in a variety of fields, including which the biomedical area is the most attractive. Currently, the most explored topic is the use of carbon nanostructures as delivery systems, due to features such as their biocompatibility, versatility, capability to load a large number of different chemical structures, and to cross the cell membrane. They seem to be attractive tools for intracellular delivery of drugs, especially anticancer ones, whose toxic effect is non-selective toward cancer cells. Anthracyclines can be mentioned as an example. The selective internalization of carbon nanostructures into tumor cells can be achieved by decorating their surface with molecules recognized by specific transporters or receptors, such as fructose or folic acid and, moreover, the enhanced permeability and retention effect can play an important role in their increased accumulation into cancer tissues.

Certainly, beside conventional anticancer drugs, these materials can be functionalized with nucleic acid derivatives, such as siRNA, and can be used in immunogenic cancer therapy, and many other kinds of molecules, among which we can mention biomolecules with a specific role in tissue regeneration. The previously mentioned decorations, together with the structural consistency of the carbon nanostructures and some other characteristics such as their conductivity, render these materials very attractive in the regenerative medicine.

Nowadays, the peculiar luminescence properties of the newer carbon nanoforms is shifting the focus from CNTs toward NDs, GQDs and CDs. In fact, their intrinsic fluorescence is an excellent base for their use as theranostic agents, thus combining both therapeutic and diagnostic effects in a single nanoconstruct, without the necessity to introduce fluorescent dyes. Moreover, a number of carbon-based nanostructures proved to efficiently

cross the blood–brain barrier, which is one of the most challenging obstacles in delivering drugs to the central nervous system. In this sense, GQDs and CDs, representing the newest frontier in nanocarbon research, widen the potential application fields. Several properties of these materials, such as biocompatibility, photoluminescence or electronic properties, can be tuned with synthetic or post-synthetic procedures. However, also in this case one of the most explored applications is on their capability to deliver drugs in the treatment of cancer, with the advantage that they allow the application of unconventional therapeutic approaches, such as two-photon photodynamic therapy, affording at the same time cell bioimaging. Promising results concerning the application of fluorescent CDs as theranostic agents have been obtained by several research groups, and many different decorations have been proposed, thus confirming the synthetic and functional versatility of this material that needs to be further explored in the future, especially considering that preparation can start from many different sources (*e.g.* orange juice, tea leaves, tryptophan) and the standardization of their production is still challenging.

References

1. (a) C. W. Lee, Y. H. Su, Y. C. Chiang, I. T. Lee, S. Y. Li, H. C. Lee, L. F. Hsu, Y. L. Yan, H. Y. Li, M. C. Chen, K. T. Peng and C. H. Lai, *Biomolecules*, 2020, **10**, 514; (b) X. Zhang, Y. Ma, S. Fu and A. Zhang, *Nanomaterials*, 2019, **9**, 1647; (c) A. Munoz, D. Sigwalt, B. M. Illescas, J. Luczkowiak, L. Rodríguez-Peŕez, I. Nierengarten, M. Holler, J. S. Remy, K. Buffet, S. P. Vincent, J. Rojo, R. Delgado, J. F. Nierengarten and N. Martín, *Nat. Chem.*, 2016, **8**, 50; (d) B. M. Illescas, J. Rojo, R. Delgado and N. Martín, *J. Am. Chem. Soc.*, 2017, **139**, 6018–6025; (e) J. Ramos-Soriano, J. J. Reina, B. M. Illescas, N. de la Cruz, L. Rodríguez-Peŕez, F. Lasala, J. Rojo, R. Delgado and N. Martín, *J. Am. Chem. Soc.*, 2019, **141**, 15403; (f) B. M. Illescas, A. Peŕez-Sanchez, A. Mallo, A. Martín-Domenech, I. Rodríguez-Crespo and N. Martín, *J. Mater. Chem. B*, 2020, **8**, 4505–4515; (g) K. Siposova, V. I. Petrenko, O. I. Ivankov, A. Musatov, L. A. Bulavin, M. V. Avdeev and O. A. Kyzyma, *ACS Appl. Mater. Interfaces*, 2020, **12**, 32410–32419.
2. H. Kazemzade and M. Mozafari, *Drug Discovery Today*, 2019, **24**, 898–905.
3. A. A. Shvedova, V. Castranova, E. R. Kisin, D. Schwegler-Berry, A. R. Murray, V. Z. Gandelsman, A. Maynard and P. Baron, *J. Toxicol. Environ. Health, Part A*, 2003, **66**, 1909–1926.
4. A. R. Murray, E. Kisin, S. S. Leonard, S. H. Young, C. Kommineni, V. E. Kagan, V. Castranova and A. A. Shvedova, *Toxicology*, 2009, **257**, 161–171.
5. M. Kaczmarek, O. A. Timofeeva, A. Karaczyn, A. Malyguine, K. S. Kasprzak and K. Salnikow, *Free Radical Biol. Med.*, 2007, **42**, 1246–1257.
6. W. Huang, Y. Wang, G. Luo and F. Wei, *Carbon*, 2003, **41**, 2585–2590.
7. Y. Li, X. Zhang, J. Luo, W. Huang, J. Cheng, Z. Luo, T. Li, F. Liu, G. Xu and X. Ke, *Nanotechnology*, 2004, **15**, 1645–1649.

8. J. Muller, F. Huaux, A. Fonseca, J. B. Nagy, N. Moreau, M. Delos, E. Raymundo-Piñero, F. Béguin, M. Kirsch-Volders, I. Fenoglio, B. Fubini and D. Lison, *Chem. Res. Toxicol.*, 2008, **21**, 1698–1705.
9. V. E. Kagan, N. V. Konduru, W. Feng, B. L. Allen, J. Conroy, Y. Volkov, I. I. Vlasova, N. A. Belikova, N. Yanamala, A. Kapralov, Y. Y. Tyurina, J. Shi, E. R. Kisin, A. R. Murray, J. Franks, D. Stolz, P. Gou, J. Klein-Seetharaman, B. Fadeel, A. Star and A. A. Shvedova, *Nat. Nanotechnol.*, 2010, **5**, 354–359.
10. C. M. Sayes, F. Liang, J. L. Hudson, J. Mendez, W. Guo, J. M. Beach, V. C. Moore, C. D. Doyle, J. L. West, W. E. Billups, K. D. Ausman and V. L. Colvin, *Toxicol. Lett.*, 2006, **161**, 135–142.
11. H. Dumortier, S. Lacotte, G. Pastorin, R. Marega, W. Wu, D. Bonifazi, J.-P. Briand, M. Prato, S. Muller and A. Bianco, *Nano Lett.*, 2006, **6**, 1522–1528.
12. D. B. Warheit, B. R. Laurence, K. L. Reed, D. H. Roach, G. A. M. Reynolds and T. R. Webb, *Toxicol. Sci.*, 2004, **77**, 117–125.
13. D. Dutta, S. K. Sundaram, J. G. Teeguarden, B. J. Riley, L. S. Fifield, J. M. Jacobs, S. R. Addleman, G. A. Kaysen, B. M. Moudgil and T. J. Weber, *Toxicol. Sci.*, 2007, **100**, 303–315.
14. C. A. Poland, R. Duffin, I. Kinloch, A. Maynard, W. A. H. Wallace, A. Seaton, V. Stone, S. Brown, W. MacNee and K. Donaldson, *Nat. Nanotechnol.*, 2008, **3**, 423–428.
15. K. Kostarelos, *Nat. Biotechnol.*, 2008, **26**, 774–776.
16. S.-T. Yang, J. Luo, Q. Zhou and H. Wang, *Theranostics*, 2012, **2**, 271.
17. L. Lacerda, M. A. Herrero, K. Venner, A. Bianco, M. Prato and K. Kostarelos, *Small*, 2008, **4**, 1130–1132.
18. R. MacDonald, B. Laurenzi, G. V. P. Ajayan and J. Stegemann, *J. Biomed. Mater. Res.*, 2005, **74**, 489–496.
19. A. Galano, *J. Phys. Chem. C*, 2008, **112**, 8922–8927.
20. (a) M. M. Elsayed, M. E. Mostafa, E. Alaaeldin, H. Sarhan, M. Shaykoon, S. Allam, A. Ahmed and B. Elsadek, *Int. J. Nanomed.*, 2019, **14**, 8445; (b) C. Falank, A. W. Tasset, M. Farrell, S. Harris, P. Everill, M. Marinkovic and M. R. Reagan, *Nanomed. Nanotechnol.*, 2019, **20**, 102025.
21. T. Saliev, *C J. Carbon Res.*, 2019, **5**, 29.
22. Y.-J. Lu, K.-C. Wei, C.-C. M. Ma, S.-Y. Yang and J.-P. Chen, *Colloids Surf., B*, 2012, **89**, 1–9.
23. (a) N. W. S. Kam, Z. Liu and H. Dai, *Angew. Chem., Int. Ed.*, 2006, **45**, 577–581; (b) K. Kostarelos, L. Lacerda, G. Pastorin, W. Wu, S. Wieckowski, J. Luangsivilay, S. Godefroy, D. Pantarotto, J.-P. Briand, S. Muller, M. Prato and A. Bianco, *Nat. Nanotechnol.*, 2007, **2**, 108–113.
24. H. A. F. M. Hassan, S. S. Diebold, L. A. Smyth, A. A. Walters, G. Lombardi and K. T. Al-Jamal, *J. Controlled Release*, 2019, **297**, 79–90.
25. L. Lacerda, J. Russier, G. Pastorin, M. A. Herrero, E. Venturelli, H. Dumortier, K. T. Al-Jamal, M. Prato, K. Kostarelos and A. Bianco, *Biomaterials*, 2012, **33**, 3334–3343.
26. N. Saito, Y. Usui, K. Aoki, N. Narita, M. Shimizu, K. Hara, N. Ogiwara, K. Nakamura, N. Ishigaki, H. Kato, S. Taruta and M. M. Endo, *Chem. Soc. Rev.*, 2009, **38**, 1897–1903.

27. (a) J. Meng, L. Song, J. Meng, H. Kong, G. Zhu, C. Wang, L. Xu, S. Xie and H. Xu, *J. Biomed. Mater. Res., Part A*, 2006, **79A**, 298–306; (b) A. O. Lobo, M. A. F. Corat, E. F. Antunes, M. B. S. Palma, C. Pacheco-Soares, E. E. Garcia and E. J. Corat, *Carbon*, 2010, **48**, 245–254.
28. G. Cellot, E. Cilia, S. Cipollone, V. Rancic, A. Sucapane, S. Giordani, L. Gambazzi, H. Markram, M. Grandolfo, D. Scaini, F. Gelain, L. Casalis, M. Prato, M. Giugliano and L. Ballerini, *Nat. Nanotechnol.*, 2009, **4**, 126–133.
29. T.-I. Chao, S. Xiang, J. F. Lipstate, C. Wang and J. Lu, *J. Adv. Mater.*, 2010, **22**, 3542–3547.
30. E. B. Malarkey, R. C. Reyes, B. Zhao, R. C. Haddon and V. Parpura, *Nano Lett.*, 2009, **9**, 264–268.
31. X. Zhang, S. Prasad, S. Niyogi, A. Morgan, M. Ozkan and C. S. Ozkan, *Sens. Actuators, B*, 2005, **106**, 843–850.
32. D. Rugar, H. J. Mamin, M. H. Sherwood, M. Kim, C. T. Rettner, K. Ohno and D. D. Awschalom, *Nat. Nanotechnol.*, 2015, **10**, 120–124.
33. J. A. Roman, T. L. Niedzielko, R. C. Haddon, V. Parpura and C. L. Floyd, *J. Neurotrauma*, 2011, **28**, 2349–2362.
34. B. Chen, H. Zhang, C. Zhai, N. Du, C. Sun, J. Xue, D. Yang, H. Huang, B. Zhang and Q. J. Xie, *Mater. Chem.*, 2010, **20**, 9895–9902.
35. O. Vittorio, S. L. Duce, A. Pietrabissa and A. Cuschieri, *Nanotechnology*, 2011, **22**, 095706.
36. A. Al Faraj, K. Cieslar, G. Lacroix, S. Gaillard, E. Canet-Soulas and Y. Crémillieux, *Nano Lett.*, 2009, **9**, 1023–1027.
37. S. Y. Hong, G. Tobias, K. T. Al-Jamal, B. Ballesteros, H. Ali-Boucetta, S. Lozano-Perez, P. D. Nellist, R. B. Sim, C. Finucane, S. J. Mather, M. L. H. Green, K. Kostarelos and B. G. Davis, *Nat. Mater.*, 2010, **9**, 485–490.
38. (a) J. T.-W. Wang, C. Spinato, R. Klippstein, P. M. Costa, M. Martincic, E. Pach, A. Perez Ruiz de Garibay, C. Ménard-Moyon, R. Feldman, Y. Michel, M. Šefl, I. Kyriakou, D. Emfietzoglou, J.-C. Saccavini, B. Ballesteros, G. Tobias, A. Bianco and K. T. Al-Jamal, *Carbon*, 2020, **162**, 410–422; (b) J. T.-W. Wang, R. Klippstein, M. Martincic, E. Pach, R. Feldman, M. Šefl, Y. Michel, D. Asker, J. K. Sosabowski, M. Kalbac, T. Da Ros, C. Ménard-Moyon, A. Bianco, I. Kyriakou, D. Emfietzoglou, J.-C. Saccavini, B. Ballesteros, K. T. Al-Jamal and G. Tobias, *ACS Nano*, 2020, **14**, 129–141.
39. C. Fabbro, H. Ali-Boucetta, T. Da Ros, K. Kostarelos, A. Bianco and M. Prato, *Chem. Commun.*, 2012, **48**, 3911–3926.
40. P. S. O. Ozgen, S. Atasoy, B. Z. Kurt, Z. Durmus, G. Yigite and A. Dag, *J. Mater. Chem. B*, 2020, **8**, 3123.
41. A. Gangrade and B. B. Mandal, *ACS Biomater. Sci. Eng.*, 2019, **5**, 2365–2381.
42. H. V. Grushevskaya and N. G. Krylova, *Curr. Pharm. Des.*, 2018, **24**, 5207–5218.
43. N. Badea, M. M. Craciun, A. S. Dragomir, M. Balas, A. Dinischiotu, C. Nistor, C. Gavan and D. Ionita, *Mater. Chem. Phys.*, 2020, **241**, 122435.

44. W. Yi, P. Zhang, J. Hou, W. Chen, L. Bai, S. Yoo, A. Khalid and X. Hou, *Int. J. Biol. Macromol.*, 2018, **120**, 1525–1532.
45. S. Pasban, H. Raissi, M. Pakdel and F. Farzad, *Int. J. Pharm.*, 2019, **568**, 118491.
46. H. Moradnia, H. Raissi and A. Bakhtiari, *J. Biomol. Struct. Dyn.*, 2019, **37**(10), 2477–2486.
47. S. K. Prajapati, A. Jain, C. Shrivastava and A. K. Jain, *Int. J. Biol. Macromol.*, 2019, **123**, 691–703.
48. P. Zhang, W. Yi, J. Hou, S. Yoo, W. Jin and Q. Yang, *Int. J. Nanomed.*, 2018, **13**, 3069–3080.
49. A. Al Faraj, A. S. Shaik, E. Ratemi and R. Halwani, *J. Controlled Release*, 2016, **225**, 240–251.
50. M. R. Berber, H. Elkhenany, I. H. Hafez, A. El-Badawy, M. Essawy and N. El-Badri, *Nanomedicine*, 2020, **15**, 793–808.
51. Y. You, N. Wang, L. He, C. Shi, D. Zhang, Y. Liu, L. Luo and T. Chen, *Dalton Trans.*, 2019, **48**, 1569–1573.
52. S. Zhu, A.-G. Huang, F. Luo, J. Li, J. Li, L. Zhu, L. Zhao, B. Zhu, F. Ling and G.-X. Wang, *ACS Appl. Mater. Interfaces*, 2019, **11**, 19006–19016.
53. N. Dlamini, H. E. Mukaya, R. L. Van Zyl, C. T. Chen, R. J. Zeevaart and X. Y. Mbianda, *Mater. Sci. Eng., C*, 2019, **104**, 109967.
54. P. J. Harsha, N. Thotakura, M. Kumar, S. Sharma, A. Mittal, R. K. Khurana, B. Singh, P. Negi and K. Raza, *J. Drug Delivery Sci. Technol.*, 2019, **53**, 101186.
55. K.-C. Tay, L. T.-H. Tan, C. K. Chan, S. L. Hong, K.-G. Chan, W. H. Yap, P. Pusparajah, L.-H. Lee and B.-H. Goh, *Front. Pharmacol.*, 2019, **10**, 820.
56. B. Guo, C. Liao, X. Liu and J. Yi, *Drug Des., Dev. Ther.*, 2018, **12**, 2815–2826.
57. M. Assali, A. N. Zaid, N. Kittana, D. Hamad and J. Amer, *Nanotechnology*, 2018, **29**, 245101.
58. G. Biagiotti, M. C. Ligi, S. Fedeli, E. Pranzini, T. Gamberi, S. Cicchi and P. Paoli, *J. Drug Delivery Sci. Technol.*, 2018, **47**, 254–258.
59. R. A. Sobh, H. E. Nasr, A. B. Moustafa and W. S. Mohamed, *J. Pharm. Invest.*, 2019, **49**, 45–55.
60. W. Zhu, C. Han, Y. Dong and B. Jian, *J. Radioanal. Nucl. Chem.*, 2019, **320**, 503–512.
61. M. A. Herrero, F. M. Toma, K. T. Al-Jamal, K. Kostarelos, A. Bianco, T. Da Ros, F. Bano, L. Casalis, G. Scoles and M. Prato, *J. Am. Chem. Soc.*, 2009, **131**(28), 9843–9848.
62. B. Kateb, M. Van Handel, L. Zhang, M. J. Bronikowski, H. Manohara and B. Badie, *NeuroImage*, 2007, **37**, S9–S17.
63. V. V. Danilenko, *Phys. Solid State*, 2004, **46**, 595.
64. R. S. Lewis, T. Ming, J. E. Wacker, E. Anders and E. Steel, *Nature*, 1987, **326**, 160.
65. (a) A. Lyamkin, E. Petrov, A. Ershov, G. Sakovich, A. Staver and V. Titov, *Dokl. Akad. Nauk SSSR*, 1988, **302**, 611; (b) N. R. Greiner, D. S. Phillips, J. D. Johnson and F. Volk, *Nature*, 1988, **333**, 440.
66. F. P. Bundy, H. T. Hall, H. M. Strong and R. H. Wentorf, *Nature*, 1955, **176**, 51.

67. I. I. Kulakova, *Phys. Solid State*, 2004, **46**, 636.
68. A. M. Schrand, S. A. Hens and O. A. Shenderova, *Crit. Rev. Solid State*, 2009, **34**, 18.
69. V. M. Mochalin, O. Shenderova, D. Ho and Y. Gogotsi, *Nat. Nanotechnol.*, 2012, **7**, 11.
70. S. Osswald, G. Yushin, V. Mochalin, S. O. Kucheyev and Y. Gogotsi, *J. Am. Chem. Soc.*, 2006, **128**, 11635.
71. (a) A. Krueger, *Adv. Mater.*, 2008, **20**, 2445; (b) Y. Liu, Z. Gu, J. L. Margrave and V. N. Khabashesku, *Chem. Mater.*, 2004, **16**, 3924; (c) V. N. Mochalin and Y. Gogotsi, *Diamond Relat. Mater.*, 2015, **58**, 161.
72. E. A. Ekimov and M. V. Kondrin, *Semicond. Semimetals*, 2020, **103**, 161–199.
73. A. Krueger, *J. Mater. Chem.*, 2011, **21**, 12571.
74. O. Faklaris, V. Joshi, T. Irinopoulou, P. Tauc, M. Sennour, H. Girard, C. Gesset, J. C. Arnault, A. Thorel, J. P. Boudou, P. A. Curmi and F. Tressart, *ACS Nano*, 2009, **3**, 3955–3962.
75. C. Gaillard, H. A. Girard, C. Falck, V. Paget, V. Simic, N. Ugolin, P. Bergonzo, S. Chevillard and J. C. Arnault, *RSC Adv.*, 2014, **4**, 3566–3572.
76. R. Kaur and I. Badea, *Int. J. Nanomed.*, 2013, **8**, 203–220.
77. D. G. Lim, R. E. Prim, K. H. Kim, E. Kang, K. Park and S. H. Jeong, *Int. J. Pharm.*, 2016, **514**, 41–51.
78. K. J. van der Laan, M. Hasani, T. Zheng and R. Schirhagl, *Small*, 2018, **14**, 1704263.
79. M. Chipaux, K. J. van der Laan, S. R. Hemelaar, M. Hasani, T. Zheng and R. Schirhagl, *Small*, 2018, **14**, 1704263.
80. (a) L. Moore, V. Grobárová, H. Shen, H. B. Man, J. Míčová, M. Ledvina, J. Štursa, M. Nesladek, A. Fišerová and D. Ho, *Nanoscale*, 2014, **6**, 11712–11721; (b) K. J. van der Laan, M. Hasani, T. Zheng and R. Schirhagl, *Small*, 2018, **14**, 1703838.
81. L. Moore, J. Yang, T. T. Ha Lan, E. Osawa, D. K. Lee, W. D. Johnson, J. Xi, E. K. H Chow and D. Ho, *ACS Nano*, 2016, **10**, 7385–7400.
82. L. W. Tsai, Y. C. Lin, E. Perevedentseva, A. Lugovtsov, A. Priezzhev and C. L. Cheng, *Int. J. Mol. Sci.*, 2016, **17**, 1111.
83. L. Fusco, E. Avitabile, V. Armuzza, M. Orecchioni, A. Istif, D. Bedognetti, T. Da Ros and L. G. Delogu, *Carbon*, 2020, **160**, 390–404.
84. (a) E. K. Chow, X.-Q. Zhang, M. Chen, R. Lam, E. Robinson, H. Huang, D. Schaffer, E. Osawa, A. Goga and D. Ho, *Sci. Transl. Med.*, 2011, **3**, 73ra21; (b) H. B. Man, H. Kim, H.-J. Kim, E. Robinson, W. K. Liu, E. K.-H. Chow and D. Ho, *Nanomed. Nanotechnol.*, 2014, **10**, 359–369; (c) J. Xiao, X. Duan, Q. Yin, Z. Zhang, H. Yu and Y. Li, *Biomaterials*, 2013, **34**, 9648–9656.
85. X. Wang, X. C. Low, W. Hou, L. N. Abdullah, T. B. Toh, M. M. A. Rashid, D. Ho and E. K. H. Chow, *ACS Nano*, 2014, **8**, 12151–12166.
86. H. B. Man, H. Kim, H. J. Kim, E. Robinson, W. K. Liu, E. K. H. Chow and D. Ho, *Nanomedicine*, 2014, **10**, 359–369.
87. R. Kaur and I. Badea, *Int. J. Nanomed.*, 2013, **8**, 203–220.

88. C. C. Fu, H. Y. Lee, K. Chen, T. S. Lim, H. Y. Wu, P. K. Lin, P. K. Wei, P. H. Tsao, H. C Chang and W. Fann, *Proc. Natl. Acad. Sci. U. S. A.*, 2007, **104**, 727–732.
89. C. C. Fu, H. Y. Lee, K. Chen, T. S. Lim, H. Y. Wu, P. K. Lin, P. K. Wei, P. H. Tsao, H. C Chang and W. Fann, *Proc. Natl. Acad. Sci. U. S. A.*, 2007, **104**, 727–732.
90. N. Kossovsky, A. Gelman, H. J. Hnatyszyn, S. Rajguru, R. L. Garrell, S. Torbati, S. S. F. Freitas and G. M Chows, *Bioconjugate Chem.*, 1995, **6**, 507–511.
91. Q. Zhang, V. N. Mochalin, I. Neitzel, I. Y. Knoke, J. Han, C. A. Klug, J. G. Zhou, P. I. Lelkes and Y. Gogotsi, *Biomater*, 2011, **32**, 87–94.
92. A. Thalhammer, R. J. Edgington, L. A. Cingolani, R. Schoepfer and R. B. Jackman, *Biomaterials*, 2010, **31**, 2097–2104.
93. J. Wehling, R. Dringen, R. N. Zare, M. Maas and K. Rezwan, *ACS Nano*, 2014, **8**, 6475–6483.
94. A. Chatterjee, E. Perevedentseva, M. Jani, C. Y. Cheng, Y. S. Ye, P. H. Chung and C. L. Cheng, *J. Biomed. Opt.*, 2015, **20**, 0510141.
95. O. Shenderova, V. Grichko, S. Hens and J. Walch, *Diamond Relat. Mater.*, 2007, **16**, 2003–2008.
96. (a) H. Sun, L. Wu, W. Wei and X. Qu, *Mater. Today*, 2013, **16**, 433–442; (b) S. Zhou, H. Xu, W. Gan and Q. Yuan, *RSC Adv.*, 2016, **6**, 110775–110788; (c) J. Ge, M. Lan, B. Zhou, W. Liu, L. Guo, H. Wang, Q. Jia, G. Niu, X. Huang, H. Zhou, X. Meng, P. Wang, C.-S. Lee, W. Zhang and X. Han, *Nat. Commun.*, 2014, **5**, 4596; (d) J. Shen, Y. Zhu, X. Yang and C. Li, *Chem. Commun.*, 2012, **48**, 3686–3699.
97. (a) D. Pan, J. Zhang, Z. Li and M. Wu, *Adv. Mater.*, 2010, **22**, 734–738; (b) J. Peng, W. Gao, B. K. Gupta, Z. Liu, R. Romero-Aburto, L. Ge, L. Song, L. B. Alemany, X. Zhan, G. Gao, S. A. Vithayathil, B. A. Kaipparettu, A. A. Marti, T. Hayashi, J. J. Zhu and P. M. Ajayan, *Nano Lett.*, 2012, **12**, 844–849; (c) Y. Li, Y. Hu, Y. Zhao, G. Shi, L. Deng, Y. Hou and L. Qu, *Adv. Mater.*, 2011, **23**, 776–780.
98. (a) Y. Li, Y. Zhao, H. Cheng, Y. Hu, G. Shi, L. Dai and L. Qu, *J. Am. Chem. Soc.*, 2012, **134**, 15–18; (b) S. Zhu, J. Zhang, X. Liu, B. Li, X. Wang, S. Tang, Q. Meng, Y. Li, C. Shi, R. Hu and B. Yang, *RSC Adv.*, 2012, **2**, 2717–2720; (c) Y. Dong, J. Shao, C. Chen, H. Li, R. Wang, Y. Chi, X. Lin and G. Chen, *Carbon*, 2012, **50**, 4738–4743.
99. L. Kittiratanawasin and S. Hannongbua, *Integr. Ferroelectr.*, 2016, **175**, 211–219.
100. L. A. Ponomarenko, F. Schedin, M. I. Katsnelson, R. Yang, E. W. Hill, K. S. Novoselov and A. K. Geim, *Science*, 2008, **320**, 356–358.
101. S. Zhu, J. Zhang, C. Qiao, S. Tang, Y. Li, W. Yuan, B. Li, L. Tian, F. Liu, R. Hu, H. Gao, H. Wei, H. Zhang, H. Sun and B. Yang, *Chem. Commun.*, 2011, **47**, 6858–6860.
102. M. Li, W. Wu, W. Ren, H.-M. Cheng, N. Tang, W. Zhong and Y. Du, *Appl. Phys. Lett.*, 2012, **101**, 103107.

103. Q. Feng, Q. Cao, M. Li, F. Liu, N. Tang and Y. Du, *Appl. Phys. Lett.*, 2013, **102**, 013111.
104. A. Wolk, M. Rosenthal, S. Neuhaus, K. Huber, K. Brassat, J. K. N. Lindner, R. Grothe, G. Grundmeier, W. Bremser and R. Wilhelm, *Sci. Rep.*, 2018, **8**, 5843.
105. S. Li, S. Zhou, Y. Li, X. Li, J. Zhu, L. Fan and S. Yang, *ACS Appl. Mater. Interfaces*, 2017, **9**, 22332–22341.
106. W.-S. Kuo, C.-Y. Chang, H.-H. Chen, C.-L. L. Hsu, J.-Y. Wang, H.-F. Kao, L. C.-S. Chou, Y.-C. Chen, S.-J. Chen, W.-T. Chang, S.-W. Tseng, P.-C. Wu and Y.-C. Pu, *ACS Appl. Mater. Interfaces*, 2016, **8**, 30467–30474.
107. R. Li, X. Wang, Z. Li, H. Zhu and J. Liu, *New J. Chem.*, 2018, **42**, 4352–4360.
108. F. Arcudi, L. Đorđević and M. Prato, *Acc. Chem. Res.*, 2019, **52**, 2070–2079.
109. Y.-P. Sun, B. Zhou, Y. Lin, W. Wang, K. A. S. Fernando, P. Pathak, M. J. Meziani, B. A. Harruff, X. Wang, H. Wang, P. G. Luo, H. Yang, M. E. Kose, B. Chen, L. M. Veca and S.-Y. Xie, *J. Am. Chem. Soc.*, 2006, **128**, 7756–7757.
110. (a) S. C. Ray, A. Saha, N. R. Jana and R. Sarkar, *J. Phys. Chem. C*, 2009, **113**, 18546–18551; (b) S. Sahu, B. Behera, T. K. Maiti and S. Mohapatra, *Chem. Commun.*, 2012, **48**, 8835–8837.
111. S.-L. Hu, K.-Y. Niu, J. Sun, J. Yang, N.-Q. Zhao and X.-W. Du, *J. Mater. Chem.*, 2009, **19**, 484–488.
112. L. Wang, S.-J. Zhu, H.-Y. Wang, S.-N. Qu, Y.-L. Zhang, J.-H. Zhang, Q.-D. Chen, H.-L. Xu, W. Han, B. Yang and H.-B. Sun, *ACS Nano*, 2014, **8**, 2541–2547.
113. H. Liu, T. Ye and C. Mao, *Angew. Chem.*, 2007, **119**, 6593–6595.
114. M. Bottini and T. Mustelin, *Nat. Nanotechnol.*, 2007, **2**, 599.
115. P.-C. Hsu, P.-C. Chen, C.-M. Ou, H.-Y. Chang and H.-T. Chang, *J. Mater. Chem. B*, 2013, **1**, 1774–1781.
116. (a) F. Arcudi, L. Đorđević and M. Prato, *Angew. Chem.*, 2016, **128**, 2147–2152; (b) F. Arcudi, L. Đorđević and M. Prato, *Angew. Chem., Int. Ed.*, 2017, **56**, 4170–4173.
117. L. Cao, X. Wang, M. J. Meziani, F. Lu, H. Wang, P. G. Luo, Y. Lin, B. A. Harruff, L. M. Veca, D. Murray, S.-Y. Xie and Y.-P. Sun, *J. Am. Chem. Soc.*, 2007, **129**, 11318–11319.
118. (a) B. Kong, A. Zhu, C. Ding, X. Zhao, B. Li and Y. Tian, *Adv. Mater.*, 2012, **24**, 5844–5848; (b) Q. Wang, X. Huang, Y. Long, X. Wang, H. Zhang, R. Zhu, L. Liang, P. Teng and H. Zheng, *Carbon*, 2013, **59**, 192–199; (c) Q. Li, T. Y. Ohulchanskyy, R. Liu, K. Koynov, D. Wu, A. Best, R. Kumar, A. Bonoiu and P. N. Prasad, *J. Phys. Chem. C*, 2010, **114**, 12062–12068.
119. S.-T. Yang, X. Wang, H. Wang, F. Lu, P. G. Luo, L. Cao, M. J. Meziani, J.-H. Liu, Y. Liu, M. Chen, Y. Huang and Y.-P. Sun, *J. Phys. Chem. C*, 2009, **113**, 18110–18114.
120. A. Salinas-Castillo, M. Ariza-Avidad, C. Pritz, M. Camprubí-Robles, B. Fernández, M. J. Ruedas-Rama, A. Megia-Fernández, A. Lapresta-Fernández, F. Santoyo-Gonzalez, A. Schrott-Fischer and L. F. Capitan-Vallvey, *Chem. Commun.*, 2013, **49**, 1103–1105.

121. Y. Zhou, K. J. Mintz, L. Cheng, J. Chen, B. C. L. B. Ferreira, S. D. Hettiarachchi, P. Y. Liyanage, E. S. Seven, N. Miloserdov, R. R. Pandey, B. Quiroga, P. L. Blackwelder, C. C. Chusuei, S. Li, Z. Peng and R. M. Leblanc, *J. Colloid Interface Sci.*, 2020, **576**, 412–425.
122. J. Mondal, V. Revuri, P. Choochana, P. Ganesan, W. J. Kang and Y.-K. Lee, *J. Pharm. Invest.*, 2020, **50**, 209–218.
123. S. Li, W. Su, H. Wu, T. Yuan, C. Yuan, J. Liu, G. Deng, X. Gao, Z. Chen, Y. Bao, F. Yuan, S. Zhou, H. Tan, Y. Li, X. Li, L. Fan, J. Zhu, A. T. Chen, F. Liu, Y. Zhou, M. Li, X. Zhai and J. Zhou, *Nat. Biomed. Eng.*, 2020, **4**, 704–716.
124. K. J. Mintz, G. Mercado, Y. Zhou, Y. Ji, S. D. Hettiarachchi, P. Y. Liyanage, R. R. Pandey, C. C. Chusuei, J. Dallman and R. M. Leblanc, *Colloids Surf., B*, 2019, **176**, 488–493.
125. S. Wang, L. Chen, J. Wang, J. Du, Q. Li, Y. Gao, S. Yu and Y. Yang, *Mater. Sci. Eng., C*, 2020, **116**, 111233.
126. Y. Zhang, C. Zhang, J. Chen, L. Liu, M. Hu, J. Li and H. Bi, *ACS Appl. Mater. Interfaces*, 2017, **9**, 25152–25163.
127. B. Unnikrishnan, R.-S. Wu, S.-C. Wei, C.-C. Huang and H.-T. Chang, *ACS Omega*, 2020, **5**, 11248–11261.
128. R. S. Li, P. F. Gao, H. Z. Zhang, L. L. Zheng, C. M. Li, J. Wang, Y. F. Li, F. Liu, N. Li and C. Z. Huang, *Chem. Sci.*, 2017, **8**, 6829–6835.
129. C. H. Li, R. S. Li, C. M. Li, C. Z. Huang and S. J. Zhen, *Chem. Commun.*, 2019, **55**, 6437–6440.
130. Y. Yuan, B. Guo, L. Hao, N. Liu, Y. Lin, W. Guo, X. Li and B. Gu, *Colloids Surf., B*, 2017, **159**, 349–359.
131. J. Li, M. Li, L. Tian, Y. Qiu, Q. Yu, X. Wang, R. Guo and Q. He, *Int. J. Pharm.*, 2020, **578**, 119122.
132. X.-W. Hua, Y.-W. Bao, Z. Chen and F.-G. Wu, *Nanoscale*, 2017, **9**, 10948–10960.
133. H. Cai, J. Ma, X. Xu, H. Chu, D. Zhang and J. Li, *J. Mater. Chem. B*, 2020, **8**, 5655–5666.
134. K. K. Lee, J.-G. Lee, C. S. Park, S. H. Lee, N. Raja, H.-S. Yun, J.-S. Lee and C.-S. Lee, *RSC Adv.*, 2019, **9**, 2708–2717.
135. S. Gogoi, S. Maji, D. Mishra, K. S. P. Devi, T. K. Maiti and N. Karak, *Macromol. Biosci.*, 2017, **17**, 1600271.
136. W. Chen, J. Li, Y. Xing, X. Wang, H. Zhang, M. Xia and D. Wang, *Pharm. Res.*, 2020, **37**, 134.
137. S. Sun, S. Zhao, K. Jiang, Y. Wang, Q. Shu, S. Jin, Z. Li and H. Lin, *ChemNanoMat*, 2020, **6**, 953–962.
138. J. Yang, G. Gao, X. Zhang, Y.-H. Ma, H.-R. Jia, Y.-W. Jiang, Z. Wang and F.-G. Wu, *Nanoscale*, 2017, **9**, 15441–15452.
139. (a) M. Pei, G. Li and P. Liu, *Mater. Sci. Eng., C*, 2020, **110**, 110719; (b) G. Li, M. Pei and P. Liu, *Mater. Sci. Eng., C*, 2020, **110**, 110653.
140. G. Li, M. Pei and P. Liu, *Colloids Surf., A*, 2020, **603**, 125258.
141. M. Zhang, P. Yuan, N. Zhou, Y. Su, M. Shao and C. Chi, *RSC Adv.*, 2017, **7**, 9347–9356.
142. W. Su, R. Guo, F. Yuan, Y. Li, X. Li, Y. Zhang, S. Zhou and L. Fan, *J. Phys. Chem. Lett.*, 2020, **11**, 1357–1363.

143. C. Scialabba, A. Sciortino, F. Messina, G. Buscarino, M. Cannas, G. Roscigno, G. Condorelli, G. Cavallaro, G. Giammona and N. Mauro, *ACS Appl. Mater. Interfaces*, 2019, **11**, 19854–19866.
144. S. Sarkar, K. Das and P. K. Das, *ACS Sustainable Chem. Eng.*, 2017, **5**, 8356–8369.
145. S. D. Hettiarachchi, R. M. Graham, K. J. Mintz, Y. Zhou, S. Vanni, Z. Peng and R. M. Leblanc, *Nanoscale*, 2019, **11**, 6192–6205.
146. H.-J. Wang, X. He, T.-Y. Luo, J. Zhang, Y.-H. Liu and X.-Q. Yu, *Nanoscale*, 2017, **9**, 5935–5947.
147. S. Kim, Y. Choi, G. Park, C. Won, Y.-J. Park, Y. Lee, B.-S. Kim and D.-H. Min, *Nano Res.*, 2017, **10**, 503–519.
148. E. Ju, T. Li, Z. Liu, S. R. Da Silva, S. Wei, X. Zhang, X. Wang and S.-J. Gao, *ACS Nano*, 2020, **14**, 476–487.
149. T. S. John, P. K. Yadav, D. Kumar, S. K. Singh and S. H. Hasan, *Luminescence*, 2020, 913–923.
150. S. M. Ardekani, A. Dehghani, P. Ye, K.-A. Nguyen and V. G. Gomes, *J. Colloid Interface Sci.*, 2019, **552**, 378–387.
151. Z. Huang, T. Zhou, Y. Yuan, N. Kłodzińska, S. Zheng, T. Sternberg, C. Mørck, H. Nielsen, Y. Sun and F. Wan, *J. Colloid Interface Sci.*, 2020, **577**, 66–74.
152. S. Malmir, A. Karbalaei, M. Pourmadadi, J. Hamedi, F. Yazdian and M. Navaee, *Carbohydr. Polym.*, 2020, **234**, 115835.
153. A. Roy, S. Samanta, K. Singha, P. Maity, N. Kumari, A. Ghosh, S. Dhara and S. Pal, *ACS Appl. Bio Mater.*, 2020, **3**, 3285–3293.

CHAPTER 2

Carbon Nanomaterials as Carriers of Anti-inflammatory Drugs

S. GUO[†a], R. SOLTANI[†a], A. BIANCO*[a] AND C. MÉNARD-MOYON*[a]

[a]CNRS, Immunology, Immunopathology and Therapeutic Chemistry, UPR3572, University of Strasbourg, ISIS, 67000 Strasbourg, France
*E-mail: a.bianco@ibmc-cnrs.unistra.fr, c.menard@ibmc-cnrs.unistra.fr

2.1 Introduction

Nanotechnology has found broad applications in different areas of science ranging from electronics and biomaterials to energy production, and it has emerged as a highly attractive and promising field especially in biomedicine. A variety of drug nanocarriers has been extensively investigated, including polymeric nanoparticles,[1] liposomes,[2] hydrogels,[3] magnetic nanoparticles[4] and carbon nanomaterials.[5] The use of a delivery system allows the main limitations of most drugs such as poor solubility and limited biodistribution to be overcome, thus enhancing their pharmacokinetics and bioavailability.

[†]These authors contributed equally to this work.

Nanoscience & Nanotechnology Series No. 48
Carbon Nanostructures for Biomedical Applications
Edited by Tatiana Da Ros, Nazario Martín and Jean-Francois Nierengarten

Published by the Royal Society of Chemistry, www.rsc.org

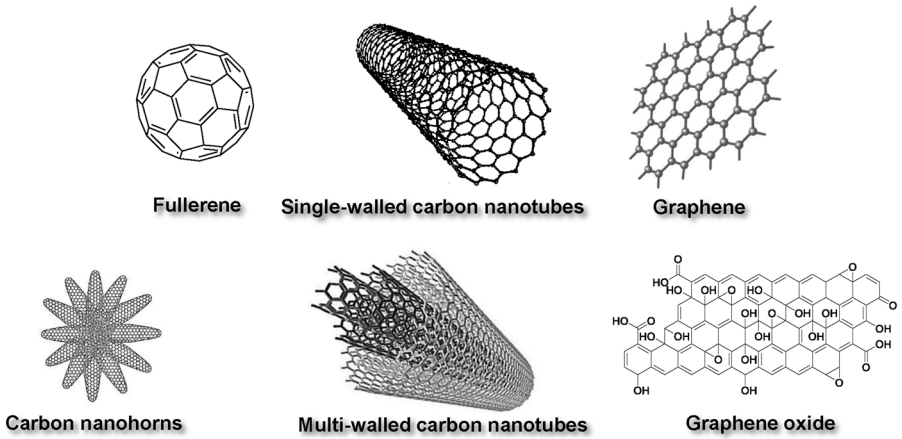

Figure 2.1 Different types of carbon nanomaterials.

Carbon nanomaterials are a class of low-dimensional carbonaceous materials that have engaged a great deal of interest in the past 35 years since the discovery of fullerene in 1985 (Figure 2.1).[6]

The most famous fullerene form of carbon is the C_{60} molecule (also called buckyball or buckminsterfullerene), which contains 60 carbon atoms arranged in 20 hexagonal and 12 pentagonal rings. The enthusiasm for another type of carbon nanomaterial, namely carbon nanotubes (CNTs), was initiated with the landmark publication of S. Iijima in 1991.[7] CNTs can be defined as hollow cylindrical structures made of rolled-up sheets constituted of hexagonally ordered carbon atoms. Depending on the number of layers, CNTs can be classified as single-walled CNTs (SWCNTs) or multi-walled CNTs (MWCNTs) with a diameter ranging from ~1 nm to tens of nanometers, and a length of several micrometers. The discovery of CNTs was followed by graphene, which is composed of a single atomic layer of sp^2-hybridized carbon atoms in the form of a two-dimensional hexagonal lattice, or its oxidized form graphene oxide (GO).[8,9] Other carbon nanomaterials have also been isolated such as carbon nanohorns (CNHs) composed of SWCNTs with long cone-shaped tips of 2–4 nm diameter and a length of 40–50 nm.[10] Great achievements have been made recently toward the use of carbon nanomaterials in nanomedicine,[11] especially for cancer therapy through their use as drug delivery systems, biosensors and photothermal agents.[12,13] Although they have been widely investigated for drug delivery in the treatment of cancer diseases, only few studies have reported their use to tackle inflammatory diseases. In this context, this book chapter will review how the different types of carbon nanomaterials have been applied as carriers for the delivery of anti-inflammatory drugs for the treatment of inflammation-associated pathologies.

2.2 Fullerenes

Fullerenes have been widely used as carriers of anti-inflammatory drugs. This section focuses on the most relevant studies reported on this topic since 2008. Dexamethasone (DEX) is a corticosteroid having anti-inflammatory and immunosuppressant effects. This drug is widely used in clinics; however, it generates severe side effects, which may be due to the generation of reactive oxygen species (ROS) likely leading to apoptosis. As C_{60} is a good ROS scavenger,[14] it was hypothesized that the conjugation of DEX to C_{60} would reduce the ROS-induced side effects. For this purpose, DEX was covalently linked to methanofullerene carboxylic acid by esterification.[15] The anti-inflammatory properties of DEX were preserved after conjugation to C_{60}, while the cytotoxicity of DEX-C_{60} on mouse thymocytes was lower compared to free DEX. It is known that the binding of DEX to the glucocorticoid receptor (GR), a cytoplasmic receptor, is involved in DEX-induced apoptosis. Indeed, after translocation of the DEX-GR complex to the nucleus, it binds to a glucocorticoid response element and modulates the expression of target genes, including interleukin (IL)-6 and nuclear factor-κB (NF-κB). Enzyme-linked immunosorbent assay (ELISA) revealed that the binding between DEX and GR was inhibited due to steric hindrance of the fullerene resulting in reduced binding to GR and therefore lower cytotoxicity because of downregulation of several apoptosis-related genes (Figure 2.2). This result was confirmed by immunostaining experiments showing that there was no GR in the nucleus due to the absence of nuclear translocation. The reduction in thymocyte apoptosis was not associated to the ROS scavenging capacity of C_{60}, contrary to the initial hypothesis. Overall, the conjugation of DEX to C_{60} preserved the anti-inflammatory properties of the drug while reducing its side effects.

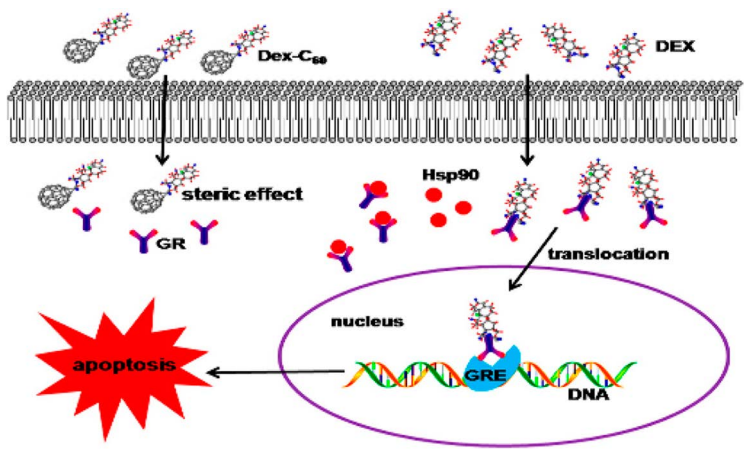

Figure 2.2 Proposed mechanism involving steric effects of C_{60} in the DEX-C_{60} conjugate on DEX-GR binding and GR activity. Reproduced from ref. 15 with permission from American Chemical Society, Copyright 2013.

In another example, C_{60} conjugated to conventional anti-inflammatory drugs augmented their anti-inflammatory effects *via* inhibition of intracellular enzymes such as cyclic 3′,5′-adenosine monophosphate phosphodiesterase (cAMP-PDE), therefore decreasing the production of pro-inflammatory substances. Xanthine derivatives are a group of alkaloids commonly used as mild stimulants and as bronchodilators in the treatment of asthma. They are also characterized by anti-inflammatory properties. The synergistic inhibitory effect of a xanthine derivative on the pro-inflammatory cytokine TNF-α and nitric oxide (NO) was evaluated during inflammation on a murine model.[16] Pentoxifylline (PTX), a xanthine analog, was conjugated to the nitrogen atom of a C_{60} fulleropyrrolidine through a triethylene glycol linker. One or two additional polar ethylene glycol chains were present on the pyrrolidine ring to improve the solubility in water, resulting in two compounds named **1a** and **1b** (Figure 2.3). A murine reticulum sarcoma cell line stimulated with lipopolysaccharide (LPS) was used for the biological experiments. Cytotoxicity based on the MTT assay revealed that C_{60}-PTX **1a** and **1b** preserved cell viability. ELISA was used to determine the amount of TNF-α, while NO was quantified by the measurement of nitrite concentration. Both conjugates had the ability to simultaneously inhibit the release of TNF-α and NO production by the cells, and it was found that **1b** was more efficient than **1a**. The suppression of TNF-α produced by the macrophages occurred through the inhibition of cAMP-PDE activity induced by the xanthine derivatives, which are known to increase the intracellular concentration of cAMP and thus suppress the production of pro-inflammatory cytokine TNF-α. Control *in vitro* experiments revealed that C_{60} alone slightly reduced NO production but could not inhibit TNF-α. Therefore, C_{60} functionalized with biologically active xanthine derivatives proved to be potent anti-inflammatory agents.

The same research group also evaluated the anti-inflammatory effects of a hybrid system based on thalidomide conjugated to C_{60} and studied the

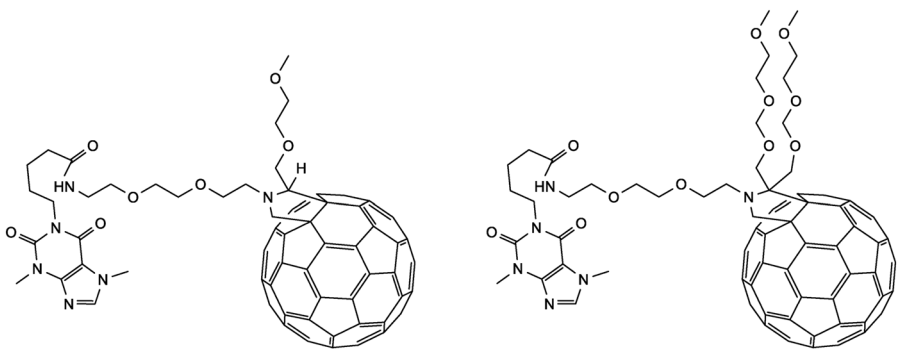

Figure 2.3 Structures of C_{60}-PTX **1a** and **1b**.

inhibition of TNF-α and NO produced by activated macrophages.[17] Thalidomide, a drug with anti-inflammatory properties, was covalently linked to C_{60} fulleropyrrolidine (CLT) through a similar approach (Figure 2.4). The cell viability was evaluated using the MTT assay on RAW 264.7 macrophages in the presence of LPS and found to be high for both CLT and C_{60} fulleropyrrolidine devoid of thalidomide (CL) (Figure 2.4). The evaluation of the anti-inflammatory effect of CL, CLT and free thalidomide on LPS-activated macrophages revealed a dose-dependent inhibitory effect on NO production and TNF-α. However, CLT exhibited higher values compared to the controls and it was 10 times more efficient in inhibiting TNF-α. On the other hand, biological tests conducted with confocal microscopy and flow cytometry showed a decrease in the ROS produced by the LPS-activated macrophages. Since inducible nitric oxide synthase (iNOS) is an enzyme that catalyzes the production of NO, the influence of the different compounds on iNOS expression was investigated. A weak expression of the protein and the suppression of intracellular ROS production were observed when macrophages were treated with CLT. Extracellular signal-regulated kinase (ERK) is a protein kinase involved in the activation of TNF-α expression in activated macrophages. The inhibition of ERK phosphorylation prevents the translocation of TNF-α mRNA from the nucleus to the cytoplasm. For this reason, the influence of CLT, CL and free thalidomide on ERK phosphorylation was studied. Cells treated with CLT had the lowest pERK1/2 expression in LPS-activated macrophages. The CLT inhibition of NO and TNF-α production was attributed to the ability to both scavenge intracellular ROS and suppress iNOS expression, and to inhibit ERK phosphorylation, respectively. This study demonstrated that the use of a hybrid system based on C_{60} fulleropyrrolidine and thalidomide to reduce NO and TNF-α secretion by activated macrophages during inflammation could ameliorate the delivery of the drug conferring a synergistic anti-inflammatory effect, which is promising for the development of a new generation of potent anti-inflammatory agents.

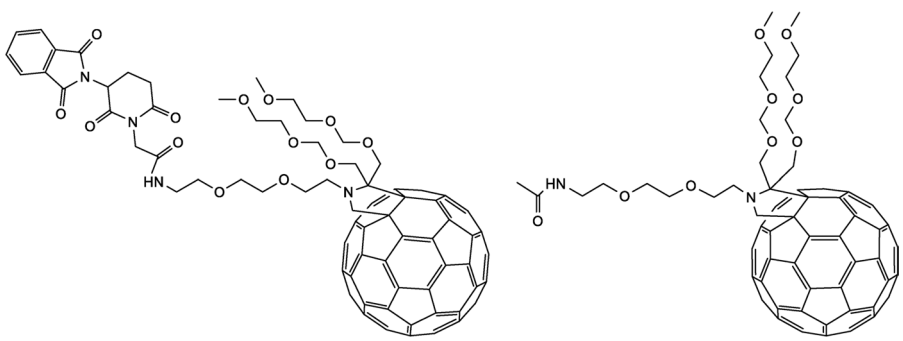

Figure 2.4 Structures of CLT (left) and CL (right).

2.3 Carbon Nanotubes

The cavity of CNTs can be exploited for encapsulation of drugs. In this context, MWCNTs were used as nanoreservoirs for drug loading and electrically-controlled release of dexamethasone.[18] DEX was incorporated into the inner cavity of oxidized MWCNTs. The controlled release of anti-inflammatory drugs or neurotropic factors allows for a stable chronic neural interface. To prevent the unwanted release of DEX, the open ends of the MWCNTs were sealed using polypyrrole (PPy), a conducting polymer forming a film by electropolymerization. Electrochemical impedance spectroscopy revealed that coating the electrode with PPy decreased the impedance and that the use of CNTs lowered the impedance even more, which is preferred for neural recording and stimulation (Figure 2.5). Electrically-controlled release of DEX loaded inside the nanotubes was studied in phosphate-buffered saline (PBS) upon electrical stimulation. The PPy films containing CNTs released more DEX compared to PPy films without CNTs, with a linear and sustainable drug release profile. The bioactivity of the released drug was tested using highly aggressively proliferating immortalized (HAPI) cells, which are microglia cells releasing pro-inflammatory cytokines and other inflammatory products such as NO when activated by a pro-inflammatory molecule (*e.g.* LPS). The DEX-free film and the released DEX from the CNT-PPy film both showed similar effective reduction of cell activation and NO production compared to the LPS control group.

Triamcinolone (TA) is a corticosteroid used to treat rheumatoid arthritis (RA). This drug can be injected directly into the inflamed joints, thus reducing inflammation. However, repetitive and long-term administrations at high doses can cause serious side effects. To overcome this problem, functionalized

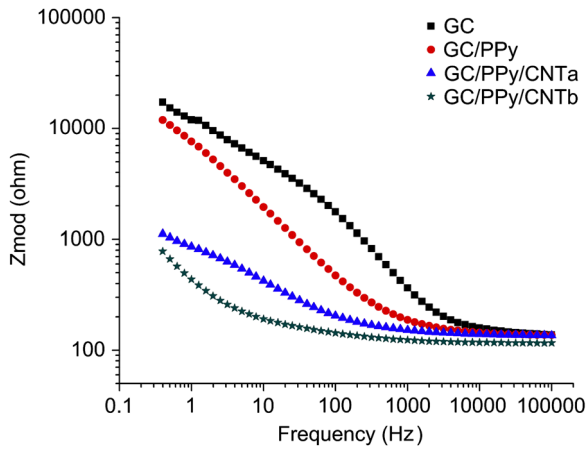

Figure 2.5 Electrochemical impedance spectroscopy of different electrodes. GC: glassy carbon electrode. CNTa: outer diameter 110–170 nm, inner diameter 3–8 nm, length 5–9 μm. CNTb: outer diameter 20–30 nm, inner diameter 5–10 nm, length 10–30 μm. Reproduced from ref. 18 with permission from Elsevier, Copyright 2011.

CNTs were used as drug carriers to improve RA treatment.[19] For this purpose, MWCNTs previously oxidized in acidic conditions were coated with polyethylene glycol (PEG) and complexed with TA. The resulting CNT-PEG-TA conjugate was then labeled with Alexa Fluor 488 to study the intracellular uptake of the drug in fibroblast-like synoviocyte (FLS) cells involved in the pathogenesis of chronic inflammatory diseases such as RA. The drug release from the PEGylated CNTs was performed at pH 7 and 5 and with lysozyme, as the pH is slightly acidic (pH 6) in synovial fluid from arthritis joints.[20] At neutral pH only 10% of TA was released, while 30% of the drug was liberated at acidic pH. Maximal release of the therapeutic agent was observed in the presence of lysozyme. The latter was found to improve the intracellular delivery of TA from the PEGylated CNTs in the FLS without drug loss in the extracellular environment. The study also suggested that the uptake mechanism of CNT-PEG-TA involved a clathrin- and macropinocytosis-mediated endocytosis. A 10 times lower dose of the CNT-PEG-TA (compared to free TA) had the same suppressive effect on the expression of pro-inflammatory cytokines (TNF-α, IL-6 and IL-1β) and matrix metalloproteinases (MMPs) MMP-1 and MMP-3, which are enzymes that induce bone erosion and cartilage destruction. In addition, a low dose of the CNT-PEG-TA also inhibited the activation of the serine/threonine kinase Akt, NF-κB, and mitogen activated protein kinases (MAPKs), signaling substances that increase the production of pro-inflammatory cytokines and MMPs in the FLS (Figure 2.6). Overall, this work demonstrated that

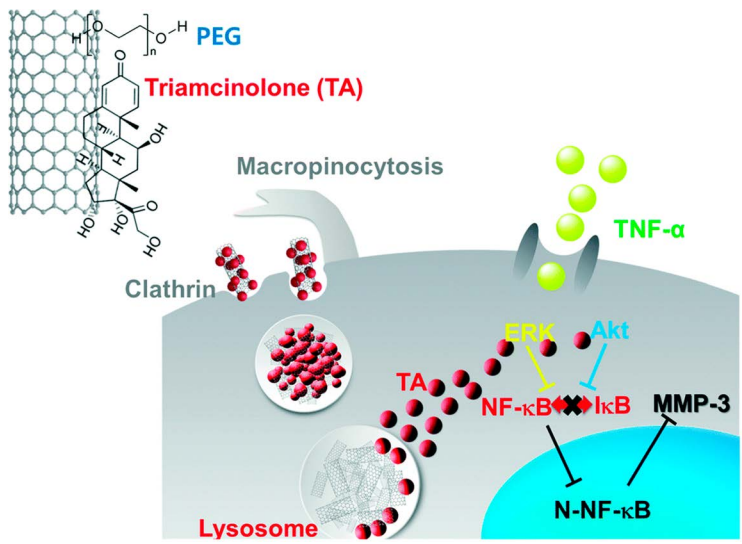

Figure 2.6 Mechanism of CNT-PEG-TA internalized by a clathrin- and macropinocytosis-mediated endocytosis leading to a significant suppression of NF-κB translocation through the inhibition of the phosphorylation of MAPKs and Akt in TNF-α-activated arthritis FLS. Reproduced from ref. 19 with permission from the Royal Society of Chemistry.

the immobilization of TA onto the CNTs enhanced the intracellular delivery of the drug *via* clathrin- and macropinocytosis-mediated endocytosis and reduced inflammation in FLS. As an increase in lysosomal content induced by CNT-PEG-TA was observed in this study, the lysosomal pathway could therefore be crucial as it operates under such low pH conditions.

Similarly, another study from the same group demonstrated that the conjugation of DEX to PEGylated MWCNTs enhanced the intracellular drug delivery and showed a highly suppressive effect of pro-inflammatory cytokines and MMPs in TNF-α-stimulated FLS even at a low dose, compared to free DEX.[21] PEG-coated MWCNTs were non-covalently functionalized with DEX and labeled with streptavidin-conjugated Alexa 488 to investigate the intracellular uptake of the MWCNT-PEG-DEX in FLS from patients with RA. The drug release was performed in two different physiological conditions. At neutral pH about 10% of the drug was released. In acidic media a release of nearly 40% was observed, whereas a higher percentage was reported after the addition of lysozyme, as observed also in the previous study. This result suggested an enhanced intracellular transport of DEX without dissociation since it was stable in the extracellular conditions (hypoxic synovial fluid) and could reach the intracellular compartments without drug loss, following a caveolin-dependent endocytosis mechanism in activated FLS. A low dose of DEX immobilized onto the MWCNTs induced a suppressive effect of pro-inflammatory cytokines and MMPs. In addition, the conjugate inhibited ROS production and rescued mitochondrial membrane damage. These two studies suggest that the use of CNTs for the delivery of corticosteroids can be used as a strategy to overcome the limitations of conventional RA treatments and reduce side effects.

A novel delivery system based on budesonide (BUD), a glucocorticoid used to treat inflammatory diseases, was designed by adsorption of the drug onto MWCNTs. The internalization of the conjugate into macrophages and the suppression of pro-inflammatory cytokine production were investigated.[22] For this purpose, a budesonide-based amphiphile was synthesized and complexed to MWCNTs. The interactions between the resulting CNT-BUD conjugate and murine macrophages were studied, as these cells are a major component of the mononuclear phagocytic system. They also play a critical anti-inflammatory role and can decrease immune reactions through the release of pro-inflammatory cytokines. As evidenced by transmission electron microscopy, individualized CNTs were localized in the cytoplasm and in the cell nucleus. It was hypothesized that CNT-BUD could escape phagosomes and reach the glucocorticoid receptor of the cells, and hence translocate to the nucleus. In addition, CNT-BUD was able to strongly inhibit the release of pro-inflammatory cytokine IL-6 by macrophages and therefore displayed high anti-inflammatory properties. The use of MWCNTs did not alter the anti-inflammatory effect of the drug and enhanced its solubility in water, which could allow the administration of lower doses of BUD and guarantee better local bioavailability.

In another study, folic acid (FA), a targeting ligand of cancer cells, was immobilized onto amino-MWCNTs.[23] FA binds with a high affinity to folate receptors, overexpressed on activated macrophages in arthritis patients. Methotrexate (MTX), an anti-inflammatory drug, was adsorbed onto the functionalized CNTs at a high percentage of drug loading (91.2%). A significant sustained release of MTX (65.8%) from the CNT-FA at pH 7.4 was measured, while it was not the case with pristine CNTs. To study the effect of CNT-FA-MTX on inflammation *in vivo*, a carrageenan-induced arthritis rat model was used and the conjugate was administered through an intravenous route by tail vein injection. Joint inflammation was determined by measuring the change in the volume of the inflamed knee joint 24 h after injection. In addition, the concentration of the drug in the plasma and tissue was measured by high-performance liquid chromatography. Pharmacodynamic and pharmacokinetic studies revealed that the percentage of arthritis inhibition after the treatment with CNT-FA-MTX was significantly higher compared to the treatment with pristine CNTs or the free drug. This result is probably due to a sustained release of the drug, thus increasing its biological half-life. The biodistribution of the free drug, the functionalized and pristine CNTs to different major organs, was investigated after intravenous administration. CNT-FA-MTX accumulated less in the liver, the kidney, the lung and the spleen compared to the pristine CNTs and the free drug. A higher amount of the drug was found in arthritic joints of the rats treated with CNT-FA-MTX. This suggests that CNTs functionalized with FA could be used as potential carriers for targeted sustained delivery of anti-inflammatory drugs.

Colitis is an inflammation of the inner lining of the colon that can be associated with diarrhea, abdominal pain, bloating, and blood in the stool. The release of inflammatory mediators may lead to mucosal ulceration and disruption. The cannabinoid 2-arachidonoylglycerol (2-AG) is a therapeutic agent that has beneficial effects on colitis. However, its poor solubility and fast hydrolysis limit its efficiency. In this context, 2-AG was immobilized onto amine-functionalized MWCNTs and the conjugate was tested for its ability to enhance the stability and the delivery of the drug.[24] *In vitro* experiments revealed a significant decrease of the drug toxicity using CNT-2-AG compared to free 2-AG. To evaluate the effects of the drug *in vivo*, colitis was induced in a rat model, which altered the colon mucosal layer, increased pro-inflammatory cytokine production and myeloperoxidase activity (as an indicator of neutrophil accumulation), as well as malondialdehyde (MDA) content (peroxidation marker). When treated by intrarectal administration of CNT-2-AG 2 days before and 8 days after the induction of colitis, inflammatory mediators such as TNF-α, IL-1β, myeloperoxidase activity and MDA content were found to be decreased. An amelioration of the colon mucosa injuries was also observed (Figure 2.7). CNT-2-AG led to a longer-lasting therapeutic effect and inhibited the release of pro-inflammatory cytokines, thus providing promising protective effects against colitis.

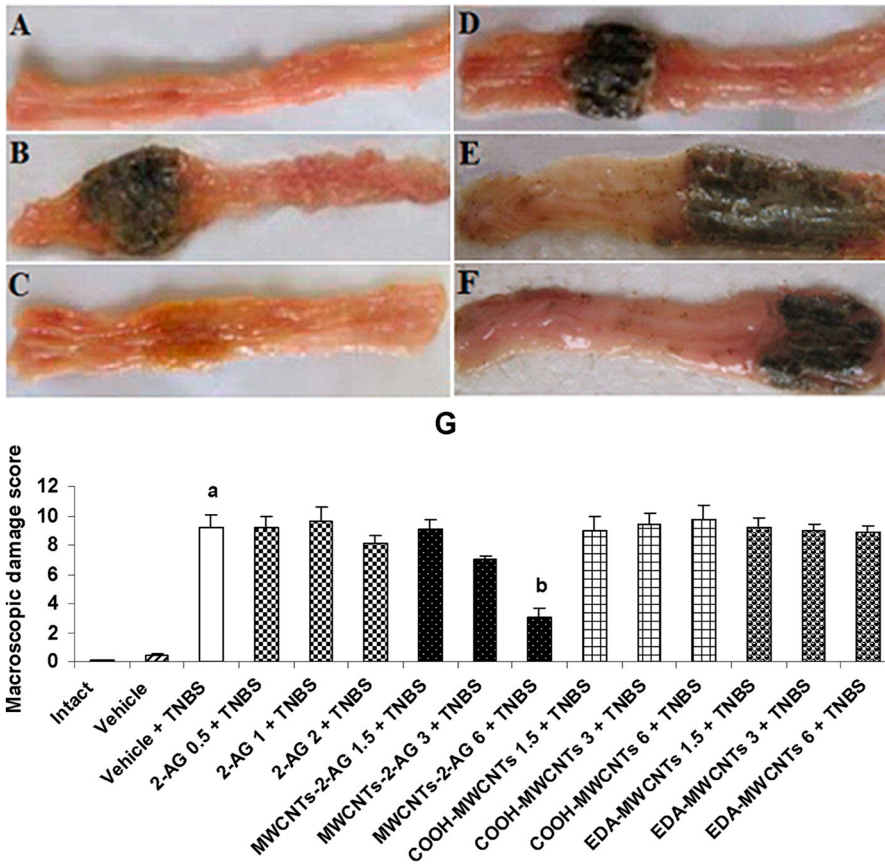

Figure 2.7 Appearance of the colon and damage score in colitic rats. (A) normal colon; (B) colitic rat treated with the vehicle; (C) treatment with 6 mg kg^{-1} of CNT-2-AG; (D) treatment with 2-AG solution; (E) treatment with CNT-COOH; (F) treatment with amine-functionalized CNTs; (G) macroscopic damage score. Reproduced from ref. 24 with permission from Elsevier, Copyright 2017.

2.4 Carbon Nanohorns

Prednisolone (PSL) is an anti-inflammatory glucocorticoid used in the treatment of allergies and many inflammatory diseases such as RA, lupus, or ulcerative colitis. Glucocorticoids are widely used to treat inflammation; however, they present many side effects. The unique physical and chemical properties of single-walled nanohorns (SWCNHs), in particular their large surface area, have been exploited as carriers for drug delivery.[25] In this context, the release of PSL adsorbed onto oxidized SWCNHs (o-SWCNHs) was investigated *in vitro* and the anti-inflammatory effect of the PSL-oSWCNH conjugate was studied in collagen-induced arthritis rats.[26] The SWCNHs were oxidized following a

slow combustion method at temperatures between 500 and 570 °C allowing the opening of holes on the walls.[27] PSL was non-covalently immobilized onto o-SWCNHs through a nano-extraction method. This strategy consists in incorporating various molecules inside nanomaterials in a liquid phase at room temperature using an appropriate solvent. Guest molecules must have a poor affinity for the solvent, but a strong affinity for the nanomaterials, while the solvent must have a poor affinity for the nanomaterials. PSL was adsorbed both outside and inside o-SWCNHs. The PSL loading was 3.2 times higher on o-SWCNHs compared to the pristine SWCNHs. The release was slow in PBS and faster in cell culture media, reaching about 9% and 40%, respectively. A burst release was noticed in the first few hours, which was due to PSL adsorbed on o-SWCNHs, followed by a slow release of PSL encapsulated inside the nanohorns. The quantity of PSL released from o-SWCNHs in cell culture media increased in a dose-dependent manner, indicating that PSL kept an equilibrium between the adsorption and the release of the drug present on or inside o-SWCNHs. PSL-oSWCNHs were locally injected into tarsal joints of female DA/Sic rats with collagen-induced arthritis. A moderate slowdown in arthritis progression was measured compared to rats treated with PSL alone and the control group (PBS). Moreover, the amount of leukocytes and C-reactive protein level (CRP) (inflammatory indicators) was lower in rats treated with PSL-oSWCNHs when compared with both control groups. Histological analysis of ankle joints evidenced that synovitis, bone destruction and inflammatory cell infiltration were observed in both control groups, while lower arthritis scores were noticed in the PSL-oSWCNH-treated rats (Figure 2.8). Immunohistological analysis using anti-CD68 antibody (marker of osteoclasts) showed accumulation of osteoclasts in the bone area of the ankle joints in the PBS control group, whereas a decreased number of osteoclasts were observed in the ankle joints of the PSL-oSWCNH-treated rats. All these results support the anti-inflammatory effect of PSL-oSWCNHs and prove that carbon nanohorns are potential drug delivery candidates that could limit the side effects of PSL.

2.5 Graphene-based Nanomaterials

Graphene oxide (GO) is an ideal carrier for the delivery of small molecules such as drugs, peptides and nucleotides for disease treatments due to its large surface area and abundance of oxygen-containing functional groups endowing GO with a good loading capacity and high biocompatibility.[5,11] The oxygenated groups can prevent drug aggregation through hydrogen bonding. Thus, the use of GO as a drug carrier allows one to improve the therapeutic efficacy of drugs and mitigate the side effects during treatment. For instance, bone morphogenetic protein 2 (BMP-2) was adsorbed onto the surface of GO with a high loading efficiency.[28] BMP-2 is important for maintaining articular cartilage and repairing damaged cartilage. A prolonged release of BMP-2 from the GO surface was observed for at least 40 days, which is crucial for osteoarthritis treatment because high doses of BMP-2 often cause serious

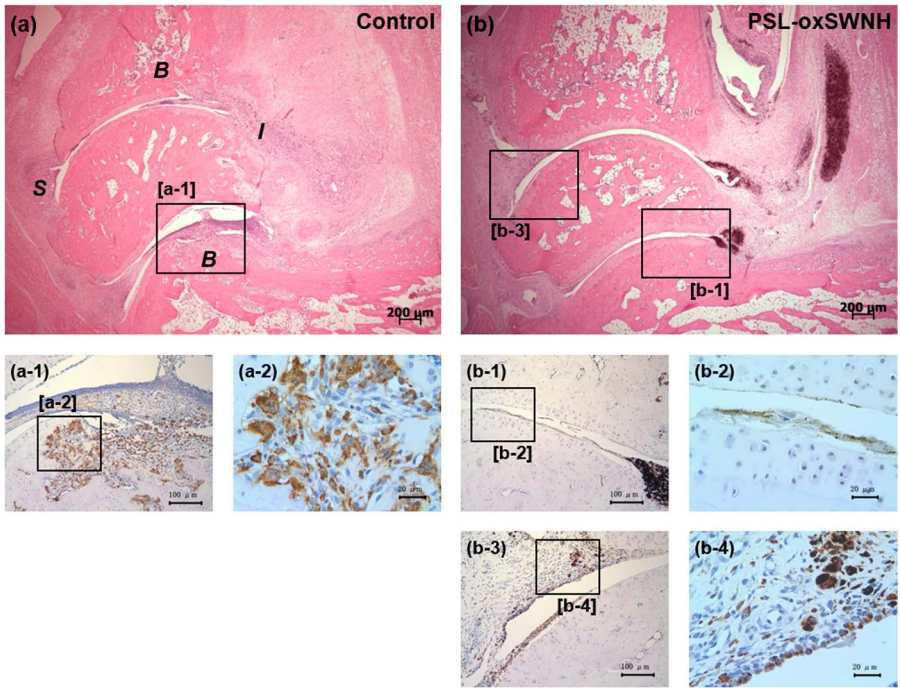

Figure 2.8 Histological analysis of ankle joints after the development of arthritis (day 28) with hematoxylin and eosin staining (a and b) and CD68 staining (a-1, a-2, b-1, b-2, b-3 and b-4). The arthritic rats were treated with PBS (a) and PSL-oSWCNHs (b). S: synovial proliferation; B: bone destruction; I: inflammatory cell infiltration. Reproduced from ref. 26 with the permission of IOP Publishing, Copyright 2011.

side effects including induction of an immune response and ectopic bone formation (Figure 2.9). GO loaded with BMP-2 significantly enhanced the therapeutic effect of the protein compared to BMP-2 alone in osteoarthritic rats. The extended release of BMP-2 avoided the activation of inflammatory factors as no inflammatory cytokines were detected in the articular cartilage after treatment with GO loaded with BMP-2.

GO has been also exploited as a gene carrier for the modulation of the immune environment in myocardial infarction (MI) for cardiac repair (Figure 2.10).[29] GO was modified with polyethylene imine (PEI) and folic acid-PEG (FA-PEG) to impart a high affinity toward inflammatory macrophages compared to other cells abundant in the region of the infarction. The functionalized GO served as an antioxidant, especially reducing hydroxyl radical species (one of the major ROS) that induce inflammatory progress and invoke heart failure. It was found that GO could attenuate inflammation and inflammatory polarization of macrophages (M1). M1 phase macrophages can remove necrotic cells and debris and initiate inflammatory reactions, whereas M2 phase macrophages can produce anti-inflammatory cytokines such as IL-4 during the inflammation resolution stage. The macrophage-targeting/polarizing GO

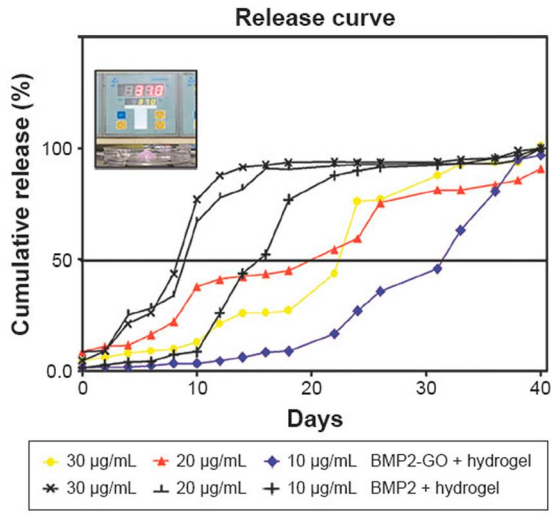

Figure 2.9 Release profiles of BMP-2 with or without immobilization on GO (for this release study, GO was resuspended in a hydrogel). Reproduced from ref. 28 with permission from Dove Medical Press, Copyright 2017.

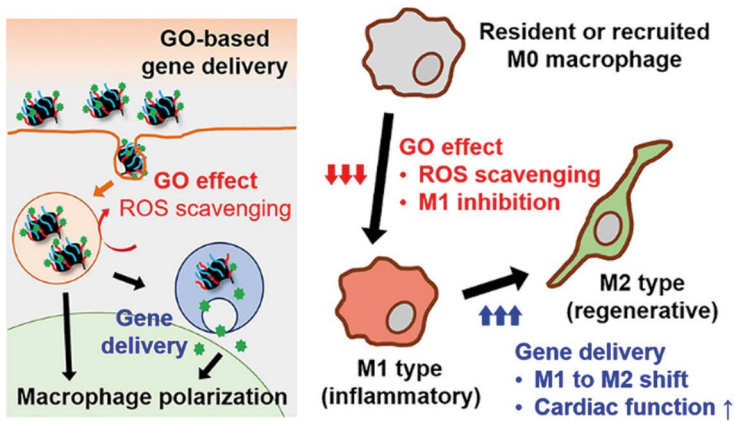

Figure 2.10 Proposed therapeutic mechanisms of MGC/IL-4 pDNA in cardiac repair. Reproduced from ref. 29 with permission from American Chemical Society, Copyright 2018.

complex (MGC) was exploited as a carrier of IL-4 plasmid DNA (IL-4 pDNA) that propagates M2 macrophages. The MGC/IL-4 pDNA induced an early shift from the inflammatory M1 phase macrophages to reparative M2 macrophages that could actively participate in cardiac repair both *in vitro* and *in vivo*. The complex could significantly reduce inflammation at infarcted regions and alleviate cardiac remodeling in MI mouse models resulting in an improved recovery of cardiac function.

The modification of GO with inorganic material can impart novel properties and extend the field of applications, in particular for drug delivery.[30] A hybrid system based on gold-GO (Au@GO) sheets incorporated with zwitterionic chitosan (ZC) was prepared using an aerosol-based method.[31] Zwitterionic polymers have recently been used as drug delivery systems due to their unique suppression of inflammatory responses. Au@GO-ZC was exposed to visible light to induce modification of ZC chemical properties by the photocatalytic activity of Au@GO flakes. Au@GO-ZC with or without visible light exposure was biocompatible and exhibited anti-inflammatory properties. The Au@GO-ZC incorporation with nystatin, a clinically used antibiotic agent, led to a significant reduction of the production of inflammatory proteins in macrophages challenged with LPS. It was hypothesized that ZC could bind to cell surface receptors, thus regulating the production of macrophage inflammatory proteins by nystatin *via* modification of cell signaling pathways. This study offers interesting perspectives for further investigation of ZC-functionalized GO in drug delivery.

Graphene nanostars (GNSs) are constituted of clusters of conical rolls of graphene sheets with cone-shaped tips named nanohorns.[32] Single-walled carbon graphene nanohorns have a typical diameter of 2 to 5 nm and a length in the range of 40–50 nm. Thousands of graphene nanohorns form spherical aggregates (nanostars) with a diameter of ~100 nm. The GNSs were covalently functionalized with a fifth-generation poly(amidoamine) (PAMAM-G5) dendrimer.[33] An anti-inflammatory plasmid (plasmid expressing the collagenase metalloproteinase 9, pMMP9) was adsorbed on the positively charged dendrimer-functionalized GNS (DGNSs) through electrostatic interactions. The expression of MMP-9 in inflamed macrophages treated with the pMMP9-DGNS complex was increased. MMP-9 can downregulate other genes related to M1 macrophages and thus promote their transition into M2 macrophages. When applied to hepatic fibrosis *in vitro* and *in vivo*, the DGNSs were able to deliver pMMP-9 to inflammatory macrophages located in the fibrotic tracts of cirrhotic livers. This induced the synthesis of MMP-9 causing collagen degradation. The pMMP9-DGNS conjugate did not cause hepatic damage as in the case for standard anti-inflammatory and anti-fibrotic drugs. In contrast, it improved the hepatic function, promoted fibrosis regression, and showed higher regeneration of the injured organ. Fibrosis contributes to ~45% of all deaths in industrialized countries. However, up to now there is no direct antifibrotic therapy. Therefore, in this context, DGNSs are promising for the treatment of diseases associated with fibrosis and inflammatory macrophage accumulation.

2.6 Conclusion and Perspectives

Due to their large surface area and the possibility of multifunctionalization, carbon nanomaterials can be functionalized covalently or non-covalently with drugs and can be used as carriers for drug delivery and gene delivery.[5,11]

In this context, they have been exploited as carriers of anti-inflammatory drugs achieving better therapeutic efficacy. They are able to enhance the stability and water solubility of the drugs, and to prolong their release, thus increasing their biological half-time and avoiding side effects caused by drug overdose. In addition, the functionalization of carbon nanomaterials with targeting ligands can improve the biodistribution of drugs. Overall, these applications illustrate the extensive potential of carbon nanomaterials for the treatment of inflammatory-related diseases. Although there are still some concerns for their toxicity and environmental impact, their applications in nanomedicine are very promising.[34–36] The type, size, functionalization and purity of the nanomaterials are crucial to increase their biocompatibility.[37,38] Their biodegradability by human enzymes or through different pathways *in vivo* offers perspectives for their real potential in the biomedical field.[39,40] Well-designed carbon nanomaterials are required for further research into the treatment of inflammatory diseases, while the elucidation of the mechanisms of interactions between the carbon nanomaterials and the immune system is also necessary.

Acknowledgements

We gratefully acknowledge the Centre National de la Recherche Scientifique (CNRS), the International Center for Frontier Research in Chemistry (icFRC), and financial support from the Agence Nationale de la Recherche (ANR) through the LabEx project Chemistry of Complex Systems (ANR-10-LABX-0026_CSC). SG is indebted to the Chinese Scholarship Council for supporting his PhD internship. Hazel Lin is gratefully acknowledged for critical reading of the chapter.

References

1. A. P. P. Kröger, N. M. Hamelmann, A. Juan, S. Lindhoud and J. M. J. Paulusse, *ACS Appl. Mater. Interfaces*, 2018, **10**, 30946.
2. Y. Lee and D. H. Thompson, *Wiley Interdiscip. Rev.: Nanomed. Nanobiotechnol.*, 2017, **9**, e1450.
3. J. Li and D. J. Mooney, *Nat. Rev. Mater.*, 2016, **1**, 16071.
4. S. M. Dadfar, K. Roemhild, N. I. Drude, S. von Stillfried, R. Knuechel, F. Kiessling and T. Lammers, *Adv. Drug Delivery Rev.*, 2019, **138**, 302.
5. K. P. Loh, D. Ho, G. N. C. Chiu, D. T. Leong, G. Pastorin and E. K. Chow, *Adv. Mater.*, 2018, **30**, e1802368.
6. H. W. Kroto, J. R. Heath, S. C. O'Brien, R. F. Curl and R. E. Smalley, *Nature*, 1985, **318**, 162.
7. S. Iijima, *Nature*, 1991, **354**, 56.
8. K. S. Novoselov, A. K. Geim, S. V. Morozov, D. Jiang, Y. Zhang, S. V. Dubonos, I. V. Grigorieva and A. A. Firsov, *Science*, 2004, **306**, 666.

9. G. Bottari, M. A. Herranz, L. Wibmer, M. Volland, L. Rodriguez-Perez, D. M. Guldi, A. Hirsch, N. Martín, F. D'Souza and T. Torres, *Chem. Soc. Rev.*, 2017, **46**, 4464.
10. S. Iijima, M. Yudasaka, R. Yamada, S. Bandow, K. Suenaga and F. Kokai, *Chem. Phys. Lett.*, 1999, **309**, 165.
11. N. Panwar, A. M. Soehartono, K. K. Chan, S. Zeng, G. Xu, J. Qu, P. Coquet, K. T. Yong and X. Chen, *Chem. Rev.*, 2019, **119**, 9559.
12. X. Cui, S. Xu, X. Wang and C. Chen, *Carbon*, 2018, **138**, 436.
13. B. P. Jiang, B. Zhou, Z. Lin, H. Liang and X. C. Shen, *Chem. - Eur. J.*, 2019, **25**, 3993.
14. N. Gharbi, M. Pressac, M. Hadchouel, H. Szwarc, S. R. Wilson and F. Moussa, *Nano Lett.*, 2005, **12**, 2578.
15. Y. Zhang, L. Wang, Y. Sun, Y. Zhu, Z. Zhong, J. Shi, C. Fan and Q. Huang, *ACS Appl. Mater. Interfaces*, 2013, **5**, 5291.
16. S. T. Huang, J. S. Liao, H. W. Fang and C. M. Lin, *Bioorg. Med. Chem. Lett.*, 2008, **18**, 99.
17. S. T. Huang, C. S. Ho, C. M. Lin, H. W. Fang and Y. X. Peng, *Bioorg. Med. Chem.*, 2008, **16**, 8619.
18. X. Luo, C. Matranga, S. Tan, N. Alba and X. T. Cui, *Biomaterials*, 2011, **32**, 6316.
19. Y. K. Lee, J. K. Choi, Y. J. Kang, H. W. Kim, S.-W. Kim, C.-K. Park, D. Khang and S.-H. Kim, *J. Mater. Chem. B*, 2016, **4**, 1660.
20. J. R. Levick, *J. Rheumatol.*, 1990, **17**, 579.
21. Y. K. Lee, S. W. Kim, J. Y. Park, W. C. Kang, Y. J. Kang and D. Khang, *Int. J. Nanomed.*, 2017, **12**, 5761.
22. S. Foillard, J. Russier, C. Seifert, H. Dumortier and E. Doris, *RSC Adv.*, 2016, **6**, 53282.
23. J. Kayat, N. K. Mehra, V. Gajbhiye and N. K. Jain, *J. Drug Targeting*, 2016, **24**, 318.
24. P. Hassanzadeh, P. Arbabi, F. Atyabi and R. Dinarvand, *Life Sci.*, 2017, **179**, 66.
25. T. Murakami, K. Ajima, J. Miyawaki, M. Yudasaka, S. Iijima and K. Shiba, *Mol. Pharm.*, 2004, **16**, 399.
26. M. Nakamura, Y. Tahara, Y. Ikehara, T. Murakami, K. Tsuchida and S. Iijima, *Nanotechnology*, 2011, **22**, 465102.
27. J. Fan, M. Yudasaka, J. Miyawaki, K. Ajima, K. Murata and S. Iijima, *J. Phys. Chem. B*, 2006, **110**, 1587.
28. C. Zhong, J. Feng, X. Lin and Q. Bao, *Int. J. Nanomed.*, 2017, **12**, 1215.
29. J. Han, Y. S. Kim, M. Y. Lim, H. Y. Kim, S. Kong, M. Kang, Y. W. Choo, J. H. Jun, S. Ryu, H. Y. Jeong, J. Park, G. J. Jeong, J. C. Lee, G. H. Eom, Y. Ahn and B. S. Kim, *ACS Nano*, 2018, **12**, 1959.
30. N. D. Q. Chau, C. Ménard-Moyon, K. Kostarelos and A. Bianco, *Biochem. Biophys. Res. Commun.*, 2015, **468**, 454.
31. J. H. Byeon and J. H. Park, *Sci. Rep.*, 2016, **6**, 34890.
32. N. Karousis, I. Suarez-Martinez, C. P. Ewels and N. Tagmatarchis, *Chem. Rev.*, 2016, **116**, 4850.

33. P. Melgar-Lesmes, A. Luquero, M. Parra-Robert, A. Mora, J. Ribera, E. R. Edelman and W. Jiménez, *Nano Lett.*, 2018, **18**, 5839.
34. J. Saleem, L. Wang and C. Chen, *Adv. Healthcare Mater.*, 2018, **7**, 1800525.
35. K. P. Loh, D. Ho, G. N. C. Chiu, D. T. Leong, G. Pastorin and E. K. Chow, *Adv. Mater.*, 2018, **30**, 1802368.
36. A. F. Rodrigues, L. Newman, D. A. Jasim, I. A. Vacchi, C. Ménard-Moyon, L. E. Crica, A. Bianco, K. Kostarelos and C. Bussy, *Arch. Toxicol.*, 2018, **92**, 3359.
37. B. Fadeel, C. Bussy, S. Merino, E. Vazquez, E. Flahaut, F. Mouchet, L. Evariste, L. Gauthier, A. J. Koivisto, U. Vogel, C. Martin, L. G. Delogu, T. Buerki-Thurnherr, P. Wick, D. Beloin-Saint-Pierre, R. Hischier, M. Pelin, F. Candotto Carniel, M. Tretiach, F. Cesca, F. Benfenati, D. Scaini, L. Ballerini, K. Kostarelos, M. Prato and A. Bianco, *ACS Nano*, 2018, **12**, 10582.
38. R. Alshehri, A. M. Ilyas, A. Hasan, A. Arnaout, F. Ahmed and A. Memic, *J. Med. Chem.*, 2016, **59**, 8149.
39. K. Bhattacharya, S. P. Mukherjee, A. Gallud, S. C. Burkert, S. Bistarelli, S. Bellucci, M. Bottini, A. Star and B. Fadeel, *Nanomedicine*, 2016, **12**, 333.
40. C. Martin, K. Kostarelos, M. Prato and A. Bianco, *Chem. Commun.*, 2019, **55**, 5540.

CHAPTER 3

Multivalent Glycosylated Carbon Nanostructures: Efficient Inhibitors of Emergent Viruses Infection

JAVIER RAMOS-SORIANO[a], ALFONSO PÉREZ-SÁNCHEZ[a], BEATRIZ M. ILLESCAS*[a], JAVIER ROJO[b], RAFAEL DELGADO[c] AND NAZARIO MARTÍN*[a]

[a]Departamento de Química Orgánica, Facultad de Química, Universidad Complutense, 28040 Madrid, Spain; [b]Glycosystems Laboratory, Instituto de Investigaciones Químicas (IIQ), CSIC – Universidad de Sevilla, Av. Américo Vespucio 49, Seville 41092, Spain; [c]Laboratorio de Microbiología Molecular, Instituto de Investigación Hospital 12 de Octubre (imas12), 28041 Madrid, Spain
*E-mail: beti@ucm.es, nazmar@ucm.es

3.1 Introduction to Emergent Viruses

The infection of humans by lethal pathogens such as emergent viruses, namely Ebola, Dengue, Zika and other related viruses, has not been properly addressed so far. Thus, Ebola virus (EBOV) is among the most lethal pathogens for humans. Since its initial description in 1976 in Zaire (now DRC), several outbreaks have been reported mainly in Central Africa.[1] EBOV belongs to the Zaire Ebolavirus species within the Ebolavirus family where

Nanoscience & Nanotechnology Series No. 48
Carbon Nanostructures for Biomedical Applications
Edited by Tatiana Da Ros, Nazario Martín and Jean-Francois Nierengarten

Published by the Royal Society of Chemistry, www.rsc.org

three additional varieties of highly pathogenic agents: Sudan, Tai forest and Bundibugyo viruses, have also been described.[2] There is a fifth variety known as Reston virus, which is endemic in certain areas in Asia, that apparently is not pathogenic for humans.[3] Although some fruit bats have been identified to be carriers of EBOV genetic sequences, still the natural reservoirs of EBOV are not clear and this is crucial information for surveillance and prevention of future outbreaks.[4–6]

The recent Ebola outbreak in West Africa (2013–2016) was caused by EBOV and has been unprecedented in the number of infected cases. Over 28 000 cases and a toll of more than 11 000 fatalities have been officially reported[7] in the main affected area of Guinea, Sierra Leona and Liberia and also some cases in neighboring countries such as Nigeria, Mali and Senegal. Apart from the devastation in West Africa, this outbreak fueled a health emergency of international concern since Ebola-infected patients traveling from or evacuated out of Africa were treated in the USA, UK, Spain, France, Germany, Italy, Switzerland and Norway.[8]

There is no specific treatment for EBOV and supportive therapy based in the treatment of complications and active fluids and electrolytes replacement remained as the basis for patient's management during this outbreak.[8,9] A variety of experimental compounds, such as EBOV specific monoclonal antibodies (ZMapp), interference RNA (TKM) or inhibitors of the viral RNA polymerase (Brincidofovir, Favipiravir (T-505) and GS-5734) (Figure 3.1) have shown therapeutic potential in experimental animal models of infection, rodents and non-human primates (NHP). Recently, an inhibitor of viral RNA polymerase has been developed. This nucleoside analog (BCX4430) has shown protection against Ebola as well as Marburg viral infection in a rodent model. Moreover, it has been demonstrated that this compound also protects non-human primates even 48 h administration after exposure to Marburg virus infection.[10] Phase 1 clinical studies with these new promising compounds are ongoing.[11–14] However, thus far, none of them have demonstrated clinical efficacy since they have only been anecdotally used in selected patients or in relatively small non-controlled clinical trials.[15–20]

At the beginning of the aforementioned last outbreak, there were also two prototypes of vaccines to prevent EBOV infection that had been tested in NHP with encouraging results but never used in human beings. In an accelerated process to fulfill the safety and immunogenicity requirements in humans, the two vaccines, both virally vectored in chimpanzee adenovirus (ChAD) and in vesicular stomatitis virus (VSV), respectively, were ready to be administered in the affected area in early 2015, at a time where the epidemic was waning and new cases started to be significantly reduced. Only results of efficacy from the VSV-based vaccine are available at this moment and, although involving a relatively small group of individuals, the vaccine showed 100% protection against EBOV when immediately administered to contacts of infected patients as compared with a control group that was vaccinated with a delay of 3 weeks.[17] Despite these promising results, questions remain on

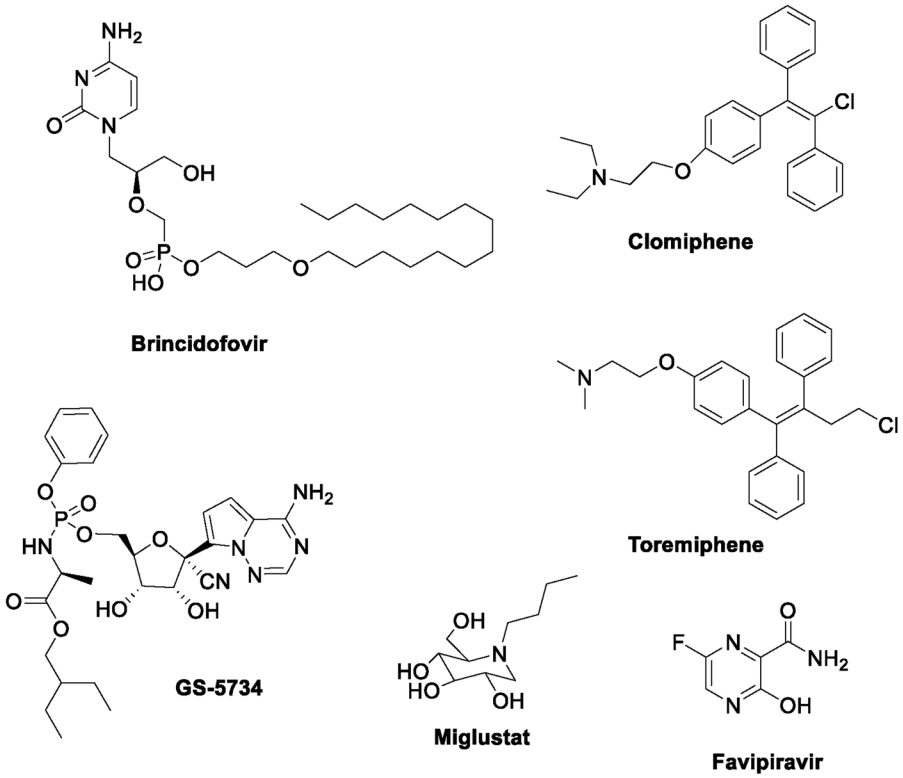

Figure 3.1 Chemical structures of Brincidofovir, Clomiphene, Toremiphene, GS-5734, Miglustat and Favipiravir.

the duration of protection and the potential coverage against other members of the ebolavirus family such as Sudan or Bundibugyo viruses.

In the search for molecules against Ebola virus infection, a variety of approaches have been addressed and promising compounds are again in the pipeline waiting for evaluation.[13] A new approach consists of the use of some small molecules that were previously FDA-approved as drugs for different indications, which have now been tested as potential Ebola virus inhibitors. These small molecules present very different chemical structures and mode of actions with different targets in the viral infection cycle. Clomiphene and Toremiphene (Figure 3.1) are FDA-approved drugs with a similar structure but different indications. Clomiphene is used to treat infertility while Toremiphene is approved to treat advanced breast cancer. Both are estrogen receptor ligands and are capable of inhibiting the EBOV entry and internalization *in vitro*. Recently, the capacity of these molecules to inhibit Ebola infection in a murine Ebola infection model has been shown.[14]

Another example is the *n*-butyl-deoxynojirimycin (Miglustat), an aminosugar derived of the D-glucose approved by the FDA to treat type I Gauche disease (GD1) (Figure 3.1). This is a well-known inhibitor of the enzyme

α-glycosidase and its antiviral activity by the modification of the *N*-glycan composition of the viral envelope glycoproteins has been proved.[15] However, a recent study using these iminosugars as inhibitors of Ebola infection in a guinea pig model showed very limited protection.[21–23]

The lack of information on the mechanism of infection, the need to use BSL4 laboratories to manipulate the wild virus – with the implications in terms of cost and accessibility that this means – as well as the scarce opportunities to carry out clinical studies on the ground with infected patients – usually concentrated in remote areas in Central Africa – are the main reasons preventing progress in this field.

The current situation on related emergent viruses is not more optimistic. Actually, there are no approved vaccines or specific treatment for Zika virus (ZIKV) infection and, as the evidence of the teratogenic effects of Zika increases, it has become even more necessary to investigate antiviral and preventive strategies to counteract its devastating potential. The social and economic cost of the recent spread of the Zika virus in Latin America and the Caribbean will total an estimated US$7–18 billion between 2015 and 2017 (United Nations Development Programme).[24,25]

ZIKV is a positive single-strand RNA virus transmitted by mosquitoes of the Aedes genus during epidemic spread and from human to human by vertical transmission (pregnant women to fetuses) and also through sexual contact since ZIKV is present at high concentrations in semen and genital fluids during and after symptomatic infection.[26] Amazingly, the infective process of ZIKV is largely unknown. However, in experiments with human skin cells, it appears that ZIKV uses C-type lectin receptor DC-SIGN (Dendritic Cell – Specific Intercellular adhesion molecule 3 Grabbing Nonintegrin) among other receptors on a host cell surface to enter the cytoplasm by receptor-mediated endocytosis.[27] DC-SIGN has been shown to be a significant receptor in the infection and pathogenesis of another flaviviruses such as Dengue virus (DENV).[28]

In this context, a question arises: what can chemistry do in the search for new strategies and approaches to solve this emergent and urgent problem? Although a variety of known chemical compounds – for other different purposes – have been disappointingly tested against virus infections, more specific molecules are dramatically required to be prepared.[29]

3.2 Supramolecular Carbohydrate–Protein Interaction

3.2.1 DC-SIGN as Target Molecule

Carbohydrates are a family of complex biomolecules involved in several relevant biological processes (physiological as well as pathological ones) such as fertilization, cell differentiation, inflammation, pathogen infection, tumor progression and metastasis, among others.[30] In fact, most mammalian cells

are covered by a dense coat of complex carbohydrates (glycolipids and glycoproteins embedded in the cell membrane) known as the glycocalix. This glycocalix is responsible for facilitating the interaction of a cell with other cells, the extracellular matrix, pathogens, *etc.* or in other words, to mediate the communication of the cell with the environment. This communication is the base of the social behavior of the cells, which means a transfer of information that takes place through the interaction between the carbohydrates of the glycocalix and the corresponding receptors. These receptors are mainly lectins, proteins that have at least one carbohydrate recognition domain (CRD).

In 1992, looking for proteins capable of interacting with gp120, a lectin (CD209) was discovered by serendipity.[31] This protein remained in the dark until the group of van Kooyk and Figdor showed that this lectin, renamed Dendritic Cell – Specific Intercellular adhesion molecule 3 Grabbing Nonintegrin (DC-SIGN) was able to recognize self-glycoproteins as intercellular adhesion molecule 3 (ICAM3).[32] Moreover, the groups of van Kooyk and Littman demonstrated that DC-SIGN played a main role in the *trans*-infection of T-cells by HIV.[33] DC-SIGN, at the surface of dendritic cells, interacts with the gp120 envelope glycoprotein of HIV to be internalized into the dendritic cells. Then, these cells mature and migrate to the lymph nodes where they present the intact HIV to T-cells, producing the infection of these cells. This discovery encouraged the interest of many groups in this lectin. Moreover, many pathogens including not only viruses such as HIV, Ebola, Dengue, SARS and others but bacteria, fungi and parasites also use DC-SIGN in their infection processes.[34] For this reason, DC-SIGN has been considered as a universal pathogen receptor and a very interesting target for the design of new anti-pathogen drugs.

In the last few decades, several contributions and a lot of information concerning DC-SIGN has been provided and is nowadays available. The first crystal structure between a pentasaccharide and the CRD of DC-SIGN was published in 2001.[35] Later, other structures of complexes between different carbohydrates and DC-SIGN have been solved, providing an overview of the binding mode of carbohydrates at the solid state.[36–39] To complement this information, NMR has been an ideal technique to obtain valuable information of carbohydrate–lectin complexes in solution,[40,41] and it has been applied to DC-SIGN to obtain binding modes, the main epitope, *etc.*[38,42–45] All this information together has provided a picture of how these carbohydrates are recognized by DC-SIGN, being the base for the design of new ligands with higher affinity and selectivity for this receptor.

DC-SIGN is found as microdomains present in patches with a diameter around 200 nm at the cell membrane of immature dendritic cells. These lectin clusters facilitate the capture of pathogens and their subsequent internalization. In this presentation, several CRDs are exposed in the cell surface to mediate multivalent interactions with pathogen surface carbohydrates leading to effective recognition processes.[46–48] So, this lectin presentation should be the real target for the design of compounds capable of competing efficiently with pathogens inhibiting their entrance into the cells.

3.2.2 Multivalency as a Concept for Efficient Inhibitors of Virus Infection

The interaction between carbohydrates and lectins presents particular features, the interaction is highly selective, in most of the cases depends on divalent metals (calcium) and presents a weak affinity (typically in the mM to μM range). Nature uses the multivalent effect to overcome the weak affinity limitation. Several copies of the carbohydrate ligands and the corresponding carbohydrate recognition domains of the receptors allow establishing simultaneous multiple interactions to increase, not only the affinity of the process (avidity) but also the selectivity. This fact, known as the cluster effect, is fundamental to the relevant carbohydrate–protein interactions.[49,50] Understanding multivalency is a hot topic in the carbohydrate field. However, this process is so complex from the molecular point of view that the explanation to justify the increment of affinity in multivalency is not clear. Several effects can contribute simultaneously to the multivalent interaction: clustering, rebinding, chelation, *etc.* It is assumed that more than one effect contributes to the outcome of the multivalent interaction simultaneously but it is not possible to evaluate the weight of each of these contributions separately.

Pathogens, including viruses, use a multivalent strategy to achieve a good docking on cell surfaces facilitating the internalization into targeting cells during the first stages of the infection process. Highly glycosylated envelope glycoproteins and the highly expressed cell surface DC-SIGN in the microdomains are the main partners to create these multivalent contacts.[45–48] Then, effective multivalent carbohydrate–protein interactions are established to facilitate the infection. Therefore, this can be considered as a target point to inhibit the infection process and to develop antiviral agents.

As mentioned above, the design of new carbohydrate glycomimetic ligands for DC-SIGN is an option to improve the development of a new antagonist of this lectin. However, this improvement, in quantitative terms, means normally dissociation constants in the μM range. To have an adequate antiviral drug, at least dissociation constants in the nanomolar range should be considered. Taking into account that achieving this value is an extraordinary challenge using monovalent ligands for DC-SIGN, carbohydrate multivalent tools are required to compete efficiently with this multivalent interaction.[51–53]

3.3 Synthesis of Suitable Functionalized Saccharides: Monomers, Trimers and Disaccharides

The search for compounds targeting the lectin DC-SIGN requires the selection of appropriate carbohydrate ligands. DC-SIGN recognizes mannosylated oligosaccharides such as high mannose, mannan, as well as fucosylated glycans, the blood type antigens Lewis a (Le^a), Lewis b (Le^b), Lewis Y (Le^y) and Lewis X (Le^x).[54] Besides these natural ligands, for which accessibility and

availability are limited, synthetic mimetics have been considered as a good alternative. In fact, the natural branched oligosaccharides are not trivial to be synthetized in the laboratory, being of high cost and time consuming. For this reason, simple monosaccharides or small oligosaccharides that contain the main epitopes of the natural ligands have been considered as potential candidates to be used as ligands for DC-SIGN.

Mannose is the smallest carbohydrate unit capable of interacting with DC-SIGN and other lectins that recognize these kinds of sugars, although the natural ligand for this lectin is the complex high mannose structure ($Man_9GlcNAc_2$) (Figure 3.2A). A middle situation between a very simple and not good ligand on one hand (mannose) and a very complex oligosaccharide on the other hand (the natural ligand high mannose) is the mannobioside disaccharide Manα1-2Man.

Although the synthesis of oligosaccharides is complex with several tedious protection and deprotection steps, the preparation of this disaccharide has been recently improved using a double strategy.[55,56] One of these strategies is based on a consecutive synthesis of the carbohydrate donor (the reducing end of the disaccharide) and its autoglycosylation.[55] In few steps with high yields and few purification steps, the disaccharide can be easily prepared on a large scale with a good overall yield in less than 3 days. The second strategy is a direct acetolysis of dried baker's yeast (*Saccharomyces cerevisiae*) that can be obtained in the supermarket at a very low cost. This acetolysis provides a mixture of peracetylated linear mannosyl oligosaccharides. The experimental conditions of this reaction can be optimized to produce mainly a mixture of peracetylated mannobioside and mannotrioside, easily separated

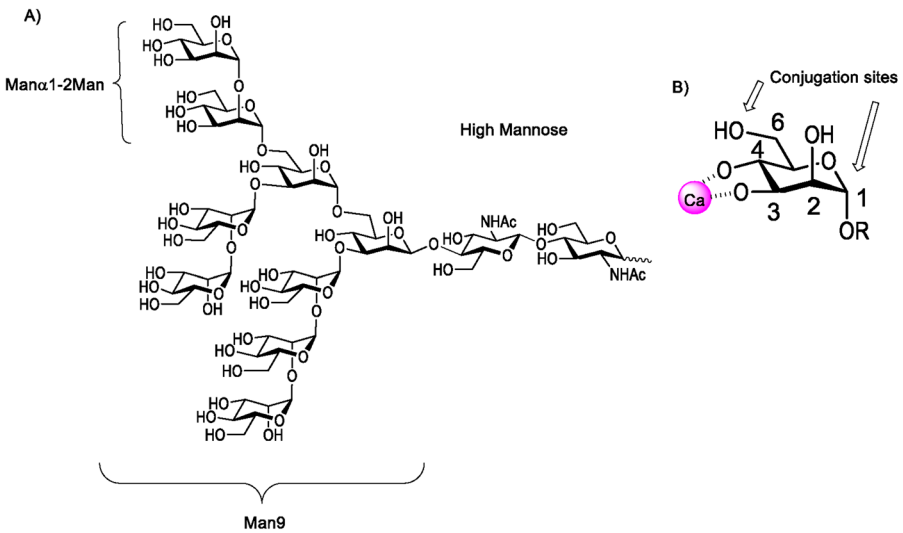

Figure 3.2 (A) Chemical structure of High Mannose ($Man_9GlcNAc_2$). (B) Mannose coordination sites to calcium and anomeric or 1 and 6 positions for conjugation.

chromatographically.[56] Therefore, in one step, from a very cheap starting material, it is possible to prepare, on a multigram scale, the disaccharide (Figure 3.3). This synthetic approach facilitates the accessibility of this relevant ligand on a large scale to create the corresponding carbohydrate multivalent systems.

It is well known, as discussed in section 2, that multivalent interactions are mandatory in carbohydrate–lectin interactions to have a biological relevance in terms of avidity. For this reason, the multivalent presentation of these carbohydrate ligands is required to establish multivalent interactions. There are plenty of examples describing many different multivalent scaffolds such as polymers, proteins, carbon nanoforms, dendrimers, nanoparticles, *etc.*, used to present carbohydrates in a multivalent way.[57] Due to space limitation and the scope of this book chapter, we are not going to discuss and analyze this plethora of multivalent scaffolds. However, it is important to discuss here how the carbohydrate ligands can be conjugated to these multivalent scaffolds without interferences with the binding mode to achieve an ideal multivalent presentation of the sugars that is critical to obtain good affinities.

C-type lectins recognize carbohydrate units by using a calcium atom present in the carbohydrate recognition domain. The sugar coordinates this Ca through the hydroxyl groups in positions 3 and 4 (Figure 3.2B).[36] Although the rest of the OH groups can be available to interact though hydrogen bonding to other residues of the binding site, in principle, these hydroxyl groups could be available to be functionalized facilitating the conjugation of these carbohydrates to the scaffolds for a multivalent presentation. For instance, the hydroxyl group in position 6 of mannose has been used to introduce a spacer with an azido terminal group to conjugate this sugar to a surface. Interaction

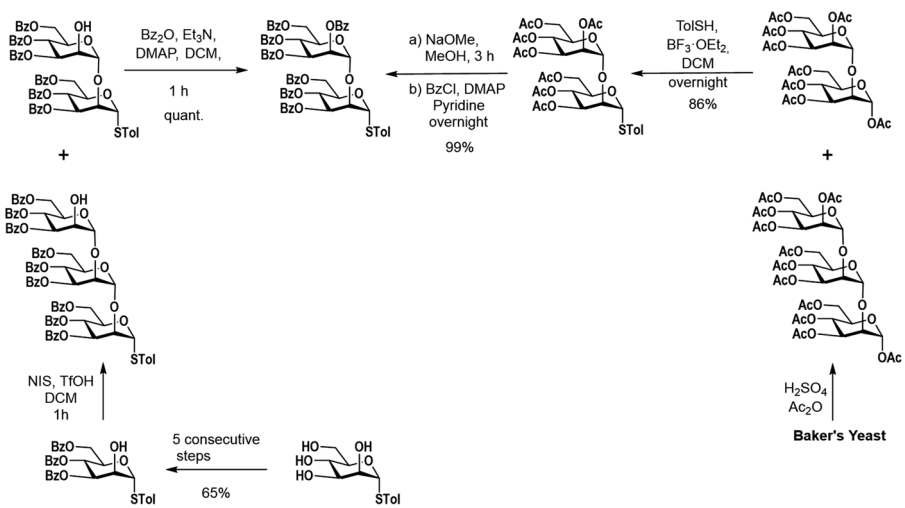

Figure 3.3 Schematic synthetic approaches to Manα1-2Man.

studies using SPR have demonstrated that the conjugation through this position does not have any negative effect on the binding capacity of this ligand to interact with DC-SIGN.[58] However, most of the glycoconjugates use the anomeric position (OH at position 1) at the reducing end of the glycan to conjugate the sugar to a scaffold (Figure 3.2B). The main reason for that, besides the non-relevant role of this position to the interaction, is the different reactivity of this hydroxyl group that facilitates its chemical manipulation. Using a selective glycosylation reaction, it is possible to introduce in this position any spacer conveniently functionalized for a subsequent conjugation.

Concerning the conjugation reaction, the simultaneous attachment of several carbohydrate units on a single scaffold requires very efficient chemistries. Full functionalization of the scaffold is fundamental, avoiding complex mixtures of compounds with similar characteristics, which makes the isolation of pure compounds leading to polydisperse materials complicated. One of the most popular approaches is the use of the well-known click chemistry, in particular the Copper (I)-Catalyzed Alkyne–Azide Cycloaddition (CuAAC). This reaction requires an azido group in one component of the reaction and a terminal alkyne group in the other.[59–61] These functional groups are compatible with many other functional groups (for instance, the OH of the deprotected carbohydrates) and can be easily incorporated in the partners to be conjugated. The reaction occurs under mild conditions in several solvents and with excellent yields. Although the introduction of these functional groups (azide or alkyne) at one end of the spacer at the anomeric position of the sugar is easy, most examples use the azido group in the glycan moiety because only one copy is required. Instead, introduction of several azido groups in the multivalent scaffold produce species that should be carefully handled due to the high concentration of nitrogen atoms leading to compounds with the potential capacity to be explosive.

An alternative to the CuAAC is a similar reaction without the intervention of metal atoms, the Strain Promoted Alkyne–Azide Cycloaddition (SPAAC).[62] In this case, the alkyne is embedded in a tensioned cycle, which provides the required reactivity driving the cyclization without the presence of a metal catalyst such as copper. This fact is of remarkable relevance in the case of biological applications of the constructed multivalent systems. Copper is a toxic residue for living cells and sometimes, the removal of the catalyst from the CuAAC reaction is not trivial – remaining traces of the toxic metal can interfere in the biological assays. For this reason, and although the introduction of the constrained cyclooctyne in one of the partners of the click reaction is synthetically more complicated than the incorporation of a simple alkyne, this SPAAC reaction can be found in many applications nowadays, in particular, in those reactions that implicate living cells.[63]

To improve the valency of the final system, on the one hand it is possible to increase the number of functional points of the scaffold introducing monovalent ligands in each point. In this case, the number of covalent bonds simultaneously created demands a very efficient conjugation strategy that is not always evident. On the other hand, higher valency can be achieved introducing multivalency in each functionalization point of the scaffold. This

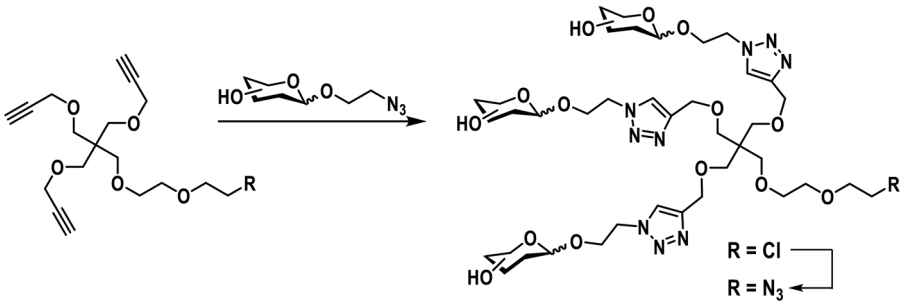

Figure 3.4 Synthesis of a trivalent glycodendron.

second approach is more interesting because the number of covalent bonds to be created simultaneously is reduced in this convergent strategy. Therefore, the approach needs the creation of a small multivalent carbohydrate system to be conjugated on the multivalent scaffold. A small glycodendron can be an easy way to achieve this goal. We have designed a trivalent glycodendron conveniently functionalized at the focal position to be conjugated using the CuAAC or the SPAAC reactions on alkynylated scaffolds.[64] Following the synthetic route depicted in Figure 3.4, a dendron with three carbohydrates (mannose or Manα1-2Man) was easily prepared in large scale with an azido group at the focal position to be conjugated with different scaffolds. In this way, the valency can be increased in a factor of three with the same number of covalent bonds created in the conjugation process.

With these tools on hand, it is possible to create, using a very efficient convergent strategy, complex carbohydrate multivalent systems as described in the next section.

3.4 Carbon Nanoform-based Glycoconjugates

3.4.1 Synthetic Approaches on Fullerenes. Chemical and Structural Characterization

One strategy to obtain antiviral agents against emergent virus infection is the design of glycoconjugates that mimic the surface of the virus and interfere with the infectious process blocking the corresponding cell-surface receptor.

In this sense, and particularly in the search for innovative scaffolds, we have focused on unexplored 3D fullerene C_{60} since it has a unique virus-like symmetrical and globular structure (~1 nm of diameter), which makes it an interesting biocompatible carbon platform for the multivalent presentation of carbohydrates.[65]

[60]Fullerene post-functionalizable hexakis-adducts with T_h symmetry constitute an attractive class of compounds that allow the globular disposition of substituents around the C_{60} core.[66] Post-functionalizable hexakis-adducts are generally easily obtained by the Bingel–Hirsch addition of malonates to C_{60}.[67] In particular, our research group have developed a straightforward strategy

based on the CuAAC reaction to click sugar residues to alkyne-substituted hexakis-adducts of [60]fullerene (Figure 3.5).[68,69] This strategy allows the introduction of 12 functional groups simultaneously in a regioselective and efficient way in few steps with good yields.

By employing this convergent strategy, we carried out for the first time the preparation of globular glycodendrofullerenes as antiviral agents against Ebola infection.[70] To study the effect of the steric congestion of these glycofullerenes on antiviral properties, two different glycodendrons were used to obtain final products with different spacers between the central fullerene core and the peripheral carbohydrate-substituted dendron appendage (Figure 3.6).

For the preparation of glycodendrofullerenes **3** and **4**, the conjugation of the hexakis adduct **1** with the corresponding glycodendron was performed using CuBr·$S(CH_3)_2$ as the catalyst in the presence of a piece of metallic Cu in DMSO affording glycodendrofullerenes with 36 mannoses in good yields.[71] Owing to the high cytotoxicity of copper, which can induce high cellular toxicity in biological assays, it was necessary to remove all traces of this metal. In this sense, a commercially available resin (QuadraSil Mercaptopropyl) was used. ICP analysis allowed the determination of the amount of copper present in the samples (copper concentration below 0.1%).

These compounds were completely characterized by using standard spectroscopic and analytical techniques (FTIR, ^{1}H and ^{13}C NMR spectroscopies and mass spectrometry). A simple FTIR analysis evidenced the absence of the typical bands for alkyne and azide groups (at ~2117 and 2092 cm^{-1}, respectively) present in the starting materials, indicating the efficiency of the cycloaddition step.

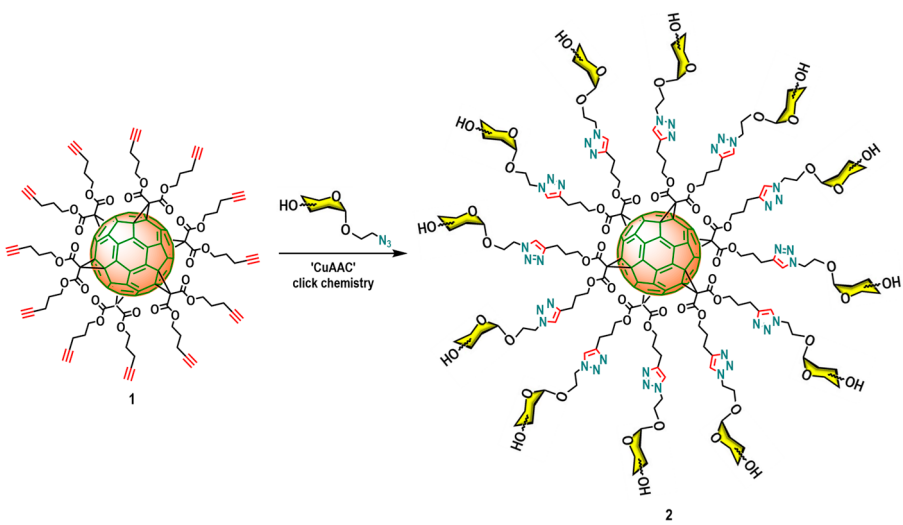

Figure 3.5 General scheme of a CuAAC reaction to click sugar moieties to an alkyne-substituted hexakis-adduct.

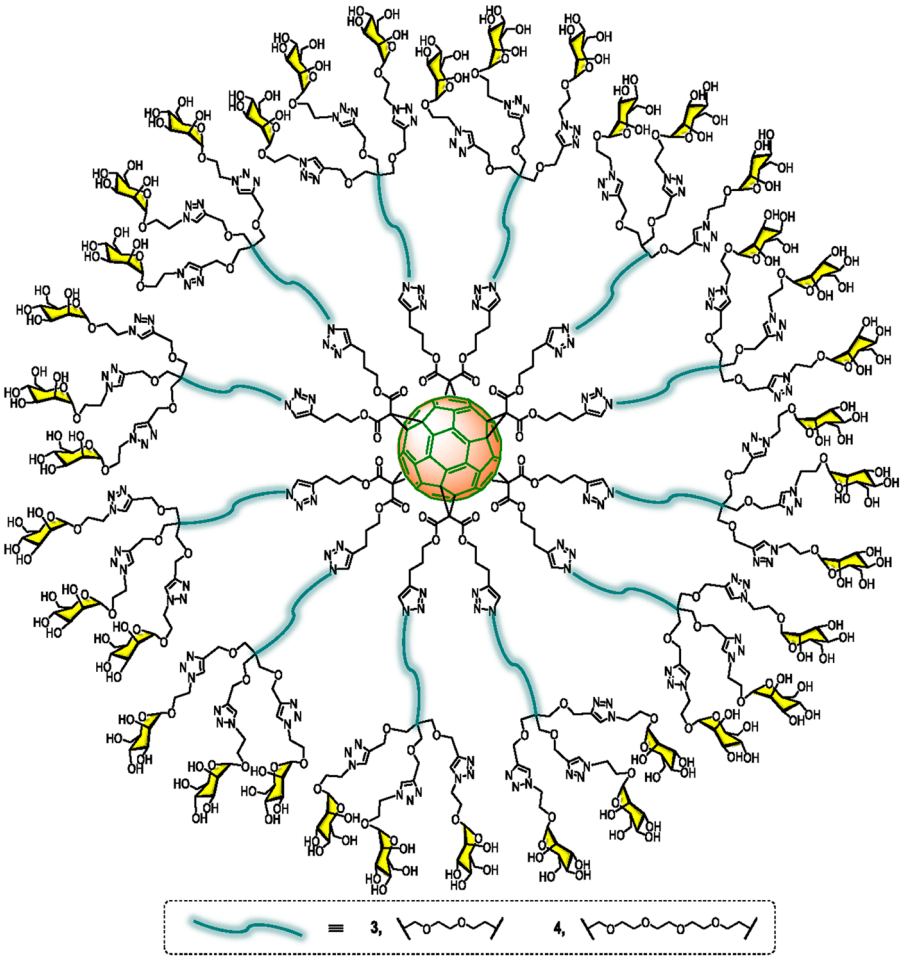

Figure 3.6 General structures of glycodendrofullerenes **3** and **4**.

Due to the success of this synthetic strategy, the preparation of tridecafullerenes in order to dramatically increase the valency and the size of the fullerene derivatives was addressed. These new tridecafullerenes, so-called 'superballs', are decorated with 120 peripheral carbohydrate ligands. They are formed by a central C_{60} scaffold in which the 12 alkyne moieties have been clicked to 12 sugar-containing [60]fullerene units (Figure 3.7).[72]

We carried out the synthesis of two different mannosylated superballs (**5** and **7**) employing the same methodology. Compound **7** contains a larger spacer between the peripheral carbohydrate-functionalized fullerenes and the fullerene central core. The aim of this ethylenglycol based linker is the increment of the flexibility of the carbohydrate moieties around the central fullerene allowing a better accessibility and availability of the sugars to interact with the cellular receptor, which could have an important influence

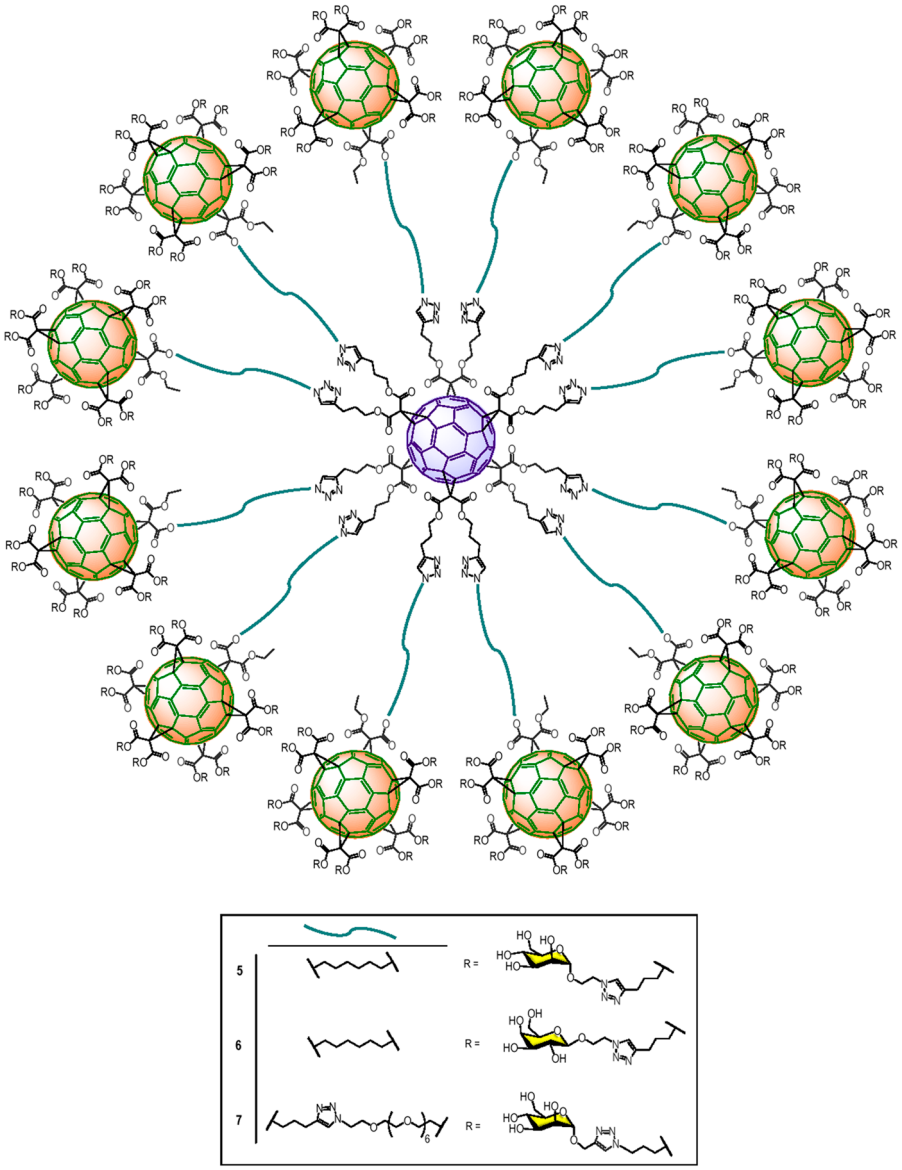

Figure 3.7 General structures of superballs **5**–**7**.

on the biological properties. Also, a tridecafullerene with 120 copies of galactose (**6**) was prepared as a negative control for the biological assays involving DC-SIGN as the target receptor, since this lectin is not able to recognize galactose.

As a typical example, the synthesis of compound **5** is depicted in Figure 3.8. The synthesis relies on the grafting of a clickable asymmetric $A_{10}B$ macromonomer onto a compact [60]fullerene hexa-adduct core bearing

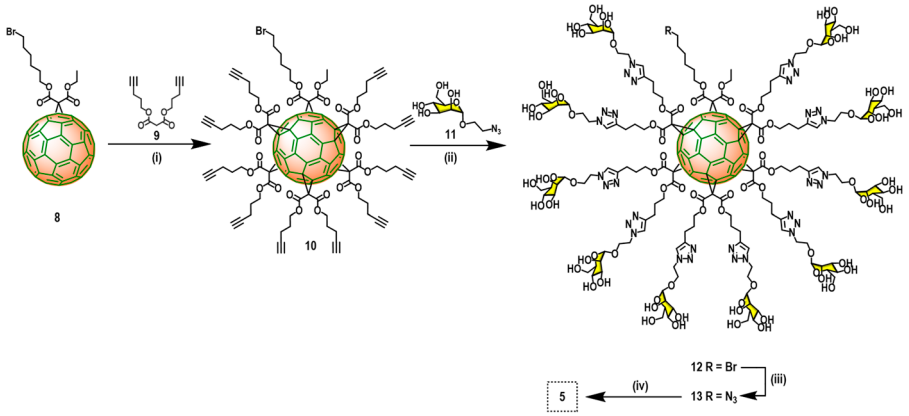

Figure 3.8 Synthetic scheme for tridecafullerene **5**. Reagents and conditions. (i) CBr_4, DBU, 20 °C, Tol, 72 h (49%); (ii) $CuBr{\cdot}S(CH_3)_2$, sodium ascorbate, Cu^0, DMSO, 72 h (86%); (iii) NaN_3, 70 °C (MW), DMSO, 3 h (84%); (iv) **1**, $CuBr{\cdot}S(CH_3)_2$, sodium ascorbate, Cu^0, DMSO, 25 °C, 48 h (73%).

12 terminal alkyne moieties. We first prepared an asymmetric $A_{10}B$ macromonomer [60]fullerene derivative **10** bearing 10 alkynes and a bromine atom at the focal point. To obtain the [5 : 1]-hexaadduct **10**, a tenfold excess of di(pent-4-yn-1-yl) malonate (**9**) and a ~50-fold excess of CBr_4 were added in the presence of 1,8-diazabicyclo[5.4.0]undec-7-ene (DBU) as the base and the methanefullerene **8**, which results from the Bingel nucleophilic cyclopropanation of C_{60} with 6-bromohexyl ethyl malonate.[73] This asymmetric compound **10** was submitted to the CuAAC reaction with 2-azidoethyl α-D-mannopyranoside (**11**) using $CuBr{\cdot}S(CH_3)_2$ as the catalyst and sodium ascorbate as the reducing agent in the presence of a piece of metallic Cu, to give derivative **12** in good yield. This derivative, after replacement of the bromine by an azide group, was then clicked to the symmetric hexa-adduct **1** under CuAAC conditions, leading to giant tridecafullerene **5** with ~70% yield. After the removal of copper, compound **5** was precipitated in the reaction medium and a pure sample was obtained. Thus, glycofullerenes containing 120 sugar moieties were obtained very efficiently in four synthetic steps by using a convergent strategy.

Despite the high molecular weights, the new compounds were characterized by standard spectroscopic techniques (FTIR, ^{1}H NMR and ^{13}C NMR spectroscopy) as well as by dynamic light scattering (DLS), transmission electron microscopy (TEM) and X-ray photoelectron spectroscopy (XPS).

^{13}C NMR characterization of fullerene derivatives is particularly relevant for demonstrating both the full functionalization of the alkyne residues and the octahedral symmetry of the structure (Figure 3.9). The absence of the typical signals corresponding to the alkyne groups (at ~69.0 and 83.0 ppm) and the signal of the CH_2 bound to the azido group at ~50 ppm indicated that

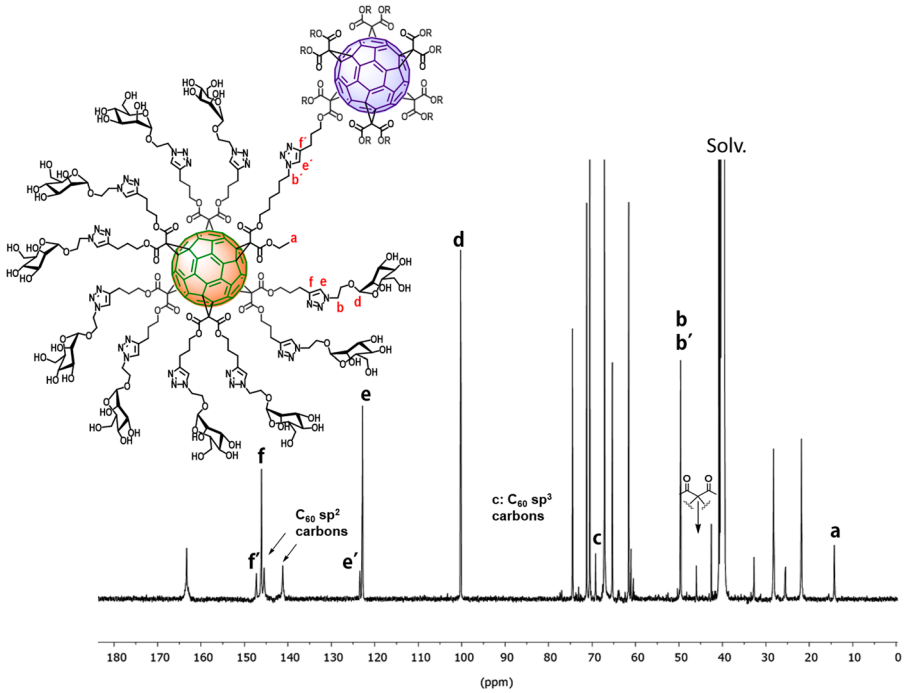

Figure 3.9 ^{13}C NMR spectrum of tridecafullerene **5** in DMSO-d_6. Assignment of the most representative signals is depicted. Adapted from ref. 72 with permission from Macmillan Publishers Ltd, Copyright 2015.

the cycloaddition step and the subsequent purification have been adequately carried out, respectively. Also, only two signals appear for the sp^2 carbons of the C_{60} cage (at ~141 and 145 ppm), together with the signal at δ ~69 for the two sp^3 carbons of the C_{60} core, thus providing evidence of the high T_h symmetry of the compound. The C atoms of the triazole rings are observed at δ ~147 and 123 ppm for the carbons of the outer triazole rings and at δ ~146 and 122 ppm for the carbons of the inner triazole rings. In addition, only one signal is detected for all the carbonyl groups (δ ~164) and the anomeric carbons of the sugar moieties (δ ~100), whereas the malonate bridgehead carbons present in the structure are observed at δ ~45 ppm. Owing to the tendency of these glycofullerenes to form aggregates in water, NMR spectra were recorded in DMSO-d_6.

TEM experiments reveal the presence of small spherical particles, corresponding to a few or even just one molecule (~4 nm), in good agreement with the experimental DLS analyses (Figure 3.10a and b).

XPS analysis provided us with the nature and relative abundance of the atoms present in the tridecafullerene. In this case, the spectrum for **5** shows

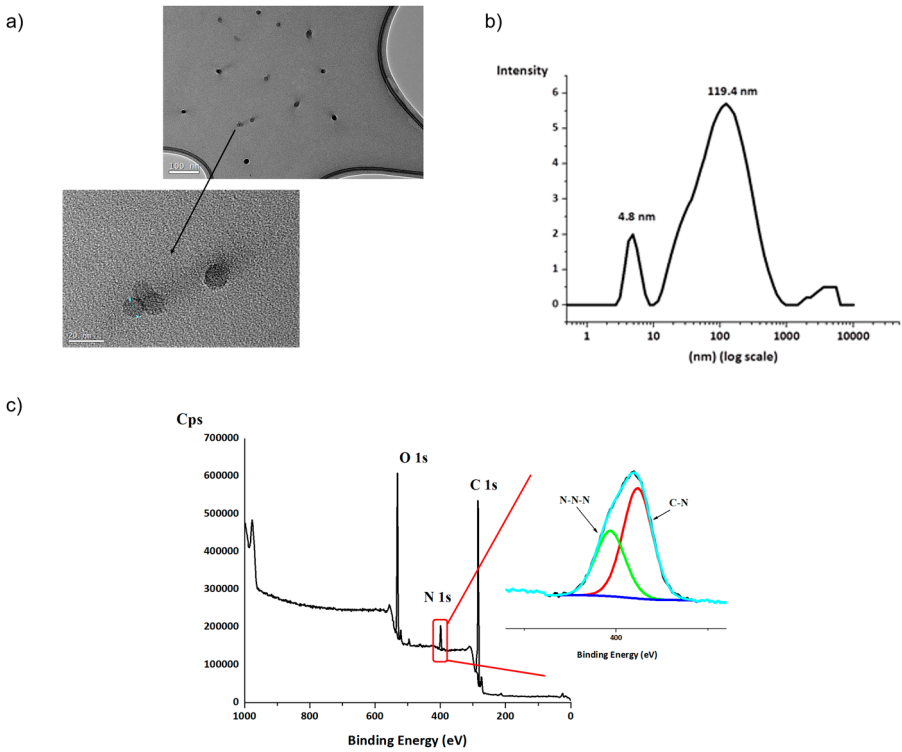

Figure 3.10 (a) TEM images of compound **5** on deposition of a 0.01 mg mL^{-1} solution in H_2O. These images show small spherical particles with a diameter of around 4 nm, which corresponds to a single molecule, together with some aggregates containing several molecules. (b) Representative DLS for **5** in H_2O, at a concentration of 0.01 M. Intensity *vs.* particle size. (c) XPS survey spectrum of compound **5** with the N 1s deconvoluted components (inset right). Adapted from ref. 72 with permission from Macmillan Publishers Ltd Copyright 2015.

the C 1s, O 1s, and N 1s features, with no additional spectroscopy signatures of possible impurities. The high-resolution N 1s core-level spectrum shows two components in a 1 : 2 ratio, attributed to one nitrogen atom of the triazole ring (N–**N**–N) and two nitrogen atoms attached to carbon atoms (C–**N**) (Figure 3.10c).

This successful methodology based on CuAAC reaction allowed us to obtain new sugarballs containing 12 to 120 sugar units. However, the use of copper (I) as the catalyst is a serious drawback, which involves a subsequent purification step for the removal of copper after the click reaction, owing to its high cytotoxicity. In addition, further increasing the multivalency of the glycoconjugates is difficult in the presence of this cytotoxic copper due to the

chelation ability of both the carbohydrate units and the triazole rings, which could affect the click reaction, lowering the yields and even, in some cases, inhibiting the reaction.[74] This is more noticeable in the particular case of the use of 1,2-mannobiosides as ligands on account of their ability for chelating copper between the two monosaccharide moieties.

To overcome these drawbacks, we proposed the synthesis of new post-functionalizable highly symmetric hexakis-adducts of [60]fullerene *via* metal-free click chemistry.[75,76] In particular, we employed a hexakis-adduct of C_{60} decorated with twelve cyclooctyne moieties to further carry out a SPAAC reaction (Figure 3.11, compound **14**).[75] The versatility of this new derivative has been tested with the addition of a variety of different natural products, including biotin, amino acids such as phenylalanine and peptide nucleic acid (PNAs) monomers such as thymine.

This new cyclooctyne-based platform allowed the addition of a variety of azides very efficiently and without the need of copper as a catalyst. Thus, the complete functionalization of the cyclooctyne moieties could be observed by ^{13}C NMR experiments, where the signals of the alkyne Csp carbons (at 110.1 and 92.8 ppm) disappeared after the click SPAAC reaction. Instead, roughly equal proportions of the two possible regioisomers was obtained at each cyclooctyne, with a slight excess of the less hindered isomer A (Figure 3.12).

Glycofullerenes based on this cyclooctyne central scaffold have also been synthesized by the addition of sugar functionalized azides very efficiently by heating the reaction mixture at 50 °C under microwave irradiation for 30 min (Figure 3.13), in contrast with the 48 h of reaction needed for a complete functionalization and lower yields obtained by employing the CuAAC

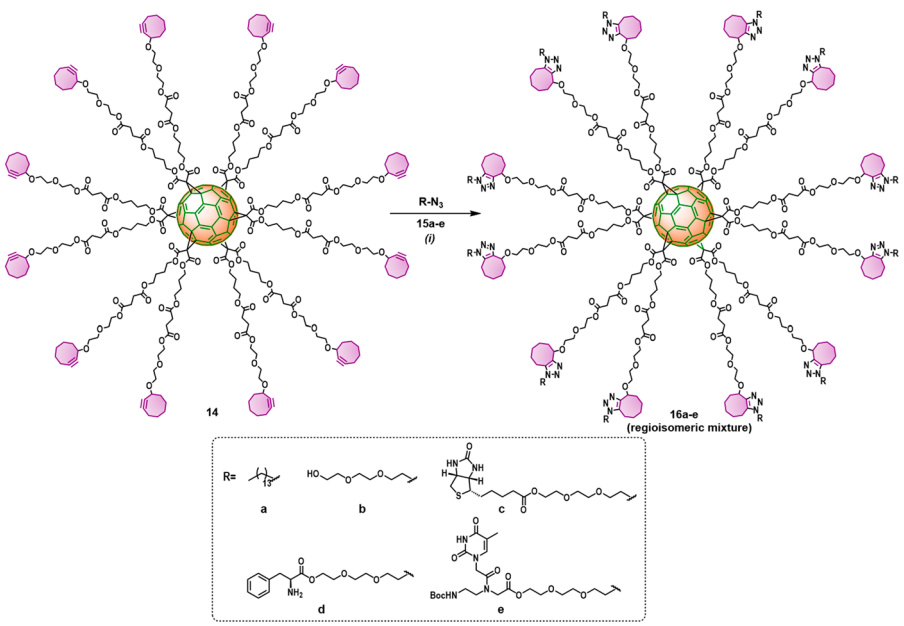

Figure 3.11 Synthetic scheme for compounds **16a–e**. Reagents and conditions. (i) DMSO, 50 °C under MW, 30 min (93–99%).

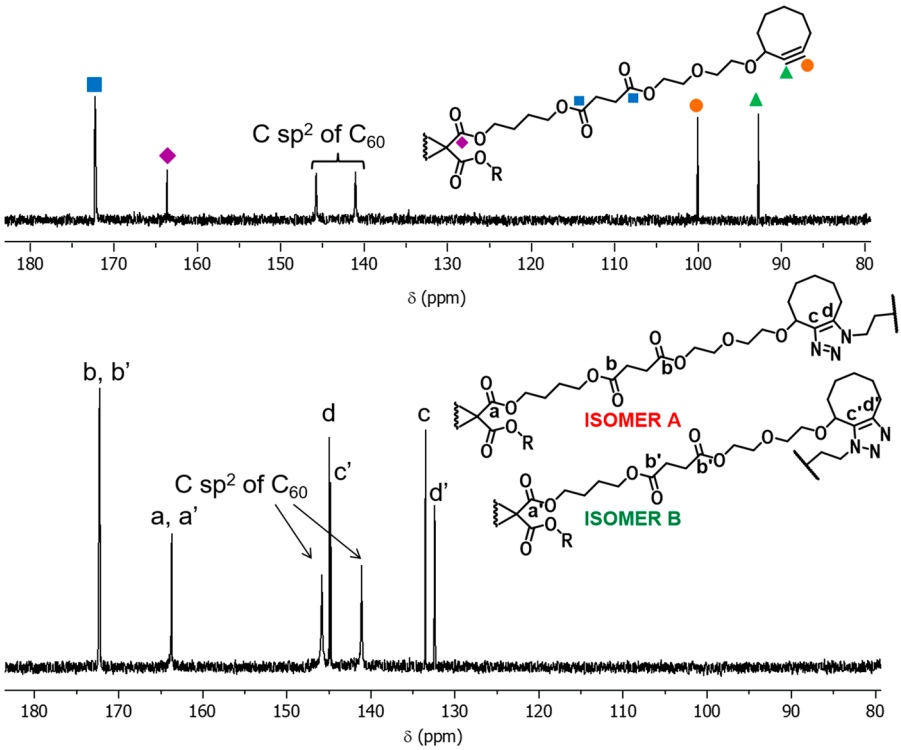

Figure 3.12 ^{13}C NMR spectra of compounds **14** (up) and **16a** (down) ($CDCl_3$, 125.8 MHz).

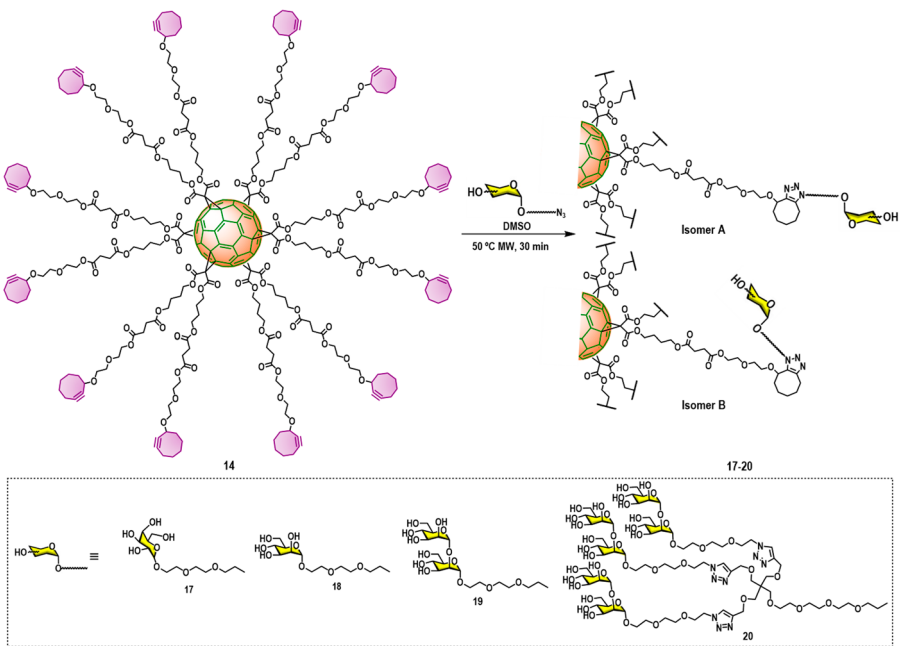

Figure 3.13 Synthesis of cyclooctyne based glycofullerenes.

strategy. Compounds **17**–**20** were purified by size-exclusion chromatography using Sephadex. The yields obtained were excellent in all cases.[77]

In order to increase the multivalency of the mannobiosylated glycofullerenes, we have carried out the synthesis of groundbreaking nanoballs decorated with 120 (**21**) and 360 (**22**) sugar functionalities. This last derivative, containing 360 disaccharides, has 41.370 atoms (C, H, O, N) and is obtained in a synthetic step which represents the fastest dendritic growth reported (Figure 3.14).

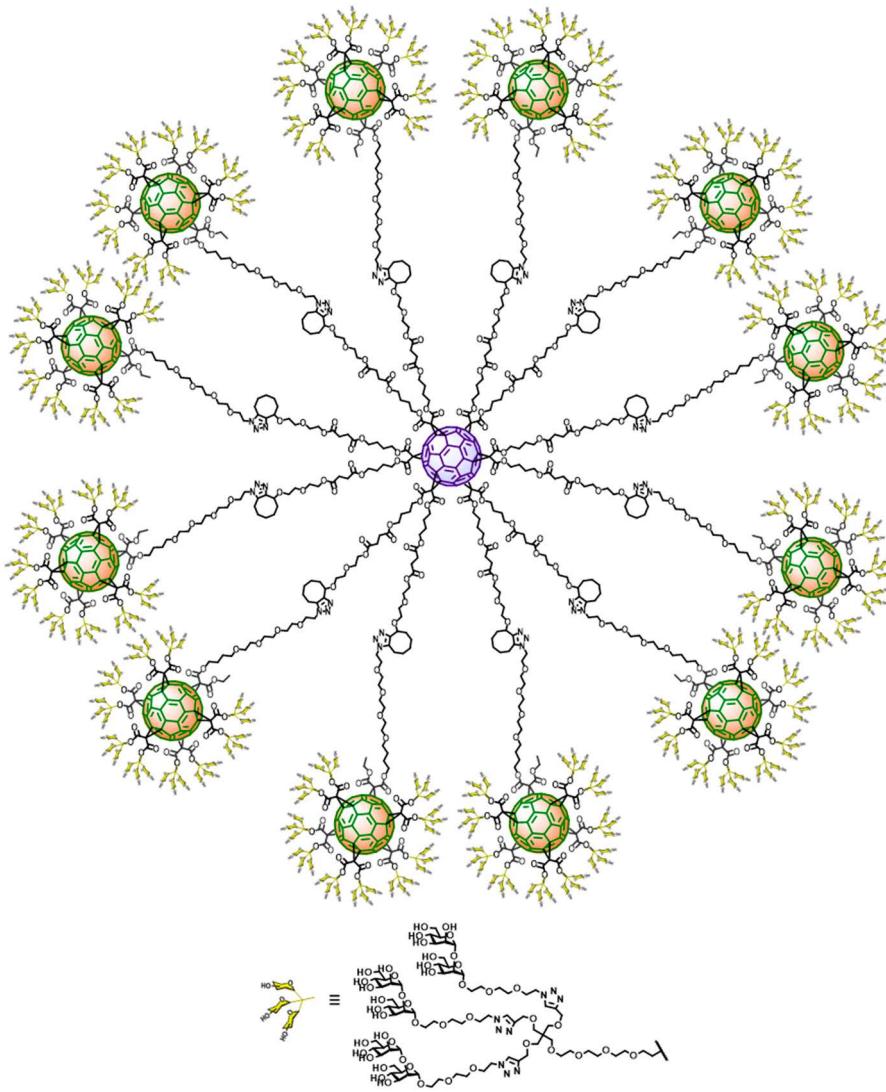

Figure 3.14 Schematic cartoon showing the chemical structure of tridecafullerene **22** appended with 360 1,2-mannobioside units synthesized by using the SPAAC click reaction.

To obtain these new tridecafullerenes **21**–**22**, a [5 : 1]-hexa-adduct derivative bearing 10 cyclooctyne moieties and a chlorine atom at the focal position was prepared according to the procedure depicted in Figure 3.15. The synthesis of this $A_{10}B$ macromonomer **29** starts from monoadduct **24**, which results from the Bingel–Hirsch nucleophilic addition of malonate

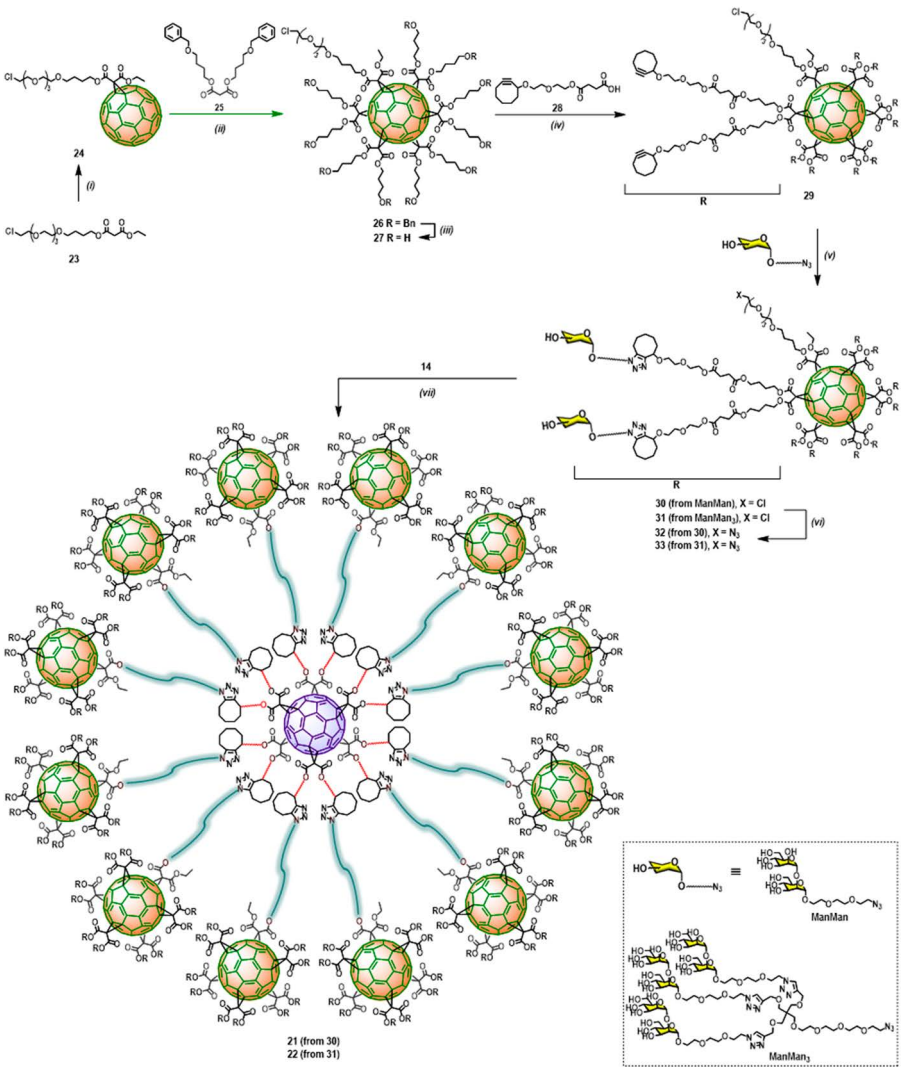

Figure 3.15 Reagents and conditions: (i) C_{60}, DBU, I_2, dry toluene, 0 °C, 4 h (71%); (ii) DBU, CBr_4, *o*-DCB, r.t., 72 h (48%); (iii) H_2, Pd/C, DCM/MeOH (3/1), r.t., overnight (quant.); (iv) DMAP, DCC, dry DCM/DMF (10/1), r.t., overnight (quant.); (v) DMSO, MW 50 °C, 30 min (quant.); (vi) NaN_3, DMF, 60 °C, 3 days (quant.); (vii) DMSO, MW 50 °C, 30 min (**21**: 98%, **22**: 94%).

23 to [60]fullerene. The reaction between methanefullerene **24** and an excess of malonate **25** (10 equiv.) in the presence of CBr_4 and DBU as the base gave the asymmetric hexakis-adduct **26** in moderate yield. After deprotection of the hydroxyl groups and esterification with cyclooctyne derivative **28**, compound **29** was quantitatively obtained. This clickable compound **29** was submitted to the SPAAC reaction under MW irradiation with azide substituted sugar **ManMan** and glycodendron **$ManMan_3$** affording the corresponding glycoderivatives **30**–**31** endowed with either ten or thirty disaccharides, respectively. The nucleophilic substitution of the chlorine atom by an azide group was carried out using sodium azide, which led to the clickable building blocks **32**–**33**. The azide-containing macromonomers **32**–**33** were then clicked to the symmetric cyclooctyne derivative **14** under SPAAC conditions to obtain nanoballs **21**–**22**, in which a central [60]fullerene scaffold is covalently bound to twelve C_{60} units, completely surrounded by mannobioside moieties. Purification of the obtained giant tridecafullerenes **21** and **22** was carried out by ultrafiltration (Amicon® Ultra-15) of a water solution.

3.4.2 Synthetic Approaches on Other Carbon Nanoforms. Chemical and Structural Characterization

Carbon nanostructures appear to be ideal candidates for the development of materials of the future. A wide variety of new carbon nanoforms (CNFs), such as single and multi-walled carbon nanotubes (SWCNTs/MWCNTs), endohedral fullerenes, carbon nanohorns (CNHs), carbon nanoonions, peapods, carbon nanotori, carbon nanobuds and more recently 2D graphene, graphene quantum dots (GQDs) and carbon quantum dots (CQDs) have given rise to a new set of carbon nanostructures which have attracted the attention of scientists (Figure 3.16).[78] Regarding biological applications, the chemical modification of these nanoforms enables an increase in their biocompatibility, providing new biological properties and preventing from toxicity by the asbestos-like behavior typically shown by them.

As not only multivalency, but also the size and shape of the platform employed for the multivalent presentation of carbohydrates seem to be very important for the interaction with cellular receptors, we decided to use different carbon nanoforms as scaffolds to generate multivalent nanosized glycoconjugates. Interestingly, these glycoconjugates mimic the shape or surface of the virus. In this sense, SWCNTs and MWCNTs with their elongated shape resemble the filamentous structure of Ebola virus, characteristic of a thread virus. For its part, HIV virus shows a roughly spherical form with a diameter of ~120 nm, comparable to the shape and size of SWCNHs. Therefore, SWCNTs, MWCNTs and SWCNHs can be considered as appropriate biocompatible platforms for the presentation of carbohydrates to interact with DC-SIGN in a multivalent way upon chemical modification.[79]

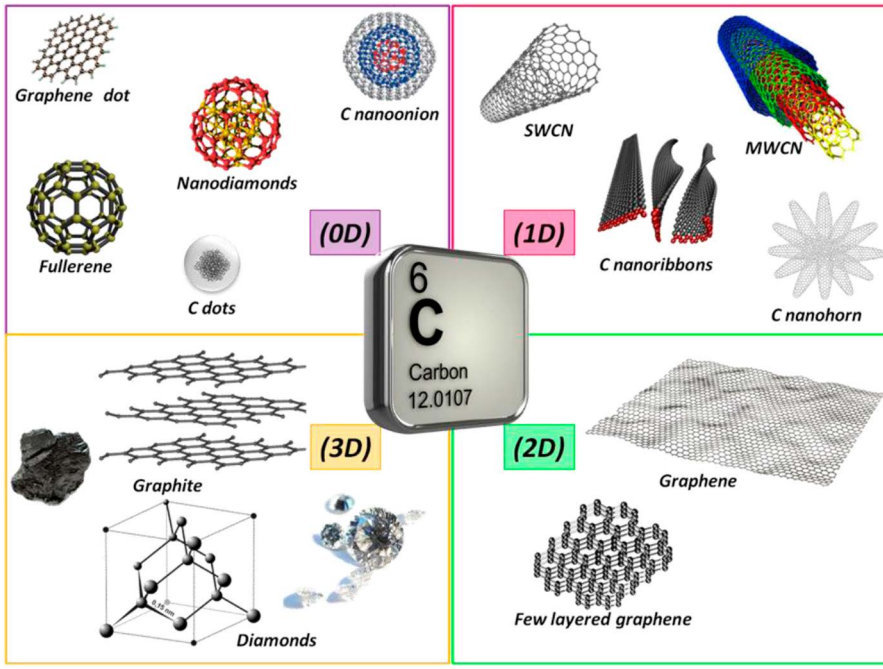

Figure 3.16 Different carbon nanostructures, all of them known allotropes of carbon.

The synthetic procedure followed for obtaining the final glycoconjugates has been carried out in an analogous manner for all the carbon nanomaterials. In a first step, the chemical modification of the carbon nanostructures to introduce protected alkyne functionalities was carried out. Later, in a second step, one pot deprotection of the terminal alkynes and CuAAC click reaction was accomplished. The introduction of the alkyne groups on the surface of the carbon nanoforms was performed by a Tour reaction by the *in situ* generation of aryl diazonium compounds from 4-[(trimethylsilyl)ethynyl]aniline and isoamyl nitrite as reactives (Figure 3.17).[80,81] This Tour reaction was performed overnight using NMP, H_2O or (1 : 1) mixtures of both solvents. Then, the reaction mixture was filtered on a 0.1 μm pore size membrane and washed with different solvents until the filtrated solution remained uncolored. Three cycles of this chemical process were necessary in order to increase the number of functional groups present on the carbon nanoform surface, followed by the same filtration methodology. Afterwards, the desired TMS-functionalized compounds were isolated.

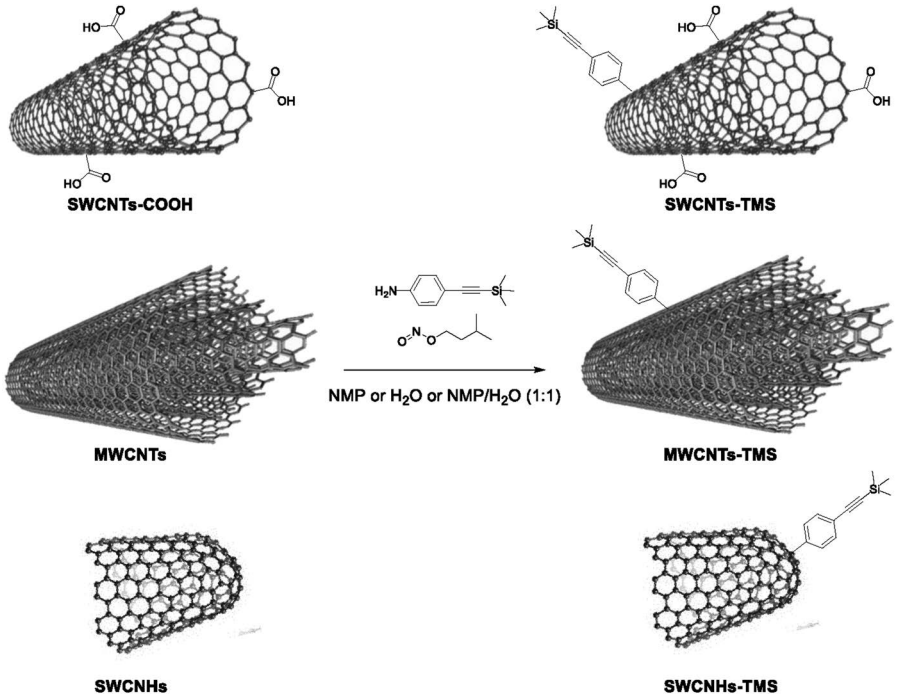

Figure 3.17 General synthetic procedure for the preparation of compounds **SWCNT-TMS**, **MWCNT-TMS** and **SWCNH-TMS**.

Afterwards, the alkyne-TMS derivatives **SWCNT-TMS**, **MWCNT-TMS** and **SWCNH-TMS** were submitted to a second step where the connection with the asymmetric azide-substituted hexakis-adducts of [60]fullerene conveniently functionalized with mannose residues was performed. For this purpose, an *in situ* desylilation based on the use of tetrabutylammonium fluoride (nBu$_4$NF) and subsequent reaction with the corresponding azide glycofullerene by means of a click chemistry methodology (CuAAC) followed by ultrasound bath sonication–filtration through a 0.1 μm membrane cycle yielded the functionalized glycoconjugates **SWCNT-C$_{60}$Man**, **MWCNT-C$_{60}$Man** and **SWCNH-C$_{60}$Man** (Figure 3.18). The click chemistry procedure was based on the use of CuBr·S(CH$_3$)$_2$ as copper catalyst, sodium ascorbate as reducing agent and some metallic copper wires, ensuring the presence of Cu^0 in the reaction media. Consecutively, the reaction mixture was filtered off and washed over a membrane several times with NMP, MeCN, *o*-DCB and MeOH. In a second washing step, the obtained solid was washed with water and acidic water (2% HNO$_3$), trying to make it free of copper materials. A galactose derivative **SWCNH-C$_{60}$Gal** was synthesized and used as a negative control in the biological assays.

To study if the presence of the [60]fullerene could have an effect on the biological activity of these hybrid glycoderivatives, the same CNFs were covalently modified with a glycodendron containing nine mannose units by

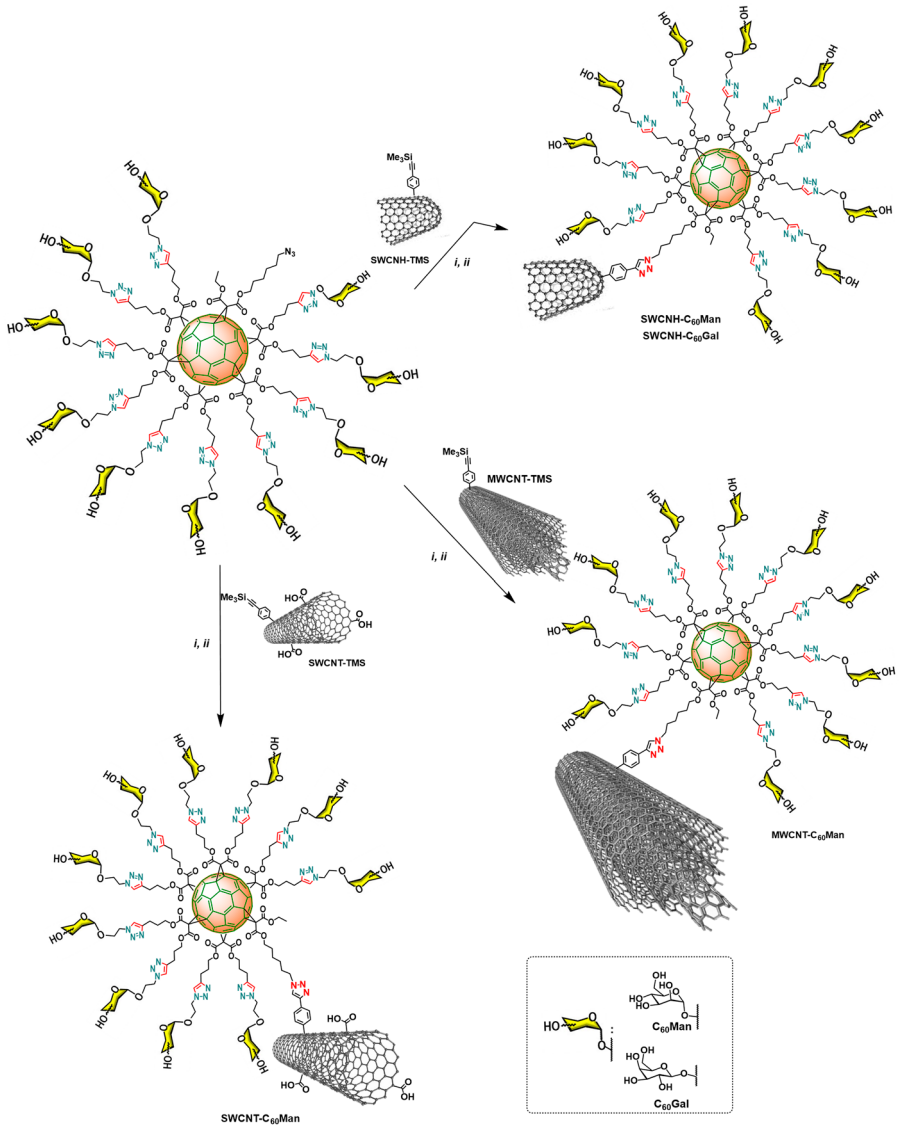

Figure 3.18 General synthetic procedure for the preparation of compounds **SWCNT-C_{60}Man**, **MWCNT-C_{60}Man**, **SWCNH-C_{60}Man** and **SWCNH-C_{60}Gal**. Conditions: (i) TBAF, NMP, 2 h; (ii) CuBr·S$(CH_3)_2$, sodium ascorbate, Cu^0, 60 °C, 6–7 days.

following the same procedure described above for the glycofullerenes. Thus, a new set of glycoconjugates was obtained, **SWCNT-glyMan**, **MWCNT-glyMan** and **SWCNH-glyMan** (Figure 3.19).

For the characterization of these hybrid materials, different techniques such as thermogravimetric analysis (TGA), Raman spectroscopy, Fourier

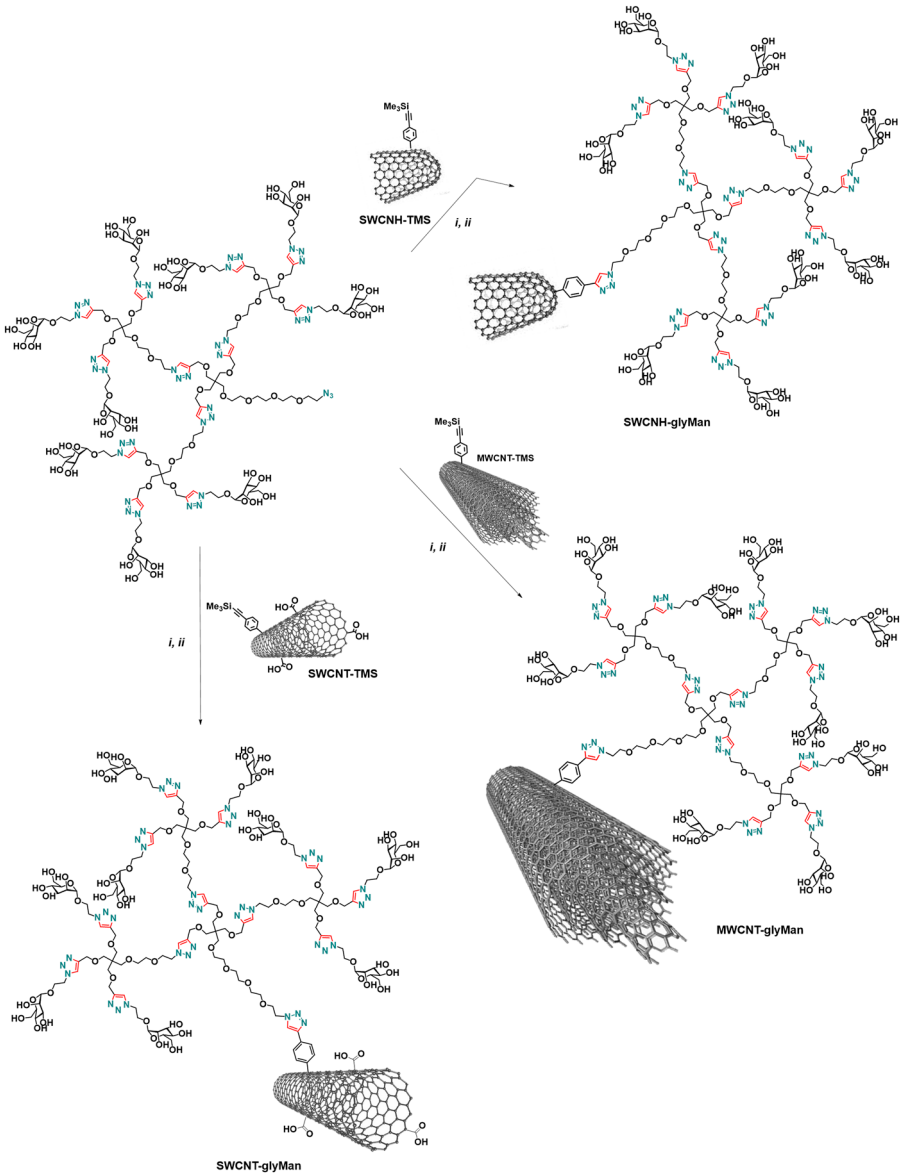

Figure 3.19 General synthetic procedure for the preparation of compounds **SWCNT-glyMan**, **MWCNT-glyMan** and **SWCNH-glyMan**. Conditions: (i) TBAF, NMP, 2 h; (ii) $CuBr{\cdot}S(CH_3)_2$, sodium ascorbate, Cu^0, 60 °C, 6–7 days.

transform infrared spectroscopy (FTIR), X-ray photoelectron spectroscopy (XPS) and transmission electron microscopy (TEM) were employed.

TGA, for instance, provides a quantitative estimation of the degree of covalent functionalization on all carbon nanoforms, therefore giving evidence of the sidewall functionalization. Pristine carbon nanoforms are stable up to 800 °C under a nitrogen atmosphere. Considering SWCNTs and its derivatives,

for example, and taking into account that SWCNTs were submitted to a previous oxidation process, the weight loss observed for this material of 26.85% at around 300 °C can be due to the oxygenated groups attached to the material surface, mainly carboxylic acid units (Figure 3.20). The weight loss associated with the decomposition of the organic phenylacetylene groups formed after the Tour reaction is measured between 100 and 600 °C. As an example, conjugate **SWCNT-TMS** shows a weight loss of 32.37% at this range of temperature. It reflects a 5.52% increase of the degree of surface functionalization from **SWCNT-COOH**. Glycofullerenes and glycodendrons decompose in a range of temperatures around 550 °C where the thermograms of **SWCNT-C_{60}Man** and **SWCNT-glyMan** show an additional weight loss of 50.08 and 45.69%, respectively. It is important to highlight that the surface reactivity of the different CNFs varies depending on the curvature of the tubes, giving rise to different functionalization degree of the walls. This different functionalization is corroborated by the decreasing weight losses observed when going from SWCNTs to SWCNHs and MWCTNs, the latter being less functionalized in agreement with their smaller curvature.

Raman spectra were recorded using a 785 nm laser wavelength for SWCNTs and MWCNTs and 532 nm for SWCNHs. These spectra show two bands with approximately equal scattering strengths related to the 'G band' and 'D band' at ~1590 and ~1300 cm^{-1}, respectively. The increase of the D-band intensity and the enlargement of the bandwidth for the tangential mode (G-band) are considered as proofs of the functionalization of the tubes' wall.[82,83] The I_D/I_G

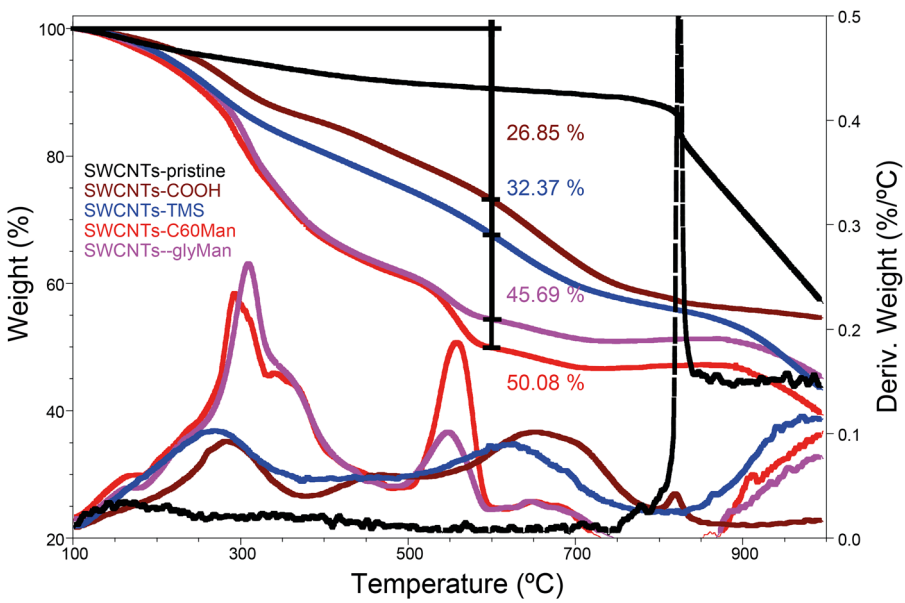

Figure 3.20 TGA under inert conditions of pristine **SWCNTs** (black), **SWCNT-COOH** (brown), **SWCNT-TMS** (blue) and the nanoconjugates **SWCNT-C_{60}Man** (red) and **SWCNT-glyMan** (purple). Reproduced from ref. 79 with permission from American Chemical Society, Copyright 2018.

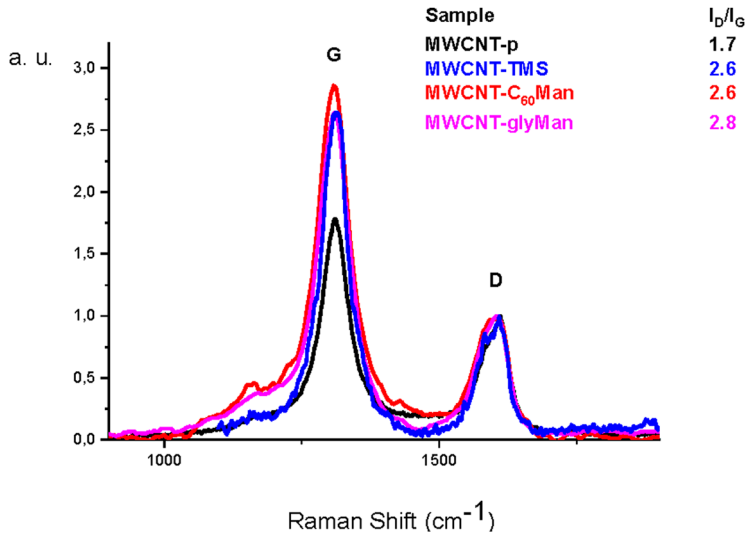

Figure 3.21 Raman spectra of pristine **MWCNT** (black), **MWCNT-TMS** (blue), **MWCNT-C_{60}Man** (red) and **MWCNT-glyMan** (pink) under 785 nm laser excitation wavelength. Reproduced from ref. 79 with permission from Amercian Chemical Society, Copyright 2018.

ratio is used to calculate the amount of covalent functionalities anchored on the CNF surface and suggests a substantial rehybridization from sp^2 carbon atoms to sp^3 going from pristine to derivatized CNFs. In the case of the nanostructures object of this study, an increase of the I_D/I_G ratio is observed when passing from the pristine material to the TMS-functionalized one, while this ratio is kept almost constant for the second functionalization step that is the CuAAC reaction (Figure 3.21). This is reasonable, as in this step no additional modification of the surface of the nanotubes is taking place.

XPS spectra are useful to analyze the elemental composition of the CNF surface. These spectra exhibit the electrons collected from C 1s, O 1s, N 1s and Si 2p core levels for all new hybrid derivatives. Other elements, which are present in very low concentration (<1%) related to solvent or surface impurities, are not considered for atomic concentration (%) calculations. As for the Raman characterization, comparison between the different derivatives gives an idea of the progress in the corresponding synthetic step.

Firstly, for derivatives **SWCNT-TMS**, **MWCNT-TMS** and **SWCNH-TMS** the absence of the N1s peak in the spectra – with the presence of the Si 2p signal related to the alkyne protecting groups – indicates correct functionalization in the Tour reaction. An increase in the oxygen peak intensity in the covalent conjugates after click chemistry reaction is due to the glycofullerene or glycodendron units, as expected. As an example, the semiquantitative analysis of **MWCNT-C_{60}Man** and **MWCNT-glyMan** reveals an oxygen content of 9.3 and 14.6%, respectively, which indicates functionalization when compared to the 4.8% measured for **MWCNT-TMS**. The N peak was observed just for sugar-functionalized derivatives formed after CuAAC (Figure 3.22).

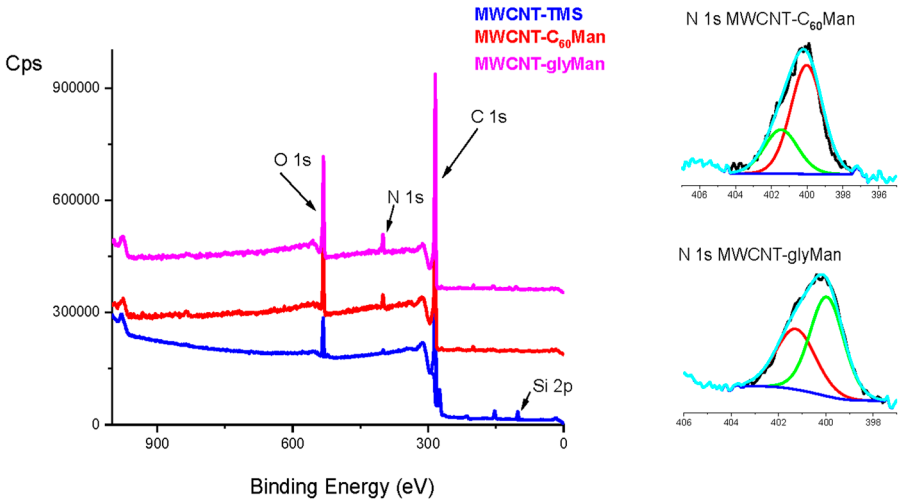

Figure 3.22 XPS spectra of **MWCNT-TMS** (blue), **MWCNT-C_{60}Man** (red) and **MWCNT-glyMan** (pink). Reproduced from ref. 79 with permission from Amercian Chemical Society, Copyright 2018.

When high-resolution spectra were performed, a C 1s signal was fitted to five components (sp^2 C=C, sp^3 C–C, C–O, C=O and COO units) for all the CNFs.[84] N 1s fitting shows two contributions, a major one at low binding energies due to N atoms directly bound to C atoms and a minor one assigned to the central N in the triazole ring.[85] No peak related to the azido group was observed.

TEM microscopy helps one to study the morphology of the new hybrid materials. In the case of the glycofullerene-appended derivatives **SWCNT-C_{60}Man**, **MWCNT-C_{60}Man** and **SWCNH-C_{60}Man**, small C_{60}-like round-shaped molecules attached to the CNTs' side wall surface or the SWCNHs' tips could be observed. The width profile for these spherical appendages is around 1 nm, in agreement with the [60]fullerene diameter. As an example, a **MWCNT-C_{60}Man** TEM image is shown in Figure 3.23.

Regarding micrographs of the glycodendron-functionalized conjugates **SWCNT-glyMan**, **MWCNT-glyMan** and **SWCNH-glyMan**, densely covered walls compared with the pristine materials were detected for all different CNFs. This can be assigned to the organic dendron functionalization covering the surface of the materials (Figure 3.24).

From the images obtained by this technique, it can be proved that SWCNTs present a high tendency to interact among them by attractive interactions such as π–π stacking and London forces, generating large bundles, even after oxidation and covalent functionalization. MWCNTs exhibit the same morphology but with fewer aggregation limitations. Finally, SWCNHs present a conical structure and a 'dahlia-like' spherical aggregation that is preserved after the different chemical steps they endure (Figure 3.24 (right panel)).

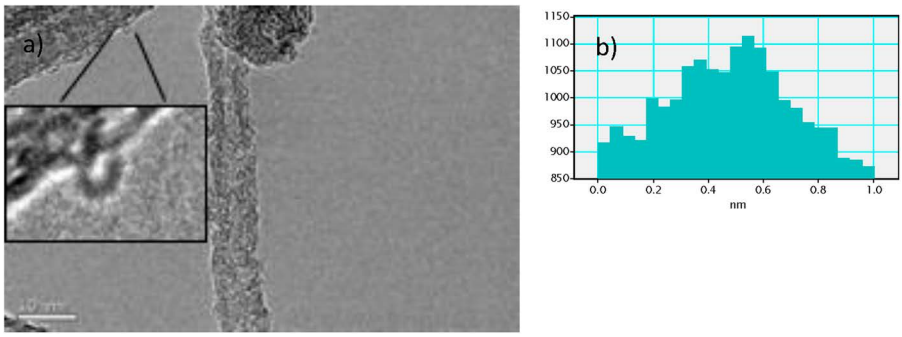

Figure 3.23 TEM image of the functionalized **MWCNTs:** (a) **MWCNT-C_{60}Man** with a scale bar of 10 nm. (b) Representative image of the width profile of the glycofullerene attached to the aggregate **MWCNT-C_{60}Man.** Reproduced from ref. 79 with permission from American Chemical Society, Copyright 2018.

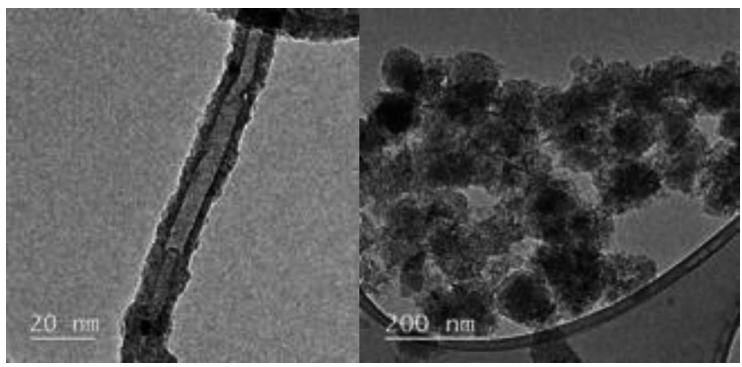

Figure 3.24 TEM image of the functionalized **MWCNTs** and **SWCNHs:** (Left) **MWCNT-glyMan** with scale bars of 20 nm. (Right) **SWCNH-glyMan** with a scale bar of 200 nm. Herein, aggregation of the nanoform is preserved, maintaining a 'dahlia-like' shape. Reproduced from ref. 79 with permission from American Chemical Society, Copyright 2018.

3.5 Biological Assays: Efficient Inhibition of Emergent Viruses Infection

3.5.1 Multivalent Glycosylated Carbon Nanostructures to Inhibit Ebola Virus Infection

As has been mentioned previously, this research is focused on the development of strategies to block a C-type lectin, DC-SIGN, which recognizes glycoconjugates present on the surfaces of several pathogens including viruses (HIV, Ebola, Cytomegalovirus, Dengue, SARS), bacteria (*M. tuberculosis, S. pneumoniae*) fungi (*C. albicans, A. fumigatus*) and parasites (*Leishmania, S. mansoni*).[34,86] It has been proven that this lectin plays a key role in the early

stages of the infection processes caused by some of these pathogens. Therefore, DC-SIGN can be selected as a new therapeutic target for the design of antiviral drugs.[87] A number of molecules, including DC-SIGN, have been proposed as receptors for Ebola virus (EBOV). Although DC-SIGN is not the main receptor in the case of the EBOV, it is thought to play a significant role in the cell entrance of this infectious agent in significant cell populations, such as dendritic cells and thus facilitates early viral dissemination. DC-SIGN is known to preferentially recognize high-mannose glycans that are *N*-linked to viral glycoproteins such the EBOV GP,[36] which contains 17 *N*-linked glycosylation sites.[88] Therefore, DC-SIGN can function as a good model for studying the first steps of pathogenesis of EBOV and screening the antiviral strategies based on DC-SIGN-targeting compounds for prevention and treatment purposes. DC-SIGN recognizes mannosylated and fucosylated oligosaccharides presented in a multivalent manner on the surface of several pathogen envelope GPs. Thus, the preparation of multivalent carbohydrate systems is necessary for an efficient interaction with this receptor as well as for effective competition with the natural ligands.

The DC-SIGN lectin receptor enhances cell-binding and infectivity of EBOV in dendritic cells and macrophages, the primary cell subsets infected during the initial stages of the disease.[89–91] To explore the role of DC-SIGN in EBOV infection, a CD4+ Jurkat T cell line modified by retroviral transduction to express DC-SIGN (Jurkat-DC-SIGN) has been used and validated.[92] T-lymphocytes such as Jurkat cells are naturally non-susceptible to EBOV infection,[92,93] nonetheless, DC-SIGN cell expression is sufficient to allow cell entry and infection by pseudotyped lentiviruses bearing EBOV GP. Recombinant viruses are produced by co-transfection in producer cells of the viral GP, along with the retroviral backbone expressing firefly luciferase as the reporter gene. The assay based on GP-pseudotyped viral particles has been extensively used for pathogenesis and antiviral screening by our group and others for different purposes, and it has been compared with live virus assays, showing strong correlation.[93–95]

In this system, cell infection with an EBOV GP-pseudotyped viral particle is completely dependent on DC-SIGN, since T-lymphocytes lack any other attachment receptors to facilitate EBOV cell entry. On one hand, this model is very appropriate to have clean experiments and to demonstrate that inhibition by the tested molecules is based exclusively on blocking the receptor DC-SIGN. On the other hand, this model permits the use of BSL2-3 laboratories, more accessible and available all around, to obtain results concerning the activity of the new candidates to inhibit Ebola infection at a reasonable cost and in a short time. As a control of the infection, viral particles pseudotyped with the envelope glycoprotein (GP) of the vesicular stomatitis virus (VSV) that does infect T-lymphocytes in a DC-SIGN-independent manner were used.

In one pioneering study, the inhibitory effect of giant globular multivalent glycofullerenes **5**–**7** was explored in an experiment with the direct infection of Jurkat cells that express the surface receptor DC-SIGN (Jurkat–DC-SIGN) with pseudotyped viral particles that present EBOV-GP.[72] These globular multivalent

systems are water soluble and show no cytotoxicity in cell lines, which allows the study of their potential biological function in preventing viral infection. All the multivalent compounds were checked for the possibility of blocking the DC-SIGN receptor in six independent experiments. The results of blocking the DC-SIGN receptor by different compounds are reported as a function of concentration (Figure 3.25). A 50% inhibition of the infection was calculated with a 95% confidence interval (CI). As a control, infection with DC-SIGN-independent vesicular stomatitis virus envelope GP (VSV-GP)-pseudotyped lentiviral particles was performed under the same conditions.

The results obtained in the infection experiment revealed the dependence of the inhibition effect on mannoses. Compound **6**, which displayed 120 galactoses, as expected, was not able to inhibit the infection process mediated by DC-SIGN. Compounds with 120 mannose-based residues (**5** and **7**) showed very strong antiviral activity at picomolar to nanomolar concentrations. Compound **5** could effectively block EBOV infection at low nanomolar concentrations, with an IC_{50} of 20.37 nM (95% CI = 14.63–28.37 nM). Compound **7** was almost one order of magnitude more potent at inhibiting the infection process, with an IC_{50} of 667 pM (95% CI = 411 pM–1.08 nM).

Previous inhibition studies using the same infection model and fullerenes that displayed up to 36 mannoses showed relative inhibitory potency (RIP) values at least two orders of magnitude smaller.[70] Moreover, huge virus-like particles (VLPs) with a radius of 16 nm and up to 1640 mannoses[64] were 18-fold less potent compared with compound **7** (see Table 3.1).[72]

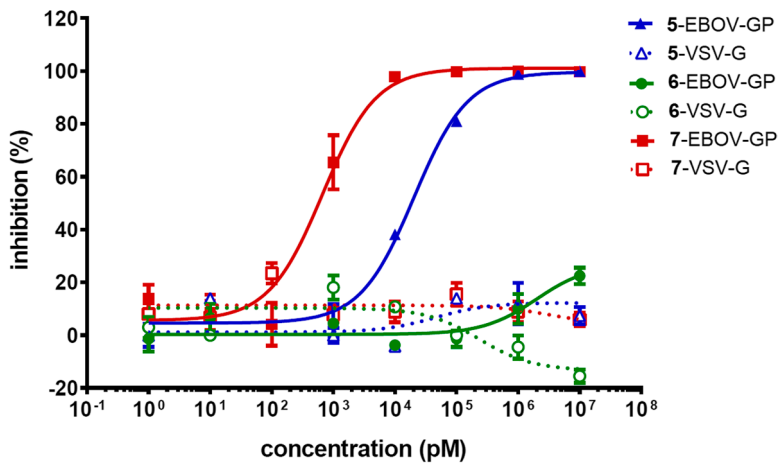

Figure 3.25 Inhibition of infection with EBOV or VSV GP-pseudotyped lentiviral particles of Jurkat DC-SIGN$^+$ cells using **5** (blue), **6** (green) and **7** (red). In the *cis*-infection experiments 2.5 × 10^5 Jurkat DC-SIGN$^+$ were challenged with 5000 TCID of recombinant lentiviral particles. Results represent the mean of 6 independent experiments +/− SEM. Adapted from ref. 72 with permission from Macmillan Publishers Limited, Copyright 2015.

Table 3.1 Comparison of IC_{50} and RIP values of different mannosylated multivalent compounds. Data obtained from inhibition studies using pseudotyped EBOV particles for the new compounds **5** and **7** in comparison with other carbohydrate multivalent systems previously reported by us. Adapted from ref. 72 with permission from Macmillan Publishers Limited, Copyright 2015.

Compound	IC_{50} (nM)	*n* Mannoses	RIP[a]	Reference
7 (120 Man)	0.667	120	1.6×10^4	96
VLP[b] (1620Man)	0.91	1620	8.6×10^2	64
5 (120 Man)	20 375	120	5.2×10^2	96
VLP[b] (540Man)	9.62	540	2.4×10^2	64
4 (36 Man)	300	36	1.2×10^2	97
3 (36 Man)	68 000	36	0.5	97
2 (12Man)	2000	12	53	97
α-Methyl Man[c]	1.27×10^6	1	1	98

[a]RIP, calculated as (IC_{50})mono/IC_{50}*valency ((IC_{50})mono, IC_{50} of the monovalent compound; IC_{50}*valency, IC_{50} of the multivalent compound multiplied by the number of ligands present in the multivalent compound); [b]virus like particles; [c]alfa-methyl-D-mannopyranoside.

Table 3.2 IC_{50} values obtained for new glycoconjugates and mannose quantification. Adapted from ref. 79 with permission from American Chemical Society, Copyright 2018.

Glycoconjugate	IC_{50} (μg mL^{-1})	Quantity of man (μg mg^{-1})[a]
2	19.01	225.92
SWCNT-C_{60}Man	15.15	30.53
SWCNT-glyMan	2.20	32.54
MWCNT-C_{60}Man	0.37	26.39
MWCNT-glyMan	1.90	21.84
SWCNH-C_{60}Man	33	13.88
SWCNH-glyMan	202	10.57

[a]Mannose quantification following the anthrone method.[100]

These results confirmed the efficiency of these systems both to interact with DC-SIGN and to compete with EBOV-GP-pseudotyped particles during their entry into target cells. These tridecafullerenes were found to block the EBOV infection efficiently in the subnanomolar concentration range. These values surpass by three orders of magnitude (two if the number of mannoses is considered) those exhibited by hexakis adducts endowed with 12 mannoses.

The antiviral activity of nanoglycocomposites decorated with mannose moieties **SWCNT-C_{60}Man**, **SWCNT-glyMan**, **MWCNT-C_{60}Man**, **MWCNT-glyMan**, **SWCNH-C_{60}Man** and **SWCNH-glyMan** was tested using the same system of pseudotyped viral particles presenting at the surface EBOV-GP.[79] The results are shown in Table 3.2.

The nanoglycocomposite **SWCNH-C_{60}Gal** displaying galactose moieties was used as a negative control and, as expected, was not able to inhibit the infection process mediated by DC-SIGN. The glycosylated carbon nanoforms had

a different performance facing DC-SIGN. Both SWCNTs (**SWCNT-C_{60}Man** and **SWCNT-glyMan**), with their rod-like shape, show antiviral activity, blocking the DC-SIGN receptor with IC_{50} values of 15.15 and 2.20 μg mL^{-1}, respectively. In contrast, MWCNTs conjugated with glycofullerenes (**MWCNT-C_{60}Man**) block the receptor in a more efficient manner than **MWCNT-glyMan**, with IC_{50} values of 0.37 and 1.90 μg mL^{-1}, respectively. However, the antiviral activity of **MWCNT-glyMan** is similar to the SWCNT analogous (**SWCNT-glyMan**). On the other hand, SWCNHs conjugated with glycofullerenes (**SWCNH-C_{60}Man**), with their globular structure, are able to inhibit Ebola virus infection more efficiently than glycodendron derivatives (**SWCNH-glyMan**), blocking the DC-SIGN receptor with an IC_{50} of 33 and 202 μg mL^{-1}, respectively (Table 3.2). After carrying out spectrophotometric measurements of the sugar content in each type of glycoconjugate following the anthrone method,[96] it was concluded that for each type of CNF, the most active derivative was that with a higher mannose content. On the other hand, the low activity of SWCNHs in comparison with SWCNTs and MWCNTs must be related, not only with the lower presence of mannose in these carbon nanoforms, but also with the size and shape of these carbon nanoforms. Comparing these results with those previously obtained for the hexakis-adduct of [60]fullerene substituted with 12 mannose units **2**, an increase of the antiviral activity in the case of glycoconjugates based on SWCNTs and MWCNTs was observed, while mannose derivatives of SWCNHs are less active than the glycofullerene itself. MWCNTs possess an ideal natural structure inhibiting viral entry, and attaching a proper glycosylated fragment, they can act as mimetics of a highly glycosylated viral capsid. On the other hand, the glycodendrimer **glyMan** itself does not show any antiviral activity DC-SIGN mediated at a concentration of 500 μg mL^{-1}. This finding demonstrates the importance of the multivalent presentation of the carbohydrate ligands provided by the CNF scaffold. In previous studies carried out with other glycodendrons in the same infection model, it was found that at least 24 copies of the ligand were needed to have a potent inhibition activity.[97,98]

3.5.2 Multivalent Glycosylated Carbon Nanostructures to Inhibit Zika and Dengue Viruses

Multiple host cell receptors have been identified to facilitate Flaviviruses entry, including DC-SIGN, which interact with Flavivirus envelope proteins (M and E) through their *N*-glycosylated envelope proteins.[99,100] *N*-glycosylation of viral proteins was shown to affect infection of different viruses, facilitating viral interaction with cellular receptors, or modifying protein immunogenicity and thus changing recognition of the virus by the host immune system.

Available data indicate that glycosylation of envelope E glycoprotein is associated with increased infectivity and proper release of mature viral particles and plays an important role in the assembly of infective particles, cellular attachment, tropism, transmission and pathogenesis.[101,102] Although the number of

N-glycosylation sites of the envelope of Zika and Dengue viruses is lower than in the glycoprotein of HIV or Ebola virus, only 4 in comparison to 18–20, the role of these *N*-glycosylation residues seems to be important for infectivity.[103]

Therefore, DC-SIGN can function as a good model for studying the first steps of pathogenesis of Flaviviruses and screening the antiviral strategies based on DC-SIGN targeting compounds for vaccination and treatment purposes.

In our study the inhibitory effect of multivalent disaccharide/fullerene nanoballs was evaluated in the experiment of direct infection of Jurkat DC-SIGN$^+$ with pseudotyped viral particles presenting Zika or Dengue virus glycoproteins.[77] The efficiency of these multivalent compounds to inhibit DC-SIGN mediated infection of ZIKV and DENV through blocking of DC-SIGN is shown in Figure 3.26.

Compound **17** displaying 12 galactoses, as expected, was not able to inhibit the infection process mediated by DC-SIGN (data not shown). However, compounds **20**, **21** and **22**, designed to present 36, 120 or 360 mannobioside residues, respectively, showed very strong antiviral activity at picomolar to nanomolar concentrations. Compound **20** could effectively block Zika and Dengue virus infection at low nanomolar concentrations with the IC_{50} of 8.35 nM (95% CI = 4.8–14.5 nM) for ZIKV and IC_{50} of 7.71 nM (95% CI = 4.85–12.24 nM) for DENV pseudotypes, respectively. Compound **21** was almost one order of magnitude more potent at inhibiting infection showing the IC_{50} of 520 pM (95% CI = 230 pM–1.150 nM) for ZIKV and IC_{50} of 98 pM (95% CI = 45 pM–213 nM) for DENV. Finally, compound **22**, containing a greater number of mannose residues (360), shows the greatest inhibitory activity with the IC_{50} of 67 pM (95% CI = 39–116 pM) for ZIKV and IC_{50} of 35 pM (95% CI = 18–68 pM) for DENV. These results have confirmed the efficiency of these systems to interact with DC-SIGN and to compete with Flavivirus glycoprotein-pseudotyped particles during their entry into target cells and highlight a potent mechanism for antiviral design to specific receptors based on recognition of carbohydrates.

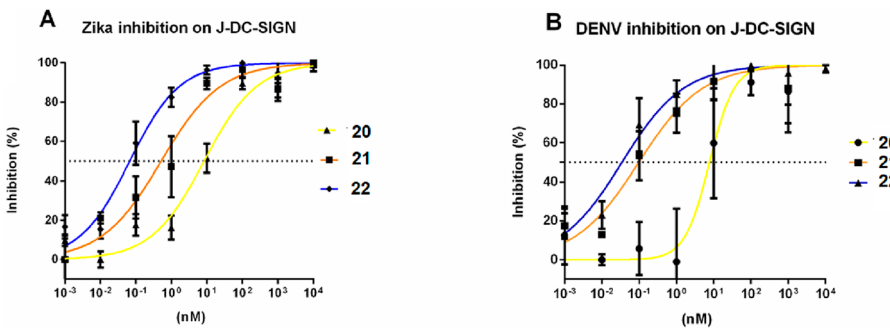

Figure 3.26 Sensitivity of (A) Zika-Paraiba and (B) DENV-1 virus transduction to the DC-SIGN inhibitors **20**, **21** and **22**. Adapted from ref. 77 with permission from Amercian Chemical Society, Copyright 2019.

3.6 Conclusions and Future Perspectives

Emergent pathogenic viruses represent nowadays one of the most dangerous causes for diseases in human beings. In the search for new pathways for addressing emergent virus infections, in the last decade we have focused on the well-known carbohydrate–protein interactions since they govern a wide variety of biological processes. Importantly, carbohydrate–protein interactions usually occur by means of the multivalent effect. Within the development of our project, we have synthesized mannosylated fullerenes containing several copies of carbohydrates in a globular presentation. These multivalent systems have a good solubility in aqueous media and a low cytotoxicity against several cell lines. Preliminary binding studies using the model lectin Concanavalin A demonstrated the potency of these glycodendrofullerenes to interact with lectins in a multivalent manner.[69] In this regard, a variety of carbohydrate multivalent systems based on dendrimers have been synthesized for the development of molecules capable of blocking DC-SIGN. In order to get a 3D globular scaffold thus resembling the most usual virus geometry, we synthesized, for the first time, new glycodendrofullerenes as antiviral agents. The antiviral activity of these compounds in an Ebola pseudotyped infection model was in the low micromolar range for fullerenes. One important factor to achieve high affinity in binding processes is not only the spatial presentation of the ligands but also the adequate accessibility of these ligands to interact with the corresponding receptor. Furthermore, the valency of the compound is an important factor to obtain good affinities in a carbohydrate–lectin interaction but, as we have shown in our studies, it is not the only factor to be taken into account.

Giant globular glycofullerenes decorated with mannoses (sugar superballs) have been synthesized and characterized by a variety of techniques. Interestingly, the so-called tridecafullerenes decorated with 120 mannoses have also shown antiviral activity with IC_{50} in the subnanomolar range. These experimental findings make these sugar superballs the most active molecules to inhibit the Ebola virus infection reported so far.

Very recently, by using a copper-free strategy based on the SPAAC click-chemistry procedure, unprecedented tridecafullerenes bearing up to 360 disaccharide residues have been synthesized and characterized in our laboratories. It is important to note that the presence of disaccharides significantly increases the biological activity when compared with previously published monosaccharides. Such compounds could not have been obtained by following a CuAAC methodology owing to the chelating ability of the mannobiosides, making the complete functionalization of the alkyne appended fullerene scaffold difficult. Although some aggregation is observed by DLS, the new hexakis-adducts, including the groundbreaking 'giant' molecule **22**, having 41.370 atoms (C, H, O, N), are totally soluble in water, thus allowing their use for biomedical purposes.

Based on the aforementioned results, fullerenes should be considered as very attractive and compatible 3D scaffolds for a globular multivalent

presentation of sugars. These promising results prompt us to search for new approaches for the design and preparation of glycodendritic key building blocks to conjugate on fullerenes. An important concept is, however, a fine control of the congestion between carbohydrates to prevent unfavorable steric hindrances in the search for better antiviral activities.

Needless to say that currently there are a great variety of known carbon nanoforms, which could also be used as potential scaffolds for the multivalent presentation of carbohydrates,[104–107] namely single and multiwall carbon nanotubes, graphene or graphene quantum dots, where the control of the carbohydrate functionalization and distribution still represents a future scientific challenge. This is also applicable to the variety of potential carbohydrates, both in terms of their own nature (monosaccharides, disaccharides, polysaccharides, *etc.*) and number of units (monomer, dimer, trimer, *etc.*). A combination of more efficient ligands and more adequate presentation on different scaffolds should eventually afford a variety of lead hybrid molecules with higher specificity and efficiency on Ebola virus infection.

A final consideration is that, although some vaccines are currently under study for the Ebola virus, the availability of chemical compounds able to fight against it at different stages of the infective process are scarce and preliminary results of clinical efficacy have been limited. The multivalent presentation of specific carbohydrates by using 3D fullerenes as controlled biocompatible carbon scaffolds represents a real advance, which, however, requires more studies to determine the optimized leads for practical purposes.

References

1. C. J. Peters and J. W. LeDuc, *J. Infect. Dis.*, 1999, **179**(Suppl 1), ix–xvi.
2. J. H. Kuhn, S. Becker, H. Ebihara, T. W. Geisbert, K. M. Johnson, Y. Kawaoka, W. I. Lipkin, A. I. Negredo, S. V. Netesov, S. T. Nichol, G. Palacios, C. J. Peters, A. Tenorio, V. E. Volchkov and P. B. Jahrling, *Arch. Virol.*, 2010, **155**, 2083–2103.
3. D. Cantoni, A. Hamlet, M. Michaelis, M. N. Wass, J. S. Rossman and C. B. Coyne, *mSphere*, 2016, **1**, e00322–16.
4. E. M. Leroy, B. Kumulungui, X. Pourrut, P. Rouquet, A. Hassanin, P. Yaba, A. Delicat, J. T. Paweska, J. P. Gonzalez and R. Swanepoel, *Nature*, 2005, **438**, 575–576.
5. A. Groseth, H. Feldmann and J. E. Strong, *Trends Microbiol.*, 2007, **15**, 408–416.
6. W. E. R. Team, *N. Engl. J. Med.*, 2016, **375**, 587–596.
7. T. M. Uyeki, A. K. Mehta, R. T. Davey Jr, A. M. Liddell, T. Wolf, P. Vetter, S. Schmiedel, T. Grunewald, M. Jacobs, J. R. Arribas, L. Evans, A. L. Hewlett, A. B. Brantsaeter, G. Ippolito, C. Rapp, A. I. Hoepelman, J. Gutman and Working Group of the U.S.-European Clinical Network on Clinical Management of Ebola Virus Disease Patients in the U.S. and Europe, *N. Engl. J. Med.*, 2016, **374**, 636–646.

8. Y. Yazdanpanah, J. R. Arribas and D. Malvy, *Intensive Care Med.*, 2015, **41**, 115–117.
9. T. K. Warren, J. Wells, R. G. Panchal, K. S. Stuthman, N. L. Garza, S. A. Van Tongeren, L. Dong, C. J. Retterer, B. P. Eaton, G. Pegoraro, S. Honnold, S. Bantia, P. Kotian, X. Chen, B. R. Taubenheim, L. S. Welch, D. M. Minning, Y. S. Babu, W. P. Sheridan and S. Bavari, *Nature*, 2014, **508**, 402–405.
10. R. Taylor, P. Kotian, T. Warren, R. Panchal, S. Bavari, J. Julander, S. Dobo, A. Rose, Y. El-Kattan, B. Taubenheim, Y. Babu and W. P. Sheridan, *J. Infect. Public Health*, 2016, **9**, 220–226.
11. D. Sissoko, C. Laouenan, E. Folkesson, A. B. M'Lebing, A. H. Beavogui, S. Baize, A. M. Camara, P. Maes, S. Shepherd, C. Danel, S. Carazo, M. N. Conde, J. L. Gala, G. Colin, H. Savini, J. A. Bore, F. Le Marcis, F. R. Koundouno, F. Petitjean, M. C. Lamah, S. Diederich, A. Tounkara, G. Poelart, E. Berbain, J. M. Dindart, S. Duraffour, A. Lefevre, T. Leno, O. Peyrouset, L. Irenge, N. Bangoura, R. Palich, J. Hinzmann, A. Kraus, T. S. Barry, S. Berette, A. Bongono, M. S. Camara, V. Chanfreau Munoz, L. Doumbouya, H. Souley, P. M. Kighoma, F. R. Koundouno, L. Rene, C. M. Loua, V. Massala, K. Moumouni, C. Provost, N. Samake, C. Sekou, A. Soumah, I. Arnould, M. S. Komano, L. Gustin, C. Berutto, D. Camara, F. S. Camara, J. Colpaert, L. Delamou, L. Jansson, E. Kourouma, M. Loua, K. Malme, E. Manfrin, A. Maomou, A. Milinouno, S. Ombelet, A. Y. Sidiboun, I. Verreckt, P. Yombouno, A. Bocquin, C. Carbonnelle, T. Carmoi, P. Frange, S. Mely, V. K. Nguyen, D. Pannetier, A. M. Taburet, J. M. Treluyer, J. Kolie, R. Moh, M. C. Gonzalez, E. Kuisma, B. Liedigk, D. Ngabo, M. Rudolf, R. Thom, R. Kerber, M. Gabriel, A. Di Caro, R. Wolfel, J. Badir, M. Bentahir, Y. Deccache, C. Dumont, J. F. Durant, K. El Bakkouri, M. Gasasira Uwamahoro, B. Smits, N. Toufik, S. Van Cauwenberghe, K. Ezzedine, E. Dortenzio, L. Pizarro, A. Etienne, J. Guedj, A. Fizet, E. Barte de Sainte Fare, B. Murgue, T. Tran-Minh, C. Rapp, P. Piguet, M. Poncin, B. Draguez, T. Allaford Duverger, S. Barbe, G. Baret, I. Defourny, M. Carroll, H. Raoul, A. Augier, S. P. Eholie, Y. Yazdanpanah, C. Levy-Marchal, A. Antierrens, M. Van Herp, S. Gunther, X. de Lamballerie, S. Keita, F. Mentre, X. Anglaret, D. Malvy and J. S. Group, *PLoS Med.*, 2016, **13**, e1001967.
12. R. T. Davey Jr, L. Dodd, M. A. Proschan, J. Neaton, J. Neuhaus Nordwall, J. S. Koopmeiners, J. Beigel, J. Tierney, H. C. Lane, A. S. Fauci, M. B. F. Massaquoi, F. Sahr and D. Malvy, *N. Engl. J. Med.*, 2016, **375**, 1448–1456.
13. A. Haque, D. Hober and J. Blondiaux, *Antimicrob. Agents Chemother.*, 2015, **59**, 5892–5902.
14. K. Y. Lai, W. Y. Ng and F. F. Cheng, *Infect. Dis. Poverty*, 2014, **3**, 43.
15. D. A. Stanley, A. N. Honko, C. Asiedu, J. C. Trefry, A. W. Lau-Kilby, J. C. Johnson, L. Hensley, V. Ammendola, A. Abbate, F. Grazioli, K. E. Foulds, C. Cheng, L. Wang, M. M. Donaldson, S. Colloca, A. Folgori, M. Roederer, G. J. Nabel, J. Mascola, A. Nicosia, R. Cortese, R. A. Koup and N. J. Sullivan, *Nat. Med.*, 2014, **20**, 1126–1129.

16. T. W. Geisbert, K. M. Daddario-Dicaprio, M. G. Lewis, J. B. Geisbert, A. Grolla, A. Leung, J. Paragas, L. Matthias, M. A. Smith, S. M. Jones, L. E. Hensley, H. Feldmann and P. B. Jahrling, *PLoS Pathog.*, 2008, **4**, e1000225.
17. A. M. Henao-Restrepo, A. Camacho, I. M. Longini, C. H. Watson, W. J. Edmunds, M. Egger, M. W. Carroll, N. E. Dean, I. Diatta, M. Doumbia, B. Draguez, S. Duraffour, G. Enwere, R. Grais, S. Gunther, P. S. Gsell, S. Hossmann, S. V. Watle, M. K. Konde, S. Keita, S. Kone, E. Kuisma, M. M. Levine, S. Mandal, T. Mauget, G. Norheim, X. Riveros, A. Soumah, S. Trelle, A. S. Vicari, J. A. Rottingen and M. P. Kieny, *Lancet*, 2017, **389**, 505–518.
18. A. S. Kondratowicz and W. J. Maury, *Future Microbiol.*, 2012, **7**, 1–4.
19. S. Yuan, *Infect. Dis. Poverty*, 2015, **4**, 23.
20. E. Picazo and F. Giordanetto, *Drug Discovery Today*, 2015, **20**, 277–286.
21. A. Mehta, N. Zitzmann, P. M. Rudd, T. M. Block and R. A. Dwek, *FEBS Lett.*, 1998, **430**, 17–22.
22. J. Chang, T. M. Block and J. T. Guo, *Antiviral Res.*, 2013, **99**, 251–260.
23. J. L. Miller, S. G. Spiro, S. D. Dowall, I. Taylor, A. Rule, D. S. Alonzi, A. C. Sayce, E. Wright, E. M. Bentley, R. Thom, G. Hall, R. A. Dwek, R. Hewson and N. Zitzmann, *PLoS One*, 2016, **11**, e0167018.
24. L. R. Petersen, D. J. Jamieson and M. A. Honein, *N. Engl. J. Med.*, 2016, **375**, 294–295.
25. G. Vogel, *Science*, 2016, **354**, 1088–1089.
26. G. Paz-Bailey, E. S. Rosenberg, K. Doyle, J. Muñoz-Jordan, G. A. Santiago, L. Klein, J. Pérez-Padilla, F. A. Medina, S. H. Waterman, C. G. Gubern, L. I. Alvarado and T. M. Sharp, *N. Engl. J. Med.*, 2018, **379**, 1234–1243.
27. R. Hamel, O. Dejarnac, S. Wichit, P. Ekchariyawat, A. Neyret, N. Luplertlop, M. Perera-Lecoin, P. Surasombatpattana, L. Talignani, F. Thomas, V. M. Cao-Lormeau, V. Choumet, L. Briant, P. Despres, A. Amara, H. Yssel and D. Misse, *J. Virol.*, 2015, **89**, 8880–8896.
28. M. Perera-Lecoin, L. Meertens, X. Carnec and A. Amara, *Viruses*, 2013, **6**, 69–88.
29. B. M. Illescas, J. Rojo, R. Delgado and N. Martín, *J. Am. Chem. Soc.*, 2017, **139**, 6018–6025.
30. A. Varki, *Glycobiology*, 2016, **27**, 3–49.
31. B. M. Curtis, S. Scharnowske and A. J. Watson, *Proc. Natl. Acad. Sci. U. S. A.*, 1992, **89**, 8356–8360.
32. T. B. Geijtenbeek, R. Torensma, S. J. van Vliet, G. C. van Duijnhoven, G. J. Adema, Y. van Kooyk and C. G. Figdor, *Cell*, 2000, **100**, 575–585.
33. T. B. Geijtenbeek, D. S. Kwon, R. Torensma, S. J. van Vliet, G. C. van Duijnhoven, J. Middel, I. L. Cornelissen, H. S. Nottet, V. N. KewalRamani, D. R. Littman, C. G. Figdor and Y. van Kooyk, *Cell*, 2000, **100**, 587–597.
34. Y. van Kooyk and T. B. Geijtenbeek, *Nat. Rev. Immunol.*, 2003, **3**, 697–709.
35. H. Feinberg, D. A. Mitchell, K. Drickamer and W. I. Weis, *Science*, 2001, **294**, 2163–2166.

36. Y. Guo, H. Feinberg, E. Conroy, D. A. Mitchell, R. Alvarez, O. Blixt, M. E. Taylor, W. I. Weis and K. Drickamer, *Nat. Struct. Mol. Biol.*, 2004, **11**, 591–598.
37. M. Thepaut, C. Guzzi, I. Sutkeviciute, S. Sattin, R. Ribeiro-Viana, N. Varga, E. Chabrol, J. Rojo, A. Bernardi, J. Angulo, P. M. Nieto and F. Fieschi, *J. Am. Chem. Soc.*, 2013, **135**, 2518–2529.
38. K. Pederson, D. A. Mitchell and J. H. Prestegard, *Biochemistry*, 2014, **53**, 5700–5709.
39. I. Sutkeviciute, M. Thepaut, S. Sattin, A. Berzi, J. McGeagh, S. Grudinin, J. Weiser, A. Le Roy, J. J. Reina, J. Rojo, M. Clerici, A. Bernardi, C. Ebel and F. Fieschi, *ACS Chem. Biol.*, 2014, **9**, 1377–1385.
40. M. C. Fernández-Alonso, D. Diaz, M. A. Berbis, F. Marcelo, J. Canada and J. Jimenez-Barbero, *Curr. Protein Pept. Sci.*, 2012, **13**, 816–830.
41. A. Arda and J. Jimenez-Barbero, *Chem. Commun.*, 2018, **54**, 4761–4769.
42. J. J. Reina, I. Diaz, P. M. Nieto, N. E. Campillo, J. A. Paez, G. Tabarani, F. Fieschi and J. Rojo, *Org. Biomol. Chem.*, 2008, **6**, 2743–2754.
43. J. Angulo, I. Díaz, J. J. Reina, G. Tabarani, F. Fieschi, J. Rojo and P. M. Nieto, *ChemBioChem*, 2008, **9**, 2225–2227.
44. C. Guzzi, J. Angulo, F. Doro, J. J. Reina, M. Thepaut, F. Fieschi, A. Bernardi, J. Rojo and P. M. Nieto, *Org. Biomol. Chem.*, 2011, **9**, 7705–7712.
45. C. Guzzi, P. Alfarano, I. Sutkeviciute, S. Sattin, R. Ribeiro-Viana, F. Fieschi, A. Bernardi, J. Weiser, J. Rojo, J. Angulo and P. M. Nieto, *Org. Biomol. Chem.*, 2016, **14**, 335–344.
46. D. A. Mitchell, A. J. Fadden and K. Drickamer, *J. Biol. Chem.*, 2001, **276**, 28939–28945.
47. A. Cambi, F. de Lange, N. M. van Maarseveen, M. Nijhuis, B. Joosten, E. M. van Dijk, B. I. de Bakker, J. A. Fransen, P. H. Bovee-Geurts, F. N. van Leeuwen, N. F. Van Hulst and C. G. Figdor, *J. Cell Biol.*, 2004, **164**, 145–155.
48. A. K. Neumann, N. L. Thompson and K. Jacobson, *J. Cell Sci.*, 2008, **121**, 634–643.
49. R. T. Lee and Y. C. Lee, *Glycoconjugate J.*, 2000, **17**, 543–551.
50. J. J. Lundquist and E. J. Toone, *Chem. Rev.*, 2002, **102**, 555–578.
51. M. Sánchez-Navarro and J. Rojo, *Drug News Perspect.*, 2010, **23**, 557–572.
52. A. Bernardi, J. Jimenez-Barbero, A. Casnati, C. De Castro, T. Darbre, F. Fieschi, J. Finne, H. Funken, K. E. Jaeger, M. Lahmann, T. K. Lindhorst, M. Marradi, P. Messner, A. Molinaro, P. V. Murphy, C. Nativi, S. Oscarson, S. Penades, F. Peri, R. J. Pieters, O. Renaudet, J. L. Reymond, B. Richichi, J. Rojo, F. Sansone, C. Schaffer, W. B. Turnbull, T. Velasco-Torrijos, S. Vidal, S. Vincent, T. Wennekes, H. Zuilhof and A. Imberty, *Chem. Soc. Rev.*, 2013, **42**, 4709–4727.
53. J. J. Reina and J. Rojo, *Braz. J. Pharm. Sci.*, 2013, **49**, 109–124.
54. E. van Liempt, C. M. Bank, P. Mehta, J. J. Garcia-Vallejo, Z. S. Kawar, R. Geyer, R. A. Alvarez, R. D. Cummings, Y. Kooyk and I. van Die, *FEBS Lett.*, 2006, **580**, 6123–6131.

55. J. J. Reina, A. Di Maio, J. Ramos-Soriano, R. C. Figueiredo and J. Rojo, *Org. Biomol. Chem.*, 2016, **14**, 2873–2882.
56. J. Ramos-Soriano, M. C. de la Fuente, N. de la Cruz, R. C. Figueiredo, J. Rojo and J. J. Reina, *Org. Biomol. Chem.*, 2017, **15**, 8877–8882.
57. J. J. Reina and J. Rojo, in *Carbohydrate Chemistry: State of the Art and Challenges for Drug Development*, 2015, pp. 419–439.
58. J. J. Reina, O. S. Maldonado, G. Tabarani, F. Fieschi and J. Rojo, *Bioconjugate Chem.*, 2007, **18**, 963–969.
59. V. V. Rostovtsev, L. G. Green, V. V. Fokin and K. B. Sharpless, *Angew. Chem., Int. Ed.*, 2002, **41**, 2596–2599.
60. C. W. Tornoe, C. Christensen and M. Meldal, *J. Org. Chem.*, 2002, **67**, 3057–3064.
61. E. Haldon, M. C. Nicasio and P. J. Perez, *Org. Biomol. Chem.*, 2015, **13**, 9528–9550.
62. J. Dommerholt, F. Rutjes and F. L. van Delft, *Top. Curr. Chem.*, 2016, **374**, 16.
63. N. J. Agard, J. A. Prescher and C. R. Bertozzi, *J. Am. Chem. Soc.*, 2004, **126**, 15046–15047.
64. R. Ribeiro-Viana, M. Sanchez-Navarro, J. Luczkowiak, J. R. Koeppe, R. Delgado, J. Rojo and B. G. Davis, *Nat. Commun.*, 2012, **3**, 1303.
65. E. Castro, A. Hernández García, G. Zavala and L. Echegoyen, *J. Mater. Chem. B*, 2017, **5**, 6523–6535.
66. A. Hirsch and O. Vostrowsky, *Eur. J. Org. Chem.*, 2001, **2001**, 829–848.
67. A. Hirsch, in *Fullerenes and Related Structures*, ed. A. Hirsch, Springer Berlin Heidelberg, Berlin, Heidelberg, 1999, pp. 1–65.
68. J. F. Nierengarten, J. Iehl, V. Oerthel, M. Holler, B. M. Illescas, A. Muñoz, N. Martín, J. Rojo, M. Sánchez-Navarro, S. Cecioni, S. Vidal, K. Buffet, M. Durka and S. P. Vincent, *Chem. Commun.*, 2010, **46**, 3860–3862.
69. M. Sánchez-Navarro, A. Muñoz, B. M. Illescas, J. Rojo and N. Martín, *Chem. - Eur. J.*, 2011, **17**, 766–769.
70. J. Luczkowiak, A. Muñoz, M. Sanchez-Navarro, R. Ribeiro-Viana, A. Ginieis, B. M. Illescas, N. Martin, R. Delgado and J. Rojo, *Biomacromolecules*, 2013, **14**, 431–437.
71. H. Isobe, K. Cho, N. Solin, D. B. Werz, P. H. Seeberger and E. Nakamura, *Org. Lett.*, 2007, **9**, 4611–4614.
72. A. Muñoz, D. Sigwalt, B. M. Illescas, J. Luczkowiak, L. Rodriguez-Perez, I. Nierengarten, M. Holler, J. S. Remy, K. Buffet, S. P. Vincent, J. Rojo, R. Delgado, J. F. Nierengarten and N. Martín, *Nat. Chem.*, 2016, **8**, 50–57.
73. H. Li, S. A. Haque, A. Kitaygorodskiy, M. J. Meziani, M. Torres-Castillo and Y.-P. Sun, *Org. Lett.*, 2006, **8**, 5641–5643.
74. C. Ornelas, J. Broichhagen and M. Weck, *J. Am. Chem. Soc.*, 2010, **132**, 3923–3931.
75. J. Ramos-Soriano, J. J. Reina, A. Perez-Sanchez, B. M. Illescas, J. Rojo and N. Martin, *Chem. Commun.*, 2016, **52**, 10544–10546.
76. J. Ramos-Soriano, J. J. Reina, B. M. Illescas, J. Rojo and N. Martin, *J. Org. Chem.*, 2018, **83**, 1727–1736.

77. J. Ramos-Soriano, J. J. Reina, B. M. Illescas, N. de la Cruz, L. Rodriguez-Perez, F. Lasala, J. Rojo, R. Delgado and N. Martin, *J. Am. Chem. Soc.*, 2019, **141**, 15403–15412.
78. J. L. Delgado, M. Á. Herranz and N. Martín, *J. Mater. Chem.*, 2008, **18**, 1417–1426.
79. L. Rodriguez-Perez, J. Ramos-Soriano, A. Perez-Sanchez, B. M. Illescas, A. Muñoz, J. Luczkowiak, F. Lasala, J. Rojo, R. Delgado and N. Martin, *J. Am. Chem. Soc.*, 2018, **140**, 9891–9898.
80. B. K. Price and J. M. Tour, *J. Am. Chem. Soc.*, 2006, **128**, 12899–12904.
81. G. Pagona, N. Karousis and N. Tagmatarchis, *Carbon*, 2008, **46**, 604–610.
82. C. A. Furtado, U. J. Kim, H. R. Gutierrez, L. Pan, E. C. Dickey and P. C. Eklund, *J. Am. Chem. Soc.*, 2004, **126**, 6095–6105.
83. R. Graupner, *J. Raman Spectrosc.*, 2007, **38**, 673–683.
84. M. E. Lipińska, S. L. H. Rebelo, M. F. R. Pereira, J. A. N. F. Gomes, C. Freire and J. L. Figueiredo, *Carbon*, 2012, **50**, 3280–3294.
85. S. Ciampi, T. Böcking, K. A. Kilian, M. James, J. B. Harper and J. J. Gooding, *Langmuir*, 2007, **23**, 9320–9329.
86. M. Bermejo-Jambrina, J. Eder, L. C. Helgers, N. Hertoghs, B. M. Nijmeijer, M. Stunnenberg and T. B. H. Geijtenbeek, *Front. Immunol.*, 2018, **9**, 590.
87. J. Rojo and R. Delgado, *J. Antimicrob. Chemother.*, 2004, **54**, 579–581.
88. A. Sanchez, S. G. Trappier, B. W. Mahy, C. J. Peters and S. T. Nichol, *Proc. Natl. Acad. Sci. U. S. A.*, 1996, **93**, 3602–3607.
89. O. Martinez, L. W. Leung and C. F. Basler, *Antiviral Res.*, 2012, **93**, 416–428.
90. T. W. Geisbert, L. E. Hensley, T. Larsen, H. A. Young, D. S. Reed, J. B. Geisbert, D. P. Scott, E. Kagan, P. B. Jahrling and K. J. Davis, *Am. J. Pathol.*, 2003, **163**, 2347–2370.
91. A. Ludtke, P. Ruibal, D. M. Wozniak, E. Pallasch, S. Wurr, S. Bockholt, S. Gomez-Medina, X. Qiu, G. P. Kobinger, E. Rodriguez, S. Gunther, S. Krasemann, J. Idoyaga, L. Oestereich and C. Munoz-Fontela, *Sci. Rep.*, 2017, **7**, 43776.
92. C. P. Alvarez, F. Lasala, J. Carrillo, O. Muniz, A. L. Corbi and R. Delgado, *J. Virol.*, 2002, **76**, 6841–6844.
93. L. G. Barrientos, F. Lasala, J. R. Otero, A. Sanchez and R. Delgado, *J. Infect. Dis.*, 2004, **189**, 1440–1443.
94. P. L. Sinn, J. E. Coffin, N. Ayithan, K. H. Holt and W. Maury, *Methods Mol. Biol.*, 2017, **1628**, 65–78.
95. K. Konduru, A. C. Shurtleff, S. Bavari and G. Kaplan, *J. Virol. Methods*, 2018, **254**, 1–7.
96. M. A. Jermyn, *Anal. Biochem.*, 1975, **68**, 332–335.
97. F. Lasala, E. Arce, J. R. Otero, J. Rojo and R. Delgado, *Antimicrob. Agents Chemother.*, 2003, **47**, 3970–3972.
98. J. Luczkowiak, S. Sattin, I. Sutkeviciute, J. J. Reina, M. Sánchez-Navarro, M. Thepaut, L. Martinez-Prats, A. Daghetti, F. Fieschi, R. Delgado, A. Bernardi and J. Rojo, *Bioconjugate Chem.*, 2011, **22**, 1354–1365.

99. B. Tassaneetrithep, T. H. Burgess, A. Granelli-Piperno, C. Trumpfheller, J. Finke, W. Sun, M. A. Eller, K. Pattanapanyasat, S. Sarasombath, D. L. Birx, R. M. Steinman, S. Schlesinger and M. A. Marovich, *J. Exp. Med.*, 2003, **197**, 823–829.
100. E. Pokidysheva, Y. Zhang, A. J. Battisti, C. M. Bator-Kelly, P. R. Chipman, C. Xiao, G. G. Gregorio, W. A. Hendrickson, R. J. Kuhn and M. G. Rossmann, *Cell*, 2006, **124**, 485–493.
101. C. W. Davis, H. Y. Nguyen, S. L. Hanna, M. D. Sanchez, R. W. Doms and T. C. Pierson, *J. Virol.*, 2006, **80**, 1290–1301.
102. S. L. Hanna, T. C. Pierson, M. D. Sanchez, A. A. Ahmed, M. M. Murtadha and R. W. Doms, *J. Virol.*, 2005, **79**, 13262–13274.
103. M. Mossenta, S. Marchese, M. Poggianella, J. L. Slon Campos and O. R. Burrone, *Biochem. Biophys. Res. Commun.*, 2017, **492**, 579–586.
104. M.-E. Ragoussi, S. Casado, R. Ribeiro-Viana, G. d. l. Torre, J. Rojo and T. Torres, *Chem. Sci.*, 2013, **4**, 4035–4041.
105. Y. Chen, A. Star and S. Vidal, *Chem. Soc. Rev.*, 2013, **42**, 4532–4542.
106. F. Wang, L. Liu and W. J. Li, *IEEE Trans. Nanobiosci.*, 2015, **14**, 818–834.
107. Z. Qi, P. Bharate, C.-H. Lai, B. Ziem, C. Böttcher, A. Schulz, F. Beckert, B. Hatting, R. Mülhaupt, P. H. Seeberger and R. Haag, *Nano Lett.*, 2015, **15**, 6051–6057.

CHAPTER 4

Carbon Nanostructures and Polysaccharides for Biomedical Materials

JOSE M. GONZÁLEZ-DOMÍNGUEZ*[a], MIGUEL Á. ÁLVAREZ-SÁNCHEZ[a], CAROLINE HADAD[b], ANA M. BENITO[a] AND WOLFGANG K. MASER[a]

[a]Group of Carbon Nanostructures and Nanotechnology (G-CNN), Instituto de Carboquímica (ICB-CSIC), C/Miguel Luesma Castan 4, 50018, Zaragoza, Spain; [b]Laboratoire de Glycochimie, des Antimicrobiens et des Agroressources, UMR CNRS 7378, Université de Picardie Jules Verne-UFR des Sciences, 33 rue Saint Leu, 80039, Amiens Cedex, France
*E-mail: jmgonzalez@icb.csic.es

4.1 Introduction

4.1.1 Carbon Nanostructures, A Brief History in Biomedical Applications: Past and Present

The term 'carbon nanostructures' covers a wide variety of carbon nanomaterials such as carbon nanotubes (CNTs), fullerenes, graphene, graphene oxide (GO), reduced graphene oxide (rGO), nanodiamonds, carbon dots, or graphene quantum dots, with at least one dimension within the nanoscale, varying in shape, size, structure and chemical surface.[1–6] The origin of all these nanostructures was the discovery in 1985 by H. Kroto, R. Smalley and R. Curl

Nanoscience & Nanotechnology Series No. 48
Carbon Nanostructures for Biomedical Applications
Edited by Tatiana Da Ros, Nazario Martín and Jean-Francois Nierengarten

Published by the Royal Society of Chemistry, www.rsc.org

of a new allotrope of carbon called fullerene.[1] The best-known member of the fullerenes is the C_{60}, a zero-dimensional closed spherical nanostructure with 60 carbon atoms at the vertices of a regular truncated icosahedron forming a closed spherical structure similar to a soccer ball. However, fullerenes with sizes ranging from 20 to hundreds of carbon atoms also exist. The authors of this finding received the Nobel Prize in 1996 and opened a new amazing area of research at the nanoscale in the field of carbon nanomaterials. In 1991, S. Iijima observed one-dimensional carbon nanostructures (CNTs) under an electronic microscope,[2] which can be considered as elongated fullerenes or rolled-up seamless graphene cylinders. Depending on the number of layers, nanotubes are classified as single-walled carbon nanotubes (SWCNTs) or multi-walled carbon nanotubes (MCWNTs). Very recently, in 2004, scientists from Manchester University, A. Geim and K. Novoselov, successfully isolated graphene,[3] a monolayer two-dimensional sheet of graphite, and contrary to the old common belief, they demonstrated that graphene is stable.[7] They were also awarded the Nobel Prize in 2010 for their discovery.

Carbon nanostructures are not only interesting from a structural point of view, but they have unique and fascinating physical, chemical, electrical, mechanical, thermal and optical properties,[8–10] which makes them promising materials for the development of endless technological applications. Fullerenes have shown superior performance in solar cells.[11–13] CNTs and graphene derivatives have been used in composites,[14–20] catalysis,[21–27] sensors,[28–32] field emission devices,[33–35] transparent conducting electrodes,[36] optoelectronic devices,[37,38] energy storage,[39–42] solar cells,[43–46] and memory devices,[47,48] among others. Also, in the field of biomedicine, there has been a significant number of publications reporting the use of carbon nanostructures as biosensors,[49–53] detection of biomarkers,[54,55] tissue engineering,[56,57] drug delivery[58,59] or actuators.[60–62] In most of these examples, the molecular basis underlying the enormous interest is the similarity of the size of carbon nanostructures with the size of biological molecules, such as enzymes membrane receptors, antibodies or DNA plasmids. In fact, due to their nanometric size, carbon nanostructures can interact with biomolecules both outside and inside the cells, thus providing valuable tools for disease diagnosis and treatment.[63] Additionally, of special interest for their application in biology and medicine, is the possibility of modulating the surface of the carbon nanostructures, improving their solubility in water, and, above all, allowing functionalization for enhancing detection response or for improving their *in vivo* stability and circulation time.[64] CNTs and pristine graphene are hydrophobic materials, with suitable properties for membrane barrier penetration systems, but they require surface modifications or stabilization agents to be water-dispersible for satisfactory biocompatibility, physiological solubility and stability.[8,65,66] For this reason, oxidized CNTs, GO and rGO (with a partial reduction degree) are preferentially used for most biological applications. Thus, these chemical derivatives are promising materials for biological applications exhibiting amphiphilicity, *i.e.* both hydrophobicity (which plays an important role in cell growth and differentiation) and high hydrophilic

character (due to their oxygen-rich chemical surface), which enables further chemical functionalization. Furthermore, the intrinsic optical, electrical and biological properties of carbon nanostructures offer unique opportunities to study and regulate complex biological processes for applications in biomedicine. However, parallel to a large number of investigations on the development and application of carbon nanomaterials in biomedicine, concerns about their toxicity and biocompatibility also emerged.[67,68] Currently, the evidence is insufficient to reach a global conclusion about the potential toxicity of carbon nanostructures, as more toxicological and pharmacological studies need to be thoroughly performed to obtain a biosafety guide for their correct use in biomedicine. Many challenges need to be addressed for implementation in diagnosis and therapy applications. Nevertheless, carbon nanostructures are fascinating materials, offering numerous and unique advantages for biomedical applications, which will bloom once a pathway is unravelled to further promote their bio-application. For the aforementioned reasons, in the following, we analyse the potential of polysaccharides as a forefront strategy to process and complement carbon nanostructures towards a reliable horizon for them to eventually be used in biomedicine.

4.1.2 Polysaccharides in Biomaterials Science

Polymeric carbohydrates, so called polysaccharides, are composed of repeating monomeric units of monosaccharides that are covalently linked to each other through glucosidic bonds with a defined stereochemistry. Together with being abundant in nature, polysaccharides are one of the most important biological macromolecules, among others such as proteins, nucleic acids, lipids, *etc.* They can exist in a linear form with a straight chain of monosaccharides or a branched form with a monosaccharide chain with arms and turns.[69] Natural polymers, compared to synthetic ones, are biodegradable, biocompatible and able to mimic the natural extracellular matrix microenvironment. In addition, since they possess a variety of functional and reactive groups, polysaccharides can be functionalized *via* chemical (*i.e.* covalent bonds, complexation)[70] or enzymatic[71] routes with other biomolecules making them ideal biomaterials for the formulation of targeted drug systems or in tissue engineering applications.[72,73] Their extraction or isolation from natural sources (plants, algae, animals or microbial organisms) are, nowadays, well described and optimized. The following figure summarizes the origins and names of the most common natural polysaccharides (Figure 4.1).

In this chapter, we will focus on four natural polysaccharides: cellulose, chitin, its derivative chitosan, and alginate, respectively. These biopolymers will be described in this section in terms of chemical composition, structure and properties. And, in subsequent sections, their potential for interfacing with carbon nanostructures will be reviewed and discussed in the biomedicine context.

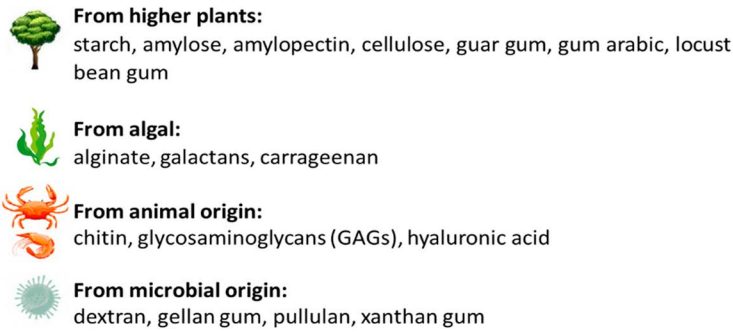

Figure 4.1 Origins and names of the natural polysaccharides.

4.1.2.1 Cellulose

Cellulose, the most abundant polysaccharide on the Earth, is the main structural material of plant cells' walls. It is a linear homopolymer of β-(1→4)-linked-D-glucopyranosyl units in which every unit is corkscrewed 180° with respect to its neighbours and with a degree of polymerization (DP) ranging from several hundred to over ten thousand monomers. The repeating unit is a dimer of glucose known as cellobiose (Figure 4.2). For industrial use, cellulose is mainly obtained from wood pulp and cotton. From the wood pulp fibres, it is possible to isolate it as microfibrillated cellulose in which van der Waals and intermolecular hydrogen bonds between hydroxyl groups and oxygens of adjacent molecules promote parallel stacking of multiple polysaccharide chains forming elementary fibrils.[74] Indeed, cellulose is biosynthesized in the form of fibrils with alternating crystalline and amorphous domains. In the ordered regions, cellulose chains are tightly packed together in crystallites, which are stabilized by a strong and very complex intra- and intermolecular network. The hydrogen-bonding network and molecular orientation in cellulose can vary widely, which give rise to cellulose polymorphs or allomorphs.[75] The amorphous regions are distributed as chain dislocations on segments along with the fibre where the cellulosic chains are distorted by internal strain and proceed to tilts and twists.

On the other hand, nanocellulose is composed of nanosized cellulose fibrils. Depending on the method with which it is obtained, nanocellulose can be classified into three main families: cellulose nanocrystals (NCCs) and nanofibrillated cellulose (NFC), obtained following a top-down approach from cellulose fibres;[76] and bacterial cellulose (BC) synthesized in pure and highly crystalline microfibrillar form (and nanosized widths) by bacteria in a bottom-up process.[77] These families, even if they have identical composition, differ on the dimension of the isolated cellulosic material, their function and their applications, but they all share unique properties such as high

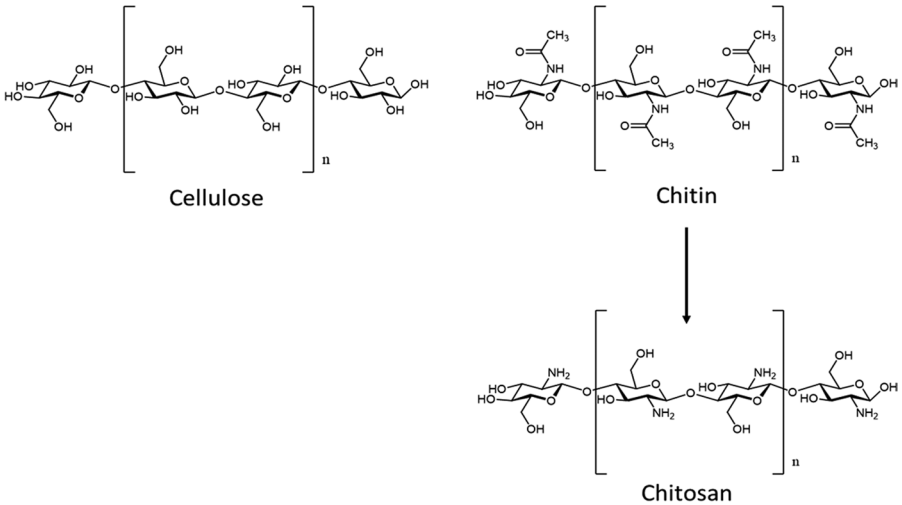

Figure 4.2 Chemical structures of cellulose, chitin and its derivative chitosan.

aspect ratio, low density, biodegradability, high strength and stiffness. They are also non-toxic, and they even possess absorbent properties when used as a basis for aerogels or foams.[78] Besides its unique properties, nanocellulose can be cost-effectively produced in large quantities and can be easily functionalized due to the presence of many hydroxyl groups along the chains. Common uses for the nanocelluloses include food packaging or additives, polymer reinforcement additives, cosmetic and skincare products, pharmaceutical excipients or even edible coatings.[79] One possible limitation in many fields of application regards the general use of hydrophilic or polar media. In order to readjust their hydrophilic–hydrophobic balance, and thus enable the nanocellulose use in other media, many examples of covalent or non-covalent functionalization have been described in the last few years. Among these modifications, esterification, etherification, silylation, urethanization, amidation or polymer grafting are some of the best examples.[80] All the families of nanocellulose exhibit good mechanical properties, which strongly depend on the ratio of crystalline/amorphous regions along the fibres. The stiffness and modulus of NCCs with an intrinsically higher content on crystalline regions should be higher than those of NFC and BC fibrils, as the latter two contain both crystalline and amorphous structures. The Young's modulus of NCCs may vary from 100–200 GPa when the one of NFC and BC is around 100 GPa (Table 4.1). These values are similar to Kevlar® (60–125 GPa) and even in some cases near that of steel (200–220 GPa). The incorporation of carbon nanostructures into a nanocellulose matrix will strongly influence these mechanical properties.

Table 4.1 Characteristics of the nanocellulose family members.

Type	Synthesis method	Sources	Width (nm)	Length (nm)	Aspect ratio	Young's modulus
NFC	"Top-down" chemical and mechanical treatment	Wood, sugar beet, potato tuber, hemp or flax	10–40	Several micro	>1000	100 GPa
NCCs	"Top-down" acid treatment	Wood, cotton, hemp, flax, wheat straw, rice straw, mulberry bark, ramie, MCC, Avicel, tunicin, algae, bacteria	10–20	100–600	10–100	100–200 GPa
BC	"Bottom-up"	Bacteria	5–6	1000–9000	160–1800	100 GPa

4.1.2.2 Chitin and Chitosan

Chitin is a polymer composed of *N*-acetylglucosamine units attached to each other by β-(1→4)-glycosidic bonds (Figure 4.2). This polysaccharide is also known as the second most abundant after cellulose and is mainly present in crustacean and insect shells, fungi, other microorganisms such as bacteria, mycetes and in minor quantities in squid feathers.[81] From a more commercial point of view, chitin products are mainly obtained from marine sources (*e.g.* shrimp, crab or krill shells). Shells, the raw biomass, are composed of chitin, proteins, minerals, secondary lipids and water.[82] Although all chitin feedstocks share those same components, the proportion of each component is different. Indeed, in crustacean shells, the mineral content usually ranges from 30% to 60% whereas chitin from insects contains a lower amount of calcium carbonate (<6%) and as a consequence, it can be more easily extracted.[83] Three crystallographic forms of chitin exist, namely α-, β- and γ-chitin, respectively, which possess different crystallographic structures depending on the orientation of the polymer chain. The α form, where chitin chains are arranged in an antiparallel manner, is present in the majority of crustacean shells and insects and is the most abundant and the most crystalline chitin form. The extraction process of chitin is generally based on an acid treatment to remove minerals followed by an alkaline treatment to remove proteins. Then, a decolorization step could also be performed in order to eliminate pigments leading to a white product. Depending on the source and the characterization technique employed, the DP can range from 50 to 200,[84] but the extraction process may have an impact on this parameter and as a consequence on the mechanical properties, gelation capability and flexibility.[85] It is also important to stress that one of the main drawbacks of this hydrophobic biopolymer is the lack of solubility in aqueous and organic solvents, which significantly limits the range of applications.[86]

Chitosan is obtained from chitin by a deacetylation step under strongly alkaline conditions resulting in partial depolymerization, so lower DP compared to chitin (Figure 4.2). The degree of deacetylation (DD), defined as the molar fraction of *N*-glucosamine (GlcN) in the copolymers composed of *N*-acetylglucosamine (GlcNAc) and GlcN, together with the molecular weight are the most important factors in assigning its application in the biomaterial field. In addition, depending on these two factors, chitosan can be soluble in acidic media. This biopolymer also possesses excellent biodegradability, biocompatibility, antimicrobial behavior, non-toxicity and anti-tumour properties and has the ability to form nanoparticles, microspheres, hydrogels, films and fibres, which are typically used for biomedical and pharmaceutical applications.[87]

4.1.2.3 Alginates

Alginates, referring to those salts from alginic acid, but also to all derivatives of alginic acid, are derived from brown algae cell walls (*i.e. Macrocystis pyrifera, Laminaria hyperborea, Ascophyllumnodosum*), and several bacteria strains (*Azotobacter, Pseudomonas*). Alginates are linear biopolymers consisting of 1,4-linked β-D-mannuronic acid (M) and 1,4 α-L-guluronic acid (G) residues arranged in homogenous or heterogenous block-like polymeric patterns (Figure 4.3). The composition (sequence of guluronic and mannuronic monomers) but also the length of the chain are related to the initial source.[88]

From an industrial point of view, it is possible to find commercially available alginates in various grades of molecular weight (ranging from 33 000 to 400 000 g mol^{-1}), diverse composition, and distribution pattern of M and G blocks. These important criteria critically influence the physicochemical properties of alginates such as viscosity, sol/gel transition conditions, and water uptake ability; and, as a consequence, on the type of potential

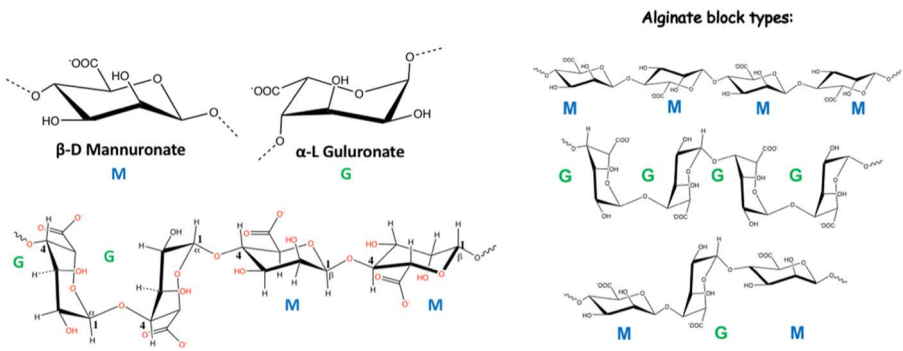

Figure 4.3 Chemical structure of alginates, where "M" stands for mannuronic and "G" for guluronic blocks, respectively.

applications. The manufacturing of processed food, cosmetic creams, cardboard and paper, and the pharmaceutical industry, are some important fields of application. These commercially available alginates are mainly obtained from algae sources using a simple multistage process. The procedure starts with a pre-treatment of the raw material using diluted mineral acid followed by the conversion of the obtained alginic acid into water-soluble sodium salt (sodium alginate) in the presence of calcium carbonate, which is one of the most widely investigated in the pharmaceutical and biomedical fields.[89] It is important to underline that alginates can be also produced by microbial fermentation to provide a kind of alginate with more defined physicochemical properties.[90] Their quality and potential applications strongly depend on their high degree of physicochemical heterogeneity. It is also important to highlight that as with cellulose and chitin/chitosan, alginic acid is insoluble in water and organic solvents. However, alginate monovalent salts and alginate esters are water-soluble, forming stable and viscous solutions of varied viscosity according to their concentration, solvent pH, temperature and the presence of divalent ions. In order to improve their physicochemical properties and/or biological activity, alginates can be easily modified through chemical or physical cross-linking leading to hydrogels that can be used for drug delivery systems and biomedical devices.[91]

4.1.3 Carbon Nanostructures and Polysaccharide Hybrids: Physical Interactions, Dispersive Action, Interfacial Synergies

Carbon nanostructures such as graphene and CNTs are unique nanoscale objects formed by a monoatomic layer of sp^2 hybridized carbon atoms arranged in a honeycomb lattice (Figure 4.4). They constitute an exciting class of 2D or 1D surface materials whose structural arrangement provides the basis for a whole bunch of exceptional mechanical, electrical, electronic, optical and thermal properties.[7,92] Being lightweight, chemically stable, and exhibiting record values for elastic moduli, as well as the highest electric and thermal conductivities, carbon nanostructures contribute to the development of novel functional materials and impact on advances in the field of structural composites,[93,94] flexible electronics,[95] thermal management,[96] energy storage and generation,[97] catalysis,[98] (bio)sensing and biomedical applications.[99,100]

To harvest the full potential of their extraordinary properties requires overcoming the strong agglomeration tendency of the individual carbon nanostructures, which is a direct consequence of strong attractive van der Waals interactions established between the hydrophobic surfaces of these nanoobjects. This results in piled-up stacks of graphene sheets and is responsible for the bundling or entanglement of SWCNTs and MWCNTs, respectively. The inherent hydrophobicity is also the origin of the poor dispersion behaviour in aqueous media. Strategies to separate the agglomerates into stable carbon

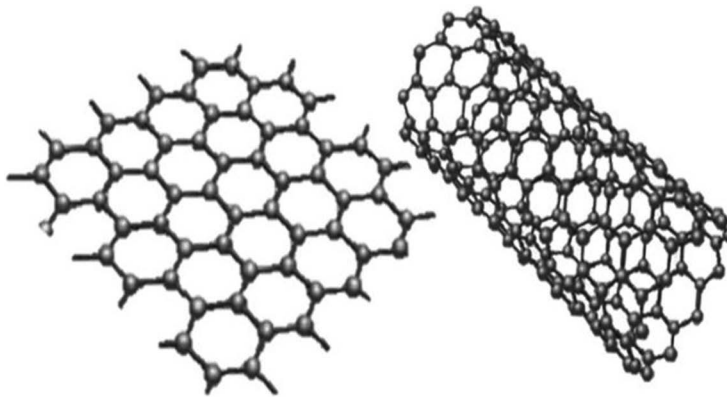

Figure 4.4 Schematic representation of a graphene sheet (left) and a carbon nanotube (right).

nanostructures (few or individually suspended) and to achieve stable colloidal dispersions typically rely on surface oxidation, covalent attachment of functional groups or the use of surfactant molecules and wrapping polymers.[99,101,102] While this ensures colloidal stability based on steric hindrance or electrostatic repulsion effects, it is accompanied by the modification of the intrinsic properties of the carbon nanostructures. An effective way out of this situation and of particular interest for biological applications is the use of water-soluble polysaccharides, such as gum arabic,[103,104] chitosan[105] or cellulose derivatives.[106] In particular, NFC or NCCs lead to irreversible CNT-cellulose associations favouring the individualization of the carbon nanostructures and the formation of stable aqueous dispersions up to very high concentrations. To understand the particular interactions resulting in the exceptional dispersion behaviour described in the recent literature, we first need to have a closer look at the structure of the most used polysaccharide for this purpose, namely cellulose.

It is worth recalling that cellulose is a linear homopolymer of ringed glucose molecules. The repeat unit is formed by two anhydroglucose ring units in the chair D-configuration connected by β-(1→4)-glycosidic linkages (Figure 4.5). The intrachain hydrogen bonding between hydroxyl groups and oxygen atoms of the adjoining rings stabilize the linkage resulting in a flat ribbon-like conformation. Van der Waals interactions and intermolecular hydrogen bonds between hydroxyl groups lead to parallel stacking of multiple cellulose chains into a crystalline microfibrillar structure of about 5–50 nm in diameter and several micrometres in length exhibiting a high axial stiffness.[107,108] The microfibrils are composed of crystalline domains of highly ordered cellulose chains and amorphous regions of disordered cellulose chains. The crystalline parts can be isolated by sulphuric acid hydrolysis leaving intact the crystalline regions thus affording rod-like NCCs with a square-like cross-section in the range of 5–30 nm and lengths of several hundreds of nm.

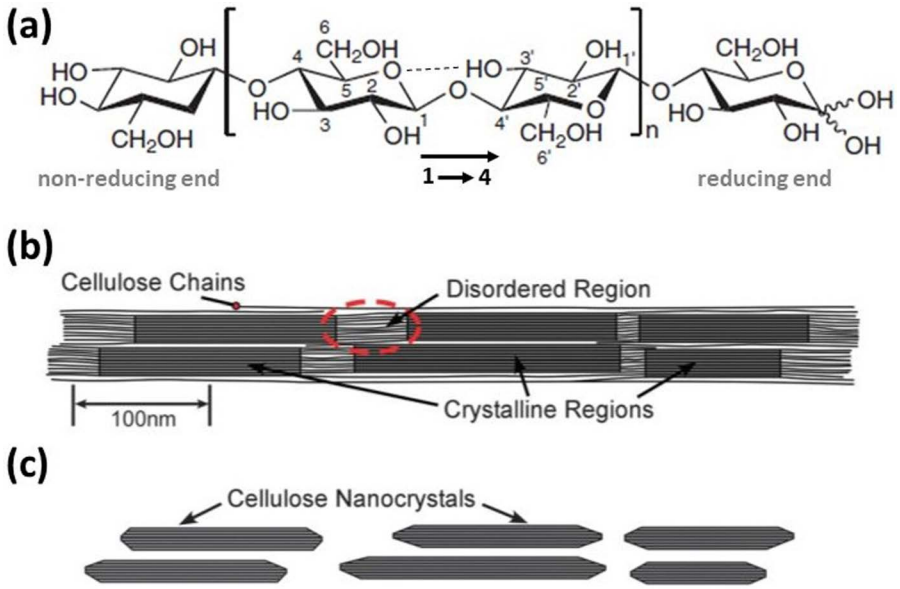

Figure 4.5 Schematic representation of (a) a single cellulose chain repeat unit, showing the directionality of the β-(1→4)-linkage, the intrachain hydrogen bonding (dotted line), as well as the non-reducing and reducing end-groups; (b) an idealized cellulose microfibril with crystalline and amorphous regions; and (c) cellulose nanocrystals after acid hydrolysis dissolved the disordered regions. Adapted from ref. 108 with permission from the Royal Society of Chemistry.

The relative position of the β-(1→4)-glycosidic bond in neighbouring chains, as well as its directionality along the chain axis (parallel up or parallel down) enables distinct possibilities for interchain interactions resulting in several cellulose polymorphs labelled type I, II, III and IV; types I and II being the most reported in the literature.[107–110] Cellulose type I is the most common allomorph being dominant in natural cellulose sources and is comprised of cellulose chains arranged in a parallel configuration. It consists of two co-existing forms I_α and I_β that differ in their kind of unit cell. Type I_α has a triclinic unit cell with one cellulose chain, whereas type I_β has a monoclinic unit cell with two chains alternately displaced by +c/4 and –c/4 in the chain direction. They have a squared cross-section with $(110)_m$ and $(1\bar{1}0)_m$ terminating surfaces (Figure 4.6).

I_α is metastable and can be transformed into I_β by hydrothermal treatments. The type II allomorph is the most thermodynamically stable structure and it has provided great technical relevance. However, its presence in natural cellulose is negligible. It is irreversibly obtained from type I by chemical modifications involving either regeneration (solubilization and recrystallization) processes, mercerization (harsh NaOH exposure) or sulphuric acid treatments.[111–113] This change from I to II entails the swelling of cellulose crystals, the break-up of existing hydrogen bonds and subsequent

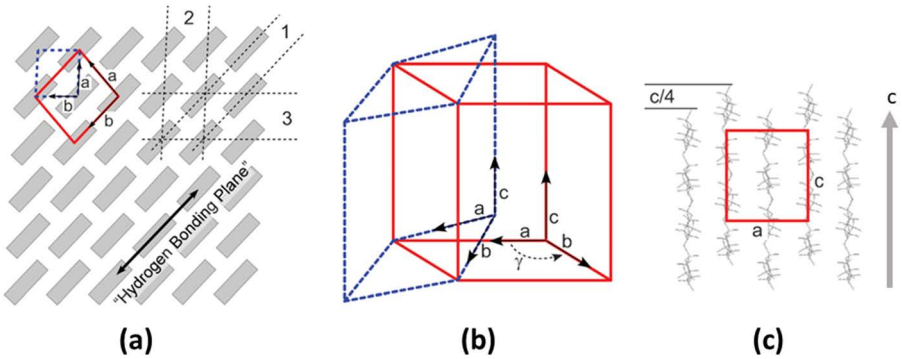

Figure 4.6 Schematic representation of the unit cell for cellulose I_α (triclinic (t), dashed) and I_β (monoclinic (m), solid). (a) Projection along the chain direction c with lattice spacing of d_1 = 0.39 nm (= $d(110)_t$ or $d(200)_m$), d_2 = 0.53 nm (=$d(010)_t$ or $d(110)_m$) and d_3 = 0.61 nm ($d(100)_t$ or $d(1\bar{1}0)_m$). (b) Relative configuration of I_α and I_β unit cell. (c) Alternating c/4 displacement of hydrogen bonding sheets for I_β polymorph. All chains are oriented in the up-configuration along the indicated c-direction. Adapted from ref. 108 with permission from the Royal Society of Chemistry.

chain intermingling causing a reorganization of neighbouring chains from a parallel to an antiparallel crystalline stacking arrangement whereby reducing and non-reducing ends point in opposite chain direction within the monoclinic unit cell. The highly ordered crystalline structure of the different polymorphs results in a highly faceted surface chemistry dictating the interactions with other species. As shown by molecular dynamics studies,[114] the square-like cross-sections of NCCs essentially exhibit two well developed surfaces defined by the hydrophilic $(110)_m$ and $(1\bar{1}0)_m$ planes for the monoclinic unit cell with a significant exposure of hydroxymethyl groups. Moreover, two minor faces are observed as blunt corners in TEM studies. These are made up by the hydrophilic $(010)_m$ plane, exhibiting hydroxymethyl groups, and the rather smooth and hydrophobic $(100)_m$ plane, rich in C–H moieties, directly attached to the glucosidic rings forming the surface backbone. This surface is characterized by the lowest surface energy and the attachment is essentially governed by van der Waals forces. However, it is important to note that the $(200)_m$ plane also possesses residual hydrophilic properties and, in turn, the dominant hydrophilic surfaces equally reveal a certain hydrophobic behaviour owing to the presence of C–H groups. Therefore, each of the surfaces constitutes an amphiphilic platform on its own with a more or less pronounced hydrophilic character. The detailed surface chemistry of the NCC depends on the employed nanocrystal isolation process, which may chemically transform the hydroxyl groups present on the surface of the native cellulose. Here, the employment of sulphuric acid (as the most commonly used hydrolysis reactant) gives rise to sulphate esters thus providing the surface a high acid content, while the (2,2,6,6-tetramethylpiperidin-1-yl)oxyl (TEMPO)-mediated oxidation process enables carboxylic acid groups (Figure 4.7) to result in highly charged surfaces.[108,109,115] Their presence is the origin of the

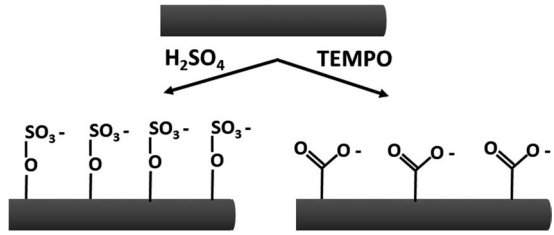

Figure 4.7 Surface functional groups on NCCs. H_2SO_4 and TEMPO-mediated isolation results in (left) sulphate esters and (right) carboxylic acid groups, respectively.

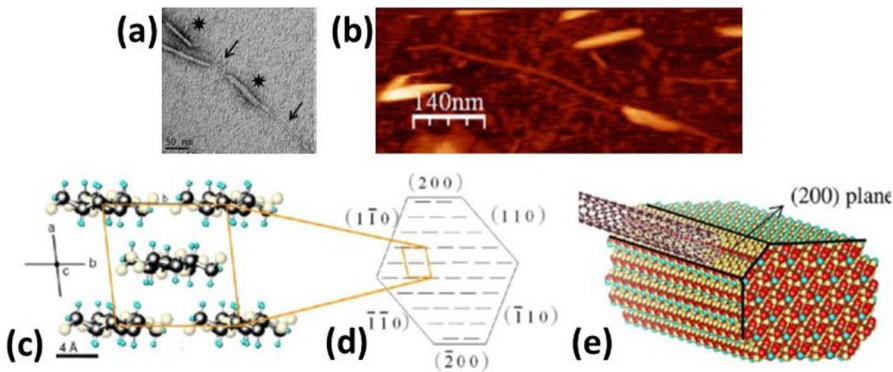

Figure 4.8 SWCNT-NCC association. (a) TEM image (arrows and stars indicate SWCNTs and NCCs, respectively) and (b) AFM image taken on a wet sample. Micrometre long SWCNTs with a co-aligned NCC can be easily identified. (c) Monoclinic unit cell and (d) cross-section of NCC with the hydrophobic $(200)_m$ and $(\bar{2}00)_m$ surfaces as preferential interaction sites with SWCNTs. (e) Representation of a SWCNT attached to the hydrophobic $(200)_m$ plane of NCC. Adapted from ref. 116 with permission from American Chemical Society, Copyright 2012.

excellent colloidal stability of the nanocrystals in aqueous media. With this background, we now proceed to the discussion of recent studies describing the interaction of NCCs with CNTs.

One of the first studies on the formation of associated SWCNT-NCC hybrid materials was presented by the group of O. Chauvet.[116] A NCC with a surface charge of 0.5 e/nm^2 was isolated from cotton linters by sulphuric acid hydrolysis. The rod-like crystals of 200 nm in length and a rectangular cross-section of 6 nm × 6.1 nm formed stable aqueous dispersions in water at a concentration of 20 g L^{-1} at pH = 4. SWCNTs (HiPCo brand) having lengths in the micrometre scale were added to the NCC suspension applying mild ultrasonication conditions to maintain the original length of the SWCNTs. In this way, NCCs were able to stabilize from 24% to 70% of SWCNTs. Transmission electron (TEM) and atomic force (AFM) microscopy studies clearly revealed that several NCCs align along the length of the SWCNTs (Figure 4.8).

AFM images taken in the wet-state confirmed that this co-alignment is a result of a self-assembly process occurring in the liquid. The authors suggest that hydrophobic interactions between the graphitic SWCNT surface and the hydrophobic (200) faces of the NCC enable the irreversible adsorption of nanocrystals along the SWCNT tube axis (Figure 4.8), thereby expelling water and stabilizing the dispersion of the SWCNT-NCC hybrids. It is emphasized that the electrostatic repulsion between NCCs may limit the number of nanocrystals associated with the hybrid structure. The partial coverage thus ensures the repulsion of the charged SWCNT-NCC complexes and keeps them dispersed in water without aggregation and further precipitation. In a follow-up work, it was demonstrated that the dispersion yield scales with the ratio of NCC concentration and the initial nanotube concentration.[117] The authors predicted dispersion yields of 100% for NCC concentrations of 10 g L^{-1}. Taking then into account the geometrical and density aspects of the SWCNTs and NCCs, it was calculated that one nanocrystal of about 120 nm in length could stabilize one SWCNT three to four times its length. This was experimentally supported by AFM observations counting the numbers of NCCs along the SWCNT length (Figure 4.9) and thus establishes a kind of stoichiometric relationship for the SWCNT-NCC hybrid association.

In the same work, it was further shown that MWCNTs could be also effectively dispersed by NCCs. The dispersion yield obeys an almost identical concentration dependency as was observed for SWCNTs whereby a maximum of 100% could be expected for NCC concentrations of 6.3 g L^{-1}. However,

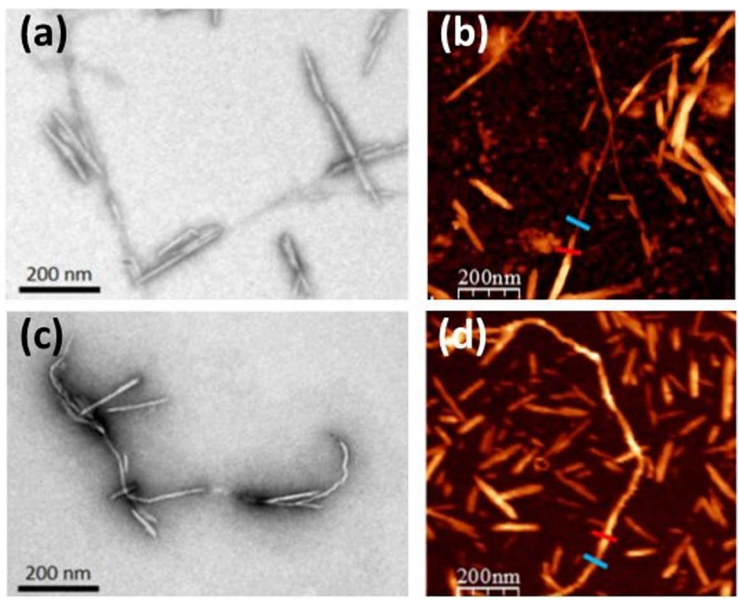

Figure 4.9 CNT-NCC hybrids. (a) TEM and (b) AFM images of SWCNT-NCC; (c) TEM and (d) AFM images of MWCNT-NCC. Adapted from ref. 117 with permission from American Chemical Society, Copyright 2016.

considerable differences arise concerning the interactions of MWCNTs with NCCs, where no co-alignment of their surfaces is observed. This is due to the fact that the MWCNT diameter is about 10 times larger resulting in a lower surface curvature and thus in reduced hydrophobic attraction towards the hydrophobic NCC surface. In addition, MWCNTs usually have many oxidative defects, which further decreases the hydrophobic interaction strength and requires many more NCCs to stabilize one MWCNT compared to a SWCNT of equal length. Therefore, the MWCNT-NCC association seems to be best achieved when interactions are established in a more random way (Figure 4.9). This most likely is assisted by the amphiphilic character of the NCC as outlined above. The authors further emphasized the importance of sufficient ultrasound exposure times required for achieving increased dispersion yields by enabling improved interactions of NCC with debundled SWCNTs or disentangled MWCNTs.

An important study to elucidate the dispersive action of nanocellulose on carbon nanomaterials was presented recently by the group of Wågberg.[118] For their investigation, they used TEMPO-mediated oxidized NFC of micrometre lengths and diameters of 3.5 nm with three different charge densities (290, 490 and 1400 μequiv g^{-1}), whereby the last one was further hydrolysed into NCCs with lengths of about 200 nm. Ultrasonicating SWCNTs in the NFC or NCC colloids provided stable dispersions with maximum dispersion yields of 60 wt% for the highest charged NFC and 75 wt% for a highly charged NCC. Dynamic light scattering (DLS) measurements revealed that higher-charged nanocellulose particles are able to disperse higher amounts of CNTs with a more efficient separation of the SWCNTs from their original bundles, thus underlining the crucial role of the surface charge of NFC or NCCs. A quantitative analysis of the interaction between nanocellulose and carbon nanomaterial surfaces was performed by using a colloidal probe AFM technique, thus offering direct access to the colloidal forces in aqueous media. Contract and retract experiments were carried out on a graphene sheet as a universal sp^2 model system probed by a NFC-coated spherical probe attached to the AFM in aqueous media (Figure 4.10).

It was demonstrated that NFC with higher charges adheres more strongly to the sp^2 carbon lattice in water. Therefore, it was suggested that upon ultrasonication, SWCNTs in the presence of NFC or NCCs are pushed toward the effective surface charged regions of the nanocellulose and associated with these highly charged structures that prevent reaggregation through electrostatic repulsion. The expulsion of water molecules in this process provides a gain in free energy favouring the stabilization of the SWCNT/NFC association. It was hypothesized that fluctuations of counterions on the surface of the nanocellulose induce polarization of the electrons in the sp^2 carbon lattice leading to attractive interactions between the two nanomaterials (Figure 4.10). The possibility of longitudinal polarizability of rod-like systems probably contributes to enhance the ion fluctuation effect and the induction of dipoles, thus leading to improved attraction in the case of CNTs. The described concept of adjusting the surface charges of NCC in order to regulate

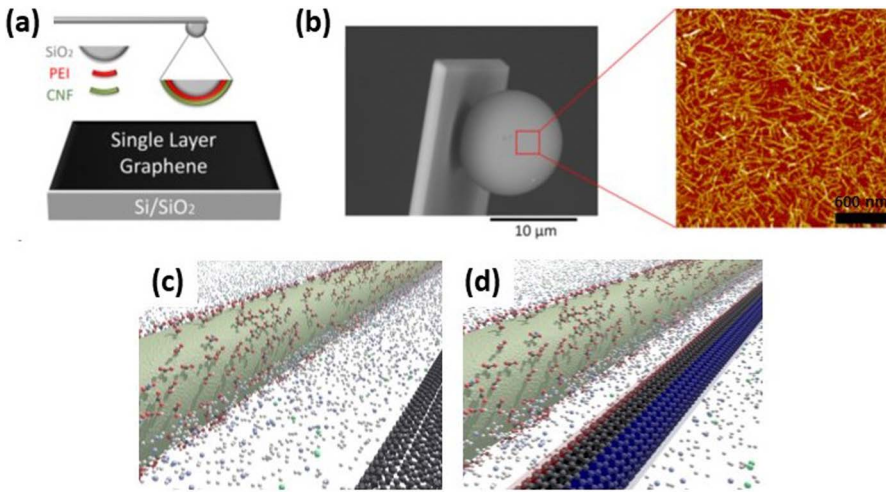

Figure 4.10 (a) Scheme of the colloidal AFM set-up probing a supported sp^2 layer (single graphene sheet) as a model surface for carbon nanostructures; (b) SEM image of the spherical SiO_2 probe of the cantilever fully covered with carbon nanofibres as seen in the AFM image; (c) schematic drawing of a charged nanocellulose rod (surface groups and counterions in water are indicated) and a SWCNT interaction in water before interaction; and (d) after induced interaction caused by dipole formation on a SWCNT. Adapted from ref. 118 with permission from American Chemical Society, Copyright 2017.

the CNT-NCC dispersion behaviour was successfully exploited by Kuzmenko *et al.*[119] By achieving a moderate decrease of electrostatic repulsion between the colloidal particles through the addition of NaOH, they were able to influence the rheological behaviour of the stable dispersion thus achieving inks with appropriate viscosities for printing applications.

The relevance of hydrogen bonding between hydroxyl and carboxyl groups on NFC and CNTs as an important mechanism for the interaction between both was emphasized by Li *et al.*[120] The authors carried out atomistic simulations and revealed that hydrogen bonding between NFC and CNTs indeed favours a strong co-alignment. They further demonstrated that a higher density of hydrogen bonds affords larger energy for breaking the NFC-CNT association and thus is responsible for improved mechanical performance.

All of the aforementioned studies show that the dispersive behaviour of NCCs for CNTs needs to take into account the action or even the joint action of different mechanisms. This involves mechanical wrapping, the interaction between hydrophobic sites of nanocellulose and CNTs, induced dipoles on the sp^2 carbon lattice surface of CNTs by fluctuations of counter ions on the surface of nanocellulose, but as well, hydrogen bonding formed upon hydroxyl and carboxyl groups. The relevance of each type may vary from case to case and needs to take into account the specific surface chemistry of the employed nanocellulose and its crystallographic arrangements.

In this context, González-Domínguez *et al.* recently studied for the first time the influence of the type of NCC polymorphs on the interaction with SWCNTs and their dispersion behaviour.[113] NCCs were isolated in a controlled way by sulphuric acid hydrolysis either of pure type I or of type II. While the NCCs of type I exhibited a needle-like morphology with lengths between 200–300 nm and widths of 5–10 nm, the type II NCCs revealed a twisted ribbon-like structure with lengths ranging from 50–100 nm and widths of 15–20 nm, thus being shorter and wider compared to type I (Figure 4.11).

Adding purified SWCNTs (without oxygen functional groups) under ultrasonication to the NCC water colloid resulted in highly stable SWCNT-NCC dispersions, withstanding ultracentrifugation forces, eventually containing 10 wt% SWCNT, independent of the NCC polymorph being used. Moreover, for both types I and II, the zeta potential of the overall SWCNT-NCC systems was higher than that of the individual components, thus indicating the formation of a stable and synergistic association. However, the morphology of the SWCNT-NCC for type I and type II hybrids appeared to be completely different. The needle-like structures of type I are observed to align along the SWCNTs, most likely established through hydrophobic interactions as outlined by Chauvet and co-workers.[116,117] On the contrary, the twisted and more flexible ribbon-like structure of type II seems to wrap-up the SWCNTs entirely forming an overall entangled network structure (Figure 4.11). The antiparallel stacking of the cellulose chains in type II NCCs most likely opened additional channels for achieving favourable interactions with SWCNTs. This may include enhanced electrostatic interactions of the highly charged nanocellulose surface based on induced dipole interactions as described by Hajian *et al.*[118] However, it should not involve hydrogen bonding as proposed by Li

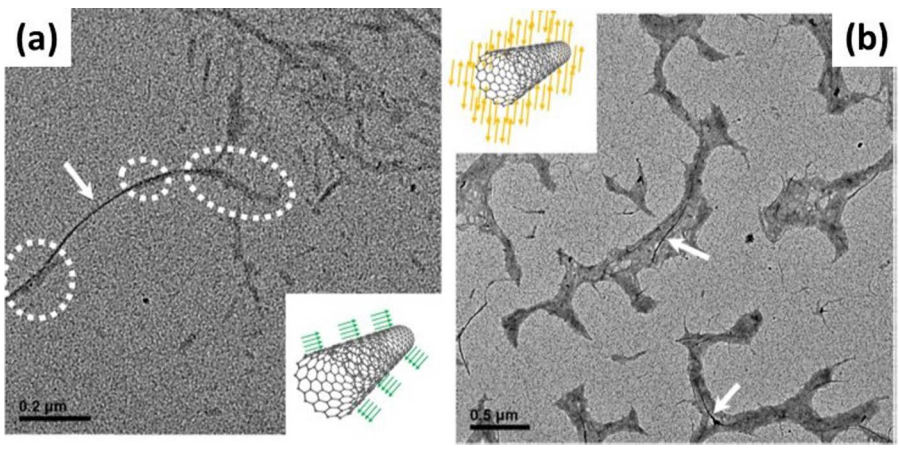

Figure 4.11 TEM images of (a) NCCs of type I aligned along SWCNTs and (b) type II NCCs wrapping-up of SWCNTs. The insets show a conceptual representation of the SWCNT dispersive interaction with the two different types of NCCs. Adapted from ref. 113 with permission from American Chemical Society, Copyright 2019.

et al.,[120] in this case, owing to the absence of carboxyl groups of the employed purified SWCNTs, despite the enhanced hydrophilic character of surfaces of the type II NCCs. Interestingly, the hydrodynamic diameters of the SWCNT-NCC hybrids were significantly reduced compared to NCC alone, further suggesting the efficient debundling and individualization ability of NCCs.

During the course of this section, it thus should have become clear that the rich surface chemistry of NCC polymorphs provides a great playground for establishing favourable interactions with carbon nanomaterials and the formation of highly stable colloidal dispersions. The basic concepts of the proposed interaction mechanism also are transferable to other types of polysaccharides, as shown for example in the case of chitosan with reduced graphene oxide.[121] Independent of the prevailing type of interaction, which definitely still needs to be elucidated in far more detail, all studies unanimously report the extraordinary ability of NCCs to associate with individual carbon nanostructures and to produce highly stable water-based colloidal dispersions. They have been successfully exploited as biocompatible and bioactive materials,[113] conductive inks,[119] mechanically flexible and conducting nanopapers, aerogels and extruded microfibres,[118,122] and as printed electrodes for tissue engineering,[119] among others, and thus offer great promise for diverse biomedical applications.

4.2 Biomedical Materials Made of Carbon Nanostructures and Polysaccharides. Examples and Applications

4.2.1 Cellulose-based Hybrids

As stated in earlier sections, cellulose is the most abundant biopolymer on Earth. It is formed by the linear polymerization of glucose monomers in a β(1→4) bonding type, containing each chain from a few hundred to many thousand monomers. Cellulose is naturally present in vegetable cell walls and generated by specific bacteria. The main sources for its industrial utilization are commonly wood pulp and cotton, due to their wide availability and high cellulose purity ratio. If the native crystalline allomorph is the so-called type I (with a parallel disposition of chains), another three artificial crystalline allomorphs are known, among which type II (with an antiparallel chain arrangement) stands out. The inherent high crystallinity owned by cellulose confers good mechanical properties, which is the reason why cellulose is widely employed for textiles, packaging, paper and cardboard manufacturing, food additives, and as a precursor of a long list of valuable derivatives such as cellulose acetate, nitrocellulose, cellophane, or rayon. Given the extremely high biocompatibility and hydrophilicity of cellulose, it has been used for a long time in medical applications, mostly in textile form (bandages, gauzes, stitches...); albeit in recent decades new uses of cellulose are starting to emerge, in consonance with the advance of carbon nanotechnology. The use

of (nano)cellulose-carbon nanostructure-based hybrids has been excellently reviewed in recent reports,[123,124] with important results in optoelectronic and structural applications. There are also reviews with a focus on biomedical applications of such hybrid materials.[125] In this section, representative examples of this new horizon on such an important biopolymer will be exposed, in particular taking into account hybrid materials that have arisen by virtue of the excellent synergy between cellulose (bulk or nanostructured) with other carbon nanostructures in biomedicine. Hybrid nanomaterials, based on carbon nanostructures, with no other component than cellulose (or nanocellulose) are being extensively studied in terms of biocompatibility, and in some cases regarding their bioactivity in specific biomedical contexts. These studies are generally performed in aqueous media, provided that (nano)cellulose enables the efficient dispersion of such carbon nanostructures in water, as described in an earlier section. In the following, landmark examples will be outlined according to the carbon nanomaterial employed.

4.2.1.1 Hybrids with Carbon Nanotubes (CNTs)

BC is a material that is being increasingly investigated due to the sustainable and 'green' procedure for its synthesis (bacteria, renewable feedstocks), its excellent physical properties (spawned by nanofibrillar morphology and high crystallinity), and the versatile possibilities to obtain membranes, films or porous aerogels by tailoring the drying conditions.[126] One of the greatest advantages of BC is its generation in the form of a hydrogel; the reason why the subsequent integration of carbon nanostructures can be accomplished in an aqueous environment. In one of the seminal works in this direction, Kim and co-workers fabricated hybrid BC materials with MWCNTs by a simple filtration procedure.[127] Over this hybrid material, glucose oxidase (GOx) enzyme was easily immobilized, and an electrode could be built. The electrochemical determinations showed that the activity of GOx was perfectly registered, and there was evidence of direct electron transfer. These results set the basis towards the construction of biosensors with such a sustainable and renewable hybrid material, to whom biocompatibility is presupposed.

In a more recent work, Kuzmenko *et al.* created hydrogel inks composed of NFC, made of carboxymethylated nanocellulose, and oxidized SWCNTs.[119] After tailoring and optimizing the rheological properties of those inks (made by the joint dispersion of both components with intense ultrasounds), they were used in a 3D printing procedure *via* the manipulation of pH. The printed structures worked as neural guidelines, tested upon the culturing of human SH-SHY5Y neuroblastoma cells. An excellent cell attachment and proliferation was observed, and ascribed to the good conductive properties of the ink, showing a promising future in the development of novel neuronal engineering approaches.

Another biomedical target of direct application is haemostasis. In this sense, an interesting work authored by Cheng and co-workers reported the

creation of haemostatic gauzes made of regenerated cellulose (recrystallized type II allomorph) with functionalized MWCNTs with terminal amine or carboxylic groups.[128] In particular, the direct attachment of amine-terminated MWCNTs to a gauze composed of oxidized (carboxylated) regenerated cellulose was carried out using glutamic acid as a cross-linker. This example showed a good water uptake and shorter haemostasis time *in vivo* (ear artery and liver injuries in a rabbit model), outperforming the blank gauze even at low loadings of MWCNTs.

If all these examples so far take advantage, in one way or another, of the biocompatible features of these (nano)cellulose-nanocarbon hybrids, little is said on their possible bioactivity. With this aim, it was discovered that SWCNT dispersions in aqueous colloids of NCCs, both in a non-oxidized form, exhibited not only biocompatibility towards human intestinal (Caco-2) cells, but also a differential bioactivity towards healthy and cancer cells within this cell line.[113] By tailoring the cell culture conditions, Caco-2 cells may behave as normal (healthy) or cancer-like, so these NCC-SWCNT hybrids could be tested in both situations, respectively (Figure 4.12). The *in vitro* results showed a critical dependence on the NCC crystalline allomorph used for creating the hybrids, namely type-I or type-II, the latter being synthesized only upon acid hydrolysis without any kind of mercerization or recrystallization steps. NCC-SWCNT hybrids containing type-II NCCs showed unprecedented bioactivity by selectively killing colon cancer cells, while being non-harmful to normal cells. On the other hand, type-I NCC-based hybrids displayed a generally innocuous trait to both kinds of Caco-2 cells (full biocompatibility

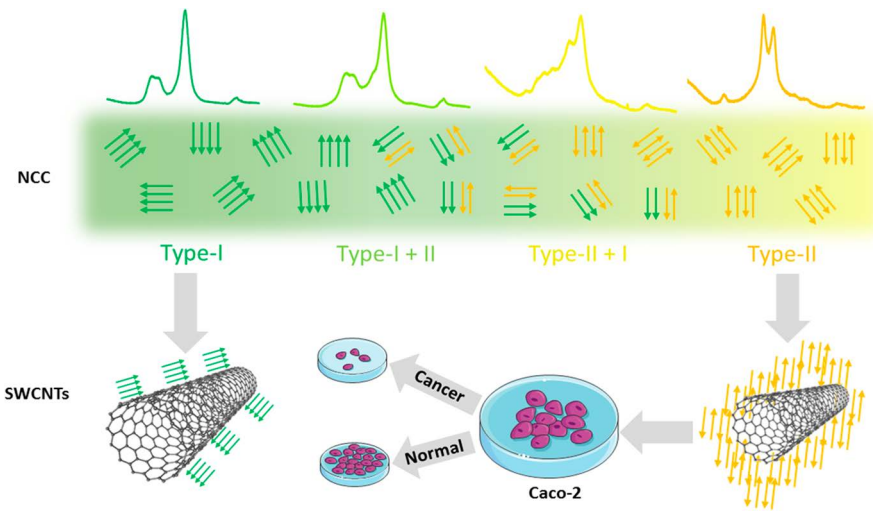

Figure 4.12 Scheme showing the use of NCC types I and II for dispersing SWCNTs in water, together with their biocompatibility and bioactivity towards human colon cancer cells. Adapted from ref. 113 with permission from American Chemical Society, Copyright 2019.

but no bioactivity), so the former hybrids could stand as promising tools for the future development of novel colon cancer therapies.

4.2.1.2 Hybrids with Graphene and Related Derivatives

An early example from Jin *et al.* showed another strategy to include carbon nanostructures into a BC matrix. These authors performed the *in situ* culture of BC with co-dispersed GO, resulting in a hybrid nanocomposite with the simultaneous reduction of GO.[129] This rGO hybrid was tested as a cell growth scaffold throughout the *in vitro* culturing of human mesenchymal stem cells (hMSCs). A satisfactory cell adhesion growth and proliferation of the hMSCs was observed, with an apparently unaltered morphology, which was ascribed to the improved physical properties and hydrophilicity of the hybrid as compared to a bare rGO film, in which the hMSCs did not develop so well. This work demonstrates the crucial role that the polysaccharide plays in boosting the biocompatibility of carbon nanostructures.

A subsequent work on hMSCs by other authors (Liu and co-workers)[130] explored not only their growth but also their osteogenic differentiation. The hybrid of choice was cellulose acetate (CA) mixed with GO in the form of nanofibrous mats, preceded by the co-dispersion of both in organic solvents and electrospinning. The authors not only found a clear osteogenic differentiation of hMSCs and an accelerated biomineralization effect, but also a concentration-dependent relationship with the GO content. The postulated hypothesis is that GO may act as a nucleation centre for calcium phosphate, revealing a biomimetic environment generated by the synergy of both components. These GO-CA hybrids could be advantageously used in the future for the development of bone-repairing materials and other possible bone regeneration applications.

If the previously mentioned examples deal with the use of GO (or rGO) with different cellulose materials, few works can be found on the use of pristine (non-oxidized) graphene. A particularly appealing work, authored by H. Luo *et al.*, directly compares the performance of graphene and GO in a BC matrix, both prepared by an *in situ* culture of bacteria with the carbon nanomaterial present in the culture medium.[131] Microscopic observation of the as-prepared hybrid nanocomposites show a homogeneous distribution of graphene or GO across the BC matrix, and through contact angle measurements. The GO-based hybrids exhibited higher wettability than the graphene counterparts as could be expected. A thorough biocompatibility study was carried out *in vitro* on mice MC3T3-E1 osteoblasts, characterized by a full set of techniques including morphology observation (preceded by selective staining), CCK-8 and alkaline phosphatase tests. The authors concluded that the graphene-based hybrid presented worse biocompatibility than the bare BC matrix, while the GO-based hybrid showed much better results, outperforming BC even in terms of bioactivity. Not much is said about these differences, but the higher hydrophilicity of GO (and thus, the higher hydrophilicity of the BC hybrid) seems to be the key.

4.2.1.3 Ternary Hybrids

Up to this point, we have presented several literature examples on hybrid nanomaterials composed exclusively of carbon nanostructures and a cellulose derivative, in order to show that the synergy between both is sufficiently strong to provide important breakthroughs in biomedicine. Nevertheless, a large pool of literature works deal with multicomponent hybrid nanomaterials, in which at least a third component is present. For instance, Ioniță *et al.* studied the joint effect of CNTs and GO as fillers in a CA membrane.[132] The resulting ternary nanocomposite exhibited the best filler distribution and mechanical properties, as compared with the binary counterparts, as well as being the most stable against hydrodynamic forces induced by flux tests. The superior performance of this ternary composite was also noticed in terms of biocompatibility, on murine 3T3E1 preosteoblasts, displaying excellent cytocompatibility. A very interesting biomedical application of these ternary hybrids, namely haemodialysis, was explored, and again the ternary nanocomposites outperformed the binary counterparts as per a +90% protein rejection (mainly haemoglobin and bovine serum albumin).

However, the most recurrent compatibilizers are synthetic polymers. These polymers are usually intended as a means to provide structural integrity or improved integration in the rest of the components. Park and co-workers used a self-synthesized amphiphilic copolymer, through the copolymerization of methyl methacrylate and ethylene glycol, to pre-disperse MWCNTs thus improving their integration into BC by the *in situ* culture method (Figure 4.13).[133] In fact, the difference between the pre-dispersion (or not) of MWCNTs was significant in their final dispersion degree within the BC matrix, which was translated into an exceedingly higher response in the biomedical application tested. This was the *in vivo* evaluation of these hybrids as scaffolds for bone regeneration in mice skulls. The ternary hybrids exhibited excellent osteoinductivity and osteoconductivity leading to a high level of bone regeneration.

The incorporation of polymers with the aim of providing structural consistency was followed by Pal and co-workers. These authors incorporated a hybrid nanomaterial (composed of rGO and NCCs) into poly(lactic acid) (PLA) films through solution casting.[134] The cell viability of these films was confirmed on NIH-3T3 fibroblasts, through both MTT assay and cell morphology observations. The biomedical application of choice was the antibacterial potential of the films, which was tested over *E. coli* and *S. aureus* pathogenic bacteria. The absence of cytotoxicity and their proven antibacterial performance makes these films potentially interesting candidates for biomedical applications.

4.2.2 Chitin-based Hybrids

Within the most important natural polysaccharides, chitin, poly (β-(1→4)-*N*-acetyl-D-glucosamine), has already been found to be the second most abundant polymer in the world after cellulose. This polymer is synthesized by crustaceans and insects forming structural components in their exoskeleton. Regarding its structure, it can be found in three different allomorphs: α, β and

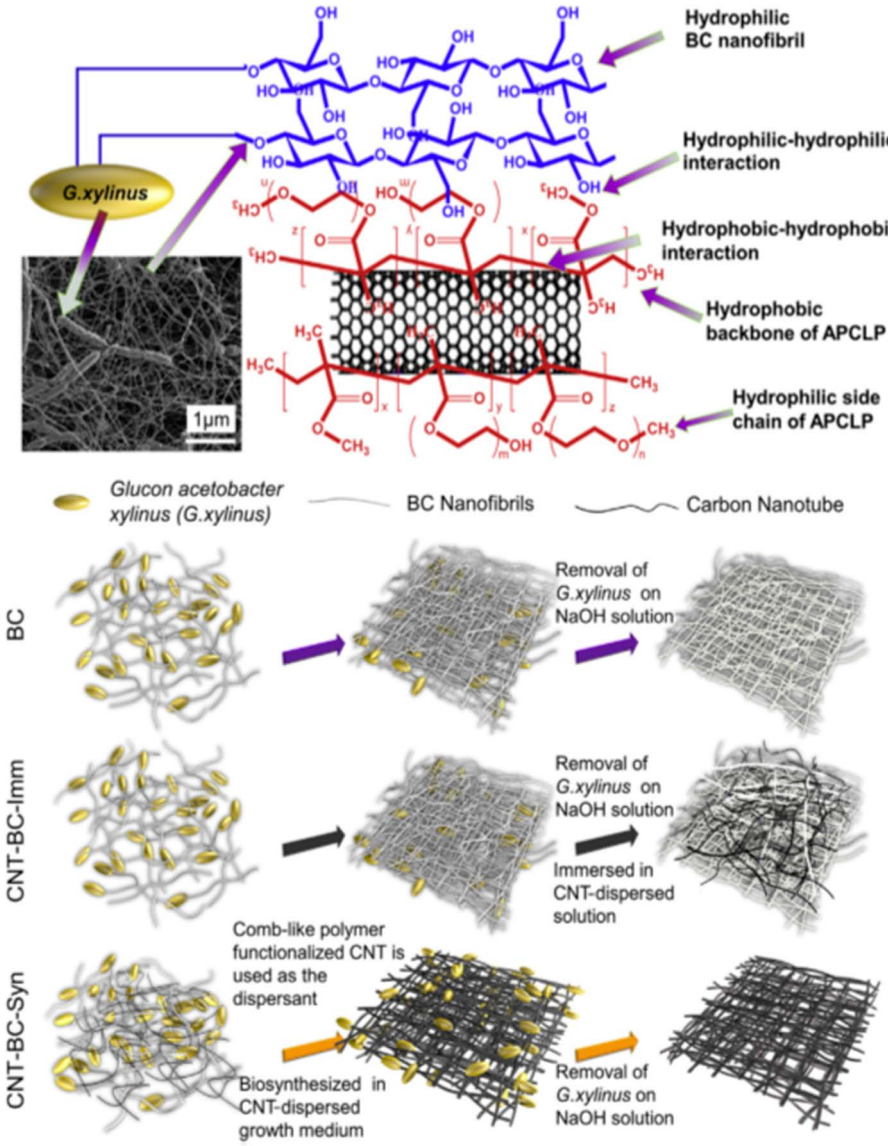

Figure 4.13 Hybridization approach to integrate MWCNTs into BC through a tailored amphiphilic polymer, and the improvements caused in the degree of dispersion. Adapted from ref. 133 with permission form Elsevier, Copyright 2015.

γ chitin, where the α-chitin is the most abundant.[135] α-chitin, which is found in fungi, krill, yeast, shrimp shells and lobster or crab tendons, is formed by recrystallization from chitin solution or enzymatic polymerization since this isomorph is thermodynamically more stable. On the other hand, β-chitin can be found in association with proteins in squid pens and vestimentiferan

worms. Crystallography analysis of the two chitin isomorphs confirms that there are two antiparallel molecules per unit cell in α-chitin but just one in a parallel fashion for β-chitin.[82]

Furthermore, chitin contains a high number of intramolecular hydrogen bonds, which produce a high degree of crystallization and, consequently, very low solubility in common solvents.[136] As an alternative to harsh chemicals or ionic liquids to process chitin, Zhang *et al.* developed an aqueous solution based on NaOH/urea with the ability to dissolve it, by freezing-thawing cycles leading to the formation of hydrogels.[137] Additional factors such as low toxicity, biodegradability, physiological inertness, hydrophilicity, antibacterial and gel-forming properties have caught the attention of researchers, making chitin a promising material for biomedical applications, such as wound healing acceleration,[138] wound dressings,[139] drug release[140] or adsorption of industrial pollutants.[141]

Additionally, the combination of chitin with carbon nanomaterials opens a new field of study in biomedicine, in which several researchers have obtained noticeable results. The joint occurrence of biocompatibility and the ability to form hydrogels turns chitin into an interesting candidate for tissue engineering. Carbon nanomaterials, such as GO, have shown advantages as cross-linkers to enhance the mechanical properties of the hydrogels, due to its large surface area, hydrophilicity and biocompatibility. The combination of chitin and GO to create a hybrid hydrogel resulted in an increase of the mechanical properties, due to the better dispersion of GO across the chitin structure, and most importantly, a high value of cell viability in L02 cells (above 90%) when this material was tested, proving its good biocompatibility as a potential candidate for tissue engineering.[142]

Apart from GO, the combination of chitin with other nanomaterials such as MWCNTs has shown potential interest in biomedicine, in particular for their excellent electrical conductivity and high aspect ratio. Hydrogels formed by these two materials can be used as scaffolds with electrical stimulation, as an alternative to metal-based conductive analogues, which display a limited lifespan *in vivo*. Singh *et al.* developed a scaffold composed of chitin and non-covalently functionalized MWCNTs with carboxymethyl cellulose (cMWCNTs) to enhance their dispersion in ionic liquids (Figure 4.14), in order to evaluate the viability and proliferation of mesenchymal stem cells. After 3 and 14 days of incubation, a LIVE/DEAD viability assay showed a large proportion of cell attachment to the chitin/cMWCNTs' scaffold, therefore confirming a successful cell proliferation.[143]

Tissue engineering is of great interest as a tool to repair several injuries in the human body. In the case of nerve injuries, whose damage is very difficult to repair,[144] the nerve regeneration induced by electrical stimulation can be promoted by bio-scaffolds based on chitin and carbon nanostructures. Chitin/MWCNT hybrids formed by the aid of ionic liquids, as mentioned above, and treated with O_2 plasma to increase their roughness, hydrophilicity, and cell adhesion, have been proven to enhance tissue regeneration. This

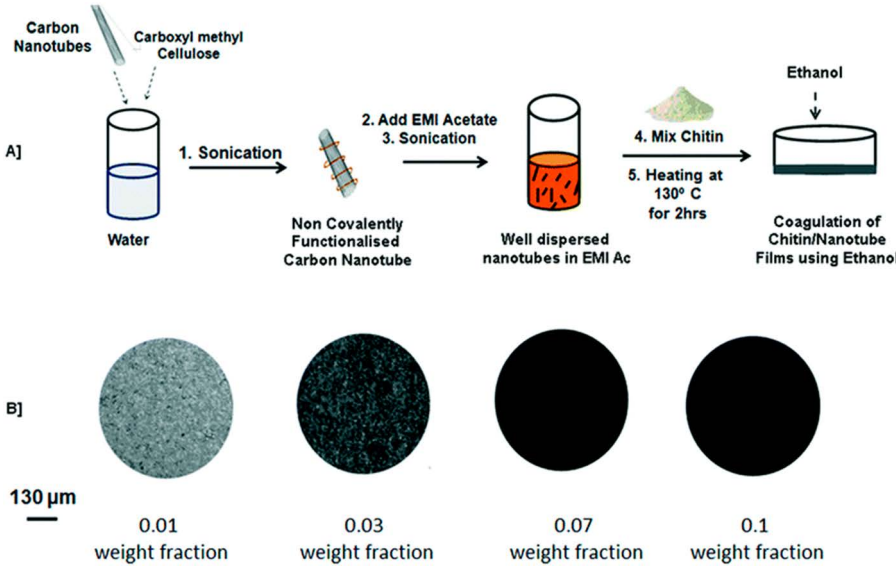

Figure 4.14 (a) Fabrication of chitin/cMWCNTs composite *via* ionic liquids dispersion. (b) Chitin/cMWCNTs composite membranes, images with different concentrations of cMWCNTs. Adapted from ref. 143 with permission from Royal Society of Chemistry.

particular scaffold was tested with neurons, where an extensive cell adhesion was found, together with a large signalling complex that produces the synapsis, detected by the PSD-95 expression (a protein involved in the synapsis between neurons).[145] Additionally, chitin/MWCNT scaffolds prepared using the aforementioned NaOH/urea solution have been used to test the viability of neuronal (PC12) and Schwann (RSC96) cells (Figure 4.15). These conditions led to migration and proliferation around the axon of injured neurons, producing neurites with large elongation and facilitating the axonal regrowth and regeneration of the nerve.[146]

Hybrid nanocomposites made of chitin and carbon nanostructures have also resulted in potential interest for other biomedical purposes, such as the healing of liver diseases. One of the most harmful problems is acute liver failure, which produces a rapid deterioration of liver function, impaired protein synthesis and hepatic encephalopathy, which derives in a significant increase of serum bilirubin.[147] Current therapeutic approaches consist of haemoperfusion, a blood purification therapy, which uses adsorbent agents to immobilize bilirubin by hydrophobic interactions and electrostatic hydrogen bonds. Chitin/CNT microspheres with immobilized lysine, a highly specific ligand to bilirubin, have exhibited an ability to remove large amounts of bilirubin in blood plasma with low side effects. These microspheres were formed by using the recurrent NaOH/urea solution, and poured over isooctane for the emulsion process.[148]

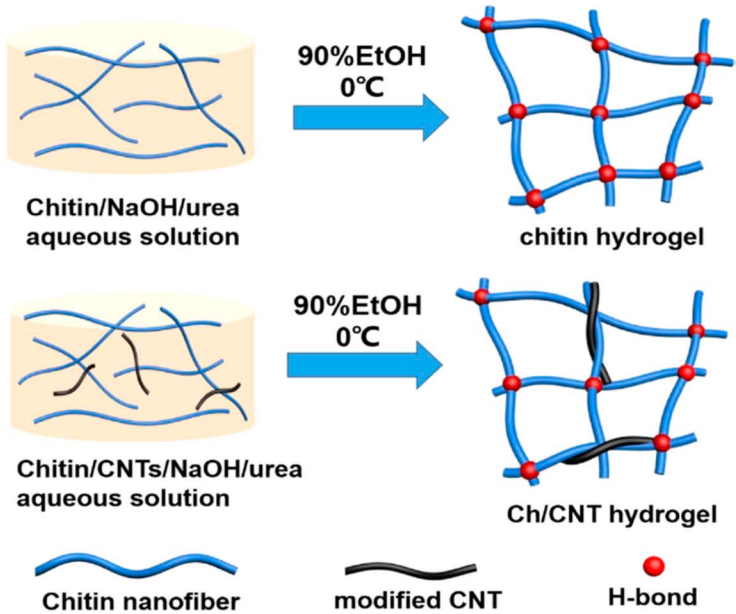

Figure 4.15 Schematic structure of chitin/CNT hydrogels prepared from aqueous NaOH/urea solution. Adapted from ref. 146, with permission from Elsevier, Copyright 2017.

4.2.3 Chitosan-based Hybrids

Owing to its excellent properties (biocompatibility, nontoxicity, biodegradability, antimicrobial and water solubility), together with its ability to form two- or three-dimensional scaffolds, chitosan has been extensively used in the biomedical field. As stated above, chitosan corresponds to partly deacetylated chitin, be it of natural or synthetic origin, so the quality of chitosan is directly linked to several factors such as the source of chitin, the extraction process and the conditions of deacetylation. In addition, depending on the molecular weight, the DD and the distribution of acetyl groups on the polymer backbone, the biological, physical and solubility properties will vary greatly. Indeed, several studies have shown that molecular weight has a huge impact on antibacterial properties. Low molecular weights allow chitosan to bind with DNA, penetrate into bacterial cells and inhibit mRNA synthesis as well as DNA transcription whereas, in the case of high molecular weights, chitosan can bind with negatively charged components of the bacterial cell walls, forming a resistant layer around them and hampering the transportation of ions into the cells.[149,150] Regardless of the DD and molecular weight, chitosan showed a stronger bactericidal effect towards Gram-negative rather than towards Gram-positive bacteria. Moreover, it has also been shown that

low pH chitosan solutions of low DD present better antibacterial activity.[151] On the other hand, for antifungal activity, the molecular weight and DD dependences were linked with the change of fungus.[151] Antioxidant activity, defined as a limitation of the oxidation of proteins, lipids, DNA or other molecules that occurs by blocking the propagation stage in oxidative chain reactions, was also highlighted for low molecular weight chitosan. These are able to scavenge the active oxygen free radicals *in vitro* through their stabilization by amino and carboxyl groups present on the chitosan's structure.[152,153] Chitosan is able to adhere to mucosal tissues and the underlying mechanism has been studied by Sogias *et al.*[154] They demonstrated that mucoadhesive interactions between chitosan and mucin are mainly due to electrostatic attraction accompanied by contributions from hydrogen bonding and hydrophobic effects. Depending on the pH of the solution and the presence of additional species (sodium chloride, urea, ethanol), the particular contribution of each physical interaction may vary. Due to its polycationic structure and its non-specific binding to cell membranes, the haemostatic properties of chitosan have been also demonstrated. Indeed, chitosan induces blood coagulation and platelet aggregation, and some studies reported a clotting time to reduce by 40% compared to whole blood alone.[155,156] Antitumoral properties of chitosan and its derivatives have also been evaluated using both *in vitro* and *in vivo* models. Chitosan nanoparticles with positive surface charge exhibited higher antitumor activity on Sarcoma-180 and mouse hepatoma H22 than other chitosan derivatives. Smaller particle size involves higher surface-to-volume ratio and specific surface area, and consequently, a more efficient dissolution arises, together with increased bioavailability of poor water-soluble molecules. The doses and administration routes also play an important role.[157,158] It is also important to highlight that chitosan depolymerisation catalysed by bioenzymes in biological organisms may occur, resulting in non-toxic degradation products namely *N*-acetyl glucose and glucosamine.

Due to these excellent biological properties, several pharmacological applications have been reported in the literature such as wound healing properties, drug delivery systems, tissue engineering and so forth.[159,160] Therefore, in the pharmaceutical industry, chitosan is mainly utilized as an excipient for tablets, gels, absorption and drug dissolution enhancers, in wound healing products, and in the development of micro/nanoparticles. The ability of chitosan to be easily processed into gels, membranes, nanofibres, nanofibrils, beads, scaffolds and sponge-like forms paves the way for new development opportunities by integrating other components, concomitantly resulting in an improvement of its mechanical properties.[161,162] Inorganic fillers such as hydroxyapatite, calcium phosphate cements, and clays are generally used to reinforce chitosan matrices but more recently, the incorporation and the effect of carbon nanostructures such as CNTs or graphene-based nanomaterials have been explored. Besides, chitosan has plenty of surface amino

groups that enable grafting-driven modifications that can be employed to strengthen the filler-matrix interactions, something that is not so common in formerly described polysaccharides.

4.2.3.1 Chitosan/CNT Hybrids

The excellent mechanical, electrical and thermal properties owned by CNTs, together with their unidimensional character make them one of the most useful nanostructures for reinforcement of polymeric matrices. However, the toxicity of CNTs continues to pose a challenge in the field of biomedicine. Surface functionalization with hydrophilic moieties such as chitosan and its derivatives may enhance their water affinity.[163,164] Even so, very few articles on the combination of chitosan/CNT have been reported. One of the first reports oriented towards biomedicine was published by Zhang *et al.* in 2004.[165] Pristine MWCNTs were mixed with an aqueous solution of chitosan to enhance the solubilisation and manipulation. Robust nanocomposite films were obtained and used as a biosensor for NADH. Mechanical properties of chitosan have also been improved by mixing it with oxidized MWCNTs. Strong interactions between the carboxylic and hydroxyl groups of oxidized MWCNTs and the functional groups of a chitosan matrix have been highlighted for many years as the cause of the extraordinary synergy between both elements, resulting in a great improvement of the tensile modulus and strength of the derived nanocomposites by about 93% and 99%, respectively, compared to neat chitosan.[105]

In a recent paper, the authors described the formation of a novel chitosan/MWCNT hybrid, suitable as a nanocarrier for the selective delivery of methotrexate (MTX) to H1299 lung cancer cells, with negligible toxicity to healthy MRC-5 cells.[166] MWCNTs were first oxidized and then non-covalently coated with chitosan, both interacting mainly *via* polar interactions. These nanohybrids possessed high biocompatibility and affinity for the drug, and compared to the free MTX that penetrated the cell membrane through passive diffusion, a longer time was required for endocytosis-mediated internalization of MTX-loaded nanohybrids.

Li *et al.* reported another chitosan/CNT hybrid that significantly inhibited tumour growth of A549 cell-bearing nude mice through active tumour-targeting ability.[167] In this study, docetaxel (DTX) was first loaded on oxidized SWCNTs *via* π–π stacking followed by the non-covalent conjugation of fluorescein- and peptide-labelled chitosan, resulting in a multicomponent hybrid.

High mechanical strength and mineralization capability are two of the most important characteristics of the bone tissue; therefore, CNT-based 3D scaffolds including chitosan matrices can also be found in the literature with this purpose.[168,169] Several methods such as controlled surface deposition and cross-linking processes, simple solution evaporation methods, thermally induced phase separation followed by freeze drying, electrodeposition, spray layer-by-layer technique, electrical actuation and wet spinning have been described for the formation of such scaffolds. Among these examples,

Venkatesan *et al.* reported the formation of a 3D-scaffold using low and high molecular weight chitosan and different concentrations of functionalized MWCNTs (0.0025, 0.005 and 0.01 weight %) by a freeze-drying method (Figure 4.16).[170] The authors observed that functionalized MWCNTs were uniformly dispersed across the chitosan matrix *via* chemical interactions,

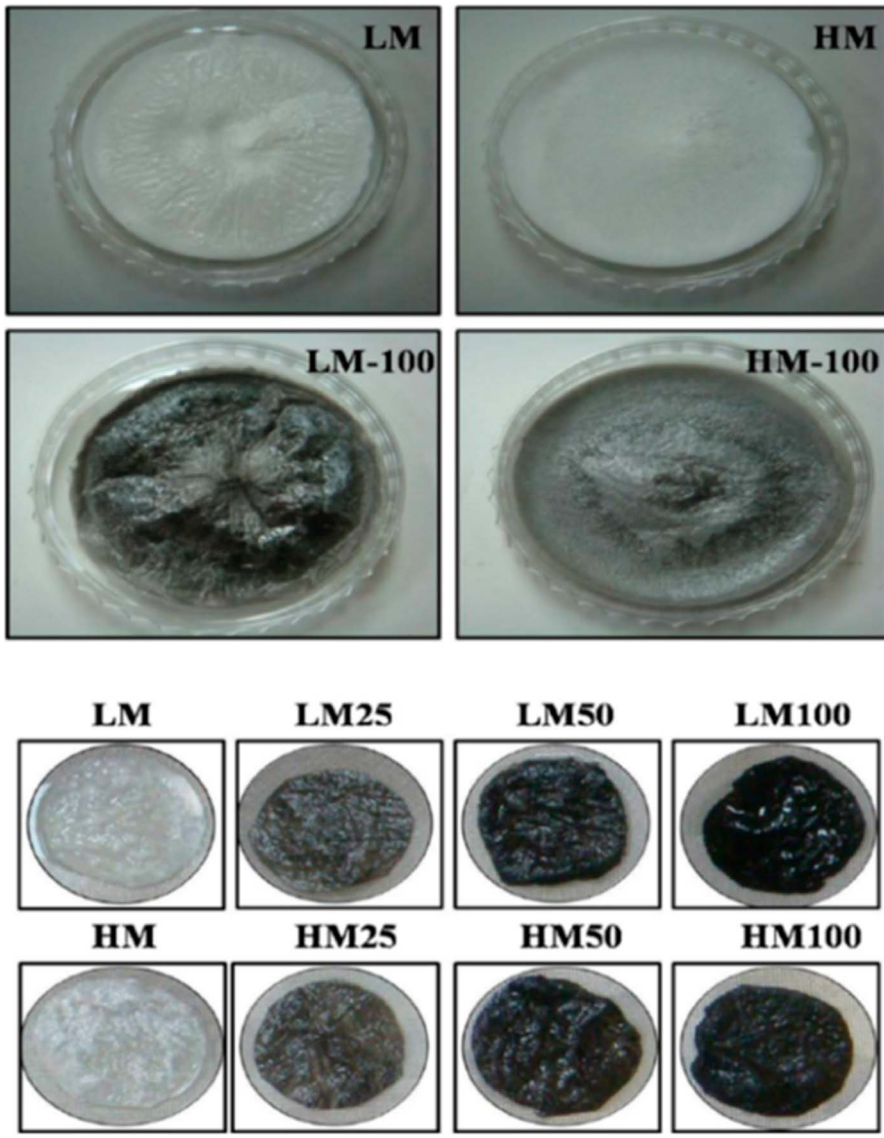

Figure 4.16 Real photographs of chitosan scaffolds reinforced with functionalized MWCNTs in the dried (top panel) and hydrated (bottom panel) state. LM = low molecular weight chitosan; HM = high molecular weight chitosan, with different MWCNT contents. Adapted from ref. 170 with permission from Elsevier. Copyright 2017.

the water uptake ability and porosity of the scaffolds, directly proportional to the amount of functionalized MWCNTs. The cell proliferation and mineral contents were higher than bare chitosan scaffolds, due to the addition of the MWCNTs, suggesting that the presence of carbon nanostructures is the key to make these scaffolds promising for bone tissue engineering.

In another representative example, novel tissue engineering scaffolds manufactured with functionalized MWCNTs, chitosan and β-glycerophosphate were obtained.[171] The effects of functionalized MWCNTS on the electrical, biological, mechanical and mineralization properties have been evaluated and the study concluded that by increasing the MWCNT content, alkaline phosphatase activity, electrical conductivity and mechanical strength increased. In addition, β-glycerophosphate used as a cross-linker showed a significant positive role in increasing alkaline phosphatase activity, which is a characteristic parameter for osteoblastic phenotype retention and differentiation.

4.2.3.2 Chitosan Hybrids with Graphene Derivatives

Given the excellent ability of chitosan to derive into water-soluble species (*e.g.* sodium salt), the largest number of works in this direction (if not all) deal with one of the most hydrophilic relatives of graphene, namely GO. Even if chitosan has been computationally determined to form energetically stable hybrids with non-oxidized graphene,[121] actual hybrid nanocomposites made of them are extremely rare. In contrast, scientific literature is full of examples dealing with GO-based hybrids, in which the concurrence of both materials enhances the hydrophilic character of the system, and largely spans the processability, enabling fibres, hydrogels or aerogels to be obtained,[172] readily available for biomedical applications. Among the many different possibilities, the chitosan/GO hybrids are mainly directed towards two well-defined biomedical focuses: controlled drug delivery and bone tissue regeneration.[173] In the following, we highlight some representative works of each of these two applications.

H. Bao and co-workers claim to have been the first in reporting the use of a chitosan/GO hybrid for the delivery of a hydrophobic drug (Camptothecin, CTP) to a very large extent (nearly 20 wt%) and also genetic material.[174] These hybrids exhibited a particularly useful pH-dependent responsiveness, able to trigger up to a 17.5 wt% release of CPT at 72 h and 30 °C. This ability entailed a powerful cancer-killing effect, tested *in vitro* on HeLa cells and assessed by an MTT assay. Apart from this drug delivery effect, the complexation of these chitosan/GO hybrids with plasmid DNA was also feasible, showing successful genetic transfection on HeLa cells, which endows a tremendous versatility and multifunctionality to these hybrids.

In another work aimed at drug delivery, reported by Justin and Chen, chitosan/GO hybrids with varying GO content (from 0.25 to 5 wt%) were synthesized in the form of films by a simple solution casting method.[175] The release of fluorescein was tested as a model, in which both the GO ratio and the

medium pH were crucial. Besides, another biomedical facet was also evaluated, namely biodegradability, and those GO-based hybrids degraded more slowly (enzymatically) compared to bare chitosan, ascribed to the strong filler-matrix interactions and the more tortuous porosity. These films were postulated as excellent candidates for transdermal drug delivery. The same authors in the same year published the reduction of GO by chitosan action at a mild temperature (37 °C) compatible with the human physiology.[176] This method is, in terms of efficiency, comparable to those more traditional at much higher temperatures and/or with more harsh chemicals, preserving the pH responsiveness and paving the way for biomedical applications.

As per the bone tissue regeneration, Depan *et al.* fabricated covalently bound chitosan/GO hybrids, forming a scaffold with visibly enhanced mechanical properties (Figure 4.17).[177] Such a strengthened and cross-linked network caused an improvement in osteoblasts' attachment, proliferation and growth, which were ascribed to the joint action of several factors: large surface area, nanoscale roughness, and the presence of surface functional groups responsible for high water affinity and retention. In particular, the surface negative charges provided by GO are postulated to be the key for such an improved osteoblast attachment and proliferation, so these hybrid scaffolds were envisioned as promising materials for bone tissue engineering.

A more recent example, reported by Hermenean and co-workers, goes much beyond by demonstrating that chitosan/GO scaffolds (prepared by solution and freeze-drying) are capable of causing osteogenic differentiation *in vitro* (3T3-E1 cells) and *in vivo* using a murine model.[178] A particularly optimal effect, and in the shortest generation time, was found for a 3 wt% content in GO, much better than lower GO ratios or chitosan alone. These conclusions were drawn after observing an increase in alkaline phosphatase activity, linked to increased osteogenesis, also supported by the detection of higher expression of proteins related to the creation of new bone cells, together with histopathological and electron microscopy observations. These works not only confirm that chitosan/GO hybrids are capable of displaying good cell proliferation and attachment, but also cell differentiation towards the generation of new bone cells, making these scaffolds very promising tools to reconstruct large bone injuries in the absence of externally-incorporated cells and growth factors, along with an invaluable biodegradable character.

4.2.4 Alginate-based Hybrids

Alginate, a promising biomaterial of marine origin, is a natural polymer belonging to the carbohydrate family (polysaccharides). It is non-toxic, biocompatible and biodegradable. Therefore, it has been largely investigated in various fields such as the food industry, agriculture, tissue engineering, wound healing, drug delivery, packaging material and other biological studies.[179–185] Alginates, which can be extracted from cell walls of brown algae,[186,187] are water-soluble linear block copolymers composed of ionic blocks of different polysaccharide polymers. These blocks consist of successive regions of acid

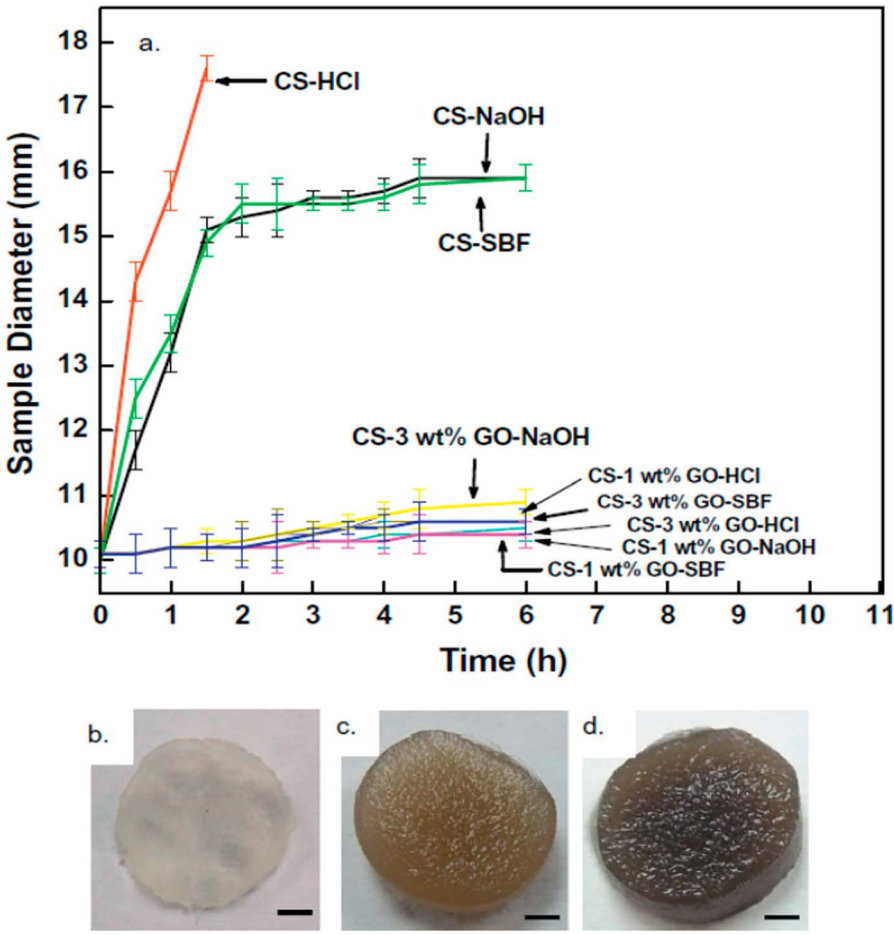

Figure 4.17 Shape retention of (a) pure chitosan and chitosan/GO scaffolds as a function of scaffold immersion time in media of different pH. Digital photographs of (b) pure chitosan, (c) 1 wt% GO chitosan hybrid, and (d) 3 wt% GO chitosan hybrid after 28 days immersion in buffer (pH 7.4). Scale bar 1 mm. Adapted from ref. 177 with permission from Elsevier, Copyright 2011.

monomers 1,4-linked β-D-mannuronic (M-blocks), regions of α-L-guluronic acid (G-blocks) and regions of dispersed M and G units (see Figure 4.3).[188,189] The properties of alginates depend on the ratio of the M/G blocks and the distribution of these blocks within the chains.[85] Sodium alginate (SA) is the most commonly available salt, readily soluble in water, giving a thick colloidal solution. SA easily jellifies in aqueous media by ionic cross-linking with divalent (also trivalent) cations forming ionic hydrogels into which other species (drugs, proteins, DNA and cells) can be entrapped while maintaining their activity due to the mild gelation conditions. In the gelation process, hydrogen bonding between the chains occurs upon cross-linking of the carboxyl groups of the G-blocks with the divalent cations. Thus, alginates that

are rich in G-blocks produce more rigid gels.[190–192] The interaction of the alginate with divalent cations is a highly selective process and its binding ability with suitable ions increases in the following order:[193] $Mn^{2+} < Zn^{2+}$, Ni^{2+}, $Co^{2+} < Fe^{2+} < Ca^{2+} < Sr^{2+} < Ba^{2+} < Cd^{2+} < Cu^{2+} < Pb^{2+}$, while establishing no interactions at all with Mg^{2+} cations. All of these alginate characteristics enable the physicochemical properties of the formed gels to be tailored by modifying the type of cation and cross-linking, the molecular weight and the chemical composition (M/G ratio) of the alginate.[182]

Unfortunately, as well as for other biopolymers, alginate itself has several disadvantages, such as poor water resistance, poor mechanical properties and low thermal stability, which restrict its use in certain applications.[194] Currently, much effort has been made to improve the performance of alginates. One of the most effective strategies has been the formation of nanocomposites. In this regard, the addition of inorganic nanofillers has proven to be successful to circumvent alginate's main weaknesses.[195–198] Likewise, the addition of carbon nanostructures not only improves alginate's mechanical and thermal properties,[199–203] but also decreases the hydrophilicity (leading to an enhanced water resistance) and adds new functionalities like antibacterial properties[204,205] and electrical conductivity.[206,207]

Aiming to obtain biomaterials that match the biological and mechanical properties of natural tissues, an important number of carbon nanostructures/alginate hybrids with improved mechanical properties have been reported (Table 4.2). Here, the mechanical properties of the hybrids can be tailored by using different types of carbon nanomaterials, selecting the adequate filler content, modifying its chemical surface and choosing the suitable fabrication methodology. In general, increased content of carbon nanomaterials in the alginate hybrid results in enhanced mechanical properties up to a certain limit beyond which these get worse, probably due to the filler aggregation within the matrix. Chemical modification of the carbon nanomaterial surface favours the establishment of a higher (and stronger) number of interactions with alginate and therefore, improved mechanical properties are obtained.[201,203,208–210] Moreover, the addition of carbon nanomaterials does not essentially alter the alginate chemical properties resulting in hybrid materials with superior mechanical properties, able to be custom designed to mimic those of natural tissues. Therefore, carbon nanomaterials are ideal candidates to prepare alginate hybrid hydrogels for biomedical purposes.

Electrical conductivity is a priceless asset that carbon nanomaterials offer when added to hydrogels. Electrically conductive biomaterials have received considerable attention as essential tools for bioelectronics due to their application in a broad range of biomedical applications, from cardiovascular, muscle and nerve tissue engineering to wearable biosensors for human health monitoring and intelligent wound care dressings, with a controlled rate of drug delivery and self-healing.[221–224] For such applications, alginate-based conductive hydrogels are commonly filled with polyelectrolytes or conductive polymers. However, they exhibit important drawbacks such as erosion, swelling, de-swelling or bending

Table 4.2 Mechanical property values for carbon nanostructure/alginate hybrids. Mechanical data for some natural tissues are also included.

Material	Tensile stress (MPa)	Young's modulus (GPa)	Elongation at break (%)	Reference
Arterial wall	0.5-1-72	0.001	—	211
Cortical bone	30–211	16–20	—	
Cancellous bone	51–93	4.6–15	—	
Hyaline cartilage	1.3–1.8	0.004–0.019	—	
Skin	2.5–16	0.006–0.040	—	
Articular cartilage	0.8–25	—	60–120	212
Tendon/ligament	30–300	0.065–2.5	—	
Alginate film	0.4	1–4	—	213
Alginate fibre	0.32	0.62	—	
0.5% CNTs/alginate electrospun fibre	11	—	—	
1% SWCNT/alginate film	0.5	1.4	92	214
1.2% SWCNT/alginate wet-spun fibre	250.0	6.97	13	215
23% SWCNT/alginate wet-spun	260.3	6.38	14	
1% GO/alginate film	69.3	3.80	6	208
3% ammonia functionalized GO/alginate film	10.6	—	15	200
4% GO/alginate wet spun fibre	1.9	4.4	—	216
6% GO/alginate film	113.0	4.2	—	199
8% GO/alginate	167.7	5.5	5	217
67% GO/alginate film	239.6	22.4	—	218
3% GO/(Fe^{3+}) alginate film	161.8	5.9	4	219
1.8% GO/polyacrylamide/alginate film (compression)	65.6	—	80	220

when an electrical field is applied. Also, the eventually reached electrical conductivity may not be high enough to achieve an effective modulation of the stimuli-responsive functional properties. Therefore, the addition of carbon nanomaterials has been proposed as a valuable approach to address these issues.[225] CNTs and graphene derivatives have been shown to be of particular interest for their excellent electrical properties and high surface area,[226–228] which facilitates their chemical functionalization solving the problem of their water insolubility, and concurrently enhancing the interaction with the hydrogel matrix.[210,229,230] Thus, it is not surprising that a large number of investigations reporting the use of carbon nanostructures, in particular CNTs, in the immobilization of enzymes or proteins,[206,225,231] or accelerating stem cell proliferation and differentiation[232–234] have been published. The addition of CNTs provides physicochemical properties matching those of soft tissue membranes due to the similarity in the viscoelastic behaviour of both systems,[235–237] the

resulting biomaterials being extremely favourable for regenerative medicine applications. Also, graphene and its derivatives have proven to be beneficial for successfully preparing hybrid scaffolds.[100,210,238] In fact, the behaviour of stem cells can be tailored by modifying the surface properties of graphene nanomaterials.[208,239–241] For instance, using GO in the proper amount significantly increases the hybrid conductivity upon GO reduction, and consequently, this enhances the signal propagation for electrical stimulation processes.[242] Nevertheless, it is not always easy to preserve the electrical conductivity of the carbon nanomaterials when forming hybrids with hydrogels, and factors such as the inhomogeneous distribution of the nanofillers hamper their advantageous effects. In this sense, new promising strategies have been developed such as the assembling of nanomaterials into macroscopically ordered structures within the hydrogel, especially in the form of fibres. From a biological point of view, almost all human tissues and organs are deposited in nanofibrous forms or structures. And, for that, different fabrication techniques such as wet spinning or electrospinning have been demonstrated as excellent methodologies to generate fine and ordered fibres at the nanosc ale.[207,213,215,243,244]

In a typical wet (also named coagulation) spinning process, alginic acid sodium salt is added to a CNT (or GO) dispersion and the resulting suspension is injected at room temperature into a rotating coagulation bath containing the coagulation dope (usually an aqueous solution of calcium salts) where the fibre forms (Figure 4.18). The spun fibres are then collected, washed, dried and characterized.[245] In the case of alginate-based systems, many examples of fibres with a high loading of CNTs and aligned along the fibre axis, showing good mechanical and electrical properties, were successfully produced by this methodology.[215] Also, the diameter of alginate spun fibres (even with carbon nanostructures) could be controlled by adjusting the inner diameter of the needle orifice used to inject the dope into the coagulation bath.[216] The use of different dispersing agents for CNTs influences the final properties of the spun fibres. Accordingly, we have observed that

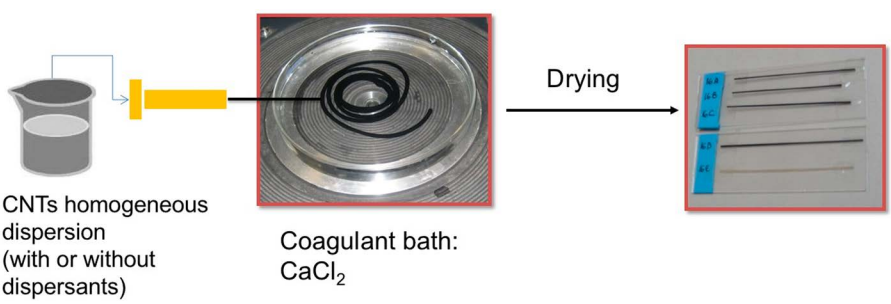

Figure 4.18 Wet spinning process represented for an in-house fabrication of coagulated spun CNT-reinforced alginate fibres.

Pluronic® F-68 block copolymer leads to alginate/CNT hybrid fibres with higher electrical conductivity than other dispersing agents (Table 4.3). As for the mechanical properties, the CNT concentration also has a direct effect on the electrical properties of the spun fibres (Figure 4.19).

The electrospinning technique has also been used in many works, although to a lesser extent, to prepare alginate-based nanofibres with carbon nanostructures with enhanced mechanical and electrical properties.[213] The technique consists of applying a high voltage to a viscoelastic polymer solution usually contained in a syringe to overcome its surface tension forces. Thus, at a given voltage, fine jets of solution are expelled from the needle of the syringe towards a grounded collector. As the solution jet follows the direction of the applied electric field, the solvent evaporates and the formed fibres are randomly deposited on the grounded collector.

Table 4.3 Effect of different CNT dispersing agents on the conductivity of coagulation-spun fibres CNT (15 wt%)/alginate (own results).

Dispersing agent[a]	Conductivity (S cm^{-1})
None	$(6.1 \pm 2.3)\times10^{-7}$
Pluronic® F-68	$(2.1 \pm 1.5)\times10^{-2}$
Gum arabic	$(1.2 \pm 1.0)\times10^{-4}$
Poly(vinyl pyrrolidone)	$(8.6 \pm 1.2)\times10^{-5}$

[a]CNT/dispersant ratio (1/5).

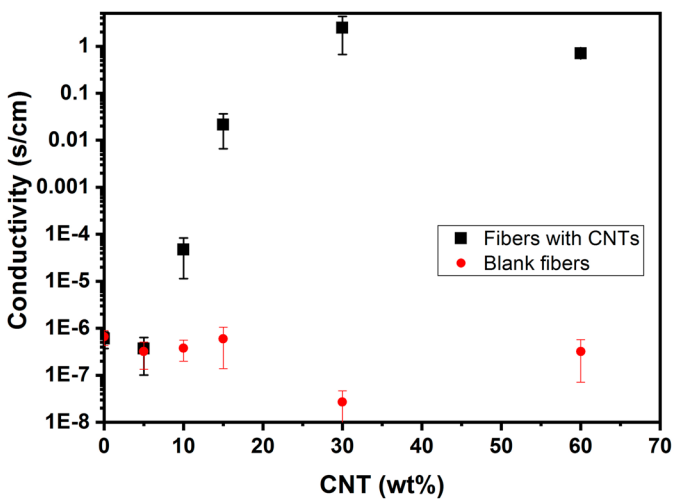

Figure 4.19 Effect of CNT content on the electrical conductivity of alginate nanocomposite fibres. Blank fibres refer to alginate spinning without CNTs, but with Pluronic® F-68 copolymer in the same concentration as homologous with CNTs (own results).

The obtained electrospun nanofibres are highly interesting as they can mimic the nanofibrous structure of the native extracellular matrix. The produced scaffolds exhibit a high surface area, which favours the cellular interaction with the material.[246]

4.3 Conclusion and Future Outlook

The inclusion of biopolymers, derived from natural resources, into the world of carbon nanostructures is a revolutionary and sustainable way to facilitate the achievement of materials and structures suitable for biomedical purposes. This approach avoids the use of organic substances, surfactants and other chemicals posing health risks and high toxicity when aiming at this goal, while being based on green and sustainable principles. We have herein shown how natural polysaccharides, and cellulose in particular, have a high adsorption affinity for carbon nanostructures (such as nanotubes), leading to stable hybrids while taking advantage of their excellent physicochemical properties. This synergistic association entails the adjustment of the hydrophilic character of the hybrid, on the one hand enhancing that of carbon nanostructures, while somewhat lowering the extremely high hydrophilic character of some polysaccharides that impedes proper processing (such as in the case of alginate derivatives). This synergy also provides optimal mechanical properties resembling those of soft tissues, being perfect assets to mimic the extracellular matrix environments. All of this ends up in the perfect balance for the aqueous processing of the hybrids, a prerequisite for their use in biomedicine. The huge processing versatility that natural polysaccharides provide to carbon nanostructures allows the manufacturing of three-dimensional hydrogels (mainly with cellulose or chitin), from which aerogels may derive, films (mainly with chitosan or chemical derivatives of cellulose) or even fibres (mainly with alginates). This diversity confers a perfect way to tailor the materials' properties towards any targeted biomedical need, in turn coupled with the high biocompatibility and possible biodegradability that natural polysaccharides exert on their hybrids. In general terms, the future of carbon nanostructures in biomedicine will definitely explore the use of polysaccharides in one way or another, as far as long-term hazards are eventually unravelled and much more *in vivo* studies are performed. The near and mid future points to three well-defined lines: (i) the use of these hybrids for biosensing applications, mostly with cellulose derivatives given their excellent mechanical performance, acting as structural support for sensing platforms, and resulting in *e.g.* glucose or pathogenic bacteria detection in very sensitive and disposable devices; (ii) drug delivery applications mainly from hybrid hydrogels in which therapeutic agents can be released in a controlled way (*e.g.* through pH stimulus), also enriched by possible degradability; (iii) tissue engineering with aerogels or fibre-based scaffolds in which specific cells may not only attach and proliferate well, but also exhibit differentiation and genesis of new-born healthy tissues from stem cells, as it was shown for the osteogenic effect of chitosan-based

hybrids. Even if biomedical outcomes are the most complex that nanoscience and nanotechnology may face, given the large amount of risks and considerations involved, it could be stated that natural polysaccharides are one of the most, if not the most, key elements pushing carbon nanostructures in big steps forward to eventual success.

List of Abbreviations

AFM	Atomic force microscopy
BC	Bacterial cellulose
CA	Cellulose acetate
CCK-8	Cell counting kit 8
cMWCNTs	Carboxymethyl cellulose-functionalized MWCNTs
CNTs	Carbon nanotubes
CPT	Camptothecin
DD	Degree of deacetylation
DLS	Dynamic light scattering
DNA	Deoxyribonucleic acid
Dox	Doxorubicin
DP	Degree of polymerization
DTX	Docetaxel
GlcN	*N*-glucosamine
GlcNAc	*N*-acetylglucosamine
GO	Graphene oxide
GOx	Glucose oxidase
hMSCs	Human mesenchymal stem cells
mRNA	Messenger ribonucleic acid
MTT	3-(4,5-dimethylthiazol-2-yl)-2,5-diphenyltetrazolium bromide
MTX	Methotrexate
MWCNTs	Multi-walled carbon nanotubes
NADH	Nicotinamide adenine dinucleotide
NCC	Nanocrystalline cellulose/cellulose nanocrystal
NFC	Nanofibrillated cellulose
rGO	Reduced graphene oxide
SA	Sodium alginate
SWCNTs	Single-walled carbon nanotubes
TEM	Transmission electron microscopy
TEMPO	(2,2,6,6-Tetramethylpiperidin-1-yl)oxyl

Acknowledgements

Financial support was obtained from MINEICO under project ENE2016-79282-C5-1-R (AEI/UE/FEDER), the Gobierno de Aragón (Grupo Reconocido T03_20R, and PhD studentship IIU/843/2019), and a 'Juan de la Cierva – Incorporación' research grant (IJCI-2016-27789).

References

1. H. W. Kroto, J. R. Heath, S. C. O'Brien, R. F. Curl and R. E. Smalley, C60: Buckminsterfullerene, *Nature*, 1985, **318**, 162.
2. S. Iijima, Helical microtubules of graphitic carbon, *Nature*, 1991, **354**, 56.
3. K. S. Novoselov, A. K. Geim, S. V. Morozov, D. Jiang, Y. Zhang, S. V. Dubonos, I. V. Grigorieva and A. A. Firsov, Electric Field Effect in Atomically Thin Carbon Films, *Science*, 2004, **306**, 666.
4. V. N. Mochalin, O. Shenderova, D. Ho and Y. Gogotsi, The properties and applications of nanodiamonds, *Nat. Nanotechnol.*, 2011, **7**, 11.
5. W. S. Hummers and R. E. Offeman, Preparation of Graphitic Oxide, *J. Am. Chem. Soc.*, 1957, **208**, 1937.
6. M. S. Dresselhaus and M. Terrones, Carbon-based nanomaterials from a historical perspective, *Proc. IEEE*, 2013, **101**, 1522.
7. A. K. Geim and K. S. Novoselov, The rise of graphene, *Nat. Mater.*, 2007, **6**, 183.
8. Y. Zhu, S. Murali, W. Cai, X. Li, J. W. Suk, J. R. Potts and R. S. Ruoff, Graphene and graphene oxide: Synthesis, properties, and applications, *Adv. Mater.*, 2010, **22**, 3906.
9. M. Terrones, Science and Technology of the Twenty-First Century: Synthesis, Properties, and Applications of Carbon Nanotubes, *Annu. Rev. Mater. Res.*, 2003, **33**, 419.
10. D. Jariwala, V. K. Sangwan, L. J. Lauhon, T. J. Marks and M. C. Hersam, Carbon nanomaterials for electronics, optoelectronics, photovoltaics, and sensing, *Chem. Soc. Rev.*, 2013, **42**, 2824.
11. G. Yu, J. Gao, J. C. Hummelen, F. Wudl and A. J. Heeger, Polymer Photovoltaic Cells: Enhanced Efficiencies *via* a Network of Internal Donor-Acceptor Heterojunctions, *Science*, 1995, **270**, 1789–1791.
12. A. M. Nardes, A. J. Ferguson, J. B. Whitaker, B. W. Larson, R. E. Larsen, K. Maturová, P. A. Graf, O. V. Boltalina, S. H. Strauss and N. Kopidakis, Beyond PCBM: Understanding the photovoltaic performance of blends of indene-C 60 multiadducts with poly(3-hexylthiophene), *Adv. Funct. Mater.*, 2012, **22**, 4115.
13. L. Sims, H. J. Egelhaaf, J. A. Hauch, F. R. Kogler and R. Steim, Plastic solar cells, *Comprehensive Renewable Energy*, 2012, vol. 1, p. 439.
14. E. Istif, J. Hernández-Ferrer, E. P. Urriolabeitia, A. Stergiou, N. Tagmatarchis, G. Fratta, M. J. Large, A. B. Dalton, A. M. Benito and W. K. Maser, Conjugated Polymer Nanoparticle–Graphene Oxide Charge-Transfer Complexes, *Adv. Funct. Mater.*, 2018, **28**, 1.
15. C. Vallés, P. Jiménez, E. Muñoz, A. M. Benito and W. K. Maser, Simultaneous reduction of graphene oxide and polyaniline: Doping-assisted formation of a solid-state charge-transfer complex, *J. Phys. Chem. C*, 2011, **115**, 10468.
16. J. M. González-Domínguez, P. Castell, S. Bespín-Gascón, A. Ansón-Casaos, A. M. Díez-Pascual, M. A. Gómez-Fatou, A. M. Benito, W. K.

Maser and M. T. Martínez, Covalent functionalization of MWCNTs with poly(p-phenylene sulphide) oligomers: a route to the efficient integration through a chemical approach, *J. Mater. Chem.*, 2012, **22**, 21285.
17. M. Cano, U. Khan, T. Sainsbury, A. O'Neill, Z. Wang, I. T. McGovern, W. K. Maser, A. M. Benito and J. N. Coleman, Improving the mechanical properties of graphene oxide based materials by covalent attachment of polymer chains, *Carbon*, 2013, **52**, 363.
18. J. G. Meier, C. Crespo, J. L. Pelegay, P. Castell, R. Sainz, W. K. Maser and A. M. Benito, Processing dependency of percolation threshold of MWCNTs in a thermoplastic elastomeric block copolymer, *Polymer*, 2011, **52**, 1788.
19. A. T. Lawal, Graphene-based nano composites and their applications. A review, *Biosens. Bioelectron.*, 2019, **141**, 111384.
20. J. M. González-Domínguez, A. M. Díez-Pascual, A. Ansón-Casaos, M. A. Gómez-Fatou and M. T. Martínez, *Polymer Nanotube Nanocomposites*, John Wiley & Sons, Inc., Hoboken, NJ, USA, 2014, vol. 9781118945, pp. 45–116.
21. M. Cano, P. Villuendas, A. M. Benito, E. P. Urriolabeitia and W. K. Maser, Carbon nanotube-supported gold nanoparticles as efficient catalyst for the selective hydrogenation of nitroaromatic derivatives to anilines, *Mater. Today Commun.*, 2015, **3**, 104.
22. M. Cano, A. M. Benito, E. P. Urriolabeitia, R. Arenal and W. K. Maser, Reduced graphene oxide: Firm support for catalytically active palladium nanoparticles and game changer in selective hydrogenation reactions, *Nanoscale*, 2013, **5**, 10189.
23. M. Cano, A. Benito, W. K. Maser and E. P. Urriolabeitia, One-step microwave synthesis of palladium-carbon nanotube hybrids with improved catalytic performance, *Carbon*, 2011, **49**, 652.
24. M. Cano, A. M. Benito, W. K. Maser and E. P. Urriolabeitia, High catalytic performance of palladium nanoparticles supported on multiwalled carbon nanotubes in alkene hydrogenation reactions, *New J. Chem.*, 2013, **37**, 1968.
25. S. Víctor-Román, E. García-Bordejé, J. Hernández-Ferrer, J. M. González-Domínguez, A. Ansón-Casaos, A. M. T. Silva, W. K. Maser and A. M. Benito, Controlling the surface chemistry of graphene oxide: Key towards efficient ZnO-GO photocatalysts, *Catal. Today*, 2020, **357**, 350.
26. R. Canton-Vitoria, L. Vallan, E. Urriolabeitia, A. M. Benito, W. K. Maser and N. Tagmatarchis, Electronic Interactions in Illuminated Carbon Dot/MoS2 Ensembles and Electrocatalytic Activity towards Hydrogen Evolution, *Chem. - Eur. J.*, 2018, **24**, 10468.
27. J. Sánchez-García, A. M. Benito, W. K. Maser and E. García-Bordejé, Ru supported on N-doped reduced graphene oxide aerogels with different N-type for alcohol selective oxidation, *Mol. Catal.*, 2020, **484**, 110737.
28. I. Sayago, E. Terrado, M. Aleixandre, M. C. Horrillo, M. J. Fernández, J. Lozano, E. Lafuente, W. K. Maser, A. M. Benito, M. T. Martinez,

J. Gutiérrez and E. Muñoz, Novel selective sensors based on carbon nanotube films for hydrogen detection, *Sens. Actuators, B*, 2007, **122**, 75.

29. I. Sayago, H. Santos, M. C. Horrillo, M. Aleixandre, M. J. Fernández, E. Terrado, I. Tacchini, R. Aroz, W. K. Maser, A. M. Benito, M. T. Martínez, J. Gutiérrez and E. Muñoz, Carbon nanotube networks as gas sensors for NO_2 detection, *Talanta*, 2008, **77**, 758.
30. Y. N. Zhang, Q. Niu, X. Gu, N. Yang and G. Zhao, Recent progress on carbon nanomaterials for the electrochemical detection and removal of environmental pollutants, *Nanoscale*, 2019, **11**, 11992–12014.
31. H. Grajek, J. Jonik, Z. Witkiewicz, T. Wawer and M. Purchała, Applications of Graphene and Its Derivatives in Chemical Analysis, *Crit. Rev. Anal. Chem.*, 2019, **1**.
32. T. Rasheed, F. Nabeel, M. Adeel, K. Rizwan, M. Bilal and H. M. Iqbal, Carbon nanotubes-based cues: A pathway to future sensing and detection of hazardous pollutants, *J. Mol. Liq.*, 2019, **292**, 111425.
33. Y. M. Lin, K. A. Jenkins, V. G. Alberto, J. P. Small, D. B. Farmer and P. Avouris, Operation of graphene transistors at giqahertz frequencies, *Nano Lett.*, 2009, **9**, 422.
34. Y. M. Lin, C. Dimitrakopoulos, K. A. Jenkins, D. B. Farmer, H. Y. Chiu, A. Grill and P. Avouris, 100-GHz Transistors from Wafer-Scale Epitaxial Graphene, *Science*, 2010, **327**, 662.
35. U. A. Palnitkar, R. V. Kashid, M. A. More, D. S. Joag, L. S. Panchakarla and C. N. R. Rao, Remarkably low turn-on field emission in undoped, nitrogen-doped, and boron-doped graphene, *Appl. Phys. Lett.*, 2010, **97**, 063102.
36. Y. Ma and L. Zhi, Graphene-Based Transparent Conductive Films: Material Systems, Preparation and Applications, *Small Methods*, 2019, **3**, 1.
37. P. Blake, P. D. Brimicombe, R. R. Nair, T. J. Booth, D. Jiang, F. Schedin, L. A. Ponomarenko, S. V. Morozov, H. F. Gleeson, E. W. Hill, A. K. Geim and K. S. Novoselov, Graphene-based liquid crystal device, *Nano Lett.*, 2008, **8**, 1704.
38. D. Wang, X. Zhao and Z. Gu, Advanced optoelectronic nanodevices and nanomaterials for sensing inside single living cell, *Opt. Commun.*, 2017, **395**, 3.
39. F. Picó, J. M. Rojo, M. L. Sanjuán, A. Ansón, A. M. Benito, M. A. Callejas, W. K. Maser and M. T. Martínez, Single-walled carbon nanotubes as electrodes in supercapacitors, *J. Electrochem. Soc.*, 2004, **151**, A831.
40. S. Nufer, P. Lynch, M. Cann, M. J. Large, J. P. Salvage, S. Víctor-Román, J. Hernández-Ferrer, A. M. Benito, W. K. Maser, A. Brunton and A. B. Dalton, Carbon Nanofoam Supercapacitor Electrodes with Enhanced Performance Using a Water-Transfer Process, *ACS Omega*, 2018, **3**, 15134.
41. D. Chen, K. Jiang, T. Huang and G. Shen, Recent Advances in Fiber Supercapacitors: Materials, Device Configurations, and Applications, *Adv. Mater.*, 2020, **32**, 1901806.

42. Y. Wang, P. Yang, L. Zheng, X. Shi and H. Zheng, Carbon nanomaterials with sp or/and sp hybridization in energy conversion and storage applications: A review, *Energy Storage Mater.*, 2020, **26**, 349.
43. X. Wang, L. Zhi and K. Müllen, Transparent, conductive graphene electrodes for dye-sensitized solar cells, *Nano Lett.*, 2008, **8**, 323.
44. X. Fu, L. Xu, J. Li, X. Sun and H. Peng, Flexible solar cells based on carbon nanomaterials, *Carbon*, 2018, **139**, 1063.
45. J. Hernández-Ferrer, A. Ansón-Casaos, S. Víctor-Román, O. Sanahuja-Parejo, M. T. Martínez, B. Villacampa, A. M. Benito and W. K. Maser, Photoactivity improvement of TiO_2 electrodes by thin hole transport layers of reduced graphene oxide, *Electrochim. Acta*, 2019, **298**, 279.
46. A. P. Litvin, X. Zhang, K. Berwick, A. V. Fedorov, W. Zheng and A. V. Baranov, Carbon-based interlayers in perovskite solar cells, *Renewable Sustainable Energy Rev.*, 2020, **124**, 109774.
47. B. Aïssa, A. Ali, A. Bentouaf, W. Khan, M. I. Hossain, J. Kroeger and N. Malik Muhammad, Functionalized single-walled carbon-nanotube-blended P3HT-based high performance memory behavior thin-film transistor devices, *Nanotechnology*, 2020, **31**, 075201.
48. T. Qu, Y. Sun, M. Chen, Z. Liu, Q. Zhu, B. Wang, T. Zhao, C. Liu, J. Tan, S. Qiu, Q. Li, Z. Han, W. Wang, H. Cheng and D. Sun, A Flexible Carbon Nanotube Sen-Memory Device, *Adv. Mater.*, 2020, **32**, 1907288.
49. Y. Wang, Y. Shao, D. W. Matson, J. Li and Y. Lin, Nitrogen-doped graphene and its application in electrochemical biosensing, *ACS Nano*, 2010, **4**, 1790.
50. S. Myung, A. Solanki, C. Kim, J. Park, K. S. Kim and K. B. Lee, Graphene-encapsulated nanoparticle-based biosensor for the selective detection of cancer biomarkers, *Adv. Mater.*, 2011, **23**, 2221.
51. S. Azzouzi, L. Rotariu, A. M. Benito, W. K. Maser, M. Ben Ali and C. Bala, A novel amperometric biosensor based on gold nanoparticles anchored on reduced graphene oxide for sensitive detection of l-lactate tumor biomarker, *Biosens. Bioelectron.*, 2015, **69**, 280.
52. R. Hernández, C. Vallés, A. M. Benito, W. K. Maser, F. X. Rius and J. Riu, Graphene-based potentiometric biosensor for the immediate detection of living bacteria, *Biosens. Bioelectron.*, 2014, **54**, 553.
53. A. T. Lawal, Progress in utilisation of graphene for electrochemical biosensors, *Biosens. Bioelectron.*, 2018, **106**, 149.
54. X. Yu, B. Munge, V. Patel, G. Jensen, A. Bhirde, J. D. Gong, S. N. Kim, J. Gillespie, J. S. Gutkind, F. Papadimitrakopoulos and J. F. Rusling, Carbon nanotube amplification strategies for highly sensitive immunodetection of cancer biomarkers, *J. Am. Chem. Soc.*, 2006, **128**, 11199.
55. B. V. Chikkaveeraiah, A. A. Bhirde, N. Y. Morgan, H. S. Eden and X. Chen, Electrochemical immunosensors for detection of cancer protein biomarkers, *ACS Nano*, 2012, **6**, 6546.
56. B. S. Harrison and A. Atala, Carbon nanotube applications for tissue engineering, *Biomaterials*, 2007, **28**, 344.

57. L. Zhang and T. J. Webster, Nanotechnology and nanomaterials: Promises for improved tissue regeneration, *Nano Today*, 2009, **4**, 66.
58. A. Bianco, K. Kostarelos and M. Prato, Applications of carbon nanotubes in drug delivery, *Curr. Opin. Chem. Biol.*, 2005, **9**, 674.
59. Z. Liu, J. T. Robinson, X. Sun and H. Dai, PEGylated nanographene oxide for delivery of water-insoluble cancer drugs, *J. Am. Chem. Soc.*, 2008, **130**, 10876.
60. R. H. Baughman, C. Cui, A. A. Zakhidov, Z. Iqbal, J. N. Barisci, G. M. Spinks, G. G. Wallace, A. Mazzoldi, D. De Rossi, A. G. Rinzler, O. Jaschinski, S. Roth and M. Kertesz, Carbon nanotube actuators, *Science*, 1999, **284**, 1340.
61. T. Sekitani, H. Nakajima, H. Maeda, T. Fukushima, T. Aida, K. Hata and T. Someya, Stretchable active-matrix organic light-emitting diode display using printable elastic conductors, *Nat. Mater.*, 2009, **8**, 494.
62. C. Li and G. Shi, Three-dimensional graphene architectures., *Nanoscale*, 2012, **4**, 5549.
63. G. M. Whitesides, The 'right' size in nanobiotechnology, *Nat. Biotechnol.*, 2003, **21**, 1161.
64. H. Liu, L. Zhang, M. Yan and J. Yu, Carbon nanostructures in biology and medicine, *J. Mater. Chem. B*, 2017, **5**, 6437.
65. D. Tasis, N. Tagmatarchis, A. Bianco and M. Prato, Chemistry of carbon nanotubes., *Chem. Rev.*, 2006, **106**, 1105.
66. A. Bianco, K. Kostarelos, C. D. Partidos and M. Prato, Biomedical applications of functionalised carbon nanotubes, *Chem. Commun.*, 2005, **5**, 571.
67. S. C. Ray and N. R. Jana, Toxicology and Biosafety of Carbon Nanomaterials, *Carbon Nanomaterials for Biological and Medical Applications*, Elsevier, 2017, pp. 205–229.
68. F. Xiaoli, C. Qiyue, G. Weihong, Z. Yaqing, H. Chen, W. Junrong and S. Longquan, Toxicology data of graphene-family nanomaterials: an update, *Arch. Toxicol.*, 2020, 1915.
69. J. N. BeMiller, *Carbohydrate Chemistry for Food Scientists*, Elsevier, 2019, pp. 75–101.
70. A. Kirschning, N. Dibbert and G. Dräger, Chemical Functionalization of Polysaccharides—Towards Biocompatible Hydrogels for Biomedical Applications, *Chem. - Eur. J.*, 2018, **24**, 1231.
71. N. Karaki, A. Aljawish, C. Humeau, L. Muniglia and J. Jasniewski, Enzymatic modification of polysaccharides: Mechanisms, Properties, And potential applications: A review, *Enzyme Microb. Technol.*, 2016, **90**, 1.
72. V. Gopinath, S. Saravanan, A. R. Al-Maleki, M. Ramesh and J. Vadivelu, A review of natural polysaccharides for drug delivery applications: Special focus on cellulose, starch and glycogen, *Biomed. Pharmacother.*, 2018, **107**, 96.
73. G. P. Rajalekshmy, L. Lekshmi Devi, J. Joseph and M. R. Rekha, *Functional Polysaccharides for Biomedical Applications*, Elsevier, 2019, pp. 33–94.

74. F. J. Martin-Martinez, Designing nanocellulose materials from the molecular scale, *Proc. Natl. Acad. Sci. U. S. A.*, 2018, **115**, 201809308.
75. K. Daicho, T. Saito, S. Fujisawa and A. Isogai, The Crystallinity of Nanocellulose: Dispersion-Induced Disordering of the Grain Boundary in Biologically Structured Cellulose, *ACS Appl. Nano Mater.*, 2018, **1**, 5774.
76. H. Kargarzadeh, M. Mariano, D. Gopakumar, I. Ahmad, S. Thomas, A. Dufresne, J. Huang and N. Lin, Advances in cellulose nanomaterials, *Cellulose*, 2018, **25**, 2151.
77. U. Römling and M. Y. Galperin, Bacterial cellulose biosynthesis: diversity of operons, subunits, products, and functions, *Trends Microbiol.*, 2015, **23**, 545.
78. N. Lavoine and L. Bergström, Nanocellulose-based foams and aerogels: processing, properties, and applications, *J. Mater. Chem. A*, 2017, **5**, 16105.
79. H. Charreau, E. Cavallo and M. L. Foresti, Patents involving nanocellulose: analysis of their evolution since 2010, *Carbohydr. Polym.*, 2020, **237**, 116039.
80. Y. Habibi, Key advances in the chemical modification of nanocelluloses, *Chem. Soc. Rev.*, 2014, **43**, 1519.
81. I. Hamed, F. Özogul and J. M. Regenstein, Industrial applications of crustacean by-products (chitin, chitosan, and chitooligosaccharides): A review, *Trends Food Sci. Technol.*, 2016, **48**, 40.
82. I. Younes and M. Rinaudo, Chitin and Chitosan Preparation from Marine Sources. Structure, Properties and Applications, *Mar. Drugs*, 2015, **13**, 1133.
83. G. Huet, C. Hadad, E. Husson, S. Laclef, V. Lambertyn, M. Araya Farias, A. Jamali, M. Courty, R. Alayoubi, I. Gosselin, C. Sarazin and A. N. Van Nhien, Straightforward extraction and selective bioconversion of high purity chitin from Bombyx eri larva: Toward an integrated insect biorefinery, *Carbohydr. Polym.*, 2020, **228**, 115382.
84. K. A. Grabińska, P. Magnelli and P. W. Robbins, Prenylation of Saccharomyces cerevisiae Chs4p Affects Chitin Synthase III Activity and Chitin Chain Length, *Eukaryotic Cell*, 2007, **6**, 328.
85. M. Rinaudo, Main properties and current applications of some polysaccharides as biomaterials, *Polym. Int.*, 2008, **57**, 397.
86. J. C. Roy, F. Salaün, S. Giraud, A. Ferri, G. Chen and J. Guan, *Solubility of Polysaccharides*, InTech, 2017, ch. 7, pp. 109–124.
87. E. Vunain, A. K. Mishra and B. B. Mamba, *Chitosan Based Biomaterials Volume 1*, Elsevier, 2017, vol. 1, pp. 3–30.
88. A. Usman, S. Khalid, A. Usman, Z. Hussain and Y. Wang, *Algae Based Polymers, Blends, and Composites*, Elsevier, 2017, pp. 115–153.
89. N. Sachan, S. Pushkar, A. Jha and A. Bhattcharya, Sodium alginate: the wonder polymer for controlled drug delivery, *J. Pharm. Res.*, 2009, **2**, 1191.
90. U. Remminghorst and B. H. A. Rehm, Bacterial alginates: From biosynthesis to applications, *Biotechnol. Lett.*, 2006, **28**, 1701.

91. J. Sun and H. Tan, Alginate-Based Biomaterials for Regenerative Medicine Applications, *Materials*, 2013, **6**, 1285.
92. H. Dai, Carbon nanotubes: Synthesis, integration, and properties, *Acc. Chem. Res.*, 2002, **35**, 1035.
93. S. Stankovich, D. A. Dikin, G. H. B. Dommett, K. M. Kohlhaas, E. J. Zimney, E. A. Stach, R. D. Piner, S. B. T. Nguyen and R. S. Ruoff, Graphene-based composite materials, *Nature*, 2006, **442**, 282.
94. P. M. Ajayan and J. M. Tour, Nanotube composites, *Nature*, 2007, **447**, 1066.
95. G. Eda, G. Fanchini and M. Chhowalla, Large-area ultrathin films of reduced graphene oxide as a transparent and flexible electronic material, *Nat. Nanotechnol.*, 2008, **3**, 270.
96. A. A. Balandin, Thermal properties of graphene and nanostructured carbon materials, *Nat. Mater.*, 2011, **10**, 569.
97. L. Dai, D. W. Chang, J. B. Baek and W. Lu, Carbon nanomaterials for advanced energy conversion and storage, *Small*, 2012, **8**, 1130.
98. B. F. MacHado and P. Serp, Graphene-based materials for catalysis, *Catal. Sci. Technol.*, 2012, **2**, 54.
99. V. Georgakilas, J. N. Tiwari, K. C. Kemp, J. A. Perman, A. B. Bourlinos, K. S. Kim and R. Zboril, Noncovalent Functionalization of Graphene and Graphene Oxide for Energy Materials, Biosensing, Catalytic, and Biomedical Applications, *Chem. Rev.*, 2016, **116**, 5464.
100. G. Reina, J. M. González-Domínguez, A. Criado, E. Vázquez, A. Bianco and M. Prato, Promises, facts and challenges for graphene in biomedical applications, *Chem. Soc. Rev.*, 2017, **46**, 4400.
101. A. Hirsch, MINIREVIEW Functionalization of Single-Walled Carbon Nanotubes, *Angew. Chem., Int. Ed.*, 2002, **41**, 1853.
102. S. Eigler and A. Hirsch, Chemistry with Graphene and Graphene Oxide-Challenges for Synthetic Chemists, *Angew. Chem., Int. Ed.*, 2014, **53**, 7720.
103. R. Bandyopadhyaya, E. Nativ-Roth, O. Regev and R. Yerushalmi-Rozen, Stabilization of Individual Carbon Nanotubes in Aqueous Solutions, *Nano Lett.*, 2002, **2**, 25.
104. A. Ansón-Casaos, J. M. González-Domínguez, I. Lafragüeta, J. A. Carrodeguas and M. T. Martínez, Optical absorption response of chemically modified single-walled carbon nanotubes upon ultracentrifugation in various dispersants, *Carbon*, 2014, **66**, 105.
105. S. F. Wang, L. Shen, W. De Zhang and Y. J. Tong, Preparation and mechanical properties of chitosan/carbon nanotubes composites, *Biomacromolecules*, 2005, **6**, 3067.
106. N. Minami, Y. Kim, K. Miyashita, S. Kazaoui and B. Nalini, Cellulose derivatives as excellent dispersants for single-wall carbon nanotubes as demonstrated by absorption and photoluminescence spectroscopy, *Appl. Phys. Lett.*, 2006, **88**, 1.
107. Y. Habibi, L. A. Lucia and O. J. Rojas, Cellulose nanocrystals: Chemistry, self-assembly, and applications, *Chem. Rev.*, 2010, **110**, 3479.

108. R. J. Moon, A. Martini, J. Nairn, J. Simonsen and J. Youngblood, Cellulose nanomaterials review: Structure, properties and nanocomposites, *Chem. Soc. Rev.*, 2011, **40**, 3941.
109. N. Lin, J. Huang and A. Dufresne, Preparation, properties and applications of polysaccharide nanocrystals in advanced functional nanomaterials: A review, *Nanoscale*, 2012, **4**, 3274.
110. S. Pérez and D. Samain, Structure and Engineering of Celluloses, *Adv. Carbohydr. Chem. Biochem.*, 2010, **64**, 25.
111. G. Sèbe, F. Ham-Pichavant, E. Ibarboure, A. L. C. Koffi and P. Tingaut, Supramolecular structure characterization of cellulose II nanowhiskers produced by acid hydrolysis of cellulose i substrates, *Biomacromolecules*, 2012, **13**, 570.
112. X. Li, J. Li, J. Gong, Y. Kuang, L. Mo and T. Song, Cellulose nanocrystals (CNCs) with different crystalline allomorph for oil in water Pickering emulsions, *Carbohydr. Polym.*, 2018, **183**, 303.
113. J. M. González-Domínguez, A. Ansón-Casaos, L. Grasa, L. Abenia, A. Salvador, E. Colom, J. E. Mesonero, J. E. García-Bordejé, A. M. Benito and W. K. Maser, Unique Properties and Behavior of Nonmercerized Type-II Cellulose Nanocrystals as Carbon Nanotube Biocompatible Dispersants, *Biomacromolecules*, 2019, **20**, 3147–3160.
114. K. Mazeau, On the external morphology of native cellulose microfibrils, *Carbohydr. Polym.*, 2011, **84**, 524.
115. A. Dufresne, Nanocellulose: A new ageless bionanomaterial, *Mater. Today*, 2013, **16**, 220.
116. C. Olivier, C. Moreau, P. Bertoncini, H. Bizot, O. Chauvet and B. Cathala, Cellulose nanocrystal-assisted dispersion of luminescent single-walled carbon nanotubes for layer-by-layer assembled hybrid thin films, *Langmuir*, 2012, **28**, 12463–12471.
117. J. B. Mougel, C. Adda, P. Bertoncini, I. Capron, B. Cathala and O. Chauvet, Highly efficient and predictable noncovalent dispersion of single-walled and multi-walled carbon nanotubes by cellulose nanocrystals, *J. Phys. Chem. C*, 2016, **120**, 22694–22701.
118. A. Hajian, S. B. Lindström, T. Pettersson, M. M. Hamedi and L. Wågberg, Understanding the Dispersive Action of Nanocellulose for Carbon Nanomaterials, *Nano Lett.*, 2017, **17**, 1439–1447.
119. V. Kuzmenko, E. Karabulut, E. Pernevik, P. Enoksson and P. Gatenholm, Tailor-made conductive inks from cellulose nanofibrils for 3D printing of neural guidelines, *Carbohydr. Polym.*, 2018, **189**, 22.
120. Y. Li, H. Zhu, Y. Wang, U. Ray, S. Zhu, J. Dai, C. Chen, K. Fu, S.-H. Jang, D. Henderson, T. Li and L. Hu, Cellulose-Nanofiber-Enabled 3D Printing of a Carbon-Nanotube Microfiber Network, *Small Methods*, 2017, **1**, 1700222.
121. O. E. Glukhova, A. S. Kolesnikova, O. A. Grishina and M. M. Slepchenkov, Structure and properties of composites based chitosan and carbon nanostructures: atomistic and coarse-grained simulation, *Proc. SPIE*, 2015, **9339**, 933911.

122. M. M. Hamedi, A. Hajian, A. B. Fall, K. Hkansson, M. Salajkova, F. Lundell, L. Wågberg and L. A. Berglund, Highly conducting, strong nanocomposites based on nanocellulose-assisted aqueous dispersions of single-wall carbon nanotubes, *ACS Nano*, 2014, **8**, 2467.
123. D. Miyashiro, R. Hamano and K. Umemura, A Review of Applications Using Mixed Materials of Cellulose, Nanocellulose and Carbon Nanotubes, *Nanomaterials*, 2020, **10**, 186.
124. E. Lizundia, D. Puglia, T.-D. Nguyen and I. Armentano, Cellulose nanocrystal based multifunctional nanohybrids, *Prog. Mater. Sci.*, 2020, **112**, 100668.
125. L. Bacakova, J. Pajorova, M. Tomkova, R. Matejka, A. Broz, J. Stepanovska, S. Prazak, A. Skogberg, S. Siljander and P. Kallio, Applications of nanocellulose/nanocarbon composites: Focus on biotechnology and medicine, *Nanomaterials*, 2020, **10**, 1.
126. V. Calvo, J. Torrubia, D. Blanco, E. García-Bordejé, W. K. Maser, A. M. Benito and J. M. González-Domínguez, Optimizing Bacterial Cellulose Production Towards Materials for Water Remediation, *NATO Science for Peace and Security Series B: Physics and Biophysics*, 2020, DOI: 10.1007/978-94-024-2018-0_31.
127. Y. H. Kim, S. Park, K. Won, H. J. Kim and S. H. Lee, Bacterial cellulose-carbon nanotube composite as a biocompatible electrode for the direct electron transfer of glucose oxidase, *J. Chem. Technol. Biotechnol.*, 2013, **88**, 1067.
128. F. Cheng, C. Liu, H. Li, X. Wei, T. Yan, Y. Wang, Y. Song, J. He and Y. Huang, Carbon nanotube-modified oxidized regenerated cellulose gauzes for hemostatic applications, *Carbohydr. Polym.*, 2018, **183**, 246.
129. L. Jin, Z. Zeng, S. Kuddannaya, D. Wu, Y. Zhang and Z. Wang, Biocompatible, Free-Standing Film Composed of Bacterial Cellulose Nanofibers–Graphene Composite, *ACS Appl. Mater. Interfaces*, 2016, **8**, 1011.
130. X. Liu, H. Shen, S. Song, W. Chen and Z. Zhang, Accelerated biomineralization of graphene oxide – incorporated cellulose acetate nanofibrous scaffolds for mesenchymal stem cell osteogenesis, *Colloids Surf., B*, 2017, **159**, 251.
131. H. Luo, H. Ao, M. Peng, F. Yao, Z. Yang and Y. Wan, Effect of highly dispersed graphene and graphene oxide in 3D nanofibrous bacterial cellulose scaffold on cell responses: A comparative study, *Mater. Chem. Phys.*, 2019, **235**, 121774.
132. M. Ioniță, L. E. Crică, S. I. Voicu, S. Dinescu, F. Miculescu, M. Costache and H. Iovu, Synergistic effect of carbon nanotubes and graphene for high performance cellulose acetate membranes in biomedical applications, *Carbohydr. Polym.*, 2018, **183**, 50.
133. S. Park, J. Park, I. Jo, S. P. Cho, D. Sung, S. Ryu, M. Park, K. A. Min, J. Kim, S. Hong, B. H. Hong and B. S. Kim, *In situ* hybridization of carbon nanotubes with bacterial cellulose for three-dimensional hybrid bioscaffolds, *Biomaterials*, 2015, **58**, 93–102.

134. N. Pal, P. Dubey, P. Gopinath and K. Pal, Combined effect of cellulose nanocrystal and reduced graphene oxide into poly-lactic acid matrix nanocomposite as a scaffold and its anti-bacterial activity, *Int. J. Biol. Macromol.*, 2017, **95**, 94.
135. M. Rinaudo, Chitin and chitosan: Properties and applications, *Prog. Polym. Sci.*, 2006, **31**, 603.
136. C. K. S. Pillai, W. Paul and C. P. Sharma, Chitin and chitosan polymers: Chemistry, solubility and fiber formation, *Prog. Polym. Sci.*, 2009, **34**, 641.
137. C. Chang, S. Chen and L. Zhang, Novel hydrogels prepared *via* direct dissolution of chitin at low temperature: Structure and biocompatibility, *J. Mater. Chem.*, 2011, **21**, 3865.
138. Y. W. Cho, Y. N. Cho, S. H. Chung, G. Yoo and S. W. Ko, Water-soluble chitin as a wound healing accelerator, *Biomaterials*, 1999, **20**, 2139.
139. T. A. Khan, K. K. Peh and H. Seng, Mechanical, bioadhesive strength and biological evaluations of chitosan films for wound dressing, *J. Pharm. Pharm. Sci.*, 2000, **3**, 303.
140. Y. I. I. Kitagawa, M. Yoshikawa, K. Kobayashi, Y. Imakura and K. S. Im, Application of Chitin and Chitosan to Pharmaceutical Preparations. I. Film Preparation and *in Vitro* Evaluation, *Chem. Pharm. Bull.*, 1989, **37**, 523.
141. C. Songkroah, W. Nakbanpote and P. Thiravetyan, Recovery of silver-thiosulphate complexes with chitin, *Process Biochem.*, 2004, **39**, 1553.
142. Y. Guo, B. Duan, L. Cui and P. Zhu, Construction of chitin/graphene oxide hybrid hydrogels, *Cellulose*, 2015, **22**, 2035.
143. N. Singh, K. K. K. Koziol, J. Chen, A. J. Patil, J. W. Gilman, P. C. Trulove, W. Kafienah and S. S. Rahatekar, Ionic liquids-based processing of electrically conducting chitin nanocomposite scaffolds for stem cell growth, *Green Chem.*, 2013, **15**, 1192–1202.
144. M. V. Sofroniew and H. V. Vinters, Astrocytes: Biology and pathology, *Acta Neuropathol.*, 2010, **119**, 7–35.
145. N. Singh, J. Chen, K. K. Koziol, K. R. Hallam, D. Janas, A. J. Patil, A. Strachan, J. G. Hanley and S. S. Rahatekar, Chitin and carbon nanotube composites as biocompatible scaffolds for neuron growth, *Nanoscale*, 2016, **8**, 8288.
146. S. Wu, B. Duan, A. Lu, Y. Wang, Q. Ye and L. Zhang, Biocompatible chitin/carbon nanotubes composite hydrogels as neuronal growth substrates, *Carbohydr. Polym.*, 2017, **174**, 830–840.
147. W. M. Lee, R. H. Squires, S. L. Nyberg, E. Doo and J. H. Hoofnagle, *Hepatology*, 2008, **47**, 1401.
148. S. Wu, B. Duan, X. Zeng, A. Lu, X. Xu, Y. Wang, Q. Ye and L. Zhang, Construction of blood compatible lysine-immobilized chitin/carbon nanotube microspheres and potential applications for blood purified therapy, *J. Mater. Chem. B*, 2017, **5**, 2952.

149. S. Rahaiee, S. A. Shojaosadati, M. Hashemi, S. Moini and S. H. Razavi, Improvement of crocin stability by biodegradeble nanoparticles of chitosan-alginate, *Int. J. Biol. Macromol.*, 2015, **79**, 423.
150. B. A. Lindborg, J. H. Brekke, C. M. Scott, Y. W. Chai, C. Ulrich, L. Sandquist, E. Kokkoli and T. D. O'Brien, A Chitosan-Hyaluronan-Based Hydrogel-Hydrocolloid Supports *In Vitro* Culture and Differentiation of Human Mesenchymal Stem/Stromal Cells, *Tissue Eng., Part A*, 2015, **21**, 1952.
151. I. Younes, S. Sellimi, M. Rinaudo, K. Jellouli and M. Nasri, Influence of acetylation degree and molecular weight of homogeneous chitosans on antibacterial and antifungal activities, *Int. J. Food Microbiol.*, 2014, **185**, 57.
152. D.-H. Ngo and S.-K. Kim, *Advances in Food and Nutrition Research*, *Antioxidant Effects of Chitin, Chitosan, and Their Derivatives*, Elsevier, 2014, ch. 2, pp. 15–31.
153. J. Huang, H. Xie, S. Hu, T. Xie, J. Gong, C. Jiang, Q. Ge, Y. Wu, S. Liu, Y. Cui, J. Mao and L. Mei, Preparation, characterization, and biochemical activities of N-(2-Carboxyethyl) chitosan from squid pens, *J. Agric. Food Chem.*, 2015, **63**, 2464.
154. I. A. Sogias, A. C. Williams and V. V. Khutoryanskiy, Why is Chitosan Mucoadhesive? *Biomacromolecules*, 2008, **9**, 1837.
155. Q. Z. Wang, X. G. Chen, Z. X. Li, S. Wang, C. S. Liu, X. H. Meng, C. G. Liu, Y. H. Lv and L. J. Yu, Preparation and blood coagulation evaluation of chitosan microspheres, *J. Mater. Sci.: Mater. Med.*, 2008, **19**, 1371.
156. X. Guo, T. Sun, R. Zhong, L. Ma, C. You, M. Tian, H. Li and C. Wang, Effects of Chitosan Oligosaccharides on Human Blood Components, *Front. Pharmacol.*, 2018, **9**, 1.
157. L. Qi and Z. Xu, *In vivo* antitumor activity of chitosan nanoparticles, *Bioorg. Med. Chem. Lett.*, 2006, **16**, 4243.
158. H. S. Adhikari and P. N. Yadav, Anticancer Activity of Chitosan, Chitosan Derivatives, and Their Mechanism of Action, *Int. J. Biomater.*, 2018, **2018**, 1.
159. D. Zhao, S. Yu, B. Sun, S. Gao, S. Guo and K. Zhao, Biomedical Applications of Chitosan and Its Derivative Nanoparticles, *Polymers*, 2018, **10**, 462.
160. S. M. Ahsan, M. Thomas, K. K. Reddy, S. G. Sooraparaju, A. Asthana and I. Bhatnagar, Chitosan as biomaterial in drug delivery and tissue engineering, *Int. J. Biol. Macromol.*, 2018, **110**, 97.
161. R. Jayakumar, M. Prabaharan, S. V. Nair and H. Tamura, Novel chitin and chitosan nanofibers in biomedical applications, *Biotechnol. Adv.*, 2010, **28**, 142.
162. R. Jayakumar, M. Prabaharan, P. T. Sudheesh Kumar, S. V. Nair and H. Tamura, Biomaterials based on chitin and chitosan in wound dressing applications, *Biotechnol. Adv.*, 2011, **29**, 322.

163. S. Vardharajula, S. Z. Ali, P. M. Tiwari, E. Eroğlu, K. Vig, V. A. Dennis and S. R. Singh, Functionalized carbon nanotubes: biomedical applications, *Int. J. Nanomed.*, 2012, **7**, 5361.
164. J. Simon, E. Flahaut and M. Golzio, Overview of Carbon Nanotubes for Biomedical Applications, *Materials*, 2019, **12**, 624.
165. M. Zhang, A. Smith and W. Gorski, Carbon nanotube-chitosan system for electrochemical sensing based on dehydrogenase enzymes, *Anal. Chem.*, 2004, **76**, 5045.
166. G. Cirillo, O. Vittorio, D. Kunhardt, E. Valli, F. Voli, A. Farfalla, M. Curcio, U. G. Spizzirri and S. Hampel, Combining Carbon Nanotubes and Chitosan for the Vectorization of Methotrexate to Lung Cancer Cells, *Materials*, 2019, **12**, 2889.
167. B. Li, X.-X. Zhang, H.-Y. Huang, L.-Q. Chen, J.-H. Cui, Y. Liu, H. Jin, B.-J. Lee and Q.-R. Cao, Effective deactivation of A549 tumor cells *in vitro* and *in vivo* by RGD-decorated chitosan-functionalized single-walled carbon nanotube loading docetaxel, *Int. J. Pharm.*, 2018, **543**, 8.
168. I. Olivas-Armendáriz, P. García-Casillas, R. Martínez-Sánchez, A. Martínez-Villafañe and C. A. Martínez-Pérez, Chitosan/MWCNT composites prepared by thermal induced phase separation, *J. Alloys Compd.*, 2010, **495**, 592.
169. S. Nardecchia, M. C. Serrano, M. C. Gutiérrez, M. T. Portolés, M. L. Ferrer and F. Del Monte, Osteoconductive performance of carbon nanotube scaffolds homogeneously mineralized by flow-through electrodeposition, *Adv. Funct. Mater.*, 2012, **22**, 4411.
170. J. Venkatesan, B. Ryu, P. N. Sudha and S.-K. Kim, Preparation and characterization of chitosan–carbon nanotube scaffolds for bone tissue engineering, *Int. J. Biol. Macromol.*, 2012, **50**, 393–402.
171. S. Gholizadeh, F. Moztarzadeh, N. Haghighipour, L. Ghazizadeh, F. Baghbani, M. A. Shokrgozar and Z. Allahyari, Preparation and characterization of novel functionalized multiwalled carbon nanotubes/chitosan/β-Glycerophosphate scaffolds for bone tissue engineering, *Int. J. Biol. Macromol.*, 2017, **97**, 365.
172. H. Yuan, L.-Y. Meng and S.-J. Park, A review: synthesis and applications of graphene/chitosan nanocomposites, *Carbon Lett.*, 2016, **17**, 11.
173. K. Pieklarz, M. Tylman and Z. Modrzejewska, Applications of Chitosan–Graphene oxide nanocomposites in medical science: A review, *Prog. Chem. Appl. Chitin Its Deriv.*, 2018, **23**, 5.
174. H. Bao, Y. Pan, Y. Ping, N. G. Sahoo, T. Wu, L. Li, J. Li and L. H. Gan, Chitosan-functionalized graphene oxide as a nanocarrier for drug and gene delivery, *Small*, 2011, **7**, 1569.
175. R. Justin and B. Chen, Characterisation and drug release performance of biodegradable chitosan–graphene oxide nanocomposites, *Carbohydr. Polym.*, 2014, **103**, 70.
176. R. Justin and B. Chen, Body temperature reduction of graphene oxide through chitosan functionalisation and its application in drug delivery, *Mater. Sci. Eng., C*, 2014, **34**, 50.

177. D. Depan, B. Girase, J. S. Shah and R. D. K. Misra, Structure-process-property relationship of the polar graphene oxide-mediated cellular response and stimulated growth of osteoblasts on hybrid chitosan network structure nanocomposite scaffolds, *Acta Biomater.*, 2011, **7**, 3432–3445.
178. A. Hermenean, A. Codreanu, H. Herman, C. Balta, M. Rosu, C. V. Mihali, A. Ivan, S. Dinescu, M. Ionita and M. Costache, Chitosan-Graphene Oxide 3D scaffolds as Promising Tools for Bone Regeneration in Critical-Size Mouse Calvarial Defects, *Sci. Rep.*, 2017, **7**, 91.
179. Y. S. Choi, S. R. Hong, Y. M. Lee, K. W. Song, M. H. Park and Y. S. Nam, Study on gelatin-containing artificial skin: I. Preparation and characteristics of novel gelatin-alginate sponge, *Biomaterials*, 1999, **20**, 409.
180. G. Orive, S. Ponce, R. M. Hernández, A. R. Gascón, M. Igartua and J. L. Pedraz, Biocompatibility of microcapsules for cell immobilization elaborated with different type of alginates, *Biomaterials*, 2002, **23**, 3825.
181. A. M. Fayaz, K. Balaji, M. Girilal, P. T. Kalaichelvan and R. Venkatesan, Mycobased synthesis of silver nanoparticles and their incorporation into sodium alginate films for vegetable and fruit preservation, *J. Agric. Food Chem.*, 2009, **57**, 6246.
182. K. Y. Lee and D. J. Mooney, Alginate: Properties and biomedical applications, *Prog. Polym. Sci.*, 2012, **37**, 106.
183. B. D. Ratner, A. S. Hoffman, F. J. Schoen and J. E. Lemons, *Biomaterials Science. An Introduction to Materials in Medicine*, Academic Press, 3rd edn, 2013.
184. S. H. Ching, N. Bansal and B. Bhandari, Alginate gel particles–A review of production techniques and physical properties, *Crit. Rev. Food Sci. Nutr.*, 2017, **57**, 1133.
185. A. Bibi, S. Rehman and A. Yaseen, Alginate-nanoparticles composites: kinds, reactions and applications, *Mater. Res. Express*, 2019, **6**, 092001.
186. P. Vauchel, R. Kaas, A. Arhaliass, R. Baron and J. Legrand, A new process for extracting alginates from Laminaria digitata: Reactive extrusion, *Food Bioprocess Technol.*, 2008, **1**, 297.
187. P. Vauchel, K. Leroux, R. Kaas, A. Arhaliass, R. Baron and J. Legrand, Kinetics modeling of alginate alkaline extraction from Laminaria digitata, *Bioresour. Technol.*, 2009, **100**, 1291.
188. A. D. Augst, H. J. Kong and D. J. Mooney, Alginate hydrogels as biomaterials, *Macromol. Biosci.*, 2006, **6**, 623.
189. P. B. Malafaya, G. A. Silva and R. L. Reis, Natural-origin polymers as carriers and scaffolds for biomolecules and cell delivery in tissue engineering applications, *Adv. Drug Delivery Rev.*, 2007, **59**, 207.
190. O. Smidsrød and A. Haug, Properties of Poly(1,4)hexuronates in the Gel State II. Comparison of Gels of Different Chemical Composition, *Acta Chem. Scand.*, 1972, **26**, 79.
191. O. Smidsrød, Molecular basis for some physical properties of alginates in the gel state, *Faraday Discuss. Chem. Soc.*, 1974, **57**, 263.
192. K. I. Draget, G. Skjåk-Bræek and O. Smidsrød, Alginate based new materials, *Int. J. Biol. Macromol.*, 1997, **21**, 47.

193. Y. Qin, Alginate fibres: an overview of the production processes and applications in wound management, *Polym. Int.*, 2008, **57**, 171.
194. J. W. Rhim, Physical and mechanical properties of water resistant sodium alginate films, *LWT--Food Sci. Technol.*, 2004, **37**, 323.
195. Y. Shchipunov, Bionanocomposites: Green sustainable materials for the near future, *Pure Appl. Chem.*, 2012, **84**, 2579.
196. M. Alboofetileh, M. Rezaei, H. Hosseini and M. Abdollahi, Effect of montmorillonite clay and biopolymer concentration on the physical and mechanical properties of alginate nanocomposite films, *J. Food Eng.*, 2013, **117**, 26.
197. B. S. Gholizadeh, F. Buazar, S. M. Hosseini and S. M. Mousavi, Enhanced antibacterial activity, mechanical and physical properties of alginate/hydroxyapatite bionanocomposite film, *Int. J. Biol. Macromol.*, 2018, **116**, 786.
198. H. Y. Mi, X. Jing, H. X. Huang, X. F. Peng and L. S. Turng, Superhydrophobic Graphene/Cellulose/Silica Aerogel with Hierarchical Structure as Superabsorbers for High Efficiency Selective Oil Absorption and Recovery, *Ind. Eng. Chem. Res.*, 2018, **57**, 1745.
199. M. Ionita, M. A. Pandele and H. Iovu, Sodium alginate/graphene oxide composite films with enhanced thermal and mechanical properties, *Carbohydr. Polym.*, 2013, **94**, 339.
200. S. Liu, Y. Li and L. Li, Enhanced stability and mechanical strength of sodium alginate composite films, *Carbohydr. Polym.*, 2017, **160**, 62.
201. A. Marrella, A. Lagazzo, F. Barberis, T. Catelani, R. Quarto and S. Scaglione, Enhanced mechanical performances and bioactivity of cell laden-graphene oxide/alginate hydrogels open new scenario for articular tissue engineering applications, *Carbon*, 2017, **115**, 608.
202. Á. Serrano-Aroca, L. Iskandar and S. Deb, Green synthetic routes to alginate-graphene oxide composite hydrogels with enhanced physical properties for bioengineering applications, *Eur. Polym. J.*, 2018, **103**, 198.
203. I. Larraza, L. Ugarte, A. Fayanas, N. Gabilondo, A. Arbelaiz, M. A. Corcuera and A. Eceiza, Influence of Process Parameters in Graphene Oxide Obtention on the Properties of Mechanically Strong Alginate Nanocomposites, *Materials*, 2020, **13**, 1081.
204. M. H. Norahan, M. Pourmokhtari, M. R. Saeb, B. Bakhshi, M. Soufi Zomorrod and N. Baheiraei, Electroactive cardiac patch containing reduced graphene oxide with potential antibacterial properties, *Mater. Sci. Eng., C*, 2019, **104**, 109921.
205. B. Salesa, M. Llorens-Gámez and Á. Serrano-Aroca, Study of 1D and 2D carbon nanomaterial in alginate films, *Nanomaterials*, 2020, **10**, 1.
206. H. Y. Zhao, W. Zheng, Z. X. Meng, H. M. Zhou, X. X. Xu, Z. Li and Y. F. Zheng, Bioelectrochemistry of hemoglobin immobilized on a sodium alginate-multiwall carbon nanotubes composite film, *Biosens. Bioelectron.*, 2009, **24**, 2352.

207. A. Grigoryev, V. Sa, V. Gopishetty, I. Tokarev, K. G. Kornev and S. Minko, Wet-spun stimuli-responsive composite fibers with tunable electrical conductivity, *Adv. Funct. Mater.*, 2013, **23**, 5903.
208. L. Nie, C. Liu, J. Wang, Y. Shuai, X. Cui and L. Liu, Effects of surface functionalized graphene oxide on the behavior of sodium alginate, *Carbohydr. Polym.*, 2015, **117**, 616.
209. B. Joddar, E. Garcia, A. Casas and C. M. Stewart, Development of functionalized multi-walled carbon-nanotube-based alginate hydrogels for enabling biomimetic technologies, *Sci. Rep.*, 2016, **6**, 1.
210. S. Homaeigohar, T. Y. Tsai, T. H. Young, H. J. Yang and Y. R. Ji, An electroactive alginate hydrogel nanocomposite reinforced by functionalized graphite nanofilaments for neural tissue engineering, *Carbohydr. Polym.*, 2019, **224**, 115112.
211. F. H. Silver and D. L. Christiansen, Mechanical Properties of Tissues: Introduction to Analysis of Tissues, *Biomaterials Science and Biocompatibility*, 1999, p. 187.
212. C. J. Little, N. K. Bawolin and X. Chen, Mechanical properties of natural cartilage and tissue-engineered constructs, *Tissue Eng., Part B*, 2011, **17**, 213.
213. M. S. Islam, M. Ashaduzzaman, S. M. Masum and J. H. Yeum, Mechanical and Electrical Properties: Electrospun Alginate/Carbon Nanotube Composite Nanofiber, *Dhaka Univ. J. Sci.*, 2012, **60**, 125.
214. E. D. Yildirim, X. Yin, K. Nair and W. Sun, Fabrication, characterization, and biocompatibility of single-walled carbon nanotube-reinforced alginate composite scaffolds manufactured using freeform fabrication technique, *J. Biomed. Mater. Res., Part B*, 2008, **87**, 406.
215. V. Sa and K. G. Kornev, A method for wet spinning of alginate fibers with a high concentration of single-walled carbon nanotubes, *Carbon*, 2011, **49**, 1859.
216. Y. He, N. Zhang, Q. Gong, H. Qiu, W. Wang, Y. Liu and J. Gao, Alginate/graphene oxide fibers with enhanced mechanical strength prepared by wet spinning, *Carbohydr. Polym.*, 2012, **88**, 1100.
217. A. S. Brady-Estévez, M. H. Schnoor, C. D. Vecitis, N. B. Saleh and M. Elimelech, Multiwalled carbon nanotube filter: Improving viral removal at low pressure, *Langmuir*, 2010, **26**, 14975.
218. X. Hu, S. Rajendran, Y. Yao, Z. Liu, K. Gopalsamy, L. Peng and C. Gao, A novel wet-spinning method of manufacturing continuous bio-inspired composites based on graphene oxide and sodium alginate, *Nano Res.*, 2016, **9**, 735.
219. H. Zheng, J. Yang and S. Han, The synthesis and characteristics of sodium alginate/graphene oxide composite films crosslinked with multivalent cations, *J. Appl. Polym. Sci.*, 2016, **133**, 43616.
220. H. Zhang, X. Pang and Y. Qi, pH-Sensitive graphene oxide/sodium alginate/polyacrylamide nanocomposite semi-IPN hydrogel with improved mechanical strength, *RSC Adv.*, 2015, **5**, 89083.

221. S. Yang, L. Jang, S. Kim, J. Yang, K. Yang, S. W. Cho and J. Y. Lee, Polypyrrole/Alginate Hybrid Hydrogels: Electrically Conductive and Soft Biomaterials for Human Mesenchymal Stem Cell Culture and Potential Neural Tissue Engineering Applications, *Macromol. Biosci.*, 2016, **16**, 1653.
222. L. Zhou, L. Fan, X. Yi, Z. Zhou, C. Liu, R. Fu, C. Dai, Z. Wang, X. Chen, P. Yu, D. Chen, G. Tan, Q. Wang and C. Ning, Soft Conducting Polymer Hydrogels Cross-Linked and Doped by Tannic Acid for Spinal Cord Injury Repair, *ACS Nano*, 2018, **12**, 10957.
223. T. Hu, Y. Wu, X. Zhao, L. Wang, L. Bi, P. X. Ma and B. Guo, Micropatterned, electroactive, and biodegradable poly(glycerol sebacate)-aniline trimer elastomer for cardiac tissue engineering, *Chem. Eng. J.*, 2019, **366**, 208.
224. B. Guo, J. Qu, X. Zhao and M. Zhang, Degradable conductive self-healing hydrogels based on dextran-graft-tetraaniline and *N*-carboxyethyl chitosan as injectable carriers for myoblast cell therapy and muscle regeneration, *Acta Biomater.*, 2019, **84**, 180.
225. C. Basavaraja, B. S. Kim and D. S. Huh, Characterization and AC electrical conductivity for the dispersed composites containing alginate-multiwalled carbon nanotubes, *Macromol. Res.*, 2011, **19**, 233.
226. C. Lynam, S. E. Moulton and G. G. Wallace, Carbon-nanotube biofibers, *Adv. Mater.*, 2007, **19**, 1244.
227. D. Y. Lewitus, J. Landers, J. R. Branch, K. L. Smith, G. Callegari, J. Kohn and A. V. Neimark, Biohybrid carbon nanotube/agarose fibers for neural tissue engineering, *Adv. Funct. Mater.*, 2011, **21**, 2624.
228. D. Y. Lewitus, K. L. Smith, J. Landers, A. V. Neimark, J. Kohn, D. Y. Lewitus, K. L. Smith, J. Landers, A. V. Neimark and J. Kohn, Bioactive agarose carbon-nanotube composites are capable of manipulating brain-implant interface, *J. Appl. Polym. Sci.*, 2014, **131**, 1.
229. Y. Liu, P. Liang, H. Y. Zhang and D. S. Guo, Cation-controlled aqueous dispersions of alginic-acid-wrapped multi-walled carbon nanotubes, *Small*, 2006, **2**, 874.
230. C. Martín, S. Merino, J. M. González-Domínguez, R. Rauti, L. Ballerini, M. Prato and E. Vázquez, Graphene Improves the Biocompatibility of Polyacrylamide Hydrogels: 3D Polymeric Scaffolds for Neuronal Growth, *Sci. Rep.*, 2017, **7**, 10942.
231. S. Sayyar, E. Murray, B. C. Thompson, S. Gambhir, D. L. Officer and G. G. Wallace, Covalently linked biocompatible graphene/polycaprolactone composites for tissue engineering, *Carbon*, 2013, **52**, 296.
232. H. Hu, Y. Ni, V. Montana, R. C. Haddon and V. Parpura, Chemically Functionalized Carbon Nanotubes as Substrates for Neuronal Growth., *Nano Lett.*, 2004, **4**, 507.

233. V. Lovat, D. Pantarotto, L. Lagostena, B. Cacciari, M. Grandolfo, M. Righi, G. Spalluto, M. Prato and L. Ballerini, Carbon nanotube substrates boost neuronal electrical signaling, *Nano Lett.*, 2005, **5**, 1107.
234. E. Mooney, P. Dockery, U. Greiser, M. Murphy and V. Barron, Carbon nanotubes and mesenchymal stem cells: Biocompatibility, proliferation and differentiation, *Nano Lett.*, 2008, **8**, 2137.
235. J. Suhr, P. Victor, L. Ci, S. Sreekala, X. Zhang, O. Nalamasu and P. M. Ajayan, Fatigue resistance of aligned carbon nanotube arrays under cyclic compression, *Nat. Nanotechnol.*, 2007, **2**, 417.
236. N. Alegret, A. Dominguez-Alfaro, J. M. González-Domínguez, B. Arnaiz, U. Cossío, S. Bosi, E. Vázquez, P. Ramos-Cabrer, D. Mecerreyes and M. Prato, Three-Dimensional Conductive Scaffolds as Neural Prostheses Based on Carbon Nanotubes and Polypyrrole, *ACS Appl. Mater. Interfaces*, 2018, **10**, 43904.
237. A. Dominguez-Alfaro, N. Alegret, B. Arnaiz, J. M. González-Domínguez, A. Martin-Pacheco, U. Cossío, L. Porcarelli, S. Bosi, E. Vázquez, D. Mecerreyes and M. Prato, Tailored Methodology Based on Vapor Phase Polymerization to Manufacture PEDOT/CNT Scaffolds for Tissue Engineering, *ACS Biomater. Sci. Eng.*, 2020, **6**, 1269.
238. S. Shah, P. T. Yin, T. M. Uehara, S. T. D. Chueng, L. Yang and K. B. Lee, Guiding stem cell differentiation into oligodendrocytes using graphene-nanofiber hybrid scaffolds, *Adv. Mater.*, 2014, **26**, 3673.
239. G. Y. Chen, D. W. P. Pang, S. M. Hwang, H. Y. Tuan and Y. C. Hu, A graphene-based platform for induced pluripotent stem cells culture and differentiation, *Biomaterials*, 2012, **33**, 418.
240. S. Kumar, S. Raj, E. Kolanthai, A. K. Sood, S. Sampath and K. Chatterjee, Chemical functionalization of graphene to augment stem cell osteogenesis and inhibit biofilm formation on polymer composites for orthopedic applications, *ACS Appl. Mater. Interfaces*, 2015, **7**, 3237.
241. R. Guo, S. Zhang, M. Xiao, F. Qian, Z. He, D. Li, X. Zhang, H. Li, X. Yang, M. Wang, R. Chai and M. Tang, Accelerating bioelectric functional development of neural stem cells by graphene coupling: Implications for neural interfacing with conductive materials, *Biomaterials*, 2016, **106**, 193.
242. N. Mansouri, S. F. Al-Sarawi, J. Mazumdar and D. Losic, Advancing fabrication and properties of three-dimensional graphene-alginate scaffolds for application in neural tissue engineering, *RSC Adv.*, 2019, **9**, 36838.
243. S. Talebian, M. Mehrali, R. Raad, F. Safaei, J. Xi, Z. Liu and J. Foroughi, Electrically Conducting Hydrogel Graphene Nanocomposite Biofibers for Biomedical Applications, *Front. Chem.*, 2020, **8**, 1.
244. Z. M. Huang, Y. Z. Zhang, M. Kotaki and S. Ramakrishna, A review on polymer nanofibers by electrospinning and their applications in nanocomposites, *Compos. Sci. Technol.*, 2003, **63**, 2223.

245. J. M. González-Domínguez, W. Neri, M. Maugey, P. Poulin, A. Ansón-Casaos and M. Teresa Martínez, A chemically reactive spinning dope for significant improvements in wet spun carbon nanotube fibres, *Chem. Commun.*, 2013, **49**, 3973.
246. S. Chew, Y. Wen, Y. Dzenis and K. Leong, The Role of Electrospinning in the Emerging Field of Nanomedicine, *Curr. Pharm. Des.*, 2006, **12**, 4751.

CHAPTER 5

Biological Applications of Magnetically Empowered Carbon Nanotubes

A. STOPIN[a] AND D. BONIFAZI*[a]

[a]Institute of Organic Chemistry, Faculty of Chemistry, University of Vienna, Währinger Strasse 38, Vienna, Austria
*E-mail: davide.bonifazi@univie.ac.at

5.1 Introduction

Carbon nanotubes (CNTs) were first described as "helical microtubules of graphitic carbons" by Iijima in 1991.[1] Due to their structure, CNTs are the nanomaterials with the highest aspect ratio having diameters ranging from 0.4 to 100 nm and length of up to the centimetre scale.[2] Their graphitic tubular structure gives them large stiffness (1.8 TPa of Young's modulus for single-wall carbon nanotubes (SWCNTs)),[3] tensile strength (up to 63 GPa for multi-wall carbon nanotubes (MWCNTs)),[4] and high axial conductivity (up to 6×10^6 A cm^{-2}).[5] Also, they possess far-infrared and far-ultraviolet absorption[6] and are excellent thermal conductors in their axial direction[7] while being thermal insulators in the radial.[8] In addition to these physical properties, CNTs possess magnetic properties which will be discussed hereafter.

The magnetisation of a material corresponds to its response to an external magnetic field. To clarify, this value is the sum of the protons and electrons magnetic dipole moments of the material. Based on this assumption, one can calculate the magnetic susceptibility χ of a material, which represents

Nanoscience & Nanotechnology Series No. 48
Carbon Nanostructures for Biomedical Applications
Edited by Tatiana Da Ros, Nazario Martín and Jean-Francois Nierengarten

Published by the Royal Society of Chemistry, www.rsc.org

the variation of magnetisation as a function of an external magnetic field H using the equation: $M = \chi H$. If $\chi < 0$, the material is diamagnetic while if $\chi > 0$, the material is paramagnetic. For CNTs, their magnetic susceptibility values are dependent on their helicity and, due to their high aspect ratio, on the angle between the tube axis and the direction of the magnetic field. Taking all this into consideration, Fujiwara *et al.* determined the χ anisotropy, due to the shape of the nanotubes, of MWCNTs to be $9 \pm 5 \times 10^{-6}$ emu mol^{-1}.[9] While low, this value is significant and similar values were found for other types of SWCNTs.[10,11] Thus, CNTs are sensitive to magnetic fields but of high intensity, in general superior to 10 T.[12,13] To improve the response towards low magnetic fields, the use of CNTs requires them to be coupled with magnetic nanoparticles (MNPs) to lead to the formation of magnetic carbon nanotubes (mCNTs).

MNPs have been reported in numerous publications for their large number of applications, such as catalysis,[14,15] data recording,[16] or wastewater treatment.[17] They have also been used for biological applications, hyperthermia and imaging among others.[18–22] By combining them with CNTs a synergy appears between the two entities (Figure 5.1).[23] The CNTs will thus confer specific properties to the MNPs. The first is cavity-confinement, protecting MNPs from the environment and thus preventing an eventual oxidation that would make them diamagnetic or soluble in the medium.[24,25] The second is templating that could happen during the synthesis of the MNPs inside the cavity of CNTs.[24,26] Finally, using the large graphitic surface of CNTs, the magnetic nanomaterials can be readily functionalised by non-covalent or covalent chemistry.[27–29] On the other hand, the magnetic behaviour of MNPs will impart new properties to the final mCNTs such as magnetically directed movement, magnetic fluid hyperthermia and magnetic resonance contrast. In the subsequent sections of this chapter, we will see the different

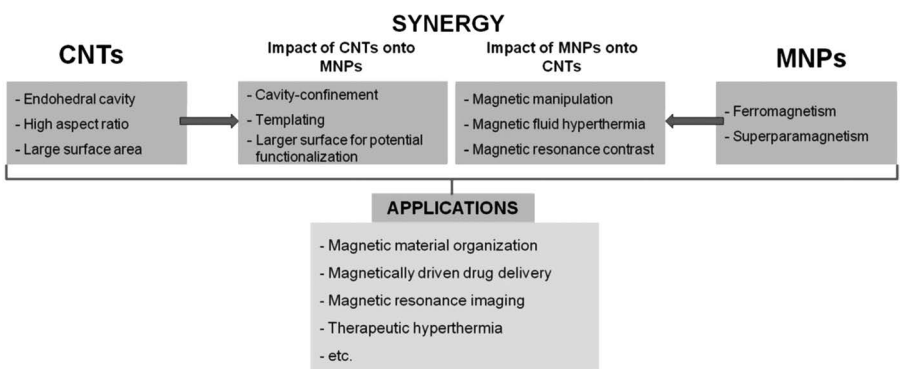

Figure 5.1 Synergy between CNTs and MNPs. Reproduced from ref. 23 with permission from John Wiley and Sons, Copyright 2015 WILEY-VCH Verlag GmbH & Co. KGaA, Weinheim.

approaches used to synthesise mCNTs, then we will detail the use of such materials in biological applications.

5.2 Preparation of Magnetic Carbon Nanotubes

The enhancement of the magnetic properties of CNTs by magnetic nanoparticles can be performed by taking advantage of the internal cavity of the CNTs, or by using their external graphitic structure (Figure 5.2). Due to the

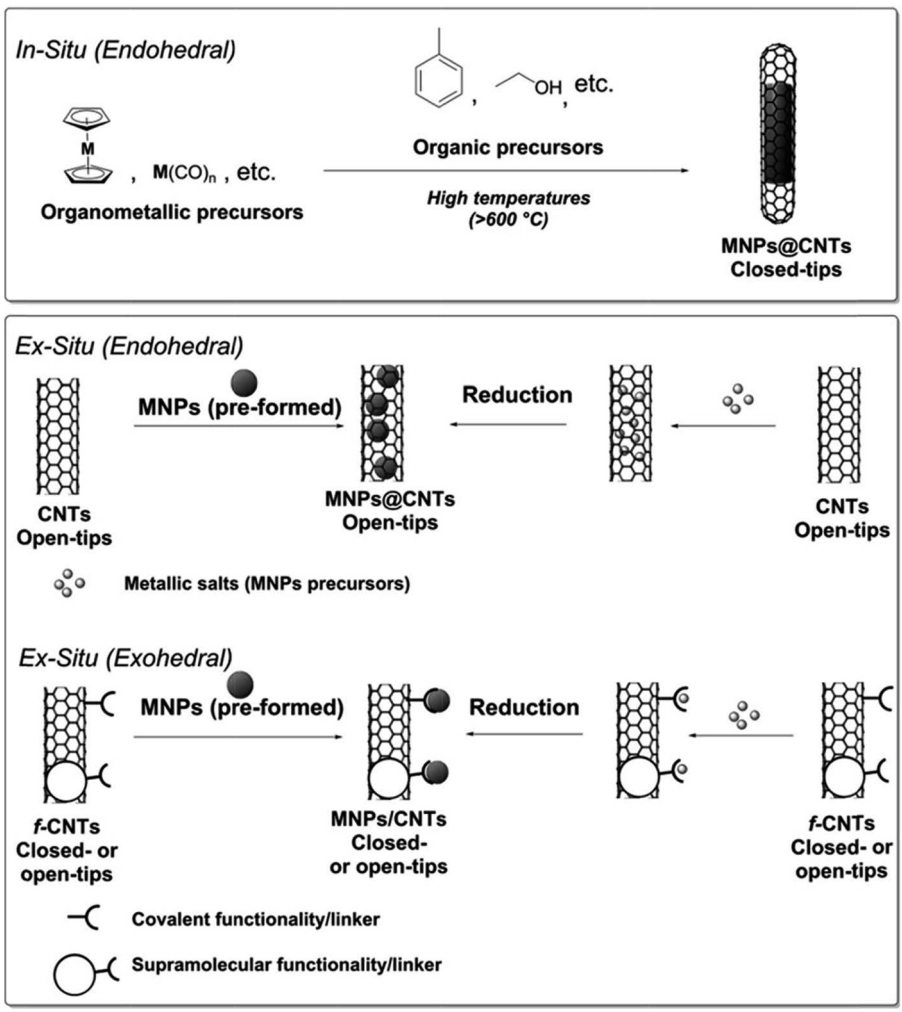

Figure 5.2 Syntheses pathways of mCNTs. Reproduced from ref. 23 with permission from John Wiley and Sons, Copyright 2015 WILEY-VCH Verlag GmbH & Co. KGaA, Weinheim.

number of reviews about the preparation of these mCNTs,[30–33] the description given here will summarise the different techniques available to the scientific community.

5.2.1 Magnetic Filling of the Cavity of the Nanotubes During the Formation of CNTs

In his seminal publication, Iijima reported the production of CNTs by arc-discharge.[1] A couple of years later, it was discovered that metallic Co nanoparticles can act as catalysts for their synthesis.[34] However, the CNTs produced were shown to possess some Co nanoparticles at their tip, making the compound ferromagnetic. In subsequent years, a report showed the production of CNTs using Ni as a catalyst on a large scale.[35] Based on these findings, the development of the chemical vapour deposition (CVD) method was reported.[36] This protocol relies on the pyrolysis of carbon precursors, such as toluene or acetylene among others, at temperatures greater than 600 °C while using metallic particles as a catalyst. These particles are, in general, deposited on a substrate and lead to the formation of nanotubes at their contact. Among all the metal particles used to produce CNTs, Co, Ni and especially Fe are now commonly used for their synthesis. However, a lot of these materials possess such a low level of metallic nanoparticles encapsulated inside their cavity that the magnetic properties of the produced materials are not greatly modified.

In order to use CNTs for magnetic-based applications using low magnetic fields, the quantity of metallic nanoparticles inside the cavity of the nanotubes should be increased. To do so, additional metallic precursors, like ferrocene, are usually employed to increase the loading of Fe inside CNTs.[37] In this case, the metallic precursors generally fulfil two duties, the formation of the metallic particles that catalyses the formation of the CNTs as well as the metal source for the additional nanoparticle's encapsulation.[38] The quantity of metal loaded in the CNTs depends on multiple factors, such as the temperature of pyrolysis, the choice and quantity of both organic and metallic precursors used as well as the CVD time.[39] In some cases, one compound can be used simultaneously as the metallic and carbon precursor. Ferrocene, for example, was used as the only material in the CVD process that led to the formation of highly loaded MWCNTs, with up to 35% Fe loading.[40,41] On the other hand, this technique presents the drawback of leading to the formation of nanotubes with the presence of Fe at the exterior of the CNTs. The non-encapsulated metal is thus sensitive to the environment and will lead to the formation of iron oxide. Acidic washings are used, in general, to remove this excess of Fe leading to the obtainment of CNTs with only encapsulated metallic nanoparticles. In a recent report, our group also demonstrated that the crystallinity of the Fe phases encapsulated in the CNTs can be tailored using post-synthetic treatments, acidic and thermal, in order to modify the magnetic properties of the materials obtained.[42]

5.2.2 Magnetic Enhancement of CNTs After Their Synthesis

5.2.2.1 Inside the Cavity of CNTs

The addition of magnetic material inside the cavity of CNTs requires, in a first step, the opening of their tip. This step is generally realised using oxidative conditions. In a second step, the open tubes are placed in contact with a fluid containing the molecule or material to be encapsulated. For some applications, the tubes are then closed again to prevent any leaching of the material. For the encapsulation of MNPs inside the cavity of the tubes, two approaches can be used: MNPs can be preformed and then inserted into the cavity or their precursors can be introduced in the cavity of nanotubes and then transformed within MNPs while already confined.

In 2005, Korneva *et al.* reported the encapsulation of preformed Fe_3O_4 nanoparticles.[43] A ferrofluid containing these MNPs was introduced inside the cavity of open-tip CNTs immobilised in an alumina support through the attraction of a permanent magnet. After removal of the solvent, mCNTs were obtained. In general, this method allows for the insertion of monodisperse MNPs inside CNTs cavities. Using the other approach described previously, Pham-Huu *et al.* filled the cavity of CNTs with precursors $Fe(NO_3)_3$ and $Co(NO_3)_3$.[44] Through a mild thermal treatment, magnetic nanowires of $CoFe_2O_4$ were formed at the tips of the CNTs. After these two seminal reports, multiple examples in the literature used adaptations of these techniques to produce mCNTs.[32,33]

5.2.2.2 On the Graphitic Structure of CNTs

The coating of the graphitic structure of CNTs can also be realised through the two approaches presented for the endohedral filling: preformed MNPs or precursor, that will be the seeds of the MNPs, can be grafted onto the surface of the nanotubes. These two different pathways require the same starting point, which is the functionalisation of the surface of CNTs by anchoring points for MNPs, either by covalent or non-covalent grafting. In 2005, Correa-Duarte *et al.* prepared mCNTs through a successive coating process.[45] In a first step, they coated their MWCNTs with poly(sodium 4-styrene sulfonate) (PSS) to enhance the dispersion of the nanotubes in water. Through electrostatic interaction with PSS, CNTs are then coated with poly(dimethyldiallylammonium chloride) (PDDA) which led to a homogeneously positively charged CNT. In the last step, PDDA is used as the anchoring point for negatively-charged iron oxide MNPs (Figure 5.3).

In 2007, Ji *et al.* prepared negatively-charged oxidised-MWCNTs to electrostatically attach Fe^{3+} cations.[46] Through a reduction of these cations by addition of polyethylene glycol and heating at 200 °C for 8 to 12 h, iron oxide MNPs were formed on the surface of the CNTs. These small 5 nm MNPs were then used as seeds for growing other iron oxide MNPs. Following these first reports, numerous developments were performed on the preparation of MNPs' decorated CNTs.[30,31]

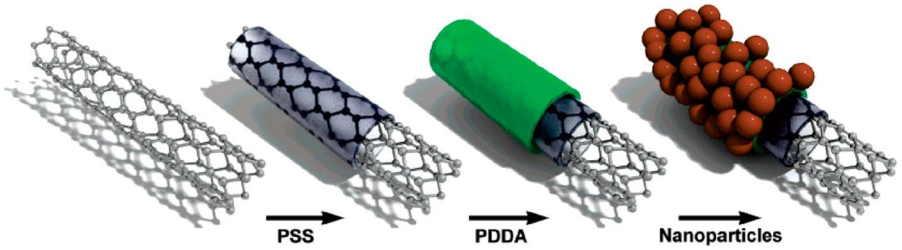

Figure 5.3 Protocol used for the synthesis of exohedrically grafted MNPs on CNTs by Correa-Duarte *et al.* Reproduced from ref. 45 with permission from American Chemical Society, Copyright 2005.

5.3 Biological Applications of Magnetically Empowered Carbon Nanotubes

The biological applications of mCNTs can be separated regarding their response to a continuous or alternating magnetic field. MNPs endohedrally-confined or exohedrally-grafted on CNTs, will move when in proximity to an external magnetic field. However, in the presence of an alternating magnetic fluid, these MNPs will produce heat in a mechanism known as magnetic fluid hyperthermia (MFH). Another common application of mCNTs is, when placed in an external magnetic field, their ability to change the relaxation time of neighbouring protons, leading to a contrast change in magnetic resonance imaging (MRI).

5.3.1 Magnetically Induced Movement

Due to their enhanced magnetic properties, mCNTs show a strong response towards permanent magnets. These induced movements can be of two different types, rotation and translation. When linked to cells, these properties can lead to cell rotation and/or cell shepherding, while these movements could also lead to pinpointed delivery.

5.3.1.1 Magnetic Stirring

As seen in the introduction, the high aspect ratio of CNTs, linked to their structure, provides them with magnetic susceptibility anisotropy making them responsive to external magnets. The alignment of CNTs inside polymeric matrixes, gels or in solution was thus reported in the literature. However, the major drawback of this approach is the intensity of the external magnetic field required to perform this alignment, *ca.* 10 T or more, leading to the need of heavy equipment. Through encapsulation of MNPs inside the cavity of CNTs or grafting of MNPs on the graphitic structure of CNTs, the hybrid materials formed are much more responsive to an external magnetic field. The mCNTs formed can be aligned with an external magnetic field as low as 0.2 T.

The application of this concept towards biological application was first reported by Gao *et al.* who managed to manipulate sheep blood cells.[47] Through the assembly of iron oxide nanoparticles on the surface of the CNTs, leading to the formation of paramagnetic CNTs, the authors were able to visualise the rotation of bundles of these magnetic CNTs upon application of a rotating external magnetic field. This rotation could also be tailored by changing the frequency of the magnetic field. After interaction with sheep blood cells and application of magnetic field of 12.7 kA m^{-1} for a frequency of 0.5 Hz, the magnetic CNTs were able to rotate these cells at a fast pace, 1 cycle per 3 s (Figure 5.4). Upon bridging two cells with magnetic CNTs and application of the same magnetic field, the pair of cells could be rotated at the same speed, opening the door for tailored manipulation of bio-objects.

In 2014, Liu *et al.* developed mCNTs for a magnetic stirrer of SKOV3 ovarian cancer cells.[48] Open-tip CNTs were immersed in a solution of MNPs' precursor that allowed the formation of MNPs inside the cavity of the CNTs in a two-step process. During the first one, the authors used precursors allowing the formation of iron oxide or cobalt-based nanoparticles inside the cavity of the nanotubes. In a second step, the mCNTs possessing iron oxide particles were subjected to the same treatment, either with an iron or cobalt precursor, and a second set of nanoparticles was obtained inside the cavity of the tubes. Following their functionalisation in order to increase their dispersibility in water, these nanotubes were incubated with tumour cells for 30 minutes. Upon applying a rotating magnetic field to these cells, mCNTs can be seen rotating at the surface of the cells. Contrary to the previous example showing cell rotation, in this case the cells do not rotate but the rotation of the mCNTs at their surface could be used as a remote stirrer.

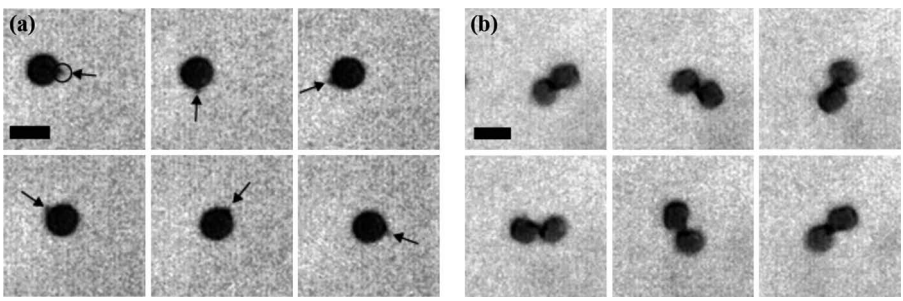

Figure 5.4 (a) Rotational motion of one sheep red blood cell showing mCNTs attached to the cells. (b) Rotational motion of two sheep red blood cells bridged by mCNTs. The frequency and intensity of the magnetic field are 0.5 Hz and 12.7 kA m^{-1}. The snapshots correspond to 0th, 0.2nd, 0.4th, 0.6th, 0.8th and 1.0th cycle of the rotational magnetic field. Reprinted from ref. 47 with permission from American Chemical Society, Copyright 2006.

5.3.1.2 Cell Shepherding

One of the most employed magnetic properties of MNPs-CNTs compared to bare CNTs is their ability to be attracted by a permanent magnet. This feature leads these new hybrid materials to be used, after carefully designed external functionalisation, in new applications such as water purification, to remove different pollutants such as metallic cations[49] or cationic dyes,[50] or recyclable catalysts,[51,52] as examples. Both these applications rely on the ability of these hybrid materials to be attracted almost quantitatively by a permanent magnet. Building on that property, these hybrid materials were used for different biomedical applications.[53]

In 2008, Pensabene *et al.* used MWCNTs possessing Fe, Co and Ni inside their cavity to proceed to the translational movement of two types of neuroblastoma cells.[54] After one-hour incubation of the hybrid mCNTs with the cells, the authors introduced a Neodymium magnet in one of the dishes used for the experiment. While the cells are homogeneously spread at the beginning of the experiment, it is clearly seen that the number of cells with mCNTs close to the magnet after three days is significantly higher than far away from the magnet. The control experiment realised in the same conditions with cells that have not been incubated with CNTs showed no preferential positioning and had the same density throughout the dish. In 2011, the same group used magnetic CNTs coated by Pluronic F127 to interact with mesenchymal stem cells (MSCs) from rat bone marrow.[55] After five days of incubating the cells with these hybrids CNTs, cytotoxicity assays were realised and revealed that the CNTs interact with the cells without any noticeable damages. Thus, the cells interacting with CNTs showed comparable viability and proliferation rate than cells in the same medium without CNTs. Upon application of an external magnetic field (1.41 T) close to the wells containing the cells for 72 h, a clear migration of the cells near the magnet could be observed when compared with cells in the absence of CNTs. Following this study *in vitro*, the authors applied their shepherding method in live rats. Thus, after incubation of mesenchymal stem cells with the hybrid CNTs for five days, one million cells were injected in the hepatic portal of rats. The shepherding of cells was engineered by placing a magnet near the liver of the rat overnight. After three weeks, the rats were sacrificed. Through treatments of the organs and colouring of the MSCs cells using Prussian blue, the quantity of MSCs treated with CNTs in three different organs, liver, kidney and lung, were evaluated and compared to rats treated in the same conditions in the absence of a magnet. On average of triplicate experiments, the livers of the rats exposed to the magnet presented three times the quantity of mCNTs than the liver of rats in the absence of a magnetic field. On the other hand, the kidneys and lungs of the rats treated with the magnets showed fewer stained cells than the control ones without a magnet. Park *et al.* also demonstrated that SWCNTs purified and functionalized by acidic treatment and containing traces of Fe, Ni and Co were able to be transfected inside NIH3T3 mouse fibroblast cells.[56] As a result, the cells could be attracted towards an external magnet. In 2013, Shen *et al.* coated the surface of CNTs with magnetic

iron oxide nanoparticles. The resulting MCNTs were noncovalently functionalised with phospholipids-PEG5000 and fluorescein isothiocyanate.[57] After incubation of the functionalised mCNTs with U87 cancer cells for two hours, fluorescence imaging revealed the presence of mCNTs in the cytoplasm of the cells. Through application of a NdFeB permanent magnet, the labelled cells showed rotation and translation. In a first avenue, the cells rotated to match the North–South poles and then started migrating towards the magnet (Figure 5.5). It is noteworthy to indicate that, also in this case, the hybrid CNT materials do not present any noticeable cytotoxicity.

In 2013, Lamanna *et al.* also showed that MWCNTs exohedrally functionalised by super-paramagnetic iron oxide nanoparticles (SPIONs), after incubation, could be internalised by human prostatic cancer cells PC3.[58] As indicated in the previous section, the use of a rotating magnetic field could enhance the uptake of the mCNTs inside the cells. The resulting cells could then be shepherded towards an external magnet and only with the presence of a micromolar concentration of mCNTs. The same year, our group synthesised Fe-filled MWCNTs and bioconjugated them with Cetuximab®, an antibody able to discriminate between EGFR+ cancer cells, such as A431 cells, from EGFR− cell lines, such as EAhy926 or CHO.[59] Through this interaction, the hybrid MCNTs were able to preferentially agglomerate around one of the three cell lines when mixed together in solution. Upon application of an

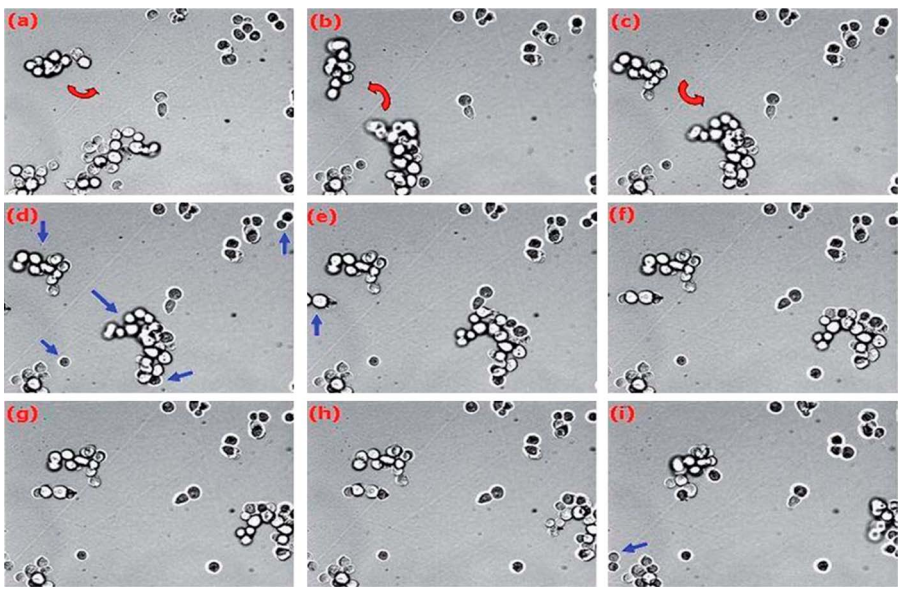

Figure 5.5 Snapshots of bright-field images of U87 cells labelled with mCNTs in the presence of an external magnetic field. (a) to (c) Rotation of a large number of cells under the influence of the magnet and (d) to (i) translation of cells (indicated by the blue arrows). The magnetically induced cell movement was monitored over 15 s. Reproduced from ref. 57 with permission from the Royal Society of Chemistry.

external magnetic field originating from a Neodymium magnet, we were able to differentiate cell lines in a matter of minutes. By removal of the supernatant, the magnetically coagulated EGFR+ cancer cells remained mainly in the original vial while the EGFR− cells were mostly found in the supernatant (Figure 5.6). A similar experiment realised by conjugation of the mCNTs with bovine serum albumin possessing no preferential targeting behaviour showed that under the same experimental conditions the three cell lines were found in the supernatant. In 2015, our group also extended this concept to magnetic cell filtration.[42] Upon bioconjugation of mCNTs with the same antibody, we studied the absorbance of the solution with or without the presence of an external static magnetic field and were able to evaluate the coagulation effectiveness (CE) of our material. In the presence of the magnet, CE reaches *ca.* 90% in 500 s while the control experiment in the absence of a magnet only shows a CE of *ca.* 35% in the same time. Following this study, we incubated the hybrid mCNTs with targeted A431 cells and proceeded to the cell fishing. After 250 s of magnetic field exposure, up to 95% of the targeted A431 cells were removed from the solution. However, in the same conditions, EA cells, not recognised by Cetuximab®, only showed a 35% cell fishing effectiveness. Interestingly, the efficiency of the fishing effectiveness is also dependent on the crystallinity of the Fe phase encapsulated in the cavity of the CNTs. It is noteworthy to indicate that the mCNTs developed by Liu *et al.*, along with their use for magnetic stirring presented previously, were also able to drive cell motion towards a permanent magnet.[48]

5.3.1.3 Delivery Through Translational Motion

Based on the same principles, it is possible to use the responses of mCNTs to external magnetic fields to induce delivery of biocompatible materials. Multiple examples are reported in the literature for the delivery of anticancer drugs or peptides, among others, by bare CNTs.[60–62] By making them magnetic through the addition of MNPs inside the cavity or on the graphitic structure of the CNTs, multiple research groups hoped to use the translational movement described previously to enhance the use of mCNTs as carriers. In 2005, Cai *et al.* developed a spearing process using magnetic CNTs.[63] After the synthesis of CNTs through plasma-enhanced chemical vapour deposition, the material obtained contained residual amounts of nickel encapsulated in the cavity of the CNTs, making them slightly magnetic and thus responsive to an external magnetic field created by a permanent magnet. Through application of a rotating magnetic field, these nanotubes can enter the cell membrane. A following static magnetic field will then lead to the pulling of the CNTs inside the cells and into the cytoplasm. By previously coating the magnetic CNTs with a DNA plasmid, encompassing the sequence for the green fluorescent protein (GFP), the authors were able to efficiently deliver their load inside specific cells. In addition, this approach of using magnetic CNTs greatly increased the efficiency of the delivery, so that femtomolar concentrations are required in the case of magnetic CNTs while

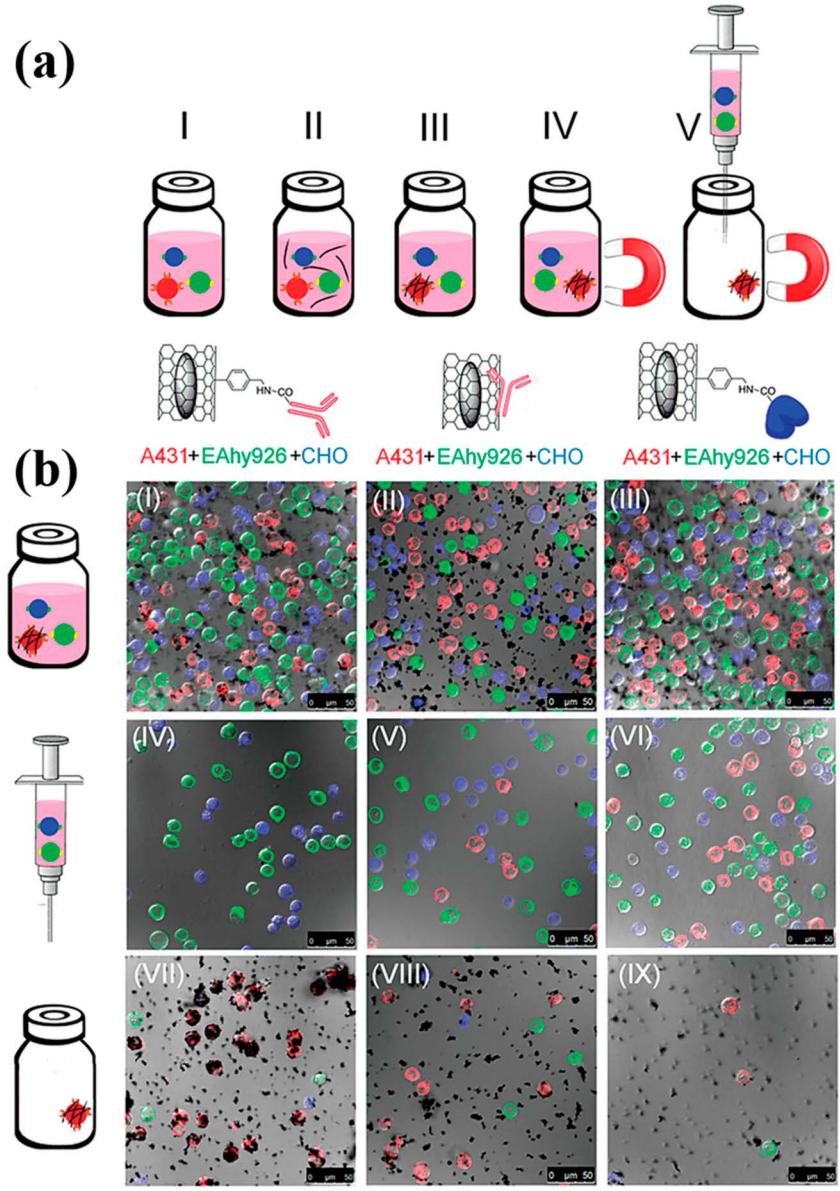

Figure 5.6 (a) Experimental steps to perform the magnetic sorting of cells and (b) confocal microscopy images of suspension containing A431 (red), and EGFR−, CHO (blue) and EAhy926 (green) cells after the magnetic filtration steps (top: mixing, middle: supernatant and bottom: precipitate) with different types of mCNTs. Reproduced from ref. 59 with permission from John Wiley and Sons, Copyright 2013 WILEY-VCH Verlag GmbH & Co. KGaA, Weinheim.

micromolar to nanomolar concentrations are needed for bare CNTs. In 2010, Gul *et al.* used magnetic SWCNTs containing Ni and Y at the tip to tag haematopoietic stem/progenitor cells with fluorescein-isothiocyanate (FITC).[64] Following the same protocol developed previously by Cai *et al.*, they used a combination of rotating and static magnetic field to lead to a high cellular uptake of the hybrid fluorophore carrier. While the cells were *ca.* 100% FITC positive, their viability was not affected compared with the control experiments. The same group later reported the uptake of the same labelled magnetic CNTs by human monocytic THP-1 leukemic cell lines showing a 100% of FITC-positive cells after 1 h. However, it is noteworthy to indicate that the fluorescence of these cells increased until 6 h, indicating that the uptake of mCNTs in the cells was still occurring. This spearing mechanism was also used more recently to extract molecules from living cells.[65] The authors prepared CNTs with Ni-coated nanoparticles enclosed at their tip and enhanced their magnetic response by an additional coating of their graphitic structure with Ni. Additional L-tyrosine electropolymerisation was realised to increase the biocompatibility of these mCNTs. Alignment and movement of these "nanospears" were then studied using an external magnet and the spearing experiment was realised on human embryonic kidney cancer cells overexpressing GFP, able to non-covalently attach to CNTs. Molecular extraction from intracellular objects was then demonstrated by cultivating the cells on a polycarbonate filter with 8 μm diameter pores (Figure 5.7). The efficiency of

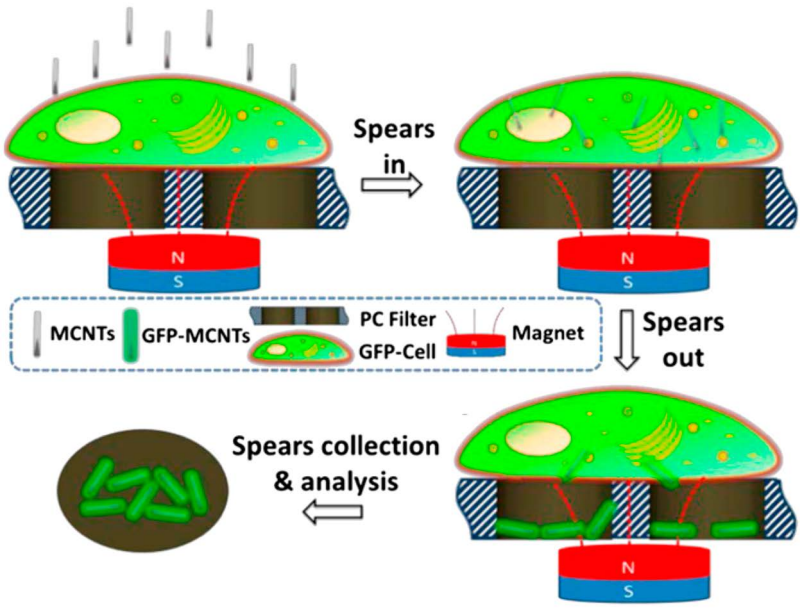

Figure 5.7 Principle of magnetic extraction using the spearing technique. Reproduced from ref. 65 with permission from Proceedings of the National Academy of Sciences, Copyright 2014.

the extraction was performed by the appearance of GFP on the mCNTs having speared in the cells and speared out through the polycarbonate filter. It is noteworthy to indicate that the spearing of mCNTs through the cells has only a negligible effect on cell viability with a drop from 98.2% to 96.4%.

In 2009, Yang *et al.* used magnetic CNTs, grafted by iron oxide nanoparticles, as lymphatic targeted drug delivery vehicles.[66] After their synthesis Gemcitabine, an anticancer drug, was loaded on the mCNTs. These materials were then used to deliver the drug into the lymphatic system of rats and the concentration of drug was evaluated in the left popliteal lymph nodes, the target of this study. Through multiple experiments, the authors demonstrated the effects of each of the materials. Thus, in absence of CNTs, the concentration of Gemcitabine is almost constant throughout the experiment, whereas, in the presence of the drug-loaded mCNTs the concentration of the drug in the targeted organ is *ca.* six times higher after 24 h. The same experiment realised in the presence of a permanent magnet sutured on the projection surface of the targeted lymph node leads to an even higher increase of the concentration of the drug in the targeted organ throughout the duration of the experiment (Figure 5.8). It is noteworthy to indicate that the same experiments in which the CNTs are replaced by nano-sized activated carbon, coated by MNPs, led to a great decrease of the concentration of the drug in the left lymph node, showing the importance of the CNTs. The efficiency of the mCNTs as drug carriers was also seen by the great decrease of the concentration of Gemcitabine in the blood plasma when using CNTs compared to the other experiments. Through this experiment, mCNTs showed their great appeal as nano-drug carriers.

In 2011, Li *et al.* developed a hybrid system composed of MWCNTs grafted by iron oxide nanoparticles for magnetic attraction, folate (FA) as the targeting unit and Doxorubicin (Dox) as the anticancer drug to kill cancer cells (Figure 5.9).[67] In a first avenue, the cytotoxicity of FA-MWCNTs@Fe was evaluated and

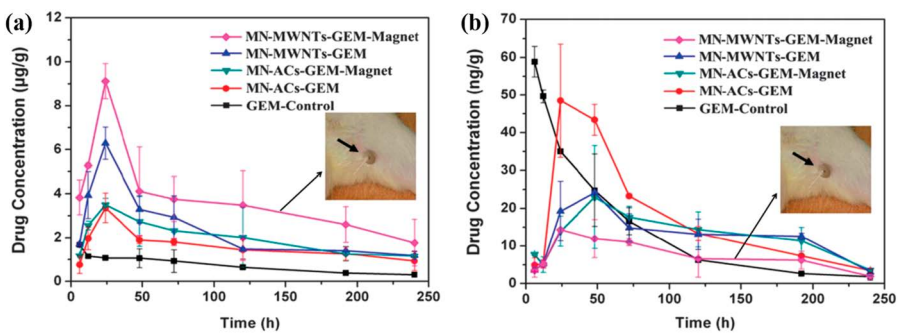

Figure 5.8 Gemcitabine concentrations at different times after subcutaneous administration: (a) in the left popliteal lymph nodes, and (b) in blood plasma. Reproduced from ref. 66 with permission from the Royal Society of Chemistry.

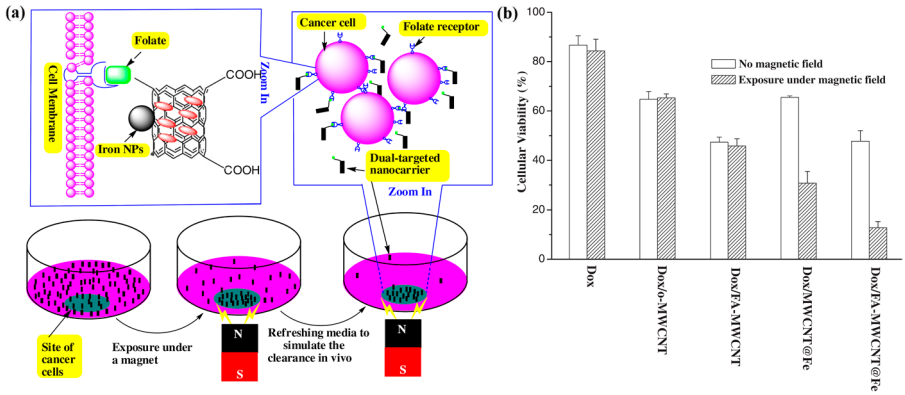

Figure 5.9 (a) Scheme for dual-targeted delivery and (b) viability of HeLa cells after 48 h in different conditions. Reproduced from ref. 67 with permission from Elsevier, Copyright 2011.

did not demonstrate any cytotoxicity of these hybrid materials towards HeLa cells. Cell viability tests were then realised in the presence of Dox. These experiments were performed on five batches: drug alone, drug loaded on oxidised-MWCNTs with or without FA and drug loaded on oxidised-MWCNTs@Fe with or without FA (Figure 5.9). In the absence of magnetic nanoparticles, the best results were obtained for Dox/FA-MWCNTs showing the affinity of FA towards cancer cells. As expected, the experiments done in the presence, or not, of an external magnet do not show any difference as the MWCNTs are not sensitive enough towards low magnetic field without the presence of MNPs. Upon addition of iron oxide nanoparticles, the hybrid materials show a cytotoxicity enhanced two to three times in the presence of a magnet compared to the same experiment without a magnet. Dox/MWCNTs-FA@Fe in the presence of a magnet even shows a 6-fold improvement compared to commercial Dox alone. These results show the efficiency of a "dual-targeted nanocarrier" in which FA acts as active targeting agent while the MNPs are passive. This property was also studied by Chen *et al.* who used Transferrin as a targeting agent for HeLa cells.[68] The authors developed a multimodal system in which iron oxide nanoparticles are encapsulated inside the cavity of CNTs whose graphitic structure is covered with PSS to anchor fluorescent SiO_2-coated quantum dots, Transferrin (Trf) as the targeting agent and Dox. Through fluorescence microscopy, the uptake of these hybrid materials by HeLa cells was demonstrated while only slight uptake was recorded for Trf-negative HEK293 cells, demonstrating the active targeting of Trf. In addition, a strong increase in the uptake of the hybrid material by the cell was observed upon addition of an external magnet. This was hypothesised to be due to the higher concentration of mCNTs in a given area also showing the passive targeting of these magnetic materials. These results allowed for the efficient delivery of Dox in the cells, showing here again a decrease in cell viability due to the drug in the presence of an external magnet.

In 2015, Al Faraj *et al.* also used mCNTs to deliver Dox to tumours.[69] After preparing SWCNTs grafted by iron oxide nanoparticles and mouse Endoglin/CD105 monoclonal antibody as the targeting agent, the authors used the graphitic surface of the SWCNTs to non-covalently attach the antitumour drug. After *in vitro* testing, the hybrid materials were injected into tumour-bearing mice. Upon injection of mCNTs bearing only the biotargeting agent, and no Dox, the tumour growth could be followed and showed metastasis after 10 to 14 days. On the other hand, if the same material bearing the anticancer drug is injected, a clear decrease of the tumour size can be seen after injection without the presence of metastasis. If a magnet is applied externally at the location of the tumour, the effect of the hybrid materials is further enhanced showing, in this example, the efficiency of magnetic targeting induced by the presence of magnetic nanoparticles grafted on CNTs.[69] In 2016, the same group used the same type of hybrid material to deliver Dox to the lungs while decreasing their uptake in the reticulo-endothelial system.[70] To do so, they used a high-energy multipole flexible magnet to guide the mCNTs towards the metastatic cancer cells in the lungs of mice injected with breast cancer. After the injection and proliferation of breast cancer cells in the left inguinal mammary fat pad of the mice, the tumour led to metastasis in the lungs in three weeks (Figure 5.10). Without treatment, the tumours keep increasing in both sites over the next four weeks, which was the end of the study. After injecting the anticancer drug alone, a decrease in growth of the tumours at both the primary site and the lungs could be observed. On the other hand, upon injection of Dox loaded on mCNTs, a clear decrease of the tumour size could be observed at the primary site while the volume of the tumour in the lungs remained constant. When the magnets are applied externally to the lungs of the mice, the mCNTs were found to colocalise with the cancerous nodules and led to a net decrease of the tumour size in the lungs to reach a similar volume to the ones seen in the control mice, without tumours. Here again, mCNTs, due to their attraction to magnets, were demonstrated to be efficient drug carriers *in vivo*. Following these studies, other research groups have used similar hybrid materials to deliver drugs such as aspirin or acetaminophen,[71] Dox[72] or Epirubicin.[73]

5.3.2 Heat Production

In the past few years, different approaches were developed to use CNTs in hyperthermal therapies. CNTs are known to produce heat through near-IR light-based hyperthermia due to their high absorption in this regime.[74,75] This method is very attractive since biological systems are transparent to these wavelengths. The use of SWCNTs as hyperthermia agents has been reported in living cells, but their use in living bodies is limited due to the low penetration of NIR light, which is only able to pass through a few centimetres of tissue. On the other hand, magnetic fields present the advantage of penetrating biological matter much deeper. However, due to their weak magnetic properties, CNT applications in magnetic-fluid hyperthermia (MFH)

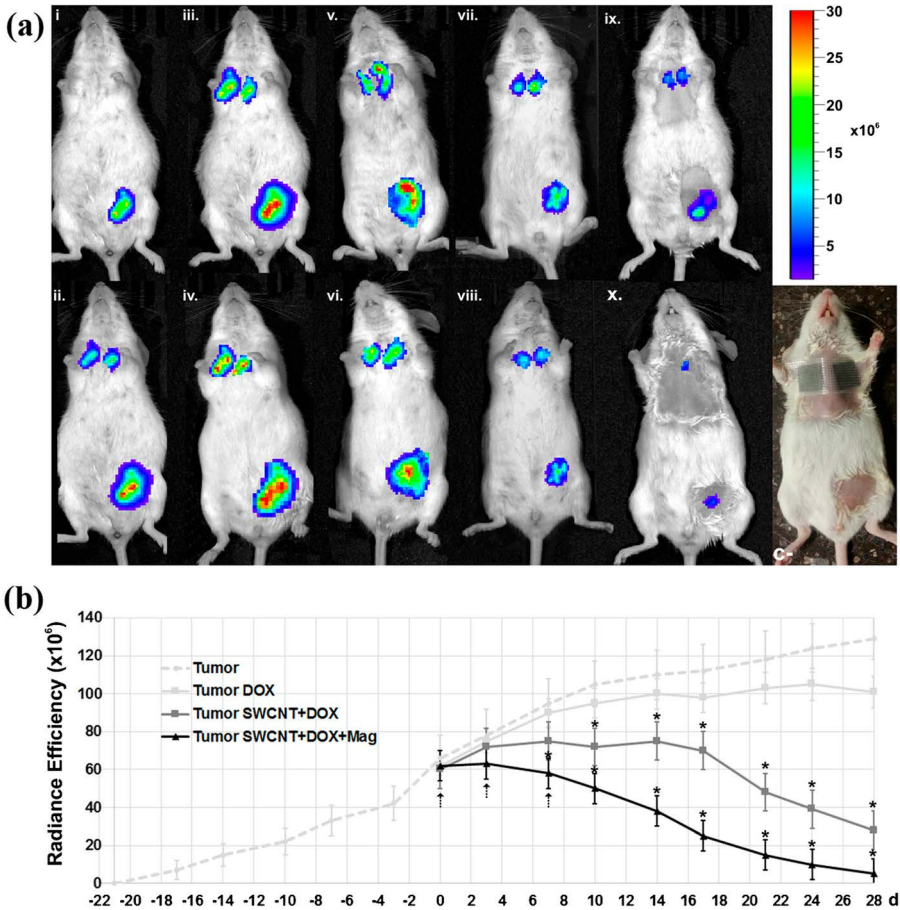

Figure 5.10 Non-invasive bioluminescence imaging assessment of the primary tumour site and lung metastasis after injection of Dox-loaded mCNTs. (a) Representative bioluminescence images of tumour-bearing mice without treatment (at i: −14 days, ii: 0 day, iii: 14 days, and iv: 28 days) and after injection of either free Dox (at v: 14 days and vi: 28 days), or Dox-loaded mCNTs without (at vii: 14 days and viii: 28 days) or with (at ix: 14 days and x: 28 days) positioning magnets over the lungs. (b) Quantitative assessments of radiance efficiency (ρ/s/cm^2/sr). The arrows represent the time of injections. The asterisks indicate significant differences as compared to the non-injected group. (c) Picture of a mouse showing the position of the small flexible magnets over the lungs. Reproduced from ref. 70 with permission from Macmillan Publishers Ltd, Copyright 2015.

treatments, while commonly used for MNPs such as SPIONs,[76] require some modifications of the CNTs. In this regard, the introduction of MNPs inside the cavity of CNTs, and especially Fe, to allow their use in MFH applications was first reported by Büchner and co-workers.[77–79] In these seminal works, the authors reported the specific absorption rates (SAR) of Fe nanowires

encapsulated inside the cavities of CNTs. In 2009, the same group expanded on these results.[80] They described the synthesis of Fe-filled MWCNTs by aerosol-assisted CVD techniques for an overall iron concentration of around 3 ± 1 wt% in the materials. Through applying alternating magnetic fields above 30 kA m^{-1}, a notable temperature increase of Fe-MWCNTs' dispersion was observed (Figure 5.11a). This heating effect could, in the conditions described in this report, reach a heating rate of 3 °C min^{-1} when the magnetic field applied was 80 kA m^{-1}. Similar experiments realised with washed CNTs, lacking Fe, or CNTs covered with non-magnetic nanoparticles, such as Cu nanowires, did not yield any temperature increase in the samples (Figure 5.11b).

Instead of using endohedrally-filled CNTs for hyperthermia application, Shi *et al.* functionalised the outer graphitic structure of MWCNTs with poly(lactic-*co*-glycolic acid) to subsequently graft quantum dots and iron oxide nanoparticles on the CNTs' surface.[81] Upon application of an alternating magnetic field, with a frequency of 956 kHz and a strength of 6.0 mT, the samples prepared reached a temperature of 45 °C after 30 minutes. Wilson *et al.* demonstrated a few years later that FeCo nanoparticles plated on MWCNTs could produce mCNTs that could also be used in hyperthermia applications.[82] Using a magnetic field of 200.2 A m^{-1} at a frequency of 282 kHz, a sample of concentration 100 mg mL^{-1} reached a temperature of *ca.* 43 °C after 800 seconds. Reaching this temperature is very important for the development of hyperthermia treatment as the thermotolerance of human and rodent cells is reported at 42.5 °C.[83,84]

Through bioconjugation of Fe-MWCNTs with Cetuximab®, an antibody able to discriminate between EGFR+ cancer cells, such as A431 cells, from EGFR− cell lines, such as EAhy926, our group demonstrated selective MFH activity.[59] A mixture of both cell lines in a thermostated solution was subjected to an alternating magnetic field of 83 kA m^{-1} and 220 kHz for 10 min and did not show any noticeable cell death. The addition of bioconjugated

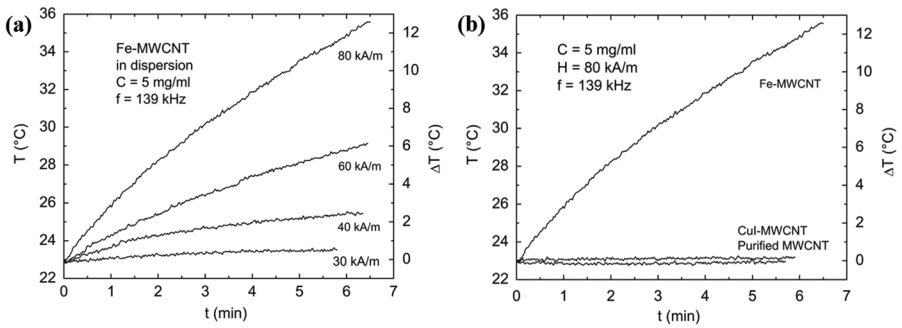

Figure 5.11 (a) Temperature increase of Fe-MWCNT dispersion in different alternating magnetic fields. (b) Comparison of Fe-MWCNT to non-magnetic control materials. Reproduced from ref. 80 with permission from Elsevier, Copyright 2009.

Fe-CNTs, with a final Fe concentration of *ca.* 7 ± 2 wt%, induced an increase in cell death for A431 and EAhy926 cell lines, *ca.* 11% and 3%, respectively. To this solution, the application of the MFH treatment described previously led to *ca.* 20–25% of A431 cell death while only 7–8% of EAhy926 cell death. We later demonstrated enhanced cytotoxicity effects upon an increase of Fe-loading of MWCNTs and use of pulsed magnetic fields, 40 seconds per minute for 30 minutes (Figure 5.12).[42] This pulsed sequence was used to prevent

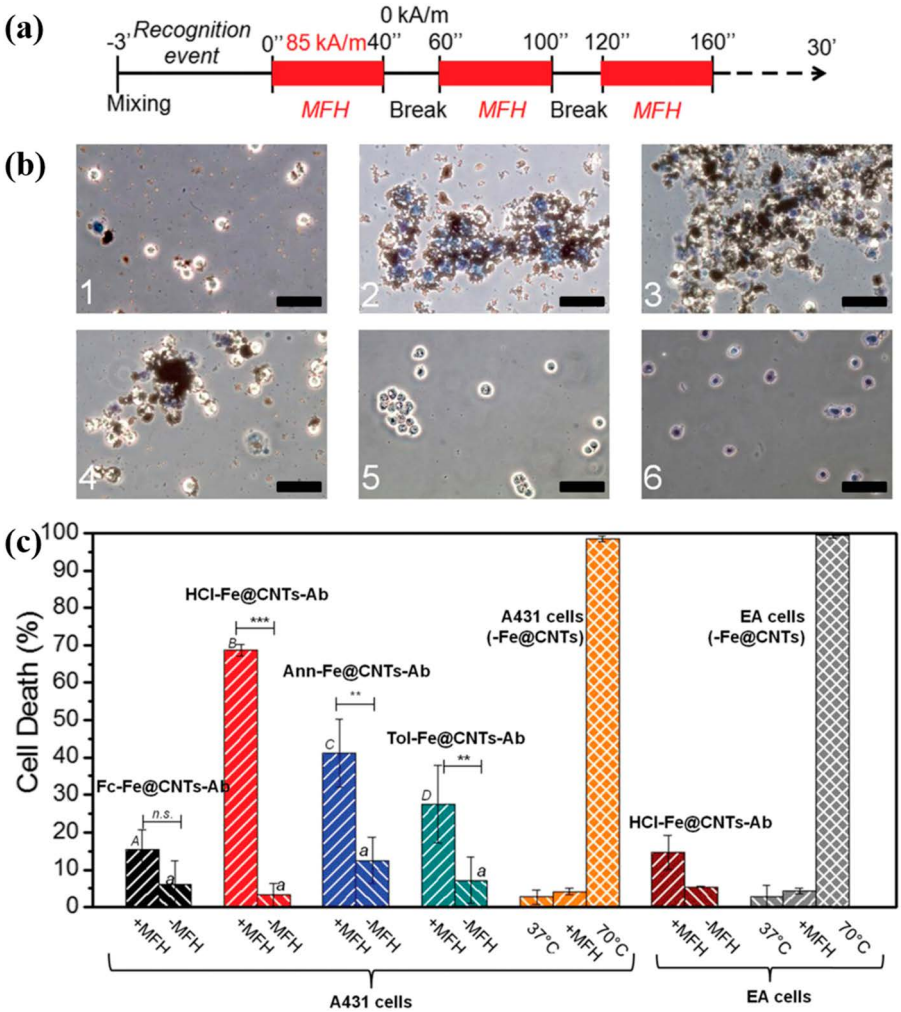

Figure 5.12 (a) Timeline of the "pulsed" MFH conditions (40 s of impulse each minute for 30 minutes). (b) Phase contrast microscopy images of EGFR+ A431 cells after "pulsed" MFH incubation with different mCNT batches and with conventional heating at 37 °C (5) and at 70 °C (6). After the incubation, cells were stained with trypan blue. Scale bar = 50 μm. (c) Cell death as assayed with trypan blue staining. Reproduced from ref. 42 with permission from the Royal Society of Chemistry.

any global heating of the whole solution and keep the heating localised in close proximity to the mCNTs. By pre- and post-modification of Fe-MWCNTs, the quantity and crystallinity of the Fe phase inside the cavity of the nanotubes was tailored. Fe-MWCNTs with a Fe concentration 19 wt% to 36 wt% presenting different ratios of α-Fe, γ-Fe, iron carbide (Fe_3C) and γ-Fe_3O_4 were bioconjugated with Cetuximab® and led to up to *ca.* 70% of targeted A431 cell death while reference Ea cells only showed 15% of cell death in the same conditions. Following these experiments, the efficiency of the killing was also proven to be highly dependent on the quantity of the Fe loading of the CNTs as well as the crystallinity of the Fe phase encapsulated. Thus, an increase in Fe_3C leads to a higher SAR of the hybrid materials and to a better hyperthermia efficiency. In 2015, Raniszewski *et al.* prepared Fe-filled CNTs and used them in hyperthermia tests showing an increase of temperature of *ca.* 30 °C when a 2 mL solution of mCNTs dispersed with DMSA was subjected to an alternating magnetic field of 11 mT at 532 kHz.[85]

In 2017, Dalal *et al.* prepared MWCNTs exohedrally grafted by Li-Zn-Co-ferrite $Li_{0.3}Zn_{0.3}Co_{0.1}Fe_{2.3}O_4$ nanoparticles using different temperatures of annealing.[86] These different samples were tested for hyperthermia applications using a magnetic field of 420 Oe at a frequency of 300 kHz. While at a concentration of 2 mg mL^{-1} of mCNTs, the MNPs reached a temperature of 42 °C in 3 min, mCNTs only reached 41 °C after 10 min. By increasing the concentration to 10 mg mL^{-1}, mCNTs reached 42 °C in 5 min under the same conditions. The following year, Zuo *et al.* studied $Zn_{0.54}Co_{0.46}Cr_{0.6}Fe_{1.4}O_4$ nanoparticles grafted on the surface of MWCNTs under an alternating magnetic field of 200 Oe with a frequency of 100 kHz.[87] Under these conditions, which could be adequate for clinical therapy,[88,89] the sample containing mCNTs reached a temperature of 42.7 °C. The same year, Sadaphal *et al.* developed CNTs covered with magnetite/gold nanoparticles.[90] These hybrid mCNTs were studied using an alternating magnetic field of 25 to 80 Oe at 155 kHz at different concentrations and showed an increase of the temperature of up to 44 K in optimal conditions. It is noteworthy to indicate that these mCNTs were also used for laser-induced hyperthermia. Combining these two techniques, the authors studied the death of PC12 cells, which reached up to *ca.* 80% after 40 min. As another example, in 2015, Peci *et al.* synthesized Fe-filled MWCNTs and coated them with gadolinium cations, Gd^{3+}.[91] Through this dual functionalisation, the authors aimed for two different applications: magnetic hyperthermia and MRI. Using an alternating magnetic field with a frequency of 696 kHz and a strength of 8 kA m^{-1}, the mCNTs produced possessed a SAR of 50 W $g_{Fe}{}^{-1}$. On the other hand, the presence of gadolinium cations could also lead to a use of these materials for MRI.

5.3.3 Magnetic Resonance Imaging

Another very important biological application of mCNTs is in magnetic resonance imaging (MRI). MRI is a commonly used technique and can acquire full-body images. This technique is non-invasive and is based on the relaxation time of protons de-excitation contained in different parts of the body.

As the data are highly dependent of the environment of the proton studied, this allows for the differentiation of the different tissues within the body.[92] However, this technique is not always sensitive enough and approximately 30% of the tests require the use of a contrast agent (CA) to enhance the contrast.[93] Thus, gadolinium-based molecules have been developed to be used as T_1, *i.e.* longitudinal, contrast agents, showing a hypersignal, *i.e.* a white zone.[94] However, it is well known that MNPs, such as iron oxide nanoparticles, can be used as T_2, *i.e.* transverse, contrast agents by reducing the T_2 relaxation times of nearby protons, leading to hyposignals, *i.e.* black zones.[95] Based on this aspect, the use of CNTs bearing MNPs, either inside their cavity or on their graphitic structure, make them excellent candidates to be used as contrast agents for MRI.[96,97]

In 2005, Sitharaman *et al.* reported the loading of ultra-short SWCNTs (US-SWCNTs) with Gd^{3+} cations through their tips or defects.[98] The hybrids obtained were superparamagnetic due to the presence of confined Gd^{3+} clusters. The presence of these clusters in the nanotubes greatly reduced the relaxation rate of the hybrid materials compared to unloaded US-SWCNTs. Remarkably, these Gd^{3+}-loaded US-SWCNTs present a proton relaxivity r_1 20 times higher that $[Gd(H_2O)_8]^{3+}$ at 60 MHz and 40 °C, increasing to 90 times at very low fields, such as 0.01 MHz, showing great promise for these materials. Since that discovery, multiple reports have expanded on these "gadonanotubes" to use them as intracellular magnetic probes or smart pH probes for NMR.[99,100]

In 2008, Richard *et al.* developed another approach to use mCNTs as T_1 CAs.[101] They non-covalently functionalised Gd^{3+} chelates, similar to GdDTPA, a clinically used Gd^{3+}-based CA, on the graphitic surfaces of MWCNTs. The material obtained showed high proton relaxivities at 20 MHz for concentrations of Gd^{3+}-chelates of 0.1 and 0.05 M with r_1 = 34.5 and 50.3 mM^{-1} s^{-1}, respectively; noticeably higher than the commercial compound measured in the same conditions (4.7 mM^{-1} s^{-1}). These compounds could also be used as T_2-weighted CAs due to their decrease of the T_2 values in comparison with pure water (Figure 5.13).

In 2014, Marangon *et al.* synthesised MWCNTs covalently functionalised by diethylenetriaminepentaacetic dianhydride (DTPA) that can chelate Gd^{3+} cations, providing paramagnetic Gd-CNTs.[102] The proton relaxivities r_1 values for this material were two-times higher than commercial Gd-DTPA at low frequency. The cellular uptake of these nanomaterials was also performed *in vitro* using RAW 264.7 mouse macrophages and showed the presence of mCNTs inside the cells after 20 h of incubation without any noticeable induced cytotoxicity. Following this study, *in vivo* imaging was performed on mice. Gd-CNTs were injected intravenously in mice at two different concentrations and the animals were monitored for 5 h. At low concentration, *ca.* 2.5 mg kg^{-1}, no significant change could be observed by T_1-weighted MRI. On the other hand, a higher concentration, *ca.* 12.5 mg kg^{-1}, led to a clear signal enhancement in the liver and spleen of the animal, with a strong one in the bladder of the animal, with an enhancement of +250% (Figure 5.14).

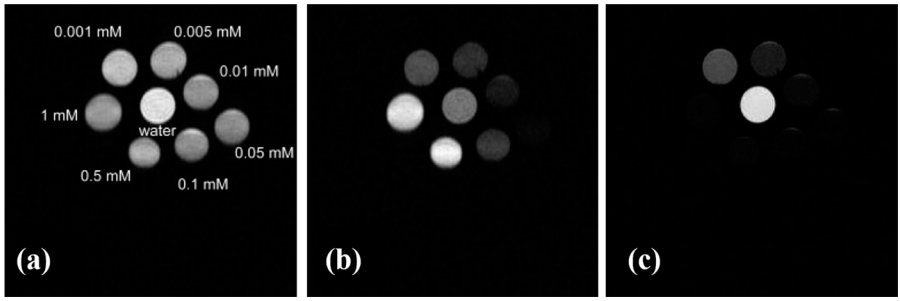

Figure 5.13 MRI images of the MWCNT-Gd complex at different concentrations and measured at 300 MHz. (a) Rho-weighted SE TR/TE = 15 s/10 ms and (b) T_1-weighted (SE TR/IR/TE = 15 s/1 s/10 ms) showing a hypersignal, (c) T_2-weighted (SE TR/TE = 15 s/33 ms) presenting a hyposignal due to the hybrid materials. Reprinted from ref. 101 with permission from American Chemical Society, Copyright 2008.

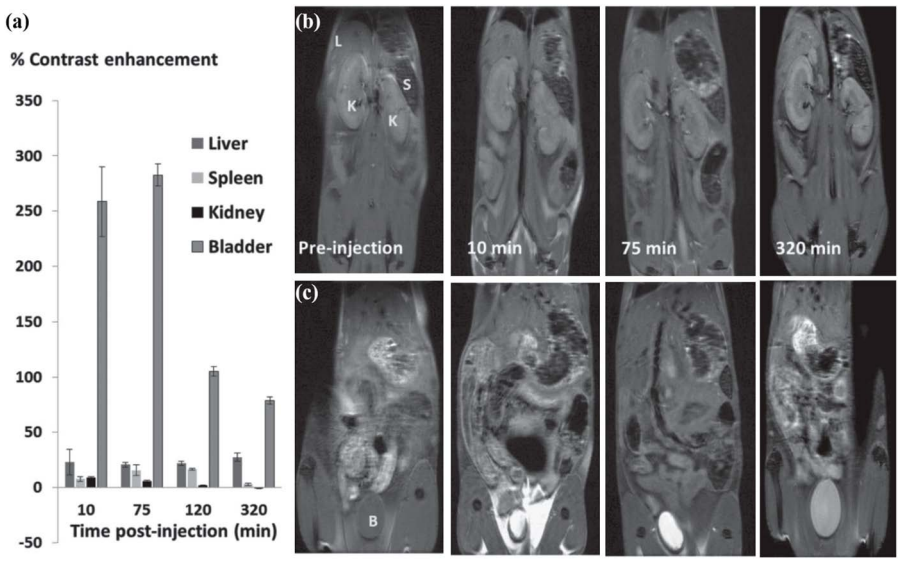

Figure 5.14 (a) MRI contrast enhancement in liver, spleen, kidneys and bladder following intravenous injection of Gd-CNT 5 (5 mg mL^{-1}, 100 μL) in comparison to the signal prior injection. Standard deviations are deduced from three independent measurements. (b, c) Example of MR slices showing liver (L), spleen (S), kidney (K) or bladder (B) at different times before and after injection of hybrid material. A fast spin echo RARE T_1-weighted sequence was used with TR/TE = 445/12 ms. Reproduced from ref. 102 with permission from John Wiley and Sons, Copyright 2014 WILEY-VCH Verlag GmbH & Co. KGaA, Weinheim.

This contrast enhancement varies differently over time in different organs, with a decrease after 2 h in the bladder while it increases in the liver over 6 h. Here again, it is noteworthy to indicate that no sign of tissue damage could be observed on the different organs and that the behaviour of the animals remained normal up to 8 days after injection.

In 2007, Choi *et al.* reported the development of T_2-weighted CA based on SWCNTs possessing iron oxide nanoparticles at their tip.[103] These mCNTs were then wrapped by DNA to improve their solubility and individualisation and then separated by magnetic separation to lead to three different samples, initial, Fe-enriched and Fe-depleted. These different hybrid mCNTs were incubated for 7 h with murine macrophage cells and, after washing, then transferred to MRI tubes. Upon T_2-weighted MR imaging of samples incubated with the Fe-enriched samples, the cells appear clearly as black spots, which demonstrates the efficiency of mCNTs as CA by reducing T_2. A clear difference can be seen on the cross-section of tubes with cells incubated with Fe-enriched (dark), initial (grey), and Fe-depleted (white), showing the efficiency of the iron oxide MNPs at the tip of the CNTs to act as CA. In another report, Wu *et al.* grafted iron oxide nanoparticles on the surface of MWCNTs and used them as T_2 CAs *in vivo*.[104] After intravenous injection of mCNTs for a dose of 2.5 mg of Fe per kg of body, a significant darkening of the spleen and liver was observed (Figure 5.15). Among other noticeable reports, in 2013,

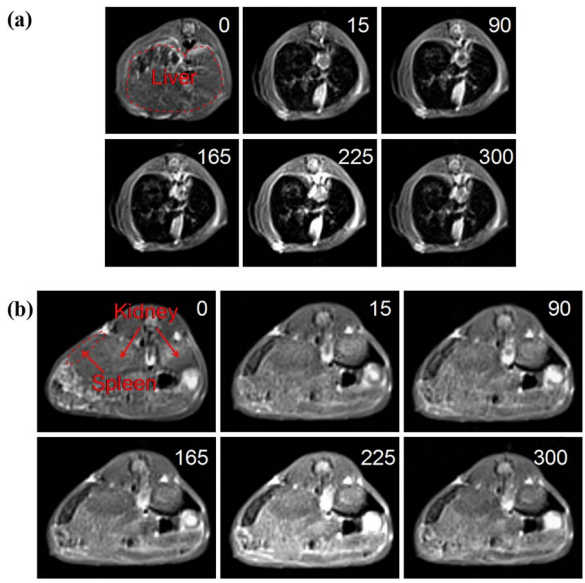

Figure 5.15 *In vivo* T_2-weighted MRI images of (a) liver and (b) kidneys/spleen taken before (time 0) and after (15, 90, 165, 225 and 300 min) intravenous administration of 2.5 mg Fe per kg body weight of MWCNT/Fe_3O_4. Reproduced from ref. 104 with permission from Elsevier, Copyright 2011.

Wang *et al.* synthesised MWCNTs decorated with super-paramagnetic iron oxide nanoparticles and used them as dual imaging agent, T_2 CA for MRI and single photon emission computed tomography (SPECT) and positron emission tomography (PET).[105] In 2014, Liu *et al.* used iron oxide nanoparticles grafted on the surface of MWCNTs, with a lactose-glycine adduct as targeting agent, as T_2 CAs *in vitro* and *in vivo*.[106] After the measurement of the magnetic properties of the mCNTs, the authors determined the relaxivity value (r_2) of their material. Thus, their hybrid mCNTs present a r_2 of 186 mM^{-1} s^{-1} while commercial Feridex, iron oxide CA, has a r_2 of 148 mM^{-1} s^{-1}. After cytotoxicity tests in mice showed that no acute toxicity was seen after 5 days upon injection of a 10 mg kg^{-1} dose, the compounds were injected into liver tumour bearing mice. After injection, a clear contrast change was observed between the normal tissue and tumour of mice indicating that the hybrid mCNTs had been internalised and taken up by the liver.

Instead of using iron oxide nanoparticles, Wu *et al.* used cobalt ferrite ($CoFe_2O_4$) grafted onto CNTs to be used as T_2 CA.[107] The efficiency of the mCNTs in MRI was measured upon different concentrations of Fe, determined by ICP-AES, showing a higher performance upon increasing Fe concentration of the hybrid materials. In addition to their potential use as CAs, the materials showed low cytotoxicity and were also used to deliver Dox, noncovalently loaded on the graphitic surface of mCNTs. Through the possibility to perform imaging and drug delivery, this report clearly shows the multimodal behaviour of mCNTs. Over the years, other types of MNPs coated on CNTs have been used as T_2 CAs, such as FePt.[108]

In 2011, Ding *et al.* used Fe-filled MWCNTs as T_2 contrast agents for MRI.[109] The authors synthesised four batches of mCNTs through CVD using increasing quantities of ferrocene catalyst in order to gradually increase the concentration of Fe encapsulated in the materials. After acidic washing of these different nanomaterials to remove any external iron, the mCNTs were dispersed in water at different concentrations and their T_2 relaxation times measured, showing a global trend in which T_2 decreases when the quantity of encapsulated Fe increases. mCNTs containing the highest quantity of encapsulated Fe were then injected in mice inoculated with murine renal carcinoma tumour fragments. 100 μg of Fe@MWCNTs were injected and their presence was followed by T_2-weighted MRI showing a clear black spot after injection. In comparison, when N-doped MWCNTs were injected in the same conditions, no MRI contrast enhancement could be observed, showing the fundamental role of encapsulated Fe. These materials were also used to perform laser-induced thermo-therapy due to their graphitic structure, here again showing the multimodal effect of mCNTs for biological applications. In 2015, Maciejewska *et al.* also used Fe-filled MWCNTs, with only 2% of Fe, as potential T_2-weighted MRI CAs *in vitro*, showing that even a small loading of Fe is sufficient to obtain a contrast enhancement.[110] This efficiency was also shown by other groups who reported mCNTs as T_2 CAs with a very small amount of Fe encapsulated.[111] Baranowska-Korczyc *et al.* also reported the use of Fe-filled MWCNTs using the CVD technique and produced mCNTs

with different Fe loading.[112] After their coating with PEG, these mCNTs were tested in MRI experiments and also showed to be efficient T_2 CAs upon good dispersibility in the solution. In 2016, Ding *et al.* reported that mCNTs encapsulating Fe-nanowires were showing a 1.5 times improvement compared to similar CNTs without metallic nanoparticles.[113] This report clearly demonstrates the synergistic behaviour of MNPs and CNTs for magnetic resonance imaging. By combining their ability to enhance contrast in MRI and to deliver drugs, these mCNTs appear as perfect materials for multimodal approaches. Lee *et al.* thus used SPIONs-covered PEG-mCNTs for Oxaliplatin delivery while following it by T_2-weighted MRI *in vivo* (Figure 5.16).[114] These

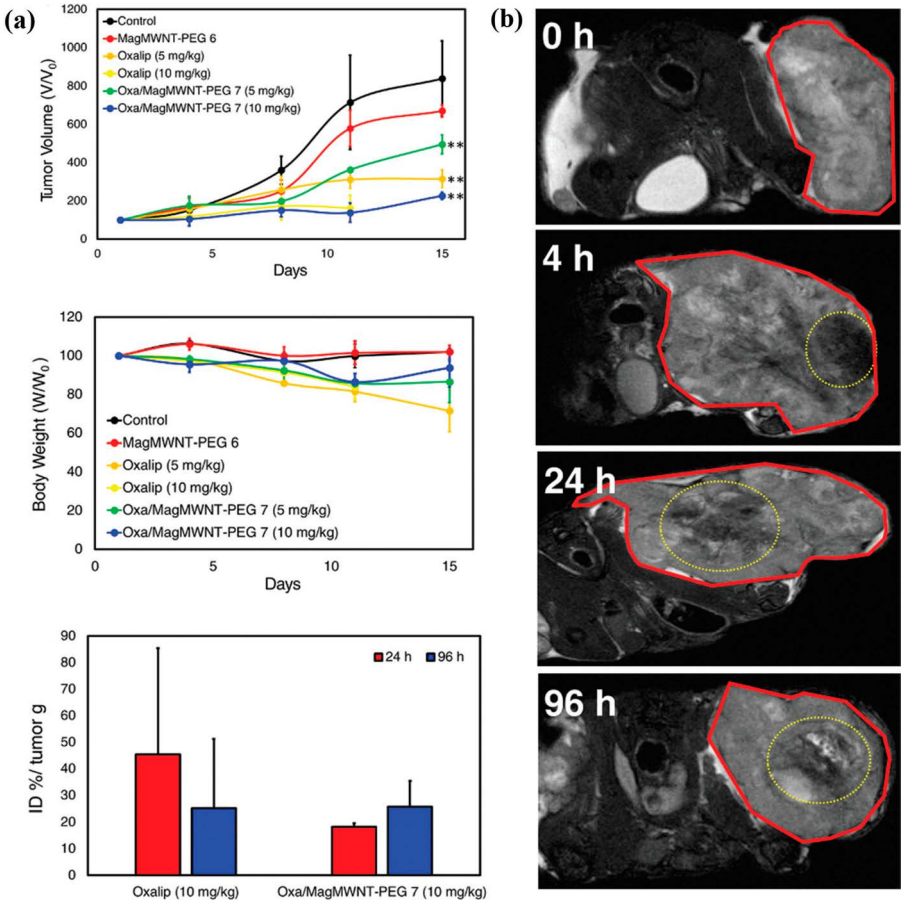

Figure 5.16 (a) Tumour volume and body weight of tumour-bearing mice after injection (**$p < 0.01$ *versus* the control group) and presence of Oxaliplatin or Oxalip in the tumour. (b) T_2-weighted MR images of the tumour before and after the injection of mCNTs bearing Oxaliplatin (the red lines correspond to the tumour and the yellow dashed circles to the presence of mCNTs aggregation). Reproduced from ref. 114 with permission from the Royal Society of Chemistry.

hybrid materials were injected into tumour-bearing mice which led to a net decrease of the tumour volume while following the presence of the mCNTs by MRI when compared to the control mice or mice injected with the free drug called Oxalip.

5.4 Conclusion

By using the synergy between MNPs and CNTs, mCNTs can be used for numerous biological applications. Magnetically driven movement by application of a low power magnet can lead mCNTs to "spear" cells and thus deliver drugs or extract intracellular compounds. By applying an external magnet at the location of a biological target, for example a tumour, the delivery efficiency of mCNTs is also enhanced. The presence of MNPs on the CNTs has also led to different reports of magnetic fluid hyperthermia. Upon targeting, selective cell killing was demonstrated through hyperthermia treatment. Finally, mCNTs offer great potential as T_2 contrast agents in magnetic resonance imaging. The low toxicity of the materials developed combined with the change in contrast they present make them very attractive for future developments. However, the synthesis and study of optimised materials is still ongoing. Through their multimodal aspect, they offer multiple possibilities for combined applications in which they are their own imaging probe to prove the efficiency of magnetically driven delivery, as one example among many.

List of Abbreviations

CA	Contrast agent
CE	Coagulation effectiveness
CNTs	Carbon nanotubes
CVD	Chemical vapour deposition
DNA	Deoxyribonucleic acid
Dox	Doxorubicin
FA	Folate
FITC	Fluorescein-isothiocyanate
GdDTPA	Gadolinium diethylenetriaminepentaacetate
GFP	Green fluorescent protein
ICP-AES	Inductively coupled plasma-atomic emission spectrometers
mCNTs	Magnetic carbon nanotubes
MFH	Magnetic fluid hyperthermia
MNPs	Magnetic nanoparticles
MRI	Magnetic resonance imaging
MSCs	Mesenchymal stem cells
MWCNTs	Multi-walled carbon nanotubes
NIR	Near infrared
NPs	Nanoparticles

PDDA	Poly(dimethyldiallylammonium chloride)
PET	Positron emission tomography
PSS	Poly(sodium 4-styrene sulfonate)
SAR	Specific absorption rate
SPECT	Single-photon emission computed tomography
SPIONs	Superparamagnetic iron oxide nanoparticles
SWCNTs	Single-walled carbon nanotubes
Trf	Transferrin
US-SWCNTs	Ultra short single-walled carbon nanotubes

Acknowledgements

The authors gratefully acknowledge the University of Vienna.

References

1. S. Iijima, *Nature*, 1991, **354**, 56.
2. X. Wang, Q. Li, J. Xie, Z. Jin, J. Wang, Y. Li, K. Jiang and S. Fan, *Nano Lett.*, 2009, **9**, 3137.
3. M. M. J. Treacy, T. W. Ebbesen and J. M. Gibson, *Nature*, 1996, **381**, 678.
4. M.-F. Yu, O. Lourie, M. J. Dyer, K. Moloni, T. F. Kelly and R. S. Ruoff, *Science*, 2000, **287**, 637.
5. T. W. Ebbesen, H. J. Lezec, H. Hiura, J. W. Bennett, H. F. Ghaemi and T. Thio, *Nature*, 1996, **382**, 54.
6. H. Kataura, Y. Kumazawa, Y. Maniwa, I. Umezu, S. Suzuki, Y. Ohtsuka and Y. Achiba, *Synth. Met.*, 1999, **103**, 2555.
7. E. Pop, D. Mann, Q. Wang, K. Goodson and H. Dai, *Nano Lett.*, 2006, **6**, 96.
8. S. Sinha, S. Barjami, G. Iannacchione, A. Schwab and G. Muench, *J. Nanopart. Res.*, 2005, **7**, 651.
9. M. Fujiwara, E. Oki, M. Hamada, Y. Tanimoto, I. Mukouda and Y. Shimomura, *J. Phys. Chem. A*, 2001, **105**, 4383.
10. S. Zaric, G. N. Ostojic, J. Kono, J. Shaver, V. C. Moore, R. H. Hauge, R. E. Smalley and X. Wei, *Nano Lett.*, 2004, **4**, 2219.
11. T. A. Searles, Y. Imanaka, T. Takamasu, H. Ajiki, J. A. Fagan, E. K. Hobbie and J. Kono, *Phys. Rev. Lett.*, 2010, **105**, 017403.
12. L. Maggini, M. Liu, Y. Ishida and D. Bonifazi, *Adv. Mater.*, 2013, **25**, 2462.
13. L. Đorđević, T. Marangoni, M. Liu, R. De Zorzi, S. Geremia, A. Minoia, R. Lazzaroni, Y. Ishida and D. Bonifazi, *ChemPlusChem*, 2019, 1270.
14. K. Zhu, Y. Ju, J. Xu, Z. Yang, S. Gao and Y. Hou, *Acc. Chem. Res.*, 2018, **51**, 404.
15. F. Kalantari, A. Ramazani and M. R. P. Heravi, *Curr. Org. Chem.*, 2019, **23**, 136.
16. B. D. Terris and T. Thomson, *J. Phys. D: Appl. Phys.*, 2005, **38**, R199.
17. F. Gao, *ChemistrySelect*, 2019, **4**, 6805.

18. M. I. Majeed, M. A. Hanif, H. Nawaz and B. Tan, in *Applied Molecular Biotechnology: The Next Generation of Genetic Engineering*, ed. M. S. Khan, I. A. Khan and D. Barh, CRC Press, Boca Raton, 2016, ch. 21, p. 485.
19. G. Latha, P. D. Kumar, K. Gopi, P. Srikanth, Y. Kusumalatha and G. V. Babu, *World J. Pharm. Res.*, 2017, **6**, 341.
20. T. Guo, M. Lin, J. Huang, C. Zhou, W. Tian, H. Yu, X. Jiang, J. Ye, Y. Shi, Y. Xiao, X. Bian and X. Feng, *J. Nanomater.*, 2018, 7805147.
21. K. Wu, D. Su, J. Liu, R. Saha and J.-P. Wang, arXiv.org, e-Print Arch., Phys., 2018, 1.
22. L. Xie, W. Jin, H. Chen and Q. Zhang, *J. Biomed. Nanotechnol.*, 2019, **15**, 215.
23. A. Stopin, F. Pineux, R. Marega and D. Bonifazi, *Chem. - Eur. J.*, 2015, **21**, 9288.
24. J. P. Tessonnier, G. Winé, C. Estournès, C. Leuvrey, M. J. Ledoux and C. Pham-Huu, *Catal. Today*, 2005, **102–103**, 29.
25. P. Kappen, A. Rider, P. J. Pigram and N. Brack, *J. Phys. Chem. C*, 2011, **115**, 21083.
26. W. Baaziz, S. Begin-Colin, B. P. Pichon, I. Florea, O. Ersen, S. Zafeiratos, R. Barbosa, D. Begin and C. Pham-Huu, *Chem. Mater.*, 2012, **24**, 1549.
27. G. Lamanna, A. Battigelli, C. Menard-Moyon and A. Bianco, *Nanotechnol. Rev.*, 2012, **1**, 17.
28. A. Battigelli, C. Menard-Moyon, T. Da Ros, M. Prato and A. Bianco, *Adv. Drug Delivery Rev.*, 2013, **65**, 1899.
29. G. Gavrel, B. Jousselme, A. Filoramo and S. Campidelli, *Top. Curr. Chem.*, 2014, **348**, 95.
30. A. Masotti and A. Caporali, *Int. J. Mol. Sci.*, 2013, **14**, 24619.
31. J. Tucek, K. C. Kemp, K. S. Kim and R. Zboril, *ACS Nano*, 2014, **8**, 7571.
32. E. Miyako, B. P. Pichon, C. Ménard-Moyon, I. A. Vacchi, C. Lefèvre, S. Bégin-Colin and A. Bianco, *Carbon*, 2016, **96**, 49.
33. M. Samadishadlou, M. Farshbaf, N. Annabi, T. Kavetskyy, R. Khalilov, S. Saghfi, A. Akbarzadeh and S. Mousavi, *Artif. Cells, Nanomed., Biotechnol.*, 2018, **46**, 1314.
34. D. S. Bethune, C. H. Kiang, M. S. de Vries, G. Gorman, R. Savoy, J. Vazquez and R. Beyers, *Nature*, 1993, **363**, 605.
35. C. Journet, W. K. Maser, P. Bernier, A. Loiseau, M. L. de la Chapelle, S. Lefrant, P. Deniard, R. Lee and J. E. Fischer, *Nature*, 1997, **388**, 756.
36. M. José-Yacamán, M. Miki-Yoshida, L. Rendón and J. G. Santiesteban, *Appl. Phys. Lett.*, 1993, **62**, 657.
37. R. Sen, A. Govindaraj and C. N. R. Rao, *Chem. Phys. Lett.*, 1997, **267**, 276.
38. K. Kuwana and K. Saito, *Carbon*, 2005, **43**, 2088.
39. U. Weissker, S. Hampel, A. Leonhardt and B. Büchner, *Materials*, 2010, **3**, 4387.
40. Q. Liu, Z.-G. Chen, B. Liu, W. Ren, F. Li, H. Cong and H.-M. Cheng, *Carbon*, 2008, **46**, 1892.
41. F. C. Dillon, A. Bajpai, A. Koós, S. Downes, Z. Aslam and N. Grobert, *Carbon*, 2012, **50**, 3674.

42. F. Pineux, R. Marega, A. Stopin, A. La Torre, Y. Garcia, E. Devlin, C. Michiels, A. N. Khlobystov and D. Bonifazi, *Nanoscale*, 2015, **7**, 20474.
43. G. Korneva, H. Ye, Y. Gogotsi, D. Halverson, G. Friedman, J.-C. Bradley and K. G. Kornev, *Nano Lett.*, 2005, **5**, 879.
44. C. Pham-Huu, N. Keller, C. Estournès, G. Ehret and M. J. Ledoux, *Chem. Commun.*, 2002, 1882.
45. M. A. Correa-Duarte, M. Grzelczak, V. Salgueiriño-Maceira, M. Giersig, L. M. Liz-Marzán, M. Farle, K. Sierazdki and R. Diaz, *J. Phys. Chem. B*, 2005, **109**, 19060.
46. B. Jia, L. Gao and J. Sun, *Carbon*, 2007, **45**, 1476.
47. C. Gao, W. Li, H. Morimoto, Y. Nagaoka and T. Maekawa, *J. Phys. Chem. B*, 2006, **110**, 7213.
48. X. Liu, I. Marangon, G. Melinte, C. Wilhelm, C. Ménard-Moyon, B. P. Pichon, O. Ersen, K. Aubertin, W. Baaziz, C. Pham-Huu, S. Bégin-Colin, A. Bianco, F. Gazeau and D. Bégin, *ACS Nano*, 2014, **8**, 11290.
49. L. Maggini, J.-M. Raquez, R. Marega, J. Jensen Ahrens, F. Pineux, F. Meyer, P. Dubois and D. Bonifazi, *ChemSusChem*, 2013, **6**, 367.
50. J.-L. Gong, B. Wang, G.-M. Zeng, C.-P. Yang, C.-G. Niu, Q.-Y. Niu, W.-J. Zhou and Y. Liang, *J. Hazard. Mater.*, 2009, **164**, 1517.
51. M. V. Bracamonte, M. Melchionna, A. Stopin, A. Giulani, C. Tavagnacco, Y. Garcia, P. Fornasiero, D. Bonifazi and M. Prato, *Chem. - Eur. J.*, 2015, **21**, 12769.
52. M. Melchionna, A. Beltram, A. Stopin, T. Montini, R. W. Lodge, A. N. Khlobystov, D. Bonifazi, M. Prato and P. Fornasiero, *Appl. Catal., B*, 2018, **227**, 356.
53. N. D. Quyen Chau, C. Ménard-Moyon, K. Kostarelos and A. Bianco, *Biochem. Biophys. Res. Commun.*, 2015, **468**, 454.
54. V. Pensabene, O. Vittorio, V. Raffa, A. Ziaei, A. Menciassi and P. Dario, *IEEE Trans. Nanobiosci.*, 2008, **7**, 105.
55. O. Vittorio, P. Quaranta, V. Raffa, N. Funel, D. Campani, S. Pelliccioni, B. Longoni, F. Mosca, A. Pietrabissa and A. Cuschieri, *Nanomedicine*, 2011, **6**, 43.
56. S. Park, J. Shin, J. Lee and M. Cha, *Mater. Lett.*, 2012, **68**, 378.
57. S. Shen, J. Ren, X. Zhu, Z. Pang, X. Lu, C. Deng, R. Zhang and X. Jiang, *J. Mater. Chem. B*, 2013, **1**, 1939.
58. G. Lamanna, A. Garofalo, G. Popa, C. Wilhelm, S. Bégin-Colin, D. Felder-Flesch, A. Bianco, F. Gazeau and C. Ménard-Moyon, *Nanoscale*, 2013, **5**, 4412.
59. R. Marega, F. De Leo, F. Pineux, J. Sgrignani, A. Magistrato, A. D. Naik, Y. Garcia, L. Flamant, C. Michiels and D. Bonifazi, *Adv. Funct. Mater.*, 2013, **23**, 3173.
60. G. Spalluto, S. Federico, B. Cacciari, A. Bianco, S. L. Cheong and M. Prato, in *Carbon Nanotubes: From Bench Chemistry to Promising Biomedical Applications*, ed. G. Pastorin, Jenny Stanford Publishing, New York, 2011, ch. 2, p. 23.
61. R. Cheng and Y. Xue, *Springer Ser. Biomater. Sci. Eng.*, 2016, **5**, 31.

62. H. He, D. Xiao, L. A. Pham-Huy, P. Dramou and C. Pham-Huy, in *Drug Delivery Approaches and Nanosystems, Volume 1: Novel Drug Carriers*, ed. R. K. Keservani, A. K. Sharma and R. K. Kesharwani, Apple Academic Press, New York, 2018, ch. 6, vol. 1, p. 163.
63. D. Cai, J. M. Mataraza, Z.-H. Qin, Z. Huang, J. Huang, T. C. Chiles, D. Carnahan, K. Kempa and Z. Ren, *Nat. Methods*, 2005, **2**, 449.
64. H. Gul, W. Lu, P. Xu, J. Xing and J. Chen, *Nanotechnology*, 2010, **21**, 155101.
65. Z. Yang, L. Deng, Y. Lan, X. Zhang, Z. Gao, C.-W. Chu, D. Cai and Z. Ren, *Proc. Natl. Acad. Sci. U. S. A.*, 2014, **111**, 10966.
66. D. Yang, F. Yang, J. Hu, J. Long, C. Wang, D. Fu and Q. Ni, *Chem. Commun.*, 2009, 4447.
67. R. Li, R. A. Wu, L. Zhao, Z. Hu, S. Guo, X. Pan and H. Zou, *Carbon*, 2011, **49**, 1797.
68. M.-L. Chen, Y.-J. He, X.-W. Chen and J.-H. Wang, *Langmuir*, 2012, **28**, 16469.
69. A. Al Faraj, A. P. Shaik and A. S. Shaik, *Int. J. Nanomed.*, 2015, **10**, 157.
70. A. Al Faraj, A. S. Shaik, R. Halwani and A. Alfuraih, *Mol. Imaging Biol.*, 2016, **18**, 315.
71. H. Bouriabadi, H. Emadi and A. N. Kharat, *J. Cluster Sci.*, 2016, **27**, 1017.
72. P. Ghoderao, S. Sahare, P. Alegaonkar, A. A. Kulkarni and T. Bhave, *ACS Appl. Nano Mater.*, 2019, **2**, 607.
73. N. Suo, M. Wang, Y. Jin, J. Ding, X. Gao, X. Sun, H. Zhang, M. Cui, J. Zheng, N. Li, X. Jin and S. Jiang, *Int. J. Nanomed.*, 2019, **14**, 1241.
74. P. Chakravarty, R. Marches, N. S. Zimmerman, A. D. E. Swafford, P. Bajaj, I. H. Musselman, P. Pantano, R. K. Draper and E. S. Vitetta, *Proc. Natl. Acad. Sci. U. S. A.*, 2008, **105**, 8697.
75. J. T. Robinson, K. Welsher, S. M. Tabakman, S. P. Sherlock, H. Wang, R. Luong and H. Dai, *Nano Res.*, 2010, **3**, 779.
76. S. M. Dadfar, K. Roemhild, N. I. Drude, S. von Stillfried, R. Knüchel, F. Kiessling and T. Lammers, *Adv. Drug Delivery Rev.*, 2019, **138**, 302.
77. A. Leonhardt, I. Mönch, A. Meye, S. Hampel and B. Büchner, *Adv. Sci. Technol.*, 2006, **49**, 74.
78. I. Mönch, A. Leonhardt, A. Meye, S. Hampel, R. Kozhuharova-Koseva, D. Elefant, M. P. Wirth and B. Büchner, *J. Phys.: Conf. Ser.*, 2007, **61**, 820.
79. R. Klingeler, S. Hampel and B. Buchner, *Int. J. Hyperthermia*, 2008, **24**, 496.
80. Y. Krupskaya, C. Mahn, A. Parameswaran, A. Taylor, K. Kraemer, S. Hampel, A. Leonhardt, M. Ritschel, B. Buechner and R. Klingeler, *J. Magn. Magn. Mater.*, 2009, **321**, 4067.
81. D. Shi, H. S. Cho, C. Huth, F. Wang, Z. Dong, G. M. Pauletti, J. Lian, W. Wang, G. Liu, S. L. Bud'ko, L. Wang and R. C. Ewing, *Appl. Phys. Lett.*, 2009, **95**, 223702.
82. L. Wilson, E. E. Kalu, L. Martin and M. E. McHenry, *J. Mater. Chem.*, 2012, **22**, 595.
83. G. C. Li and G. M. Hahn, *Cancer Res.*, 1980, **40**, 4501.

84. L. Roizin-Towle and J. P. Pirro, *Int. J. Radiat. Oncol., Biol., Phys.*, 1991, **20**, 751.
85. G. Raniszewski, A. Miaskowski and S. Wiak, *J. Nanomater.*, 2015, **2015**, 8.
86. M. Dalal, J.-M. Greneche, B. Satpati, T. B. Ghzaiel, F. Mazaleyrat, R. S. Ningthoujam and P. K. Chakrabarti, *ACS Appl. Mater. Interfaces*, 2017, **9**, 40831.
87. X. Zuo, C. Wu, W. Zhang and W. Gao, *RSC Adv.*, 2018, **8**, 11997.
88. M. Johannsen, U. Gneveckow, B. Thiesen, K. Taymoorian, C. H. Cho, N. Waldöfner, R. Scholz, A. Jordan, S. A. Loening and P. Wust, *Eur. Urol.*, 2007, **52**, 1653.
89. K. Maier-Hauff, F. Ulrich, D. Nestler, H. Niehoff, P. Wust, B. Thiesen, H. Orawa, V. Budach and A. Jordan, *J. Neuro-Oncol.*, 2011, **103**, 317.
90. V. Sadaphal, S. Mukherjee and S. Ghosh, *Appl. Phys. Express*, 2018, **11**, 097001.
91. T. Peci, T. J. S. Dennis and M. Baxendale, *Carbon*, 2015, **87**, 226.
92. B.-T. Doan, S. Meme and J.-C. Beloeil, in *Chemistry of Contrast Agents in Medical Magnetic Resonance Imaging*, ed. A. Merbach, L. Helm and E. Toth, John Wiley & Sons Ltd, 2013, p. 1.
93. R. H. Hashemi, W. G. Bradley and C. J. Lisanti, *MRI: The Basics: The Basics*, Lippincott Williams & Wilkins, Philadelphia, 2012.
94. E. Toth, L. Helm and A. Merbach, in *Chemistry of Contrast Agents in Medical Magnetic Resonance Imaging*, ed. A. Merbach, L. Helm and E. Toth, John Wiley & Sons Ltd, 2013, p. 25.
95. S. Laurent, L. Vander Elst and R. N. Muller, in *Chemistry of Contrast Agents in Medical Magnetic Resonance Imaging*, ed. A. Merbach, L. Helm and E. Toth, John Wiley & Sons Ltd, 2013, p. 427.
96. N. Kuznik and M. M. Tomczyk, *Beilstein J. Nanotechnol.*, 2016, **7**, 1086.
97. Y. Gao, *J. Funct. Biomater.*, 2018, **9**, 16.
98. B. Sitharaman, K. R. Kissell, K. B. Hartman, L. A. Tran, A. Baikalov, I. Rusakova, Y. Sun, H. A. Khant, S. J. Ludtke, W. Chiu, S. Laus, E. Toth, L. Helm, A. E. Merbach and L. J. Wilson, *Chem. Commun.*, 2005, 3915.
99. B. Sitharaman and L. J. Wilson, *Int. J. Nanomed.*, 2006, **1**, 291.
100. R. Sethi, Y. Mackeyev and L. J. Wilson, *Inorg. Chim. Acta*, 2012, **393**, 165.
101. C. Richard, B.-T. Doan, J.-C. Beloeil, M. Bessodes, E. Toth and D. Scherman, *Nano Lett.*, 2008, **8**, 232.
102. I. Marangon, C. Menard-Moyon, J. Kolosnjaj-Tabi, M. L. Beoutis, L. Lartigue, D. Alloyeau, E. Pach, B. Ballesteros, G. Autret, T. Ninjbadgar, D. F. Brougham, A. Bianco and F. Gazeau, *Adv. Funct. Mater.*, 2014, **24**, 7173.
103. J. H. Choi, F. T. Nguyen, P. W. Barone, D. A. Heller, A. E. Moll, D. Patel, S. A. Boppart and M. S. Strano, *Nano Lett.*, 2007, **7**, 861.
104. H. Wu, G. Liu, Y. Zhuang, D. Wu, H. Zhang, H. Yang, H. Hu and S. Yang, *Biomaterials*, 2011, **32**, 4867.
105. J. T.-W. Wang, L. Cabana, M. Bourgognon, H. Kafa, A. Protti, K. Venner, A. M. Shah, J. K. Sosabowski, S. J. Mather, A. Roig, X. Ke, G. Van Tendeloo, R. T. M. de Rosales, G. Tobias and K. T. Al-Jamal, *Adv. Funct. Mater.*, 2014, **24**, 1880.

106. Y. Liu, T. C. Hughes, B. W. Muir, L. J. Waddington, T. R. Gengenbach, C. D. Easton, T. M. Hinton, B. A. Moffat, X. Hao and J. Qiu, *Biomaterials*, 2014, **35**, 378.
107. H. Wu, G. Liu, X. Wang, J. Zhang, Y. Chen, J. Shi, H. Yang, H. Hu and S. Yang, *Acta Biomater.*, 2011, **7**, 3496.
108. W. Chen, X. Zheng, S. Li, W. Zhang, X. Wen, L. Yue and J. Wang, *J. Nanopart. Res.*, 2015, **17**, 444.
109. X. Ding, R. Singh, A. Burke, H. Hatcher, J. Olson, R. A. Kraft, M. Schmid, D. Carroll, J. D. Bourland, S. Akman, F. M. Torti and S. V. Torti, *Nanomedicine*, 2011, **6**, 1341.
110. B. M. Maciejewska, A. Warowicka, A. Baranowska-Korczyc, K. Załęski, T. Zalewski, K. K. Kozioł and S. Jurga, *Carbon*, 2015, **94**, 1012.
111. O. Vittorio, S. L. Duce, A. Pietrabissa and A. Cuschieri, *Nanotechnology*, 2011, **22**, 095706.
112. A. Baranowska-Korczyc, M. Jasiurkowska-Delaporte, B. M. Maciejewska, A. Warowicka, L. E. Coy, T. Zalewski, K. K. Kozioł and S. Jurga, *RSC Adv.*, 2016, **6**, 49891.
113. W. Ding, C. Lou, J. Qiu, Z. Zhao, Q. Zhou, M. Liang, Z. Ji, S. Yang and D. Xing, *Nanomedicine*, 2016, **12**, 235.
114. P.-C. Lee, C.-Y. Lin, C.-L. Peng and M.-J. Shieh, *Biomater. Sci.*, 2016, **4**, 1742.

CHAPTER 6

Carbon Nanomaterials for Neuronal Tissue Engineering

MYRIAM BARREJÓN ARAQUE[a] AND SUSANNA BOSI*[b]

[a]Universidad de Castilla-La Mancha, Instituto de Nanociencia, Campus Tecnológico Antigua Fábrica de Armas, Nanotecnología y Materiales Moleculares (INAMOL), Avda. Carlos III, s/n, 45071 Toledo, Spain; [b]Dipartimento di Scienze Chimiche e Farmaceutiche, Università di Trieste, via Licio Giorgieri 1, 34127 Trieste, Italy
*E-mail: susanna.bosi@gmail.com

6.1 Introduction

Over the past few years, converging research between nanotechnology and neuroscience has potentially emerged,[1,2] leading to extensive investigation in both fields within the scientific community. Nanotechnology covers the branch of science that deals with materials at the nanoscale level to engineer new structures, devices, and systems on a near-atomic size scale. The interaction of this field with neuroscience leads to the tailoring of materials, devices and systems with the primary goal of achieving direct communication with the central nervous system (CNS).[3] One of the biggest successes of this convergence has been the development of neuroprostheses. Neuroprostheses are devices designed to interact with the CNS and restore function that has been lost.[4] These devices consist of electrodes that allow either the electrical recording of extracellular signals or electrical stimulation of neurons.[3,4] To optimize the neuroprosthesis efficiency and minimize the side effects, an intimate contact between the electrodes and neural cells is required, which

Nanoscience & Nanotechnology Series No. 48
Carbon Nanostructures for Biomedical Applications
Edited by Tatiana Da Ros, Nazario Martín and Jean-Francois Nierengarten

Published by the Royal Society of Chemistry, www.rsc.org

will improve the performance of the final device.[5,6] In this sense, the use of carbon nanomaterials (CNMs) has been at the forefront of the field, allowing the design of nanoscale-sized systems able to interact with neural cells in a controlled way, inducing the desired physiological response.[4,7,8]

CNMs show unique properties such as a high electrochemically accessible surface area, high mechanical strength and excellent thermal and electrical conductivity.[9,10] The high surface area of CNMs is an important factor to enable the increment of the electrode charge injection capacity and decrease the interfacial impedance with neurons.[11,12] Furthermore, their intrinsic good electrical conductivity and biocompatibility make them promising candidates for the development of neural interfacing materials with high efficiency recording and stimulation of the neuronal activity.[12] It is also important to notice that their biocompatibility and properties can be modulated through chemical modification, allowing an optimal design of interface between the conductive materials and target tissue. Thus, the chemical modification of CNMs can be used to influence the CNM/neuronal interaction and modify cell behavior.[13–16]

Three naturally occurring carbon allotropes are known to exist (amorphous carbon, diamond and graphite). However, the valency of carbon allows the arrangement of bonds in multiple forms, yielding different synthetic carbon allotropes such as fullerenes, graphene (GR), carbon nanotubes (CNTs), carbon nanohorns (CNHs) and nanodiamonds (Figure 6.1).[10]

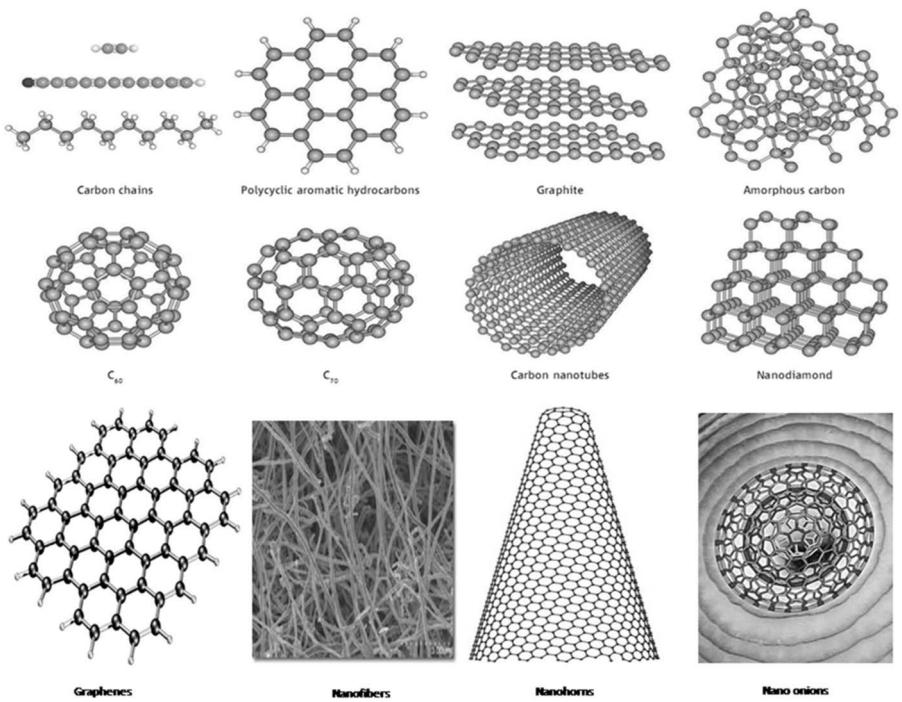

Figure 6.1 Different types of existing carbon allotropes. Reprinted from ref. 183, https://doi.org/10.3390/ma8063068, under the terms of the CC BY 4.0 International License https://creativecommons.org/licenses/by/4.0/.

Among these allotropes, CNTs and GR have been the most extensively studied in the field of neuroscience due to their peculiar properties.[17] The excellent mechanical strength of GR and CNTs, combined with their very low dimensions and flexibility, provide an intimate contact with the neural cells, enabling the design of systems that behave as both support and/or interface materials.[12,17]

The purpose of this chapter is to describe the chronological evolution the most common CNMs use in the field of neuroscience and to report the most recent advances.

6.2 Carbon Nanomaterials in Neuroscience (History and Perspectives)

In this section an overview of the main advances that have been realized in the development of neural interfacing materials involving different types of carbon nanostructures is provided. The history and the current journey towards the design of advanced carbon-based materials aimed at interfacing with the CNS will be discussed.

6.2.1 Carbon Nanotubes

CNTs were first observed as early as 1952 by the Russian scientists Radushkevich and Lukyanovich when they reported the electron microscopy observation of hollow carbon fibers.[18] However, the first breakout in the discovery of CNTs came in 1991 when Sumio Iijima published a paper in *Nature*, in which he reported the discovery of a new type of carbon structure with the appearance of needle-like tubes.[19] These structures consisted of concentric shell structures containing from 2 to 50 layers of graphene, which are nowadays known as multi-walled carbon nanotubes (MWCNTs). Two years later, Iijima[20] and Donald Bethune[21] independently observed single-walled nanotubes (SWCNTs), structures consisting of just one layer of graphene rolled up in the form of a cylinder with a diameter of around 1 nm.

The first application of CNTs as substrates for neuronal growth was performed nearly two decades ago by Mattson *et al.*,[22] who grew hippocampal neurons on glass coverslips coated with the permissive substrate polyethyleneimine (PEI) and overcoated with MWNTs. In the same work, they also reported the improvement in the growth of neurons by modifying the MWNT with the bioactive molecule 4-hydroxynonenal, a modification that was accomplished *via* physical adsorption. In a later study, in an effort to investigate whether the chemical modification of CNTs could be used to affect neurite outgrowth, Hu *et al.* grew neurons on MWCNTs with different charges.[13] Thus, negatively charged MWNTs were prepared by attaching carboxyl groups to the caps of CNTs. Then, the carboxy-CNTs were further modified by reacting with oxalyl chloride and either poly-*m*-aminobenzene sulfonic acid (PABS) or ethylenediamine (EN), yielding zwitterionic and positively charged CNTs, respectively. In this work, the functional groups were

covalently attached to the CNTs, providing a much more permanent modification compared to that of physisorption. The authors concluded that positively charged MWCNTs allowed an increase in the length and branching of neurites.[13] In an attempt to obtain a more permissive CNT-based substrate, the same group conducted a new study where they functionalized SWCNTs with PEI.[23] The results demonstrated that SWNT-PEI exerted modulation of neurite outgrowth and branching with intermediate effects between that of PEI and MWNTs. Lovat *et al.*[24] studied the possibility of using CNTs to promote an increase in the neural signal transfer. To improve the adhesion properties of CNTs to the commonly employed glass coverslips and obtain a homogeneous distribution of CNTs on the surface, MWCNTs were functionalized *via* 1,3-dipolar cycloaddition of azomethine ylides (Figure 6.2, left), yielding MWCNTs modified with pyrrolidine groups. Subsequent defunctionalization of the MWCNTs was achieved by annealing under N_2 atmosphere at 350 °C, leaving purified and nonfunctionalized MWNTs on the glass (Figure 6.2, right).[24]

Postnatal hippocampal cells were then cultured on either uncoated glass coverslips or coverslips coated with nonfunctionalized MWNT films. After eight days of culturing, single cell patch clamp recording demonstrated a six-fold greater frequency of spontaneous postsynaptic currents of the neurons grown on MWCNT films (Figure 6.2, right). The authors attributed this increase in the efficacy of neural signal transmission to the high electrical conductivity of CNTs.[24]

The importance of the type of chemical modification was further evidenced by the study performed by Liopo *et al.*[25] The authors demonstrated that the covalent chemical modification of SWCNTs with 4-benzoic acid or 4-*tert*-butylphenyl functional groups exerted a negative effect in the viability and cell attachment of neuronal cells, showing them to be less supportive substrates than unmodified SWCNTs. Such a result was attributed to the hydrophobicity of the groups anchored to the sidewall of the CNTs. Most importantly, during these studies Liopo and colleagues showed for the first time electrical stimulation of neurons using the electrical properties of SWCNTs. The electrical coupling between CNTs and neurons was confirmed when electrically stimulated transparent, conductive SWCNT films elicited a neural response that was monitored by whole-cell current recordings.[25] However, these studies did not prove the possibility of evoking synaptic activity in long-term neural circuits. In this direction, new insights were obtained by Mazzatenta *et al.*,[5] who grew hippocampal cells on glass coverslips coated with SWNT films. Electrophysiological recordings indicated that neurons grown on SWNT substrates displayed prominent spontaneous electrical activity. Furthermore, under a current clamp, a strong increase in the average frequency of spontaneous action potentials was observed in neurons grown on SWNTs. Finally, effective stimulation of the neural network allowed the emergence of synaptic responses in neurons due to action potentials elicited by CNTs' electrical stimulations of the pre-synaptic cells.[5] In a later study, Cellot *et al.*[26] demonstrated that the presence of "intimate contacts" between hippocampal neurons and SWCNTs created a physical

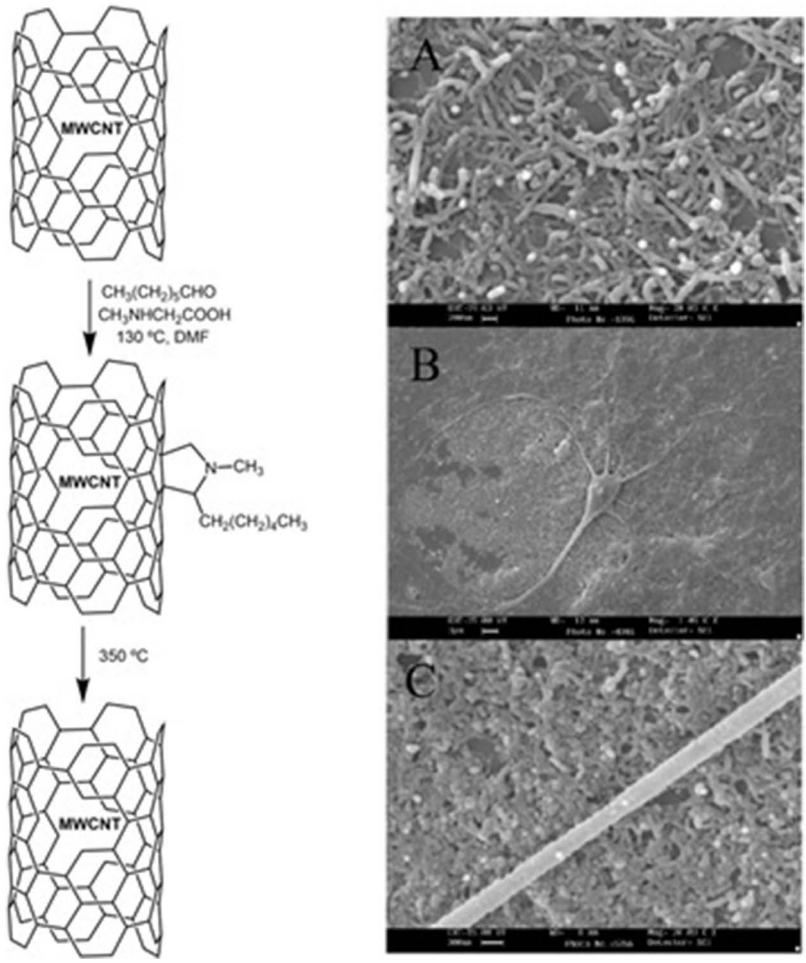

Figure 6.2 Left: Schematic representation of the chemical modification of MWCNTs *via* 1,3-dipolar cycloaddition reaction. Right: (A) Micrographs taken by scanning electron microscopy showing the retention on glass of MWNT films after an 8-day testing culturing conditions. (B) Neonatal hippocampal neuron growing on dispersed MWNT after 8 days in culture. The surface structure, composed of films of MWNT and peptide-free glass, allows neuron adhesion. Dendrites and axons extend across MWNT, glia cells and glass. The relationship between the dendrite and MWNT is very clear in the image in (C), were a neurite is traveling in close contact to carbon nanotubes.[24] Reprinted from ref. 24 with permission from American Chemical Society, Copyright 2005.

channel, which would electrically couple nanotubes to neurons favoring electrical shortcuts between the proximal and distal compartments of the neuron. They demonstrated also the presence of an additional somatic membrane depolarization that occurred indirectly due to dendritic calcium electrogenesis.[26]

Functional stimulation, especially in applications of the nervous system, often requires small-size electrodes with high current density. In this direction, several studies have been reported that incorporate directionally oriented CNTs into the electrodes.[27,28] The high packing density and high degree of alignment in these systems enhance the electrical properties of the electrodes.[29] Thus, Galvan-Garcia *et al.*[27] reported directionally oriented MWCNTs in the form of sheets or yarns. These nanomaterials were demonstrated to be viable substrates to promote cell attachment, differentiation and cell growth. Additionally, the purity of the CNTs also affected the interaction with the neurons. When highly purified CNTs were interfaced with neurons, extended processes whose number and length were comparable to those of neurons grown on a planar permissive substrate, represented by polyornithine pre-treated glass, were observed. Wang *et al.*[28] reported the first neural interface consisting of CNT microelectrode arrays (MEAs) integrated onto substrates with pre-patterned micro-circuitry. The MEA was based on vertically aligned MWCNT arrays and offered a high charge injection ability (1–1.6 mC cm^{-2}). Stimulation of embryonic rat hippocampal neurons with the MEA was demonstrated and neuronal activity was optically monitored by live calcium imaging.[28] Shein *et al.*[30] reported CNT-based MEAs consisting of metal electrodes coated by a layer of dense and entangled CNTs that formed islands. The CNT regions attracted and anchored neurons and glial cells. Electrical stimulation allowed the detection of neuronal activity over an extended time period *in vitro* (up to two months).[30] Similarly, Shoval *et al.*[31] reported the application of CNT MEAs as interfaces for retinal recording and stimulation. Neural spontaneous activity was monitored minutes after retinas were placed over the electrodes. Most importantly, a gradual increase in amplitude was recorded over several hours that was attributed to an improved coupling between the neurons and the CNT electrodes.[31] In order to reduce the neural damage and immune response after implantation, a flexible CNT MEA was developed by Chen and collaborators.[32] The presence of CNTs improved both the electrode impedance and the charge-transfer capacity by more than six times. To ensure good electrode adhesion, the CNTs were grown directly on the polyimide substrate. The as-prepared MEA showed improved signal-to-noise ratio during the recording of electrocorticograms from the rat cortex *in vivo*.[32] In another study, neurons were grown on CNT modified MEAs and the onset of the electrical activity was developed as early as four days after seeding compared to seven days in control cultures.[33] The authors concluded that the presence of CNTs increase the surface roughness of the microelectrodes allowing the adhesion of cells with a larger surface area, boosting the activation of integrins, and promoting a faster neuronal differentiation.[33] More recently, an all-carbon-nanotube flexible MEA was developed by David-Pur *et al.*[34] consisting of conducting MWCNT films embedded in a polymeric support. Recording and stimulation tests with chick retinas developed neuronal activity at currents as low as 4 μA, similar to values obtained with TiN commercial devices.

Another important issue in the development of implantable scaffolds based on CNT substrates has been the achievement of free-standing structures, instead of CNT-based materials attached to supportive glass or plastics. The first example of free-standing CNT-based substrates was reported by Gheith *et al.*[35] and consisted in layer-by-layer (LBL) films of SWCNTs modified by polyacrylic acid polymer. The SWCNT LBL films were demonstrated to support the growth, viability, and differentiation of neuronal NG108-15 neuroblastoma/glioma hybrid cells. In a later study, the same authors studied the capability of the LBL-assembled CNT-based substrates to stimulate the neurophysiological activity of NG108-15 cells.[36] The results showed a clear electrical excitation of neurons when current passed through the SWCNT films.

Krukiewicz *et al.*[37] prepared self-supporting flexible CNT films from MWCNT arrays for the design of neural interfaces. The films were fabricated by spray-coating a dispersion of MWCNTs onto a Kapton foil. The subsequent detachment from the substrate and annealing yielded the self-supporting MWCNT films with a uniform thickness of 10 μm that were employed as neural interfaces. The as-prepared CNT films were found to facilitate neurite outgrowth, as well as decrease the presence of reactive astrocytes *in vitro*, observed by the decrease in astrocyte cell area.[37] In this framework, very recent research has demonstrated that self-supporting SWCNTs films with high mechanical performance can be designed through the chemical cross-linking of the SWCNTs.[16] Most importantly, the electrical conductivity of the resulting CNT-films can be tuned just by modifying the degree of cross-linking, which, in turn, regulates neural circuit outputs. Immunofluorescence studies confirmed that neurons and glial cells were able to grow and survive on the CNT substrates for at least 9–11 days. Finally, calcium imaging recording was accomplished revealing that those films with a lower degree of cross-linking and higher electrical conductivity generated bursts with higher rate, due to an improved efficiency in axonal signaling and to the increase in synaptic connections (Figure 6.3).[16]

Much of our early knowledge about neural interfaces has been acquired from studies based on 2D structures. However, beyond the development of 2D constructs, in recent years biologists have focused their attention on the development of three-dimensional (3D) structures that mimic the 3D microenvironment in which cells operate *in vivo*.[38] In 2009, Ghibaudo and co-workers[39] showed that the topography of the substrates played an important role in cell shape and migration by modifying cell-to-substrate interactions. Cells that were cultured on 3D structures exhibited a more branched shape than those cultured on 2D substrates. In a recent study, Alegret *et al.*[40] reported 3D porous and conductive composites consisting of CNTs and polypyrrole (PPy), a conjugated polymer demonstrated to reduce gliosis, improve adaptability and increase charge-transfer efficiency in brain–machine interfaces. The authors developed a novel strategy for the construction of 3D porous composites based on the vapor phase polymerization of pyrrole

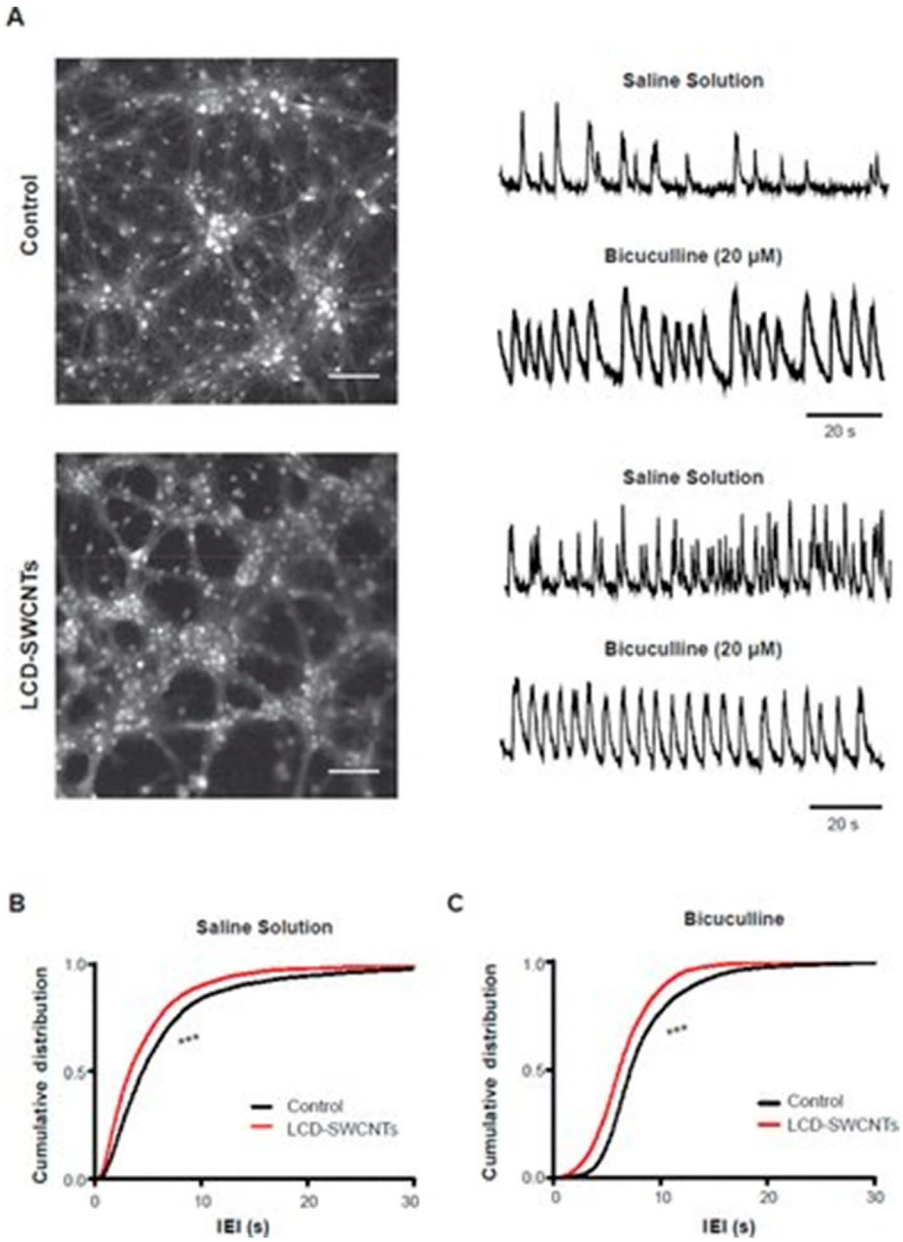

Figure 6.3 (A) Top left: Snapshots of representative fields of neuronal cultures grown on SWCNTs with low cross-linking degree and high conductivity (LCD-SWCNTs), stained with the Oregon Green 488-BAPTA-1AM. Scale bar: 50 μm. Right: Repetitive Ca^{2+}-events spontaneously or bicuculline induced recorded in hippocampal cultures of 10 DIV for LCD-SWCNTs. (B) Bottom left: Snapshots of representative fields of neuronal cultures grown on SWCNTs with high cross-linking degree and low conductivity (HCD-SWCNTs), stained with the Oregon Green 488-BAPTA-1AM. Scale bar: 50 μm. (C) Right: Repetitive Ca^{2+}-events spontaneously or bicuculline induced recorded in hippocampal cultures of 10 DIV for HCD-SWCNTs. Reproduced from ref. 16 with permission from American Chemical Society, Copyright 2019.

inside the CNT 3D template. Finally, astrocytic cells were cultured on the as-prepared scaffolds in order to evaluate its biocompatibility. After 48 h of incubation, the PPy/CNT scaffolds showed a huge stimulation effect in the cell growth, regeneration and shape, showing the potential of these scaffolds for the future development of neural prostheses.[40] Gui *et al.*[41] reported the synthesis of sponge-like bulk materials consisting of self-assembled, interconnected CNTs reinforced by polymer infiltration. The as-prepared sponges showed very high porosity, mechanical flexibility and robustness, electrical conductivity, thermal stability and resistance to harsh environments. Encouraged by the promising properties of these sponge-like materials, Bosi *et al.*[42] developed 3D PDMS porous scaffolds containing CNT carpets stably entrapped in the PDMS matrix (Figure 6.4). The 3D CNT sponges showed an increase in neuronal signals and boosted synchronization *in vitro*. Interestingly, when the 3D scaffolds were implanted in the rat primary visual cortex *in vivo* a more limited scar formation was observed in comparison with control experiments.[17] More recently, the PDMS-CNT 3D scaffolds were interfaced to spinal organotypic slices conferring increased neuronal activity in the spinal networks and guiding regrowing axons toward functional reconnection of separated spinal explants.[43] Additionally, the 3D constructs were implanted into the adult rat visual cortex for 2, 4 and 8 weeks to study the biocompatibility. These studies indicated that the scaffolds were largely biocompatible *in vivo* and supported their application as neural interfaces.[43]

Since biocompatibility studies of CNTs with neuronal tissues have shown promising results over the years,[44,45] other *in vivo* studies using CNT-based neural interfaces have also been reported.[7,17,46] *In vivo* recordings have been reported in the motor cortex of anesthetized rats and in the visual cortex of monkeys by using conventional metal electrodes coated with CNTs.[47] Compared with bare metal electrodes, the CNT coating enhanced both recording and electrical stimulation of neurons due to the decrease of the electrode impedance and the increase of charge transfer capacity. Roman *et al.*[48] studied the neuroregenerative capacity of CNTs in spinal cord injury model rats. For this purpose, polyethyleneglycol (PEG) functionalized SWCNTs, which have been shown to increase the length of selected neurites *in vitro*,[49] were administered post-injury in the lesion site resulting in the promotion of axonal survival and repair. Additionally, in delayed administration experiments, the PEG-SWCNTs were able to achieve a concentration-dependent reduction in the lesion volume and an increase in the number of neurofilament-positive fibers in the lesion epicentre. A dose-dependent modest functional recovery in treated rats was achieved. In a later study, *in vivo* chronic studies in Parkinsonian rodents were accomplished by using CNT fiber microelectrodes.[50] The authors demonstrated that the stimulation of neurons with these electrodes was as effective as that observed for metal electrodes. These results were attributed to the active site surface area of the CNT fiber microelectrodes that was ten times larger than that of metal electrodes resulting in a minimization of impedance and significantly reduced inflammatory response.[50]

The future direction and perspective in research for the application of CNTs in neuroscience is focused in the field of human–machine interfaces (HMI) that bidirectionally connect humans and machines.[51–53] Very recent research suggests a potential breakthrough in the application of SWCNTs for the development of multifunctional human–machine interfaces of the future.[54] In this work, the authors reported the fabrication of a transparent, stretchable, and highly sensitive strain sensor consisting of a novel sandwich-like stacked nanohybrid film of SWCNTs and a conductive elastomeric composite with tuneable electrical and optical properties. The manufactured patchable strain sensor is demonstrated to be useful for sensing emotions

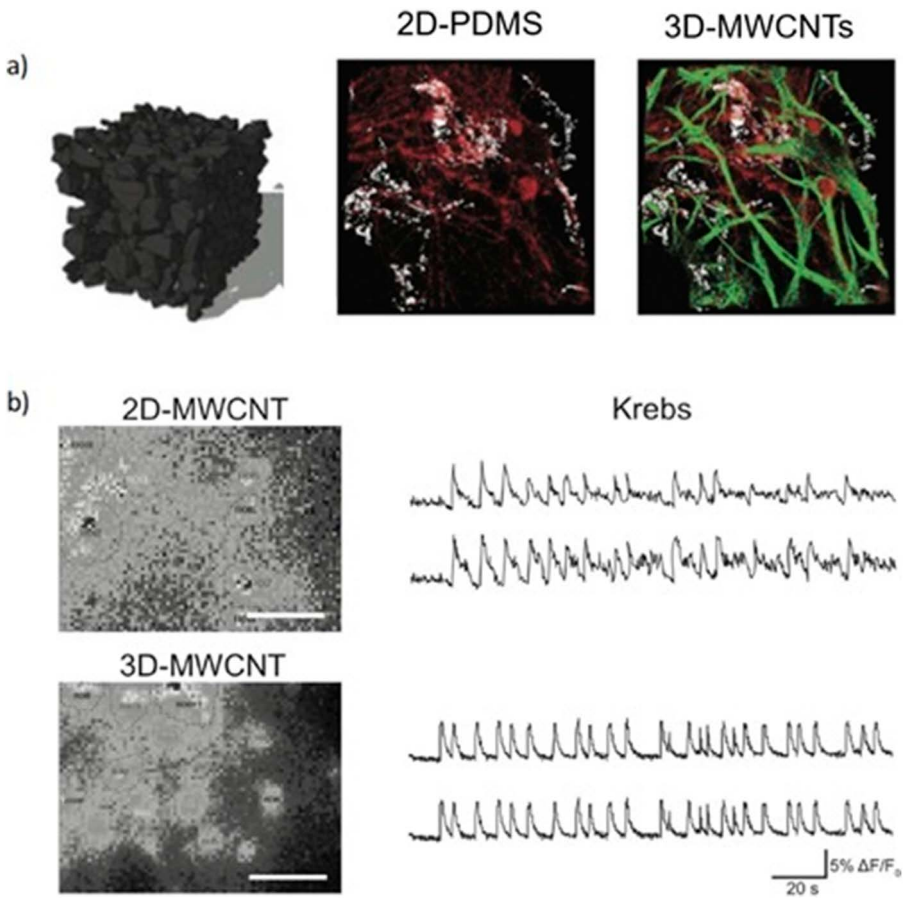

Figure 6.4 (a) Left: Sketch of the PDMS-MWCNTs scaffold, and right: confocal micrographs show hippocampal cultures grown (9 DIV) on 2D-PDMS and 3D-MWCNTS immune-stained for β-tubulin III (in red), GFAP (green) and DAPI (blue). Scale bar: 100 μm. (b) Repetitive Ca^{2+} activities spontaneously recorded in 2D- and 3D-MWCNTs. Adapted from ref. 42, https://doi.org/10.1038/srep09562, under the terms of the CC BY 4.0 International License https://creativecommons.org/licenses/by/4.0/.

such as laughing and crying or detection of eye movements. The high electrical transport of SWCNTs was crucial to get an effective sensor. These results, along with the outstanding achievements of CNT-based interfaces described above, clearly indicate the future potential of CNTs for the development of smart HMI.

6.2.2 Graphene

In the early 21st century, Geim and Novoselov discovered how to obtain isolated sheets from graphite, yielding a new allotrope of carbon named graphene (GR), which overcame the expectations of any other material (Figure 6.1).[55] GR consists of a two-dimensional grid of sp^2 hybridized carbon atoms arranged in hexagons. Among the outstanding properties of GR it has to be highlighted that it is the thinnest compound known to man (a one atom thick crystal), the world's lightest material, the strongest material ever measured (between 100 and 300 times stronger than steel and with a tensile stiffness of 150 000 000 psi), an excellent heat conductor and also the best conductor of electricity with reported values in excess of 15 000 $cm^2\ V^{-1}\ s^{-1}$.[56]

Despite the fact that CNTs are the most studied carbon nanomaterials for biomedical applications,[57,58] in the past few years the scientific community has shown a growing interest in GR-based materials.[59,60] The biological application of GR is a relatively new area with significant potential. Since the reported use of graphene oxide (GO) as an efficient nanocarrier for drug delivery by Dai *et al.*[61] in 2008, the first study on GR for biomedical applications, many efforts have been made to explore the use of this material for possible biomedical applications, such as cellular imaging and drug/gene delivery,[62] biological sensing,[63] stem cell research and as a biocompatible scaffold for cell culture.[64,65]

Interfacing GR with neural cells has been demonstrated to be very advantageous for exploring their electrical behavior or facilitating neuronal regeneration through the controlled elongation of neuronal processes.[66] Its mechanical and electronic features make it a strong candidate for replacing current neural interface devices allowing the design of highly sensitive electrodes for neural signal recording and GR-based platforms for electrical local stimulation.[67,68]

In early studies in the field, GR films were employed for primary cultures of mouse hippocampal neurons.[69] The authors observed an increase in the number of neurites and the average neurite length during 2–7 days after cell seeding compared with tissue culture polystyrene substrates. Additionally, expression of growth-associate protein-43 (GAP-43) was examined on the GR substrates, as compared to the polystyrene substrates, showing that GAP-43 expression was greatly enhanced on the GR substrates. This protein is considered as an important component for the effective regenerative response in nervous systems. The results indicated that using GR substrates for neuronal growth may effectively boost neurite sprouting and outgrowth.[69]

Fabbro *et al.*[70] developed GR-based substrates (GBSs) produced by liquid phase exfoliation (LPE) or ball milling (BM). The authors tested the effects of GBSs on brain cell cultures by measuring functional and synaptic integrity of

the emerging neuronal networks. To this end, neurons were investigated by electron microscopy and immunofluorescence and their density was quantified by immunofluorescence staining (Figure 6.5c–f). Similarly, the glial cells density was also investigated (Figure 6.5g–i). The results showed that GBSs were inert as neuron-interfacing materials, preserving the basal physiological level of neuronal activity as well. Most importantly, they demonstrated the uncommon ability of GBSs to support neuronal development (in terms of neuronal passive properties, spontaneous synaptic activity, synaptogenesis and short-term synaptic plasticity) without precoating with adhesion-promoting peptides (*e.g.*, polylysine or polyornithine).[70]

Very recent studies demonstrated that single-layer GR increases neuronal firing by altering membrane-associated functions in cultured cells, causing an increase in neuronal synaptic activity.[17] The tuning of the distribution of extracellular ions at the interface with neurons, a key regulator of neuronal excitability, was also observed, which was maximized when a single layer GR

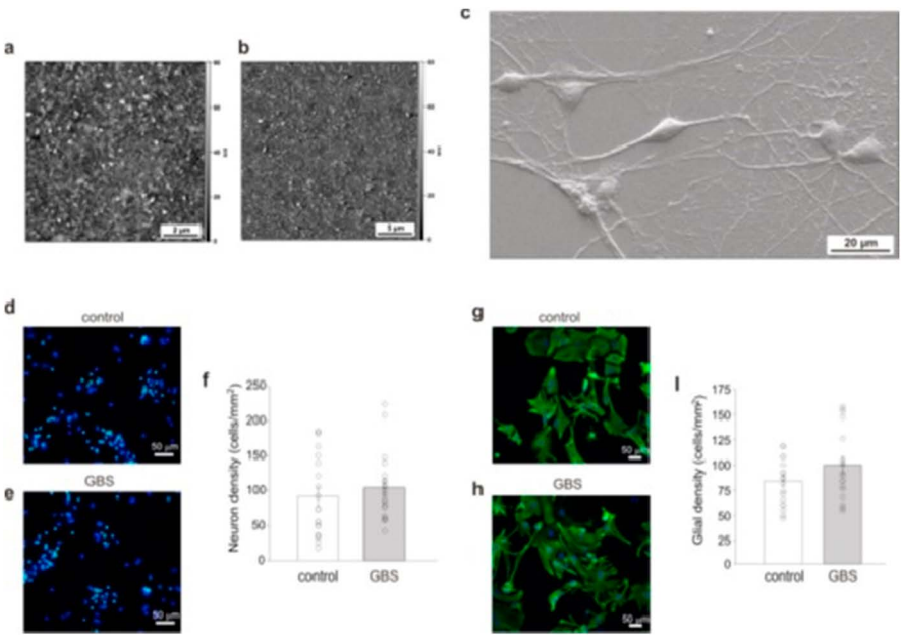

Figure 6.5 AFM images of (a) LPE-GBS and (b) BM-GBS. (c) SEM image of dissociated hippocampal neurons grown onto LPE-GBS. Immunofluorescence staining of cultures developed on (d) control and (e) LPE-GBS substrates, marked for neurons (NeuN, green) and nuclei (DAPI, blue). (f) Plot summaries of neuronal density in the two GBSs culturing conditions. Immunofluorescence staining for glial cells (marked for GFAP, green; DAPI in blue) on (g) control and (h) LPE-GBS. (i) Plot summaries of glial cells density in the two GBSs' culturing conditions. Histograms are mean ± standard error. Reprinted from ref. 70 with permission from American Chemical Society, Copyright 2016.

was deposited on electrically insulated substrates. These biophysical changes caused a significant shift in neuronal firing phenotypes and affected network activity.[17]

GR microelectrode arrays (GRMEAs) have also been studied as neural interfaces.[71] The first GRMEA was reported by Park *et al.*[72] and consisted of a transparent graphene-based, carbon-layered device. The authors demonstrated that the GRMEA was successfully implanted on the brain surface in rodents and, in addition to direct optogenetic stimulation and fluorescence imaging at the microelectrode sites, they were able to detect high resolution neural signals *in vivo*.[72] Furthermore, Kuzum *et al.*[73] combined transparent GRMEAs with calcium imaging. The combination of both techniques revealed temporal and spatial characteristics of high-frequency bursting activity and synaptic potentials in hippocampal slices with high precision.[73] GR was also used by Kireev *et al.* for the development of flexible MEAs.[74] Extracellular recordings were tested by measuring electrical activities from acute heart tissue and cardiac muscle cells. GRMEAs fabricated in a dense array on a flexible polyimide substrate showed excellent robustness and extracellular recordings with excellent signal-to-noise ratios of up to 65 ± 15.[74] Using a flexible array of GR field-effect transistors, Hébert *et al.*[75] developed neural interfaces that were placed on the surface of the cerebral cortex in rats for the recording of neural activity, exhibiting a signal-to-noise ratio similar to platinum black electrodes in the frequency range below 100 Hz and a recording limit for signals above 1 kHz. Additionally, the implants successfully detected slow–wave activity, synchronous epileptic activity and audio-visual responses in rats, showing similar performance to poly(3,4-ethylenedioxythiophene) polystyrene sulfonate (PEDOT:PSS) organic electrochemical transistors, which are currently considered the state-of-the art flexible transistor technology for neural recordings.[75] Thunemann *et al.*[76] reported transparent GR-microelectrode arrays that were employed to enable crosstalk-free integration of three different modalities, two-photon imaging, optogenetic stimulation and electrical recording experiments at the same time. Such technology allowed simultaneous mapping of surface local field potentials and high-resolution two-photon imaging of neuronal calcium transients *in vivo*.[76]

Due to its highly reactive surface, single layer GR production is difficult and challenging. For this reason, graphene oxide (GO) is sometimes preferred for biological applications. Based on the previous studies on CNTs about the influence of surface charge on neurite outgrowth and branching,[13] and considering that GR-based materials and CNTs have similar properties, Tu *et al.*[77] reported the influence of surface charge on GO-based materials. To this end, carboxylated GO was chemically modified with amino- ($-NH_2$), poly-*m*-aminobenzene sulfonic acid- ($-NH_2/-SO_3H$), or methoxyl- ($-OCH_3$) terminated functionalities changing its surface charge. Primary rat hippocampal neurons were cultured on the resulting GO-based substrates confirming that, as in CNTs, the outgrowth and branching of neuronal processes can be controlled through this method. Additionally, positively charged GO was found

to be more beneficial for neurite outgrowth and branching.[77] In a later study, Rauti *et al.*[78] performed a comparative study by exposing primary neuronal cultures to equal amounts of large GO nanosheets (>200 nm) and small GO nanosheets (<200 nm). The authors demonstrated that small GO nanosheets specifically interfered with synapses in cultured neurons, reducing synaptic activity at glutamatergic synapses without affecting cell viability, while the larger sheets induced unequivocal hippocampal cell loss, thus hampering any further evaluation of membrane/flake interactions.[78] Following these studies, recently, Musto *et al.*[79] investigated the CNS tissue reactivity upon prolonged exposure to GO nanosheets in 3D organotypic spinal cultures. The glial responses to small GO nanosheets' exposure were investigated by immunofluorescence and confocal microscopy, focusing on resident microglia, tested in organotypic spinal slices and in isolated neuroglia cultures. The authors concluded that long-term accumulation of small GO sheets affected resident microglia and may induce a subtle, although chronic, reactive state, potentially trimming down synaptic activity, although in the absence of an effective activation of inflammatory response and in the absence of neuronal cell death.[79]

One of the main goals in neuroscience is focused on the development of interfacing materials that cause less or no neuroinflammation. As in CNTs, 3D graphene culture systems (3D GR) represent a more physiologically accurate model than traditional 2D cultures (2D GR).[66,80]

The first reported application of a 3D porous GR foam in neuroscience was reported by Li *et al.*[81] as a novel scaffold for neural stem cell growth *in vitro*. The 3D scaffolds not only supported neural stem cell growth, but also kept cells at a more active proliferation state with upregulation of Ki67 expression than that of 2D GR films. These findings suggested the great potential of 3D GR scaffolds for their application in neural tissue engineering and neural prostheses.[81] Song *et al.*[82] conducted a comparative study to investigate the pro- and anti-inflammatory responses of microglia on 2D GR films or 3D GR foam culturing systems. In the brain, most of the damage caused by nanomaterials is caused by the microglia, a macrophage-like, phagocytic cell that is normally inactive unless confronted with potentially damaging foreign chemicals (xenobiotics). The results indicated that 3D GR elicited milder neuroinflammation on microglial cells in comparison to 2D GR, which provided new insights into the effects of the material's topographical structure in inflammatory behaviors.[82] Using dissociated hippocampal neurons, Severino *et al.*[83] compared the properties of cultures grown on flat 2D substrates with those grown on 3D GR foam scaffolds. After one week of culture, moderate synchronous activity was observed in 2D networks, while the spontaneous electrical activity of GR 3D networks was more synchronous. The results showed that dimensionality determines the properties of neuronal networks. Several properties were identified and two of them were of particular importance in the study: firstly, the coexistence of segregated and global electrical activity, and secondly, the existence of neuronal assemblies that change their degree of correlated activity both in time and in space,

generating a variety of rhythms.[83] In a recent study, 3D scaffolds consisting of hybrid GR hydrogels were employed to support the growth of living primary neurons,[84] demonstrating that GR improves the neuronal biocompatibility of 3D scaffolds. López-Dolado *et al.*[85] reported the first work concerning the study of *in vivo* tissue responses of GR porous 3D scaffolds. Here, the 3D scaffolds were implanted at an injured rat spinal cord and the generated subacute tissue response was explored. The results evidenced the capacity of these scaffolds to regain tissue integrity after injury and to prevent additional scarring, avoiding the extension of the lesion.[85]

Beyond the use of 3D GR based scaffolds for *in vivo* systems, further *in vivo* experiments involving the use of GR were reported by Defterali *et al.*[86] who studied the biocompatibility of thermally reduced GR oxide (rGO) with neurons and glia, as well as with the generation of new neurons in the adult brain *in vivo*. After direct injection into the brain, rGO was demonstrated to be a permissive substrate for the survival of neurons and astrocytes as well as for the generation of new neurons.[86] In a recent study, Mendonça *et al.*[87] used an *in vivo* rat model to explore the effects of PEGylated rGO (rGO-PEG) on the key components of the blood–brain barrier (BBB), such as astrocytes and endothelial cells. The results suggested dose- and time-dependent toxicity of rGO-PEG for key components of the BBB. After intravenous injection of rGO-PEG, a notable long-lasting downregulation of astrocyte markers (GFAP and connexin-43), endothelial tight (occludin) and adherens (β-catenin) junctions and basal lamina (laminin) was observed, due to oxidative stress-mediated damage. The authors concluded that the attachment of PEG to rGO induced deleterious effects in comparison with the effects caused by non-PEGylated rGO.[87]

The studies reported here suggest that GR-based materials are promising for next generation bioelectronic systems, to be used as neural interfaces for the CNS. Their ability to integrate with the neural tissue, their flexibility and uncommon ability to support neural development in terms of growth and synaptic activity, make them ideal candidates for the future design of electrically functional implants that are promising as neural interfacing materials.

6.2.3 Other Carbon-based Materials

To a lesser extent, other carbon nanomaterials have been also employed as neural interfaces for the CNS.[7,12] For example, fullerene, which can be considered the third allotrope of carbon after graphite and diamond, attracted great attention during the early years of carbon-based neural interfacing materials.[88] However, the rising concerns regarding fullerenes' toxicity has contributed to a reduction of interest in clinical neuroscience. In particular, their ability to induce lipid peroxidation has caused serious concern.[89]

Fullerenes are zero-dimensional materials that include a broad family of carbon-based molecules with different symmetries and interesting chemical and physical properties. Among them, the most common fullerene, buckminsterfullerene, consists of 60 carbon atoms arranged in a series of

interlocking hexagonal shapes, and was the first and the smallest stable fullerene isolated.

Fullerenes were pioneering nanomaterials investigated *in vivo* in the CNS, and were the first found to distribute in the brain after systemic administration.[90] Intravenous administration of ^{14}C-radiolabeled carboxylated-C_{60} derivative in rats revealed that the material was able to cross the BBB despite its high molecular weight. No toxic effects were observed after intravenous administration, while toxicity was observed after intraperitoneal injection. Later results demonstrated that C_{60} displays acute toxicity when employed locally in the CNS at high concentrations, thus, its dilution in the bloodstream seems to supress the inflammatory response.[91]

Basso *et al.*[92] employed a water-soluble adamantyl-oligoethyleneglycol-fullerene hybrid (ABS-75) attached to an *N*-methyl-D-aspartate receptor antagonist, which combines antioxidant and anti-excitotoxic properties to block axonal degeneration; a process that plays an important role in the progressive neurological disability in multiple sclerosis. After the disease onset, *in vivo* experiments with fullerene ABS-75 treatment reduced the clinical progression of chronic experimental allergic encephalomyelitis (EAE). This effect was associated with the reduced axonal loss and demyelination in the spinal cord.[92] Norton *et al.*[93] synthesized a panel of fullerene derivatives to test their ability to prevent the release of mediators from activated mast cells thus blocking their effects that can cause allergic diseases. The results evidenced that fullerene derivatives are potent reactive oxygen species (ROS) scavengers that produce oxidative stress mediating mast cells signaling and multiple sclerosis pathology.[93] Their antioxidant ability has been also used recently to inhibit organophosphate (OP)-induced acetylcholinesterase that induces toxicity leading to neuronal damage.[94]

Despite the promising results that have been observed during the past few years in the application of fullerenes for interfacing the CNS, their accumulation in organs, the difficulties to be excreted from the body, and their toxicity, are major concerns that nowadays have limited their applications in the biomedical field. For this reason, fullerenes are currently considered the "past" of carbon nanomaterials in the CNS research field.[7,12]

Diamond has been also widely employed for neural interfacing. It is the hardest known carbon-material, shows the highest bulk modulus and highest thermal conductivity, is a wide band gap semiconductor showing therefore high electrical resistivity and shows broad optical transparency from ultraviolet to infrared. Nanodiamonds (NDs) are diamonds with a size below 1 micrometer. One of the most important features of NDs is their chemical and biochemical inertness, being considered non-cytotoxic biocompatible materials, the reason for which they have been also widely explored for applications in the biomedical field.[95,96] In the field of neural interfaces the major goal is the development of materials with long-term stability and high-fidelity connections with neurons; in this direction, diamond's longevity, biocompatibility and biochemical inertness make it a highly promising material with which to achieve this goal.[97]

The chemical functionalization of the ND surface has been widely employed to modify its conductive properties allowing the fabrication of biomedical electronic devices.[96] Thus, phosphorus-doped diamond-like carbon has been demonstrated to direct neuronal growth when primary cortical neurons are cultured on it.[98] Similarly, novel electrode materials consisting mainly of boron-doped diamond microelectrodes transferred to a flexible substrate were developed by Bergonzo *et al.*[99] The main goal of these studies was the integration of diamond on flexible substrates, which represents a major challenge for the retinal implant community. This successful method has been used to fabricate a range of diamond-based MEA types enabling the fabrication of flexible implants for retinal stimulation.[100] Furthermore, later studies have demonstrated that despite the toxicity of elemental boron, when used as a dopant in diamond it has no adverse effect on cell survival, neurite formation and the apoptosis levels of cells.[101] Thus, boron has been one of the most widely used dopants employed to change the electrical conductivity of NDs for neuronal studies.[102]

Due to their unique electrical, chemical and mechanical properties, NDs have been also used for the development of biosensors aiming to record neuronal activity. Thus, Ariano *et al.*[103] reported the design and fabrication of devices based on hydrogen terminated conductive diamonds that were useful for the recording of extracellular activity of cultured neurons. GT1-7 cells cultured on the H-terminated diamond surface maintained their functional properties for several days. The recorded extracellular electrical activity matched that recorded by means of conventional MEAS.[103] In a different study, Chan *et al.*[104] reported the fabrication of polycrystalline boron-doped diamond-based microprobes that were used as electrode materials, providing a chemically stable surface for both chemical and electrical detections in neural studies. The probes were successfully implanted in the auditory cortex area of guinea pig brain for *in vivo* neural studies, showing a recorded signal amplitude of 30–40 μV with a duration of 1 ms.[104]

Recently, Guarina *et al.*[105] employed fluorescent NDs (FNDs) to evaluate their effect on cultured hippocampal neurons, using MEA recordings. The advantage of FNDs is related to their photostability, that allows their monitoring along neuronal branches with high spatio-temporal resolution. Two different stages of culture development were evaluated (7 DIV for young cultures and 14 DIV for mature cultures), concluding that the firing frequency of neurons was differently affected depending on the developmental stage of incubation. When FNDs were applied at 14 days *in vitro* they drastically reduced the neuronal firing frequency.[105]

Although the current results provide evidence that diamond is a promising material for the fabrication of neural interfaces for neuroscience studies, this material is still of limited use owing to its extreme hardness, lack of ductility and weldability. Therefore, future work and the development of new techniques is still needed to improve the performance of diamond as a substrate material for the construction of better performing diamond-based interfaces.[7]

Carbon nanofibers (CNFs) are defined as cylindrical nanostructures with graphene layers constructed in the shape of cups, cones, or plates, showing an average diameter of *ca.* 100 nm and an average length of 50–200 μm.[106] CNFs have emerged in recent years as promising materials for the development of neural interfaces due to their superior electrical, chemical, and physical properties, such as chemical stability and inertness in physiological environment, biocompatibility for long-term implantation due to their covalent carbon structure, electrical conductivity for signal detection and high surface-to-volume ratio, which reduces contacting electrical impedance.[107] Thus, multiple CNF-based materials have been developed as electroconductive scaffolds to facilitate communication with the CNS through neural interfaces.[107]

In early studies, CNFs were proposed as coating materials for neural prosthetic devices, as they show good compatibility with neuronal cells and demonstrate to favor neuronal *vs.* glial/astrocytic proliferation.[108]

Vertically aligned carbon nanofiber (VACNF) electrode arrays have been also widely employed for the development of electrodes with small size and excellent electrical conductivity.[109] Thus, Nguyen-Vu *et al.*[110,111] fabricated a VACNF electrode array coated with a thin film of electronic conductive polypyrrole polymers for neural implants. The authors demonstrated that the nanoelectrode array showed a stronger 3D structure with better electrical conductivity and allowed an intimate neural–electrical interface between cells and nanofibers, crucial for the development of neural prosthesis. Two types of VACNF electrode arrays were also reported by McKnight *et al.*[112] to characterize the performance of these arrays for electroanalytical measurement of several easily oxidizable neurotransmitters. The authors demonstrated that these VACNF arrays were responsive for the detection of oxidized species generated by the cultured cells.[112] Furthermore, in a later study, the same authors showed that the recording of spontaneous and induced neuroelectrical activity in organotypic hippocampal slice cultures was possible with ultramicroelectrode VACNF arrays.[113] Recently, Guo and collaborators reported a neural probe consisting of a polymer composite with CNFs aligned during thermal drawing.[114] The as-prepared microelectrode contributes to a drastic improvement of electrical conductivity by two orders of magnitude compared to conventional polymer electrodes. Additionally, it has a miniature footprint with a size-reduced recording size that matches single neurons yet maintaining impedance value to capture neural signals. Its capability for both acute and chronic recording, along with biocompatibility and minimal tissue response over long implantation periods in wild-type mice was demonstrated.[114]

The above reported results and the promising properties of CNFs suggest that these materials show a promising future for the development of smart systems for the diagnosis and treatment of neurological diseases, allowing the modulation of neural activity by neurostimulation and showing real-time detection of electrical and chemical information from the nervous system.

6.3 Carbon Nanomaterials as Biocompatible Substrates for Stem Cell Growth and Differentiation

6.3.1 Stem Cells in Neuronal Tissue Engineering

Over the past few years, both embryonic and adult stem cells have been identified as ideal cell sources in the field of tissue engineering and regenerative medicine. Although several tissues are important sources of therapeutically relevant differentiated cells, an inevitable problem is the difficulty of harvesting sufficient cells for implantation. Lineages such as neurons and cardiac cells, being terminally differentiated and non-regenerative, impose the biggest challenge. In this light, pluripotent stem cells have attracted much attention due to their unique capabilities of self-renewal in an undifferentiated state for prolonged time as well as multilineage differentiation after proper stimuli.

The most explored adult stem cells are mesenchymal stem cells (MSCs), owing to their wide range of sources, ease of expansion *in vitro* and multilineage differentiation abilities. They are attractive, being readily isolated from bone marrow, umbilical cords, umbilical cord blood, lacrimal glands, glomeruli and other easily accessible sources, such as adipose tissue and peripheral blood. Advances in stem cell biology have shown that adult human mesenchymal stem cells (hMSCs) can differentiate into a variety of connective tissue cells, including osteocytes, chondrocytes, adipocytes, myocytes and even *trans*-differentiate into other cell types like hepatocytes[115] and neurons.[116] in response to appropriate biological cues *in vitro*. In addition, they possess immunoregulation abilities that further expand their clinical applications, for instance in inflammatory diseases.[117] They have been identified also as key components of the hematopoietic stem cell (HSC) *niche*, *i.e.*, the extracellular microenvironment that surrounds HSCs and ensures their viability and self-renewal.[118] This kind of cell is easy to access and does not present ethical issues as is the case for embryonic stem cells, although it is clear that further stringent definitions of MSCs are required to ensure progress in the understanding of such a heterogeneous cell population.[119] In recent years, adipose tissue-derived stem cells (ADSCs) have gained great attention as a SC source. This kind of SC is similar to the MSCs, but the cells are obtained from the stromal-vascular fraction of the fat tissue. A third kind of SC used is the hematopoietic stem cell (HSC), which is found in bone marrow. This kind of blood cell gives rise to all kinds of blood cells. Finally, another well-known SC is the neuro-stem cell (NSC) that can differentiate into an amazing array of neurons and neural-support cells such as oligodendrocytes and astrocytes.[120]

In most native tissues, cells are contained within a specific tissue, three-dimensional (3D) extracellular matrix (ECM), which comprises a complex network of nanoscale protein fibers forming hierarchically structured local microenvironments that play a pivotal role in maintaining tissue homeostasis

and health.[121] Cellular communication, transport of oxygen and nutrients, and removal of cellular metabolism waste require such an environment, where cellular orientation can be polarized and movement of contents can be directional. Hence, in tissue engineering, a 3D framework is needed to organize the cells into a higher ordered assembly so as to achieve the desired tissue function. In addition, most of the engineered tissues/organs need support, which could be provided by a "scaffold", for their correct organization from cell constituents. Stem cell fate is controlled by a complex set of signals found in the cellular microenvironment. These signals can exist in the form of soluble factors, the extracellular matrix (ECM), the biophysical environment and inter cellular contacts instructing whether the stem cell should undergo apoptosis, proliferate, differentiate or remain quiescent. It is generally hypothesized that a close imitation to the natural ECM could provide a scaffold with a more conducive environment to support the adhesion, migration, proliferation and differentiation of stem cells.[122]

Typically, the classical method to control stem cell differentiation is by using biochemical factors. However, in recent years there has been growing evidence that the physical microenvironment where the cell resides (stem cell *niche*) is also capable of directing stem cell fate by other means. Investigation of the mechanotransduced responses of stem cells subjected to mechanical interaction with nanoscale features has led to the identification of other key factors of a physical nature, such as the scaffold stiffness, roughness and porosity, playing a pivotal role in directing stem cell fate.[123] It is noteworthy that cellular response is usually accompanied by alterations in cellular morphology. In fact, changes in cell shape are often used as an early indicator of modulated cell functions.

It would be ideal to eliminate the need for chemical and biological agents to guide stem cell differentiation: they are expensive, their half-lives are short (in minutes) and the dose that is effective *in vitro* might not mirror the *in vivo* requirements. More importantly, there is no well-recognized way of controlling the optimal concentrations of the inducers for efficient differentiation with reduced or no side effects *in vivo*. The majority of studies nowadays use static culture where the period of medium changes and diffusion of growth factors vary between laboratories. Uncertainties in using these biomolecule approaches, such as safety issues, still exist.[124] In this respect, the observed commitment of hMSCs guided by nanomaterials in the absence of additional biochemical inducing agents is a major advancement of stem cell application for tissue engineering.[125,126] Indeed, working at the nanoscale offers unprecedented opportunities to tailor the scaffold properties and control stem cell fate.

Tissue engineering requires complex interactions between the SC, the growth factors and the ECM. The secret is to develop scaffolds that mimic the ECM surface, thus providing to the SC the biomaterial instructions to afford their best adaptation and modify their fate accordingly. In that line, nanomaterial-based scaffolds have become promising candidates to make the desired interactions happen, due to their large surface area and easy

interaction with nano- and micrometric systems. Beyond their biocompatibility, scaffolds are stable once they are implanted, and allow the homing, proliferation and differentiation of the SC they are carrying. In particular, based on the composition and structure, the scaffolds would transmit specific signals to cells that these will decode into biochemical signals. Thus, surface topography, mechanics, morphology, and electrical properties are key features for directing cell fate.[127]

The chemical arrangement of the nanomaterial surface is a key feature influencing the characteristics of the surface and, accordingly, the type of stem cell nanomaterial interaction.[128] First of all, considering the chemical nature of the nanomaterial surface that comes into contact with stem cells, organic surfaces often appear preferable over inorganic alternatives.[129] Secondly, the introduction of minimal adhesive motifs (*e.g.*, integrin peptide ligands) has to follow precise parameters in terms of nanoscale density and distance between ligand clusters. Although there is a consensus on such general requirements in order to achieve the appropriate formation of focal adhesion and cell spreading, the exact numbers (*i.e.*, how many ligand units per cluster, distance amongst clusters, and geometrical design of clusters surface topography) vary greatly, depending upon the experimental settings.[130] Thirdly, surface roughness of the nanomaterial scaffolds also plays a crucial role in stem cell substrate interaction. It was postulated that nanoscale surface roughness resembling the nanoarchitecture of the natural ECM increased the opportunity for protein adsorption on scaffolds, thus facilitating stem cell survival and differentiation.

Due to the complexity of the human nervous system and inherent lack of regenerative capacity, disorders affecting the central nervous system and the associated loss of function are difficult to treat. Stem cells with the potential for neural differentiation have long been viewed as a potential therapeutic avenue for treating many of these disorders. In addition to clinical transplantation, stem cells offer a unique opportunity to study neurological disease *in vitro*.[131] The molecular mechanisms underlying human disease are incompletely understood, particularly in the nervous system. This is in part due to the lack of suitable models that recapitulate the complex environment of human neural tissue. Animal models and *ex vivo* tissue slices often fail to fully recapitulate hallmarks of human disease due to fundamental biological differences between species. Despite the progress made, precisely defined environments will need to be engineered to induce the specific differentiation of stem cell populations to mature, functional neural cell populations or the formation of reproducible tissue models.

At least on paper, carbon nanomaterials such as carbon nanotubes and graphene *etc.*, possess all the features for being ideal substrates for neuronal cells: they are conductive, they confer a certain nanotopography to the substrate where they are incorporated or deposited and they are biocompatible. They have indeed been demonstrated to be such a good terrain for the survival of these kinds of cells, as illustrated in the previous paragraph. Furthermore, they can be chemically functionalized to incorporate useful

domains such as growth or differentiating factors and this can be of paramount importance when dealing with the idea of supporting the survival of stem cells. In the following paragraphs we will explore the most significant studies involving the main classes of different CNMs and their peculiar capacity of hosting stem cells.

6.3.2 Carbon Nanotubes

During the last decade, a variety of scaffolds manufactured from nanofibers, nanotubes and nanoparticles have been investigated to manipulate stem cell fate. Within the different biocompatible natural or synthetic materials that have been studied as candidates for stem cell engineering, carbon nanotubes (CNTs) have stood out as excellent candidates.[132] Their anisotropic morphology and especially their unique physical and chemical properties offer a tremendous opportunity to make a qualitative leap forward in the progress of innovative therapeutic solutions, although their clinical translation is not trivial.[133]

Given that CNTs possess a nanostructure similar to neuronal processes (axons and dendrites), numerous studies have documented the unexpected and exciting impact of CNTs on neuronal signaling. The molecular mechanisms driving these phenomena, however, remain elusive to date. In a recent study, CNT multilayers fabricated using the layer-by-layer assembly of negatively charged MWCNTs and positively charged poly(diallyldimethylammonium chloride) (PDDA) provided a permissive substrate for neuronal differentiation, neurite outgrowth and electrophysiological maturation of NSC-derived neurons.[134] This study postulated that signal transduction—the process by which physicochemical stimuli of the CNT-multilayered substrate were transmitted through a cell as a series of molecular events—most commonly involved protein phosphorylation catalyzed by protein kinases, which were ultimately integrated into the cellular responses.

One of the main characteristics that CNTs confer to scaffolds is the nanotopological feature of the surface that can be tuned by choosing the appropriate size and chemical functionalization. There are studies that support a key role of nanomaterial surface roughness for cell adhesion and tissue regeneration. For instance, the surface nano-roughness displayed by single-wall CNT films used as scaffolds for MSC culture was suggested as the responsible factor for the transient upregulation of neuronal markers, opening the way for nanomaterial-driven stem cell differentiation without the need for soluble (bio)chemical inducers.[135] Three-dimensional (3D) micropatterned CNT templates are used to effectively direct human neurite stem cell growth. By exploiting the mechanical flexibility, electrical conductivity and texture of the 3D CNT micropillars, a perfect environment is created to achieve specific guidance of human neurites, which may lead to enhanced therapeutic effects within the injured spinal cord or peripheral nerves. It is found that the 3D CNT micropillars grant excellent anchoring for adjacent neurites to form seamless neuronal networks that can be grown to any arbitrary shape and size (Figure 6.6).[136]

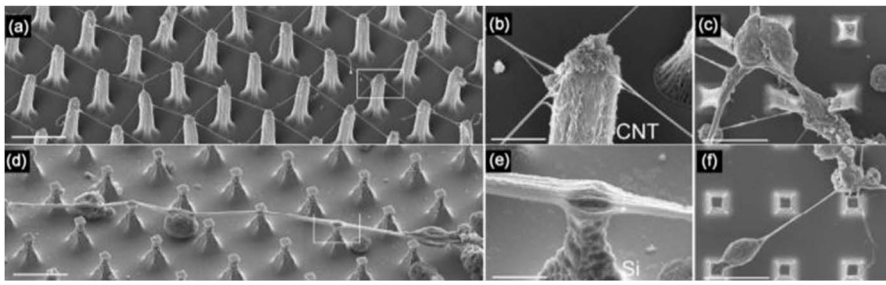

Figure 6.6 SEM images of human NSCs on 3D micropillared arrays of CNTs and Si. (a) Well-ordered squared pattern network of neurites stretching between the arrayed pillars of CNTs. Scale bar, 5 μm. (b) Neurites anchored at different locations of the same CNTs pillar. Scale bar, 2 μm. (c) Human NSCs deforming the mechanically flexible pillars of CNTs. Scale bar, 10 μm. (d) A single tight bundle of microtubules spanning across Si micropillars. Scale bar, 5 μm. (e) Tip of a Si pillar wrapped around by the tight bundle of microtubules. Scale bar, 2 μm. (f) Human NSCs attached to rigid micropillars of Si. Scale bar, 10 μm. Reproduced from ref. 136 with permission from Macmillan Publishers Ltd, Copyright 2019.

CNT elongated morphology gives one the option to create anisotropic materials where the nanostructures can be ordered and aligned directionally. Their incorporation into scaffolds by means of suitable nanomaterial processing methods, such as electrospinning, allows for the hierarchical translation of the anisotropic features across several size scales, whilst maintaining a high level of porosity within the scaffold to ensure good exchange of nutrients and catabolites.[137] This approach appears particularly promising also for the regeneration of anisotropic tissue, such as cardiac[138] or skeletal myofibers.[139]

CNT/poly-L-lactic (PLLA) composite scaffolds were applied to enhance neural differentiation of mouse embryonic stem cells (ESCs) even in the absence of soluble inductive factors.[140] Thin film scaffolds composed of biocompatible polymer poly(acrylic acid) or silk grafted with CNTs were also shown to promote human ESC-derived embryoid body (EB) differentiation into neural cells with heightened cell viability.[141] In addition to nanofibrous materials and CNT composite scaffolds with random nanotopological features, well controlled nanoscale surface patterns such as nanoscale ridge/groove arrays also improved significantly the differentiation of human ESCs into neural lineages without any soluble inductive factor.[142] Interestingly, human ESCs cultured on such nanoscale ridge/groove arrays preferentially differentiated into neurons but not glial cells, such as astrocytes. Such selective suppression of glial cell formation is desirable for potential applications in therapies for spinal cord injury, as astrocytes are known to contribute to glial scar formation, creating barriers to axons in the CNS.[143]

In 2018, a conductive polycaprolactone fumarate–carbon nanotube (PCLF-CNT) scaffold was synthesized using ultraviolet (UV)-induced photo-crosslinking for peripheral nerve regeneration applications. The embedding of CNT in PCLF appended several appropriate properties to the scaffold including improved surface roughness, reduced polymer impedance, decreased tensile modulus, and accelerated biodegradation ability. These properties not only increased PC12 cell growth and differentiation, but also promoted cellular migration and intracellular connections.[144] Also, Wang *et al.* observed that nanofibrous scaffolds composed of PLGA and carboxyl-modified MWCNTs (MWCNTs–COOH) support the proliferation, differentiation, maturation and neurite extension of PC12 cells.[145] More recently, the emerging technique of 3D printing has been applied to produce innovative CNT based substrates. Lee *et al.* designed 3D-printed electroconductive scaffolds made of amine-functionalized MWCNTs incorporated in a poly(ethylene glycol) diacrylate (PEGDA) matrix to evaluate NSC differentiation after applying a 500 μA current.[146] The result of bioassays indicated that this electroactive scaffold, coupled with electrical stimulation, exhibited significantly higher TUJ1 and glial fibrillary acidic protein expression relative to the bare PEGDA group without electrical stimulation. In a comprehensive study, Shao *et al.* prepared a multilayer of CNT nanocomposites *via* a layer-by-layer assembly of negatively charged MWCNTs and positively charged poly(dimethyldiallylammonium chloride). These nanostructures regulated the interactions between neural cells and nanomaterials themselves, leading to increased neuronal differentiation, enhanced neurite outgrowth, and improved electrophysiological maturation of NSC-derived neurons (Figure 6.7).[134]

A relevant question arising from studies on the interactions between CNT-based nanomaterials and cultured stem cell behavior is which biochemical pathways are affected, and how. It would appear very reasonable to firstly probe for adhesion-dependent pathways, for instance those integrin-mediated,[147] as we can expect that such biochemical cascades will be activated once cells adhere on the nanomaterial scaffolds. Interestingly, Namgung *et al.* found that actin filaments aligned over ordered CNT networks, resulting in high cytoskeletal tension, and upregulation of a FAK-mediated RhoA/ROCK pathway.[148] Since RhoA/ROCK and FAK favor the advance of the cell cycle.[149]

Being electrically conductive materials, CNTs have been taken into consideration as ideal substrates for neuronal lineage differentiation of stem cells. Indeed, the excellent electrical conductivity of CNTs not only supports and directs stem cell differentiation toward neural lineages, but also promotes the signal transmission among neurons. For example, single-walled CNT (SWCNT) films were found to be highly biocompatible and supportive of hMSCs' growth for neural regeneration.[134] Laminin/SWNT thin films were found to support NSCs' proliferation and differentiation, as shown by the synaptic connections on differentiated NSCs.[150] In another study, neural stem cells have been cultured on a MWNT-based substrate produced by a

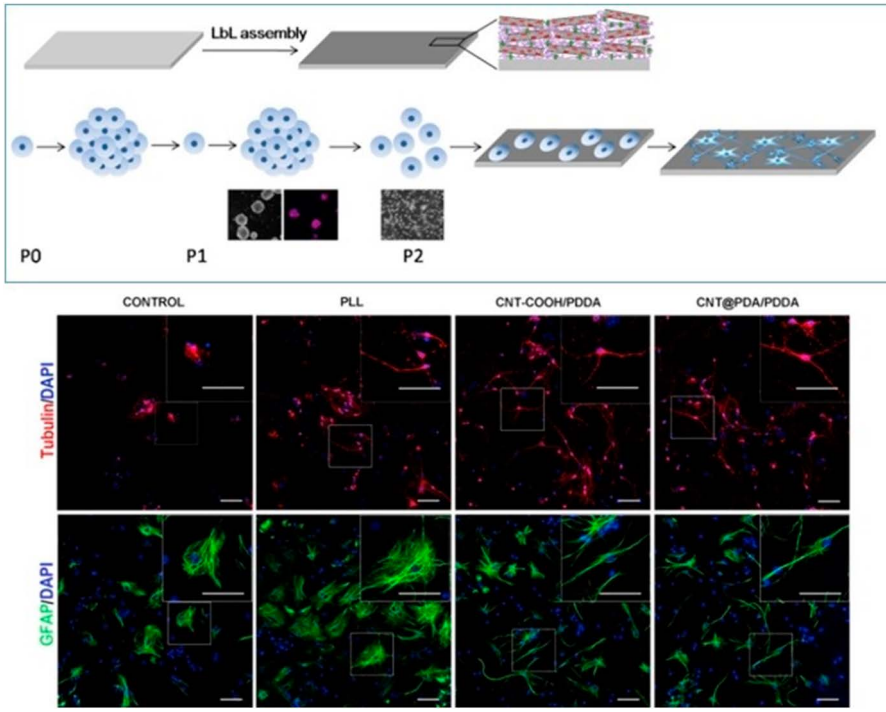

Figure 6.7 Upper part: Schematic diagram of the NSC differentiation on CNT-multilayered substrates. CNT multilayers were fabricated using the LBL assembly of negatively charged CNTs and positively charged PDDA. After being passaged twice, E14.5 NSCs (P2) were cultured on the CNT-multilayered substrates in the differentiation medium. Lower part: NSC differentiation on various substrates *in vitro*. (A) Immunohistochemical staining of neurons (red, β III tubulin) and astrocytes (green, GFAP). Cell nuclei were stained using DAPI. Reproduced from ref. 134 with permission from Elsevier, Copyright 2018.

LBL technique. These substrates not only induced differentiation of NSCs, but also allowed the electrical stimulation of cells that have shown how cells are able to establish synaptic connections.

Besides electrical conductivity, surface modifications of nanomaterial scaffolds are widely used to improve protein attachment and thus enhance stem cell proliferation and neuronal differentiation. CNTs are always reported to be modified with polymers: poly(methacrylic acid) grafted CNT films promoted hESCs' differentiation into neural cells, as seen in numerous synaptic vesicles with strong expression of motor neuron marker synapsin I on this platform;[151] poly(acrylic acid) grafted CNT (PAA-g-CNT) thin films enhanced neuron differentiation efficiency of hESCs according to the fluorescence image analysis stained with neuron specific marker tubulin III.[152] To evaluate scaffold toxicity, the cell viability analysis of hESCs on PAA-g-CNT films

after 5 days incubation was investigated. The PAA-g-CNT films did not show any detrimental effect on hESCs' growth and had no significant difference in cytotoxic effect with poly-L-ornithine (PLO) surface, a conventionally used substrate for hESCs to survive and differentiate.

6.3.3 Graphene

In recent years, graphene has taken over the leading role of carbon nanotubes in many fields of application. Due to the biocompatibility at low concentration and to the 2D nature with ultra-large surface area, GR and its oxide (GO) have recently captured interest as innovative cell culture substrates.

Despite having one of the highest Young's modulus (up to 1 TPa) among any known material, GR is remarkably not brittle. In addition, GR can be transferred onto any substrate, be it a flat or irregular surface; if the support is flexible, it can easily be bent into any required shape without damage to the graphene coating.[153] As a substrate for stem cell culture, GR has interesting effects on cell differentiation and, as observed for CNTs, it appears this is not just owing to its high modulus. Combined effects rather play a role, including graphene's ability to sustain lateral stress, thus providing the appropriate tension for optimal cytoskeleton anchoring.[154] This is consistent with another study that called for activation of integrin-mediated mechanotransduction pathways as a key factor leading to differentiation of NSCs cultured on a graphene-PCL hybrid nanofiber scaffold.

In recent years, numerous studies have demonstrated that GR and its derivatives are excellent cell culture platforms for adhesion, growth, proliferation and differentiation of various cells.[155,156] Shah *et al.* developed a GR-based nanomaterial for the design of hybrid nanofibrous scaffolds to guide rat NSCs' differentiation into oligodendrocytes.[157] The authors demonstrated that GO is an effective coating material in combination with electrospun nanofibers for the selective differentiation of NSCs into oligodendrocytes, even in the absence of inductive factors in the culture medium. They found that the GO coating promoted the overexpression of several integrin-related signaling molecules that are known to induce oligodendrocyte survival, differentiation and myelination. The superior electrical conductivity of GR, which effectively supplies the charge transport required for neuronal stimulation, suggests the strong potential of these carbon nanomaterials for nerve tissue engineering.

In 2019, Wang *et al.* modified the surface of *Antheraea pernyi* silk fibroin (ApSF)/poly(L-lactic acid-co-caprolactone) (PLCL) composite through an *in situ* redox reaction of GO. Results confirmed that rGO coating improved the electrical and mechanical properties of nanofibrous scaffold without destroying its nanoscale structure. Likewise, this scaffold created an ideal interface for SC migration, proliferation, myelination and PC12 cell differentiation under a DC electric field of 100 mV cm^{-1}.[158] Qing *et al.* fabricated a novel heterostructure composite scaffold based on aligned electrospinning

silk nanofibers coated on reduced GR paper (rGOP) with high conductivity and good biocompatibility.[159] The experimental results showed that this scaffold effectively enhanced oriented growth and neural differentiation of SH-SY5Y cells. SH-SY5Y is a human bone-marrow-derived cell line that is often utilized for neuronal differentiation *in vitro* (Figure 6.8).[160]

In another study, the coating of aligned PLLA nanofibrous scaffolds with GO significantly improved the growth of Schwan cells and induced PC12 cell differentiation and neurite growth.[161] In a study conducted by Guo and co-workers, both gene expression and immunofluorescence staining data suggested that a porcine acellular dermal matrix (PADM)–rGO hybrid can direct the neural differentiation of rat bone-marrow-derived mesenchymal stem cells (BMMSCs).[162] As shown by Rotman *et al.*, a conductive nerve guide channel consisting of the polymer poly(trimethylene carbonate) (PTMC) and the conductive filler rGO increased the rate of axonal regeneration, resulting in improved functional recovery of a transected peripheral nerve.[163] Biomolecules such as interferon-γ (IFN-γ) and platelet-derived growth factor (PDGF) are utilized for neuronal or oligodendrocyte lineage differentiation of stem

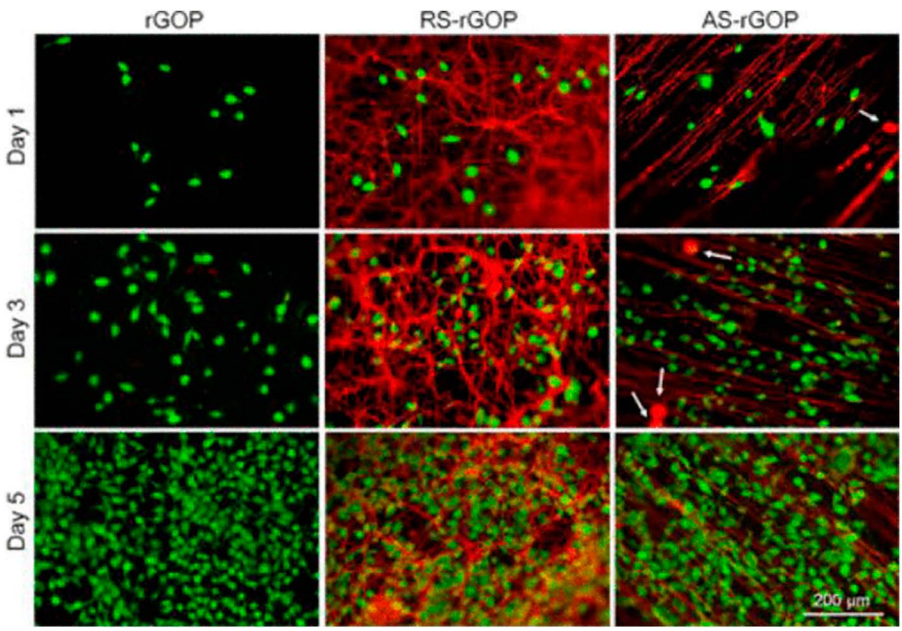

Figure 6.8 Viability and proliferation of SH-SY5Y cells on composite materials. (A) LIVE/DEAD fluorescent images of SH-SY5Y cells cultured on reduced graphene paper (rGOP), random silk nanofibers-rGOP (RS–rGOP) scaffold, and aligned silk nanofibers-rGOP (AS–rGOP) scaffold. The dead cells stained with red color are indicated by the white arrows. Reproduced from ref. 159 with permission from American Chemical Society, Copyright 2018.

cells. Weaver and Cui investigated the behavior of NSCs seeded on the surface poly(3,4-ethylenedioxythiophene) (PEDOT) and GO nanocomposites conjugated with IFN-γ and PDGF. This surface-modified conductive scaffold supported the higher cell density and improved neuronal differentiation as compared to unmodified surfaces.[164]

Another intriguing characteristic of GR is its capability to form a functional neural network. In a study by Tang *et al.*, neurospheres derived from NSCs were seeded on graphene substrates and after 14 days of culture the process of network formation was visualized by β-tubulin immunostaining.[165] Also, Li *et al.* discovered the great potential of using GR for neural interfacing, as it could promote neurite sprouting and outgrowth in primary culture of hippocampal neurons, enhance neural performance in networks differentiated by NSCs, and be used as an electric field stimulator for effective cerebral blood volume enhancement.[69] Novel applications of GR as a neural interface material seem to be encouraged by a study of Song *et al.*, who established anti-inflammatory effects of 3D GR foams cultured with murine microglial cells – the macrophages of the brain and spinal cord that are first activated by damage caused by nanomaterials.[82] The pioneering work described here demonstrates the potential of GR for applications in tissue engineering of the CNS. The rationale provided to explain such outcomes in cell culture includes not only the inherent mechanical properties of graphene substrates, but also selective protein adsorption and interaction with the aromatic surface. This is not surprising if we consider that, in the case of the more-studied CNTs, it is well-known that proteins can establish a variety of interactions with the graphitic surface, and with different results on their function preservation.[166] Similarly, it appears that proteins, and, generally, differentiation inducers, adsorb and pre-concentrate on both graphene and graphene oxide (GO), thus accelerating stem cell commitment to specific lineages.[167–170]

Similar to cell differentiation effects observed for protein adsorption on graphene, also cell proliferation can be favored through adsorption of cell adhesion promoters. For instance, the use of poly-D-lysine-coated surfaces with GR micropatterned *via* laser ablation allows for the formation of neural networks following specific designs. Polylysine adsorbs all over the surface, initially leading to random cell attachment; however, the polypeptide forms a thicker film on GR that affects neural cell movement, which over time becomes directional and with a preference towards GR-coated areas.[171]

Alternatively, even epigenetic reprogramming of fibroblasts to iPSCs can be promoted on GR substrates, suggesting that graphene can be used as an excellent nanomaterial for promoting cell fate changes associated with reprogramming and thus may give rise to various applications in iPSC-based regenerative medicine.[172]

GR nanomaterial engineering has also advanced towards 3D scaffolds, which generally perform better in stem cell culture than the 2D counterparts. Differentiation into artificial tissues of high complexity in terms of

different cell types is nowadays a reality. Specifically, culture of embryonic neural progenitor cells within 3D highly porous GO scaffolds over two weeks leads to the formation of highly interconnected neural networks from both neurons and glial cells, and rich on dendrites, axons and synaptic connections.[173] In addition, it has been shown that laminin-coated 3D graphene foams perform better than the 2D film analogs in NSC culture and differentiation. The foam scaffolds keep cells at a more active proliferation state as measured through upregulation of specific markers, owing to efficient exchange of nutrients and removal of cell metabolism products through the elaborate microtopography. Besides, the 3D scaffolds provide a much stronger charge injection ability than the 2D films for the electrical stimulation of cells. The conductive properties of graphene derivatives allow for unprecedented performance also towards the 3D printing of an artificial heart. 3D cellularized heart tissues can be prepared with a LBL technique by seeding alternate layers of cells and adhesive GO-bearing sheets, on a basal plane of GO-gelatin-acrylate hydrogel, thus forming a stand-alone multilayer cardiac tissue capable of spontaneous beating and programmable pumping.[174] Remarkably, 3D GR foams, but not 2D GR films, show anti-inflammatory properties, as they rescue neuroinflammation, probably through restriction of microglia morphological changes within the 3D nanotopography.[82] This finding could have resonance to reduce the typical issue of scar formation around neural implants.

Since stem cell biology is a relatively new field of research, several challenges must be overcome before pluripotent stem cells can be used in clinical settings. First, although stem cells provide an abundant resource of pluripotent cells, our present knowledge is limited in how to efficiently push all stem cells into a particular lineage during differentiation. Present methods in directed differentiation are laborious and low yield, even when supplemented with known growth factors. To overcome this issue, more studies are needed in order to elucidate the molecular and cellular mechanisms of cell differentiation and basic human developmental biology. Second, although induced pluripotent stem cells provide an attractive *in vitro* model for the study of diseases in a patient-specific manner, it is unclear whether results from these studies accurately predict diseases *in vivo*. Standard preclinical evaluation of potential drug candidates will still require *in vivo* testing. Third, since a hallmark characteristic of pluripotent stem cells is the ability to form teratomas,[175] stem cells must first be terminally differentiated before using them as cell-based therapies. It is unclear whether introducing induced pluripotent stem cell-derived cells into matched-patients will cause abnormal teratoma growth since the frequency of teratoma formation seems to directly correspond to the degree of immunosupression,[176] as shown in animal studies. Furthermore, it is unknown how the host environment will react to the introduced cells, regardless of the cell source, after cell transplantation. It might not be possible to rely on cell-based therapy as a mode to treat autoimmune diseases since the host immune system may also target

and destroy these transplanted cells, as they already eradicate endogenous host cells.

6.3.4 Other Carbon Nanomaterials

Fullerene C60 has been widely studied as a potential carrier in the drug delivery of a variety of substances. Water-soluble C60 derivatives with different types of linkages between the fullerene cage and the solubilizing addend have been synthesized in order to study their efficacy in repairing CNS damage and killing brain tumors.[177] *In vitro* experiments were performed on NSCs and it has been observed that, with some particular appendages on the fullerene cage, the derivatives increased the expression of β-tubulin (a neural precursor marker) and of MAP2 (a mature neuronal marker) than the control at 7 days, suggesting that they could promote the neuronal differentiation of NSCs. Furthermore, the same compounds might sustain the self-renewal of some neuroprogenitors. This activity is ascribed by authors to a direct action on mitochondrial functions.

Another interesting study demonstrates how highly aligned C60 nanowhiskers are able to support the adhesion, the proliferation and the differentiation in neurons of NSCs, proved by a significant upregulation of β-tubulin and MAP2.[178]

Nanodiamonds have been taken into consideration also for neural stem cells. The interaction of nanodiamond monolayers with hNSCs has been investigated by Taylor *et al.* The effect of altering the surface functionalization of nanodiamonds on hNSC adhesion and proliferation has shown that confluent cellular attachment occurs on oxygen terminated nanodiamonds (O–NDs), but not on hydrogen terminated nanodiamonds (H–NDs). Analysis of H and O–NDs by atomic force microscopy, contact angle measurements and protein adsorption suggests that differences in topography, wettability, surface charge and protein adsorption of these surfaces may underlie the difference in cellular adhesion of hNSCs reported.[179] The same authors have successively confirmed how the topography of ND monolayers is an exceptional platform for hNSC adhesion, proliferation and differentiation. The observed preference for neuronal differentiation was confirmed *via* semiquantitative polymerase chain reaction (PCR) and immunocytochemistry of spontaneous differentiated hNSCs, where inducing factors were removed from the culture medium. This study shows for the first time the spontaneous differentiation of hNSCs on NDs, with extremely promising results.[180]

Carbon nanofibers are close relatives of carbon nanotubes and share with them many interesting properties. From the point of view of the interaction with stem cells, CNFs have been interfaced with a variety of them in order to achieve an efficient differentiation process towards neural lineages.

Human endometrial stem cells (hEnSCs) have been cultured on electrospun CNFs with random and aligned topographies and it was demonstrated that hEnSCs could attach, proliferate and differentiate into neural cells on

both random and aligned CNFs.[181] However, the proliferation, differentiation and morphology of cells were affected by CNF morphology. Under the proliferative condition, hEnSCs showed lower proliferation on aligned CNFs than on random CNFs and on tissue culture plate (TCP) control. When cultured on aligned CNFs in neural induction media, hEnSCs showed significant upregulation of neuronal markers, NF–H and Tuj-1, and downregulation of neural progenitor marker (nestin) compared to that on random CNFs and on TCP. In contrast, hEnSCs showed higher expression of nestin and slight upregulation of oligodendrocyte marker (OLIG-2) on random CNFs compared to that on aligned CNFs and on TCP.

With a very elegant approach, nanostructured microfibers derived from reduced GO were synthesized by a dimensionally confined hydrothermal reduction strategy, which presents the possibility for the application of rGO in neuronal tissue engineering *in vitro*.[182] By assessing the cytocompatibility and differentiation of NSCs on the nanostructured rGO microfiber, the adhesion and proliferation of NSCs were studied, and the regulating effects of the differentiation of NSCs to neurons were proven. With its excellent cytocompatibility and protein adsorption ability, the nanostructured rGO microfiber can not only support NSCs' growth but also keep the cells at a more active differentiation state with Tuj1 expression while inhibiting the expression of GFAP. The experimental results prove that the nanostructured rGO microfiber can regulate the NSCs' differentiation into neurons. Furthermore, the NSCs can form a dense neural network around the nanostructured rGO microfiber, just like a functional nerve graft.

6.4 Conclusions

The great success achieved by carbon nanomaterials in a multitude of different technological applications is reflected also in the biological and biomedical field. The interest initially aroused by these materials as potential substrates for neuronal tissue regeneration has been materialized by many promising studies where their applicability has been confirmed. In this chapter a quick journey through the multiple possibilities offered by the most famous CNMs as CNTs and GR has been taken both for tissue regeneration and for neuronal stem cell proliferation and differentiation. Many challenges on the practical implementation of these materials still remain in terms of long-term applicability, potential toxicity and production costs, but it is clear that their interesting features will be further studied and exploited in the future by many research groups.

References

1. A. Kumar, A. Tan, J. Wong, J. C. Spagnoli, J. Lam, B. D. Blevins, G. Natasha, L. Thorne, K. Ashkan, J. Xie and H. Liu, *Adv. Funct. Mater.*, 2017, **27**, 1.

2. A. P. Ramos, M. A. E. Cruz, C. B. Tovani and P. Ciancaglini, *Biophys. Rev.*, 2017, **9**, 79.
3. S. M. Won, E. Song, J. Zhao, J. Li, J. Rivnay and J. A. Rogers, *Adv. Mater.*, 2018, **30**, 1800534.
4. P. Zarrintaj, M. R. Saeb, S. Ramakrishna and M. Mozafari, *Curr. Opin. Biomed. Eng.*, 2018, **6**, 99.
5. A. Mazzatenta, M. Giugliano, S. Campidelli, L. Gambazzi, L. Businaro, H. Markram, M. Prato and L. Ballerini, *J. Neurosci.*, 2007, **27**, 6931.
6. J. E. Collazos-Castro, J. L. Polo, G. R. Hernández-Labrado, V. Padial-Cañete and C. García-Rama, *Biomaterials*, 2010, **31**, 9244.
7. M. Baldrighi, M. Trusel, R. Tonini and S. Giordani, *Front. Neurosci.*, 2016, **10**, 250.
8. S. Marchesan, L. Ballerini and M. Prato, *Science*, 2017, **356**, 1010.
9. M. S. Dresselhaus, *Phys. Scr.*, 2012, T146.
10. A. Hirsch, *Nat. Mater.*, 2010, **9**, 868.
11. B. N. A. Kotov, J. O. Winter, I. P. Clements, E. Jan, S. Pathak, A. Mazzatenta, B. P. Timko, C. M. Lieber, M. Prato, R. V. Bellamkonda, G. A. Silva, N. Wong, S. Kam, F. Patolsky and L. Ballerini, *Adv. Mater.*, 2009, **21**, 3970.
12. R. Rauti, M. Musto, S. Bosi, M. Prato and L. Ballerini, *Carbon*, 2019, **143**, 430.
13. H. Hu, Y. Ni, V. Montana, R. C. Haddon and V. Parpura, *Nano Lett.*, 2004, **4**, 507.
14. J. Liu, F. Appaix, O. Bibari, G. Marchand, A. L. Benabid, F. Sauter-Starace and M. Waard, *Nanotechnology*, 2011, **22**, 195101.
15. S. Bosi, A. Fabbro, C. Cantarutti, M. Mihajlovic, L. Ballerini and M. Prato, *Carbon*, 2016, **97**, 87.
16. M. Barrejon, R. Rauti, L. Ballerini and M. Prato, *ACS Nano*, 2019, **13**, 8879.
17. N. Pampaloni, R. Rauti, M. Giugliano, D. Scaini and L. Ballerini, *Front. Neurosci.*, 2019, **12**, 953.
18. L. Radushkevich and V. Lukyanovich, *Zurn. Fisc. Chim.*, 1952, **26**, 88.
19. S. Iijima, *Nature*, 1991, **354**, 56.
20. S. Iijima and T. Ichihashi, *Nature*, 1993, **17**, 603.
21. S. Iijima, *Nature*, 1993, **363**, 605.
22. M. P. Mattson, R. C. Haddon and A. M. Rao, *J. Mol. Neurosci.*, 2000, **14**, 175.
23. E. B. Malarkey and V. Parpura, *Nanotechnol. Neurosci.*, 2007, **4**, 292.
24. V. Lovat, D. Pantarotto, L. Lagostena, B. Cacciari, M. Grandolfo, M. Righi, G. Spalluto, M. Prato and L. Ballerini, *Nano Lett.*, 2005, **5**, 1107.
25. A. V. Liopo, M. P. Stewart, J. Hudson, J. M. Tour and T. C. Pappas, *J. Nanosci. Nanotechnol.*, 2006, **6**, 1365.
26. G. Cellot, E. Cilia, S. Cipollone, V. Rancic, A. Sucapane, S. Giordani, L. Gambazzi, H. Markram, M. Grandolfo, D. Scaini, F. Gelain, L. Casalis, M. Prato, M. Giugliano and L. Ballerini, *Nat. Nanotechnol.*, 2009, **4**, 126.

27. P. Galvan-Garcia, E. W. Keefer, F. Yang, S. Fang, A. A. Zakhidov, R. H. Baughman and M. I. Romero, *J. Biomater. Sci. Polym. Ed.*, 2007, 1245.
28. K. Wang, H. A. Fishman, H. Dai and J. S. Harris, *Nano Lett.*, 2006, **6**, 2043.
29. T. Souier, S. Santos, A. Al Ghaferi, M. Stefancich and M. Chiesa, *Nanoscale Res. Lett.*, 2012, **7**, 630.
30. M. Shein, A. Greenbaum, T. Gabay, R. Sorkin, M. David-Pur, E. Ben-Jacob and Y. Hanein, *Biomed. Microdevices*, 2009, **11**, 495.
31. A. Shoval, C. Adams, M. David-Pur, M. Shein, Y. Hanein and E. Sernagor, *Front. Neuroeng.*, 2009, **2**, 1.
32. Y. Chen, H. Hsu, Y. Lee, H. Su, S. Yen, C. Chen, W. Hsu, T. Yew, S.-R. Yeh, D.-J. Yao, Y.-C. Chang and H. Chen, *J. Neural Eng.*, 2011, **8**, 34001.
33. M. Khraiche, N. Jackson and J. Muthuswamy, *Annu. Int. Conf. IEEE Eng. Med. Biol. Soc.*, 2009, 777.
34. M. David-Pur, L. Bareket-Keren, G. Beit-Yaakov, D. Raz-Prag and Y. Hanein, *Biomed. Microdevices*, 2014, **16**, 43.
35. M. K. Gheith, V. A. Sinani, J. P. Wicksted, R. L. Matts and N. A. Kotov, *Adv. Mater.*, 2005, **17**, 2663.
36. M. K. Gheith, T. C. Pappas, A. V. Liopo, V. A. Sinani, B. S. Shim, M. Motamedi, J. P. Wicksted and N. A. Kotov, *Adv. Mater.*, 2006, **18**, 2975.
37. K. Krukiewicz, D. Janas, C. Vallejo-Giraldo and M. J. P. Biggs, *Electrochim. Acta*, 2019, **295**, 253.
38. B. M. Baker and C. S. Chen, *J. Cell Sci.*, 2012, **125**, 3015.
39. M. Ghibaudo, L. Trichet, J. Le Digabel, A. Richert, P. Hersen and B. Ladoux, *Biophys. J.*, 2009, **97**, 357.
40. N. Alegret, A. Dominguez-Alfaro, J. M. González-Domínguez, B. Arnaiz, U. Cossío, S. Bosi, E. Vázquez, P. Ramos-Cabrer, D. Mecerreyes and M. Prato, *ACS Appl. Mater. Interfaces*, 2018, **10**, 43904.
41. B. X. Gui, J. Wei, K. Wang, A. Cao, H. Zhu, Y. Jia, Q. Shu and D. Wu, *Adv. Mater.*, 2010, **22**, 617.
42. S. Bosi, R. Rauti, J. Laishram, A. Turco, D. Lonardoni, T. Nieus, M. Prato, D. Scaini and L. Ballerini, *Sci. Rep.*, 2015, **5**, 9562.
43. E. R. Aurand, S. Usmani, M. Medelin, D. Scaini, S. Bosi, F. B. Rosselli, S. Donato, G. Tromba, M. Prato and L. Ballerini, *Adv. Funct. Mater.*, 2017, 1700550.
44. S. Yang, W. Guo, Y. Lin, X. Deng, H. Wang, H. Sun, Y. Liu, X. Wang, W. Wang, M. Chen, Y. Huang and Y. Sun, *J. Phys. Chem. C*, 2007, **111**, 17761.
45. C. Bussy, C. Hadad, M. Prato, A. Bianco and K. Kostarelos, *Nanoscale*, 2016, **8**, 590.
46. W. Lee and V. Parpura, *Brain Protection in Schizophrenia, Mood and Cognitive Disorders*. ed. M. Ritsner, Springer, Dordrecht, 2010, p. 325.
47. E. W. Keefer, B. R. Botterman, M. I. Romero, A. F. Rossi and G. W. Gross, *Nat. Nanotechnol.*, 2008, **3**, 434.
48. J. A. Roman, T. L. Niedzielko, R. C. Haddon, V. Parpura and C. L. Floyd J, *Neurotrauma*, 2011, **28**, 2349.

49. Y. Ni, H. Hu, E. B. Malarkey, B. Zhao, V. Montana, R. C. Haddon and V. Parpura, *J. Nanosci. Nanotechnol.*, 2005, **5**, 1707.
50. F. Vitale, S. R. Summerson, B. Aazhang, C. Kemere and M. Pasquali, *ACS Nano*, 2015, **9**, 4465.
51. K. E. Schroeder and C. A. Chestek, *Front. Neurosci.*, 2016, **10**, 291.
52. G. A. Silva, *Front. Neurosci.*, 2018, **12**, 843.
53. T. Kim, M. Cho and K. J. Yu, *Materials*, 2018, **11**, 1163.
54. E. Roh, B. Hwang, D. Kim, B. Kim and N. Lee, *ACS Nano*, 2015, **9**, 6252.
55. K. S. Novoselov, A. K. Geim, S. Morozov, D. Jiang, Y. Zhang, S. V. Dubonos, I. V. Grigorieva and A. A. Firsov, *Science*, 2004, **306**, 666.
56. Z. Xu, *Graphene. Fabrication, Characterizations, Properties and Applications*, ed. H. Zhu, Academic Press Books-Elsevier, 2018, p. 73.
57. M. Lamberti, P. Pedata, N. Sannolo, S. Porto, A. De Rosa and M. Caraglia, *Int. J. Immunopathol. Pharmacol.*, 2015, **28**, 4.
58. R. Alshehri, A. M. Ilyas, A. Hasan, A. Arnaout, F. Ahmed and A. Memic, *J. Med. Chem.*, 2016, **59**, 8149.
59. T. P. Dasari, S. Danielle, M. Asok and K. D. Paul, *Nano-Micro Lett.*, 2018, **10**, 53.
60. H. Zhang, G. Grüner and Y. Zhao, *J. Mater. Chem. B*, 2013, **1**, 2542.
61. Z. Liu, J. T. Robinson, X. Sun and H. Dai, *J. Am. Chem. Soc.*, 2008, **130**, 10876.
62. X. Sun, Z. Liu, K. Welsher, J. T. Robinson, A. Goodwin, S. Zaric and D. Hongjie, *Nano Res.*, 2008, **1**, 203.
63. P. Suvarnaphaet and S. Pechprasarn, *Sensors*, 2017, **17**, s17102161.
64. W. Cheng Lee, K. Ping Loh and C. Teck Lim, *Biomaterials*, 2018, **155**, 236.
65. A. Halim, Q. Luo, Y. Ju and G. A. Song, *Nanomaterials*, 2018, **8**, 736.
66. M. Bramini, G. Alberini, E. Colombo, M. Chiacchiaretta, M. L. Difrancesco, J. F. Maya-vetencourt and L. Maragliano, *Front. Syst. Neurosci.*, 2018, **12**, 12.
67. K. Kostarelos, M. Vincent, C. Hebert and J. A. Garrido, *Adv. Mater.*, 2017, **29**, 1700909.
68. G. Reina, J. M. González-Domínguez, A. Criado, E. Vàzquez, A. Bianco and M. Prato, *Chem. Soc. Rev.*, 2017, **46**, 4400.
69. N. Li, X. Zhang, Q. Song, R. Su, Q. Zhang, T. Kong, L. Liu, G. Jin, M. Tang and G. Chen, *Biomaterials*, 2011, **32**, 9374.
70. A. Fabbro, D. Scaini, V. León, E. Vázquez, G. Cellot, G. Privitera, A. C. Ferrari, L. Ballerini and M. Prato, *ACS Nano*, 2016, **10**, 615.
71. X. Du, L. Wu, J. Cheng, S. Huang, Q. Cai, Q. Jin and J. Zhao, *J. Biol. Phys.*, 2015, **41**, 339.
72. D. Park, A. A. Schendel, S. Mikael, S. K. Brodnick, T. J. Richner, J. P. Ness, M. R. Hayat, F. Atry, S. T. Frye, R. Pashaie, S. Thongpang, Z. Ma and J. C. Williams, *Nat. Commun.*, 2014, **5**, 5258.
73. D. Kuzum, H. Takano, E. Shim, J. C. Reed, H. Juul, A. G. Richardson, J. De Vries, H. Bink, M. A. Dichter, T. H. Lucas, D. A. Coulter, E. Cubukcu and B. Litt, *Nat. Commun.*, 2014, **5**, 5259.

74. D. Kireev, S. Seyock, M. Ernst, V. Maybeck, B. Wolfrum and A. Offenhäusser, *Biosensors*, 2017, **7**, 1.
75. R. Garcia-Cortadella, E. Masvidal-Codina, J. M. De la Cruz, N. Schäfer, G. Schwesig, C. Jeschke, J. Martinez-Aguilar, M. V. Sanchez-Vives, R. Villa, X. i. Illa, A. Sirota, A. Guimerà and J. A. Garrido, *Adv. Funct. Mater.*, 2018, **28**, 1703976.
76. M. Thunemann, Y. Lu, X. Liu, M. Desjardins, M. Vandenberghe, S. Sadegh, P. A. Saisan, Q. Cheng, K. L. Weldy, H. Lyu, S. Djurovic, O. A. Andreassen, A. M. Dale, A. Devor and D. Kuzum, *Nat. Commun.*, 2018, **9**, 2035.
77. Q. Tu, L. Pang, Y. Chen, Y. Zhang, R. Zhan, B. Lu and J. Wang, *Analyst*, 2014, **139**, 105.
78. R. Rauti, N. Lozano, V. León, D. Scaini, M. Musto, I. Rago, K. Kostarelos, M. Prato and L. Ballerini, *ACS Nano*, 2016, **10**, 4459.
79. M. Musto, R. Rauti, A. F. Rodrigues, E. Bonechi, C. Ballerini, K. Kostarelos and L. Ballerini, *Front. Syst. Neurosci.*, 2019, **13**, 1.
80. P. M. D. Watson, E. Kavanagh, G. Allenby and M. Vassey, *SLAS Discov.*, 2017, **22**, 583.
81. N. Li, Q. Zhang, S. Gao, Q. Song, R. Huang, L. Wang, L. Liu, J. Dai, M. Tang and G. Cheng, *Sci. Rep.*, 2013, **3**, 1604.
82. Q. Song, Z. Jiang, N. Li, P. Liu, L. Liu, M. Tang and G. Cheng, *Biomaterials*, 2014, **35**, 6930.
83. F. P. Severino, J. Ban, Q. Song, M. Tang, G. Bianconi, G. Cheng and V. Torre, *Sci. Rep.*, 2016, **6**, 26640.
84. C. Martín, S. Merino, J. M. González-Domínguez, R. Rauti, L. Ballerini, M. Prato and E. Vázquez, *Sci. Rep.*, 2017, **7**, 10942.
85. E. López-Dolado, A. González-Mayorga, M. T. Portolés, M. J. Feito, M. L. Ferrer, F. del Monte, M. C. Gutiérrez and M. C. Serrano, *Adv. Healthcare Mater.*, 2015, **4**, 1861.
86. Ç. Defteralı, R. Verdejo, L. Peponi, E. D. Martín, R. Martínez-Murillo, M. Á. López-Manchado and C. Vicario-Abejón, *Biomaterials*, 2016, **82**, 84.
87. M. Culturato, P. Mendonça, E. S. Soares, M. B. de Jesus, H. J. Ceragioli, A. G. Batista, J. Molnár, I. Wihelm, M. R. Maróstica, I. Krizbai and M. A. da Cruz-Höfling, *Mol. Pharm.*, 2016, **13**, 3913.
88. J. L. Gilmore, X. Yi, L. Quan and A. V. Kabanov, *J. Neuroimmune Pharmacol.*, 2008, **3**, 83.
89. C. M. Sayes, A. M. Gobin, K. D. Ausman, J. Mendez, J. L. West and V. L. Colvin, *Biomaterials*, 2005, **26**, 7587.
90. S. Yamago, H. Tokuyama, E. Nakamural, S. Kananish, K. Sueki, S. Enomoto and F. Ambe, *Chem. Biol.*, 1995, **2**, 6.
91. A. M. Lin, S. Fang, S. Lin, C. Chou, Y. Luh and L. Ho, *Neurosci. Res.*, 2002, **43**, 317–321.
92. A. S. Basso, M. Gozin, H. L. Weiner, D. Frenkel, F. J. Quintana, F. A. Costa-Pinto, S. Petrovic-Stojkovic, L. Puckett, A. Monsonego, A. Bar-shir and Y. Engel, *J. Clin. Invest.*, 2008, **118**, 1532.

93. S. K. Norton, A. Dellinger, Z. Zhou, R. Lenk, D. Macfarland, B. Vonakis, D. Conrad and C. L. Kepley, *Clin. Transl. Sci.*, 2010, **3**, 159.
94. M. Ehrich, R. Van Tassell, Y. Li, Z. Zhou and C. L. Kepley, *Toxicol. In Vitro*, 2011, **25**, 301.
95. N. Prabhakar and J. M. Rosenholm, *Curr. Opin. Colloid Interface Sci.*, 2019, **39**, 220.
96. K. Turcheniuk and V. N. Mochalin, *Nanotechnology*, 2017, **28**, 252001.
97. D. J. Garrett, W. Tong, D. A. Simpson and H. Meffin, *Carbon*, 2016, **102**, 437.
98. S. Kelly, E. M. Regan, J. B. Uney, A. D. Dick, J. P. Mcgeehan, T. Bristol, B. Group, E. J. Mayer and F. Claeyssens, *Biomaterials*, 2008, **29**, 2573.
99. P. Bergonzo, A. Bongrain, E. Scorsone, A. Bendali, L. Rousseau, G. Lissorgues, P. Mailley, Y. Li, T. Kauffmann, F. Goy, B. Yvert, J. A. Sahel and S. Picaud, *IRBM*, 2011, **32**, 91.
100. M. Cottance, S. Nazeer, R. Lionel, G. Lissorgues, A. Bongrain, R. Kiran, E. Scorsone, P. Bergonzo, A. Bendali, S. Picaud, S. Joucla and B. Yvert, *Symposium on Design, Test, Integration and Packaging of MEMS/MOEMS (DTIP)*, Barcelona, 2013, p. 1.
101. P. A. Nistor, P. W. May, F. Tamagnini, A. D. Randall and M. A. Caldwell, *Biomaterials*, 2015, **61**, 139.
102. P. A. Nistor and P. W. May, *J. R. Soc., Interface*, 2017, **14**, 20170382.
103. P. Ariano, A. Lo Giudice, A. Marcantoni, E. Vittone, E. Carbone and D. Lovisolo, *Biosens. Bioelectron.*, 2009, **24**, 2046.
104. H. Chan, D. M. Aslam, S. Member, J. A. Wiler and B. A. Casey, *J. Microelectromech. Syst.*, 2009, **18**, 511.
105. L. Guarina, C. Calorio, D. Gavello, E. Moreva, P. Traina, A. Battiato and S. D. Tchernij, *Sci. Rep.*, 2018, **8**, 2221.
106. Y. A. Kim, T. Hayashi, M. Endo and M. S. Dresselhaus, *Springer Handbook of Nanomaterials*, Springer-Verlag, Berlin Heidelberg, 2013, p. 233.
107. H. Zhang, M. Yu, L. Xie, L. Jin and Z. Yu, *J. Nanomater.*, 2012, 280902.
108. T. J. Webster, M. C. Waid, J. L. Mckenzie, R. L. Price and J. U. Ejiofor, *Nanotechnology*, 2004, **15**, 48.
109. P. A. Tran, L. Zhang and T. J. Webster, *Adv. Drug Delivery Rev.*, 2009, **61**, 1097.
110. T. D. B. Nguyen-Vu, H. Chen, A. M. Cassell, R. J. Andrews, M. Meyyappan and J. Li, *IEEE Trans. Biomed. Eng.*, 2007, **54**, 1121.
111. T. D. B. Nguyen-Vu, H. Chen, A. M. Cassell, R. J. Andrews, M. Meyyappan and J. Li, *Small*, 2006, **2**, 89–94.
112. T. E. Mcknight, A. V. Melechko, B. L. Fletcher, S. W. Jones, D. K. Hensley, D. B. Peckys, G. D. Griffin, M. L. Simpson and M. N. Ericson, *J. Phys. Chem. B*, 2008, **110**, 15317.
113. Z. Yu, T. E. Mcknight, M. N. Ericson, A. V. Melechko, M. L. Simpson and B. M. Iii, *Nano Lett.*, 2008, **7**, 2188–2195.
114. Y. Guo, S. Jiang, J. B. Grena, I. F. Kimbrough, E. Thompson, Y. Fink, H. Sontheimer, T. Yoshinobu and X. Jia, *ACS Nano*, 2017, **11**, 6574.
115. D. K. Bishi, S. Mathapati, K. M. Cherian, S. Guhathakurta and R. S. Verma, *PLoS One*, 2014, **9**, e92397.

116. H. L. Tsai, W. P. Deng, W. F. T. Lai, W. T. Chiu, C. B. Yang, Y. H. Tsai, S. M. Hwang and P. F. Renshaw, *PLoS One*, 2014, **9**, e104937.
117. S. Ma, N. Xie, W. Li, B. Yuan, Y. Shi and Y. Wang, *Cell Death Differ.*, 2014, **21**, 216.
118. P. S. Frenette, S. Pinho, D. Lucas and C. Scheiermann, *Annu. Rev. Immunol.*, 2013, **31**, 285.
119. C. Nombela-Arrieta, J. Ritz and L. E. Silberstein, *Nat. Rev. Mol. Cell Biol.*, 2011, **12**, 126.
120. R. H. Miller, *Brain Res.*, 2003, **1091**, 258.
121. J. D. Humphrey, E. R. Dufresne and M. A. Schwartz, *Nat. Rev. Mol. Cell Biol.*, 2014, **15**, 802.
122. M. F. Griffin, P. E. Butler, A. M. Seifalian and D. M. Kalaskar, *World J. Stem Cells*, 2015, **7**, 37.
123. L. R. Smith, S. Cho and D. E. Discher, *Physiology*, 2018, **33**, 16.
124. A. C. Mitchell, P. S. Briquez, J. A. Hubbell and J. R. Cochran, *Acta Biomater.*, 2016, **30**, 1.
125. X. Liu and S. Wang, *Chem. Soc. Rev.*, 2014, **43**, 2385.
126. S. M. Hosseini, A. Vasaghi, N. Nakhlparvar, R. Roshanravan, T. Talaeikhozani and Z. Razi, *Neural Regener. Res.*, 2015, **10**, 1312.
127. E. M. Place, N. D. Evans and M. M. Stevens, *Nat. Mat.*, 2009, **8**, 457.
128. H. K. Kim, E. Kim, H. Jang, Y. K. Kim and K. Kang, *Chem. Nano Mat.*, 2017, **3**, 278.
129. K. S. Brammer, C. Choi, C. J. Frandsen, S. Oh, G. Johnston and S. Jin, *Acta Biomater.*, 2011, **7**, 2697.
130. M. J. Dalby, N. Gadegaard and R. O. Oreffo, *Nat. Mater.*, 2014, **13**, 558.
131. M. Grskovic, A. Javaherian and B. Strulovici, *et al.*, *Nat. Rev. Drug Discovery*, 2011, **10**, 915.
132. C. Cha, S. R. Shin, N. Annabi, M. R. Dokmeci and A. Khademhosseini, *ACS Nano*, 2013, **7**, 2891.
133. S. Marchesan, M. Melchionna and M. Prato, *Fullerenes, Nanotubes, Carbon Nanostruct.*, 2013, **22**, 190.
134. H. Shao, T. Li, R. Zhu, X. Xu, J. Yu and S. Chen, *et al.*, *Biomaterials*, 2018, **175**, 93.
135. C. Y. Tay, H. Gu, W. S. Leong, H. Yu, H. Q. Li, B. C. Heng, H. Tantang, S. C. J. Loo, L. J. Li and L. P. Tan, *Carbon*, 2010, **48**, 1095.
136. G. S. Lorite, *Nano Res.*, 2019, **12**, 2894.
137. B. Sun, X. J. Jiang, S. Zhang, J. C. Zhang, Y. F. Li, Q. Z. You and Y. Z. Long, *J. Mater. Chem. B*, 2015, **3**, 5389.
138. N. Masoumi, N. Annabi, A. Assmann, B. L. Larson, J. Hjortnaes, N. Alemdar, M. Kharaziha, K. B. Manning, J. E. Mayer Jr and A. Khademhosseini, *Biomaterials*, 2014, **35**, 7774.
139. S. Ostrovidov, X. Shi, L. Zhang, X. Liang, S. B. Kim, T. Fujie, M. Ramalingam, M. Chen, K. Nakajima, F. Al-Hazmi, H. Bae, A. Memic and A. Khademhossein, *Biomaterials*, 2014, **35**, 6268.

140. M. Kabiri, M. Soleimani, I. Shabani, K. Futrega, N. Ghaemi, H. H. Ahvaz, E. Elahi and M. R. Doran, *Biotechnol. Lett.*, 2012, **34**, 1357.
141. Y. Sun, C. S. Chen and J. Fu, *Annu. Rev. Biophys.*, 2012, **41**, 519.
142. M. R. Lee, K. W. Kwon, H. Jung, H. N. Kim, K. Y. Suh, K. Kim and K. S. Kim, *Biomaterials*, 2010, **31**, 4360.
143. K. N. Chua, C. Chai, P. C. Lee, S. Ramakrishna, K. W. Leong and H. Q. Mao, *Exp. Hematol.*, 2007, **35**, 771.
144. Z. Zhou, X. Liu, W. Wu, S. Park, A. L. Miller II, A. Terzic and L. Lu, *Biomater. Sci.*, 2018, **6**, 2375.
145. J. Wang, N. Chen, S. Ramakrishna, L. Tian and X. Mo, *Polymers*, 2017, **9**, 713.
146. S. J. Lee, W. Zhu, M. Nowicki, G. Lee, D. N. Heo, J. Kim, Y. Y. Zuo and L. G. Zhang, *J. Neural Eng.*, 2018, **15**, 016018.
147. C. G. Gahmberg, S. C. Fagerholm, S. M. Nurmi, T. Chavakis, S. Marchesan and M. Gronholm, *Biochim. Biophys. Acta*, 2009, **1790**, 431.
148. S. Namgung, K. Y. Baik, J. Park and S. Hong, *ACS Nano*, 2011, **5**, 7383.
149. M. A. Wozniak and C. S. Chen, *Nat. Rev. Mol. Cell Biol.*, 2009, **10**, 34.
150. N. W. Kam, E. Jan and N. A. Kotov, *Nano Lett.*, 2009, **9**, 273.
151. T. I. Chao, S. Xiang, J. Faye Lipstate, C. Wang and J. Lu, *Adv. Mater.*, 2010, **22**, 3542.
152. T. I. Chao, S. Xiang, C. S. Chen, W. C. Chin, A. J. Nelson, C. Wang and J. Lu, *Biochem. Biophys. Res. Commun.*, 2009, **384**, 426.
153. Y. Lee, S. Bae, H. Jang, S. Jang, S. E. Zhu, S. H. Sim, Y. I. Song, B. H. Hong and J. H. Ahn, *Nano Lett.*, 2010, **10**, 490.
154. T. R. Nayak, H. Andersen, V. S. Makam, C. Khaw, S. Bae, X. Xu, P. L. R. Ee, J. H. Ahn, B. H. Hong, G. Pastorin and B. Özyilmaz, *ACS Nano*, 2011, **5**, 4670.
155. S. Goenka, V. Sant and S. Sant, *J. Controlled Release*, 2014, **173**, 75.
156. O. Akhavan, E. Ghaderi, S. A. Shirazian and R. Rahighi, *Carbon*, 2016, **97**, 71.
157. S. Shah, P. T. Yin, T. M. Uehara, S. T. Dean Chueng, L. Yang and K. B. Lee, *Adv. Mater.*, 2014, **11**, 3673.
158. J. Wang, Y. Cheng, L. Chen, T. Zhu, K. Ye, C. Jia, H. Wang, M. Zhu, C. Fan and X. Mo, *Acta Biomater.*, 2019, **84**, 98.
159. H. Qing, G. Jin, G. Zhao, G. Huang, Y. Ma, X. Zhang, B. Sha, Z. Luo, T. J. Lu and F. Xu, *ACS Appl. Mater. Interfaces*, 2018, **10**, 39228.
160. A. O. Pires, A. Neves-Carvalho, N. Sousa and A. J. Salgado, *Stem Cells Int.*, 2014, 438352.
161. K. Zhang, H. Zheng, S. Liang and C. Gao, *Acta Biomater.*, 2016, **37**, 131.
162. W. Guo, S. Wang, X. Yu, J. Qiu, J. Li, W. Tang, Z. Li, X. Mou, H. Liu and Z. Wang, *Nanoscale*, 2016, **8**, 1897.
163. S. G. Rotman, Z. Guo, D. W. Grijpma and A. A. Poot, *Polym. Adv. Technol.*, 2017, **28**, 1233.
164. C. L. Weaver and X. T. Cui, *Adv. Healthcare Mater.*, 2015, **4**, 1408.

165. M. Tang, Q. Song, N. Li, Z. Jiang, R. Huang and G. Cheng, *Biomaterials*, 2013, **34**, 6402.
166. S. Marchesan and M. Prato, *Chem. Commun.*, 2015, **51**, 4347.
167. W. C. Lee, C. H. Y. X. Lim, H. Shi, L. A. L. Tang, Y. Wang, C. T. Lim and K. P. Loh, *ACS Nano*, 2011, **5**, 7334.
168. Y. Luo, H. Shen, Y. Fang, Y. Cao, J. Huang, M. Zhang, J. Dai, X. Shi and Z. Zhang, *ACS Appl. Mater. Interfaces*, 2015, **7**, 6331.
169. W. C. Lee, C. H. Lim, Kenry, C. Su, K. P. Loh and C. T. Lim, *Small*, 2015, **11**, 963.
170. H. H. Yoon, S. H. Bhang, T. Kim, T. Yu, T. Hyeon and B.-S. Kim, *Adv. Funct. Mater.*, 2014, **24**, 6455.
171. M. Lorenzoni, F. Brandi, S. Dante, A. Giugni and B. Torre, *Sci. Rep.*, 2013, **3**, 1954.
172. J. Yoo, J. Kim, S. Baek, Y. Park, H. Im and J. Kim, *Biomaterials*, 2014, **35**, 8321.
173. M. C. Serrano, J. Patino, C. Garcia-Rama, M. L. Ferrer, J. L. G. Fierro, A. Tamayo, J. E. Collazos-Castro, F. del Monte and M. C. Gutierrez, *J. Mater. Chem. B*, 2014, **2**, 5698.
174. S. R. Shin, B. Aghaei-Ghareh-Bolagh, X. Gao, M. Nikkhah, S. M. Jung, A. Dolatshahi-Pirouz, S. B. Kim, S. M. Kim, M. R. Dokmeci, X. S. Tang and A. Khademhosseini, *Adv. Funct. Mater.*, 2014, **24**, 6136.
175. M. Baker, *Nat. Rep. Stem Cells*, 2009, DOI: 10.1038/stemcells.2009.36.
176. R. Dressel, J. Schindehütte, T. Kuhlmann, L. Elsner, P. Novota, P. C. Baier, A. Schillert, H. Bickeböller, T. Herrmann, C. Trenkwalder, W. Paulus and A. Mansouri, *PLoS One*, 2008, **3**, e2622.
177. F.-Y. Hsieh, A. V. Zhilenkov, I. I. Voronov, E. A. Khakina, D. V. Mischenko, P. A. Troshin and S. Hsu, *ACS Appl. Mater. Interfaces*, 2017, **9**, 11482.
178. F.-Y. Hsieh, L. K. Shrestha, K. Ariga and S. Hsu, *Chem. Commun.*, 2017, **53**, 11024.
179. A. C. Taylor, C. H. González, B. S. Miller, R. J. Edgington, P. Ferretti and R. B. Jackman, *Sci. Rep.*, 2017, **7**, 7307.
180. A. C. Taylor, C. H. González, P. Ferretti and R. B. Jackman, *Adv. Biosyst.*, 2019, **3**, 1800299.
181. E. Mirzaei, J. Ai, S. Ebrahimi-Barough, J. Verdi, H. Ghanbari and R. Faridi-Majidi, *Mol. Neurobiol.*, 2016, **53**, 4798.
182. W. Guo, J. Qiu, J. Liu and H. Liu, *Sci. Rep.*, 2017, **7**, 5678.
183. A. C. Tripathi, S. A. Saraf and S. K. Saraf, *Materials*, 2015, **8**, 3068–3100.

CHAPTER 7

Carbon Nanotubes for Cardiac Applications

BRISA PEÑA*[a, b, c], NURIA ALEGRET[d], MELISSA LAUGHTER[c], MATTHEW R. G. TAYLOR[a], LUISA MESTRONI[a] AND MAURIZIO PRATO*[e, f, g]

[a]Cardiovascular Institute, University of Colorado Anschutz Medical Campus, 12700 E.19th Avenue, Aurora, Colorado, 80045, USA; [b]Consortium for Fibrosis Research & Translation, University of Colorado, Anschutz Medical Campus, 12700 E.19th Avenue, Aurora, Colorado, 80045, USA; [c]Bioengineering Department, University of Colorado Denver Anschutz Medical Campus, at Bioscience 2 1270 E. Montview Avenue, Suite 100, Aurora, Colorado, 80045, USA; [d]POLYMAT University of the Basque Country UPV/EHU, Avenida de Tolosa 72, 20018 Donostia-San Sebastián, Spain; [e]Center for Cooperative Research in Biomaterials (CIC biomaGUNE), Basque Research and Technology Alliance (BRTA), Paseo de Miramon 182, 20014, Donostia San Sebastián, Spain; [f]Department of Chemical and Pharmaceutical Sciences, University of Trieste, Via Giorgieri 1, Trieste, 34127, Italy; [g]Ikerbasque, Basque Foundation for Science, 48013 Bilbao, Spain
*E-mail: brisa.penacastellanos@cuanschutz.edu, prato@units.it

7.1 CNTs in Neural Cells: First Studies that Attracted the Use of CNTs for Cardiac Tissue Engineering Approaches

Multiple experimental studies suggest that the use of nanoparticles in medicine may revolutionize the therapeutic success in numerous diseases, *e.g.*, neoplastic, heart and neurodegenerative diseases.[1,2] Since their discovery

Nanoscience & Nanotechnology Series No. 48
Carbon Nanostructures for Biomedical Applications
Edited by Tatiana Da Ros, Nazario Martín and Jean-Francois Nierengarten

Published by the Royal Society of Chemistry, www.rsc.org

in 1991 by Ijima,[3] CNTs have become integral to advancing multiple nanotechnology strategies due to their unique electrical, mechanical and thermal properties. Their high mechanical strength and low weight combined with their conductivity and stability make them useful materials for field emission, energy storage and molecular electronics, and also provides great potential in biomedical applications.[4,5] More specifically, CNTs are one of the most promising materials to interface with the central nervous system (CNS) when being used as growth substrate scaffolds for nerve tissue engineering, electrode coating, long-term implants, drug delivery agents and molecular sensors.[6,7] In 2000, Matson *et al.* reported the first *in vitro* study showing the biocompatibility of CNTs for neuronal growth in hippocampal cells from E18 rat embryos. They found that CNTs promote the growth of neurons and extension of their axonal processes in all directions.[8] Since then, multiple studies have shown how interfacing neurons with CNTs emerged as an effective tool to modulate neuronal behavior at either the structural and functional level[9–14] and even induce neuronal differentiation.[7]

The positive influence of CNTs on neuronal networks comes from the physical interface along the cylindrical aspect of the nanomaterial and the electrical contact between the conductive nanomaterial and the electroactive cells.[15] Mazzatenta *et al.* have previously shown that the frequency of spontaneous events in networks cultured on CNT substrates was increased when compared with peptide-free glass surfaces controls.[16] They observed that neuronal membranes establish a tight contact with the CNTs (Figure 7.1), and hypothesized that CNTs can provide a shortcut between the proximal and distal compartments of the neuron, promoting axon excitability and synaptic activity of neuronal networks.[17,18] Furthermore, the impact of CNT substrates on CNS tissue was also demonstrated.[19,20] Spinal cord and dorsal

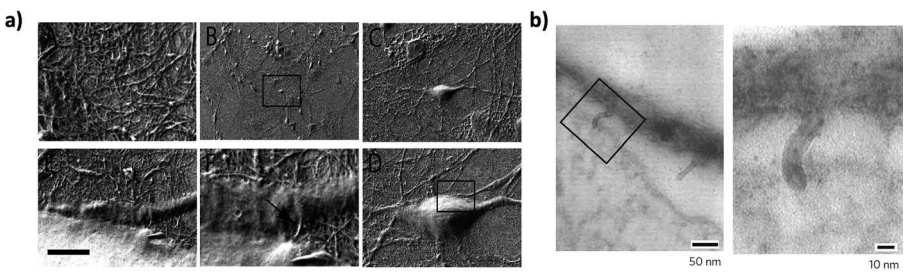

Figure 7.1 (a) SEM images showing the intimate contacts between CNTs and cultured hippocampal neurons. Scale bar (in E): A, 1 μm; B, 200 μm; C, 25 μm; D, 10 μm; E, 2 μm; F, 450 nm. (b) TEM micrographs from planar sections of hippocampal cultures grown on CNTs, showing a single nanotube 'pinching' the neuronal membrane. Reprinted from (a) ref. 15 under the terms of an Open Access license, https://www.jneurosci.org/content/rights-permissions, Copyright 2007 Society for Neuroscienceand (b) ref. 17 with permission from Macmillan Publishers Ltd, Copyright 2008.

root ganglia multilayered explants co-cultured on CNT substrates showed a higher number of longer neuronal processes, and the integration of CNTs as their own supports or exoskeletons.[20] When sensory afferent pathways were exogenously activated, the resulting synaptic responses recorded from single neurons not in direct contact with the CNT layer were strongly increased, indicating that the boosting effects of CNTs at the interface was transferred from the layers of neurons directly exposed to the CNTs to those functionally connected, yet physically far from the interface.[20]

Scaffolds made of different kinds of biomaterials have been investigated to favor neuronal growth and axonal regeneration. In order to provide stromal support for lesions at the level of the CNS or peripheral nervous systems (PNS) and to overcome the inhibitory environment,[21–23] scaffolds selected for neuronal tissue engineering have to be biocompatible with the host tissue without inducing inflammatory and immune reactions. Furthermore, they must reduce astrocytic reactions and glial scar formation, allow neuronal adhesion and axonal extension within a tridimensional architecture, offer proper physical support to cells and axons, provide physical properties similar to the native environment, and have a tunable rate of degradation without inflammatory degradation products.[24,25] CNT scaffolds have been shown to be excellent materials to address many of these requirements. The architecture of the scaffold structure is crucial for neuronal regeneration. For example, the introduction of longitudinal tubular constructs provides physical guidance for axonal regrowth and cell migration, and thus may enhance nerve regeneration.[26] Moreover, the micro- and nanotopography at the cellular level are fundamental for successful nerve regeneration. Several studies have shown that cells behave differently on aligned *vs.* randomly oriented fibers.[27–29] The main characteristic of these materials is a longitudinal organization mimicking the natural structure of axonal pathways within the brain and spinal cord. Finally, it is worth noting that the nature of the material used is crucial. Roberts *et al.* demonstrated how primary embryonic rat motor neurons grown on thin films of alternating stripes of hyaluronic acid (HA)/CNTs and silicon oxide (SiO_2) selectively migrate toward and adhere to the CNT-containing substrate.[30]

Different kinds of polymers (biodegradable, non-biodegradable, synthetic and natural) have been used as support materials for CNTs, allowing modulation of the shape, dimensions and stiffness of the final scaffold.[31–33] We previously demonstrated that the exceptionally unique capabilities of CNTs to improve and boost neuronal functionality also work in three dimensions. Such three-dimensional (3D) cellular organization is able to induce neuronal network outputs that strongly differ from the standard 2D constructs. Polydimethylsiloxane (PDMS)/CNT porous 3D constructs showed great potential in neuronal colonization and 3D synaptic network reconstruction of hippocampal neurons and spinal cord explants (Figure 7.2).[34,35] Conductive polymers have been proven to down-regulate glial reaction without affecting neuronal viability and function.[36] Alegret *et al.* and Dominguez-Alfaro *et al.* demonstrated that highly conductive scaffolds, composed of Polypyrrole (PPy)

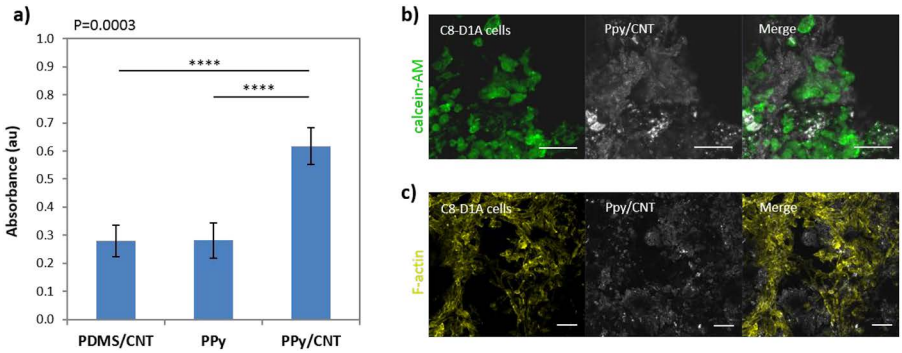

Figure 7.2 (a) *In vitro* LDH assay of C8-D1A astrocytes cultivated for 48 h on polypyrrole 3D scaffolds in the presence or absence of CNTs. Confocal images after (b) calcein-AM stain of viable cells (green) and (c) the F-actin cytoskeleton (yellow) staining of PPy/CNT scaffolds after 2 days of culture. The elongated morphology of the cells indicates a good biocompatibility of the material. Scale bar = 50 μm. Reprinted from ref. 37 with permission from American Chemical Society, Copyright 2018.

or Poly(3,4-ethylenedioxythiophene) (PEDOT) in combination with CNTs, are able to support neuronal growth and regeneration more than non-conductive matrices.[37,38]

Due to the beneficial therapeutic uses of CNTs in neuron tissue engineering, several authors have now explored their use for other electric cells such as cardiomyocytes. The following sections will provide an overview of recent developments that have occurred in the design and engineering of various CNT substrates for cardiac tissue engineering efforts such as injectable hydrogels, polymeric patches and other biomaterials.

7.2 Epidemiology of Heart Failure

7.2.1 Introduction to Heart Failure

Chronic heart failure (HF) is a life-threatening condition in which cardiac output fails to meet systemic demands resulting in damage to other organs and tissues. Chronically, the heart experiences cardiomyocyte (CM) loss, matrix degradation and fibrosis.[39–42] The most frequent cause of HF is ischemic heart disease, in particular myocardial infarction (MI).[43] During MI, a blocked coronary artery decreases blood flow to part of the heart, causing ischemia and eventually necrosis to the infarcted region.[44] After the initial damage, the surrounding heart wall becomes thinner, leading to ventricular dilation and progression towards HF.[45,46]

As patients progress through the stages of HF, they can experience an escalating distress, increased disability and reduced quality of life. There are four stages of HF: A, B, C and D. The stages range from high risk of developing

HF to advanced HF.[47] Treatment at each stage may involve medical management, lifestyle behaviors and cardiac devices.[48] These treatments are aimed at reducing symptoms, slowing disease progression and reducing mortality; however, they are not aimed at repairing heart muscle or restoring function.[49] Furthermore, even with these treatments, approximately half of patients with HF will die within five years of their diagnosis.[50,51] Cardiac transplantation remains the only definitive treatment for those affected with end-stage HF, but the availability of donor hearts remains a major limitation.[52,53]

The American Heart Association's (AHA) statistical update in 2020 reported that from 1987 to 2012, over 40 253 people waited for heart transplants in the United States (US).[54] According to data from the Organ Procurement and Transplantation Network, in 2018 there were 3408 heart transplants performed in the US.[54] There are 256 hospitals in the US with the capabilities to perform heart transplantations from which 143 heart transplantations were performed in 2018.[54] In the US, the average cost of heart transplantation is $808 770 [55] with a mean recovery length of 45 days and an in-hospital mortality of 7.84%. The overall cost to treat HF continues to rise. In the US, the total cost for HF was estimated to be $30.7 billion per year in 2012,[56] from which more than two-thirds was attributable to direct medical costs. It is predicted that by 2030, the total cost to treat HF will increase by 127%.[57]

7.2.2 Prevalence and Incidence of Heart Failure

HF remains a rising global epidemic affecting at least 23 million people worldwide.[58] According to the AHA statistical update from 2020, about 6.5 million adults in the US are affected by HF and the prevalence of HF continues to rise.[54] Projections show that the prevalence of HF in the US will increase 46% from 2012 to 2030, resulting in more than 8 million adults with HF.[54] Additionally, it is predicted that the total percentage of the population with HF will increase from 2.42% in 2012 to 2.97% in 2030.[59]

Based on ARIC Community Surveillance data from 2014, the incidence of HF in patients over the age of 55 was around 1 000 000 in the US.[60] The incidence of HF was slightly higher in women compared to men, 505 000 and 495 000 people, respectively. There were over 80 480 fatalities in 2017 due to HF from which 43 656 (54.2%) were women and 36 824 were men (45.8%). Regarding hospital discharges (including discharged alive, deceased and status unknown), there were 809 000 hospital discharges in the US by 2016 (the data include patients of all ages from 1997 to 2016) from which 394 000 were women and 415 000 were men.[60] Additionally, it was observed that there is an increased burden of HF within the Black population followed by Hispanic, White and Asian populations.[61] Table 7.1 shows the prevalence of HF in the US per population group in adult patients (over the age of 20) from 2013 to 2016.[54]

According to the National Health and Nutrition Examination Survey,[62] the prevalence of HF among US adults from 2013 to 2016 was: 0.2 and 0.3% in the age range of 20–39 years old in female and male, respectively; 1.7 and

Table 7.1 Heart failure in the United States by population group.

Population group								
Non-hispanic white		Non-hispanic black		Hispanic		Non-hispanic asian		Non-hispanic american indian or Alaskan native
Female	Male	Female	Male	Female	Male	Female	Male	N/A
1.9%	2.2%	3.9%	3.5%	2.1%	2.5%	0.7%	1.7%	—

1.2% in the age range of 40–59 years old in female and male, respectively; 4.8 and 6.9% in the age range of 60–79 years old in female and male, respectively; and 12 and 12.8% above the age of 80 years old in female and male, respectively.[54] Finally, the number of deaths due to HF was around 80 480 in 2017 (36 824 males and 43 656 females). The number of deaths attributable to HF was 42.3% higher in 2017 (80 480 deaths) than it was in 2007 (56 565 deaths).[63]

7.2.3 Future Directions for Heart Failure

Although prevention of HF is the most effective way to improve quality of life and reduce health-care costs,[64] the incidence and prevalence of HF is still increasing worldwide.[57] Due to the limited supply of donor hearts for heart transplantation and the poor regenerative ability of the myocardium, investigators have turned to therapeutic approaches aimed at improving myocardial function.[65] As previously mentioned, CNTs have become the leading edge of nanotechnology due to their unique electrical, mechanical and thermal properties.[66] Their beneficial therapeutic uses in electric cells, such as neurons, have now been expanded to cardiac cells. In the following sections, we will address the therapeutic effects of CNT for cardiac repair and their use in cardiac tissue engineering.

7.3 CNT Applications in Heart Disease

7.3.1 CNTs in Myocardial Infarction: Atherosclerosis

Atherosclerosis is a progressive multi-factorial disease that affects the vasculature. This disease results in gradual accumulation of lipids within the intima of mostly medium to large sized arteries. Previously thought to be a disease solely of excess lipids, it is now well-accepted to also be characterized by chronic inflammation. In fact, the first step in disease progression is the secretion of pro-inflammatory cytokines and the subsequent expression of cell adhesion molecules on endothelial cells.[67] These adhesion molecules provide a contact point for monocytes and leukocytes to migrate into the intimal layer of the vessel. Once within the intima, monocytes increase

their uptake of oxidized lipids and continue to mediate the inflammatory response.[68] Over time, these lesions can progress into mature atherosclerotic plaques with thin fibrous caps, internal necrosis and even neovascularization. Not only can these plaques cause narrowing of blood vessels and decrease in blood flow, but also may rupture causing sudden occlusion of the artery and complete blockage of downstream blood flow. In the heart, the rupture of atherosclerotic plaques can lead to MI, whereas in the brain, rupture of atherosclerotic plaques can lead to ischemic stroke. In addition, rupture of plaques in other vessels throughout the body can result in kidney damage, lower limb ischemia and abdominal aortic aneurysms.[67]

CNTs may be synthesized and functionalized to possess various chemical and surface properties making them useful in a wide array of applications. CNTs can be categorized as either single-walled (SWCNTs) or multi-walled (MWCNTs) (double-walled being a subset of this category). CNTs that have not been functionalized nor purified have previously been investigated in *in vitro* studies that have shown that endothelial cells cultured with 0.1 ug/mL SWCNT suspended in culture media[69] and HUVEC cells cultured with MWCNTS suspended in culture media[70] produced increased reactive oxygen species (ROS). These studies indicate that non-functionalized or unpurified CNTs may encourage the production of ROS and propel oxidative stress and inflammation thus presenting concern that CNTs could accelerate atherosclerosis. In fact, one study by Suzuki *et al.* showed that non-functionalized or unpurified SWCNTs and MWCNTs can increase the expression level of adhesion molecules, which could influence atherosclerotic development through increased monocyte adhesion.[71] On the other hand, another study demonstrated that catalytically grown and purified SWCNTs and MWCNTs can trigger a dose-dependent disruption of cell function and intercellular contact on human aortic endothelial cells.[72] However, although the CNTs used in this study were purified, traces of metal content were identified in the CNTs after purification. Unfortunately, the authors did not provide specific information regarding the purification protocol used for their investigation. As we will further discuss in the toxicity section, metal impurities in CNTs are the one of the main reasons for their toxicity.

In vivo studies conducted by Cao *et al.* showed that pulmonary exposure to non-functionalized or unpurified MWCNTs in ApoE (−/−) mice had increased atherosclerotic plaque progression in the aorta with largely unaltered oxidative damage in lunge tissue.[73] Interestingly, one *in vivo* study examining the pulmonary and atherosclerotic effects of pharyngeal aspiration of non-functionalized or unpurified MWCNT in a mouse model of atherosclerosis, showed increased pulmonary injury and inflammation but no increase in atherosclerotic lesions.[74] Although these studies show the potential negative impact of CNTs when used alone without a functionalization method or purification protocol, the *in vivo* effects of CNTs are largely dictated by the delivery or route of exposure as well as the construct of the CNTs themselves. For instance, CNTs in the previously discussed studies not only were non-functionalized or unpurified, but also, they were not conjugated

or encapsulated within a delivery modality and, thus, were capable of dispersing freely. These important factors that influence CNT toxicity are discussed in more detail in the toxicity section of this chapter. For example, one study showed markedly different effects of MWCNTs with repeated oral *vs.* pulmonary exposures.[75] Another study showed that specifically pulmonary exposure to MWCNTs in mice induced changes in plasma acute phase response (APR), lipid composition and hepatic gene expression, which could cause an increase in cardiovascular disease risk.[76] Although, it seems that the delivery route of CNTs may influence the effects on lung tissue and vasculature, certain *in vivo* studies display varying results despite similar exposure mechanisms. This may be due to the large variety of CNTs that exist, whether or not they are purchased commercially or grown in a lab. Furthermore, all of the above *in vivo* studies were conducted using non-functionalized and unpurified CNTs as well as animal models with poor lipoprotein clearance or accumulation of cholesterol particles in the blood potentially making atherosclerotic effects more severe.

As discussed in later sections, several investigators have demonstrated that using CNTs to functionalize biomaterials or biomolecules has a tremendous potential for cardiac applications. For example, carbon composite beads with CNTs have been utilized to decrease the amount of LDL in plasma with the goal of preventing the formation of atherosclerotic plaques. In a study by Gong *et al.*, porous carbon composite beads with CNTs absorbed and lowered LDL levels through electrostatic interactions between the CNTs and electropositive LDLs.[77] Owning to the highly diverse nature of CNT applications, CNTs have also been functionalized with α-bromoacid and 2-(methacryloloxy) ethyl phosphorylcholine (MPC) to specifically repel oxidized LDLs making them candidates for the treatment of atherosclerosis and prevention of restenosis following stent placement.[78]

The functionalizable and highly versatile nature of CNTs have also made them useful for diagnostic approaches of both atherosclerosis and MI. Layer-by-layer assembled CNTs and graphene complexes were used as a novel diagnostic approach to detect elevated concentrations of hypoxanthine (Hx) and uric acid (UA), important biomarkers in human serum following MI.[79] Along similar lines, other researchers used SWCNTs functionalized with tissue plasminogen activator (tPA) monoclonal antibodies to detect levels of tPA, another important biomarker that increases in concentration following MI.[80] Further diagnostic modalities utilized electro-analysis of myoglobin following MI and screen-printed electrodes modified with MWCNT.[81] Potentially most in line with clinically used MI diagnostic techniques, carboxylated MWCNTs embedded nanofibers were used to construct a cardiac Troponin I (cTnl) sensor reliable enough for point-of-care MI diagnosis.[82] CNTs have also been utilized to improve imaging modalities and characterization of atherosclerosis *in vivo*. In one study by Wait *et al.*, micro-computed tomography (micro-CT) imaging using a novel CNT as an X-ray source was used to evaluate vascular calcifications in living mice.[83] Similarly, one study took advantage of

CNT accumulation in atherosclerotic macrophages to demonstrate their utilization as a platform for targeted imaging of macrophage laden plaques and vascular inflammation.[84]

7.3.2 CNT in Arrhythmias

The heart is responsible for pumping blood to the lungs for oxygenation and to the peripheral tissue for oxygen delivery. The coordinated contraction of the heart relies on electrical impulses traveling through the myocardium. In normal, healthy heart tissue these electrical impulses occur in sequential and regular intervals.[85] However, abnormalities in the electrical impulses can cause accelerations, slowing or irregular rates depending on where these abnormal impulses originate (*i.e.* atria, AV node, or ventricle). Importantly, certain alterations in electrical conduction can lead to the development of lethal arrhythmias, such as ventricular tachycardia or ventricular fibrillation. Arrhythmias can be caused by a multitude of different mechanisms, although a significant number of arrhythmias in developed countries result from ischemic or scarred myocardium as a consequence of MI.[86] Treatment of arrhythmias will depend on the type of arrhythmia experienced by the patient. Medical management typically involves antiarrhythmic drugs that work by decreasing the myocardial conduction velocity but can have significant toxic effects and are only suitable for certain types of arrythmias.[87] For more life-threatening arrhythmias, such as ventricular tachycardia, treatment rests on the implantation of cardioverter defibrillators to deliver an anti-tachycardic shock in order to restore regular conduction velocity.[86] However, this type of treatment does not prevent the initiation of these deadly arrhythmias but instead relies solely on reversal once the arrhythmia has already started. Finally, ablation of aberrant heart tissue can be used to deliberately destruct aberrant myocardium, but again this treatment is only useful for specific types of arrhythmias.

Attempts have been made to restore conduction across ischemic and damaged myocardium to prevent aberrant circuits from occurring in the first place. Researchers have investigated a number of modalities to accomplish this including stem cell therapy, biomaterials and gene therapy; however, CNTs have also been researched as this material can be easily modified and possesses inherent conduction capabilities.[88] In fact, super aligned carbon-nanotube sheets (SA-SNTs) cultured with cardiomyocytes induced aligned cell morphology and provided signal–transmission pathways to synchronize cells and potentially decrease risk of arrhythmias.[89] In one *in vivo* study by McCauley *et al.*, carbon nanotube fibers (CNTfs) were sewn across epicardial scars in sheep following radiofrequency ablation to create a conduction delay. CNTfs not only improved conduction across the epicardial scar, but also maintained conduction for one month post atrioventricular nodal ablation.[88] Similarly, CNTs fabricated into nanotube patches have been employed to improve cardiac conduction across surgically impaired epicardium.[90]

Together these studies and others display the promising application of CNTs for cardiac resynchronization therapy in patients at risk of cardiac arrhythmias following myocardial scarring.

In other applications, CNTs have been used to improve upon current ablation methods for the treatment of arrhythmias. CNTs have been used extensively in oncology to sensitize tumors to radiofrequency (RF) ablation. As discussed previously, CNTs have high thermal conductivity and a broad spectrum of electromagnetic frequency absorbance which includes RF bands. With this information, researchers have begun to investigate the use of CNTs to enhance thermal conductivity and RF heating during myocardial ablation procedures. In one study conducted by Nguyen *et al.*, CNT-treated myocardial tissue showed altered electrical and thermal conductivity following the application of RF, demonstrating the ability of CNTs to possibly bolster ablative techniques.[91]

As mentioned previously, CNTs present the potential to be used in cardiac applications. However, in order to explore their therapeutic properties in a safe manner, CNTs would be ideally used to functionalize biomaterials for cardiac tissue engineering. However, a proper purification methodology is needed prior to their use. The following section shows the advances in cardiac tissue engineering using CNTs to improve the electrical cues of polymeric materials.

7.4 CNTs in Tissue Engineering

7.4.1 Biological Effect of CNTs in Cardiomyocyte

CNT-based biomaterials have been shown to promote cardiomyocyte maturation and improve cardiomyocyte function.[92–96] The effects of CNTs on the electrophysiological behavior of cardiomyocytes was first characterized by Martinelli *et al.*[97] when they cultured neonatal rat ventricular myocytes (NRVMs) on MWCNT substrates. Using transmission electron microscopy (TEM), they found that CNTs tightly interact with the cell membrane of NRVMs (see Figure 7.3). In addition, they found that this close interaction promoted cardiomyocyte proliferation during the first three days of culture and enhanced NRVM electrophysiological properties when compared with NRVMs cultured in traditional gelatin-coated tissue culture dishes. In another publication, Martinelli *et al.*[98] found that CNTs increased Cx43 expression and promoted a gene expression profile characteristic of terminal differentiation and physiological growth on NRVMs when compared with the gelatin controls. These studies attracted the use of CNTs to improve biomaterials for cardiac tissue engineering. However, in order to understand the positive effect that CNTs have on cardiomyocytes, several investigations studied the biological pathways that lead to the mechanisms underlying this process.

Sun *et al.*[99] studied the effect of CNTs on NRVMs using SWCNTs dispersed into collagen type I. Through immunohistochemical staining and western blotting, they found that the incorporation of CNTs into the collagen

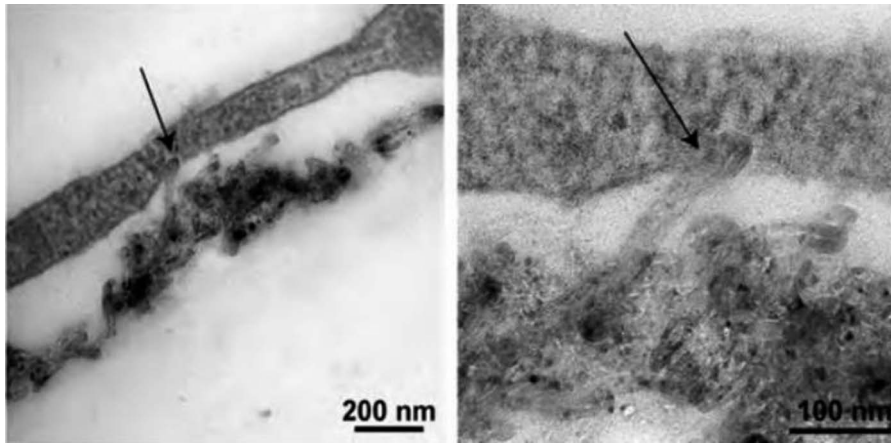

Figure 7.3 CNT interaction with cardiac myocyte membranes (arrows). The images show a tight interaction between the CNTs and the cardiomyocyte cell membrane. Reprinted from ref. 97 with permission from American Chemical Society, Copyright 2012.

substrates promoted the assembly and formation of intercalated discs (ID) within cardiomyocytes. They further explored the effect of CNTs on the integrin pathway, the signaling pathway that is involved in the regulation of intercalated disc formation. Through western blot analysis, they found an elevated expression of β1-integrin in NRVMs cultured in the CNT-collagen substrates when compared with the collagen substrates without CNTs. They concluded that β1-integrin is activated on NRVMs due to the presence of CNTs in the collagen substrates. They next investigated the phosphorylation levels of focal adhesion kinase (FAK) and Src along with the expression level of integrin-linked kinase (ILK) in NRVMs cultured in the CNT-collagen substrates. These markers are all involved in the intracellular signaling pathways that can be activated by β1-integrin[100–105] and are thus important for the regulation of electrical and mechanical junction proteins.[106–108] They found that a notably higher expression of p-FAK was observed in the NRVMs cultured in the CNT-collagen substrates when compared with NRVMs cultured in the collagen substrates without CNTs. No differences were observed between the groups for the p-Src and ILK pathways. The phosphorylation of FAK can activate several downstream signaling kinases,[109] such as AKT (protein kinase B)[110] and extracellular signal-regulated kinases (ERK),[111] both of which are involved in the upregulation of ID-related proteins.[112] Sun *et al.* found that expression of p-ERK in NRVMs cultured in CNT-collagen was increased when compared to NRVMs cultured in the collagen substrates without CNTs. They did not observe any apparent change of p-AKT expression between the two groups. Since Cx43 is the main gap junction protein increased in NRVMs cultured in CNT substrates, they investigated the mRNA expression of transcription factors that regulate expression of the connexin gene, such as AP-1, c-fos,

myocyte enhancer factor-2 (MEF-2c), NKX2.5 and GATA-binding protein 4 (GATA4).[113–116] Through semi-quantitative polymerase chain reaction (RT-PCR) they determined the expression levels of AP-1, c-fos, MEF-2c, NKX2.5 and GATA4 in NRVMs cultured in CNT-collagen substrates. They found that the mRNA levels of GATA4 and MEF-2c were elevated in the NRVMs cultured in the CNT-collagen substrates when compared with NRVMs cultured in collagen substrates without CNTs. They did not find changes in the level of expression of AP-1, c-fos, or NKX2.5 between the two groups. They concluded that CNTs promote the acceleration of gap junction formation by activating the β1-integrin-mediated FAK/ERK/GATA4 pathway.

Furthermore, Sun *et al.*[117] cultured NRVMs in SWCNTs incorporated into gelatin with methacrylate anhydride (CNT/GelMA) hydrogels and performed similar studies to those mentioned previously. Using immunohistochemical staining and western blotting, they found that the incorporation of CNTs in GelMA hydrogels promotes the assembly and formation of intercalated discs within cardiomyocytes. Pathways such as wnt and p38 mitogen-activated protein kinase, have also shown to regulate intercalated disc formation.[118–120] Thus, the authors further analyzed the expression levels of integrin and β-catenin in NRVMs cultured in both CNT/GelMa and GelMa hydrogels using quantitative western blotting. They found again that the β1-integrin was highly expressed in NRVMs cultured in the CNT/GelMa hydrogel (3 times more) than in NRVMs cultured in the hydrogel without CNTs. No changes in β-catenin were observed between the two groups. As previously mentioned, β1-integrin signaling activates FAK as well as small G proteins, like RhoA,[121] which play an important role in the formation of cell–cell junctions.[122] Thus, the authors further investigated the phosphorylation levels of FAK and the expression level of RhoA in NRVMs cultured on CNT/GelMa hydrogels. They found that the expression of p-FAC and RhoA was higher in the NRVMs cultured in the CNTs when compared with NRVMs cultured in hydrogels without CNTs. The authors concluded that through the activation of β1-integrin signaling, CNTs trigger downstream signaling kinases FAK and Rho, thus promoting gap and mechanical junction formations within cardiomyocytes.

To further study the integrin pathways activated by CNTs, Lee *et al.*[123] studied the expression of integrin receptors on NRVMs cultured for three and five days in GelMA hydrogels containing dispersed CNTs and reduced-graphene oxide (rGO). Using quantitative RT-PCR, they analyzed various integrin subunits (α1, α2, α3, α5, α7 and β1) responsible for mechanotransduction initiating intracellular signaling. They found that NRVMs cultured on the CNTs-GelMA hydrogel have higher expressions of α1, α2, α3, and β1 on day three and five than those cultured on the rGO-GelMA hydrogel. They also found that NRVMs cultured on the rGO-GelMA hydrogel have higher expression for α5 and α7 on day three and five than NRVMs cultured on the hydrogel with CNTs. NRVMs cultured on CNT-GelMA hydrogels display higher expression levels of distinct integrin receptors such as α1β1 and α2β1. They further investigated this integrin engagement by assessing gene expression profiles pertinent to mechanotransduction, cytoplasmic structure, and growth in

NRVMs cultured in CNT-GelMa and rGO-GelMa hydrogels for three and five days. Although the panels of transcripts related to cytoplasmic structure and Rho family expressed higher levels in cells cultured in the CNT-GelMA hydrogels on day 3, there were no significant differences detected on day 5 between the two hydrogels. On the other hand, NRVMs cultured on CNT-GelMA for five days exhibited a much higher expression level of mechanotransduction related transcripts (focal adhesion and YAP/TAZ) than NRVMs cultured in the rGO-GelMA hydrogels. It has been reported that small GTPase Rho indirectly regulates YAP/TAZ activation by inducing the assembly of actin stress fibers to encourage the spreading of cells across the extracellular matrix (ECM).[124] The authors concluded that NRVMs cultured in the CNT-GelMA hydrogels had increased functionality through integrin-mediated mechanotransduction (*via* YAP/TAZ) in contrast to NRVMs cultured in the rGO-GelMA hydrogels.

Although there are no current *in vivo* studies looking at the pathways activated by CNT-functionalized hydrogels, the discussed *in vitro* studies suggest that CNTs promote the formation of gap junctions, improve cardiomyocyte activity and activate integrin pathways.

7.4.2 Injectable Hydrogel

7.4.2.1 Introduction to Injectable Hydrogels

For patients with end-stage HF, therapeutic options are limited and cardiac transplantation remains challenging due to a shortage of donor hearts and high surgical risk.[54,125,126] In this regard, efforts in cardiac tissue engineering have sought to overcome these limitations by developing novel biomaterials, such as injectable hydrogels[66,127] or polymeric patches,[125,126] that can mimic the cardiac tissue and promote cardiac repair.[128–130] Due to co-morbidities in patients affected with end-stage HF, ideally, biomaterials should be delivered with a minimally invasive procedure to prevent any additional damage incurred through surgical implantation.[131] For this reason, injectable hydrogels are particularly desirable due to their minimally invasive delivery approach and their unique modifiable properties.[65,132] Injectable hydrogels can be designed to have specific physical, chemical and electrical properties to provide structural and electrical support to the damaged cardiac tissue.[93,133,134] Additionally, they can also serve as a delivery vehicle for cells and biomolecules to further promote cardiac repair.[93,135–138] In fact, injectable acellular alginate-based hydrogels have been already tested in clinical trials in patients with previous MI and HF with favorable tolerability.[139,140] These results support the use of injectable hydrogels for cardiac repair. However, due to the complexity of cardiac tissue, the ideal injectable hydrogel for cardiac repair has not yet been developed, particularly a hydrogel that mimics the cardiac electrical cues.[96] Native cardiac muscle has unique electrophysiological behavior that transfers electrical signals through CM coupled with nonmyocytes cells such as fibroblasts, smooth muscle cells, endothelial cells and macrophages.[123,141] Due to the loss of CMs and the pathogenic

cardiac remodeling during HF, abnormalities in the electrical signaling of the injured heart are commonly observed.[142] Unfortunately, the majority of polymeric materials are electrically insulated.[143] To this end, investigations have moved to modify injectable hydrogels by conjugating or dispersing CNTs to provide electrical cues into hydrogels.[144] For the purpose of this section, an overview of injectable hydrogels functionalized with CNTs for cardiac tissue engineering will be discussed.

7.4.2.1.1 CNTs in Natural Injectable Hydrogels. Natural hydrogels are attracting attention for cardiac tissue engineering applications as they preserve the biological properties and biocompatibility of the host tissue.[145] Among them, ECM-derived hydrogels are increasingly used as scaffolds for cardiac repair.[146] Previous investigations have shown that porcine myocardial ECM-derived hydrogels improved cardiac function and attenuated pathogenic left ventricle remodeling in both rat[147] and pig[148] MI models. However, ECM-derived hydrogels lack electrical cues which are needed for efficient cardiac function. To overcome this limitation, Roshanbinfar *et al.*[149] proposed the dispersion of carbodihydrazide MWCNTs into sheep decellularized pericardial tissue. They found that culturing HL-1 cardiomyocytes in the 3D CNT-pericardial matrix promoted cell proliferation, increased expression of connexin 43 (Cx43) (cardiac specific gap junction protein) and improved synchronous contraction when compared with cells cultured in pericardial matrix without CNTs. Furthermore, in another study, Roshanbinfar *et al.*[150] tested the same sheep pericardial matrix with dispersed carbohydrazide MWCNTs in human-induced pluripotent stem cell derived cardiomyocytes (hiPSC-CM). They found that the hiPSC-CM cultured in the 3D CNT pericardial sheep matrix present an enhanced Cx43 expression with improved cellular alignment and more organized sarcomeres when compared with cells growing in Matrigel. In addition, they observed an enhanced calcium handling with better response to external electrical and pharmaceutical stimulation in hiPSC-CM cultured in the 3D CNT pericardial sheep matrix. Although ECM-derived hydrogels have shown promise in both *in vivo* and *in vitro* studies, a more cost-effective extraction method to reduce the denaturalization of ECM proteins is still needed.[151]

To this end, several investigators have developed and studied other natural injectable hydrogels for cardiac repair. Collagen has attracted great interest as it is the major protein component in the native cardiac ECM.[152] Thus, it naturally exhibits good biocompatibility. However, similar to other ECM-derived hydrogels, collagen hydrogels are electrically insulated, which leads to poor functionality of the constructed tissues. In order to improve collagen hydrogels' conductivity, Sun *et al.*[153] suspended SWCNTs into collagen type 1 solution to produce CNT-collagen hydrogels. They tested this CNT-collagen hydrogel as a 3D scaffold *in vitro* using NRVMs and found that the incorporation of CNTs into the collagen hydrogels improved cell alignment and function. Similarly, Yu *et al.*[154] dispersed carboxyl-functionalized MWCNT into collagen type I solutions and tested its effect on NRVMs. They found

that NRVMs cultured in the 3D CNT-collagen matrix showed improved cardiac cell function compared with cells cultured in collagen hydrogels without CNTs. Although collagen hydrogels have shown good biocompatibility, and the dispersion of CNTs within the hydrogel improves cardiac cell function, there are still concerns regarding the batch-to-batch variability of collagen hydrogel synthesis and the lack of chemically-bonded CNTs, which can increase the risk of CNT release and toxicity.

7.4.2.1.2 CNTs in Synthetic Injectable Hydrogels. Although natural injectable hydrogels have shown promise to be used in cardiac tissue engineering applications, high cost purification methods and their variability properties in batch-to-batch synthesis make them not ideal for clinical applications.[65] Thus, investigations have moved towards synthetic materials.[155–158] Synthetic materials can be easily modified to fulfill specific properties, such as chemical functionalization, increased mechanical strength, improved porosity, controlled degradation and gelation rate. Additionally, synthetic materials are more easily controlled avoiding batch to batch variability.

Poly(*N*-isopropylacrylamide) (PNIPAAm)-based hydrogels are common thermosensitive synthetic materials broadly used in the biomedical field.[159,160] PNIPAAm-based hydrogels remain in solution at room temperature and turn to a physical gel at body temperature.[161,162] Thus, these synthetic hydrogels can be injected into a specific side of interest and will conform to the irregularities of the injury site *via in situ* gelation.[163] Moreover, PNIIPAAm-based hydrogels can be chemically modified to covalently incorporate CNT into the polymer backbone. Pena *et al.*[66] developed a reverse thermal gel functionalized with carbon nanotubes (CNT): poly(serinol hexamethylene urea)-poly-(*N*-isopropylacrylamide)-poly-(lysine)-CNT (PSHU-PNIPAAm-lysine-CNT) or RTG-CNT. They first synthetized CNT with COOH groups by incorporating amino benzyl groups to commercial MWCNT *via* the diazonium salt arylation reaction route. Then, they chemically conjugated the MWCNT-COOH to the primary amine groups of the PSHU-PNIPAAm-lysine hydrogel. They further performed long-term 3D cell cultures using NRVMs for up to 21 days. They found that NRVMs cultured in the 3D RTG-CNT hydrogel have stronger and more homogeneous spontaneous calcium transients and an increased and more organized localization Cx43 when compared with NRVMs cultured in the 3D hydrogel without CNTs or in their 2D gelatin controls (standard controls for NRVM culture). Moreover, they observed that the culture of NRVMs in the 3D RTG-CNT promoted cardiomyocyte proliferation during the first four days of culture. These results demonstrated that conductive CNTs have the capacity to improve NRVMs' function and promote early cardiomyocyte proliferation.

CNTs can also be dispersed into PNIPAAm solutions. Li *et al.*[164] used PNIPAAm's unique abilities to inject and localize brown adipose derived stem cells (BASCs) into the myocardium of a rat myocardial infarction model and they improved cell engraftment, cardiac repair and function when SWCNTs were dispersed in the PNIPAAm hydrogel. Thus, the incorporation of CNTs

not only enhances function *in vitro*, but also improves cell integration and therapeutic benefit *in vivo*.

As previously discussed, injectable hydrogels are ideal systems for patients with other co-morbidities that put them at risk during invasive surgeries. However, polymeric patches can be also used for cardiac repair for other cardiac injuries in which injectable hydrogels are not ideal. The following section will discuss and describe the use of CNTs in polymeric patches for cardiac tissue engineering applications.

7.4.3 3D Cardiac Patches

As previously mentioned, the main difficulty in repairing the heart by itself after infarction is the limited regenerative capacity of the myocardium. The artificial regeneration of the heart muscle could be an effective therapy, and the implantation of cell supportive cardiac patches directly into the diseased myocardium has become a potential solution to achieve such purpose. Ideally, cardiac patches should be able to mimic the myocardium ECM for a successful integration with the tissue. More specifically, they should be electrically conductive, as the host tissue, and mechanically robust and elastic, to support the heart contraction. In most of the reported cardiac patches, the function of the cardiomyocytes is restricted because of mismatches in the mechanics, conductivity and submicrometric structure of the matrix.[154] The introduction of CNTs has been proven to overcome such restrictions, providing the patch with enhanced conductive and mechanical properties. Moreover, CNTs have been shown to increase the cardiac tissue functionality against other conductive carbon nanomaterials, such as graphene oxide and reduced graphene oxide.[123]

Several tissue engineering strategies aimed to produce artificial cardiac tissues through the development of 'sheets' or 'two-dimensional (2D) patches' using a wide array of natural and synthetic polymer composites and blends. Coating substrates containing CNTs have shown to promote cell adhesion, spreading and growth of stem cells, accelerating the maturation of derived cardiomyocytes.[165] However, conventional methods of engineering cardiac tissue through sheet engineering approaches have not been able to recapitulate the extremely complex structure and functionality of the native myocardium. For these, several investigations have shown that tridimensional (3D) scaffolds have become the most effective strategy for tissue regeneration as they have large surface areas for cell or biomaterial attachment, proliferation, sensing, *etc.*[166] Additionally, cellular behavior and cellular responses are more similar to the native tissue in 3D cell cultures which may provide a more realistic biological behavior. Even though studies in the literature regarding the manufacture of 3D conductive cardiac patches indicate that it has not been an easy task, tissue engineers have succeeded in the development of implantable patches. In this section we will review these advances.

7.4.3.1 Hydrogel Patches

Hydrogels are outstanding biomimetic materials for soft tissue applications as they can successfully integrate living cells with good viability within their polymeric matrix.[167,168] Their highly hydrated nature, flexibility and softness can be adjusted to create microenvironments for cells and biomolecules. Moreover, CNTs can be easily dispersed within their polymeric matrix before gelation, providing electrical cues to the hydrogel material. Gelatin-based scaffolds have shown improved performance *in vitro* and *in vivo* when used as engineered cardiac tissue.[169] However, gelatin-based scaffolds are not electrically conductive. To provide electrical cues to gelatin hydrogels, Cabiati *et al.* dispersed CNTs into gelatin polymeric solutions and the resulting gelatin scaffolds provided enhanced cellular electrical excitability with a more mature cardiac phenotype on myoblast H9c2 rat cells when compared with hydrogels without CNTs.[169] Gelatin methacrylate (GelMA) hydrogels functionalized with CNTs have also successfully been obtained and further tested in cardiac cells. Results showed that NRVMs cultured in CNT-GelMA hydrogels have higher spontaneous synchronous beating rates and a lower excitation threshold when compared with NRVMs cultured on GelMA hydrogels without CNTs.[143]

The use of aligned CNTs has brought interest for cardiac tissue engineering as they can be used as electrodes for tissue stimulation. Aligned-CNT microelectrodes can allow pacing in close contact with cells and lower voltages, thus controlling the electrical pulses between cells and tissue constructs and regulating their behavior and function. This kind of platform, which possesses high similarity to the nanofibrous microstructure of native ECM, enables localized stimulation and, hence, guidance of cardiac cells. Although micropatterned hydrogels with aligned CNTs are not easy to manufacture at first glance, a few scientists have succeeded in their production. For example, Shin *et al.* fabricated first a vertically aligned CNT forest by chemical vapor deposition (CVD), and then, encapsulated them within CNT-GelMA and PEG hydrogel layers.[170] They then tested these hydrogels with vertically aligned CNTs using NRVMs. They found that cardiomyocytes cultured in the CNT-GelMA-PEG hydrogel showed homogeneous cell organization with good cell-to-cell coupling associated with maturation and continuous beating. In another study, Ahadian *et al.* also used GelMA to encapsulate CNTs and aligned them using dielectrophoresis. They then tested the hydrogel using mouse embryoid bodies. The authors observed a superior cardiac differentiation of mouse embryoid bodies upon applying electrical stimulation in the aligned CNT-GalMA hydrogel group when compared with non-conductive GelMA and randomly dispersed CNT-GelMA hydrogel groups.[171]

Three-dimensional printing techniques have recently emerged as a promising industrial manufacturing strategy for tissue engineering applications, and biomedical engineering has become one of the cradles of its development. Integrating UV-lighting into a 3D bioprinter provides a new tool to

draw photo-crosslinkable hydrogels into predefined complex structures, curing the gel while it is printed. For example, Izadifar *et al.* generated a hybrid hydrogel composed of a CNTs-incorporated alginate framework and human coronary artery endothelial cells' (HCAECs) laden methacrylated collagen. The nanofilamentous patterned networks were composed of strings between 25 and 500 nm. They observed that CNTs improved not only the electrical and mechanical properties of the hydrogel, but also the HCAECs' cellular attachment and elongation when compared with hydrogels without CNTs.[172] Such low dimensions and complex designed patterns have also been achieved using photolithography techniques. For example, Wang *et al.* developed star-like and stingray-like micropatterns as robotic systems. The authors used CNT/GelMA hydrogels to engineer cardiac muscle tissue from NRVM: the hydrogel was previously attached to poly(ethylene glycol) diacrylate (PEGDA), which provided structural cartilage-like support, and flexible gold microelectrodes, for electrical stimulation control.[173] They concluded that including electrically conductive nanoparticles, such as CNTs, not only improved the electrical coupling of the cardiac tissue, but also induced an excellent *in vitro* tissue architecture and arrangement. In summary, an artificial tissue construct using nanosized-patterned hydrogels is one step closer to implementing robotic systems that can mimic complex living behaviors and thus, shows more reliable biological effects for biomedical studies.

7.4.3.2 Solid Fibrous Patches

Nanofibers with diameters of a few hundred nanometers are considered to be promising materials for 3D cardiomyocyte cultures,[174] as their shape and distribution can be modified to mimic the ECM more effectively than other biomaterials.[175] However, due to the non-conductive nature of natural or synthetic fibers, the challenge remains to introduce conductive additives without influencing the scaffold's biocompatibility. As previously mentioned, CNTs are the perfect nanomaterial to provide electrical cues to non-conductive materials along with enhanced mechanical properties and reduction in degradability. For example, Wickham *et al.* demonstrated that the inclusion of CNTs into 3D poly-caprolactone (PCL) fibrous meshes increased their mechanical strength without altering their morphology, resulting in enhanced proliferation of stem/progenitor cells (CPCs) from murine hearts.[176] In the same work, the authors analyzed the effect of the substrate topology and showed that 3D electrospun meshes supported adhesion, proliferation and differentiation of CPCs, while solvent casted sheets were not able to support cellular attachment nor spreading.

Most of the conductive fibers are produced by electrospinning a solution containing a polymer solution and CNTs. This produces a fibrous mesh with the nanomaterial embedded and trapped within the non-conductive matrix, ensuring mechanical and conductive stability. However, the synthesis of a polymer solution with a homogeneous distribution of nanomaterial by electrospinning can sometimes be unattainable. For example, Hou *et al.*

developed spider silk fibrous matrices containing CNTs using a dry-coating and wet collapsing method that showed high flexibility, lightweight properties, stretching ability, strength and softness.[177] They further tested these matrices with neonatal cardiac chicken cells and found that the CNT-silk fibers have an intimate contact with cardiomyocytes and this can direct cell growth and stimulate cell beating. In materials such as spider silk, coating or electrospray techniques are needed to attach CNTs on the fibrous surfaces.[174]

Nanofibrous matrices with aligned morphologies have been highlighted to induce the formation of oriented engineered cardiac tissues with enhanced functionalities and mature phenotype.[178] Such alignment guides the oriented organization of cardiac cells, sarcomeres and gap junctions, and favors the electric propagation and subsequent synchronized contractions. As reported by Ren *et al.*, super aligned 3D sheets obtained from a spinnable CNT forest have been proven to induce an elongated and aligned cell morphology of cultured neonatal rat ventricular cardiomyocytes and provide efficient extracellular signal–transmission pathways, resulting in regular and synchronous beating. CNTs have also been shown to improve the fibrous alignment of poly(glycerol sebacate):gelatin (PG) polymeric matrices and, together with enhanced electrical conductivity and toughness, promote stronger spontaneous and synchronous beating of NRVMs.[179]

Micropatterns with multiple structures have been also developed. Liu *et al.* formed square, rectangle and honeycomb micropatterned fibrous matrices by deposition of electrospun poly(ethylene glycol)-poly(DL-lactide) (PELA) containing CNT for the co-culture of primary neonatal rat CMs with cardiac fibroblasts and endothelial cells. In their work, the authors observed that the cells cultured in the honeycomb patterned CNT-fibrous matrices showed higher cell viability, better cell elongation, more ECM synthesis, higher production of organized contractile proteins and a pulsation frequency close to that of the atrium when compared with cells cultured in the fibrous matrices without CNT.[180] Furthermore, 3D printing strategies have recently emerged to manufacture superaligned structures. Conductive inks incorporating CNTs have been prepared to print 3D cardiac patches.[90] For example, Vaithilingam *et al.* have used 3D printing approaches to fabricate 3D biomimetic substrates of an acrylate matrix containing CNTs with a linear pattern.[181] Cardiomyocytes derived from human pluripotent stem cells were cultured in the patterned substrates, and the authors demonstrated that cellular behavior could be modulated due to the scaffold architecture and electric properties provided by the CNTs.

Finally, the addition of conductive properties to porous scaffolds has become key for electric stimulation and providing a new kind of interaction with biological systems. Several studies demonstrated that local electrical stimulation favored and accelerated the regeneration and healing processes of electroactive tissues, enhancing cell–cell and cell–substrate interaction.[182] Similarly, even though there is no clear observation of the impact of CNTs on cellular differentiation, the combination of a CNT-based conductive scaffold with electrical stimulation does promote differentiation of cardioprogenitor

cells and, therefore, cardiomyogenesis.[183] To this end, Mombini *et al.* produced 3D nanofiber scaffolds composed on polyvinyl alcohol (PVA), chitosan (CS) and CNTs for cardiac differentiation of rat mesenchymal stem cells (MSCs). In their work, they applied electrical stimulation to favor differentiation and showed that the substrates containing 1% CNTs had optimal conditions for this purpose.[184]

7.5 Toxicities Associated with CNTs

Given the increased usage of CNTs in biomedicine, the concern about a potential toxicity has been raised. Even though strong efforts of one part of the scientific community have been made to devalue them, relatively little is known about the biological effects of these materials. Therefore, the biosafety of CNTs in biomedical applications is still an important consideration and one that typically generates controversy. To this end, there are multiple studies supporting the positive effects of CNTs while others defend their inconvenient usage.[185] Due to their small size and intrinsic properties, CNTs can reach regions of the body that larger particles cannot.[186] This fact can be beneficial when using them as nanocarriers to cross the blood–brain barrier (BBB), one of the main obstacles to get therapeutic substances into the brain. However, this fact can have negative effects when deposited or aggregated into unwanted organs and tissues.[187] Other concerns arise from the high heterogeneity of CNTs used in the experimental studies (*i.e.* length, size, purity, number of walls and surface properties). Furthermore, it has also been highlighted that the tests commonly used have not been adapted to nanosized materials.[188] In this section we will try to untangle this topic and clarify the conditions and considerations that should be taken into account for the biomedical use of CNTs, with special attention to the toxicity or non-toxicity to the heart and the cardiovascular system.

Previous studies demonstrated that CNTs can penetrate cell membranes by endocytosis or simple passive diffusion and recruited into lysosomes, as shown in Figure 7.4. This can lead to oxidative stress, inflammation and cytotoxicity. CNTs are also able to enter organelles and the nucleus. Afterwards, they are excreted by exocytosis or autophagic microvesicles.[189] The cell uptake of CNTs was higher than other carbon nanomaterials, such as graphene oxide (GO), while the cytotoxicity observed between them showed no significant differences.[190,191] The main mechanism of CNT toxicity comes from its high chemical reactivity that favors the production of reactive oxygen species (ROS) and free radicals. This can cause oxidative stress, inflammation, and damage to proteins and DNA.[192] Similarly, Salehcheh *et al.* exposed mitochondria from hearts to a suspension of free CNTs, which resulted in high mitochondrial toxicity. To solve this, the authors also then tested CNT functionalized with naringin (a natural sugar extract from citric fruits) and found that the incorporation of naringin reduced cardiotoxicity.[193]

As an alternative to reduce toxicity and improve biocompatibility, CNTs have been functionalized by incorporating chemical groups or biomolecules.[194,195] For example, oxidation of CNTs was shown to dramatically reduce

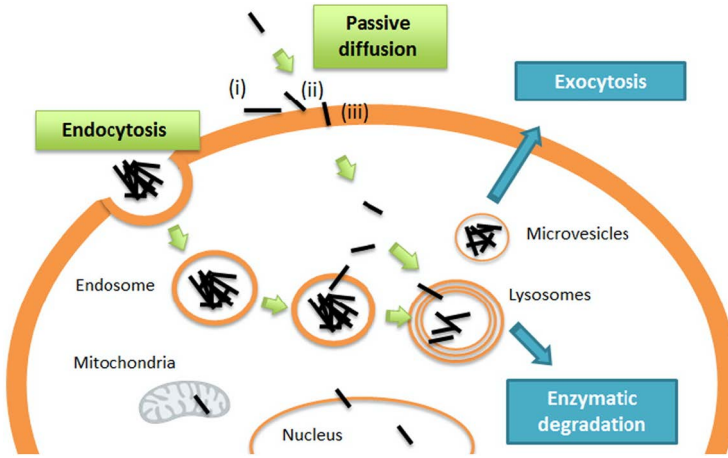

Figure 7.4 Uptake and cellular fate of *f*-CNTs in mammalian cells. Reproduced from ref. 189, https://doi.org/10.1016/j.jconrel.2016.09.033 under the terms of the CC-BY 4.0 license https://creativecommons.org/licenses/by/4.0/.

their toxic effects, making them biodegradable by enzymatic digestion or microglia shattering.[196,197] Chatterjee *et al.* demonstrated that the sensitivity order to cause toxicity was oxidation, hydroxylation-oxygenation, amination and pristine.[198] Cell integration depends on the surface chemistry of the CNTs. Furthermore, another advantage of CNTs is that they can be functionalized with effective carriers of various molecules, including peptides, proteins, plasmids, nucleic acids and chemotherapeutics.[195] Modified CNTs with polyethylene-glycol (PEG) and injected into mouse models showed extended blood circulation times and low uptake by the reticuloendothelial system (RES). In this study, no toxic evidence was detected and the mice did not display any damaging effects, such as weight loss and fatigue.[199]

The toxicity of CNTs has been mostly associated with its physicochemical properties, surface chemistry and functionalization. Other factors that can influence the toxicity are the presence of metal impurities, such as nickel that can generate asthma and dermatitis,[188] and mechanisms such as aggregation, cellular processes, biodistribution and degradation kinetics.[200,201] Xu *et al.* demonstrated that CNT aggregates attenuate the behavior and neurochemical effects of methamphetamine in mice, although no significant change in the common behavior of mice, *e.g.*, feeding, drinking, or locomotion was detected.[202] In any case, the most important toxicity factor at the *in vivo* level is related to the route of CNT delivery into the body (*i.e.* dermal, ingestion, intravenous injection and inhalation). Indeed, inhalation of CNTs may induce a range of harmful effects in laboratory animals, such as inflammation, fibrosis and cancer.[188,203] Several data revealed that free CNTs within the body behave as nano-needles and can have adverse effects comparable to inhaled pathogenic particles and fibers, such as silica and asbestos.[204,205] In particular, inhaled CNTs can interact with the heart, causing muscle

damage, cardiovascular alterations, cell proliferation and disruption in blood flow. These effects can result in atherosclerosis (as previously discussed in Section 7.3.1), hemolysis and blood clotting.[5] Zheng *et al.* reported a detailed study of the effects of inhaled MWCNTs on the cardiovascular system and evaluated the correlation between alterations in heart rate and changes in cardiovascular function.[206] The authors concluded that the cardiovascular alterations where a consequence of changes in the sympathetic and parasympathetic nervous system, and that further studies are required. Currently, few reports study CNT-exposed human beings and the results are inconclusive. It seems that there are multiple signaling pathways involved and the mechanisms associated with heart and vascular toxicity are poorly understood.

It is worth noting that many of the reports proposing that CNTs are harmful evaluate only the effects after inhaling CNT powder or injection of CNT dispersions, most of them using unpurified CNTs. However, in tissue engineering and cardiac engineering in particular, CNTs are embedded in polymeric matrices, making them more stable and localized within the area of interest. CNTs embedded or conjugated into polymeric matrices behave more like particulate materials without interacting with the cellular cytoskeleton and do not act like nanometric materials.[188] All of the CNT-based biomaterials discussed within this book chapter demonstrated no cytotoxicity, inflammation or any negative effect when tested in animal models or in *in vitro* studies for cardiac applications. In fact, 3D meshes of CNTs have been implanted into adult rat visual cortex and not only showed excellent biocompatibility and low tissue reaction after 4 weeks, but also did not induce an inflammatory response. During this experiment, there were no significant effects of scaffold implantation on general animal behavior and/or well-being.[34] Similarly, Pedrotty *et al.* constructed cardiac patches with CNTs and demonstrated that they can restore cardiac conduction when passively applied to surgically disrupted epicardial myocardium in canines.[90] Ren *et al.* developed a flexible superaligned CNT-electrode (SA-CNT) able to synchronously pace *ex vivo* three isolated hearts, imitating the application in cardiac resynchronization therapy, as well as pacing a mouse heart *in vivo*.[89] Unfortunately, few *in vivo* experiments have been performed using CNT-based biomaterial and thus, more animal studies are needed to determine the biological effects of CNTs.

7.6 Conclusions and Future Directions

HF is a leading cause of death worldwide.[207] The gold-standard treatment for end-stage HF is heart transplantation.[53] However, cardiac transplantation remains challenging due to several complications including the limited availability of donated organs, immune rejection, surgical risk and hospitalization costs.[52,53] Advances in cardiac tissue engineering have sought to overcome these limitations by developing novel biomaterials engineered to mimic native cardiac tissue and promote cardiac repair.[66,125–130] In this regard, the incorporation of CNTs has been largely studied to provide electrical cues to non-conductive biomaterials, making them more similar to

native tissue.[95,96] Although there are difficulties in introducing CNTs homogeneously within polymeric matrices, multiple works succeeded in developing hydrogels with homogeneously distributed CNTs and homogeneous CNT-filamentous porous tridimensional conductive substrates. Moreover, aligned-CNTs and nanofilamentous patterned networks have been proven to guide the organization of cardiac cells into a more mature phenotype, mimicking the biological oriented cardiac tissue, and favoring the electric propagation and subsequent synchronized contractions.[168,170,178]

Regarding the cellular pathways activated by CNT in cardiac cells, CNT-functionalized hydrogels have been shown to stimulate cardiac cell function *in vitro* by activating β1-integrin pathways associated with intercalated disc formation.[99,117] In addition, *in vivo* studies using CNT-functionalized biomaterials have shown favorable results in MI animal models, inducing cardiac repair and improving myocardium function.[164] However, the biological pathways relating CNTs with improvement in cardiac function *in vivo* are still unknown and require further investigation.

All this being said, concerns have been raised regarding the potential toxicity of CNTs and research surrounding this remains controversial.[188,198] As previously discussed, unpurified pristine CNTs, not chemically functionalized, integrated nor dispersed within biomaterials, have been associated with atherosclerosis.[69–73] These results were mainly observed due to the delivery route, the animal model assessed and the fact that non-functionalized free CNTs were used. Furthermore, pristine CNTs without proper purification can lead to the presence of toxic metal impurities and CNT aggregates can lead to cellular toxicity.[188,200,201] We have previously demonstrated the importance of CNT functionalization to promote their solubility through synthesizing CNTs with COOH groups by incorporating amino benzyl groups on commercial MWCNT *via* the diazonium salt arylation reaction route.[66] We found that these functionalized CNTs were well dispersed in organic solvents, whereas commercial CNT-COOH formed agglomerates. Therefore, CNT functionalization and proper purification are key to improve CNT dispersion and biocompatibility. However, standard toxicological procedures are still needed to assess CNTs and CNT-functionalized biomaterials. These procedures may include conjugation of the proper chemical groups or biomolecules to properly disperse the CNTs as well targeting delivery methods.

In summary, CNTs have great potential to be used in cardiac tissue engineering applications to not only repair the injured myocardium, but properly mimic its intended electroconductive function. It is likely that CNTs must be functionalized and ideally used in conjunction with biomaterials to improve their efficacy and minimize unwanted effects. However, additional studies are needed to properly design, optimize and advance this potentially life-saving technology.

Acknowledgements

This study was supported by generous grants from the NIH/NHLBI K25HL148386 (BP) and R01HL147064 9 (LM and BP).

References

1. G. R. Rudramurthy and M. K. Swamy, *J. Biol. Inorg Chem.*, 2018, **23**, 1185–1204.
2. F. Gorjikhah, S. Davaran, R. Salehi, M. Bakhtiari, A. Hasanzadeh, Y. Panahi, M. Emamverdy and A. Akbarzadeh, *Artif. Cells, Nanomed., Biotechnol.*, 2016, **44**, 1609–1614.
3. S. Iijima, *Nature*, 1991, **354**, 56–58.
4. V. R. Raphey, T. K. Henna, K. P. Nivitha, P. Mufeedha, C. Sabu and K. Pramod, *Mater. Sci. Eng. C*, 2019, **100**, 616–630.
5. S. K. Prajapati, A. Malaiya, P. Kesharwani, D. Soni and A. Jain, *Drug Chem. Toxicol.*, 2020, 1–15.
6. G. A. Silva, *Nat. Rev. Neurosci.*, 2006, **7**, 65–74.
7. R. Rauti, M. Musto, S. Bosi, M. Prato and L. Ballerini, *Carbon*, 2019, **143**, 430–446.
8. M. P. Mattson, R. C. Haddon and A. M. Rao, *J. Mol. Neurosci.*, 2000, **14**, 175–182.
9. A. Fabbro, M. Prato and L. Ballerini, *Adv. Drug Delivery Rev.*, 2013, **65**, 2034–2044.
10. A. Fabbro, S. Bosi, L. Ballerini and M. Prato, *ACS Chem. Neurosci.*, 2012, **3**, 611–618.
11. H. Hu, Y. Ni, V. Montana, R. C. Haddon and V. Parpura, *Nano Lett.*, 2004, **4**, 507–511.
12. E. B. Malarkey, K. A. Fisher, E. Bekyarova, W. Liu, R. C. Haddon and V. Parpura, *Nano Lett.*, 2009, **9**, 264–268.
13. N. P. Pampaloni, D. Scaini, F. Perissinotto, S. Bosi, M. Prato and L. Ballerini, *Nanomedicine*, 2018, **14**, 2521–2532.
14. S. Fiorito, J. Russier, A. Salemme, M. Soligo, L. Manni, E. Krasnowska, S. Bonnamy, E. Flahaut, A. Serafino, G. I. Togna, L. N. J. L. Marlier and A. R. Togna, *Carbon*, 2018, **129**, 572–584.
15. A. Mazzatenta, M. Giugliano, S. Campidelli, L. Gambazzi, L. Businaro, H. Markram, M. Prato and L. Ballerini, *J. Neurosci.*, 2007, **27**, 6931–6936.
16. V. Lovat, D. Pantarotto, L. Lagostena, B. Cacciari, M. Grandolfo, M. Righi, G. Spalluto, M. Prato and L. Ballerini, *Nano Lett.*, 2005, **5**, 1107–1110.
17. G. Cellot, E. Cilia, S. Cipollone, V. Rancic, A. Sucapane, S. Giordani, L. Gambazzi, H. Markram, M. Grandolfo, D. Scaini, F. Gelain, L. Casalis, M. Prato, M. Giugliano and L. Ballerini, *Nat. Nanotechnol.*, 2009, **4**, 126–133.
18. G. Cellot, F. M. Toma, Z. K. Varley, J. Laishram, A. Villari, M. Quintana, S. Cipollone, M. Prato and L. Ballerini, *J. Neurosci.*, 2011, **31**, 12945–12953.
19. A. Fabbro, A. Sucapane, F. M. Toma, E. Calura, L. Rizzetto, C. Carrieri, P. Roncaglia, V. Martinelli, D. Scaini, L. Masten, A. Turco, S. Gustincich, M. Prato and L. Ballerini, *PLoS One*, 2013, **8**, 1–14.
20. A. Fabbro, A. Villari, J. Laishram, D. Scaini, F. M. Toma, A. Turco, M. Prato and L. Ballerini, *ACS Nano*, 2012, **6**, 2041–2055.
21. S. A. Busch and J. Silver, *Curr. Opin. Neurobiol.*, 2007, **17**, 120–127.
22. M. T. Fitch and J. Silver, *Exp. Neurol.*, 2008, **209**, 294–301.

23. A. Rolls, R. Shechter and M. Schwartz, *Nat. Rev. Neurosci.*, 2009, **10**, 235–241.
24. A. Accardo, C. Cirillo, S. Lionnet, C. Vieu and I. Loubinoux, *Brain Res. Bull.*, 2019, **152**, 202–211.
25. L. Papadimitriou, P. Manganas, A. Ranella and E. Stratakis, *Mater. Today Bio*, 2020, **6**, 100043.
26. E. C. Spivey, Z. Z. Khaing, J. B. Shear and C. E. Schmidt, *Biomaterials*, 2012, **33**, 4264–4276.
27. J. M. Corey, D. Y. Lin, K. B. Mycek, Q. Chen, S. Samuel, E. L. Feldman and D. C. Martin, *J. Biomed. Mater. Res., Part A*, 2007, **83**, 636–645.
28. S. Y. Park, B. S. Kang and S. Hong, *Nanomedicine*, 2013, **8**, 715–723.
29. E. Hasanzadeh, S. Ebrahimi-Barough, E. Mirzaei, M. Azami, S. M. Tavangar, N. Mahmoodi, A. Basiri and J. Ai, *J. Biomed. Mater. Res., Part A*, 2019, **107**, 802–814.
30. M. J. Roberts, M. K. Leach, M. Bedewy, E. R. Meshot, D. Copic, J. M. Corey and A. J. Hart, *J. Neural Eng.*, 2014, **11**, 036013.
31. S. J. Lee, W. Zhu, M. Nowicki, G. Lee, D. N. Heo, J. Kim, Y. Y. Zuo and L. G. Zhang, *J. Neural Eng.*, 2018, **15**, 016018.
32. X. Liu, A. L. Miller, S. Park, B. E. Waletzki, A. Terzic, M. J. Yaszemski and L. Lu, *J. Mater. Chem. B*, 2016, **4**, 6930–6941.
33. K. Shah, D. Vasileva, A. Karadaghy and S. P. Zustiak, *J. Mater. Chem. B*, 2015, **3**, 7950–7962.
34. S. Usmani, E. R. Aurand, M. Medelin, A. Fabbro, D. Scaini, J. Laishram, F. B. Rosselli, A. Ansuini, D. Zoccolan, M. Scarselli, M. De Crescenzi, S. Bosi, M. Prato and L. Ballerini, *Sci. Adv.*, 2016, **2**, e1600087.
35. S. Bosi, R. Rauti, J. Laishram, A. Turco, D. Lonardoni, T. Nieus, M. Prato, D. Scaini and L. Ballerini, *Sci. Rep.*, 2015, **5**, 9562.
36. G. Cellot, P. Lagonegro, G. Tarabella, D. Scaini, F. Fabbri, S. Iannotta, M. Prato, G. Salviati and L. Ballerini, *Front. Neurosci.*, 2016, **9**, 521.
37. N. Alegret, A. Dominguez-Alfaro, J. M. González-Domínguez, B. Arnaiz, U. Cossío, S. Bosi, E. Vázquez, P. Ramos-Cabrer, D. Mecerreyes and M. Prato, *ACS Appl. Mater. Interfaces*, 2018, **10**, 43904–43914.
38. A. Dominguez-Alfaro, N. Alegret, B. Arnaiz, J. M. González-Domínguez, A. Martin-Pacheco, U. Cossío, L. Porcarelli, S. Bosi, E. Vázquez, D. Mecerreyes and M. Prato, *ACS Biomater. Sci. Eng.*, 2020, **6**, 1269–1278.
39. E. Braunwald, *JACC Heart Fail.*, 2013, **1**, 1–20.
40. B. Ziaeian and G. C. Fonarow, *Nat. Rev. Cardiol.*, 2016, **13**, 368–378.
41. F. M. Chen and X. Liu, *Prog. Polym. Sci.*, 2016, **53**, 86–168.
42. A. L. Bui, T. B. Horwich and G. C. Fonarow, *Nat. Rev. Cardiol.*, 2011, **8**, 30–41.
43. A. Schäfer, N. Werner, D. Burkhoff, J.-T. Sieweke, A. Zietzer, M. Masyuk, N. L. Junker Udesen, R. Westenfeld and J. E. Møller, *Front. Cardiovasc. Med.*, 2020, **7**, 74.
44. A. Albakri, *Clin. Med. Invest.*, 2018, **3**, 1–15.
45. M. F. Minicucci, P. S. Azevedo, B. F. Polegato, S. A. R. Paiva and L. A. M. Zornoff, *Clin. Cardiol.*, 2011, **34**, 410–414.

46. P. S. Azevedo, B. F. Polegato, M. F. Minicucci, S. A. R. Paiva and L. A. M. Zornoff, *Arq. Bras. Cardiol.*, 2016, **106**, 62–69.
47. S. S. Gidding, D. Lloyd-Jones, J. Lima, B. Ambale-Venkatesh, S. J. Shah, R. Shah, C. E. Lewis, D. R. Jacobs and N. B. Allen, *Circ.: Heart Failure*, 2019, **12**, 1–11.
48. E. B. Friedrich and M. Böhm, *Heart*, 2007, **93**, 626–631.
49. L. M. Monteiro, F. Vasques-Nóvoa, L. Ferreira, P. Pinto-do-Ó and D. S. Nascimento, *npj Regener. Med.*, 2017, **2**, 9.
50. I. Bytyçi and G. Bajraktari, *Anadolu Kardiyol. Derg.*, 2015, **15**, 63–68.
51. C. J. Taylor, J. M. Ordóñez-Mena, A. K. Roalfe, S. Lay-Flurrie, N. R. Jones, T. Marshall and F. D. R. Hobbs, *BMJ*, 2019, **364**, 1–10.
52. J. Garbade, M. J. Barten, H. B. Bittner and F.-W. Mohr, *Clin. Cardiol.*, 2013, **36**, 378–382.
53. P. Macdonald, D. Verran, M. O'Leary, E. Cavazzoni and K. Dhital, *Transplantation*, 2015, **99**, 1101–1102.
54. S. S. Virani, A. Alonso, E. J. Benjamin, M. S. Bittencourt, C. W. Callaway, A. P. Carson, A. M. Chamberlain, A. R. Chang, S. Cheng, F. N. Delling, L. Djousse, M. S. V. Elkind, J. F. Ferguson, M. Fornage, S. S. Khan, B. M. Kissela, K. L. Knutson, T. W. Kwan, D. T. Lackland, T. T. Lewis, J. H. Lichtman, C. T. Longenecker, M. S. Loop, P. L. Lutsey, S. S. Martin, K. Matsushita, A. E. Moran, M. E. Mussolino, A. M. Perak, W. D. Rosamond, G. A. Roth, U. K. A. Sampson, G. M. Satou, E. B. Schroeder, S. H. Shah, C. M. Shay, N. L. Spartano, A. Stokes, D. L. Tirschwell, L. B. VanWagner, C. W. Tsao, S. S. Wong and D. G. Heard, *Heart Disease and Stroke Statistics—2020 Update: A Report from the*, American Heart Association, 2020.
55. M. E. Helmuth, Q. Liu, M. N. Turenne, J. M. Park, M. Oguntimein, S. K. Dutcher, R. Balkrishnan, P. Sharma, J. Zee, A. B. Leichtman and A. R. Smith, *Clin. J. Am. Soc. Nephrol.*, 2019, **14**, 421–430.
56. J. B. Echouffo-Tcheugui, K. G. Bishu, G. C. Fonarow and L. E. Egede, *Am. Heart J.*, 2017, **186**, 63–72.
57. G. Savarese and L. H. Lund, *J. Card Fail Rev.*, 2017, **3**, 7–11.
58. V. L. Roger, *Circ. Res.*, 2013, **113**, 646–659.
59. P. A. Heidenreich, N. M. Albert, L. A. Allen, D. A. Bluemke, J. Butler, G. C. Fonarow, J. S. Ikonomidis, O. Khavjou, M. A. Konstam, T. M. Maddox, G. Nichol, M. Pham, I. L. Piña and J. G. Trogdon, *Circ.: Heart Failure*, 2013, **6**, 606–619.
60. P. P. Chang, L. M. Wruck, E. Shahar, J. S. Rossi, L. R. Loehr, S. D. Russell, S. K. Agarwal, S. H. Konety, C. J. Rodriguez and W. D. Rosamond, *Circulation*, 2018, **138**, 12–24.
61. J. E. A. Blair, M. Huffman and S. J. Shah, *Curr. Cardiol. Rev.*, 2013, **9**, 128–146.
62. S. Komanduri, Y. Jadhao, S. S. Guduru, P. Cheriyath and Y. Wert, *J. Community Hosp. Intern. Med. Perspect.*, 2017, **7**, 15–20.

63. E. J. Benjamin, S. S. Virani, C. W. Callaway, A. M. Chamberlain, A. R. Chang, S. Cheng, S. E. Chiuve, M. Cushman, F. N. Delling, R. Deo, S. D. De Ferranti, J. F. Ferguson, M. Fornage, C. Gillespie, C. R. Isasi, M. C. Jiménez, L. C. Jordan, S. E. Judd, D. Lackland, J. H. Lichtman, L. Lisabeth, S. Liu, C. T. Longenecker, P. L. Lutsey, J. S. MacKey, D. B. Matchar, K. Matsushita, M. E. Mussolino, K. Nasir, M. O'Flaherty, L. P. Palaniappan, A. Pandey, D. K. Pandey, M. J. Reeves, M. D. Ritchey, C. J. Rodriguez, G. A. Roth, W. D. Rosamond, U. K. A. Sampson, G. M. Satou, S. H. Shah, N. L. Spartano, D. L. Tirschwell, C. W. Tsao, J. H. Voeks, J. Z. Willey, J. T. Wilkins, J. H. Y. Wu, H. M. Alger, S. S. Wong and P. Muntner, Heart disease and stroke statistics - 2018 update: A report from the American Heart Association, *Circulation*, 2018, **137**, e67–e492.
64. B. Ziaeian and G. C. Fonarow, *Prog. Cardiovasc. Dis.*, 2016, **58**, 379–385.
65. B. Peña, M. Laughter, S. Jett, T. J. Rowland, M. R. G. Taylor, L. Mestroni and D. Park, *Macromol. Biosci.*, 2018, **18**, 1–22.
66. B. Peña, S. Bosi, B. A. Aguado, D. Borin, N. L. Farnsworth, E. Dobrinskikh, T. J. Rowland, V. Martinelli, M. Jeong, M. R. G. G. Taylor, C. S. Long, R. Shandas, O. Sbaizero, M. Prato, K. S. Anseth, D. Park and L. Mestroni, *ACS Appl. Mater. Interfaces*, 2017, **9**, 31645–31656.
67. G. K. Hansson and P. Libby, *Nat. Rev. Immunol.*, 2006, **6**, 508–519.
68. K. J. Moore and I. Tabas, *Cell*, 2011, **145**, 341–355.
69. L. K. Vesterdal, K. Jantzen, M. Sheykhzade, M. Roursgaard, J. K. Folkmann, S. Loft and P. Moller, *Nanotoxicology*, 2014, **8**, 61–71.
70. Y. Y. Guo, J. Zhang, Y. F. Zheng, J. Yang and X. Q. Zhu, *Mutat. Res.*, 2011, **721**, 184–191.
71. Y. Suzuki, S. Tada-Oikawa, Y. Hayashi, K. Izuoka, M. Kataoka, S. Ichikawa, W. Wu, C. Zong, G. Ichihara and S. Ichihara, *Part. Fibre Toxicol.*, 2016, **13**, 54.
72. V. G. Walker, Z. Li, T. Hulderman, D. Schwegler-Berry, M. L. Kashon and P. P. Simeonova, *Toxicol. Appl. Pharmacol.*, 2009, **236**, 319–328.
73. Y. Cao, N. R. Jacobsen, P. H. Danielsen, A. G. Lenz, T. Stoeger, S. Loft, H. Wallin, M. Roursgaard, L. Mikkelsen and P. Møller, *Toxicol. Sci.*, 2014, **138**, 104–116.
74. S. G. Han, D. Howatt, A. Daugherty and G. Gairola, *J. Toxicol. Environ. Health, Part A*, 2015, **78**, 244–253.
75. D. V. Christophersen, N. R. Jacobsen, M. H. G. Andersen, S. P. Connell, K. K. Barfod, M. B. Thomsen, M. R. Miller, R. Duffin, J. Lykkesfeldt, U. Vogel, H. Wallin, S. Loft, M. Roursgaard and P. Møller, *Toxicology*, 2016, **371**, 29–40.
76. S. S. Poulsen, A. T. Saber, A. Mortensen, J. Szarek, D. Wu, A. Williams, O. Andersen, N. R. Jacobsen, C. L. Yauk, H. Wallin, S. Halappanavar and U. Vogel, *Toxicol. Appl. Pharmacol.*, 2015, **283**, 210–222.
77. Y. Lu, Q. Gong, F. Lu, J. Liang, L. Ji, Q. Nie and X. Zhang, *J. Mater. Sci.: Mater. Med.*, 2011, **22**, 1855–1862.

78. C. I. Santana, L. M. Hoyos, J. F. Pérez, J. Bustamante and A. G. García, *Mater. Sci. Eng. C*, 2017, **79**, 30–36.
79. Y. Si, J. W. Park, S. Jung, G. S. Hwang, E. Goh and H. J. Lee, *Biosens. Bioelectron.*, 2018, **121**, 265–271.
80. H. Saify Nabiabad, K. Piri, F. Kafrashi, A. Afkhami and T. Madrakian, *Anal. Bioanal. Chem.*, 2018, **410**, 3683–3691.
81. V. V. Shumyantseva, T. V. Bulko, L. V. Sigolaeva, A. V. Kuzikov, P. V. Pogodin and A. I. Archakov, *Biosens. Bioelectron.*, 2016, **86**, 330–336.
82. B. Rezaei, A. M. Shoushtari, M. Rabiee, L. Uzun, W. C. Mak and A. P. F. Turner, *Talanta*, 2018, **182**, 178–186.
83. J. M. S. Wait, H. Tomita, L. M. Burk, J. Lu, O. Z. Zhou, N. Maeda and Y. Z. Lee, *J. Am. Heart Assoc.*, 2013, **2**, e003358.
84. H. Kosuge, S. P. Sherlock, T. Kitagawa, R. Dash, J. T. Robinson, H. Dai and M. V. McConnell, *J. Am. Heart Assoc.*, 2012, **1**, e002568.
85. G. Tse, *J. Arrhythmia*, 2016, **32**, 75–81.
86. A. E. Buxton, K. L. Lee, J. D. Fisher, M. E. Josephson, E. N. Prystowsky and G. Hafley, *N. Engl. J. Med.*, 1999, **341**, 1882–1890.
87. J. Camm, *Int. J. Cardiol.*, 2012, **155**, 362–371.
88. M. D. Mccauley, F. Vitale, J. S. Yan, C. C. Young, B. Greet, M. Orecchioni, S. Perike, A. Elgalad, J. A. Coco, M. John, D. A. Taylor, L. C. Sampaio, L. G. Delogu, M. Razavi and M. Pasquali, *Circ.: Arrhythmia Electrophysiol.*, 2019, **12**, e007256.
89. J. Ren, Q. Xu, X. Chen, W. Li, K. Guo, Y. Zhao, Q. Wang, Z. Zhang, H. Peng and Y. G. Li, *Adv. Mater.*, 2017, **29**, 1702713.
90. D. M. Pedrotty, V. Kuzmenko, E. Karabulut, A. M. Sugrue, C. Livia, V. R. Vaidya, C. J. Mcleod, S. J. Asirvatham, P. Gatenholm and S. Kapa, *Circ.: Arrhythmia Electrophysiol.*, 2019, **12**, e006920.
91. D. T. Nguyen, W. Barham, L. Zheng, B. Shillinglaw, W. S. Tzou, B. Neltner, L. Mestroni, S. Bosi, L. Ballerini, M. Prato and W. H. Sauer, *J. Cardiovasc. Electrophysiol.*, 2014, **25**, 1385–1390.
92. R. Amezcua, A. Shirolkar, C. Fraze and D. Stout, *Nanomaterials*, 2016, **6**, 133.
93. G. Camci-Unal, N. Annabi, M. R. Dokmeci, R. Liao and A. Khademhosseini, *NPG Asia Mater.*, 2014, **6**, e99.
94. K. N. Alagarsamy, W. Yan, A. Srivastava, V. Desiderio and S. Dhingra, *Rev. Cardiovasc. Med.*, 2019, **20**, 221–230.
95. K. Ashtari, H. Nazari, H. Ko, P. Tebon, M. Akhshik, M. Akbari, S. N. Alhosseini, M. Mozafari, B. Mehravi, M. Soleimani, R. Ardehali, M. Ebrahimi Warkiani, S. Ahadian and A. Khademhosseini, *Adv. Drug Delivery Rev.*, 2019, **144**, 162–179.
96. B. Gorain, H. Choudhury, M. Pandey, P. Kesharwani, M. M. Abeer, R. K. Tekade and Z. Hussain, *Biomed. Pharmacother.*, 2018, **104**, 496–508.
97. V. Martinelli, G. Cellot, F. M. Toma, C. S. Long, J. H. Caldwell, L. Zentilin, M. Giacca, A. Turco, M. Prato, L. Ballerini and L. Mestroni, *Nano Lett.*, 2012, **12**, 1831–1838.

98. V. Martinelli, G. Cellot, A. Fabbro, S. Bosi, L. Mestroni and L. Ballerini, *Front. Physiol.*, 2013, **4**, 1–6.
99. H. Sun, S. Lü, X. X. Jiang, X. Li, H. Li, Q. Lin, Y. Mou, Y. Zhao, Y. Han, J. Zhou and C. Wang, *Biomaterials*, 2015, **55**, 84–95.
100. A. R. C. Santos, R. G. Corredor, B. A. Obeso, E. F. Trakhtenberg, Y. Wang, J. Ponmattam, G. Dvoriantchikova, D. Ivanov, V. I. Shestopalov, J. L. Goldberg, M. E. Fini and M. L. Bajenaru, *PLoS One*, 2012, **7**, e48332.
101. T. Shibue and R. A. Weinberg, *Proc. Natl. Acad. Sci. U. S. A.*, 2009, **106**, 10290–10295.
102. S. Isaeli-Rosenbergr, A. M. Manso, H. Okada and R. S. Ross, *Circ. Res.*, 2014, **114**, 572–586.
103. D. J. Lee, M. A. Cavasin, A. J. Rocker, D. E. Soranno, X. Meng, R. Shandas and D. Park, *J. Biol. Eng.*, 2019, **13**, 1–13.
104. F. Meng and C. A. Lowell, *EMBO J.*, 1998, **17**, 4391–4403.
105. B. Meder, I. G. Huttner, F. Sedaghat-Hamedani, S. Just, T. Dahme, K. S. Frese, B. Vogel, D. Kohler, W. Kloos, J. Rudloff, S. Marquart, H. A. Katus and W. Rottbauer, *Mol. Cell. Biol.*, 2011, **31**, 3424–3435.
106. S. J. Parsons and J. T. Parsons, *Oncogene*, 2004, **23**, 7906–7909.
107. A. Salameh and S. Dhein, *Biochim. Biophys. Acta, Biomembr.*, 2013, **1828**, 147–156.
108. J. J. Saucerman, P. M. Tan, K. S. Buchholz, A. D. McCulloch and J. H. Omens, *Nat. Rev. Cardiol.*, 2019, **16**, 361–378.
109. J. T. Parsons, *J. Cell Sci.*, 2003, **116**, 1409–1416.
110. T. Akagi, K. Murata, T. Shishido and H. Hanafusa, *Mol. Cell. Biol.*, 2002, **22**, 7015–7023.
111. A. E. Aplin, S. A. Stewart, R. K. Assoian, R. L. Juliano, A. E. Aplin, S. A. Stewart, R. K. Assoian and R. L. Juliano, *J. Cell Biol.*, 2001, **153**, 273–282.
112. J. R. McMullen, *Hypertension*, 2009, **54**, 713–715.
113. M. Oyamada, K. Takebe and Y. Oyamada, *Biochim. Biophys. Acta, Biomembr.*, 2013, **1828**, 118–133.
114. V. L. F. Linhares, N. A. S. Almeida, D. C. Menezes, D. A. Elliott, D. Lai, E. C. Beyer, A. C. Campos De Carvalho and M. W. Costa, *Cardiovasc. Res.*, 2004, **64**, 402–411.
115. N. J. A. Scott, L. J. Ellmers, J. G. Lainchbury, N. Maeda, O. Smithies, A. M. Richards and V. A. Cameron, *Biochim. Biophys. Acta, Mol. Basis Dis.*, 2009, **1792**, 1175–1184.
116. D. L. Lefebvre, M. Piersanti, X. Hui Bai, Z. Qing Chen and S. J. Lye, *Reprod., Fertil. Dev.*, 1995, **7**, 603–611.
117. H. Sun, J. Tang, Y. Mou, J. Zhou, L. Qu, K. Duval, Z. Huang, N. Lin, R. Dai, C. Liang, Z. Chen, L. Tang and F. Tian, *Acta Biomater.*, 2017, **48**, 88–99.
118. H. R. Manring, L. E. Dorn, A. Ex-Willey, F. Accornero and M. A. Ackermann, *Biophys. Rev.*, 2018, **10**, 961–971.
119. J. Moncayo-Arlandi and R. Brugada, *Nat. Rev. Cardiol.*, 2017, **14**, 744–756.
120. A. Keren, E. Bengal and D. Frank, *Dev. Biol.*, 2005, **288**, 73–86.
121. C. D. Lawson and K. Burridge, *Small GTPases*, 2014, **5**, 37–41.

122. R. J. Marjoram, E. C. Lessey and K. Burridge, *Curr. Mol. Med.*, 2014, **14**, 199–208.
123. J. Lee, V. Manoharan, L. Cheung, S. Lee, B. H. Cha, P. Newman, R. Farzad, S. Mehrotra, K. Zhang, F. Khan, M. Ghaderi, Y. D. Lin, S. Aftab, P. Mostafalu, M. Miscuglio, J. Li, B. B. Mandal, M. A. Hussain, K. T. Wan, X. S. Tang, A. Khademhosseini and S. R. Shin, *ACS Nano*, 2019, **13**, 12525–12539.
124. G. Nardone, J. Oliver-De La Cruz, J. Vrbsky, C. Martini, J. Pribyl, P. Skládal, M. Pešl, G. Caluori, S. Pagliari, F. Martino, Z. Maceckova, M. Hajduch, A. Sanz-Garcia, N. M. Pugno, G. B. Stokin and G. Forte, *Nat. Commun.*, 2017, **8**, 15321.
125. L. Ye, W. H. Zimmermann, D. J. Garry and J. Zhang, *Circ. Res.*, 2013, **113**, 922–932.
126. C. Castells-Sala and C. E. Semino, *Curr. Opin. Organ Transplant.*, 2012, **17**, 681–687.
127. B. Peña, V. Martinelli, M. Jeong, S. Bosi, R. Lapasin, M. R. G. G. Taylor, C. S. Long, R. Shandas, D. Park and L. Mestroni, *Biomacromolecules*, 2016, **17**, 1593–1601.
128. G. A. Truskey, *F1000Research*, 2016, **5**, 1045.
129. C. P. Jackman, I. Y. Shadrin, A. L. Carlson and N. Bursac, *Curr. Opin. Chem. Eng.*, 2015, **7**, 57–64.
130. L. L. Y. Chiu and M. Radisic, *Curr. Opin. Chem. Eng.*, 2013, **2**, 41–52.
131. A. Moorthi, Y.-C. Tyan and T.-W. Chung, *Biomater. Sci.*, 2017, **5**, 1976–1987.
132. B. Peña, M. Maldonado, A. J. Bonham, B. A. Aguado, A. Dominguez-Alfaro, M. Laughter, T. J. Rowland, J. Bardill, N. L. Farnsworth, N. Alegret Ramon, M. R. G. Taylor, K. S. Anseth, M. Prato, R. Shandas, T. A. McKinsey, D. Park and L. Mestroni, *ACS Appl. Mater. Interfaces*, 2019, **11**, 18671–18680.
133. Z. Li and J. Guan, *Polymers*, 2011, **3**, 740–761.
134. S. Khan, A. Ullah, K. Ullah and N. U. Rehman, *Des. Monomers Polym.*, 2016, **19**, 456–478.
135. C. L. Hastings, E. T. Roche, E. Ruiz-Hernandez, K. Schenke-Layland, C. J. Walsh and G. P. Duffy, *Adv. Drug Delivery Rev.*, 2015, **84**, 85–106.
136. J. A. Burdick, R. L. Mauck and S. Gerecht, *Cell Stem Cell*, 2016, **18**, 13–15.
137. H. Wang, J. Zhou, Z. Liu and C. Wang, *J. Cell. Mol. Med.*, 2010, **14**, 1044–1055.
138. Z. Wu, G. Chen, J. Zhang, Y. Hua, J. Li, B. Liu, A. Huang, H. Li, M. Chen and C. Ou, *Sci. Rep.*, 2017, **7**, 1–11.
139. N. Frey, A. Linke, T. Süselbeck, J. Müller-Ehmsen, P. Vermeersch, D. Schoors, M. Rosenberg, F. Bea, S. Tuvia and J. Leor, *Circ.: Cardiovasc. Interventions*, 2014, **7**, 806–812.
140. S. D. Anker, A. J. S. Coats, G. Cristian, D. Dragomir, E. Pusineri, M. Piredda, L. Bettari, R. Dowling, M. Volterrani, B. A. Kirwan, G. Filippatos, J. L. Mas, N. Danchin, S. D. Solomon, R. J. Lee, F. Ahmann, A. Hinson, H. N. Sabbah and D. L. Mann, *Eur. Heart J.*, 2015, **36**, 2297–2309.

141. N. Tandon, C. Cannizzaro, P.-H. G. Chao, R. Maidhof, A. Marsano, H. T. H. Au, M. Radisic and G. Vunjak-Novakovic, *Nat. Protoc.*, 2009, **4**, 155–173.
142. E. L. Ongstad and R. G. Gourdie, *Semin. Cell Dev. Biol.*, 2016, **58**, 41–54.
143. S. R. Shin, S. M. Jung, M. Zalabany, K. Kim, P. Zorlutuna, S. B. Kim, M. Nikkhah, M. Khabiry, M. Azize, J. Kong, K. T. Wan, T. Palacios, M. R. Dokmeci, H. Bae, X. Tang and A. Khademhosseini, *ACS Nano*, 2013, **7**, 2369–2380.
144. V. Martinelli, S. Bosi, B. Penã, G. Baj, C. S. Long, O. Sbaizero, M. Giacca, M. Prato and L. Mestroni, *ACS Appl. Bio Mater.*, 2018, **1**, 1530–1537.
145. X. Liao, X. Yang, H. Deng, Y. Hao, L. Mao, R. Zhang, W. Liao and M. Yuan, *Front. Bioeng. Biotechnol.*, 2020, **8**, 1–18.
146. M. T. Spang and K. L. Christman, *Acta Biomater.*, 2018, **68**, 1–14.
147. J. M. Singelyn, P. Sundaramurthy, T. D. Johnson, P. J. Schup-Magoffin, D. P. Hu, D. M. Faulk, J. Wang, K. M. Mayle, K. Bartels, M. Salvatore, A. M. Kinsey, A. N. Demaria, N. Dib and K. L. Christman, *J. Am. Coll. Cardiol.*, 2012, **59**, 751–763.
148. S. B. Seif-Naraghi, J. M. Singelyn, M. A. Salvatore, K. G. Osborn, J. J. Wang, U. Sampat, O. L. Kwan, G. M. Strachan, J. Wong, P. J. Schup-Magoffin, R. L. Braden, K. Bartels, J. A. DeQuach, M. Preul, A. M. Kinsey, A. N. DeMaria, N. Dib and K. L. Christman, *Sci. Transl. Med.*, 2013, **5**, 1883–1889.
149. K. Roshanbinfar, J. Hilborn, O. P. Varghese and O. P. Oommen, *RSC Adv.*, 2017, **7**, 31980–31988.
150. K. Roshanbinfar, Z. Mohammadi, A. Sheikh-Mahdi Mesgar, M. M. Dehghan, O. P. Oommen, J. Hilborn and F. B. Engel, *Biomater. Sci.*, 2019, **7**, 3906–3917.
151. Y. Seo, Y. Jung and S. H. Kim, *Acta Biomater.*, 2018, **67**, 270–281.
152. R. K. Li, Z. Q. Jia, R. D. Weisel, D. A. Mickle, A. Choi and T. M. Yau, *Circulation*, 1999, **100**, II63-9.
153. H. Sun, J. Zhou, Z. Huang, L. Qu, N. Lin, C. Liang, R. Dai, L. Tang and F. Tian, *Int. J. Nanomed.*, 2017, **12**, 3109–3120.
154. H. Yu, H. Zhao, C. Huang and Y. Du, *ACS Biomater. Sci. Eng.*, 2017, **3**, 3017–3021.
155. P. Varilly and D. Chandler, *Sci. China Chem.*, 2014, **57**, 490–500.
156. P. A. Gunatillake, R. Adhikari and N. Gadegaard, *Eur. Cells Mater.*, 2003, **5**, 1–16.
157. D. Ozdil and H. M. Aydin, *J. Chem. Technol. Biotechnol.*, 2014, **89**, 1793–1810.
158. E. S. Place, J. H. George, C. K. Williams and M. M. Stevens, *Chem. Soc. Rev.*, 2009, **38**, 1139.
159. J. Wu, F. Zeng, X.-P. Huang, J. C.-Y. Chung, F. Konecny, R. D. Weisel and R.-K. Li, *Biomaterials*, 2011, **32**, 579–586.
160. E. H. Kim, M. K. Joo, K. H. Bahk, M. H. Park, B. Chi, Y. M. Lee and B. Jeong, *Biomacromolecules*, 2009, 2476–2481.

161. M. Nakayama, T. Okano, T. Miyazaki, F. Kohori, K. Sakai and M. Yokoyama, *J. Control. Release*, 2006, **115**, 46–56.
162. D. C. Coughlan, F. P. Quilty and O. I. Corrigan, *J. Control. Release*, 2004, **98**, 97–114.
163. D. Schmaljohann, *Adv. Drug Delivery Rev.*, 2006, **58**, 1655–1670.
164. X. Li, J. Zhou, Z. Liu, J. Chen, S. Lu, H. Sun, J. Li, Q. Lin, B. Yang, C. Duan, M. M. Xing and C. Wang, *Biomaterials*, 2014, **35**, 5679–5688.
165. H. Sun, Y. Mou, Y. Li, X. Li, Z. Chen, K. Duval, Z. Huang, R. Dai, L. Tang and F. Tian, *Int. J. Nanomed.*, 2016, **11**, 4381–4395.
166. J. S. Choi, J. S. Park, B. Kim, B. T. Lee and J. H. Yim, *Polymer*, 2017, **124**, 95–100.
167. F. Zhao, D. Yao, R. Guo, L. Deng, A. Dong and J. Zhang, *Nanomaterials*, 2015, **5**, 2054–2130.
168. M. B. Runge, M. Dadsetan, J. Baltrusaitis, T. Ruesink, L. Lu, A. J. Windebank and M. J. Yaszemski, *Biomacromolecules*, 2010, **11**, 2845–2853.
169. M. Cabiati, F. Vozzi, F. Gemma, F. Montemurro, C. De Maria, G. Vozzi, C. Domenici and S. Del Ry, *J. Biomed. Mater. Res., Part B*, 2018, **106**, 2750–2762.
170. S. R. Shin, C. Shin, A. Memic, S. Shadmehr, M. Miscuglio, H. Y. Jung, S. M. Jung, H. Bae, A. Khademhosseini, X. Tang and M. R. Dokmeci, *Adv. Funct. Mater.*, 2015, **25**, 4486–4495.
171. S. Ahadian, S. Yamada, J. Ramón-Azcón, M. Estili, X. Liang, K. Nakajima, H. Shiku, A. Khademhosseini and T. Matsue, *Acta Biomater.*, 2016, **31**, 134–143.
172. M. Izadifar, D. Chapman, P. Babyn, X. Chen and M. E. Kelly, *Tissue Eng., Part C*, 2018, **24**, 74–88.
173. T. Wang, B. Migliori, B. Miccoli and S. R. Shin, *J. Vis. Exp.*, 2020, **156**, e60717.
174. S. Asadpour, H. Yeganeh, J. Ai, S. Kargozar, M. Rashtbar, A. Seifalian and H. Ghanbari, *ACS Biomater. Sci. Eng.*, 2018, **4**, 4299–4310.
175. A. S. Tayi, E. T. Pashuck, C. J. Newcomb, M. T. McClendon and S. I. Stupp, *Biomacromolecules*, 2014, **15**, 1323–1327.
176. A. M. Wickham, M. M. Islam, D. Mondal, J. Phopase, V. Sadhu, É. Tamás, N. Polisetti, A. Richter-Dahlfors, B. Liedberg and M. Griffith, *J. Biomed. Mater. Res., Part B*, 2014, **102**, 1553–1561.
177. J. Hou, Y. Xie, A. Ji, A. Cao, Y. Fang and E. Shi, *ACS Appl. Mater. Interfaces*, 2018, **10**, 6793–6798.
178. G. Zhao, X. Zhang, B. Li, G. Huang, F. Xu and X. Zhang, *ACS Biomater. Sci. Eng.*, 2020, **6**, 1630–1640.
179. M. Kharaziha, S. R. Shin, M. Nikkhah, S. N. Topkaya, N. Masoumi, N. Annabi, M. R. Dokmeci and A. Khademhosseini, *Biomaterials*, 2014, **35**, 7346–7354.
180. Y. Liu, J. Lu, G. Xu, J. Wei, Z. Zhang and X. Li, *Mater. Sci. Eng. C*, 2016, **69**, 865–874.
181. J. Vaithilingam, P. Sanjuan-Alberte, S. Campora, G. A. Rance, L. Jiang, J. Thorpe, L. Burroughs, C. J. Tuck, C. Denning, R. D. Wildman, R. J. M. Hague, M. R. Alexander and F. J. Rawson, *Adv. Funct. Mater.*, 2019, **29**, 1902016.

182. R. Balint, N. J. Cassidy and S. H. Cartmell, *Tissue Eng., Part B*, 2013, **19**, 48–57.
183. E. Mooney, J. N. Mackle, D. J. P. Blond, E. O'Cearbhaill, G. Shaw, W. J. Blau, F. P. Barry, V. Barron and J. M. Murphy, *Biomaterials*, 2012, **33**, 6132–6139.
184. S. Mombini, J. Mohammadnejad, B. Bakhshandeh, A. Narmani, J. Nourmohammadi, S. Vahdat and S. Zirak, *Int. J. Biol. Macromol.*, 2019, **140**, 278–287.
185. M. Marcaccio and F. Paolucci, *Top. Curr. Chem.*, 2013, **348**, v–vi.
186. R. Duffin, N. L. Mills and K. Donaldson, *Yonsei Med. J.*, 2007, **48**, 561–572.
187. C. Bussy, A. Bianco, M. Prato and K. Kostarelos, *Nanoscale Horiz.*, 2017, **2**, 284–296.
188. B. R. C. De Menezes, K. F. Rodrigues, B. C. D. S. Fonseca, R. G. Ribas, T. L. D. A. Montanheiro and G. P. Thim, *J. Mater. Chem. B*, 2019, **7**, 1343–1360.
189. P. M. Costa, M. Bourgognon, J. T. W. Wang and K. T. Al-Jamal, *J. Control. Release*, 2016, **241**, 200–219.
190. X. Zhang, W. Hu, J. Li, L. Tao and Y. Wei, *Toxicol. Res.*, 2012, **1**, 62–68.
191. C. Xiang, Y. Zhang, W. Guo and X. J. Liang, *Acta Pharm. Sin. B*, 2020, **10**, 239–248.
192. M. Kulmala, H. Vehkamäki, T. Petäjä, M. Dal Maso, A. Lauri, V. M. Kerminen, W. Birmili and P. H. McMurry, *J. Aerosol Sci.*, 2004, **35**, 143–176.
193. M. Salehcheh, S. Alboghobeish, M. A. Dehghani and L. Zeidooni, *Environ. Sci. Pollut. Res.*, 2020, **27**, 13447–13456.
194. S. Bosi, A. Fabbro, C. Cantarutti, M. Mihajlovic, L. Ballerini and M. Prato, *Carbon*, 2016, **97**, 87–91.
195. A. Battigelli, C. Ménard-Moyon, T. Da Ros, M. Prato and A. Bianco, *Adv. Drug Delivery Rev.*, 2013, **65**, 1899–1920.
196. A. Nunes, C. Bussy, L. Gherardini, M. Meneghetti, M. A. Herrero, A. Bianco, M. Prato, T. Pizzorusso, K. T. Al-Jamal and K. Kostarelos, *Nanomedicine*, 2012, **7**, 1485–1494.
197. A. E. Goode, D. A. Gonzalez Carter, M. Motskin, I. S. Pienaar, S. Chen, S. Hu, P. Ruenraroengsak, M. P. Ryan, M. S. P. Shaffer, D. T. Dexter and A. E. Porter, *Biomaterials*, 2015, **70**, 57–70.
198. N. Chatterjee, J. Yang, H. M. Kim, E. Jo, P. J. Kim, K. Choi and J. Choi, *J. Toxicol. Environ. Health, Part A*, 2014, **77**, 1399–1408.
199. Z. Liu, W. Cai, L. He, N. Nakayama, K. Chen, X. Sun, X. Chen and H. Dai, *Nat. Nanotechnol.*, 2007, **2**, 47–52.
200. M. P. Holsapple, W. H. Farland, T. D. Landry, N. A. Monteiro-Riviere, J. M. Carter, N. J. Walker and K. V. Thomas, *Toxicol. Sci.*, 2005, **88**, 12–17.
201. B. Song, J. Gong, W. Tang, G. Zeng, M. Chen, P. Xu, M. Shen, S. Ye, H. Feng, C. Zhou and Y. Yang, *Sci. Total Environ.*, 2020, **713**, 136645.
202. X. Xue, J. Y. Yang, Y. He, L. R. Wang, P. Liu, L. S. Yu, G. H. Bi, M. M. Zhu, Y. Y. Liu, R. W. Xiang, X. T. Yang, X. Y. Fan, X. M. Wang, J. Qi, H. J. Zhang, T. Wei, W. Cui, G. L. Ge, Z. X. Xi, C. F. Wu and X. J. Liang, *Nat. Nanotechnol.*, 2016, **11**, 613–620.
203. J. Dong and Q. Ma, *Nanotoxicology*, 2019, **13**, 1244–1274.

204. J. Palomäki, E. Välimäki, J. Sund, M. Vippola, P. A. Clausen, K. A. Jensen, K. Savolainen, S. Matikainen and H. Alenius, *ACS Nano*, 2011, **5**, 6861–6870.
205. K. Donaldson, C. A. Poland, F. A. Murphy, M. MacFarlane, T. Chernova and A. Schinwald, *Adv. Drug Delivery Rev.*, 2013, **65**, 2078–2086.
206. W. Zheng, W. McKinney, M. L. Kashon, D. Pan, V. Castranova and H. Kan, *Nanoscale Res. Lett.*, 2018, **13**, 189.
207. K. L. Fujimoto, Z. Ma, D. M. Nelson, R. Hashizume, J. Guan, K. Tobita and W. R. Wagner, *Biomaterials*, 2009, **30**, 4357–4368.

CHAPTER 8

Nanodiamonds and Their Biological Applications

CHANDRA P. EPPERLA*[a,b], HSIN-HUNG LIN[a] AND HUAN-CHENG CHANG[a]

[a]Institute of Atomic and Molecular Sciences, Academia Sinica, Taipei, 106, Taiwan; [b]Institute of Organic Chemistry and Biochemistry of the CAS, Flemingovo nam. 2, 166 10 Prague, Czech Republic
*E-mail: epperlaprakash@gmail.com

8.1 Introduction

Diamonds are the hardest known naturally occurring mineral on Earth. Diamonds are made up of purely carbon atoms that are arranged in a cubic crystal structure. They are naturally formed in the Earth's mantle at extreme conditions of high temperature and pressure. In addition to this, diamonds are also found in space,[1,2] in metamorphic rocks as a result of continental plate collisions,[3,4] and are also formed by the impacts of meteorites on Earth.[5] Although 'bulk' diamonds are most commonly used for jewelry purposes, 'tiny' diamond particles are used in a wide range of scientific applications owing to their unique physical properties. These 'tiny' diamonds are called nanodiamonds (NDs) and their size is in the order of few hundreds of nanometers. NDs, similar to bulk diamonds, also possess a cubic crystal structure and are made up of carbon atoms and impurities (dopants) to a certain extent in ppm levels due to their different

Nanoscience & Nanotechnology Series No. 48
Carbon Nanostructures for Biomedical Applications
Edited by Tatiana Da Ros, Nazario Martín and Jean-Francois Nierengarten

Published by the Royal Society of Chemistry, www.rsc.org

preparation schemes. In comparison to other carbon allotropes, NDs are unique in that they solely consist of sp^3 hybridized carbon atoms and thus are optically transparent and biologically inert. NDs have attracted much attention in biomedical research especially due to their numerous unique properties such as easy surface functionalization, high thermal conductivity and photostability, biocompatibility and extended far-red fluorescence emission, *etc.*[6]

This chapter focuses on giving a brief introduction about NDs, their color centers and biocompatibility studies, and then their various applications in biology and medicine are finally discussed in detail.

8.2 Production of NDs

The problem that attracted many great scientists 200 years ago was diamond synthesis. The first credit to diamond synthesis has been given to Henry Moisson in 1893 when he claimed to have made diamonds by dissolving sugar charcoal in molten iron and then rapidly cooling the molten mass in water. Many scientists and workers have failed when attempting to reproduce the same results. Nevertheless, over the decades many methodologies have evolved for preparing diamonds among which the widely used methods are high pressure and high temperature (HPHT), detonation and chemical vapor deposition (CVD).

It was not until 1955 that the first reproducible nanodiamond synthesis was reported.[7] By applying high pressure and high temperature to a carbon source, such as graphite, in a belt apparatus at pressures greater than 100 000 atm and temperatures above 2000 °C, diamond particles were produced. Diamond crystals grown by this technique are of high quality and their sizes range from tens of nanometers to about 1 cm. Later, in 1963, a group of Soviet Union scientists observed that detonation of carbon containing explosives such as a trinitrotoluene/hexogen mixture produced diamond particles in the soot.[8] Diamond particles obtained by this method are called 'detonation nanodiamonds (DNDs)'. The product of detonation synthesis includes both diamond and graphite like structures along with other impurities such as metals and oxides that originate from the steel walls of the explosion chamber. A further purification process of this DND by both mechanical and chemical means took place to obtain NDs with an average size of 5 nm. Around the same time in the 1960s, a chemical vapor deposition (CVD) method was developed to produce NDs.[9] In contrast to the both HPHT and DND synthesis where high pressures are needed, low pressures are used in the CVD technique. Briefly, a mixture of a carbon source such as methane or acetylene and hydrogen is taken in a gas chamber in a typical ratio of 1 : 99 where it is heated to temperatures above 1000 °C. At this temperature all the molecular bonds are broken and plasma is created where the free atoms in the plasma are deposited on the substrate surface forming a diamond layer.

In addition to the most commonly used techniques such as HPHT, detonation and CVD, many other techniques have been developed over the past decades. For example, ion irradiation of graphite,[10] femtosecond laser irradiation of graphite,[11] electron irradiation of carbon onions,[12] chlorination of carbides,[13] ultrasound cavitation,[14] laser ablation of graphite,[15] microplasma-assisted ND formation are just a few. Since several papers have been published explaining the methods of HPHT, detonation and the CVD method, these are not discussed in detail in here.

8.3 Color Centers

Color centers are crystal defects in the diamond lattice that are created due to impurities present during the production of diamonds. Although pure diamonds are optically transparent due to their wide band gap (5.5 eV), defects or imperfections within the crystal lattice bring about interesting light–matter interactions. If both the ground and excited states of defects are located inside the band gap, then an optical dipole transition is allowed between them. Then these defects become luminescent under excitation and give a characteristic color to the crystal, thus these defects are called color centers. Diamonds host more than 500 different color centers emitting from the deep ultraviolet (UV) to the far infrared (IR) region. Among the several color centers listed in nanodiamonds, the negatively charged nitrogen-vacancy and silicon-vacancy color centers have gained widespread applications.

8.3.1 NV Color Centers

Nitrogen (N) is the most common impurity found in diamonds.[18] As a matter of fact, diamonds are classified based on the concentration of nitrogen and boron impurities present and the way they are arranged in the lattice.[19] Diamonds with high concentration of nitrogen such as 200–4000 ppm are classified as Type I and with low concentration of nitrogen (*i.e.*, less than 100 ppm) classified as Type II. Based on the atomic dispersions of nitrogen impurities Type I diamonds are further classified as Type Ia (aggregated 'N' impurities) or Type Ib (Isolated single 'N' impurities). Whereas based on the presence or absence of boron (B) impurities, Type II are classified as Type IIa (No 'B' impurities) and Type IIb ('B' impurities).

In a Type Ib diamond crystal lattice, nitrogen replaces one carbon atom and acts as an electron donor. When an N impurity becomes associated with a neighboring vacant (V) lattice site, it forms an optically active center that is called the nitrogen-vacancy (N-V) center. A schematic of both the atomic structure and the energy levels of the NV center is shown in Figure 8.1a and b, respectively. Upon excitation with green yellow light, the N-V center in NDs exhibits a wide range of emission wavelengths (550–850 nm) with near unity quantum yield and a longer lifetime (~25 ns). The N-V center contains two charge states, namely NV^0 and NV^- with a corresponding zero phonon line

(ZPL) at 575 and 637 nm, respectively[20] (Figure 8.1c). Both NV^0 and NV^- emit photoluminescence that extends from their respective ZPL to a higher wavelength due to vibronic phonon sidebands. The emitted far-red fluorescence is perfectly stable, showing no sign of photobleaching or photoblinking even under continuous high-laser power excitation.[20] The N-V center with its unique optical and spin properties is one of the most studied defect centers in diamonds, particularly the negatively charged NV^- center owing to its potential for applications in quantum information processing and sensing (spin qubits and spin sensing), optically detected magnetic resonance (ODMR), fluorescence enabled bioimaging and long-term tracking applications, *etc.*

8.3.2 SiV Color Centers

Silicon-vacancy (SiV) color centers have recently gained an increasing amount of interest in the diamond applications field. These are caused by the impurities of silicon present in the diamond lattice that are either implanted by the ion implantation method[21] or *in situ* 'Si' doping during the growth of the diamond. The SiV color center consists of a single silicon atom adjacent to

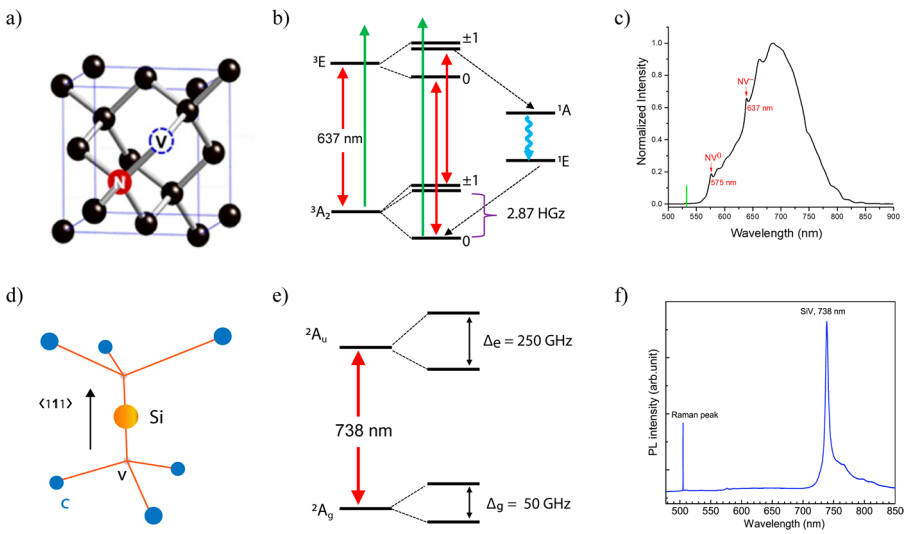

Figure 8.1 Atomic structure of a NV center (a) and SiV center (d). (b) and (e) show the energy levels of the NV and SiV center, respectively. (c) and (f) display the photoluminescence of the NV and SiV center, respectively. Reproduced from ref. 6 with permission from American Chemical Society, Copyright 2016. Reproduced from ref. 21 with permission from American Physical Society, Copyright 2016. Reproduced from ref. 23 with permission from Elsevier, Copyright 2017 respectively.

two vacancies in the diamond lattice.[22] A schematic illustration of the atomic structure and energy levels of the SiV center is shown in Figure 8.1d and e, respectively. SiV centers exist in either a negatively charged state SiV^- with ZPL at 738 nm[23] (Figure 8.1f) or in a neutral charge state SiV^0 with ZPL around 947 nm. Most of the emitted fluorescence (>90%) of SiV^- is concentrated in the ZPL at room temperature making it favorable for single photon source applications.[17] In addition, the center also exhibits a short excited-state lifetime (~1.2 ns) and a ZPL narrow linewidth of ~1.6 nm, which makes it suitable for application in quantum technologies.[17]

8.3.3 Production of Color Centers in NDs

Most of the applications of NDs involve their intrinsic color centers. Color centers are a result of dopants or impurities involved during the production of NDs. Diamonds host more than 500 different color centers. Among them NV centers are most notably studied. Nitrogen-vacancy (N-V) color centers are formed as a result of nitrogen impurities, silicon-vacancy (Si-V) color centers are a result of Si impurities and boron color centers are a result of boron impurities during the preparation method of NDs. These various color centers in NDs can serve in different applications of quantum computing, quantum entanglement, quantum memory, biolabeling, fluorescence and super-resolution imaging of cells, tracking cells and quantum sensing, *etc.* Due to these various advantages, growing NDs with color centers has become a recent trend.

The most commonly studied color centers in NDs are involved with vacancies in the crystal lattice. The first step in creating a color center in a diamond is to form vacancies. Vacancies in a diamond can be created by irradiation with high-energy electrons, protons, neutrons, helium ions or gamma rays. The structural defects created at this stage are typically stationary and do not form any complexes with the impurities present in the diamond crystal yet. Upon annealing this sample in vacuum at 800 °C for 2 h, the vacancies are moved in the lattice and captured by the impurities such as nitrogen atoms, thus forming complexes such as NV, N3, NVN depending on the type of starting material used in the production (Table 8.1). Oxidation in air at 450 °C for 2 h more will result in removal of the graphitic structures that had formed on the surface of the diamond powder. Further washing of these samples in an

Table 8.1 Vacancy-related color centers in ND and their properties.

Centers	Zero phonon line (nm)	τ (ns)	Quantum yield	Reference
V^0 (GR1)	741	2.55	0.014	16
NV^0	575	—	—	16
NV^-	637	11.6	0.99	16
N-V-N (H3)	503	16	0.95	16
N3 + V (N3)	415	41	0.29	16
SiV^-	738	1.28	0.05	17

acid mixture such as H_2SO_4 : HNO_3 at 100 °C will remove metals and any other impurities. This method is mostly used for creating nitrogen-related color centers in the diamond. The fluorescent nanodiamonds (FNDs) created by this method are further reduced in size by ball-milling, high-pressure crushing or sonication. Later, a differential centrifugation technique is applied to collect the smaller FNDs such as 50 nm or sub-20 nm. The disadvantage of some of these methods results in FNDs with highly polydisperse sizes, crystal defects due to the extruding pressure applied and increased sp^2 carbon due to surface graphitization.

In order to address the aforementioned problems, a controlled synthesis of high-purity diamonds with color centers is required. Y.-K. Tzeng *et al.* have developed a method where diamonds were grown in a microwave plasma CVD (MPCVD) and simultaneously the color centers were introduced using a vertically oriented stage-substrate geometry.[24] By this method, the authors were able to grow very small, high quality single crystal diamonds in the 10 nm size range. Briefly, a diamondoid seed, [1(2,3)4]-pentamantane was chemically bonded to oxidized surfaces of silicon wafers *via* phosphonyl dichloride. Then this substrate was rotated 90° to a vertical configuration for MPCVD diamond growth (Figure 8.2a). In this configuration, the substrate and diamond seeds are exposed to systematic variations in plasma density, local temperature and different growth conditions along the vertical axis of the substrate. A diamond was grown in a MPCVD with growth conditions of H_2, 300 sccm; CH_4, 0.5 sccm; stage temperature, 350 °C; microwave power, 400 W; pressure, 23 Torr. The vertical geometry generates a temperature and plasma electron density gradient along the substrate, allowing the seeds to be exposed to different conditions from top to bottom of the wafer.

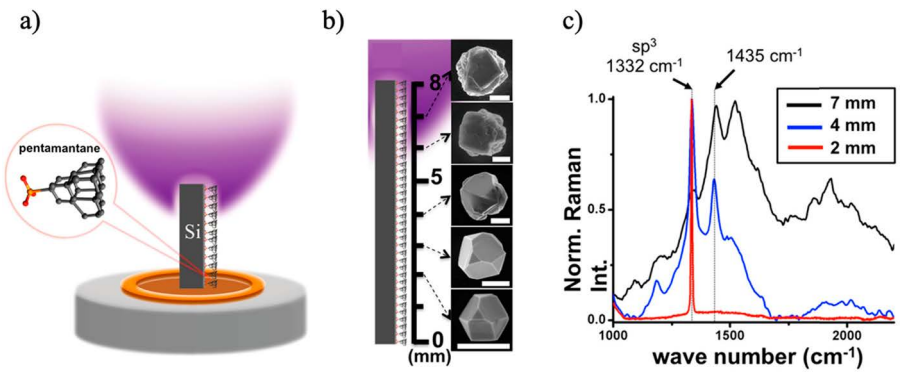

Figure 8.2 (a) Schematic illustration of vertical-substrate MPCVD diamond growth. (b) Different morphology of diamonds along the Si-wafer substrate at different heights and their Raman spectra in (c). The diamond peak of sp^3 carbon is at 1332 cm^{-1} and the peak at 1435 cm^{-1} is most likely *trans*-polyacetylene. Scale bar: 1 μm in (b). Reproduced from ref. 24 with permission from American Chemical Society, Copyright 2017.

Representative scanning electron microscope (SEM) images of diamond growth along the length of the vertical substrate are shown in Figure 8.2b. Diamond particles, formed at the top of the wafer, displayed polycrystallinity whereas a well-faceted and single-crystal particle formed near the bottom of the silicon substrate. This phenomenon is the result of a higher concentration of hydrogen acting as sp^2 etchant near the bottom of the surface. The bottom region of the substrate (at the height of 2 mm) produced around 20–30% of high quality, single crystal diamond. Diamond particles occurred 2–3 mm from the bottom of the wafer and showed a very sharp 1332 cm^{-1} sp^3 Raman peak with full width at half-maximum line width of 5.75 cm^{-1} (Figure 8.2c). Since silicon or silicon carbide substrates are used in this process, the resulting diamonds contain Si-V color centers without additional Si sources. The lifetime of these grown Si-V color centers is about 0.602 ± 0.008 ns similar to the literature value of 0.7–1.2 ns. This method produced very high-quality single crystal diamonds in the 10 nm size range and also a Si-V center containing diamonds in ~75 nm size range.

This synthetic method could also be applicable to growing other color centers containing diamonds. For example, Tzeng *et al.*[24] applied the same method to grow chromium color centers by simply depositing a $[Cr(H_2O)_6](NO_3)_3$ onto the Si substrate. These diamonds grown under the same conditions of Si-V synthesis showed clear optical signatures of Cr color centers with photoluminescence peaks at 750 and 758 nm. This synthesis method did not need an additional second impurity atom (*i.e.*, O, N, or Si), suggesting that vertical-substrate MPCVD could be a general means of creating a wide variety of color centers containing diamonds.

8.4 Biocompatibility

The applications of NDs in the biomedical field has expanded significantly. NDs have shown to be useful in bioimaging and tracking applications, nanoscale magnetic resonance, drug delivery, temperature sensing in live cells to cancer therapy. So, in order to validate the application of NDs for biological studies, it is important to understand the behavior and potential risks of NDs in both *in vitro* and *in vivo* systems. *In vitro* cytotoxic assessments of NDs included studying various cellular functions such as enzyme activity, oxidative stress levels, cell proliferation and differentiation, ATP (adenosine triphosphate) production and nucleotide uptake activity, *etc.* Various methods or assays that are being used to test the biocompatibility of nanomaterials are listed in Table 8.2. Several studies have been performed in light of understanding the biocompatibility of NDs in both cells and animals.

8.4.1 *In Vitro* Studies

Cellular toxicity of NDs was first reported by Yu *et al.*[37] when they incorporated high-density ensembles of NV centers containing NDs in human embryonic kidney cells. The MTT assay displayed no noticeable toxicity of

Table 8.2 Summary of various methods to test the biocompatibility of nanomaterials.[a]

Cell death testing	Means of testing	Detection/Indicators	Reference
Necrosis	• Trypan blue		25
	• Propidium iodide	Plasma membrane integrity	26
	• Ethidium homodimer		27
Apoptosis	• Annexin V assay	- Detection of phosphatidylserine - a cell death signaling molecule	28
	• Caspase assay	- Detection of caspases-a protein cleaving enzyme	29
	• TUNEL assay	- Detection of DNA fragmentation	30
Cell viability	• MTT assay • XTT assay • WST-1 assay	- Reduction of tetrazolium salts to a soluble colored formazan salts by metabolically active cells	31
Genotoxicity	• Comet assay	- Measurement of DNA breaks in cells by gel electrophoresis	32
	• Micronucleus assay	- Measurement of chromosome alterations	33
Hemocompatibility	• Hemolytic activity	- Disruption of blood cells and release of hemoglobin	34
	• Thrombogenicity	- Measurement of thrombin generation by APTT kit	35
	• Cytokine production	- Measurement of cytokine levels in blood by ELISA	36

[a]Abbreviations: TUNEL- terminal deoxynucleotidyl transferase dUTP nick end labeling, MTT-3-(4,5-dimethylthiazole-2-yl)-2, 5-diphenyltetrazolium bromide, XTT- 2,3-bis-(2-methoxy-4-nitro-5-sulfophenyl)-2*H*-tetrazolium-5-carboxanilide, WST-1- 4-[3-(4-Iodophenyl)-2-(4-nitro-phenyl)-2 *H*-5-tetrazolio]-1,3-benzene sulfonate, APTT- activated partial thromboplastin time.

FNDs at concentrations as high as 100 μg mL^{-1}. Later, Schrand *et al.* studied the cytotoxicity of NDs using a MTT and ATP production assay. It was shown that NDs did not induce significant toxicity on a variety of cell lines.[38] In their subsequent study, they compared the toxicity of NDs with other carbon nano-materials such as carbon black (CB), multi-walled carbon nanotubes (MWNTs) and single-walled carbon nanotubes (SWNTs) on neuroblastoma cells and macrophages.[39] It was observed that SWNTs were found to be more toxic, followed by MWNTs and CB, respectively. Interestingly NDs displayed the least toxicity amongst all the carbon materials studied.[39]

Although cell viability, proliferation and differentiation of cells display that NDs are least toxic, it is also important to evaluate the potential genotoxicity and mutagenic activity of NDs in cells. In order to address this, Paget at al[40] have made a thorough and systematic investigation of NDs on six human cell lines. Genotoxicity of NDs was assessed by γ-H2Ax foci detection, which is considered the most sensitive technique for studying DNA

double-strand breaks. Their results indicated that NDs with nominal sizes of 20 and 100 nm could effectively enter cells but did not induce any genotoxicity with a concentration up to 250 μg mL^{-1}. In a separate study, Hemelaar *et al.* performed an in-depth analysis of the biological impact of FNDs uptake on HeLa cells by studying their cellular mRNA, protein levels and reactive oxygen species (ROS) generation.[41] Rounded FNDs of 25 nm and FNDs with varying sizes of 120 nm, 70 nm and 40 nm were used in this study. A maximum concentration of 10 μg mL^{-1} and incubation time of 24 h were chosen as this results in already more than a few diamonds per cell to study their impact on cells. Hydrogen peroxide was used as a control. Cell viability from the MTT assay (Figure 8.3a) and total ROS activity (Figure 8.3b) by the HeLa cells show that FNDs did not affect the cells. Further, analysis of changes in mRNA (Figure 8.3c) and protein levels (Figure 8.3d) are measured inside the cells. Most stress-related genes are down-regulated after incubation with FNDs. A summary of their study indicates that the shape, size and concentrations of diamonds did not influence the cell viability or the total free radical levels inside the cells. Although down-regulated transcription of genes involved in oxidative stress was observed, there was no change in protein levels inside the cells.

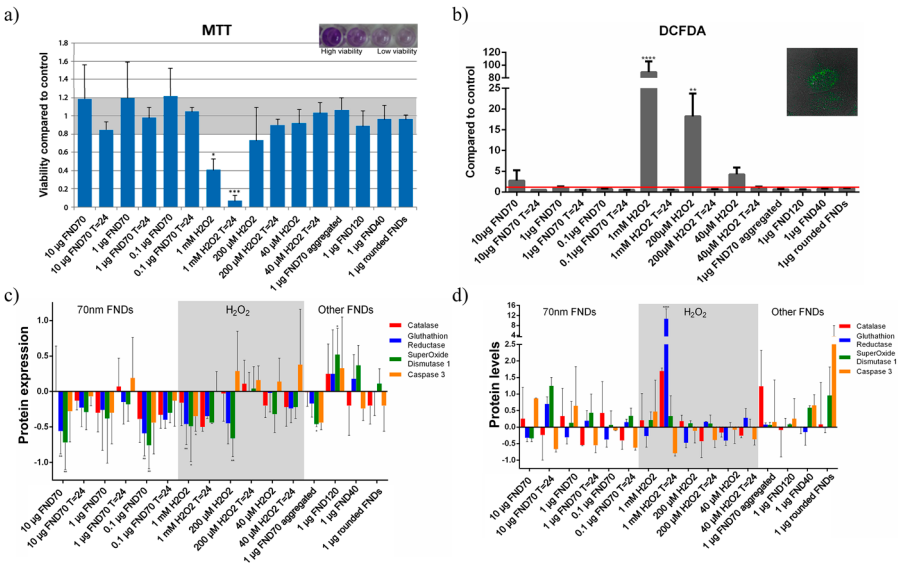

Figure 8.3 (a) HeLa cell viability after FND uptake. When the viability compared to the control is between 0.8 and 1.2, then it is considered that cells are unaffected. (b) The mean free radical production. ROS production can be measured by the conversion of 2′,7′-dichlorodihydrofluorescein diacetate (DCFDA) to its fluorescent metabolite DCF. (c) and (d) display the expression levels of oxidative stress-related genes and proteins, respectively. Error bars show the standard deviations. Reproduced from ref. 41, https://doi.org/10.3390/s18020355 under the terms of the CC-BY 4.0 license, https://creativecommons.org/licenses/by/4.0/.

Even though NDs were found to be nontoxic to a wider range of cells, how they influence the cellular functions of the primary cell lines remains a concern. H. S. Jung *et al.* compared the toxicity of FNDs and poly(vinylpyrrolidone) (PVP)-coated FNDs with quantum dots (QDs).[42] The authors studied the cell viability, toxicity and inflammatory immune responses in bone marrow-derived dendritic cells (BMDCs) and human non-small cell lung carcinoma cells (H1299). Both FNDs and FND@PVP particles were not toxic to BMDCs or H1299 cells over the concentrations (up to 250 nM) or incubation times (up to 16 h) tested. In contrast, QDs showed significant toxicity with approximately 50% of the cells dying at the maximum concentration or incubation time. In addition to dendritic cells, Wu *et al.*[43] reported that treating lung stem/progenitor cells (LSCs) and mouse embryonal primary neurons with 100 nm FNDs did not eliminate the self-renewal and differentiation abilities. In conclusion, most of the studies reported that NDs displayed the least cytotoxicity or highest biocompatibility compared to not only other carbon-based nanomaterials[44,45] but also quantum dots.

8.4.2 *In Vivo* Studies

The primary requirement for clinical application studies in humans is animal safety and toxicological studies over an extended period of time. The validation of NDs for potential therapeutic or clinical applications is incomplete without these *in vivo* studies. Several model organisms including *Caenorhabditis elegans* (*C. elegans*), mice, rats, zebrafish embryos and *Xenopus* embryos are studied for the *in vivo* biocompatibility of NDs. Methods of ND administration to animals included oral, intradermal (i.d), intraperitoneal (i.p), intravenous (i.v) and subcutaneous injections. The effects of NDs on these tested animals were assessed by several parameters such as survival rates, metabolic responses, biodistribution, histological analysis and pharmacokinetics. A proper evaluation of these parameters in animals is essential before NDs can progress towards a clinical translation.

C. elegans is a small free-living nematode worm with a fully mapped genome and nervous system. Owing to its short life cycle, ease in handling and high sensitivity to various types of stresses, *C. elegans* is an ideal model organism to study the innate immunity and stress responses against nanoparticles. Mohan *et al.* performed toxicity assessments of FNDs in *C. elegans*.[46] In this study, FNDs were either fed orally or microinjected into *C. elegans*. Their studies proved that FNDs did not cause any change in longevity or reproductive potential of the organism. Moreover, FNDs did not cause any detectable stress to the organism. When FNDs were microinjected into gonads of the *C. elegans*, the particles were subsequently delivered to their embryos, a second generation of the organism. FNDs did not cause any abnormality in cell division, differentiation or morphogenesis during the embryogenesis and especially did not elicit any detectable stress. These studies prove that FNDs were biologically inert and nontoxic to *C. elegans*. Continuing from this work, Chang *et al.* also microinjected FNDs

into yolk cells of zebrafish embryos at the one-cell stage.[47] Due to the bright fluorescence of the NDs, they were able to track the FND particles from dividing cells in the blastomeres to whole fishes without any apparent morphological anomalies during their embryogenesis.[48] As an extension of FND biocompatibility studies, the group of Chang *et al.* have further studied the long-term stability and biocompatibility of FNDs in rats over five months.[49] Their results indicate that there was no significant difference in water consumption, body weight and organ index between the control and FND-treated rats. Even after intraperitoneal injection of FNDs up to 75 mg kg^{-1} body weight of rats, histopathological analysis of various tissues and organs indicated that FNDs are nontoxic and did not cause any inflammation over the three-month course of study.

Formation of blood clots are the major cause of heart attacks and strokes. 'αIIbβ3' is a membrane protein receptor on platelets that plays a crucial role during platelet aggregation,[50] and 'bitistatin' is a platelet aggregation inhibitory ligand that binds with high affinity to αIIbβ3 integrin. Diagnosis of vascular clot location is hampered by a lack of proper detection tools. Recently, Gerstenhaber *et al.* bioengineered FND particles conjugated with bitistatin. This bioengineered FND successfully binds to platelet-rich plasma clots *in vitro*[51] and rats.[52] Due to near infrared fluorescence of FNDs, their study demonstrates the potential ability of FNDs for both visualization and identification of blood clots. So, in order to test the potential preclinical development of FNDs as a tool for imaging vascular blood clots, Barone *et al.*[53] have intravenously administered 800 nm FNDs in rats at a single dose of 60 mg kg^{-1} and studied the safety, tolerability, pharmacokinetics and biodistribution for two weeks. This pilot study revealed no change in morbidity or mortality and preserved normal motor and sensory functions in rats.[53] In this acute/subacute study, it was observed that FNDs were rapidly cleared from the circulation of blood and majorly accumulated in the liver or spleen. As a follow up of this study, the same group studied the long-term *in vivo* biocompatibility of FNDs in rats over three months.[54] Their studies also reveal that there is neither morbidity nor mortality observed over the 12 week period of study. The FND particles were largely entrapped in liver and to a lesser amount in spleen, whereas other organs such as heart, kidney and brain had no identifiable amounts of FND deposits. Despite prolonged entrapments of FNDs in liver and spleen, neither biochemical biomarkers nor specific histopathologic adverse effects were noted in these organs. Finally, there is no alteration in the central and peripheral nervous system as evidenced by the several sensory, motor and cognitive tests.[54] The same group further studied the localization of FNDs in the liver specimens that are obtained from the above-mentioned studies.[55] It was observed that FNDs were present in the hepatic lobules including parenchymal and non-parenchymal cells as well as in the micro-circulation and their presence was not associated with macro or micro histopathological signs. Taken together, all their data suggest liver biocompatibility of FNDs and that FNDs could potentially be well tolerated by humans when administered through an intravenous route.

In another recent study by Moore *et al.*,[56] detonation diamonds of size 100 nm were systemically infused to either rats or monkeys. The study was done in two cohorts that lasted for two weeks in rats and six months in monkeys including histological, serum and urine analysis. Their results indicate that NDs are well tolerated at clinically relevant doses of 6.75–13.5 mg kg^{-1}. Even after exposures over six months, no adverse effects of particles to the animals were observed.

To conclude, NDs were biocompatible both *in vitro* and *in vivo* and caused no severe toxicity to cells or the organisms. The *in vitro* studies suggest that NDs cause none or low cytotoxicity compared to other carbon nanomaterials or quantum dots. The *in vivo* studies suggest that NDs were well tolerated in the animals over the period of study; although more detailed studies, such as longer than six months, need to be carried out to better understand toxicity and safety to animals in the long-term. In addition, for future clinical translation of NDs, more comprehensive biodistribution and pharmacokinetics analyses are required.

8.5 Biological Application of NDs

The nanotechnology revolution offers many expectations for the application of NDs in the biomedical field. After establishing safety and bio-compatibility in recent studies, NDs have been investigated for their use in the biomedical field. NDs have a high surface-area-to-volume ratio that allows for very efficient biomolecule loading and delivery. The NV centers provide fluorescence that is highly photostable without photobleaching or photoblinking, making NDs a good contrast agent for long-term cell tracking and super-resolution imaging applications. The unique spin properties of NV^- centers make NDs useful for ultrasensitive detection of temperatures at the nanoscale. Due to these properties, the ND has emerged as a novel imaging probe for several biological applications. Having discussed the physical and chemical properties and biocompatibility of NDs, a few applications of NDs are now reported in the following sections.

8.5.1 NDs in Cell Tracking

In recent years, cell-and gene-based therapies (CGTs) offer the promise of treating and altering the course of diseases that cannot be addressed adequately by existing pharmaceuticals. In CGTs live whole cells or maturation of a specific cell population are introduced to a patient's body to replace, repair, reconstruct, or supplement damaged cells/tissues. In light of the tremendous potential of this therapeutic approach, there is an imperative need to develop general and reliable methods to measure the biodistribution and pharmacokinetics of these cell products *in vivo* for preclinical evaluation. Such information is critical in clinical trials since it is vitally important to know whether the transplanted CGT cell products completely home to the

target organs and disease sites instead of unwanted distribution that will induce inappropriate differentiation leading to cancer development.

A critical step in generating pharmacokinetic models of the CGT cell product is tracking the fate of cells following transplantation. The current available methods for quantitative CGT cell detection are polymerase chain reaction (PCR), flow cytometry, optical imaging, magnetic resonance imaging (MRI) and radio isotope labeling. But these methods have lower detection limits and offer only semi-quantitative information on the biodistribution of the transplanted cells. An ideal quantification technique should have the following features: single-cell detection sensitivity and specificity, long-term detection and monitoring, and quantification of cell numbers at any anatomic location. Recently, FNDs have emerged as an attractive option for tracking cells. One of the critical issues in tracking cells *in vivo* is autofluorescence and background noise. Sarkar *et al.* demonstrated a way of contrast enhancement for FNDs *in vivo* using an external modulated magnetic field (MMF).[57] This MMF method relies on simple subtraction of images with and without a magnetic field, which results in background-free detection of FNDs. This background-free imaging technique improves the signal-to-background ratio for *in vivo* imaging up to 100-fold. Hui *et al.* also presented another approach to achieve background-free fluorescence imaging of FNDs both *in vitro* and *in vivo* by using an intensified charge-coupled device (ICCD) as the detector.[58] Having longer life times for FNDs (~25 ns), ICCD is useful to suppress short-lifetime autofluorescence backgrounds and provides time-gated fluorescence images with high contrast. These technologies enabled FNDs to be useful for cell labeling, imaging and tracking applications *in vitro* and *in vivo*.

One of the first studies to show FNDs for tracking cells *in vivo* was demonstrated by Wu *et al.*[43] The authors labeled primary cells such as lung stem cells (LSCs) with 100 nm FNDs through endocytosis. Later, these FND-labeled LSCs were injected intravenously in mice to determine their tissue-specific engraftment and regenerative capacity. By combining FNDs with fluorescence life time imaging (FLIM), fluorescence-activated cell sorting (FACS) and immunostaining analysis, they were able to identify, unequivocally, transplanted cells in histological lung sections with single-cell resolution. Inspired by this work, Su *et al.* demonstrated the quantitative tracking of FND-labeled human mesenchymal stem cells (MSCs) in miniature pigs.[59] Briefly, MSCs were labeled with human serum albumin (HSA)-conjugated 100 nm FNDs at a concentration of 100 μg mL^{-1}. By using the MMF method, an average weight of ~100 pg for the FNDs in one cell or an average number of ~5.5×10^4 particles/cell were determined. Later, FND-labeled MSCs were transplanted into miniature pigs by intravenous administration. After sacrificing the animals at specific time points, five major organs were extracted. Acid digestion of the organs enabled one to determine the absolute amount of FNDs and thus the labeled cells in the individual organs with both high sensitivity and accuracy. Figure 8.4 displays the results of the experiment. By applying the MMF method, background-free detection of FNDs directly

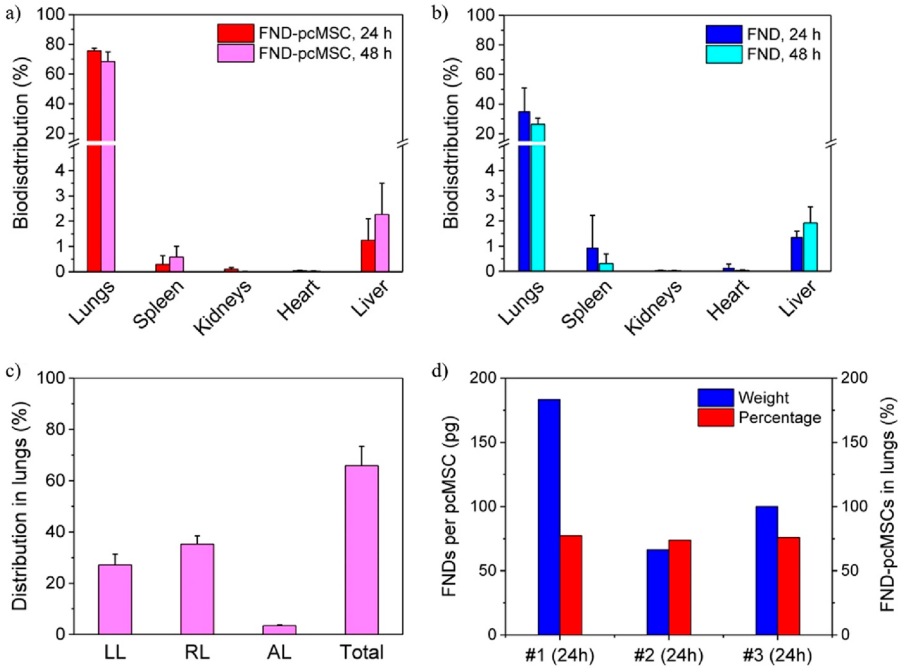

Figure 8.4 FND labeled cell tracking and quantification. (a) and (b) biodistribution of HSA-FND-labeled MSCs and HSA-FNDs in five different organs at two different points. (c) Distribution of HSA- FND-labeled MSCs in different sections of the lungs at 48 h after injection. LL-left lobes, RL-right lobes and AL-accessory lobe. (d) Amounts of HSA-FNDs taken up by three sets of MSCs (blue) and the corresponding percentages of HSA-FND-labeled MSCs (red) found in the lungs 24 h after intravenous injection. The HSA-FND concentration used for the labeling was 100 μg mL^{-1}. Experiments (a–c) were repeated in triplicate and the error bars represent one standard deviation of uncertainty. Reproduced from ref. 59 with permission from Macmillan Publishers Ltd, Copyright 2017.

in the digests without purification is achieved. Engraftment of the stem cells in tissues was finally identified by time-gated fluorescence imaging with single-cell resolution.

In conclusion, the combination of the MMF method together with FNDs as well as the large quantity of the nanoparticles taken up by the cells, has permitted studies of the biodistribution and pharmacokinetics of FND-labeled cells in a preclinical setting. The technique has excellent compatibility with time-gated fluorescence imaging, which has been shown to be a powerful means of acquiring high-contrast fluorescence imaging of FND-labeled cells in tissues. The ability to find single CGT cells is particularly valuable for *ex vivo* histological detection of these cells in clinical trials. This combined approach represents an appealing alternative to hazardous radioisotope labeling techniques in cell tracking applications.

8.5.2 Intracellular Delivery of Functional Proteins with NDs

Biomolecules have been immobilized on nanoparticles through a variety of techniques including covalent conjugation or by noncovalent interactions such as hydrophobic interaction, electrostatic binding and specific recognition. The development of nanomaterials carrying biomolecules towards a translation application may significantly improve efficacy and safety in the treatment of a spectrum of diseases that have proven challenging to address through conventional means. However, care must be taken to conserve their functionalities when loading the macromolecules onto the particles since the strong interaction between nanoparticles and biomolecules may cause structural changes of the biomolecules. A spectroscopic study of bovine serum albumin (BSA) on NDs has suggested that while the adsorbed BSA may undergo some minor conformational changes due to the protein–surface interactions, most of the structural features of the protein are preserved.[60] A study had similar findings for α-bungarotoxin, which is a neurotoxin from *Bungarus Multicinctus* and can maintain its bioactivity after physical adsorption onto carboxylated nanodiamond surfaces.[61] The same conclusion was reached for rabbit anti-mouse antibodies covalently immobilized on NDs.[62] In an intensive and thorough research, Shimkunas *et al.*[63] explored the feasibility of using monodisperse NDs (~5 nm in diameter) for insulin therapy, where the protein molecules serve as a potential promoting agent for wound healing and vascularization for severe burns and other possible conditions. The study demonstrated an efficient method for non-covalent conjugation of insulin with the nanodiamond surface and, moreover, when immersed in an alkaline environment, the attached insulin could be readily released from the complexes. Both cytotoxicity and polymerase chain reaction analysis revealed that the protein's functionality remains active after desorption but is inactive when adsorbed onto the nanodiamond surface; a behavior attributed to the rapid formation of stable insulin aggregates at the interfaces.[64] In addition to insulin, the same research group also investigated the feasibility of using NDs as a protein delivery vehicle for transforming growth factor beta antibody (anti-TGF-β), which is a potential anti-scarring agent.[65] Enzyme-linked immunosorbent assays (ELISA) verified the preservation of the protein activity after release. The studies together support the notion that the ND is a useful delivery vehicle of protein molecules, including possibly enzymes.

Immobilization of enzymes on a substrate is an important process in biotechnology for commercial uses. Many disadvantages of using free enzymes, such as short-term stability and complications in recovery and recycling, can be eliminated and improved by noncovalent or covalent immobilization of the protein molecules on the surface. According to previous research, NDs show high affinity with biomolecules such as proteins,[66,67] enzymes,[68,69] and antibodies,[65] which indicates that NDs serve as an exceptional platform for biomolecule adsorption and immobilization. When using NDs as enzyme carriers, a question arises: can enzyme-linked NDs be used as therapeutic and

diagnostic agents in medicine? In order to study this, Su *et al.* have used a FND as a biocompatible nanocarrier for firefly enzyme-luciferase (Luc) and successfully delivered it into MSCs for human stem cell labeling.[69] First, the FND surface was physically adsorbed with luciferase and then further covered with BSA for better dispersion and stabilization of the particles. It was observed that FND-bound luciferase molecules are intact and retain their catalytic activities even after being trapped in endosomes of labeled MSCs for hours. Later these Luc-FND+BSA labeled MSCs were subcutaneously injected into a mouse. Figure 8.5 shows the experimental results. Both fluorescence and bioluminescence imaging of these particles allowed the cells to be tracked *in vitro* as well as *in vivo* demonstrating that Luc-FNDs are useful as multifunctional labels of human stem cells for diverse theranostic applications. This platform can be applicable to dual-modality imaging of cancer cells as well.

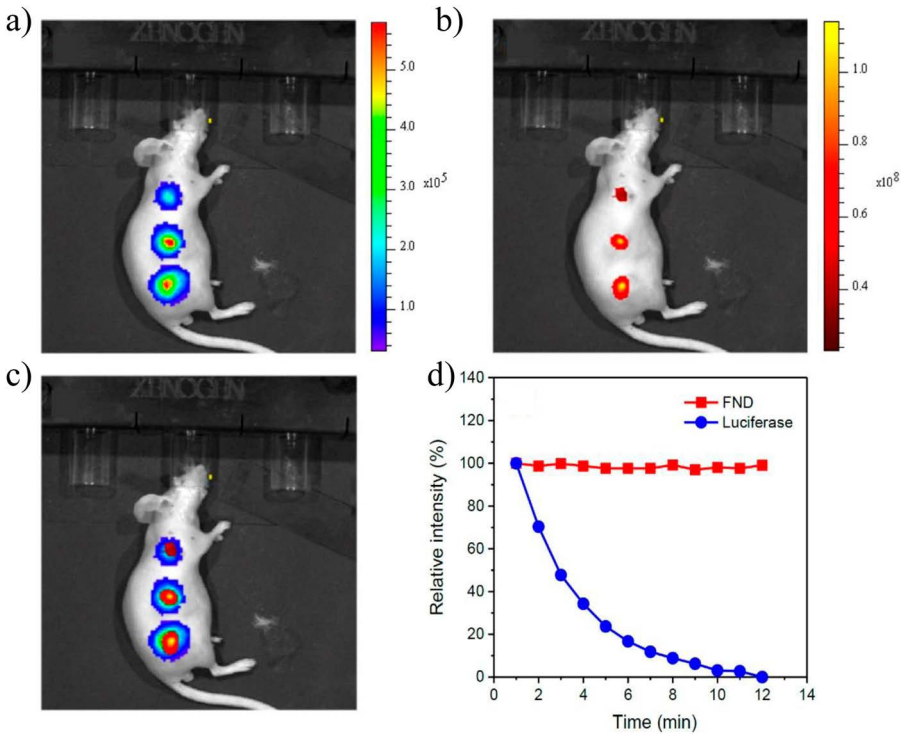

Figure 8.5 *In vivo* imaging of Luc-FND+BSA-labeled MSCs. (a) Merged bright-field and bioluminescence image of a mouse injected with Luc-FND+BSA-labeled MSCs at a dose of 1×10^5, 5×10^5, 1×10^6 cells (top to bottom). (b) Merged bright-field/fluorescence image of the same mouse in (a). (c) Merged bright-field/bioluminescence/fluorescence image of the same mouse in (a) and (b), showing colocalization of bioluminescence and fluorescence signals. (d) Decays of the luminescence intensities of FND and luciferase for Luc-FND+BSA-labeled MSCs in the mouse. The spectrum gradient bars in (a) and (b) correspond to the bioluminescence and fluorescence intensities in unit of photons/s/cm^2/sr. Reproduced from ref. 69 with permission from American Chemical Society, Copyright 2019.

8.5.3 Bioimaging

8.5.3.1 FNDs for Single Particle Tracking

Fluorescence labeling and imaging is one of the most important and powerful methods in molecular biology. A good fluorophore is one that emits a decent number of photons before it gets photobleached, exhibits high quantum yield, longer fluorescence lifetime, low or no toxicity and is inert to the environment. Although organic dyes and fluorescent proteins are good compatible biolabels for imaging, their photostability is a major concern. The FND turns out to be an exceptional candidate for bioimaging applications due to its superlative physical and chemical properties. A few examples are now discussed to demonstrate both the advantages and applications of FND as a bioprobe.

The NV^- centers in FNDs, which act as built-in fluorophores, exhibit high photostability. This enables FNDs to be good contrast agents for both single particle tracking (SPT) and long-term cell imaging. A number of studies have shown that FNDs could be easily internalized by the cells in culture through an energy-dependent, clathrin-mediated endocytosis pathway and are eventually trapped inside endosomes.[70–73] Fu *et al.*[74] were among the first group to conduct single particle tracking of FNDs inside live cells. Both 35 and 100 nm FNDs were spontaneously taken up by the cells and their motions in three dimensions inside the HeLa cells are tracked at the single particle level. Analysis of the trajectories for more than 200 seconds indicates a diffusion coefficient of $D = 3.1 \times 10^{-3}$ μm^2 s^{-1}, which is comparable to other nanoparticles such as quantum dots trapped inside endosomes or lysosomes. This study laid the foundation for several upcoming bioapplications of FNDs. In addition to the intracellular tracking of FNDs, the same group demonstrated the FND as a biomarker to study intercellular dynamics. For this, Epperla *et al.*[75] applied protein-coated FNDs to track the endosomal vesicles inside membrane nanotubes (MNTs) to study intercellular communication. MNTs are one of the intercellular communication pathways through which the transport of proteins and other cytoplasmic components can occur.[76] These MNTs are also known to contribute in the pathogenesis of many diseases including HIV, Parkinson's and Alzheimer's.[77] These nanotubes are typically 30 μm in length and up to 1 μm in diameter. The 100 nm FNDs loaded with either BSA or green fluorescent protein (GFP) were easily internalized by human embryonic kidney cells (HEK293T) through endocytosis. SPT accomplished by fluorescence microscopy revealed the active transport of FNDs and the dynamics of cargo transport along the nanotubes. Simultaneous imaging of both GFP and FND indicated the FNDs' ability for protein transport from the cytoplasm of one cell towards another cell through the MNTs. Interestingly, the protein-loaded FNDs were observed to take a molecular motor mediated motion inside the nanotubes with ‘stop and go’ or ‘to-and-fro’ motions. A similar behavior of motion was also observed for molecular motors that are traveling along the actin cytoskeleton.[78] The detailed SPT analysis of FND transport indicated that the particles are moving with a diffusion coefficient

of $D = 0.08\ \mu m^2\ s^{-1}$ with an active transport velocity of $v = 0.54\ \mu m\ s^{-1}$ along the nanotubes. This study demonstrates the ability of the surface functionalized FNDs for the intercellular delivery of various biomolecules at the single particle level.

The biological cell membrane is a highly complex and dynamic system on which several important activities occur. Membrane proteins (MPs) in particular play crucial roles in biological processes by interacting with other intracellular and extracellular components. Real-time monitoring and long-term visualization are essential to better understand the role and dynamics of these membrane associated proteins. Commonly used organic dyes or fluorescent protein molecules are comparable in size for labeling of MPs, but this is limited to short-term imaging due to photobleaching. There is a need for a bio-label that can withstand continuous imaging for long-term periods without compromising the fluorescence and at the same time providing both high temporal and spatial resolution. In order to address this, Hsieh *et al.* developed a facile method where alkyne-functionalized FNDs were bio-orthogonally labeled to azide-modified sialoglycoproteins on human fibroblasts (HFW) cells and continuously tracked them for both short-term and long-term periods.[79] Sialoglycoproteins are a group of proteins that span the cell membrane, which are important determinants in the social behavior of the cell. Both 50 and 100 nm alkyne-FNDs were used to label the sialoglycoproteins, specifically integrin α5 and β1 on the HFW cell membrane. The specific labeling of the 100 nm alkyne-FND with integrin α5 was carried through an azido-modified anti-integrin α5 antibody. Epifluorescence imaging of the FND coupled with an electron multiplying charge-coupled device (EMCCD) for a relatively short time (5 min) displayed an active and random movement of integrin α5 on the cell surface. A detailed analysis of the trajectories revealed that integrins were moving with a diffusion coefficient of $0.041 \pm 0.032\ \mu m^2\ s^{-1}$, which is in agreement ($0.01–0.1\ \mu m^2\ s^{-1}$) with nanogold-labeled integrins β1, β3 and α4 moving on the surface of mouse fibroblasts. In order to gain a better understanding of how these proteins interact or behave, a long-term tracking of integrin α5 enabled by FNDs was carried out. For this, initially integrin α5 was labeled with alkyne FNDs and then with Alexa 488-conjugated wheat term agglutinin. What seemed like a random movement during short-term imaging, the seemingly aimless transports of integrin α5 actually have a predefined destination over long-term imaging. The integrin molecules moved toward the direction of the cell migration, an event that could not be unveiled by either short-term imaging or the conventional dye labeling of the integrin molecules. Due to the long-term photostability and no fluorescence bleaching or blinking of FNDs, continuous long-term tracking of FNDs attached to the cell surface antigens was conducted. This method could open new avenues for specific targeting and tracking of membrane proteins on live cells for better understanding of their functional role.

Another innovative application of a FND based SPT technique is to probe the abnormalities in intraneuronal transport induced by brain-disease-related genetic risk factors. Without going into too much detail, Haziza *et al.*[80]

tracked FNDs inside the branches of dissociated neurons of a transgenic mouse with a spatial resolution of 12 nm and a temporal resolution of 50 ms. The transgenic mouse lines mimic the slight changes in protein concentration (~30%) found in the brains of patients on intraneuronal transport. The FND tracking assay is sufficiently sensitive enough to detect modifications of intraneuronal transport parameters such as velocity, run length, molecular motor stopping duration and frequency between neurons in control and transgenic mice.

One of the first SPT studies of FNDs was carried out by Chang *et al.*[48] for studying the cytoplasmic dynamics in zebrafish yolk cells. When 100 nm BSA-coated FNDs were introduced into the yolk of a zebrafish embryo at the one-cell stage, it was observed that microinjected FNDs trafficked unidirectionally with a stop-and-go manner within the yolk cell. An analysis of the trajectories revealed that the BSA-FNDs were moving with a velocity of 0.19–0.40 $\mu m\ s^{-1}$ along the axial streaming. Interestingly, these particles traveled into the dividing cells and dispersed in the fish's body when the embryos developed into larvae and eventually into adult fish. In another study, Simpson *et al.*[81] studied the embryogenesis of the *drosophila melanogaster*, a model organism for genetic studies. BSA-coated FNDs were microinjected into the embryos and observed to diffuse both freely and in a driven motion in furrow periplasm and sub-nuclear periplasms by SPT. The observed differences of diffusion coefficients and velocity of FND in furrow (D = 0.006 $\mu m^2\ s^{-1}$, v = 0.13 $\mu m\ s^{-1}$) and sub-nuclear periplasm (D = 0.063 $\mu m^2\ s^{-1}$, v = 0.27 $\mu m\ s^{-1}$) correspond well to the fact that cytoskeletal networks are much denser in furrow periplasm hindering the FND diffusion. Yet in another interesting study, Igarashi *et al.*[82] studied the real-time background free detection of FNDs in *C. elegans* and mice. In order to overcome the autofluorescence generated from the organisms and thus to improve the effective image contrast, a selective imaging method based on ODMR was employed. This approach enabled them to conduct long-term imaging of 200 nm FNDs in both *C. elegans* and mice, achieving good image contrast by deleting the strong background autofluorescence. This selective ODMR based imaging method is expected to be applicable to a wide range of living systems.

8.5.3.2 FNDs in Super-resolution Imaging

In conventional fluorescence microscopy, the resolution is diffraction limited (~200 nm) making it difficult to distinguish similar features that are spatially closer. But in the past two decades, super-resolution optical microscopy has been developed to observe sub-cellular and ultra-fine structures that are beyond the diffraction limit.[83] Without going into the technical details of super-resolution microscopy methods, several applications of FNDs have been discussed below.

One of the first developed methods for sub-diffraction imaging is the stimulated emission depletion (STED) microscopy by S. W. Hell.[84] In STED microscopy two lasers are used. One is a normal pulsed laser to excite the

fluorophore under study and the other is a doughnut-shaped STED laser to deplete the fluorescence signal by stimulated emission. Since high powered lasers are required to obtain the efficient depletion of fluorescence in this technique, highly photostable fluorophores are required. The NV^- centers in FNDs are perfectly photostable without photo-bleaching or blinking, making them a well-suited contrasting agent for STED imaging. Most of the FND applications in super-resolution are centered around this STED microscopy. Hell and his coworkers first used STED microscopy to image the individual nitrogen-vacancy centers in a bulk diamond with a nanoscale resolution of 5.8 nm.[85] This remarkable resolution is up to 6-fold improvement over confocal fluorescence microscopy for 35 nm FNDs dispersed on a glass slide.[86] In a follow up work, Camejo *et al.* applied STED microscopy to image individual NV centers in FNDs of various sizes (40–250 nm). They were able to resolve single NV^- centers in nanodiamonds with a resolution of 10 nm and discern individual NV centers within a nanodiamond to a relative distance of 15 nm.[87] Their work demonstrated the emerging potential of NV centers as photostable fluorophore tags in far-field fluorescence nanoscopy.

In order to demonstrate the FND as a fluorescent label for super-resolution imaging of cells, Tzeng *et al.* performed the imaging of single 35 nm FNDs in fixed HeLa cells by STED microscopy.[88] In order to avoid the aggregation of FNDs and to see single particles inside the cell with high precision, BSA was conjugated to FNDs. These BSA-functionalized FNDs were readily internalized by HeLa cells and trapped inside endosomes. Upon continuous-wave mode excitation with a green laser (λ_{ex} = 532 nm) and doughnut-shaped depletion laser (λ_{ex} = 740 nm), a lateral resolution of 40 nm was achieved for the FND particles by STED microscopy, whereas the conventional confocal microscopy for the same showed a resolution of 240 nm, which is diffraction-limited (Figure 8.6a, b and c). In addition to NV centers that emit red color fluorescence, STED imaging of the NVN centers in the nanodiamond that exhibit green fluorescence has also been conducted.[89] Utilization of green fluorescent nanodiamonds (gFNDs) opened the door for long-term two-color STED imaging. In order to compensate for the absorption cross-section of NVN, which is half of the NV centers, larger size (70 nm) gFNDs are chosen that contain a large number of NVN color centers (~60 NVN centers/particle). Using 488 nm pulsed excitation and 590 nm CW depletion (~130 MW cm^{-2}), a resolution of 70 nm was achieved for gFNDs dried on a covered glass slide. Followed by this, sub-diffraction STED images were obtained for 70 nm gFND internalized HeLa cells. Two-color confocal imaging of cells by confocal microscopy Z-sections reveals that gFNDs are inside the cytoplasm. What seemed to be an aggregated ensemble of gFNDs in confocal imaging, STED imaging resolves more details of the nanocrystals at the single particle level. Due to high photostability, gFNDs are promising candidates as a second color nonbleaching probe for STED microscopy based bioapplications. Although several studies have explored the possibility of NV centers for super-resolution work,[85,90] very few studies have actually employed FNDs for super-resolution of cellular features.[88,89]

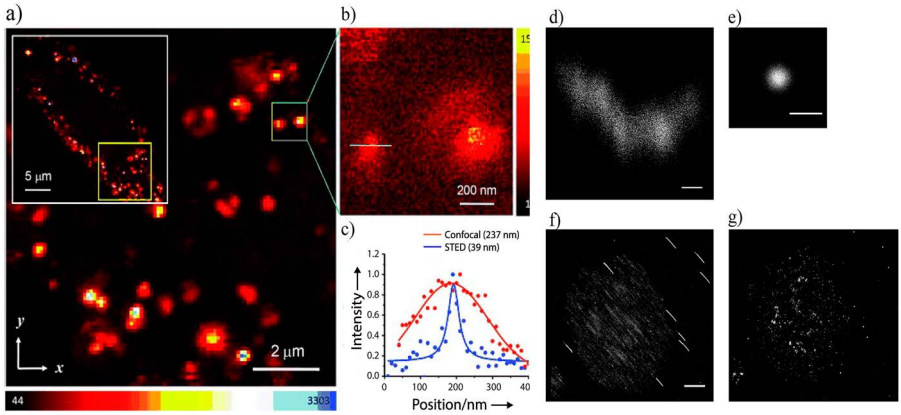

Figure 8.6 (a) Confocal fluorescence image of BSA-conjugated FNDs in HeLa cells. (b) A STED image of the single FND particles enclosed within the green box in (a). (c) Confocal and STED fluorescence intensity profiles of the particle indicated in (b) with a blue line. (d) and (e) show a single FND particle localized in 30 000 image frames before (d) and after (e) drift correction. (f) and (g) show images of the activated Jurkat T cell stained with anti-phosphorylated SLP76 (Y128) antibody and FND fiducial markers before and after drift correction, respectively. Reproduced from ref. 88 with permission from John Wiley & Sons, Copyright 2011 WILEY-VCH Verlag GmbH & Co. KGaA, Weinheim and ref. 91 with permission from JOVE.

Unlike STED microscopy where super-resolution is achieved based on optics alone, there are other techniques such as stochastic optical reconstruction microscopy (STORM) or photoactivation localization microscopy (PALM) where super-resolution is achieved based on photo-switchable probes and their single molecule localization accuracy. During the image acquisition, mechanical movement of the stage hampers the localization precision of the single molecule and thus compromises the final super-resolution image. Even nanoscale drifts in the microscope stage is a greater issue for STORM and PALM techniques since longer acquisition times are required for obtaining super-resolution images. In order to correct the stage drift, a bright fluorescence marker with high photostability is required where the probe acts like an anchor between several images. Since fluorescent dyes bleach very fast and quantum dots suffer from photoblinking, they cannot be used. In order to address this, Yi *et al.* have used FNDs as fiducial markers for imaging drift correction in the super-resolution imaging of T cells using multiplexed antibody size-limited direct STORM (madSTORM).[91] First, 100 nm FNDs are spin coated on coverslips and later Jurkat T cells are added and incubated at 37 °C. These T cells covered by coverslips are imaged by madSTORM. By calculating the centroid position of 100 nm FNDs in each image and applying this drift correction factor to the entire image stack, a super-resolved image of the Alexa 647 antibody-labeled Jurkat T cells were

obtained (Figure 8.6d and e). Figure 8.6f and g shows before and after stage drift correction using FNDs. This FND-assisted madSTORM method can be applied to other systems including *in vitro* molecular complexes, different cell types and tissue sections.

Similar studies were also carried by other researchers. For example, Prabhakar *et al.* have used FNDs as intracellular dual contrast markers for STED-TEM correlative microscopy.[92] Hsieh *et al.* employed lipid encapsulated FNDs as fiducial markers in correlative light and electron microscopy (CLEM) to obtain the spatial distribution of CD44 antigens on the HeLa cell surface.[93] These are just a couple of studies to mention. The deeply embedded NV centers in FNDs and their exceptional photostability are unaffected by surface modifications or environmental changes at room temperature, which makes them a good contrasting agent in both super-resolution and CLEM microscopy.

8.5.4 Temperature Sensing

Temperature is one of the most critical parameters for the activities of living organisms at various levels. Intracellular thermometry is of great significance in studying cellular activities such as mitochondrial thermogenesis, disease diagnosis and tumor therapy. The ability to monitor or sense the temperature fluctuations at the nanoscale inside the cell is quite challenging. In the past decade, several nanoparticle-based luminescent thermometers have been developed to measure temperature and distributions inside the cell.[94] Luminescence thermometry usually suffers from biological environmental factors such as pH and ionic strength, thus affecting the accuracy and reliability of the measured temperature. FNDs have recently joined this class of nanothermometers presenting their unique robustness and invariability to the local chemical environment such as pH, ion concentration, viscosity, molecular interaction and organic solvent.[95] FNDs can be applied over a wide range of temperatures (200–600 K) making them interesting nanothermometers for the study of nanoscale chemical reactions.

The NV^- center in the FND acts as a robust artificial solid-state system with optically readable spin states. In order to understand how a FND acts as a temperature sensor, it is necessary to look at the energy diagram of the NV center (Figure 8.1b). It has two triplet states, namely $^3A_2$ and ^3E, where each state is further split into three spin sublevels, namely $m_s = 0$ and ± 1. The $m_s = 0$ is energetically lower and the two $m_s = \pm 1$ states are energetically degenerate. The crystal field splitting between the spin sublevels is $D = 2.87$ GHz for the ground state and $D = 1.42$ GHz for the excited state, where D is called the zero-field splitting. The metastable singlet states ^1E and ^1A play a pivotal role in the magneto-optical behavior of the NV center. The optical transitions between $^3A_2$ and ^3E are spin-state conserved, whereas occasionally, intersystem crossing (ISC) occurs from the excited state ^3E ($m_s = \pm 1$) to the singlet state ^1A singlet state. The ISC rate from ^3E $m_s = \pm 1$ state to the ^1A singlet state is higher than the ^3E $m_s = 0$ to the singlet state. The ^1A singlet state then decays into the ground state $m_s = 0$ spin sublevel, selectively

populating through non-radiative processes. When a resonant microwave field is applied corresponding to the energy difference between ground state m_s = 0 and ±1, the electron spin transition occurs resulting in about 30% reduction of the fluorescence intensity. This phenomenon of reading the spin state of electrons by fluorescence is called optically detected magnetic resonance (ODMR). Interestingly this magnetic resonance frequency corresponding to the ground state spin sublevels is temperature dependent due to the thermally induced lattice strains and can be observed by ODMR spectra. Acosta *et al.* were the first to investigate the temperature dependent shifts in the magnetic resonance spectra of the NV^- center in bulk diamond samples using ODMR.[96] Figure 8.7a shows a typical ODMR spectra of the HPHT ND obtained at two different temperatures. A thermal shift ($\Delta D/\Delta T$) of −75 kHz K^{-1} was determined around 300 K for NV^- centers in NDs.

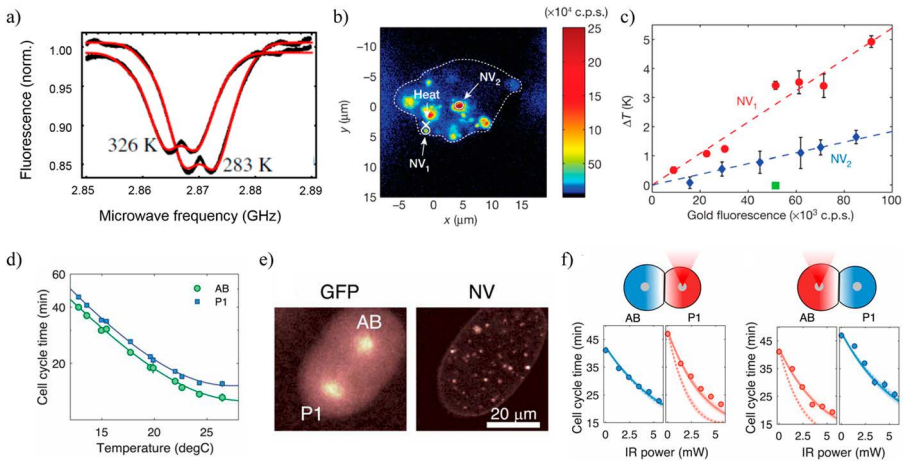

Figure 8.7 Nanothermometry of NDs with the ODMR approach. (a) Zero field ODMR spectra (black line) of NDs with NV^- concentration of 0.3 ppm at 283 K and 326 K with fits (solid red line). (b) Confocal scan of a single cell under laser excitation at 532 nm. The cross marks the position of the gold nanoparticle used for heating and the circles represent the location of the NDs (NV_1 and NV_2) used for thermometry. The dotted line provides the outlines of the cell membrane. The color bar indicates the fluorescence in counts per seconds. (c) Measured change in temperature at the positions of NV_1 and NV_2 relative to the incident laser power applied to the gold nanoparticle. Dashed lines are linear fits to the data. (d) Cell-cycle times for AB and P1 as a function of global ambient temperature with solid lines as fits to the data. (e) Confocal images of a GFP-labeled embryo in the two-cell stage with GFP imaging (left) and ND fluorescence (right). (f) Cell-cycle times of a two-cell embryo subject to local heating as a function of laser power with AB nucleus heating (left) and P1 nucleus heating (right). Solid and dashed lines are theoretical predictions based on the average and nuclei temperatures of individual cells, respectively. Reproduced from ref. 96 with permission from American Physical Society, Copyright 2010. Reproduced from ref. 97 with permission from Macmillan Publishers Ltd, Copyright 2013. Reproduced from ref. 99 with permission from PNAS.

Kucksо *et al.* first demonstrated FNDs as nanoscale thermometers in living cells.[97] First, they spin coated both the NDs and gold nanoparticles (GNPs) with a nominal diameter of 100 nm on covered glass. While locally heating the GNPs with a continuous green laser, temperatures were measured at the nanodiamond location using ODMR spectra with a precision of 0.1 K and a resolution of 100 nm. Later, to demonstrate the nanodiamond thermometry in cells, both FNDs and GNPs were introduced into the human embryonic fibroblast cells and the local temperature changes – caused by illuminating the gold nanoparticles – were measured. As shown in Figure 8.7b, while locally heating the gold nanoparticle, the temperatures at two different diamond locations (NV_1 and NV_2) were measured. The location of NV_1 is significantly closer to the heat source than NV_2 and has a stronger temperature dependence as a function of the laser power. By measuring the temperatures at the diamond locations, the temperatures at the gold location were estimated. It is observed that a temperature gradient is created around the GNPs with temperature differences of up to 5 K over a distance of approximately 7 μm (Figure 8.7c). The authors demonstrated a sensitivity of 44 ± 10 mK. Inspired by this work, Tsai *et al.* developed dual functional gold/diamond nanohybrids by conjugating gold nanorods (GNRs) directly onto the FND using polyarginine as the interface.[98] These nanohybrids were used as a combined nanoheater (the GNRs) and nanothermometer (the FNDs) for highly localized hyperthermia applications in HeLa cells. By using a near-infrared laser (808 nm) to excite the GNRs, a temperature rise of 10 K is readily achieved in cells. By increasing the laser power, the temperature rise can be significantly increased, which is good enough for conducting photothermal applications in the cells as a means for tumor therapy.

In a separate study, Choi *et al.* studied the embryogenesis of *C. elegans* using nanoscale NV thermometry.[99] In this study, the authors demonstrated a method to probe and control the cell-division timing in *C. elegans* embryos using a combination of infrared (IR) laser heating and ND nanothermometry. Embryonic development of *C. elegans* starts with a single P0 cell, which subsequently divides into smaller daughter cells, AB and P1. The daughter cells exhibit asynchronous division in which AB undergoes mitosis earlier than P1. Cell-cycle times for AB and P1 change as a function of global ambient temperature (Figure 8.7d). Making use of this temperature dependence of division time, cell-cycle durations were manipulated selectively by heating a cell (either AB or P1) with an IR laser, which created a temperature gradient across the embryo. NDs are incorporated inside the embryo to measure the resultant temperature distribution. Figure 8.7e shows the confocal images of the GFP-labeled embryo (left) in the two-cell stage and the ND fluorescence (right). When the IR laser was focused on the nucleus of the P1 cell, the cell-cycle times for both AB and P1 monotonically decreased with increasing IR power, with a greater decrease in P1, leading to a narrowing of the division-timing differences between the two cells. In contrast, AB nucleus heating produced an even larger timing difference between the two cells. The observed differences in cell-cycle acceleration rates can be attributed to a

difference in local temperature under cell-selective laser heating. Temperature distribution measured by the NV thermometers to estimate the expected cell-cycle times revealed that the cell-cycle time is not solely determined by the DNA replication occurring in the nucleus of the cell, but is also dependent on the kinetics of cyclins and other proteins throughout the cytoplasm (Figure 8.7f). Under P1 cell heating, the P1 cell division substantially sped up relative to the AB cell, and examination of the cell-cycle time differences in more detail indicated that the P1 cell consistently divided faster than the AB cell at high laser powers. The data imply that cell-cycle timings are controlled in a cell-autonomous manner with no significant contribution from cell–cell communication.

Imaging of cell-division under controlled laser heating accompanied with temperature distribution mapping inside the embryo with NV centers in NDs provided insights into the timing-regulation mechanism during early embryogenesis. These results open multiple future directions of exploration of cell-cycle timing control at later developmental stages and further investigations of the developmental consequence of perturbing cell-cycle times as well as additional thermogenetic control.

As illustrated above, probing the thermal shifts of the spin resonances of the NV^- center shows that FNDs are an effective means of nanoscale temperature sensors providing both high temporal and spatial resolution. However, the ODMR method is technically demanding as microwave excitation is delivered through a metal wire for reducing the fluorescence emission. The requirement of keeping the metal wire in such close proximity to the sample limits the application of the ODMR method in life sciences research.

Alternatively, there is an all-optical method where shifts in the ZPL line of the NV^- center (637 nm) are observed with temperature. Davies first observed the temperature shifts of the visible ZPL energy and provided an accurate vibronic model for observed thermal shifts of ZPL.[100] His vibronic model considered the thermal response of the ZPL to the stress induced by the thermal expansion of the bulk diamond lattice and the electron–phonon interactions at the center. At room temperature, a thermal shift of $(\Delta(\mathrm{ZPL})/\Delta T) = 0.015$ nm K^{-1} is observed accompanied by a full width at half-maximum of ~5 nm for bulk diamonds. Figure 8.8a shows the fluorescence spectra of FNDs dispersed in water at different temperatures. While the overall feature of the emission band does not change with temperature over 28–75 °C, the ZPL is red-shifted as the solution temperature increases. Compared to the ODMR method, this all-optical method provides a much simpler, straightforward approach and is readily implementable by any confocal microscope equipped with a CCD-based spectrometer.

All-optical based ND thermometry enables researchers to study how local temperature changes affect the cellular activities and their functions. Using this approach, Tsai *et al.*[101] studied the membrane stability of cells with respect to temperature and also performed hyperlocalized hyperthermia on cells as means for tumor therapy. In this study, the authors developed two-in-one dual-functional nanohybrids that can heat and sense the temperature

simultaneously by conjugating GNRs onto the FND surface through the polyethyleneimine (PEI) interface. They were able to put more than 50 such GNRs onto a single 100 nm FND surface forming a shell-like structure. Figure 8.8b shows the absorption spectrum of 10 nm × 16 nm (diameter × length) GNRs and fluorescence emission of FNDs. GNR-FND nanohybrids could be individually heated and imaged at the same time with a single laser. In order to avoid the fluorescence background from the NV^0 center, which interferes in the later spectral analysis, and to selectively excite NV^- centers in FNDs, nanohybrids were irradiated with a 594 nm laser. The technical details of the method development and the data analysis can be read in other papers.[101,102] These dual-functional GNR-FND hybrids were then successfully introduced into the human embryonic kidney (HEK293T) cells through an endocytosis process.[101] Fluorescence imaging of the FND revealed that some of these

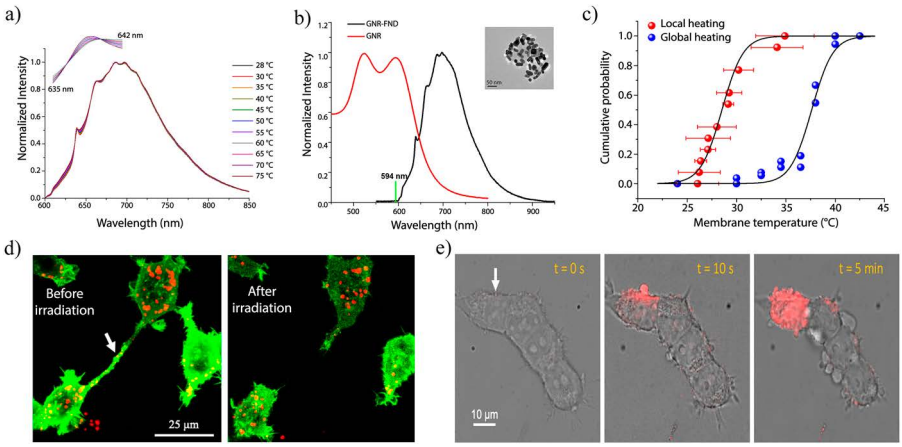

Figure 8.8 FND based temperature sensing and hyperlocalized hyperthermia in HEK293T cells. (a) Area-normalized temperature-dependent fluorescence spectra of 100 nm FNDs illuminated by a 594 nm laser in solution. Inset: Enlarged view of the temperature-induced shift of the ZPLs for spectra acquired at 28–75 °C. (b) Comparison between the absorption spectrum of 10 nm × 16 nm GNRs and the emission of 100 nm GNR-FNDs. The thick green bar denotes the excitation wavelength at 594 nm. Inset: TEM image of a typical GNR-decorated FND. (c) Empirical cumulative distribution plot of the membrane temperatures at which MNTs are ruptured by local heating and global heating of the GFP-transduced HEK293T cells. (d) Fluorescence imaging of HEK293T cells transduced with actin-GFP fusion protein (green) and labeled with GNR-FNDs (red). The MNT was broken and retracted upon excitation of the GNR-FND particle (white arrow). (e) Merged bright-field and fluorescence images of the HEK293T cell cluster with GNR-FNDs attached to plasma membrane in the presence of PI dye at different time points. Intracellular PI was observed almost immediately after laser irradiation of the GNR-FND particle shown by the white arrow. Reproduced from ref. 101 with permission from John Wiley and Sons, Copyright 2017 Wiley-VCH Verlag GmbH & Co. KGaA, Weinheim.

GNR-FNDs were inside the membrane nanotubes (MNTs) that were formed between the HEK293T cells. At first, the MNTs were globally heated using an on-stage incubator and the temperatures at which these MNTS were ruptured were observed. For local heating, single GNR-FND particles inside the MNTs were irradiated with a 594 nm laser and FND temperatures were measured at which MNTs were ruptured (Figure 8.8d). Interestingly for MNTs, a temperature difference of up to 10 °C was found between global heating and local heating (Figure 8.8c). The authors attributed this difference to the large temperature gradient (>10 °C μm^{-1} at the MNT membrane) created by the local heating but not by the global heating.

Further, the authors applied the hyperlocalized hyperthermia on the membrane of HEK293T cells. The hyperlocalized hyperthermia surpasses conventional thermal therapy by reducing the heating zone down to the nanometer size. When GNR-FNDs were sparsely anchored on the cell membrane, laser excitation with low power (30 μW) did not damage the cell membrane. But when the laser power increased by a factor of 10, a severe membrane blebbing was observed as indicated by the penetrated propidium iodide (PI) dye (Figure 8.8e). PI is a membrane impermeable dye which is used to label dead cells and its fluorescence intensity is increased by more than 10-fold once bound to nucleic acids inside the cytoplasm. The blebbing is a signature of cell death due to necrosis, as the cell membrane was compromised by heating of the attached single GNR-FND particle. This is the first demonstration of a technology that enables the simultaneous heating, measurement of temperature, and observation of the cellular response to heat spots. The dual-functional nanohybrids provide a powerful new tool for single cell laser surgery and precision hyperthermia cancer therapy applications.

8.5.5 Gene Delivery

Gene therapy or delivery is a technique used to treat or prevent diseases by using genes. By introducing genetic material into the target pathological cells or tissues, the abnormal or mutated genes in the specimen can be modified to restore their function. Naked genetic molecules such as DNA, plasmid DNA, mRNA and siRNA are unstable in a biological environment and cannot be internalized by cells efficiently. One of the challenging issues in gene therapy is to find better ways of delivering genes and targeting them to particular cells. Although viral gene delivery is highly effective, concerns regarding safety have limited its application. Recently, nanosized materials for gene delivery have attracted wide attention. Successful gene delivery requires both effective cellular uptake and cytosolic release of the gene. Studies show that NDs emerged as an efficient tool for gene delivery, by which the efficiency of gene therapy is much increased.

Zhang *et al.* have introduced polymer-functionalized NDs as vehicles for gene delivery.[103] Briefly, the ND surface is modified either covalently or noncovalently with low molecular weight (800 Da) polyethyleneimine (PEI800). Later, negatively-charged DNA (luciferase plasmid) was surface immobilized

onto positively-charged ND-PEI800 *via* electrostatic interactions. Along with ND-PEI800, different nanoparticles (unmodified ND and amine terminated ND) were also tested for comparison. Upon administering these nanoparticles to HeLa cells different transfection efficiencies were shown. The transfection efficiency followed the trend of ND-PEI800>PEI800>ND-NH_2>ND>naked DNA. Interestingly, ND-PEI800 is 400 and 800 times more efficient than ND-NH_2 and unmodified ND, respectively. In addition, ND-PEI800 particles efficiently deliver and express another plasmid encoding for GFP in HeLa cells. Strong GFP-expression could be easily visualized in the cytoplasm by confocal microscopy when ND-PEI800 particles were used, whereas only weak GFP was observed when PEI800 or NDs are used as gene carriers.

Ewing sarcoma (ES) is a genetic disease, causing bone cancer in children. In most cases of ES (85%) a chromosomal translocation occurs at chromosomes t(11,22) producing a fusion gene, *EWS-FLi1*, which is finally expressed as a chimeric protein.[104] One of the treatments for this cancer is siRNA targeting the *EWS-FLi1* junction at the mRNA level. Alhaddad *et al.* used NDs for siRNA delivery to ES cells.[105] Briefly, cationic NDs (50 nm) were produced by surface coating with amino rich polymers: poly(allylamine hydrochloride) (PAH) or PEI. Later, SiRNA targeting the *EWS-FLi1* gene are attached to the PEI or PAH coated NDs. The particles were introduced through endocytosis into the NIH/3T3 and A673 cells expressing human *EWS-FLi1* oncogene. It was observed by qPCR results that a maximum efficiency of 50% for ND-PEI in inhibiting the *EWS-FLi1* mRNA expression in NIH/3T3 cells and 55% in A673 cells, whereas ND-PAH appears to be a less efficient transfection agent and free siRNA do not inhibit *EWS-FLi1* expression at all. When lipofectamine was used to deliver the siRNA, a 65% inhibition is observed in the cells, but it caused more toxicity than the ND-PAH or ND-PEI. This study showed that NDs induce a larger efficiency in inhabiting the *EWS-FLi1* expression, combined with lower toxicity to the cell. Although the applications of NDs for the treatment of human diseases is promising, the U.S. Food and Drug Administration (FDA) requirements state that therapeutic agents injected into the body should not accumulate for long periods of time. In order to test the ND-mediated gene delivery combined with their distribution and elimination pathways, Claveau *et al.* studied the activity of ND-mediated siRNA delivery *in vivo* in ES tumor xenografted mice.[106] In this study, hydrogenated or tritiated (tritium, isotope of hydrogen) DNDs (3–8 nm) were used instead of polycation-NDs as mentioned in the previous study. Hydrogenation of DNDs provided a positive zeta potential (+50 mV) on the DND surface. In order to establish H-DNDs for anticancer gene delivery in mice, siRNA was bound to cationic H-DND and the inhibition of *EWS-FLi1* was first tested in A673 cells. In the presence of serum, 35% inhibition is obtained for cationic H-DNDs, whereas only 18% is observed for lipofectamine 2000 under same conditions (Figure 8.9a). Later, radioisotope tritium-labeled DNDs (T-DNDs) are used instead of H-DNDs for studies on mice. Radioactivity from T-DNDs allowed the study of the distribution and elimination pathways of T-DNDs in mice. T-DNDs complexed with siRNA or without any complexation were

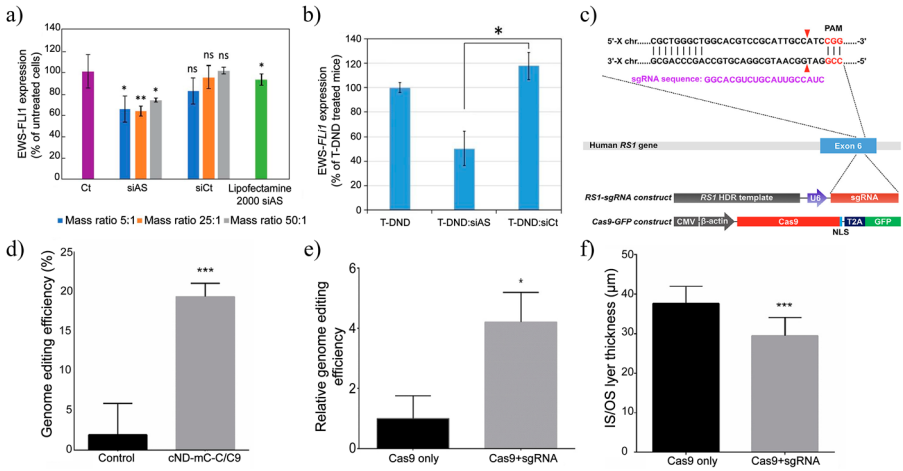

Figure 8.9 ND-mediated gene delivery and the inhibition efficiencies *in vitro* and *in vivo*. (a) Inhibition of *EWS-FLi1* expression in A673 cells by H-DND : siRNA or Lipofectamine 2000. The indicated mass ratio is for H-DND : siRNA. siAS: antisense siRNA directed against *EWS-FLi1* oncogene; siCt: control irrelevant siRNA sequence. (b) Inhibition of *EWS-FLi1* expression on tumor xenografted on mice (n = 6 to 8 animals per condition) treated for 24 h by T-DND : siRNA at a mass ratio of 5 : 1 (T-DND : siRNA). (c) A schematic showing the design of CRISPR-Cas9 constructs to introduce c.625C>T mutation into the mouse RS1 gene. The fragment of RS1 exon 6 sequence containing the cleavage site (red arrowhead) and PAM sequence (red font) shown at the top. The maps of Cas9-GFP and RS1-sgRRNA are shown at the bottom. (e) ddPCR analysis of RS1 c.625C>T copy number in GFP-sorted population of hiPSCs treated for 24 h (d) and in mouse retinas treated for two weeks with control (Cas9 construct only) and RS1 targeting ND-mC-C/C9 nanoparticles (Cas9 + sgRNA). (f) Quantification of thickness of the inner and outer segment (IS/OS) layers in mouse retinas. The data are expressed as means ± standard deviation error bars. Reproduced from ref. 106, https://doi.org/10.3390/nano10030553 under the terms of the CC-BY 4.0 license https://creativecommons.org/licenses/by/4.0/. Reproduced from ref. 107 with permission from Elsevier, Copyright 2020.

injected into the tail vein of mice. After 24 h, the mice were sacrificed and RNA was extracted from the tumors. RT-qPCR analysis revealed that T-DNDs complexed with antisense siRNA were able to inhibit the *EWS-FLi1* expression by about 50%, whereas T-DNDs complexed with control irrelevant siRNA had no effect (Figure 8.9b). These results confirm that H/T-DNDs complexed with siRNA are able to inhibit the *EWS-FLi1* gene expression in an ES tumor model grafted on mice. The biodistribution and elimination pathways of the T-DND : siRNA particles were also studied. Radioactivity of tritium enabled the observation that T-DND : siRNA particles were mainly accumulated in kidney, spleen, heart and lung with a slow increase from 4 to 24 h and their transfer to the intestine lumen by bile may be the main way for T-DND elimination from the bodies of the mice. Overall, this study shows a significant

step towards the use of ultra-small solid nanoparticles for the efficient delivery of siRNA to tumor cells in animals that are also eliminated subsequently from their bodies.

In another recent study, Yang *et al.* studied the ND-mediated CRISPR-Cas9 delivery of human retinoschisis mutation into human stem cells and mouse retinas.[107] X-linked retinoschisis (XLRS) is a retinal disease caused by mutations in the *RS1* gene, which affects males in early life. The most characteristic features of this disease include mild to severe loss in central vision, splitting of the retinal layers and damage of the photoreceptor cells. In order to establish the ND as a CRISPR-Cas9 (C/C9) carrier, the authors of this study introduced a mutation in the RS1 gene that is associated with XLRS in healthy cells and mouse retinas. For this, carboxylated DNDs with a diameter of 3 nm are covalently conjugated with fluorescent mCherry protein (mC). Two linear DNA constructs were then attached to the conjugated mC. One encoded Cas9 endonucleases and GFP reporter, another one encoded sgRNA and contained an insert of a HDR template designed to introduce mutation in the *RS1* gene (Figure 8.9c). Initially, the efficiency of these prepared ND-mC-C/C9 particles were tested to introduce the mutation to the RS1 gene in human induced pluripotent stem cells (hiPSCs). The prepared ND-mC-C/C9 particles were diluted in 3% BSA in PBS for better stabilization, which in turn also increased the efficiency of internalization through endocytosis. The phosphoryl imidazole covalent bond between mCherry and the DNA construct was compromised in a lower pH environment such as exists in late endosomes, thus releasing the DNA into the cytosol. Fluorescence signals from both mCherry and GFP show that the particles were internalized by hiPSCs and the attached DNA was transcribed. Cell viability assessment of these particles by CCK8 assay shows that in a range of concentrations between 1.5 and 24 μg mL^{-1}, the ND-mC-C/C9 particles did not affect the viability of hiPSCs. Two days after the internalization, the GFP expressing cells were sorted by flow cytometry and the gene mutation in genomic DNA was analyzed by droplet digital PCR (ddPCR). It was shown that the nucleotide was edited in 19.3% of all alleles (Figure 8.9d). Later these particles (ND-mC-C/C9) were injected into the eyes of mice. Two weeks after the injection, ddPCR analysis of retinal lysates showed that four times the percentage of edited alleles than the background signal were detected in the retina of mice injected with ND particles carrying Cas-GFP construct only (Figure 8.9e). Further investigation by immunofluorescence staining of a retinal tissue section revealed a reduction of thickness in the outer retinal layer and defects in the organization of photoreceptor cells (Figure 8.9f). All these results indicate the successful introduction of mutation to the *RSI* gene in a mouse retina. Overall, the delivery of ND based C/C9 showed great potential for establishing *in vitro* and *in vivo* disease models of XLRS.

In conclusion, the ND has been shown to be a good delivery agent. Although there is a low transfection efficiency compared to conventional delivery agents such as lipofectamine 2000, the advantage of NDs is based on

their safety as an inert and low immunogenicity material. The transfection efficiency can be improved by loading more genetic material onto NDs and also by increasing the concentration of NDs for genetic delivery applications.

8.6 Conclusions

In the past few years, NDs have emerged in the field of nanomedicine and nanotechnology with great potential for a broad range of biomedical applications. Their biocompatibility together with their unique spin-optical properties of color centers make the ND an outstanding nanoparticle for therapeutic delivery and bioimaging applications as well as quantum sensing in a biological environment. It has become quite easy to modify the ND surface with biomolecules and probe the functions of a living cell at the molecular level with single particle detection sensitivity. NDs have shown to be a novel carrier of biomolecules for targeted delivery and controlled release in live cells. A large variety of bioactive molecules have been delivered with NDs and shown increased therapeutic efficiency and reduced systematic toxicity *in vitro* and *in vivo*. The highly stable near-infrared fluorescence of NV centers in NDs combined with their magnetic modulation characteristic is essential for the studies of biodistribution and pharmacokinetics of therapeutic cells in a preclinical setting. These advanced technologies are promising for theranostic patient-centered care to allow sensitive multimode diagnostics together with targeted gene therapy within one nanoparticle.

It should also be stressed that many challenges and limitations still need to be addressed before the translation of these techniques from the laboratory to the clinic can be made. More detailed studies of cellular fate, re-aggregation prevention, excretion or accumulation in the human body, and the long-term effects of ND based treatments are needed. In addition, sufficiently bright sub-10 nm FND particles can have great impact in sensing and fluorescence modulation applications. But it is difficult to produce such smaller and brighter NDs with sizes comparable to conventional dyes and other fluorescent nanomaterials. Recently, core–shell particles have gained more interest with ND being core and gold, silver and iron particles acting as shells. The biocompatibility and cytotoxicity of these nanohybrids are still yet to be studied along with their other potential uses in the life science field. Multicolor FNDs seem to have more applications in clinical use, where fluorescence imaging guides the surgical resection *in vivo*.

Furthermore, the interdisciplinary nature of ND based medicine requires the cooperation of scientists from different fields; chemists are working on developing different color centers in NDs and physicists are working on exploring the applications of these prepared color centers. In the near future, more collaborative research between chemists, physicists, biologists and even physicians is needed to explore more ND applications in the life science and clinical research fields for fast and safe development of nanomedicines.

Acknowledgements

This work was supported by Academia Sinica and the Ministry of Science and Technology, Taiwan, with grant no. 107-2113-M-001-018-MY3.

References

1. H.-C. Chang, *J. Phys.: Conf. Ser.*, 2016, **728**, 062004.
2. H.-C. Lu, Y.-C. Peng, S.-L. Chou, J.-I. Lo, B.-M. Cheng and H.-C. Chang, *Angew. Chem., Int. Ed.*, 2017, **56**, 14469–14473.
3. X. Shutong, S. Wen, L. Yican, J. Laili, J. Shouyuan, A. I. Okay and A. M. Sengör, *Science*, 1992, **256**, 80–82.
4. N. V. Sobolev and V. S. Shatsky, *Nature*, 1990, **343**, 742–746.
5. A. El Goresy, P. Gillet, M. Chen, F. Künstler, G. Graup and V. Stähle, *Am. Mineral.*, 2001, **86**, 611–621.
6. W. W. W. Hsiao, Y. Y. Hui, P. C. Tsai and H. C. Chang, *Acc. Chem. Res.*, 2016, **49**, 400–407.
7. F. P. Bundy, H. T. Hall, H. M. Strong and R. H. Wentorf, *Nature*, 1955, **176**, 51–55.
8. V. Y. Dolmatov, *Russ. Chem. Rev.*, 2001, **70**, 607–626.
9. K. E. Spear, J. P. Dismukes and Electrochemical Society, *Synthetic Diamond: Emerging CVD Science and Technology*, Wiley, 1994.
10. F. Gorrini, M. Cazzanelli, N. Bazzanella, R. Edla, M. Gemmi, V. Cappello, J. David, C. Dorigoni, A. Bifone and A. Miotello, *Sci. Rep.*, 2016, **6**, 35244.
11. C.-H. Nee, S.-L. Yap, T.-Y. Tou, H.-C. Chang and S.-S. Yap, *Sci. Rep.*, 2016, **6**, 33966.
12. J. Xiao, G. Ouyang, P. Liu, C. X. Wang and G. W. Yang, *Nano Lett.*, 2014, **14**, 3645–3652.
13. S. Welz, Y. Gogotsi and M. J. McNallan, *J. Appl. Phys.*, 2003, **93**, 4207–4214.
14. A. K. Khachatryan, S. G. Aloyan, P. W. May, R. Sargsyan, V. A. Khachatryan and V. S. Baghdasaryan, *Diamond Relat. Mater.*, 2008, **17**, 931–936.
15. L. Basso, F. Gorrini, N. Bazzanella, M. Cazzanelli, C. Dorigoni, A. Bifone and A. Miotello, *Appl. Phys. A*, 2018, **124**, 72.
16. G. Davies, S. C. Lawson, A. T. Collins, A. Mainwood and S. J. Sharp, *Phys. Rev. B*, 1992, **46**, 13157–13170.
17. S. Lagomarsino, A. M. Flatae, S. Sciortino, F. Gorelli, M. Santoro, F. Tantussi, F. De Angelis, N. Gelli, F. Taccetti, L. Giuntini and M. Agio, *Diamond Relat. Mater.*, 2018, **84**, 196–203.
18. W. Kaiser and W. L. Bond, *Phys. Rev.*, 1959, **115**, 857–863.
19. J. Walker, *Rep. Prog. Phys.*, 1979, **42**, 1605–1659.
20. Y.-R. Chang, H.-Y. Lee, K. Chen, C.-C. Chang, D.-S. Tsai, C.-C. Fu, T.-S. Lim, Y.-K. Tzeng, C.-Y. Fang, C.-C. Han, H.-C. Chang and W. Fann, *Nat. Nanotechnol.*, 2008, **3**, 284–288.
21. R. E. Evans, A. Sipahigil, D. D. Sukachev, A. S. Zibrov and M. D. Lukin, *Phys. Rev. Appl.*, 2016, **5**, 44010.
22. J. P. Goss, R. Jones, S. J. Breuer, P. R. Briddon and S. Öberg, *Phys. Rev. Lett.*, 1996, **77**, 3041–3044.

23. F. Treussart and I. I. Vlasov, in *Micro and Nano Technologies*, ed. J.-C. Arnault, Elsevier, 2017, pp. 155–181.
24. Y.-K. Tzeng, J. L. Zhang, H. Lu, H. Ishiwata, J. Dahl, R. M. K. Carlson, H. Yan, P. R. Schreiner, J. Vuč, Z.-X. Shen, N. Melosh and S. Chu, *Nano Lett.*, 2017, **17**, 1489–1495.
25. W. Strober, *Curr. Protoc. Immunol.*, 1997, **21**, A.3B.1–A.3B.2.
26. L. Zamai, E. Falcieri, G. Marhefka and M. Vitale, *Cytometry*, 1996, **23**, 303–311.
27. J. Markovits, B. P. Roques and J.-B. Le Pecq, *Anal. Biochem.*, 1979, **94**, 259–264.
28. B. Schutte, R. Nuydens, H. Geerts and F. Ramaekers, *J. Neurosci. Methods*, 1998, **86**, 63–69.
29. S. Shalini, L. Dorstyn, S. Dawar and S. Kumar, *Cell Death Differ.*, 2015, **22**, 526–539.
30. W. Gorczyca, J. Gong and Z. Darzynkiewicz, *Cancer Res.*, 1993, **53**, 1945–1951.
31. M. V. Berridge, P. M. Herst and A. S. Tan, *Biotechnology Annual Review*, Elsevier, 2005, vol. 11, pp. 127–152.
32. A. R. Collins, *Mol. Biotechnol.*, 2004, **26**, 249.
33. M. Kirsch-Volders, I. Decordier, A. Elhajouji, G. Plas, M. J. Aardema and M. Fenech, *Mutagenesis*, 2011, **26**, 177–184.
34. M. A. Dobrovolskaia, J. D. Clogston, B. W. Neun, J. B. Hall, A. K. Patri and S. E. McNeil, *Nano Lett.*, 2008, **8**, 2180–2187.
35. S. Braune, R. A. Latour, M. Reinthaler, U. Landmesser, A. Lendlein and F. Jung, *Adv. Healthcare Mater.*, 2019, **8**, 1900527.
36. M. Elsabahy and K. L. Wooley, *Chem. Soc. Rev.*, 2013, **42**, 5552–5576.
37. S.-J. Yu, M.-W. Kang, H.-C. Chang, K.-M. Chen and Y.-C. Yu, *J. Am. Chem. Soc.*, 2005, **127**, 17604–17605.
38. A. M. Schrand, H. Huang, C. Carlson, J. J. Schlager, E. Ōsawa, S. M. Hussain and L. Dai, *J. Phys. Chem. B*, 2007, **111**, 2–7.
39. A. M. Schrand, L. Dai, J. J. Schlager, S. M. Hussain and E. Osawa, *Diamond Relat. Mater.*, 2007, **16**, 2118–2123.
40. V. Paget, J. A. Sergent, R. Grall, S. Altmeyer-Morel, H. A. Girard, T. Petit, C. Gesset, M. Mermoux, P. Bergonzo, J. C. Arnault and S. Chevillard, *Nanotoxicology*, 2014, **8**, 46–56.
41. S. Hemelaar, B. Saspaanithy, S. L'Hommelet, F. Perona Martinez, K. van der Laan, R. Schirhagl, S. R. Hemelaar, B. Saspaanithy, S. R. M. L'Hommelet, F. P. Perona Martinez, K. J. Van der Laan and R. Schirhagl, *Sensors*, 2018, **18**, 355.
42. H.-S. Jung, K.-J. Cho, S.-J. Ryu, Y. Takagi, P. A. Roche and K. C. Neuman, *ACS Appl. Mater. Interfaces*, 2020, **12**, 6641–6650.
43. T.-J. Wu, Y.-K. Tzeng, W.-W. Chang, C.-A. Cheng, Y. Kuo, C.-H. Chien, H.-C. Chang and J. Yu, *Nat. Nanotechnol.*, 2013, **8**, 682–689.
44. X. Zhang, W. Hu, J. Li, L. Tao and Y. Wei, *Toxicol. Res.*, 2012, **1**, 62–68.
45. Y. Zhu, J. Li, W. Li, Y. Zhang, X. Yang, N. Chen, Y. Sun, Y. Zhao, C. Fan and Q. Huang, *Theranostics*, 2012, **2**, 302–312.

46. N. Mohan, C.-S. Chen, H.-H. Hsieh, Y.-C. Wu and H.-C. Chang, *Nano Lett.*, 2010, **10**, 3692–3699.
47. N. Mohan, B. Zhang, C.-C. Chang, L. Yang, C.-S. Chen, C.-Y. Fang, H.-H. Hsieh, C.-Y. Cho, Y.-C. Wu, J.-H. Weng, B. Chung and H.-C. Chang, *MRS Proc.*, 2011, **1362**, 25–35.
48. C.-C. Chang, B. Zhang, C.-Y. Li, C.-C. Hsieh, G. Duclos, F. Treussart and H.-C. Chang, *Proc. SPIE*, 2012, **8272**, 827205.
49. V. Vaijayanthimala, P.-Y. Cheng, S.-H. Yeh, K.-K. Liu, C.-H. Hsiao, J.-I. Chao and H.-C. Chang, *Biomaterials*, 2012, **33**, 7794–7802.
50. B. Kamila, S. S. Smyth and E. F. Plow, *Circ. Res.*, 2013, **112**, 1189–1200.
51. C. Marcinkiewicz, J. A. Gerstenhaber, M. Sternberg, P. I. Lelkes and G. Feuerstein, *Int. J. Nanomed.*, 2017, **12**, 3711–3720.
52. J. A. Gerstenhaber, F. C. Barone, C. Marcinkiewicz, J. Li, A. O. Shiloh, M. Sternberg, P. I. Lelkes and G. Feuerstein, *Int. J. Nanomed.*, 2017, **12**, 8471–8482.
53. F. C. Barone, C. Marcinkiewicz, J. Li, M. Sternberg, P. I. Lelkes, D. A. Dikin, P. J. Bergold, J. A. Gerstenhaber and G. Feuerstein, *Int. J. Nanomed.*, 2018, **13**, 5449–5468.
54. F. C. Barone, C. Marcinkiewicz, J. Li, F. Yi, M. Sternberg, P. I. Lelkes, D. P. Rosenbaum, J. A. Gerstenhaber and G. Z. Feuerstein, *Int. J. Nanomed.*, 2019, **14**, 1163–1175.
55. J. A. Gerstenhaber, C. Marcinkiewicz, F. C. Barone, M. Sternberg, M. R. D'Andrea, P. I. Lelkes and G. Z. Feuerstein, *Int. J. Nanomed.*, 2019, **14**, 6451–6464.
56. L. Moore, J. Yang, T. T. H. Lan, E. Osawa, D.-K. Lee, W. D. Johnson, J. Xi, E. K.-H. Chow and D. Ho, *ACS Nano*, 2016, **10**, 7385–7400.
57. S. K. Sarkar, A. Bumb, X. Wu, K. A. Sochacki, P. Kellman, M. W. Brechbiel and K. C. Neuman, *Biomed. Opt. Express*, 2014, **5**, 1190–1202.
58. Y. Y. Hui, L.-J. Su, O. Y. Chen, Y.-T. Chen, T.-M. Liu and H.-C. Chang, *Sci. Rep.*, 2014, **4**, 5574.
59. L.-J. Su, M.-S. Wu, Y. Y. Hui, B.-M. Chang, L. Pan, P.-C. Hsu, Y.-T. Chen, H.-N. Ho, Y.-H. Huang, T.-Y. Ling, H.-H. Hsu and H.-C. Chang, *Sci. Rep.*, 2017, **7**, 45607.
60. H.-D. Wang, C. H. Niu, Q. Yang and I. Badea, *Nanotechnology*, 2011, **22**, 145703.
61. K.-K. Liu, M.-F. Chen, P.-Y. Chen, T. J. F. Lee, C.-L. Cheng, C.-C. Chang, Y.-P. Ho and J.-I. Chao, *Nanotechnology*, 2008, **19**, 205102.
62. K. V. Purtov, A. I. Petunin, A. E. Burov, A. P. Puzyr and V. S. Bondar, *Nanoscale Res. Lett.*, 2010, **5**, 631–636.
63. R. A. Shimkunas, E. Robinson, R. Lam, S. Lu, X. Xu, X.-Q. Zhang, H. Huang, E. Osawa and D. Ho, *Biomaterials*, 2009, **30**, 5720–5728.
64. S. Li and R. M. Leblanc, *J. Phys. Chem. B*, 2014, **118**, 1181–1188.
65. A. H. Smith, E. M. Robinson, X.-Q. Zhang, E. K. Chow, Y. Lin, E. Osawa, J. Xi and D. Ho, *Nanoscale*, 2011, **3**, 2844.
66. X. L. Kong, L. C. L. Huang, C.-M. Hsu, W.-H. Chen, C.-C. Han and H.-C. Chang, *Anal. Chem.*, 2005, **77**, 259–265.
67. L.-C. L. Huang and H.-C. Chang, *Langmuir*, 2004, **20**, 5879–5884.
68. T.-T.-B. Nguyen, H.-C. Chang and V. W.-K. Wu, *Diamond Relat. Mater.*, 2007, **16**, 872–876.

69. L.-J. Su, H.-H. Lin, M.-S. Wu, L. Pan, K. Yadav, H.-H. Hsu, T.-Y. Ling, Y.-T. Chen and H.-C. Chang, *Bioconjugate Chem.*, 2019, **30**, 2228–2237.
70. V. Vaijayanthimala, Y.-K. Tzeng, H.-C. Chang and C.-L. Li, *Nanotechnology*, 2009, **20**, 425103.
71. O. Faklaris, V. Joshi, T. Irinopoulou, P. Tauc, M. Sennour, H. Girard, C. Gesset, J.-C. Arnault, A. Thorel, J.-P. Boudou, P. A. Curmi and F. Treussart, *ACS Nano*, 2009, **3**, 3955–3962.
72. E. Perevedentseva, S.-F. Hong, K.-J. Huang, I.-T. Chiang, C.-Y. Lee, Y.-T. Tseng and C.-L. Cheng, *J. Nanopart. Res.*, 2013, **15**, 1834.
73. C.-Y. Fang, V. Vaijayanthimala, C.-A. Cheng, S.-H. Yeh, C.-F. Chang, C.-L. Li and H.-C. Chang, *Small*, 2011, **7**, 3363–3370.
74. C.-C. Fu, H.-Y. Lee, K. Chen, T.-S. Lim, H.-Y. Wu, P.-K. Lin, P.-K. Wei, P.-H. Tsao, H.-C. Chang and W. Fann, *Proc. Natl. Acad. Sci. U. S. A.*, 2007, **104**, 727–732.
75. C. P. Epperla, N. Mohan, C.-W. Chang, C.-C. Chen and H.-C. Chang, *Small*, 2015, **11**, 6097–6105.
76. S. Abounit and C. Zurzolo, *J. Cell Sci.*, 2012, **125**, 1089–1098.
77. R. Mittal, E. Karhu, J.-S. Wang, S. Delgado, R. Zukerman, J. Mittal and V. M. Jhaveri, *J. Cell. Physiol.*, 2019, **234**, 1130–1146.
78. W. Jung, A. P. Tabatabai, J. J. Thomas, S. M. A. Tabei, M. P. Murrell and T. Kim, *Cytoskeleton*, 2019, **76**, 517–531.
79. F.-J. Hsieh, S. Sotoma, H.-H. Lin, C.-Y. Cheng, T.-Y. Yu, C.-L. Hsieh, C.-H. Lin and H.-C. Chang, *ACS Appl. Mater. Interfaces*, 2019, **11**, 19774–19781.
80. S. Haziza, N. Mohan, Y. Loe-Mie, A.-M. Lepagnol-Bestel, S. Massou, M.-P. Adam, X. L. Le, J. Viard, C. Plancon, R. Daudin, P. Koebel, E. Dorard, C. Rose, F.-J. Hsieh, C.-C. Wu, B. Potier, Y. Herault, C. Sala, A. Corvin, B. Allinquant, H.-C. Chang, F. Treussart and M. Simonneau, *Nat. Nanotechnol.*, 2017, **12**, 322–328.
81. D. A. Simpson, A. J. Thompson, M. Kowarsky, N. F. Zeeshan, M. S. J. Barson, L. T. Hall, Y. Yan, S. Kaufmann, B. C. Johnson, T. Ohshima, F. Caruso, R. E. Scholten, R. B. Saint, M. J. Murray and L. C. L. Hollenberg, *Biomed. Opt. Express*, 2014, **5**, 1250–1261.
82. R. Igarashi, Y. Yoshinari, H. Yokota, T. Sugi, F. Sugihara, K. Ikeda, H. Sumiya, S. Tsuji, I. Mori, H. Tochio, Y. Harada and M. Shirakawa, *Nano Lett.*, 2012, **12**, 5726–5732.
83. L. Schermelleh, R. Heintzmann and H. Leonhardt, *J. Cell Biol.*, 2010, **190**, 165–175.
84. T. A. Klar, S. Jakobs, M. Dyba, A. Egner and S. W. Hell, *Proc. Natl. Acad. Sci. U. S. A.*, 2000, **97**, 8206–8210.
85. E. Rittweger, K. Y. Han, S. E. Irvine, C. Eggeling and S. W. Hell, *Nat. Photonics*, 2009, **3**, 144–147.
86. K. Y. Han, K. I. Willig, E. Rittweger, F. Jelezko, C. Eggeling and S. W. Hell, *Nano Lett.*, 2009, **9**, 3323–3329.
87. S. Arroyo-Camejo, M.-P. Adam, M. Besbes, J.-P. Hugonin, V. Jacques, J.-J. Greffet, J.-F. Roch, S. W. Hell and F. Treussart, *ACS Nano*, 2013, **7**, 10912–10919.
88. Y.-K. Tzeng, O. Faklaris, B.-M. Chang, Y. Kuo, J.-H. Hsu and H.-C. Chang, *Angew. Chem., Int. Ed.*, 2011, **50**, 2262–2265.

89. G. Laporte and D. Psaltis, *Biomed. Opt. Express*, 2016, **7**, 34–44.
90. M. Pfender, N. Aslam, G. Waldherr, P. Neumann and J. Wrachtrup, *Proc. Natl. Acad. Sci. U. S. A.*, 2014, **111**, 14669–14674.
91. J. Yi, A. Manna, V. A. Barr, J. Hong, K. C. Neuman and L. E. Samelson, *J. Visualized Exp.*, 2017, 55997.
92. N. Prabhakar, M. Peurla, S. Koho, T. Deguchi, T. Näreoja, H.-C. Chang, J. M. Rosenholm and P. E. Hänninen, *Small*, 2018, **14**, 1701807.
93. F.-J. Hsieh, Y.-W. Chen, Y.-K. Huang, H.-M. Lee, C.-H. Lin and H.-C. Chang, *Anal. Chem.*, 2018, **90**, 1566–1571.
94. K. Okabe, R. Sakaguchi, B. Shi and S. Kiyonaka, *Pfluegers Arch.*, 2018, **470**, 717–731.
95. T. Sekiguchi, S. Sotoma and Y. Harada, *Biophys. Physicobiol.*, 2018, **15**, 229–234.
96. V. M. Acosta, E. Bauch, M. P. Ledbetter, A. Waxman, L.-S. Bouchard and D. Budker, *Phys. Rev. Lett.*, 2010, **104**, 70801.
97. G. Kucsko, P. C. Maurer, N. Y. Yao, M. Kubo, H. J. Noh, P. K. Lo, H. Park and M. D. Lukin, *Nature*, 2013, **500**, 54–58.
98. P.-C. Tsai, O. Y. Chen, Y.-K. Tzeng, Y. Y. Hui, J. Y. Guo, C.-C. Wu, M.-S. Chang and H.-C. Chang, *EPJ Quantum Technol.*, 2015, **2**, 19.
99. J. Choi, H. Zhou, R. Landig, H.-Y. Wu, X. Yu, S. E. Von Stetina, G. Kucsko, S. E. Mango, D. J. Needleman, A. D. T. Samuel, P. C. Maurer, H. Park and M. D. Lukin, *Proc. Natl. Acad. Sci. U. S. A.*, 2020, **117**, 14636–14641.
100. G. Davies, *J. Phys. C: Solid State Phys.*, 1974, **7**, 3797–3809.
101. P.-C. Tsai, C. P. Epperla, J.-S. Huang, O. Y. Chen, C.-C. Wu and H.-C. Chang, *Angew. Chem., Int. Ed.*, 2017, **56**, 3025–3030.
102. T. Plakhotnik, H. Aman and H.-C. Chang, *Nanotechnology*, 2015, **26**, 245501.
103. X.-Q. Zhang, M. Chen, R. Lam, X. Xu, E. Osawa and D. Ho, *ACS Nano*, 2009, **3**, 2609–2616.
104. K. A. Ross, N. A. Smyth, C. D. Murawski and J. G. Kennedy, *ISRN Oncol.*, 2013, **2013**, 759725.
105. A. Alhaddad, M.-P. Adam, J. Botsoa, G. Dantelle, S. Perruchas, T. Gacoin, C. Mansuy, S. Lavielle, C. Malvy, F. Treussart and J.-R. Bertrand, *Small*, 2011, **7**, 3087–3095.
106. S. Claveau, É. Nehlig, S. Garcia-Argote, S. Feuillastre, G. Pieters, H. A. Girard, J.-C. Arnault, F. Treussart and J.-R. Bertrand, *Nanomaterial*, 2020, **10**, 553.
107. T.-C. Yang, C.-Y. Chang, A. A. Yarmishyn, Y.-S. Mao, Y.-P. Yang, M.-L. Wang, C.-C. Hsu, H.-Y. Yang, D.-K. Hwang, S.-J. Chen, M.-L. Tsai, Y.-H. Lai, Y. Tzeng, C.-C. Chang and S.-H. Chiou, *Acta Biomater.*, 2020, **101**, 484–494.

CHAPTER 9

Carbon Nanomaterials for the Development of Biosensors for Microbe Detection and Diagnosis

NHAN DAI THIEN TRAM[a], XIAO ZHU[a], PUI LAI RACHEL EE[a] AND GIORGIA PASTORIN*[a]

[a]Pharmacy Department, National University of Singapore, 18 Science Drive 4, Singapore 117543
*E-mail: phapg@nus.edu.sg

9.1 Introduction

9.1.1 Traditional Methods for the Detection of Microorganisms

The demand for improvements in diagnostic techniques for infectious diseases is a medical necessity that has been globally recognized. More accessible tools with better performance are required to enable more timely medical decisions. Historically, a few conventional methods have been routinely employed, namely plate count, polymerase chain reaction (PCR), and enzyme-linked immunosorbent assay (ELISA). The specific pros and cons of each technique are described below, and the state-of-the-affairs indicate that these methods are not sufficiently robust to meet current diagnostic needs. Advancements in the field of biosensors may potentially overcome these limitations. Biosensors offer multiple advantages

Nanoscience & Nanotechnology Series No. 48
Carbon Nanostructures for Biomedical Applications
Edited by Tatiana Da Ros, Nazario Martín and Jean-Francois Nierengarten

Published by the Royal Society of Chemistry, www.rsc.org

over the traditional methods, such as shorter processing time, greater sensitivity and selectivity. In addition, biosensors designed as lab-on-a-chip devices allow for rapid and convenient on-site diagnosis of infectious diseases, an area that traditional methods have failed to address. It has been projected that biosensors are on track to be adopted as the technique of choice.[1]

Plate count is the oldest method that remains in routine use today. It is time-consuming to culture microbes, up to days, and requires a considerable amount of laboratory equipment and consumables.[2,3] Since plate counting mainly relies on the visual assessment of colony growth, the quality of the results hinge upon the experience and proficiency of the operator. This baseline requirement gravely undermines the utility of this method in underdeveloped areas where trained personnel are scarce.[1,3]

PCR is another established method, the principle of which revolves around the amplification of nucleic acids in the samples. Among the various PCR techniques,[4–6] the ability of multiplex PCR to concurrently identify the presence of several microbes proves to be particularly useful in clinical contexts.[4] Compared to the plate counting method, it requires much less time and offers superior sensitivity.[7] However, potential sample contamination poses a concern because the presence of confounding nucleic acids could severely mislead diagnostic efforts. In addition, PCR requires primers, the design of which depends on the availability of prior sequence data. This could limit its applicability when dealing with pathogens whose genomic information has yet been established in the database. Apart from these common limitations, each individual PCR technique has its own drawbacks which are briefly summarized in Table 9.1.

Table 9.1 Advantages and limitations of traditional pathogen detection techniques.[1,8,9]

Detection method	Advantages	Limitations
PCR	• High sensitivity • High specificity • Could be coupled with other detection techniques • Less time-consuming • Does not require post-amplification processing (real-time PCR) • Concurrent detection of multiple species (multiplex PCR)	• DNA purification required to eliminate interference from PCR inhibitors • Challenge to distinguish between viable and non-viable cells • Reverse transcriptase PCR can overcome this
ELISA	• High specificity • Less labor- and time-consuming if automated • Also capable of detecting bacterial toxins • Can handle large numbers of samples	• Low sensitivity • Potential cross-reactivity • Pre-enrichment required
Colony counting method	• Standard detection method • Well-established	• Very time-consuming • A variety of selective media required • Could be labor-intensive (most-probable number method)

The remaining standard method, namely ELISA, employs immunological reactions, whereby antibodies are coupled to an enzyme for the recognition of microbial antigens. This approach has inspired the development of multiple biosensor applications.[1]

Despite its high specificity and reproducibility, ELISA exhibits a number of shortcomings that have limited its clinical utility.[10] It necessitates relatively sophisticated laboratory equipment, sizeable sample volume, intricate processing steps and skilled personnel. Besides, the commonly reported limit of detection (LOD) values of ELISA systems are barely below the nanomolar range, which greatly limits its performance.[11]

9.1.2 Recent Advances in Biosensor Technologies

To meet the demand for less time-consuming, more affordable, and more accessible pathogen detection techniques, biosensors have emerged over the past few decades as a promising option to complement and/or replace traditional methods. Not only do biosensors shorten the total analysis duration from days to potentially minutes,[12–15] technological advancements have also endowed biosensors with outstanding levels of sensitivity and selectivity.[13,16–18] In general, biosensors contain bio-recognition elements that are immobilized onto materials closely associated with a transducing system, which in turn transmit signals to a detector for signal read-outs. The recognition component is designed to bind target ligands with a desirable level of sensitivity and specificity. A vast array of detection techniques, ranging from electrochemical to chemiluminescent, have been employed for biosensor-based detection of either pathogens or pathogen-specific biomolecules. Such a diverse toolbox will undoubtedly empower these diagnostic systems to better meet current medical requirements.

More recently, the incorporation of nanomaterials has facilitated the growth of biosensor technologies.[19] With a very high specific surface area, these nano-sized scaffolds allow for the conjugation of a greater density of bio-recognition elements than previously achievable. Among them, carbon nanomaterials (CNMs) such as graphene, carbon nanotubes (CNTs), and carbon dots (CDs) have garnered much attention for their potential applications in the fields of biomedicine and bioelectronics (Figure 9.1). With exceptional physical and chemical properties, these materials are emerging as appealing building blocks of sensitive and selective biosensors for detecting microbes – namely bacteria, viruses and fungi. One of CNMs' virtues most relevant to biosensor technologies is the ease of organic functionalizations.[19] Chemical functionalizations at the surface of materials have been applied to not only render the physicochemical properties of CNMs more suitable for biomedical applications, but also to introduce functional groups to which a variety of bio-components can be conjugated.[20,21]

CNTs, including single-walled CNTs (SWCNTs) and multi-walled CNTs (MWCNTs), offer appealing attributes such as mechanical durability, vast surface area, exceptional electrical properties and electrochemical stability.[22–24] Both these CNTs consist of rolled up graphene sheets (single

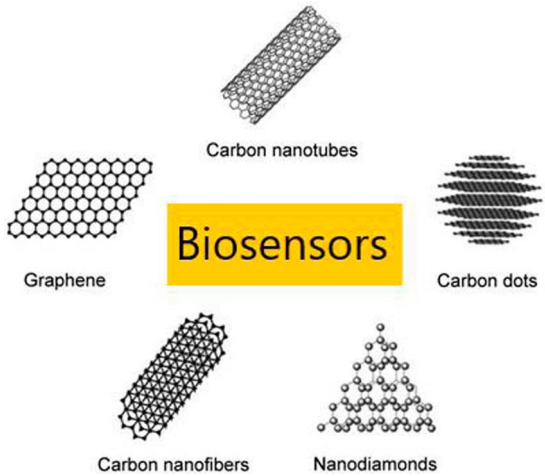

Figure 9.1 Common types of CNMs employed in biosensors for pathogen detection. Reproduced from ref. 27 with permission from the Royal Society of Chemistry.

sheet for SWCNTs and multiple, concentric ones for MWCNTs) forming cylindrical nanostructures, with hexagonal lattices of carbon atoms. With pronounced photostability and negligible auto-fluorescence, CNTs are also compatible with optical detection techniques.[25] Besides, functionalization of CNTs has been reported to improve their biocompatibility and suppress cytotoxicity.[26]

Alongside CNTs, graphene has gained tremendous attention in the field of bioelectronics by virtue of its large surface area, high electrical conductivity and adsorption kinetics.[28] The structure of graphene consists of a hexagonal arrangement of carbon atoms into flat sheets. The extensive network of π-conjugation gives rise to the material's desirable thermal, mechanical and electrical properties.[29] Graphene is usually prepared by subjecting its precursor graphite, a naturally occurring form where carbon atoms are arranged in a hexagonal lattice, through chemical modifications.[30] In brief, after being oxidized into graphite oxide, the material could be subjected to chemical, thermal, or electrochemical reduction.[31] The resulting chemical variants of graphene are structurally distinct from the pristine version. Such differences could have an impact on their properties and applicability for biosensors with electrochemical transducers.[30] Among them, graphene oxide (GO), which can be reduced at high temperature, was found to possess attributes most ideal for electrochemical performance.

Aside from whole cells, these sensor platforms are capable of detecting a host of microbe-specific biomarkers, such as proteins, nucleic acids and antigens. The aim of this chapter is to offer a comprehensive discussion and evaluation of biosensors employing a variety of bio-recognition elements, ranging from the more widely reviewed aptamers and antibodies, to the less explored bacteriophage, DNAzyme and peptides. Through state-of-the-art examples (Table 9.2), which are grouped into sections based on

Table 9.2 Recent examples of CNM-based biosensors for microbe detection published from 2017.

Target of detection	Type of CNM	Detection method	Duration	LOD	Linear range	Specificity validation[a]	Test sample[b]	Reference
Immunosensor								
HIV-1gp 140_{MS}	GO	Electrochemical	12 s	8.3 fM	670 fM to 0.1 μM	Bovine serum albumin	Serum	Nehra *et al.*[38]
S. cerevisiae	GO	Amperometric	N/A	~4 CFU mL^{-1}	10^1 to 10^7 CFU mL^{-1}	*Z. fermentati*, *H. uvarum*, *T. delbrueckii*	Wine	Borisova *et al.*[16]
Norovirus VLP	Graphene	Colorimetric	N/A	92.7 pg mL^{-1}	100 pg mL^{-1} to 10 μg mL^{-1}	Bovine serum albumin, influenza virus A	Serum	Ahmed *et al.*[17]
Zika virus antigen NS1	Graphene	Capacitance	5 min	0.45 nM	N/A	Japanese, Encephalitis NS1	Serum	Afsahi *et al.*[12]
E. coli	GO	Conductivity	50 s	10^3 CFU mL^{-1}	10^3 to 10^5 CFU mL^{-1}	*S. typhimurium*, *S. pneumonia*	River water	Thakur *et al.*[35]
Aptasensor								
S. aureus	CNP	Impedimetric	30 min	1 CFU mL^{-1}	1.2×10^1 to 1.2×10^8 CFU mL^{-1}	*S. aureus, P. aeruginosa, E. coli* O157, *S. flexneri, S. typhimurium*	Serum	Ranjbar *et al.*[13]
M. tuberculosis H37Rv	SWCNT	Electrochemical	70 min	100 CFU mL^{-1}	10^3 to 10^7 CFU mL^{-1}	*M. smegmatis*, BCG	Sputum	Zhang *et al.*[39]
M. tuberculosis DNA	Graphene	Impedimetric	1 min	10 fM	10 fM to 0.1 μM	DNA from *Leptospira* sp., *E. coli, V. cholera*	N/A	Perumal *et al.*[14]
HPV	rGO	Voltammetric	N/A	1.75 pM	3.5 pM to 35.3 pM	N/A	Serum, saliva	Chekin *et al.*[40]
Dengue virus DNA	Graphene QD	Voltammetric	N/A	9.4 fM	10^{-14} to 10^{-6} M	Norovirus, zika, influenza virus DNA	N/A	Chowdhury *et al.*[18]

(*continued*)

Table 9.2 (*continued*)

Target of detection	Type of CNM	Detection method	Duration	LOD	Linear range	Specificity validation[a]	Test sample[b]	Reference
AMP								
E. coli	CD	Fluorescence	N/A	460 CFU mL^{-1}	3.81×10^2 to 2.44×10^4 CFU mL^{-1}	*S. aureus*	Urine, apple juice, tap water	Chandra *et al.*[41]
S. aureus, E. coli, P. aeruginosa, K. pneumoniae, E. cloacae, E. faecalis, C. albicans	SWCNT	Piezoelectric	15 min	10 to 100 CFU mL^{-1}	N/A	N/A	Sheep blood	Shi *et al.*[15]
Bacteriophage								
P. aeruginosa	Graphene	Electrochemi-luminescent	30 min	56 CFU mL^{-1}	1.4×10^2 to 1.4×10^6 CFU mL^{-1}	*E. coli, Salmonella.*, *S. aureus*, *M. luteus*, *B. subtilis*	Urine, milk, insulin injection	Yue *et al.*[42]
S. typhimurium	GO	Impedimetric	40 min	12 CFU mL^{-1}	10^2–10^8 CFU mL^{-1}	*E. coli*, *S. aureus*		Quiton *et al.*[43]
DNAzyme								
E. coli	Graphene	Fluorescence	N/A	10^4 CFU mL^{-1}	N/A	N/A	Blood	Liu *et al.*[44]
Polymer								
HIV-1 p24	MWCNT	Electrochemical	N/A	0.083 pg mL^{-1}	10^{-4} to 2 ng mL^{-1}	N/A	Serum	Ma *et al.*[45]

[a]Listed are the interference species tested.
[b]Biological samples are from humans, unless stated otherwise.

the bio-recognition element, we hope to foster awareness of recent advancements in the field, thereby catalyzing further progress in the development of microbe biosensors to meet the increasing demand for more refined diagnostic tools of infectious diseases.

9.2 Antibodies as Bio-recognition Elements

There are three major classes of antibodies: polyclonal, monoclonal and recombinant antibodies. The choice of antibody class primarily depends on the intended diagnostic purpose, desired sensitivity and specificity of the system. A rigorous discussion of antibodies and their applications in immunosensors can be found in another review.[32]

Of the different kinds of microbes, bacteria appear to be the most extensively studied as targets of CNM-based sensors. For sensing *E. coli* O157:H7, antibody-decorated nanodiamonds were anchored to interdigitated electrodes.[33] The nanodiamond seeds were employed for their electrical conductivity, which allowed for impedance-based detection of the bacteria. In another instance, GO was employed as the energy acceptor, in conjunction with antibody-tagged quantum dots (QDs) as energy donors, in a fluorescence resonance energy transfer (FRET) detection system.[34] Antibody-QD probes were printed onto a glass slide to generate a microarray for testing. In the absence of the target cells, the GO platelet effectively quenched the fluorescence of QDs. Conversely, the addition of *E. coli* would disrupt the binding equilibrium and shift the tide towards microorganism-QD affinity. The removal of GO from QD proximity would consequently halt its check on QD fluorescence, hence allowing a detectable fluorescence signal. This description of working principles in general applies to most FRET-based diagnostic systems. In a disposable immunosensor reported for real-time sensing of *E. coli*, gold nanoparticles (AuNPs) served as site of antibody immobilization.[35] To enable field-effect transistor (FET) detection, the GO channel was covered by a nano-sized layer of Al_2O_3 in order to block out interfering signals. The thickness of the Al_2O_3 layer was identified to be an essential parameter that required optimization. While its thickness ought to be sufficiently sizeable to curtail oxidative vulnerability, it was restrained by the Debye length limitation, above which the ensuing FET signals in response to the inclusion of target bacteria would be too miniscule for practical applications.[36] Since the Debye–Hückel equation dictates that temperature and ionic strength of the solvent affect the Debye length,[37] these parameters should naturally be taken into consideration as well. After proper fine-tuning, however, not only was the sensor able to process 1 μL of sample in merely 50 s, it could also be promptly regenerated with a simple washing protocol.

Concurrently, signal amplification strategies have been adopted to enhance sensitivity. Yang *et al.* encaged hundreds of CDs inside breakable organosilica nanocapsules, the surface of which was decorated with antibodies specific to *Staphylococcus aureus* (*S. aureus*).[46] As the CDs were maintained in close proximity of one another within the nano-sized enclosure,

self-quenching took place.[47] After target isolation using magnetite NPs, the reductive rupture of the nanocapsules with $NaBH_4$ would liberate the hoard of antibody-labeled CDs, which would inundate *S. aureus* cells. The system yielded a much improved sensitivity level (approximately 30 000 times lower LOD) as compared to that acquired by the more orthodox approach, whereby CDs were directly employed as fluorescent probes without being encapsulated.[48]

In conjunction with signal amplification, sample enrichment *via* magnetic separation could be tapped for concentrating the targets of interest, often with the help of antibody-functionalized magnetite NP.[46,49–51] The utility of magnetic enrichment is by no means limited to a single species of bacteria. By tagging multicolored carbon dots with two kinds of antibodies, an immunosensor was bestowed with the capability to concurrently isolate methicillin-resistant *S. aureus* (MRSA) and *Salmonella* bacteria in spiked whole blood samples.[50] On top of that, pardaxin, an antimicrobial peptide (AMP), was included in the set-up for bactericidal effect.[52] Conjugation to the NPs was required for bioactivity of pardaxin, which failed to work as free AMP.

In diseases like tuberculosis, where the causative pathogens exhibit a low rate of growth, whole cells may not be the most clinically practical option as the target for diagnostic purposes.[53] Instead, researchers have experimented with biomolecular predictors such as culture filtrate protein (CFP-10), a secretory antigen strongly indicative of an active disease state. It can be detected in the host circulation early on in the course of tuberculosis, and is unique to tuberculous mycobacteria.[54] An immunosensor was developed from AuNPs, QDs and graphene to quantify CFP-10 concentration through plasmon-induced photoluminescence.[55] The antibody of choice was selective enough to permit the differentiation of CFP-10 from antigen 85 (Ag85), another antigenic predictor of *Mycobacterium tuberculosis* (*M. tuberculosis*).[56] With a LOD of 4.5 pg mL^{-1}, this biosensor was far more sensitive than many other systems in the literature.[57–59] Azmi *et al.* combined functionalized graphene and a screen-printed gold electrode to generate a sandwich assay for sensing CFP-10.[60] Whereas practical applicability of the sensor was demonstrated in sputum samples, its sensitivity was relatively mediocre, with a LOD of 15 ng mL^{-1}.

By virtue of antibodies' wide-ranging binding affinity, microbes other than bacteria could also be detected. A disposable carbon SPE decorated with GO was devised for amperometric sensing of *Saccharomyces cerevisiae* (*S. cerevisiae*), a yeast species.[16] Propionic acid was introduced to the surface of GO to provide the requisite functional groups for covalently immobilizing antibody molecules. Concanavalin A-peroxidase conjugate was employed for recognizing surface glycoproteins of *S. cerevisiae*.[61] The density of antibodies encasing the electrode had to be optimized, since an excessive amount could impair the signal. Specificity of the sensor was validated in the presence of several other yeast species. In another example, a carbon screen-printed electrode (SPE) with AuNPs-GO nanocomposite was applied for the detection of *Brettanomyces bruxellensis*, another yeast species.[62]

CNM-based immunosensors have also been implemented for the diagnosis of viruses – fowl adenovirus,[63] influenza virus of different serotypes[64] and avian influenza virus subtype H5,[65] to name a few. To design a point-of-care (POC) device, Wiriyachaiporn *et al.* assembled a lateral flow immunoassay facilitating direct visual interpretation of the results.[66] Antibody-tagged carbon nanoparticles (CNPs) were packed into the conjugate pad region of the device. If influenza A viruses were present in the sample, antigen-antibody-CNP complexes would form when the sample was added to the device. It would then flow through different compartments for matrix isolation. Upon reaching the nitrocellulose membrane, stationary antibodies would capture the incoming complexes in a sandwich-like fashion. As the CNP-containing complex amassed at the designated test zone, a visually discernible black spot would emerge, thus facilitating result read-out by the naked eye. Specificity of the system was illustrated by ruling out cross-talks with other viruses, including influenza B.

Biosensors capable of multiplexed detection of both bacteria and viruses have been reported. Fullerene was incorporated into a multi-chamber microfluidic device for chemiluminescent detection of *E. coli* O157:H7, *Campylobacter jejuni* and adenovirus at the same time.[67] A poly(methylmethacrylate) surface was functionalized with antibodies for capturing the flowing pathogens. One sample could be analyzed in just 35 min. Although the use of chemiluminescence agents could prove to be costly, the device would enable multiplexed detection of up to sixteen different microbes.

Whenever a standardized culture system for growing viruses is not available, researchers have justifiably turned their attention to virus-like particles (VLPs), as immunogenic mimics. VLPs are sophisticated protein structures that display epitopes closely resembling those found on the template virus of interest. They are capable of inducing the formation of antibodies specific to the virus itself.[68] Moreover, these antigenic surrogates are bereft of genetic content. This eliminates safety concerns associated with the handling of viruses.[69] For discerning the presence of novovirus VLPs, immunosensors have been fabricated from a graphene-AuNPs nanocomposite,[17] flexible inkjet-printed graphene sensor,[70] or as a paper-based device integrating either GO or MWCNT.[71]

Viral diseases can be diagnosed through the detection of their antigens, either surface-bound or secreted. Afsahi *et al.* applied a commercially available graphene chip for detecting nonstructural protein 1 (NS1), a glycoprotein found on Zika virus.[12] With a response time of merely 5 min, it could be an exceptional option for real-time diagnosis of the Zika virus. There are well-founded concerns regarding the potential cross-reactivity with other flaviviruses such as dengue, among which the expressed NS1 analogs share a reasonably high degree of sequence homology.[72] Even though a retrospective study documented zero cases of cross-talks when applying dengue NS1 tests on Zika-infected samples,[73] cases of NS1 false positives tests have been reported.[74] To address this potential limitation, Afsahi *et al.* demonstrated the absence of noticeable response when the biosensor was subjected to

recombinant NS1 of Japanese encephalitis virus.[12] Investigation into the crystal structure of Zika NS1 had formerly revealed distinctive electrostatic properties of its C-terminal region, which set it apart from its counterparts expressed by other flaviviruses.[75] Nonetheless, testing against other flaviviruses still needs to be conducted to ascertain the sensor's specificity. This case study of NS1 detection underlined the need to keep specificity in mind while deciding on the target viral antigen. Undoubtedly, an antigen unique to the pathogen of interest without any close homolog is the most desirable. p24 capsid protein of human immunodeficiency virus (HIV) is another antigen that has garnered much interest as a viral biomarker. Given its much earlier appearance in circulation, p24 is preferable to anti-HIV antibodies as the biomolecular indicator of early stage HIV infection.[76] Immunosensors constructed from GO and other CNMs have been fabricated for the identification of p24 using either electrochemiluminescence,[77] or electrochemical techniques.[78]

Aside from circulating proteins in the bloodstream, ribonucleic acid (RNA) of HIV has also been examined as a potential biomarker. Safavieh *et al.* designed a flexible paper microchip with a graphene-coated silver electrode for the impedimetric detection of HIV-1 RNA (Figure 9.2A).[79] To enhance the sensitivity of the system, the loop-mediated isothermal amplification (LAMP) technique was used. This affordable microchip only consumed a

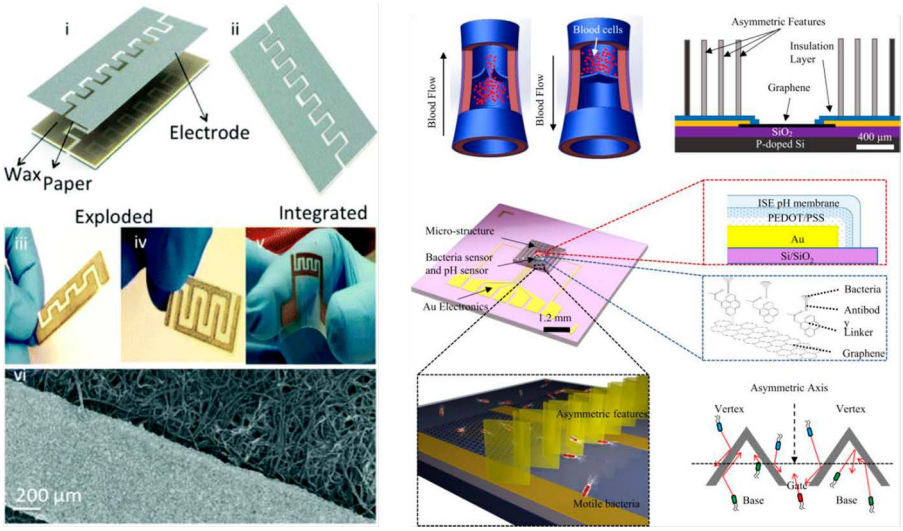

Figure 9.2 CNM-based biosensors with antibodies as bio-recognition components. (A) Paper microchip for POC diagnosis of HIV-1. Reproduced from ref. 79 with permission from The Royal Society of Chemistry (B) Microfluidic device drawing inspiration from venous valves for microbial isolation (Li *et al.*[80]). Reproduced from ref. 80, https://doi.org/10.1016/j.bios.2018.09.087 under the terms of the CC-BY 4.0 license https://creativecommons.org/licenses/by/4.0/.

total processing time of 60 min, including preparation steps, and an estimated cost of $2 per test. Therefore, it is an ideal candidate for bedside applications.

Moving beyond traditional antibodies, researchers have explored the use of hybrid versions in immunosensors as well. Nehra *et al.* conceptualized an antibody domain fusion construct for the targeting of $gp140_{MS}$ envelope glycoprotein of HIV-1.[38] The use of layered GO laminates conferred stability to the system. With the LOD and response time being 8.3 fM and 12 s, respectively, the biosensor showed great promise for ultrasensitive real-time diagnosis. In another unconventional immunosensor design, researchers swapped the role of antibody and antigen. In response to hepatitis B virus (HBV) infection, the immune system produces immunoglobulins IgG and IgM, the latter of which could persist in the circulation for a really long time.[81] Thus, IgG has been acclaimed as the most suitable marker for identifying prior HBV infection. Muain *et al.* utilized the HBV core antigen as the recognition element for anti-HBV antibodies, using a reduced graphene oxide (rGO) nanocomposite as the sensing surface.[82]

Besides the performance of the device, special attention has also been devoted to include unconventional mechanical features in immunosensors to ameliorate their utility. Flexible electrodes with outstanding mechanical and electrical properties can be assembled from graphene nanosheet building blocks to generate free-standing graphene paper.[83–85] An impedimetric immunosensor constructed from reduced GO paper and AuNPs was devised for the detection of *E. coli* O157:H7 serotype.[86] Biotinylated antibodies were anchored to the electrode surface through streptavidin–biotin interaction. The sensor was selective enough to distinguish between the pathogenic O157:H7 serotype and the non-pathogenic DH5α strain. Apart from flexibility, the graphene-based paper electrode displayed excellent durability and performance robustness. Flexible free-standing GO film has been applied for sensing the virus as well (*e.g.* rotavirus[87]). More recently, Li *et al.* reported the fabrication of a graphene-based microfluidic chip for sensing *E. coli* (Figure 9.2B).[80] Drawing inspiration from bicuspid valves found inside veins,[88] the authors implemented asymmetric micro-sized gateways to regulate monodirectional movement of motile *E. coli* into the assay chamber. This allowed for the isolation and concentration of the bacteria within the chamber, thereby enhancing the sensitivity of subsequent detection steps. As a result, the biosensor achieved a remarkable LOD of 1 colony-forming unit (CFU) mL^{-1}.

9.3 Aptamers as Bio-recognition Elements

Aptamers are single-stranded oligonucleotides with the ability to recognize biomolecules with remarkable affinity.[89] Exact sequences of aptamers specific to intended targets could be selected using the systematic evolution of ligands by exponential enrichment (SELEX) process.[90,91]

Given the prevalence of *S. aureus* in the environment, there is a substantial likelihood of host pre-exposure.[92] Antibodies generated as a consequence of immune responses could remain in the bloodstream at the point of testing.[93] This might in turn intervene with the operation of immunosensors.[94] When it comes to the detection of *S. aureus* and microorganisms with similar interference concerns, aptasensors are preferred, since their target biomarkers do not persist in circulation. For instance, an impedimetric aptasensor was devised by modifying a glassy carbon electrode (GCE) with rGO-AuNP-single-stranded DNA (ssDNA) nanocomposite, where the thiolated single-strand DNA served as a linker between rGO and AuNPs.[95] When the AuNP-anchored DNA capture probes immobilized the targets, a resulting change in impedance signal was magnified by the nanocomposite. The system managed to yield a LOD of 10 CFU mL^{-1} within 60 min. Another impedimetric system was reported with an even more impressive performance, yielding a LOD of 1 CFU mL^{-1} and a wider linear dynamic range of 12–1.2 × 10^8 CFU mL^{-1} in just 30 min.[13] Besides, the sensor exhibited selective responsiveness towards live bacteria. Harsh thermal treatment could have damaged the surface epitopes, which may account for the reduced affinity between the probes and target cells. A potentiometric sensor based on CNMs was also capable of sensing *S. aureus* at the level of 1 CFU mL^{-1}, with the additional advantage of consuming only a few minutes.[96] In two related systems, Hernández *et al.* affixed DNA aptamer either covalently to GO or non-covalently to rGO, both of which were, in turn, coated onto a GCE. Although the former platform produced a noisier baseline, its precision was superior. Additionally, the GO-based sensor displayed greater reproducibility, which was attributed to the simplification of the graphene preparation steps. The system could be easily regenerated by immersing the electrodes in 2 M NaCl for 1 h, followed by washing with distilled water. Under such hypertonic condition, alterations in the aptamer structure impaired probe–target interaction, hence dislodging bacteria from the electrode surface.

Researchers have previously reported the combination of two different kinds of CNMs in a single sensor system. A nanocomposite constituted of rGO and MWCNTs was electrodeposited onto a GCE for the impedimetric detection of *Salmonella enterica* serovar typhimurium (*S. typhimurium*).[99] π–π interaction between rGO and MWCNTs rendered the composite sturdier than a composite between either one of them and metal NPs. rGO served as the transducer layer for signal amplification, whereas MWCNTs offered numerous sites for DNA aptamer immobilization.

Fluorescence is another quantification technique employed for sensing *S. typhimurium*. GO was employed as an energy acceptor, and 5-Carboxyfluorescein (FAM) as the energy donor in a FRET system.[100] The sensor was selective enough to distinguish among different *Salmonella* serovars. Notably, not all aptamers described in the literature are capable of ruling out inter-serovar cross-talk. While the ssDNA probe reported by Hasan *et al.* displayed species-specific differentiating power, it failed to differentiate between various *Salmonella* serovars.[101] Depending on the diagnostic aims,

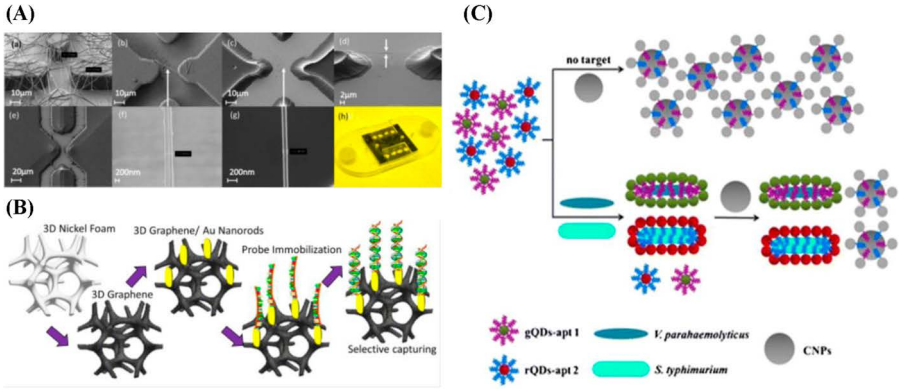

Figure 9.3 CNM-based biosensors with aptamers as bio-recognition components (A) Lab-on-a-chip biosensor employing carbon nanowire for rapid detection of *S. typhimurium* (Thiha *et al.*[97]). Reproduced from ref. 97 with permission from Elsevier, Copyright 2018 (B) 3D construct constituted of graphene and AuNPs for anchoring anti-*M. tuberculosis* probes (Perumal *et al.*[14]). Reproduced from ref. 14 with permission from Elsevier, Copyright 2018 (C) Dual FRET system using CNPs and multicolor QDs for simultaneous detection of multiple microbial species (Duan *et al.*[98]). Reproduced from ref. 98 with permission from Elsevier, Copyright 2014.

this level of selectivity may, however, suffice to inform an appropriate therapeutic decision. The performance level of fluorescence-based sensors relies heavily on the choice of fluorescent probes. Metallic QDs have been widely implemented as the fluorescent probe of choice by virtue of their optical properties and large Stokes shift.[102] Nevertheless, they have their fair share of limitations, including challenging preparation procedures and a lack of biocompatibility. CDs have recently emerged as a promising alternative.[103] DNA aptamer was immobilized onto carboxyl-functionalized CDs for the specific recognition of *S. typhimurium*.[104] The exceptional optical properties of CDs ensured that sensitivity of this sensor outperformed that of the FAM-GO platform mentioned above.[100]

By deviating from the one-donor-one-acceptor *modus operandi*, FRET-based aptasensors have also been adapted for multiplexed assays. Using CNPs as the sole energy acceptor, Duan *et al.* employed two kinds of dual-colored QDs as energy donors, each attached to a separate aptamer sequence (Figure 9.3C).[98] The sensor was able to simultaneously monitor the concentration of *Vibrio parahaemolyticus* (*V. parahaemolyticus*) and *S. typhimurium*, at a satisfactory level of sensitivity (25 and 35 CFU mL^{-1}, respectively). Another group went a step further and integrated three dye–aptamer pairs instead of two.[105] With FAM, Cy3, and 6-carboxy-X-rhodamine as the fluorescent probes, the sensor could concurrently detect *V. parahaemolyticus*, *S. aureus* and *S. typhimurium*.

Despite a host of appealing attributes, CNTs and graphene-derived nanomaterials suffer from structural and compositional heterogeneity.[106]

Furthermore, control over shape manipulation of these materials proves to be intractable. To overcome these hurdles, some groups have resorted to carbon nanowires. Thiha *et al.* applied this CNM in a microfluidic chip for chemiresistive diagnosis of *S. typhimurium* (Figure 9.3A).[97] The carbon nanowires were generated in suspension by combining electrospinning and carbon-microelectromechanical system (C-MEMS) techniques. The resulting nanofibers, being extremely fine with diameters below 100 nm, served as the electrode. The sensor required only 5 μL of sample volume and 5 min of processing time, inclusive of the incubation step, to attain a LOD of 10 CFU mL^{-1}. With respect to chemiresistive and FET-based sensors, aptamers largely overshadow antibodies as the bio-recognition biomolecule of choice. The former's comparatively small size benefits the sensitivity of the system through a reduction in the Debye screening effect.[107]

Aside from the frequently reported GCE, other kinds of electrodes have been utilized in aptasensors. In one such system, SWCNT-linked ssDNA aptamer was anchored onto a gold interdigital electrode for the detection of *M. tuberculosis* H37Rv strain.[39] As mycobacteria dislodged SWCNTs from aptamer probes, the change in electrical signals could be picked up. Specificity of the system was validated against the closely related *Mycobacterium smegmatis* (*M. smegmatis*) and Bacillus Calmette-Guerin strain (BCG).

Similar to immunosensors, aptasensors are capable of detecting not just whole cells, but also biomolecular markers. Graphene QDs and AuNPs were used as the donor–acceptor system for FRET-based sensing of *S. aureus mecA* gene.[108] mecA is the gene responsible for methicillin resistance and is thus recruited as a biomarker for MRSA strains.[109] IS6110 of *M. tuberculosis* is another bacterial gene that has been considered as an infectious disease indicator. An amperometric sensor employed polyalanine-functionalized tufted CNTs for the holding signal probe, and functionalized fullerene as a platform for immobilizing the capture probe.[110] It was able to quantify as low as 0.33 fM of the IS6110 gene. In another IS6110-targeting system, Au nanorods were sputtered onto 3D graphene, which had been assembled using the chemical vapor deposition (CVD) method (Figure 9.3B).[14] The graphene-derived 3D network provided an extensive surface area for probe anchoring. While the sensor only managed a LOD of 10 fM, its response time of 1 min was remarkably short.

As discussed in the previous section, secreted antigens are reliable biomarkers for virulent *M. tuberculosis*. CNM-based aptasensors have been designed for specifically recognizing early secreted antigenic targets (ESAT-6)[111] and Ag85.[112] Mycolic acid has also been evaluated as a biomarker. It is an integral cell wall component of mycobacteria, including non-pathogenic species such as *M. smegmatis*.[113] It follows that mycolic acid is not unique to the disease-causing *M. tuberculosis*, seemingly undercutting its utility as a disease predictor. Nonetheless, three chemically distinct forms of mycolic acid could be characterized – α-, methoxy- and keto-mycolic acid.[114] Their expression profiles considerably vary among mycobacterial species, and their surface-enhanced Raman scattering (SERS) spectra are readily discernible.[115,116]

In principle, the profile of relative occurrence of the three mycolic acid analogs could provide the identification of *M. tuberculosis* in the presence of non-tuberculous mycobacteria. As opposed to their secretory counterpart, surface-expressed antigens may not allow for a clinically satisfactory level of specificity. Thakur *et al.* described a graphene-based voltammetric biosensor targeting MPT64, a surface antigen of mycobacteria.[117] Unfortunately, MPT64 is also expressed by non-tuberculous mycobacteria such as *Mycobacterium bovis* (*M. bovis*) and particularly BCG strains.[118]

Whenever the rate of false negative needs to be lowered, researchers have resorted to multiple biomarkers, each of which is indicative of a single microorganism. One such system employed separate QDs-aptamer pairs as energy donors and GO as energy acceptor for the simultaneous detection of *hlyA* genes and *iap* genes, both of which originated from *Listeria monocytogenes* (*L. monocytogenes*) cells in the samples.[119]

Besides bacteria, aptasensors have been developed to detect whole viruses. Chekin *et al.* reported a voltammetric sensor, where the GCE was decorated with porous rGO and molybdenum disulfide, for sensing human papilloma virus (HPV) through the recognition of L1-major capsid protein.[40] Porous rGO offered a larger surface area for anchoring aptamer probes, and permitted the diffusion of analytes across the pores, which in turn facilitated the detection process.[120]

In chronic HBV infection, HBV DNA is the most reliable marker for viral replication, regardless of the viral load.[121] A sensor in which the GCE was modified with graphene QDs was capable of detecting HBV DNA as low as 1 nM.[122] Other sensor systems integrating CNMs have been designed to identify nucleic acids from Ebola virus,[123] HIV,[124] influenza virus H5N1 subtype,[125] or H1N1 subtype and norovirus.[126] Chowdhury *et al.* adopted an intriguing two-pronged approach for dengue virus diagnosis.[18] Using a novel class of graphene QDs nanocomposite, the authors combined the electrochemical quantification of target DNA with serotype discernment *via* fluorescence spectroscopy. The system could successfully distinguish among the four serotypes of dengue virus.[127]

9.4 Antimicrobial Peptides (AMPs) as Bio-recognition Elements

Peptides, especially those with antimicrobial activity, have been employed as bio-recognition elements. This capability chiefly stems from their selective interactions with microbial membranes.[128] Significant variations in membrane compositions only exist among major groups of organisms (*e.g.* Gram-positive bacteria, Gram-negative bacteria, mycobacteria, fungi and eukaryotes). To the best of our knowledge, no AMP with specific affinity to one single species or subspecies of microorganism has been discovered or designed. Exceptions lie in those that act on either biological pathways or intracellular targets, in neither of which cases their mechanism of action

could be readily adopted to distinguish between species. Nonetheless, peptides could still be useful as bio-recognition elements where therapeutic decisions do not hinge upon the precise identification of the causative pathogen.

Andrade *et al.* encased a gold electrode with CNTs, which were in turn functionalized with clavanin A as the AMP probe.[129] Gram-negative bacteria such as *E. coli* and *Klebsiella pneumoniae* (*K. pneumoniae*) elicited a distinctly greater impedimetric signal than the Gram-positive counterparts. Therefore, clavanin A was functional as a Gram-selective biosensing probe. Notwithstanding its broad-spectrum activity,[130,131] there exist nuances between the way clavanin A interacts with the Gram-negative membrane and the Gram-positive membrane, which were electrochemically perceptible. Unfortunately, the LOD of 100 CFU mL^{-1} paled in comparison to those of the aforementioned biosensors.[13,34,80,96] In another CNT-based sensor, pleurocidin was employed as the bio-recognition element.[15] Akin to clavanin A, pleurocidin is a broad-spectrum AMP.[132] While pleurocidin could detect a variety of pathogenic species in spiked blood samples, it failed to distinguish between Gram-positive bacteria, Gram-negative bacteria and fungi.

By combining GO nanocomposites and AMP-functionalized magnetite NPs, Yuan *et al.* coupled magnetic isolation with diagnosis of infectious diseases (Figure 9.4A).[133] The deficient photothermal stability of metallic NPs was overcome by the inclusion of GO. In addition, GO safeguarded them against oxidation, hence limiting unwelcome fluctuations in the signals. Conjugation with 4-mercaptophenylboronic acid (4-MPBA) was implemented to magnify the differentiating prowess of the SERS spectra, which relied on silver-coated AuNPs as the substrate. Furthermore, 4-MPBA served as a SERS internal standard to account for any electromagnetic interference. As the biosensing component, bacitracin A attracted bacteria by forming hydrogen bonds with pyrophosphate molecules.[134] After being immobilized onto magnetite NPs, the AMP retained its antimicrobial activity. With the aid of discriminant analysis (DA), the signature Raman bands could be processed for differentiating *Pseudomonas aeruginosa (P. aeruginosa)*, *S. aureus* and *E. coli.* Together, SERS and DA helped actualize species-specificity of this AMP-based sensor.

Vancomycin, a glycopeptide antibiotic, was conjugated to CDs for fluorescent detection of Gram-positive bacteria.[48] Unlike broad-spectrum AMPs, vancomycin is preferentially active against Gram-positive bacteria by strongly interacting with the D-Ala-D-Ala terminus of peptidoglycan, a key component of the Gram-positive cell wall.[135] As a result, it could distinguish between Gram-positive (*S. aureus*, Bacillus subtilis (*B. subtilis*), and *L. monocytogenes*) and Gram-negative (Salmonella, *P. aeruginosa* and *E. coli*) bacteria. Upon the addition of target pathogens, the fluorescence signal of the system vastly decreased. Aggregation of the CDs supposedly culminated in their self-quenching, hence the drop in emission.

Meanwhile, fluorogens, whose emission level heightens in response to the formation of aggregates, have also found usage in pathogen biosensors.[136] The mechanism behind this phenomenon of aggregation-induced

emission (AIE) has been discussed in detail elsewhere.[137] Feng *et al.* conjugated vancomycin to AIEgen for the sensing of Gram-positive bacteria such as vancomycin-resistant Enterococcus (VRE).[138] To facilitate a visual read-out of fluorescence results, a substantial concentration of vancomycin-tagged AIEgen was necessary. The resulting background noise would be too high were it not for GO quenching. Interestingly, the AIEgen could double as a photosensitizer for photodynamic killing of pathogens.[139]

The same group later combined vancomycin with an aptamer for the simultaneous sensing of *B. subtilis* and the chain B of ricin toxin,[140] the constituent responsible for triggering uptake of the toxin into the host cell and ensuing toxicity.[141] The two biosensing elements were conjugated to different kinds of AIEgens, which emitted distinct colors in response to the initiation of aggregation. GO was again included in the system for its quenching ability, which ceased with the addition of the respective targets. Chandra *et al.* reported another system capable of multiplexed detection of both a pathogen and a chemical species.[41] CDs were functionalized with colistin, a cyclic peptide antibiotic preferentially interacting with the outer membrane of Gram-negative bacteria *via* lipopolysaccharide (LPS).[142] It served as the probe for both *E. coli* and Fe^{3+} ions. Interaction between colisin-CD and the latter was revealed to be through chelation.[143]

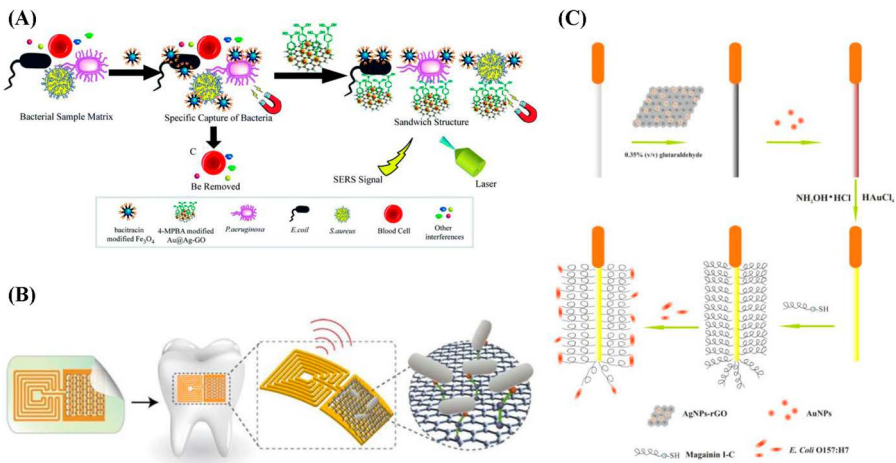

Figure 9.4 CNM-based biosensors with AMPs as bio-recognition components. (A) Metallic GO nanocomposites and magnetite NPs were combined for both SERS detection of bacteria and magnetic isolation. Reproduced from ref. 133 with permission from The Royal Society of Chemistry (B) Graphene-containing silk film capable of wireless data transfer was attached to tooth enamel for pathogenic monitoring of saliva and breath (Manu *et al.*[147]). Reproduced from ref. 147 with permission from Elsevier, Copyright 2012 (C) A fiber optic was encased in AgNP-rGO nanocomposite for detecting E. coli O157:H7 (Zhou *et al.*[148]). Reproduced from ref. 148 with permission from Elsevier, Copyright 2018.

In spite of a dissimilarity in chemical structure, non-peptide antibiotics have also been investigated as a reporter probe for bacteria sensing. Chandra *et al.* conjugated CDs with amikacin, a glycoside antibiotic active against Gram-negative bacteria,[144] for the fluorescent sensing of *E. coli*.[145] Its bacterial recognition utility primarily stems from its binding affinity towards ribosomal RNA (rRNA) small subunits.[146] Specificity of the system was established in the presence of *S. aureus*. In fact, rRNA binding behavior of amikacin is an attribute shared among aminoglycosides. Therefore, other members in this class of antibiotics might prove just as useful as biosensor probes.

LPS presents another viable biomolecular target for the diagnosis of Gram-negative bacteria. Lim *et al.* conjugated KC-13, an LPS-binding peptide, to tetramethylrhodamine fluorescent dye.[149] Together, they were adsorbed onto GO for fluorescence quenching prior to sample testing. The sequence of KC-13 was identified using a phage display method.[150] Despite structural variations of LPS among different Gram-negative species,[151] the sensor successfully responded to the presence of LPS from a variety of Gram-negative bacteria, namely *E. coli*, *K. pneumoniae*, *Salmonella thyphosa* (*S. thyphosa*) and *P. aeruginosa*.[149]

Interfacing of biosensors with biomedical devices has paved the way for expanding their clinical applications. Graphene-embedded silk film was bio-transferred onto tooth enamel for pathogenic monitoring of a patient's saliva and breath (Figure 9.4B)[147]. Graphene was modified with a hybrid peptide comprising a graphene-binding domain and odorranin as the AMP probe[152]. The sensor could detect a diverse range of bacteria, including *Helicobacter pylori*[153]. Advanced bioelectronics (i.e. resonant coil) enabled wireless transfer of electrochemical data to an external reader for real-time tracking. Incidentally, Zhou *et al.* overlaid a fiber optic with a nanocomposite of reduced GO and silver NPs (Figure 9.4C)[148]. A layer of gold film was added on top to enhance the surface plasmon resonance signal. Magainin 1 was utilized as the probe for recognizing *E. coli* O157:H7. The sensor was specific enough to differentiate between pathogenic and non-pathogenic strains of *E. coli*.

9.5 Less Explored Bio-recognition Elements

9.5.1 Polymers

Molecularly imprinted polymers (MIPs) are synthetic polymers onto which target binding sites could be imprinted using a template, either a cell or a molecule. Various imprinting methods have been reported, namely covalent, non-covalent and semi-covalent imprinting. A detailed review on MIPs and their preparation procedures could be found elsewhere.[154] In general, a functional monomer is co-polymerized with a cross-linker in

the presence of the template. For complexation between the monomers and template molecules to happen, appropriate functional groups have to be present on the two components. After the template is removed, pockets whose shape complements the contour of the target are retained on the material outline.

For the detection of p24 protein of HIV, Ma *et al.* enlisted acrylamide as the monomer for producing MIP-functionalized MWCNTs, which was in turn conjugated to the GCE.[45] This sensor achieved a remarkable sensitivity. Its LOD of 0.083 pg mL^{-1} was much lower than those of the aforementioned p24-targeting immunosensors (*i.e.* 1 pg mL^{-1} [77] and 0.15 pg mL^{-1} [78]). A MIP-based sensor has also been applied for the detection of whole viruses. Tancharoen *et al.* incorporated MIPs for the fabrication of an electrochemical sensor of the Zika virus.[155] A MIP-GO composite was applied onto a gold electrode, followed by imprinting the Zika virus template under exposure to ultraviolet (UV) light. Although the LOD in PBS was found to be 2×10^{-4} plaque-forming units (PFU) mL^{-1}, it increased 100-fold in media with interfering viruses. In light of this finding, serum samples had to be diluted to minimize the background noise. The same group had previously employed MIP for the identification of the dengue virus.[156] With several target templates for molding the MIP probe, the authors managed to discern among the four serotypes of dengue virus. Notably, if the viruses had been exposed to corresponding antibodies prior to testing, their physical properties were altered. The resulting signal was sufficiently discernible from the one without antibody pre-exposure. With minor modifications in the operation, the sensor can double as an antibody detector.

Other than MIPs, ordinary polymers without the imprinted binding sites could still be exploited as reporter probes for microorganisms. For instance, a chemiresistive biosensor for the dengue virus was fabricated from heparin-modified SWCNTs.[157] Applicability of heparin in dengue sensing stemmed from its chemical homology to heparan sulfate, a surface receptor for the dengue virus.[158] As the negatively charged heparin interacted with the dengue envelope, which also exhibited a net negative charge, change in resistance intensity was indicative of a target binding event. On top of that, the outstanding photothermal stability of heparin warrants a long shelf-life.[159] In another example, nanodiamonds were decorated with saccharides for the detection and agglutination of uropathogenic *E. coli*.[160]

9.5.2 DNAzyme

Like aptamer, DNAzyme is an oligonucleotide-derived bio-recognition molecule endowed with inherently good binding affinity and specificity. What sets it apart is its enzymatic cleaving ability.[161] Similar to SELEX, a sequence of DNAzyme could be identified through *in vitro* selection from a massive pool of single-stranded nucleic acids.[162] Capitalizing on its

unique attributes, Liu *et al.* employed a 125-nucleotide DNAzyme alongside graphene for the sensing of *E. coli*.[44] The authors designed a DNAzyme construct, whereby a fluorophore was tethered using a RNA linker which could be cleaved by the DNAzyme itself. In the absence of target bacteria, the DNAzyme constructs are immobilized to graphene *via* π–π stacking interactions.[163] Close proximity of the DNAzyme-attached fluorophore to graphene permitted the quenching of fluorescence emission. Upon binding of the target bacteria to the construct, the enzymatic action of the DNAzyme became activated. Subsequent release of the fluorophore distanced itself from the graphene platform, thereby enabling quantifiable fluorescence emission.

Aside from whole-cell pathogens, DNAzymes can also be used to recognize molecular biomarkers. For example, a multifunctional DNAzyme was employed for the fluorescent quantification of hepatitis C virus (HCV) mRNA.[164] This rGO-based system was devised to deliver DNAzyme into human liver cells, where mRNA of non-structural gene 3 (NS3) from HCV could be detected. The protein encoded by NS3 is essential for a multitude of HCV life functions, including replication in host cells.[165] It is worth highlighting the intracellular locality of NS3, as opposed to the usual supernatant occurrence of biomarkers. Unlike the sensor design by Liu *et al.*,[44] catalytic activity of the DNAzyme was directed towards NS3 mRNA. In addition to sensing function, the construct was capable of silencing the NS3 gene, thereby suppressing the HCV multiplication process inside human liver cells. By targeting the TcdC transcription factor, DNAzyme could be selected to capture a specific pathogenic strain of *Clostridium difficile* (*C. difficile*) regardless of other confounding intra-species strains.[166]

9.5.3 Bacteriophage

Bacteriophages are viruses that specifically infect bacteria. Superb specificity potentially to an inter-strain level, durability under harsh conditions (*e.g.* temperature, solvent, pH), and suitability for live/dead differentiation render bacteriophages appealing biosensing probes for bacteria.[167,168] Quiton *et al.* anchored a bacteriophage probe onto a SPE electrode, which was functionalized with GO, for impedimetric detection of *S. typhimurium*.[43] The phage was prepared from sewage water and subsequently enriched to produce a sufficient titer. Specificity of the sensor was demonstrated in the presence of *E. coli* and *S. aureus*. Yue *et al.* devised a phage-based biosensor using graphene-decorated GCE for recognizing *P. aeruginosa*.[42] PaP1 phage was prepared from hospital sewage using lambda phage isolation protocol. The electrochemiluminescent detection technique was employed, with luminol chosen as the substrate. As the target bacteria interacted with the probes, the luminescence intensity of

luminol was suppressed, the extent of which allowed for quantification of the pathogen density. The assay duration totaled 30 min. In another system employing graphene SPE, the diagnosis of *Staphylococcus arlettae* was achieved within an even shorter response timeframe of only 2 min.[169] The sensor possessed a clinically relevant level of stability, yielding reproducible readings after three months of storage. Furthermore, the electrode could be regenerated through simple washing with phosphate-buffered saline.

Whereas most groups performed immobilization of bacteriophages onto the electrode surface *via* covalent bonds, Zhou *et al.* opted for a charge-directed strategy.[170] In brief, polyethylenimine was introduced to the surface of MWCNTs to confer positive charges. By applying a positive electric potential onto the electrode, T2 phages could be anchored through their negatively charged capsid. Enrichment of T2 phage was conducted using a soft agar overlay technique. Notwithstanding its outstanding specificity, which permitted the discernment between *E. coli* B from *E. coli* K strains, lytic cycle of bacteriophage could limit its utility. To address this, Shin *et al.* resorted to recombinant C-terminal fiber tail protein J of bacteriophage lambda.[171] This phage protein component had previously been shown to exhibit affinity towards LamB, an outer membrane protein of *E. coli* K-12.[172]

9.6 Conclusions and Perspectives

There is a wide array of available options for the bio-recognition element, and this could generate confusion for new researchers in the field. Arguably, the specificity of the bio-sensing component is the property most essential to the selection process. In general, antibodies and aptamers could be selected using well-established procedures to display very high binding specificity to target ligands. DNAzyme, which can also be selected using the SELEX process like aptamers, also displays potential for high specificity. Although more widely studied than DNAzyme for CNM-based biosensors, specificity of AMPs as bio-sensing molecules is inferior. In some cases, reported AMP only allowed for Gram-selective differentiation. Meanwhile, bacteriophage is less explored despite the superb species-specificity. In reported examples, the phage had to be isolated from hospital sewage, instead of standardized preparation protocols in the cases of antibodies and aptamers. This might have discouraged interest from researchers. Additionally, sensing applicability of phage is restricted to whole cells and hence cannot be employed to detect disease biomarkers.

The bio-recognition elements can be immobilized using different methods, ranging from chemical (*e.g.* covalent bonding and cross-linking) to

physical methods (*e.g.* non-covalent adsorption and encapsulation).[176] In the context of CNM-based biosensors, the aforementioned ease of chemical functionalization facilitates covalent anchoring of the sensor molecule in most cases. The stable chemical bonds between the CNM scaffold and the sensor element dispel any concern over leaching problems generally associated with non-covalent conjugation.[177]

With respect to the clinical utility of the system, the type of sensor target could play a determining role. As mentioned above, detection of whole cells is not the most ideal option under many circumstances. In the case of HIV diagnosis, p24 antigen is the biomarker of choice.[76] Likewise, CFP-10 antigen is preferred for monitoring the active tuberculosis disease state.[54] Meanwhile, influence of the choice of bio-recognition component is largely constrained to the specificity of the sensor.

To demonstrate applicability of the biosensors in analyzing real samples whereby a complex assortment of biomolecules and osmolytes in the samples could interfere, researchers have assessed the systems in relevant human samples spiked with the target of interest.[8,30,33,39,40,42,44,59,72,75,86,90,111,120,125,126,133] In other studies, the tests were conducted on food samples (*e.g.* milk,[42,46,100,105,119,145] fruit juice,[41,46,48,148,169] or wine[16]). We believe most of these sensors could be repurposed for human disease diagnosis, given the appropriate modifications and verifications if need be.

In most cases, selectivity was validated by testing samples in the presence of other microbes or biomolecules. However, rarely were the criteria for choosing these confounding species clearly outlined. In order to further enhance clinical relevance of the systems, it is imperative to ensure the inclusion of microbial species or relevant biomarkers, which have an established likelihood to affect therapeutic decisions.

The development of CNM-based biosensors, or any kind of biosensor for that matter, should take into consideration the influence from environmental cues. For instance, deviation in surrounding temperature has been shown to instigate transformation in the structural dynamics of dengue viral icosahedral particles.[178] Consequential restructuring of surface epitopes, especially the E-dimer dependent epitopes,[179] could disrupt antibody–antigen interactions, thereby impairing the efficiency of immunosensors. Even more astounding is the fact that this transfiguration was only observed in one out of the four dengue virus serotypes.[178] From a chemistry viewpoint, epitope-paratope affinity is essentially governed by weak chemical interactions, whose equilibrium can be swayed by a multitude of factors (*e.g.* pH, osmolality, ionic strength).[180] It follows that these parameters need to be evaluated to ensure reproducibility and robustness of the system.

Moving forward, more studies need to incorporate biosensors into microchips for POC testing,[12,79,97,181] or bio-transferrable films for organ-specific remote monitoring.[147] More information on POC devices and their utility for on-site diagnosis of infectious diseases can be found in a review article we previously published.[182] As of late, bio-inspired medical devices are on the rise. Wearable sensors have been described in the literature for various applications (Figure 9.5).[173–175,183–187] With

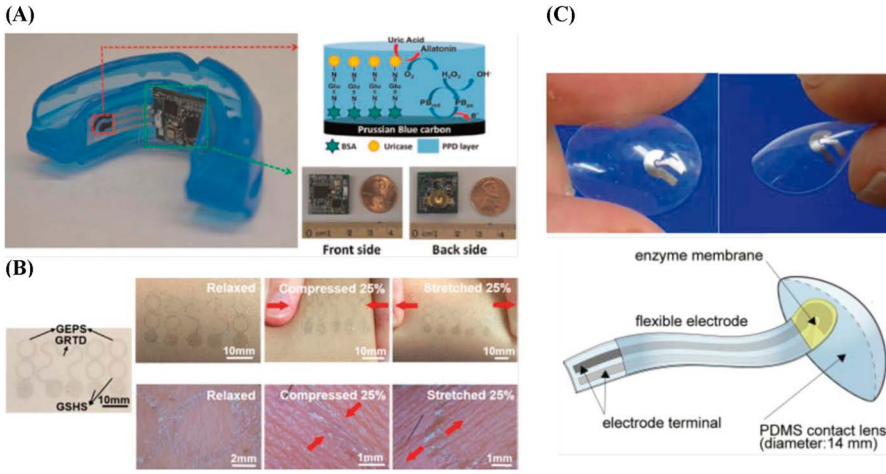

Figure 9.5 Wearable sensor designs that may be adopted for CNM-based detection of microbes (A) Mouthguard with embedded biosensor and wireless transceiver for monitoring of saliva metabolite level (Kim *et al.*[173]). Reproduced from ref. 173 with permission from Elsevier, Copyright 2015 (B) Stretchable graphene-based tattoo sensor for monitoring of multiple physiological factors (Ameri *et al.*[174]) (C) Soft contact lens biosensor with flexible electrode for monitoring of tear glucose (Chu *et al.*[175]). Reproduced from ref. 175 with permission from Elsevier, Copyright 2011.

the necessary adjustments, we could adopt these innovative design features for non-invasive CNM-based monitoring of microbes and relevant biomarkers.

References

1. O. Lazcka, F. J. D. Campo and F. X. Muñoz, Pathogen detection: a perspective of traditional methods and biosensors, *Biosens. Bioelectron.*, 2007, **22**(7), 1205–1217.
2. B. W. Brooks, J. Devenish, C. L. Lutze-Wallace, D. Milnes, R. H. Robertson and G. Berlie-Surujballi, Evaluation of a monoclonal antibody-based enzyme-linked immunosorbent assay for detection of campylobacter fetus in bovine preputial washing and vaginal mucus samples, *Vet. Microbiol.*, 2004, **103**(1–2), 77–84.
3. P. Rajapaksha, A. Elbourne, S. Gangadoo, R. Brown, D. Cozzolino and J. Chapman, A review of methods for the detection of pathogenic microorganisms, *Analyst*, 2019, **144**(2), 396–411.
4. J. J. Waggoner, L. Gresh, A. Mohamed-Hadley, G. Ballesteros, M. J. V. Davila, Y. Tellez, M. K. Sahoo, A. Balmaseda, E. Harris and B. A. Pinsky, Single-reaction multiplex reverse transcription PCR for detection of Zika, Chikungunya, and Dengue viruses, *Emerging Infect. Dis.*, 2016, **22**(7), 1295–1297.

5. K. E. Hanson, E. S. Slechta, J. A. Killpack, C. Heyrend, T. Lunt, J. A. Daly, A. C. Hemmert and A. J. Blaschke, Preclinical assessment of a fully automated multiplex pcr panel for detection of central nervous system pathogens, *J. Clin. Microbiol.*, 2016, **54**(3), 785–787.
6. P. Kralik and M. A. Ricchi, Basic guide to real time PCR in microbial diagnostics: definitions, parameters, and everything, *Front. Microbiol.*, 2017, **8**, 108.
7. A. K. Deisingh and M. Thompson, Strategies for the detection of *Escherichia Coli* O157:H7 in foods, *J. Appl. Microbiol.*, 2004, **96**(3), 419–429.
8. G. López-Campos, J. V. Martínez-Suárez, M. Aguado-Urda and V. López-Alonso, *Detection, Identification, and Analysis of Foodborne Pathogens*, Springer, Boston, MA, 2012, pp. 13–32, DOI: 10.1007/978-1-4614-3250-0_2.
9. J. W.-F. Law, N.-S. Ab Mutalib, K.-G. Chan and L.-H. Lee, Rapid methods for the detection of foodborne bacterial pathogens: principles, applications, advantages and limitations, *Front. Microbiol.*, 2014, **5**, 770.
10. S. Hosseini, P. Vázquez-Villegas, M. Rito-Palomares and S. O. Martinez-Chapa, *Advantages, Disadvantages and Modifications of Conventional ELISA*, Springer, Singapore, 2018, pp. 67–115, DOI: 10.1007/978-981-10-6766-2_5.
11. D. M. Rissin, C. W. Kan, T. G. Campbell, S. C. Howes, D. R. Fournier, L. Song, T. Piech, P. P. Patel, L. Chang and A. J. Rivnak, *et al.*, Single-molecule enzyme-linked immunosorbent assay detects serum proteins at subfemtomolar concentrations, *Nat. Biotechnol.*, 2010, **28**(6), 595–599.
12. S. Afsahi, M. B. Lerner, J. M. Goldstein, J. Lee, X. Tang, D. A. Bagarozzi, D. Pan, L. Locascio, A. Walker and F. Barron, *et al.*, Novel graphene-based biosensor for early detection of Zika virus infection, *Biosens. Bioelectron.*, 2018, **100**, 85–88.
13. S. Ranjbar and S. Shahrokhian, Design and fabrication of an electrochemical aptasensor using Au nanoparticles/carbon nanoparticles/cellulose nanofibers nanocomposite for rapid and sensitive detection of *Staphylococcus Aureus*, *Bioelectrochemistry*, 2018, **123**, 70–76.
14. V. Perumal, M. S. M. Saheed, N. M. Mohamed, M. S. M. Saheed, S. S. Murthe, S. C. B. Gopinath and J.-M. Chiu, Gold nanorod embedded novel 3D graphene nanocomposite for selective bio-capture in rapid detection of *Mycobacterium Tuberculosis*, *Biosens. Bioelectron.*, 2018, **116**, 116–122.
15. X. Shi, X. Zhang, Q. Yao and F. He, A novel method for the rapid detection of microbes in blood using pleurocidin antimicrobial peptide functionalized piezoelectric sensor, *J. Microbiol. Methods*, 2017, **133**, 69–75.
16. B. Borisova, A. Sánchez, P. E. D. Soto-Rodríguez, A. Boujakhrout, M. Arévalo-Villena, J. M. Pingarrón, A. Briones-Pérez, C. Parrado and R. Villalonga, Disposable amperometric immunosensor for Saccharomyces cerevisiae based on carboxylated graphene oxide-modified electrodes, *Anal. Bioanal. Chem.*, 2018, **410**(30), 7901–7907.

17. S. R. Ahmed, K. Takemeura, T.-C. Li, N. Kitamoto, T. Tanaka, T. Suzuki and E. Y. Park, Size-controlled preparation of peroxidase-like graphene-gold nanoparticle hybrids for the visible detection of norovirus-like particles, *Biosens. Bioelectron.*, 2017, **87**, 558–565.
18. A. Dutta Chowdhury, A. B. Ganganboina, F. Nasrin, K. Takemura, R. Doong, D. I. S. Utomo, J. Lee, I. M. Khoris and E. Y. Park, Femtomolar detection of Dengue virus DNA with serotype identification ability, *Anal. Chem.*, 2018, **90**(21), 12464–12474.
19. M. Holzinger, A. Le Goff and S. Cosnier, Nanomaterials for biosensing applications: a review, *Front. Chem.*, 2014, **2**, 63.
20. S. Vardharajula, S. Z. Ali, P. M. Tiwari, E. Eroğlu, K. Vig, V. A. Dennis and S. R. Singh, Functionalized carbon nanotubes: biomedical applications, *Int. J. Nanomed.*, 2012, **7**, 5361–5374.
21. A. Bianco, K. Kostarelos, C. D. Partidos and M. Prato, Biomedical applications of functionalised carbon nanotubes, *Chem. Commun.*, 2005, **0**(5), 571.
22. B. Q. Wei, R. Vajtai and P. M. Ajayan, Reliability and current carrying capacity of carbon nanotubes, *Appl. Phys. Lett.*, 2001, **79**(8), 1172–1174.
23. B. Peng, M. Locascio, P. Zapol, S. Li, S. L. Mielke, G. C. Schatz and H. D. Espinosa, Measurements of near-ultimate strength for multiwalled carbon nanotubes and irradiation-induced crosslinking improvements, *Nat. Nanotechnol.*, 2008, **3**(10), 626–631.
24. J. J. Davis, K. S. Coleman, B. R. Azamian, C. B. Bagshaw and M. L. H. Green, Chemical and biochemical sensing with modified single walled carbon nanotubes, *Chem. - Eur. J.*, 2003, **9**(16), 3732–3739.
25. M. Sireesha, V. Jagadeesh Babu, A. S. Kranthi Kiran and S. Ramakrishna, A review on carbon nanotubes in biosensor devices and their applications in medicine, *Nanocomposites*, 2018, **4**(2), 36–57.
26. A. Erdely, M. Dahm, B. T. Chen, P. C. Zeidler-Erdely, J. E. Fernback, M. E. Birch, D. E. Evans, M. L. Kashon, J. A. Deddens and T. Hulderman, *et al.*, Carbon nanotube dosimetry: from workplace exposure assessment to inhalation toxicology, *Part. Fibre Toxicol.*, 2013, **10**(1), 53.
27. Z. Wang and Z. Dai, Carbon nanomaterial-based electrochemical biosensors: an overview, *Nanoscale*, 2015, **7**(15), 6420–6431.
28. A. K. Geim and K. S. Novoselov, The rise of graphene, *Nat. Mater.*, 2007, **6**(3), 183–191.
29. M. J. Allen, V. C. Tung and R. B. Kaner, Honeycomb carbon: a review of graphene, *Chem. Rev.*, 2010, **110**(1), 132–145.
30. A. Ambrosi, A. Bonanni, Z. Sofer, J. S. Cross and M. Pumera, Electrochemistry at chemically modified graphenes, *Chem. - Eur. J.*, 2011, **17**(38), 10763–10770.
31. D. R. Dreyer, S. Park, C. W. Bielawski and R. S. Ruoff, The chemistry of graphene oxide, *Chem. Soc. Rev.*, 2010, **39**(1), 228–240.
32. B. Byrne, E. Stack, N. Gilmartin and R. O'Kennedy, Antibody-based sensors: principles, problems and potential for detection of pathogens and associated toxins, *Sensors*, 2009, **9**(6), 4407–4445.

33. W. Zhang, K. Patel, A. Schexnider, S. Banu and A. D. Radadia, Nanostructuring of biosensing electrodes with nanodiamonds for antibody immobilization, *ACS Nano*, 2014, **8**(2), 1419–1428.
34. E. Morales-Narváez, A.-R. Hassan and A. Merkoçi, Graphene oxide as a pathogen-revealing agent: sensing with a digital-like response, *Angew. Chem., Int. Ed.*, 2013, **52**(51), 13779–13783.
35. B. Thakur, G. Zhou, J. Chang, H. Pu, B. Jin, X. Sui, X. Yuan, C.-H. Yang, M. Magruder and J. Chen, Rapid detection of single *E. Coli* bacteria using a graphene-based field-effect transistor device, *Biosens. Bioelectron.*, 2018, **110**, 16–22.
36. G. Wu, M. Meyyappan and K. W. C. Lai, Graphene field-effect transistors-based biosensors for *Escherichia Coli* detection, in *2016 IEEE 16th International Conference on Nanotechnology*, IEEE-NANO, IEEE, 2016, pp. 22–25, DOI: 10.1109/NANO.2016.7751414.
37. G. M. Kontogeorgis, B. Maribo-Mogensen and K. Thomsen, The Debye-Hückel Theory and its importance in modeling electrolyte solutions, *Fluid Phase Equilib.*, 2018, **462**, 130–152.
38. A. Nehra, W. Chen, D. S. Dimitrov, A. Puri and K. P. Singh, Graphene oxide-polycarbonate track-etched nanosieve platform for sensitive detection of Human Immunodeficiency Virus envelope glycoprotein, *ACS Appl. Mater. Interfaces*, 2017, **9**(38), 32621–32634.
39. X. Zhang, Y. Feng, Q. Yao and F. He, Selection of a new *Mycobacterium Tuberculosis* H37Rv aptamer and its application in the construction of a SWCNT/Aptamer/Au-IDE MSPQC H37Rv sensor, *Biosens. Bioelectron.*, 2017, **98**, 261–266.
40. F. Chekin, K. Bagga, P. Subramanian, R. Jijie, S. K. Singh, S. Kurungot, R. Boukherroub and S. Szunerits, Nucleic aptamer modified porous reduced graphene oxide/MoS_2 based electrodes for viral detection: application to Human Papillomavirus (HPV), *Sens. Actuators, B*, 2018, **262**, 991–1000.
41. S. Chandra, T. K. Mahto, A. R. Chowdhuri, B. Das and S. K. Sahu, One step synthesis of functionalized carbon dots for the ultrasensitive detection of *Escherichia Coli* and iron (III), *Sens. Actuators, B*, 2017, **245**, 835–844.
42. H. Yue, Y. He, E. Fan, L. Wang, S. Lu and Z. Fu, Label-free electrochemiluminescent biosensor for rapid and sensitive detection of *Pseudomonas Aeruginosa* using phage as highly specific recognition agent, *Biosens. Bioelectron.*, 2017, **94**, 429–432.
43. P. A. Quiton, B. M. Carreon, D. M. Dela Cruz-Papa and J. J. Bergantin, Bacteriophage-modified graphene oxide screen-printed electrodes for the impedimetric biosensing of *Salmonella*, *Sens. Transducers*, 2018, **28**, 38–42.
44. M. Liu, Q. Zhang, J. D. Brennan and Y. Li, Graphene-DNAzyme-based fluorescent biosensor for *Escherichia Coli* detection, *MRS Commun.*, 2018, **8**(3), 687–694.

45. Y. Ma, X.-L. Shen, Q. Zeng, H.-S. Wang and L.-S. Wang, A multi-walled carbon nanotubes based molecularly imprinted polymers electrochemical sensor for the sensitive determination of HIV-P24, *Talanta*, 2017, **164**, 121–127.
46. L. Yang, W. Deng, C. Cheng, Y. Tan, Q. Xie and S. Yao, Fluorescent immunoassay for the detection of pathogenic bacteria at the single-cell level using carbon dots-encapsulated breakable organosilica nanocapsule as labels, *ACS Appl. Mater. Interfaces*, 2018, **10**(4), 3441–3448.
47. J. Park, Y. Park and S. Kim, Signal amplification *via* biological self-assembly of surface-engineered quantum dots for multiplexed subattomolar immunoassays and apoptosis imaging, *ACS Nano*, 2013, **7**(10), 9416–9427.
48. D. Zhong, Y. Zhuo, Y. Feng and X. Yang, Employing carbon dots modified with Vancomycin for assaying gram-positive bacteria like *Staphylococcus Aureus*, *Biosens. Bioelectron.*, 2015, **74**, 546–553.
49. F. Zhu, G. Zhao and W. Dou, Electrochemical sandwich immunoassay for *Escherichia Coli* O157:H7 based on the use of magnetic nanoparticles and graphene functionalized with electrocatalytically active Au@Pt core/shell nanoparticles, *Microchim. Acta*, 2018, **185**(10), 455.
50. A. Pramanik, S. Jones, F. Pedraza, A. Vangara, C. Sweet, M. S. Williams, V. Ruppa-Kasani, S. E. Risher, D. Sardar and P. C. Ray, Fluorescent, magnetic multifunctional carbon dots for selective separation, identification, and eradication of drug-resistant superbugs, *ACS Omega*, 2017, **2**(2), 554–562.
51. J. Fei, W. Dou and G. Zhao, Amperometric immunoassay for the detection of *Salmonella Pullorum* using a screen - printed carbon electrode modified with gold nanoparticle-coated reduced graphene oxide and immunomagnetic beads, *Microchim. Acta*, 2016, **183**(2), 757–764.
52. H.-N. Huang, C.-Y. Pan, Y.-L. Chan, J.-Y. Chen and C.-J. Wu, Use of the antimicrobial peptide pardaxin (GE33) to protect against methicillin-resistant *Staphylococcus Aureus* infection in mice with skin injuries, *Antimicrob. Agents Chemother.*, 2014, **58**(3), 1538–1545.
53. N. Caceres, C. Vilaplana, C. Prats, E. Marzo, I. Llopis, J. Valls, D. Lopez and P.-J. Cardona, Evolution and role of corded cell aggregation in *Mycobacterium Tuberculosis* cultures, *Tuberculosis*, 2013, **93**(6), 690–698.
54. C. Liu, Z. Zhao, J. Fan, C. J. Lyon, H.-J. Wu, D. Nedelkov, A. M. Zelazny, K. N. Olivier, L. H. Cazares and S. M. Holland, *et al.*, Quantification of circulating *Mycobacterium Tuberculosis* antigen peptides allows rapid diagnosis of active disease and treatment monitoring, *Proc. Natl. Acad. Sci. U. S. A.*, 2017, **114**(15), 3969–3974.
55. J. Lee, J. Kim, S. R. Ahmed, H. Zhou, J.-M. Kim and J. Lee, Plasmon-induced photoluminescence immunoassay for tuberculosis monitoring using gold-nanoparticle-decorated graphene, *ACS Appl. Mater. Interfaces*, 2014, **6**(23), 21380–21388.

56. M. K. Z. Babaki, S. Soleimanpour and S. A. Rezaee, Antigen 85 complex as a powerful *Mycobacterium Tuberculosis* immunogene: biology, immune-pathogenicity, applications in diagnosis, and vaccine design, *Microb. Pathog.*, 2017, **112**, 20–29.
57. S. C. Hong, H. Chen, J. Lee, H.-K. Park, Y. S. Kim, H.-C. Shin, C.-M. Kim, T. J. Park, S. J. Lee and K. Koh, *et al.*, Ultrasensitive immunosensing of tuberculosis CFP-10 based on SPR spectroscopy, *Sens. Actuators, B*, 2011, **156**(1), 271–275.
58. P.-C. Soo, C.-J. Kung, Y.-T. Horng, K.-C. Chang, J.-J. Lee and W.-P. Peng, Detonation nanodiamonds for rapid detection of clinical isolates of *Mycobacterium Tuberculosis* complex in broth culture media, *Anal. Chem.*, 2012, **84**(18), 7972–7978.
59. T.-T. Feng, C.-M. Shou, L. Shen, Y. Qian, Z.-G. Wu, J. Fan, Y.-Z. Zhang, Y.-W. Tang, N.-P. Wu and H.-Z. Lu, *et al.*, Novel monoclonal antibodies to ESAT-6 and CFP-10 antigens for ELISA-based diagnosis of pleural tuberculosis, *Int. J. Tuberc. Lung Dis.*, 2011, **15**(6), 804–810.
60. U. Mohd Azmi, N. Yusof, N. Kusnin, J. Abdullah, S. Suraiya, P. Ong, N. Ahmad Raston, S. Abd Rahman, M. Mohamad Fathil and U. Z. Mohd Azmi, *et al.*, Sandwich electrochemical immunosensor for early detection of tuberculosis based on graphene/polyaniline-modified screen-printed gold electrode, *Sensors*, 2018, **18**(11), 3926.
61. J. M. Smeekens, H. Xiao and R. Wu, Global analysis of secreted proteins and glycoproteins in *Saccharomyces Cerevisiae*, *J. Proteome Res.*, 2017, **16**(2), 1039–1049.
62. B. Borisova, M. L. Villalonga, M. Arévalo-Villena, A. Boujakhrout, A. Sánchez, C. Parrado, J. M. Pingarrón, A. Briones-Pérez and R. Villalonga, Disposable electrochemical immunosensor for *Brettanomyces Bruxellensis* based on nanogold-reduced graphene oxide hybrid nanomaterial, *Anal. Bioanal. Chem.*, 2017, **409**(24), 5667–5674.
63. S. R. Ahmed, J. Mogus, R. Chand, E. Nagy and S. Neethirajan, Optoelectronic fowl adenovirus detection based on local electric field enhancement on graphene quantum dots and gold nanobundle hybrid, *Biosens. Bioelectron.*, 2018, **103**, 45–53.
64. J. Lee, S. R. Ahmed, S. Oh, J. Kim, T. Suzuki, K. Parmar, S. S. Park, J. Lee and E. Y. Park, A plasmon-assisted fluoro-immunoassay using gold nanoparticle-decorated carbon nanotubes for monitoring the Influenza virus, *Biosens. Bioelectron.*, 2015, **64**, 311–317.
65. Z. Xie, J. Huang, S. Luo, Z. Xie, L. Xie, J. Liu, Y. Pang, X. Deng and Q. Fan, Ultrasensitive electrochemical immunoassay for Avian Influenza subtype H5 using nanocomposite, *PLoS One*, 2014, **9**(4), e94685.
66. N. Wiriyachaiporn, H. Sirikett, W. Maneeprakorn and T. Dharakul, Carbon nanotag based visual detection of Influenza A virus by a lateral flow immunoassay, *Microchim. Acta*, 2017, **184**(6), 1827–1835.
67. N. Matos Pires, T. Dong, N. M. Matos Pires and T. Dong, Microfluidic biosensor array with integrated Poly(2,7-Carbazole)/Fullerene-based photodiodes for rapid multiplexed detection of pathogens, *Sensors*, 2013, **13**(12), 15898–15911.

68. A. Zeltins, Construction and characterization of virus-like particles: A review, *Mol. Biotechnol.*, 2013, **53**(1), 92–107.
69. I. Voráčková, P. Ulbrich, W. E. Diehl and T. Ruml, Engineered retroviral virus-like particles for receptor targeting, *Arch. Virol.*, 2014, **159**(4), 677–688.
70. L. Xiang, Z. Wang, Z. Liu, S. E. Weigum, Q. Yu and M. Y. Chen, Inkjet printed flexible biosensor based on graphene field effect transistor, *IEEE Sens. J.*, 2016, 8359–8364.
71. X. Weng and S. Neethirajan, Rapid detection of Norovirus using paper-based microfluidic device, *bioRxiv*, 2017, 162396.
72. J. Blok, S. M. McWilliam, H. C. Butler, A. J. Gibbs, G. Weiller, B. L. Herring, A. C. Hemsley, J. G. Aaskov, S. Yoksan and N. Bhamarapravati, Comparison of a Dengue-2 virus and its candidate vaccine derivative: Sequence relationships with the Flavi viruses and other viruses, *Virology*, 1992, **187**(2), 573–590.
73. S. Matheus, R. Boukhari, B. Labeau, V. Ernault, L. Bremand, M. Kazanji and D. Rousset, Specificity of Dengue NS1 antigen in differential diagnosis of Dengue and Zika Virus infection, *Emerging Infect. Dis.*, 2016, **22**(9), 1691–1693.
74. S. J. Chung, P. U. Krishnan and Y. S. Leo, Two cases of false-positive Dengue Non-Structural Protein 1 (NS1) antigen in patients with hematological malignancies and a review of the literature on the use of NS1 for the detection of Dengue infection, *Am. J. Trop. Med. Hyg.*, 2015, **92**(2), 367–369.
75. L. Dai, J. Song, X. Lu, Y.-Q. Deng, A. M. Musyoki, H. Cheng, Y. Zhang, Y. Yuan, H. Song and J. Haywood, *et al.*, Structures of the Zika Virus envelope protein and its complex with a Flavi virus broadly protective antibody, *Cell Host Microbe*, 2016, **19**(5), 696–704.
76. S. Bystryak and C. Acharya, Detection of HIV-1 P24 antigen in patients with varying degrees of Viremia using an ELISA with a photochemical signal amplification system, *Clin. Chim. Acta*, 2016, **456**, 128–136.
77. L. Zhou, J. Huang, B. Yu, Y. Liu and T. You, A novel electrochemiluminescence immunosensor for the analysis of HIV-1 P24 antigen based on P-RGO@Au@Ru-SiO_2 composite, *ACS Appl. Mater. Interfaces*, 2015, **7**(44), 24438–24445.
78. Y.-S. Fang, X.-J. Huang, L.-S. Wang and J.-F. Wang, An enhanced sensitive electrochemical immunosensor based on efficient encapsulation of enzyme in silica matrix for the detection of Human Immunodeficiency Virus P24, *Biosens. Bioelectron.*, 2015, **64**, 324–332.
79. M. Safavieh, V. Kaul, S. Khetani, A. Singh, K. Dhingra, M. K. Kanakasabapathy, M. S. Draz, A. Memic, D. R. Kuritzkes and H. Shafiee, Paper microchip with a graphene-modified silver nano-composite electrode for electrical sensing of microbial pathogens, *Nanoscale*, 2017, **9**(5), 1852–1861.
80. B. Li, H. Tan, S. Anastasova, M. Power, F. Seichepine and G.-Z. Yang, A bio-inspired 3D micro-structure for graphene-based bacteria sensing, *Biosens. Bioelectron.*, 2019, **123**, 77–84.

81. Q. Yuan, L.-W. Song, D. Cavallone, F. Moriconi, B. Cherubini, P. Colombatto, F. Oliveri, B. A. Coco, G. Ricco and F. Bonino, *et al.*, Total Hepatitis B core antigen antibody, a quantitative non-invasive marker of Hepatitis B virus induced liver disease, *PLoS One*, 2015, **10**(6), e0130209.
82. M. F. Abd Muain, K. H. Cheo, M. N. Omar, A. S. Amir Hamzah, H. N. Lim, A. B. Salleh, W. S. Tan and A. Ahmad Tajudin, Gold nanoparticle-decorated reduced-graphene oxide targeting anti Hepatitis B virus core antigen, *Bioelectrochemistry*, 2018, **122**, 199–205.
83. D.-W. Wang, F. Li, J. Zhao, W. Ren, Z.-G. Chen, J. Tan, Z.-S. Wu, I. Gentle, G. Q. Lu and H.-M. Cheng, Fabrication of Graphene/Polyaniline composite paper *via in Situ* anodic electropolymerization for high-performance flexible electrode, *ACS Nano*, 2009, **3**(7), 1745–1752.
84. B. G. Choi, H. Park, T. J. Park, M. H. Yang, J. S. Kim, S.-Y. Jang, N. S. Heo, S. Y. Lee, J. Kong and W. H. Hong, Solution chemistry of self-assembled graphene nanohybrids for high-performance flexible biosensors, *ACS Nano*, 2010, **4**(5), 2910–2918.
85. F. Xiao, J. Song, H. Gao, X. Zan, R. Xu and H. Duan, Coating graphene paper with 2D-assembly of electrocatalytic nanoparticles: a modular approach toward high-performance flexible electrodes, *ACS Nano*, 2012, **6**(1), 100–110.
86. Y. Wang, J. Ping, Z. Ye, J. Wu and Y. Ying, Impedimetric immunosensor based on gold nanoparticles modified graphene paper for label-free detection of *Escherichia Coli* O157:H7, *Biosens. Bioelectron.*, 2013, **49**, 492–498.
87. F. Liu, K. S. Choi, T. J. Park, S. Y. Lee and T. S. Seo, Graphene-based electrochemical biosensor for pathogenic virus detection, *BioChip J.*, 2011, **5**(2), 123–128.
88. J. M. Karamichalis, H. Aguib, A. Anastasopulos and M. Yacoub, Design, dynamism, and valve repair, *J. Thorac. Cardiovasc. Surg.*, 2017, **153**(2), 396–398.
89. Z. Zhuo, Y. Yu, M. Wang, J. Li, Z. Zhang, J. Liu, X. Wu, A. Lu, G. Zhang and B. Zhang, Recent advances in SELEX technology and aptamer applications in biomedicine, *Int. J. Mol. Sci.*, 2017, **18**(10), 2142.
90. A. D. Ellington and J. W. Szostak, *In vitro* selection of RNA molecules that bind specific ligands, *Nature*, 1990, **346**(6287), 818–822.
91. C. Tuerk and L. Gold, Systematic evolution of ligands by exponential enrichment: RNA ligands to bacteriophage T4 DNA polymerase, *Science*, 1990, **249**(4968), 505–510.
92. V. Templier and Y. Roupioz, On the challenges of detecting whole *Staphylococcus Aureus* cells with biosensors, *J. Appl. Microbiol.*, 2017, **123**(5), 1056–1067.
93. N. J. Verkaik, C. P. de Vogel, H. A. Boelens, D. Grumann, T. Hoogenboezem, C. Vink, H. Hooijkaas, T. J. Foster, H. A. Verbrugh and A. van Belkum, *et al.*, Anti-staphylococcal humoral immune response in persistent nasal carriers and noncarriers of *Staphylococcus Aureus*, *J. Infect. Dis.*, 2009, **199**(5), 625–632.

94. L. J. Wheat, R. B. Kohler, Z. Tabbarah and A. White, Circulating staphylococcal antigen in humans and immune rabbits with endocarditis due to *Staphylococcus Aureus*: Inhibition of detection by preexisting antibodies, *J. Infect. Dis.*, 1979, **140**(1), 54–61.
95. F. Jia, N. Duan, S. Wu, X. Ma, Y. Xia, Z. Wang and X. Wei, Impedimetric aptasensor for *Staphylococcus Aureus* based on nanocomposite prepared from reduced graphene oxide and gold nanoparticles, *Microchim. Acta*, 2014, **181**(9–10), 967–974.
96. R. Hernández, C. Vallés, A. M. Benito, W. K. Maser, F. Xavier Rius and J. Riu, Graphene-based potentiometric biosensor for the immediate detection of living bacteria, *Biosens. Bioelectron.*, 2014, **54**, 553–557.
97. A. Thiha, F. Ibrahim, S. Muniandy, I. J. Dinshaw, S. J. Teh, K. L. Thong, B. F. Leo and M. Madou, All-carbon suspended nanowire sensors as a rapid highly-sensitive label-free chemiresistive biosensing platform, *Biosens. Bioelectron.*, 2018, **107**, 145–152.
98. N. Duan, S. Wu, S. Dai, T. Miao, J. Chen and Z. Wang, Simultaneous detection of pathogenic bacteria using an aptamer based biosensor and dual fluorescence resonance energy transfer from quantum dots to carbon nanoparticles, *Microchim. Acta*, 2015, **182**(5–6), 917–923.
99. F. Jia, N. Duan, S. Wu, R. Dai, Z. Wang and X. Li, Impedimetric *Salmonella* aptasensor using a glassy carbon electrode modified with an electrodeposited composite consisting of reduced graphene oxide and carbon nanotubes, *Microchim. Acta*, 2016, **183**(1), 337–344.
100. Y. F. Duan, Y. Ning, Y. Song and L. Deng, Fluorescent aptasensor for the determination of *Salmonella Typhimurium* based on a graphene oxide platform, *Microchim. Acta*, 2014, **181**(5–6), 647–653.
101. M. R. Hasan, T. Pulingam, J. N. Appaturi, A. N. Zifruddin, S. J. Teh, T. W. Lim, F. Ibrahim, B. F. Leo and K. L. Thong, Carbon nanotube-based aptasensor for sensitive electrochemical detection of whole-cell *Salmonella*, *Anal. Biochem.*, 2018, **554**, 34–43.
102. C. Carrillo-Carrión, B. M. Simonet and M. Valcárcel, Colistin-functionalised CdSe/ZnS quantum dots as fluorescent probe for the rapid detection of *Escherichia Coli*, *Biosens. Bioelectron.*, 2011, **26**(11), 4368–4374.
103. A. B. Bourlinos, A. Stassinopoulos, D. Anglos, R. Zboril, M. Karakassides and E. P. Giannelis, Surface functionalized carbogenic quantum dots, *Small*, 2008, **4**(4), 455–458.
104. R. Wang, Y. Xu, T. Zhang and Y. Jiang, Rapid and sensitive detection of *Salmonella Typhimurium* using aptamer-conjugated carbon dots as fluorescence probe, *Anal. Methods*, 2015, **7**(5), 1701–1706.
105. N. Duan, W. Gong, Z. Wang and S. Wu, An aptasensor based on fluorescence resonance energy transfer for multiplexed pathogenic bacteria determination, *Anal. Methods*, 2016, **8**(6), 1390–1395.
106. W. Yang, K. R. Ratinac, S. P. Ringer, P. Thordarson, J. J. Gooding and F. Braet, Carbon nanomaterials in biosensors: should you use nanotubes or graphene? *Angew. Chem., Int. Ed.*, 2010, **49**(12), 2114–2138.

107. A. Zhang, G. Zheng and C. M. Lieber, *Nanowire Field-Effect Transistor Sensors*, Springer, Cham, 2016, pp. 255–275, DOI: 10.1007/978-3-319-41981-7_10.
108. J. Shi, C. Chan, Y. Pang, W. Ye, F. Tian, J. Lyu, Y. Zhang and M. Yang, A Fluorescence Resonance Energy Transfer (FRET) biosensor based on Graphene Quantum Dots (GQDs) and Gold Nanoparticles (AuNPs) for the detection of MecA gene sequence of *Staphylococcus Aureus*, *Biosens. Bioelectron.*, 2015, **67**, 595–600.
109. C. L. C. Wielders, A. C. Fluit, S. Brisse, J. Verhoef and F. J. Schmitz, MecA gene is widely disseminated in *Staphylococcus Aureus* population, *J. Clin. Microbiol.*, 2002, **40**(11), 3970–3975.
110. Y. Chen, S. Guo, M. Zhao, P. Zhang, Z. Xin, J. Tao and L. Bai, Amperometric DNA biosensor for *Mycobacterium Tuberculosis* detection using flower-like carbon nanotubes-polyaniline nanohybrid and enzyme-assisted signal amplification strategy, *Biosens. Bioelectron.*, 2018, **119**, 215–220.
111. L. Li, Y. Yuan, Y. Chen, P. Zhang, Y. Bai and L. Bai, Aptamer based voltammetric biosensor for *Mycobacterium Tuberculosis* antigen ESAT-6 using a nanohybrid material composed of reduced graphene oxide and a metal-organic framework, *Microchim. Acta*, 2018, **185**(8), 379.
112. N. Ansari, K. Ghazvini, M. Ramezani, M. Shahdordizadeh, R. Yazdian-Robati, K. Abnous and S. M. Taghdisi, Selection of DNA aptamers against *Mycobacterium Tuberculosis* Ag85A, and its application in a graphene oxide-based fluorometric assay, *Microchim. Acta*, 2018, **185**(1), 21.
113. H. Marrakchi, M.-A. Lanéelle and M. Daffé, Mycolic acids: structures, biosynthesis, and beyond, *Chem. Biol.*, 2014, **21**(1), 67–85.
114. G. Shui, A. K. Bendt, I. A. Jappar, H. M. Lim, M. Laneelle, M. Hervé, L. E. Via, G. H. Chua, M. W. Bratschi and S. Z. Zainul Rahim, *et al.*, Mycolic acids as diagnostic markers for tuberculosis case detection in humans and drug efficacy in mice, *EMBO Mol. Med.*, 2012, **4**(1), 27–37.
115. J. Perumal, U. S. Dinish, A. K. Bendt, A. Kazakeviciute, C. Y. Fu, I. L. H. Ong and M. Olivo, Identification of mycolic acid forms using surface-enhanced raman scattering as a fast detection method for Tuberculosis, *Int. J. Nanomed.*, 2018, **13**, 6029–6038.
116. Y. Yuan, Y. Zhu, D. D. Crane and C. E. Barry, The effect of oxygenated mycolic acid composition on cell wall function and macrophage growth in *Mycobacterium Tuberculosis*, *Mol. Microbiol.*, 1998, **29**(6), 1449–1458.
117. H. Thakur, N. Kaur, P. Sabherwal, D. Sareen and N. Prabhakar, Aptamer based voltammetric biosensor for the detection of *Mycobacterium Tuberculosis* antigen MPT64, *Microchim. Acta*, 2017, **184**(7), 1915–1922.
118. H. Yang, Z.-H. Liu, L.-T. Zhang, J. Wang, H.-S. Yang, L.-H. Qin, R.-L. Jin, Y.-H. Feng, Z.-L. Cui and R.-J. Zheng, *et al.*, Selection and application of peptide mimotopes of MPT64 protein in *Mycobacterium Tuberculosis*, *J. Med. Microbiol.*, 2011, **60**(1), 69–74.

119. Y. Liao, X. Zhou and D. Xing, Quantum dots and graphene oxide fluorescent switch based multivariate testing strategy for reliable detection of *Listeria Monocytogenes*, *ACS Appl. Mater. Interfaces*, 2014, **6**(13), 9988–9996.
120. S. Han, D. Wu, S. Li, F. Zhang and X. Feng, Porous graphene materials for advanced electrochemical energy storage and conversion devices, *Adv. Mater.*, 2014, **26**(6), 849–864.
121. J.-M. Pawlotsky, Hepatitis B virus (HBV) DNA assays (Methods and Practical Use) and viral kinetics, *J. Hepatol.*, 2003, **39**, 31–35.
122. Q. Xiang, J. Huang, H. Huang, W. Mao and Z. Ye, A label-free electrochemical platform for the highly sensitive detection of Hepatitis B virus DNA using graphene quantum dots, *RSC Adv.*, 2018, **8**(4), 1820–1825.
123. J. Wen, W. Li, J. Li, B. Tao, Y. Xu, H. Li, A. Lu and S. Sun, Study on rolling circle amplification of *Ebola Virus* and fluorescence detection based on graphene oxide, *Sens. Actuators, B*, 2016, **227**, 655–659.
124. Y.-D. Ye, L. Xia, D.-D. Xu, X.-J. Xing, D.-W. Pang and H.-W. Tang, DNA-stabilized silver nanoclusters and carbon nanoparticles oxide: a sensitive platform for label-free fluorescence turn-on detection of HIV-DNA sequences, *Biosens. Bioelectron.*, 2016, **85**, 837–843.
125. Y. Fu, V. Romay, Y. Liu, B. Ibarlucea, L. Baraban, V. Khavrus, S. Oswald, A. Bachmatiuk, I. Ibrahim and M. Rümmeli, *et al.*, Chemiresistive biosensors based on carbon nanotubes for label-free detection of DNA sequences derived from Avian Influenza Virus H5N1, *Sens. Actuators, B*, 2017, **249**, 691–699.
126. J. Lee, M. Morita, K. Takemura and E. Y. Park, A multi-functional gold/iron-oxide nanoparticle-CNT hybrid nanomaterial as virus DNA sensing platform, *Biosens. Bioelectron.*, 2018, **102**, 425–431.
127. S. B. Halstead, Pathogenesis of dengue: Challenges to molecular biology, *Science*, 1988, **239**(4839), 476–481.
128. M. D. Lad, F. Birembaut, L. A. Clifton, R. A. Frazier, J. R. P. Webster and R. J. Green, Antimicrobial peptide-lipid binding interactions and binding selectivity, *Biophys. J.*, 2007, **92**(10), 3575–3586.
129. C. A. S. Andrade, J. M. Nascimento, I. S. Oliveira, C. V. J. de Oliveira, C. P. de Melo, O. L. Franco and M. D. L. Oliveira, Nanostructured sensor based on carbon nanotubes and Clavanin A for bacterial detection, *Colloids Surf., B*, 2015, **135**, 833–839.
130. O. N. Silva, I. C. M. Fensterseifer, E. A. Rodrigues, H. H. S. Holanda, N. R. F. Novaes, J. P. A. Cunha, T. M. B. Rezende, K. G. Magalhães, S. E. Moreno and M. S. Jerônimo, *et al.*, Clavanin A improves outcome of complications from different bacterial infections, *Antimicrob. Agents Chemother.*, 2015, **59**(3), 1620–1626.
131. E. J. M. van Kan, D. N. Ganchev, M. M. E. Snel, V. Chupin, A. van der Bent and B. de. Kruijff, The peptide antibiotic Clavanin A interacts strongly and specifically with lipid bilayers, *Biochemistry*, 2003, **42**(38), 11366–11372.

132. N. Saint, H. Cadiou, Y. Bessin and G. Molle, Antibacterial peptide pleurocidin forms ion channels in planar lipid bilayers, *Biochim. Biophys. Acta, Biomembr.*, 2002, **1564**(2), 359–364.
133. K. Yuan, Q. Mei, X. Guo, Y. Xu, D. Yang, B. J. Sánchez, B. Sheng, C. Liu, Z. Hu and G. Yu, *et al.*, Antimicrobial peptide based magnetic recognition elements and Au@Ag-GO SERS tags with stable internal standards: a three in one biosensor for isolation, discrimination and killing of multiple bacteria in whole blood, *Chem. Sci.*, 2018, **9**(47), 8781–8795.
134. A. C. Pawlowski, W. Wang, K. Koteva, H. A. Barton, A. G. McArthur and G. D. Wright, A diverse intrinsic antibiotic resistome from a cave bacterium, *Nat. Commun.*, 2016, **7**, 13803.
135. F. Wang, H. Zhou, O. P. Olademehin, S. J. Kim and P. Tao, Insights into key interactions between vancomycin and bacterial cell wall structures, *ACS Omega*, 2018, **3**(1), 37–45.
136. D. Ding, K. Li, B. Liu and B. Z. Tang, Bioprobes based on AIE fluorogens, *Acc. Chem. Res.*, 2013, **46**(11), 2441–2453.
137. Y. Hong, J. W. Y. Lam and B. Z. Tang, Aggregation-induced emission: phenomenon, mechanism and applications, *Chem. Commun.*, 2009, **0**(29), 4332.
138. G. Feng, Y. Yuan, H. Fang, R. Zhang, B. Xing, G. Zhang, D. Zhang and B. Liu, A light-up probe with Aggregation-Induced Emission Characteristics (AIE) for selective imaging, naked-eye detection and photodynamic killing of gram-positive bacteria, *Chem. Commun.*, 2015, **51**(62), 12490–12493.
139. Y. Yuan, G. Feng, W. Qin, B. Z. Tang and B. Liu, Targeted and image-guided photodynamic cancer therapy based on organic nanoparticles with aggregation-induced emission characteristics, *Chem. Commun.*, 2014, **50**(63), 8757.
140. R. Zhang, X. Cai, G. Feng and B. Liu, Real-time naked-eye multiplex detection of toxins and bacteria using AIEgens with the assistance of graphene oxide, *Faraday Discuss.*, 2017, **196**(0), 363–375.
141. L. G. Doan, Ricin: Mechanism of toxicity, clinical manifestations, and vaccine development. a review, *J. Toxicol., Clin. Toxicol.*, 2004, **42**(2), 201–208.
142. M. E. Evans, D. J. Feola and R. P. Rapp, Polymyxin B sulfate and colistin: Old antibiotics for emerging multiresistant gram-negative bacteria, *Ann. Pharmacother.*, 1999, **33**(9), 960–967.
143. Q. Ma, J. Song, S. Wang, J. Yang, Y. Guo and C. Dong, A general sensing strategy for detection of Fe^{3+} by using amino acid-modified graphene quantum dots as fluorescent probe, *Appl. Surf. Sci.*, 2016, **389**, 995–1002.
144. G. K. Daikos, J. C. Kosmidis, J. M. Hamilton-Miller and W. Brumfitt, Amikacin in treatment of infections caused by gram-negative bacteria resistant to gentamicin and other aminoglycosides: clinical and bacteriologic results, *J. Infect. Dis.*, 1976, **134**(SUPPL), S286–S290.

145. S. Chandra, A. R. Chowdhuri, T. K. Mahto, A. Samui and S. K. Sahu, One-Step Synthesis of amikacin modified fluorescent carbon dots for the detection of gram-negative bacteria like *Escherichia Coli*, *RSC Adv.*, 2016, **6**(76), 72471–72478.
146. M. Dudek, J. Romanowska, T. Wituła and J. Trylska, Interactions of Amikacin with the RNA model of the ribosomal A-site: computational, spectroscopic and calorimetric studies, *Biochimie*, 2014, **102**, 188–202.
147. M. S. Mannoor, H. Tao, J. D. Clayton, A. Sengupta, D. L. Kaplan, R. R. Naik, N. Verma, F. G. Omenetto and M. C. McAlpine, Graphene-based wireless bacteria detection on tooth enamel, *Nat. Commun.*, 2012, **3**(1), 763.
148. C. Zhou, H. Zou, M. Li, C. Sun, D. Ren and Y. Li, Fiber optic surface plasmon resonance sensor for detection of *E. Coli* O157:H7 based on antimicrobial peptides and AgNPs-RGO, *Biosens. Bioelectron.*, 2018, **117**, 347–353.
149. S. K. Lim, P. Chen, F. L. Lee, S. Moochhala and B. Liedberg, Peptide-assembled graphene oxide as a fluorescent turn-on sensor for lipopolysaccharide (Endotoxin) detection, *Anal. Chem.*, 2015, **87**(18), 9408–9412.
150. M. M. Suzuki, M. Matsumoto, A. Yamamoto, M. Ochiai, Y. Horiuchi, M. Niwa, H. Omi, T. Kobayashi and T. Takagi, Molecular design of LPS-binding peptides, *J. Microbiol. Methods*, 2010, **83**(2), 153–155.
151. M. Lukáčová, I. Barák and J. Kazár, Role of structural variations of polysaccharide antigens in the pathogenicity of gram-negative bacteria, *Clin. Microbiol. Infect.*, 2008, **14**(3), 200–206.
152. L. Chen, Y. Li, J. Li, X. Xu, R. Lai and Q. Zou, An antimicrobial peptide with antimicrobial activity against *Helicobacter Pylori*, *Peptides*, 2007, **28**(8), 1527–1531.
153. M. F. Dixon, Patterns of inflammation linked to ulcer disease, *Best Pract. Res., Clin. Gastroenterol.*, 2000, **14**(1), 27–40.
154. L. Chen, X. Wang, W. Lu, X. Wu and J. Li, Molecular imprinting: Perspectives and applications, *Chem. Soc. Rev.*, 2016, **45**(8), 2137–2211.
155. C. Tancharoen, W. Sukjee, C. Thepparit, T. Jaimipuk, P. Auewarakul, A. Thitithanyanont and C. Sangma, Electrochemical biosensor based on surface imprinting for Zika virus detection in serum, *ACS Sens.*, 2019, **4**(1), 69–75.
156. K. Navakul, C. Warakulwit, P. Yenchitsomanus, A. Panya, P. A. Lieberzeit and C. Sangma, A novel method for dengue virus detection and antibody screening using a graphene-polymer based electrochemical biosensor, *Nanomedicine*, 2017, **13**(2), 549–557.
157. D. Wasik, A. Mulchandani and M. V. Yates, A heparin-functionalized carbon nanotube-based affinity biosensor for Dengue virus, *Biosens. Bioelectron.*, 2017, **91**, 811–816.
158. Y. Chen, T. Maguire, R. E. Hileman, J. R. Fromm, J. D. Esko, R. J. Linhardt and R. M. Marks, Dengue virus infectivity depends on envelope protein binding to target cell heparan sulfate, *Nat. Med.*, 1997, **3**(8), 866–871.

159. L. Fu, L. Li, C. Cai, G. Li, F. Zhang and R. J. Linhardt, Heparin stability by determining unsubstituted amino groups using hydrophilic interaction chromatography mass spectrometry, *Anal. Biochem.*, 2014, **461**, 46–48.
160. M. Hartmann, P. Betz, Y. Sun, S. N. Gorb, T. K. Lindhorst and A. Krueger, Saccharide-modified nanodiamond conjugates for the efficient detection and removal of pathogenic bacteria, *Chem. - Eur. J.*, 2012, **18**(21), 6485–6492.
161. M. Liu, D. Chang and Y. Li, Discovery and biosensing applications of diverse RNA-cleaving DNAzymes, *Acc. Chem. Res.*, 2017, **50**(9), 2273–2283.
162. J. Achenbach, W. Chiuman, R. Cruz and Y. Li, DNAzymes: from creation *in vitro* to application *in vivo*, *Curr. Pharm. Biotechnol.*, 2004, **5**(4), 321–336.
163. N. Varghese, U. Mogera, A. Govindaraj, A. Das, P. K. Maiti, A. K. Sood and C. N. R. Rao, Binding of DNA nucleobases and nucleosides with graphene, *ChemPhysChem*, 2009, **10**(1), 206–210.
164. S. Kim, S.-R. Ryoo, H.-K. Na, Y.-K. Kim, B.-S. Choi, Y. Lee, D.-E. Kim and D.-H. Min, Deoxyribozyme-loaded nano-graphene oxide for simultaneous sensing and silencing of the Hepatitis C virus gene in liver cells, *Chem. Commun.*, 2013, **49**(74), 8241.
165. H. Jang, S.-R. Ryoo, Y.-K. Kim, S. Yoon, H. Kim, S. W. Han, B.-S. Choi, D.-E. Kim and D.-H. Min, Discovery of Hepatitis C virus NS3 helicase inhibitors by a multiplexed, high-throughput helicase activity assay based on graphene oxide, *Angew. Chem., Int. Ed.*, 2013, **52**(8), 2340–2344.
166. Z. Shen, Z. Wu, D. Chang, W. Zhang, K. Tram, C. Lee, P. Kim, B. J. Salena and Y. Li, A catalytic DNA activated by a specific strain of bacterial pathogen, *Angew. Chem., Int. Ed. Engl.*, 2016, **55**(7), 2431–2434.
167. U. Farooq, Q. Yang, M. W. Ullah and S. Wang, Bacterial biosensing: recent advances in phage-based bioassays and biosensors, *Biosens. Bioelectron.*, 2018, **118**, 204–216.
168. Ł. Richter, M. Janczuk-Richter, J. Niedziółka-Jönsson, J. Paczesny and R. Hołyst, Recent advances in bacteriophage-based methods for bacteria detection, *Drug Discovery Today*, 2018, **23**(2), 448–455.
169. N. Bhardwaj, S. K. Bhardwaj, J. Mehta, G. C. Mohanta and A. Deep, Bacteriophage immobilized graphene electrodes for impedimetric sensing of bacteria (*Staphylococcus Arlettae*), *Anal. Biochem.*, 2016, **505**, 18–25.
170. Y. Zhou, A. Marar, P. Kner and R. P. Ramasamy, Charge-directed immobilization of bacteriophage on nanostructured electrode for whole-cell electrochemical biosensors, *Anal. Chem.*, 2017, **89**(11), 5734–5741.
171. H. J. Shin and W. K. Lim, Rapid label-free detection of *E. Coli* using a novel SPR biosensor containing a fragment of tail protein from phage lambda, *Prep. Biochem. Biotechnol.*, 2018, **48**(6), 498–505.
172. J. Wang, M. Hofnung and A. Charbit, The C-terminal portion of the tail fiber protein of bacteriophage lambda is responsible for binding to LamB, its receptor at the surface of *Escherichia Coli* K-12, *J. Bacteriol.*, 2000, **182**(2), 508–512.

173. J. Kim, S. Imani, W. R. de Araujo, J. Warchall, G. Valdés-Ramírez, T. R. L. C. Paixão, P. P. Mercier and J. Wang, wearable salivary uric acid mouthguard biosensor with integrated wireless electronics, *Biosens. Bioelectron.*, 2015, **74**, 1061–1068.
174. S. Kabiri Ameri, R. Ho, H. Jang, L. Tao, Y. Wang, L. Wang, D. M. Schnyer, D. Akinwande and N. Lu, Graphene electronic tattoo sensors, *ACS Nano*, 2017, **11**(8), 7634–7641.
175. M. X. Chu, K. Miyajima, D. Takahashi, T. Arakawa, K. Sano, S. Sawada, H. Kudo, Y. Iwasaki, K. Akiyoshi and M. Mochizuki, Soft contact lens biosensor for *in situ* monitoring of tear glucose as non-invasive blood sugar assessment, *Talanta*, 2011, **83**(3), 960–965.
176. T. Bhardwaj, A review on immobilization techniques of biosensors, *Int. J. Eng. Res. Technol.*, 2014, **3**(5), 294–298.
177. R. Singhal, A. Gambhir, M. K. Pandey, S. Annapoorni and B. D. Malhotra, Immobilization of urease on Poly(N-Vinyl Carbazole)/Stearic acid langmuir–blodgett films for application to urea biosensor, *Biosens. Bioelectron.*, 2002, **17**(8), 697–703.
178. X.-X. Lim, A. Chandramohan, X. Y. E. Lim, N. Bag, K. K. Sharma, M. Wirawan, T. Wohland, S.-M. Lok and G. S. Anand, Conformational changes in intact Dengue virus reveal serotype-specific expansion, *Nat. Commun.*, 2017, **8**, 14339.
179. W. Dejnirattisai, W. Wongwiwat, S. Supasa, X. Zhang, X. Dai, A. Rouvinski, A. Jumnainsong, C. Edwards, N. T. H. Quyen and T. Duangchinda, *et al.*, A new class of highly potent, broadly neutralizing antibodies isolated from viremic patients infected with Dengue virus, *Nat. Immunol.*, 2015, **16**(2), 170–177.
180. R. Reverberi and L. Reverberi, Factors affecting the antigen-antibody reaction, *Blood Transfus.*, 2007, **5**(4), 227–240.
181. M. S. Khan, S. K. Misra, K. Dighe, Z. Wang, A. S. Schwartz-Duval, D. Sar and D. Pan, Electrically-receptive and thermally-responsive paper-based sensor chip for rapid detection of bacterial cells, *Biosens. Bioelectron.*, 2018, **110**, 132–140.
182. D. T. N. Tram, H. Wang, S. Sugiarto, T. Li, W. H. Ang, C. Lee and G. Pastorin, Advances in nanomaterials and their applications in Point of Care (POC) devices for the diagnosis of infectious diseases, *Biotechnol. Adv.*, 2016, **34**(8), 1275–1288.
183. X. Liu, D. Liu, J. Lee, Q. Zheng, X. Du, X. Zhang, H. Xu, Z. Wang, Y. Wu and X. Shen, *et al.*, Spider-web-inspired stretchable graphene woven fabric for highly sensitive, transparent, wearable strain sensors, *ACS Appl. Mater. Interfaces*, 2019, **11**(2), 2282–2294.
184. X. Jing, H.-Y. Mi, X.-F. Peng and L.-S. Turng, Biocompatible, self-healing, highly stretchable polyacrylic acid/reduced graphene oxide nanocomposite hydrogel sensors *via* mussel-inspired chemistry, *Carbon*, 2018, **136**, 63–72.
185. Z. Song, W. Li, Y. Bao, W. Wang, Z. Liu, F. Han, D. Han and L. Niu, Bioinspired microstructured pressure sensor based on a janus graphene film for monitoring vital signs and cardiovascular assessment, *Adv. Electron. Mater.*, 2018, **4**(11), 1800252.

186. Z. Chen, J. Wang, D. Pan, Y. Wang, R. Noetzel, H. Li, P. Xie, W. Pei, A. Umar and L. Jiang, *et al.*, Mimicking a dog's nose: scrolling graphene nanosheets, *ACS Nano*, 2018, **12**(3), 2521–2530.
187. X. Li, R. Zhang, W. Yu, K. Wang, J. Wei, D. Wu, A. Cao, Z. Li, Y. Cheng and Q. Zheng, *et al.*, Stretchable and Highly Sensitive Graphene-on-Polymer Strain Sensors, *Sci. Rep.*, 2012, **2**, 870.

CHAPTER 10

Biotechnology Applications of Nanocarbons in Plant and Algal Systems

ALESSANDRA ANTONUCCI, ALICE J. GILLEN AND ARDEMIS A. BOGHOSSIAN*

[a]École Polytechnique Fédérale de Lausanne, 1015 Lausanne, Switzerland
*E-mail: ardemis.boghossian@epfl.ch

10.1 Introduction

Quantum confinement effects can give rise to unusual optical and electronic properties in low-dimensional carbon materials that are not attainable in bulk carbons such as diamond or graphite.[1–3] These exceptional properties make nanocarbons (NCs) particularly interesting for a range of applications, spanning from photonics,[4–6] electronics,[7–9] and sensing,[10,11] to energy[12,13] and environmental engineering.[14] The last ten years have seen an exponential rise in the use of NCs for biomedical and biotechnological research.[15–18] The characteristically small dimensions of NCs (from 1 nm to 1 μm) are very similar in size to most biomolecules involved in vital physiological functions, enabling an effective geometrical coupling of nano- and bio-materials. In addition to coupling, NCs can traverse cellular barriers and localize within

Nanoscience & Nanotechnology Series No. 48
Carbon Nanostructures for Biomedical Applications
Edited by Tatiana Da Ros, Nazario Martín and Jean-Francois Nierengarten

Published by the Royal Society of Chemistry, www.rsc.org

targeted organelles, providing alternative tools for the characterization and manipulation of important processes at a cellular level. NCs have thus found further application as molecular scaffolds for facilitating the transport of genetic material, biomolecules, and drugs across cellular barriers.[19–21] In addition, the distinct optical properties of specific NCs make them ideal candidates for both bioimaging and biosensing technologies.

NCs typically employed for biological applications include carbon nanotubes (CNTs), fullerenes, graphene, graphene oxide (GO), carbon quantum dots (CDs), carbon nanohorns, and carbon nanofibers. However, owing to the significant progress in NC synthesis and functionalization procedures, researchers today have access to an ever-growing set of synthetic nano-probes that can be used to investigate a range of complex molecular dynamics at the nanoscale.

Graphitic nanomaterials, including graphene and CNTs, consist of a network of sp^2-hybridized carbon atoms. The resulting electronic structure is characterized by strong optical transitions in the near-infrared regions of the electromagnetic spectrum (between 700 and 1300 nm), where light absorption by blood, skin, and organ tissues is minimized.[22] Hence, due to low cross-contamination with biological autofluorescence and increased tissue penetration, these nanostructures are excellent options for *in situ* photo-thermal therapy,[23,24] deep-tissue imaging,[25] and sensing.[26,27] Within the family of synthetic sp^2 carbon allotropes, semiconducting single-walled carbon nanotubes (SWCNTs) show intrinsic fluorescence emissions in the second near-infrared window (NIR-II), from 1000 to 1350 nm.[28] The optical transparency of biological tissue to light from this region of the spectrum, together with the elevated photostability and single-molecule sensitivity of the SWCNT fluorescence emissions, substantiates their applicability for *in vivo* bioimaging,[29–31] intracellular nanoparticle tracking,[32] and analyte detection.[33,34]

In addition to CNTs, CDs have found broad application in several branches of biomedical and biotechnological research.[3] Spherical-shaped graphitic CDs are the most commonly reported form in the literature, although several other variants exist, possessing different core structures or containing various mixtures of sp^2- and sp^3-hybridized carbons.[35] An advantage of CDs over other similar NCs is their high quantum efficiency and the ability to regulate the wavelength of this bright fluorescence emission, which can be tuned over the entire visible spectrum. Similarly, nanodiamonds, which consist mostly of sp^3 carbon atoms, have recently been identified as more promising candidates for bioimaging and therapy applications due to their elevated photostability and considerably higher quantum efficiency.[36,37] These advantages, alongside their excellent biocompatibility, make these NCs suitable for use as *in vivo* fluorescent markers[38] and quantum sensors,[39] as well as photodynamic therapy agents.[40,41]

The myriad of potential applications offered by the combination of tunable NCs with the numerous biological systems available has given rise to an expansion of nanobiotechnology applications. For example, the emerging

field of "plant nanobionics" aims to improve the native performances of photosynthetic organisms.[42] Plant nanobionics involves the incorporation of synthetic nanomaterials within targeted cellular compartments of plant systems, where they can carry out a diverse range of functions. By broadening the limited light-absorption cross-section of plants and algae, NCs that possess distinct light-harvesting or electron-transfer capabilities have the potential to boost the natural photosynthetic activities of these organisms.[42–44] Beyond light-harvesting, the agronomic application of NCs can expedite the development of "smart crops".[12] Synthetic nanoparticles can impart plants with unprecedented capabilities, such as self-regulation, analyte-monitoring, or an ability to responsively release agrochemicals, thereby revolutionizing agronomy. Furthermore, NCs can also serve as efficient alternatives for targeted biomolecule and gene delivery, as they can be used as vectors to deliver biomolecules into living cells,[45–49] enabling streamlined genetic modification of plant and algal metabolism.[19]

Interfacing synthetic NCs with living organisms poses challenges associated with the poor biocompatibility of pristine nanomaterials, as well as species-dependent cellular responses upon nanoparticle exposure. A thorough characterization of the effects and underlying mechanisms of nanoparticle interaction is therefore needed to take advantage of the multiple opportunities provided by the synergistic combination of NCs and photosynthetic organisms. Despite the growing number of studies elucidating the impact of NCs on mammalian organisms, the analogous understanding of NC fate and behavior within plant and algal systems has lagged far behind. Coupled with the large diversity of plant and algal ecosystems, this uncertainty motivates ongoing research efforts between NCs and photosynthetic systems. The present chapter focuses on the fundamental principles governing NC interaction with photosynthetic organisms. In particular, the chapter focuses on NC uptake mechanisms, as well as localization and functionality post-uptake. The following sections will specifically highlight the major applications of several NCs and present future possible directions within this burgeoning research field.

10.2 Traversal of NCs Across Biological Barriers of Photosynthetic Systems

Because of their highly hydrophobic nature, pristine NCs are practically insoluble in aqueous solutions and exhibit a very strong tendency to self-associate, forming thick, toxic aggregates.[16] NC surface chemistry therefore plays a fundamental role in promoting nanoparticle dispersion in physiological environments and improving NC biocompatibility, as demonstrated by numerous studies, such as those by Lacerda *et al.* and Wu *et al.*[50,51] In addition to imparting solubility, chemical functionalization can give NCs the ability to bypass most cellular barriers, enabling them to reach specific targets of interest within the cell.[42] Although previous studies have explored the

importance of factors such as species type, growth conditions, NC physical and chemical properties, and dosage on nanoparticle interaction with subcellular organelles, cells and organisms,[52–54] a fundamental understanding of the nature of these interactions remains elusive.

The ability of functionalized NCs to cross biological barriers is particularly advantageous in plants and algae, where the additional cell wall acts as a strong physical barrier against the free passage of exogenous nanostructures. Several bio-conjugation approaches have already been optimized to increase NC solubility and facilitate their transport across the cell wall of different photosynthetic species. The majority of these approaches rely on noncovalent functionalization of the NCs with biological or synthetic polymers.[55] These noncovalent strategies preserve the unique optical behavior of many NCs, allowing imaging and tracking of NCs across cell boundaries using the NC fluorescence.

10.2.1 NC Internalization within Isolated Organelles and Protoplasts

Photosynthetic organelles and protoplasts represent model systems for studying NC interaction with intact photosynthetic machinery. Protoplasts are plant cells where the outer wall has been removed, typically through enzymatic digestion.[56] Like protoplasts, isolated organelles such as chloroplasts present a photosynthetic system that is surrounded only by a lipid bilayer membrane. These membrane-bound systems have allowed researchers to directly explore internalization effects of NCs without the need to engineer mechanisms for penetrating the thick cell wall. For example, by taking advantage of the intrinsic fluorescence properties of SWCNTs, Giraldo *et al.* and Wong *et al.* demonstrated rapid transport of these NCs into both isolated plant chloroplasts and subcellular compartments of plant protoplasts *via* passive uptake mechanisms.[32,42] This passive SWCNT internalization was shown to largely depend on the nanoparticle size and zeta potential. Specifically, nanoparticles that were sufficiently charged, either positively or negatively, induced a potential drop across the lipid bilayer, which led to local pore formation inside the membrane that, in turn, promoted nanoparticle entry.

The surface charge of the SWCNT can be modulated by using a variety of wrappings, such as single- or double-stranded DNA, proteins, or synthetic polymers.[18,34,55,57–59] SWCNTs that are functionalized with highly charged biopolymers (such as DNA or chitosan with zeta potentials of -44.6 ± 1.9 mV and 48.5 ± 1.0 mV, respectively) can rapidly localize inside plant protoplasts and isolated chloroplasts, while SWCNTs possessing an almost neutral zeta-potential (such as those suspended using PVA, zeta potential of -6.4 ± 3.4 mV) are incapable of penetrating the lipid envelopes.[42,60] The irreversible adsorption of lipid molecules onto the surface of the nanotube during penetration of the membrane, possibly due to this charged coating, is hypothesized to act

as the driving force for SWCNT translocation in both plant chloroplasts and protoplasts. This mechanism is believed to prevent nanoparticle escape following internalization. In support of this hypothesis, lipid-coated SWCNTs are unable to penetrate the chloroplast outer envelope, independent of their significantly negative zeta potential of -35.2 ± 2.6 mV. This inability to traverse the chloroplast membrane was attributed to membrane trapping inhibition due to the lipid coating on the SCWNT.[42,60]

NCs possessing larger aspect ratios, such as multi-walled carbon nanotubes (MWCNTs), are also capable of cellular internalization into plant protoplasts. Serag *et al.* discovered that MWCNTs labeled with fluorescein isothiocyanate (FITC) can penetrate the cell membrane of plant protoplasts *via* a direct internalization mechanism.[61] Furthermore, these functionalized MWCNTs could target specific cellular substructures, including plastids, vacuoles, and the nucleus.[61] However, the subcellular distribution of MWCNTs was found to strongly depend on nanoparticle size, with shorter MWCNTs (30–100 nm) more readily able to penetrate into the subcellular organelles. Similar observations have been reported for SWCNTs, although the larger radial dimension of the MWCNTs appears to exaggerate this effect.[61] In summary, although SWCNT and MWCNT internalization in protoplasts offer a model basis for studying NC interactions with photosynthetic systems, delivery applications motivate the need to develop methods of internalizing NCs in intact whole cells, where they must additionally penetrate the cell walls.[56]

10.2.2 NC Internalization within Plant Cells

The delivery of exogenous NCs into intact plant cells presents many additional challenges compared to their wall-less counterparts. The cell wall, which varies in composition amongst different species, typically consists of a network of cellulose microfibrils cross-linked with hemi-cellulose and interpenetrated by pectin.[62] These thick cellulosic layers provide the cell with increased rigidity and structural support, thereby largely determining the shape. In addition, the cell wall offers increased protection, acting as an additional filtering mechanism and impeding the passage of larger macromolecules to the cell interior.[63] This limited permeability is partly due to the small dimensions of the cell wall pores, ranging on average between 5 and 30 nm, which impede the translocation of larger macromolecules and nanostructures.[64] Although a number of reports have documented the traversal of larger nanoparticles across the thick plant cell wall, the underlying mechanisms of the cell membrane translocation remain largely unclear, with both energy-dependent (active processes) and passive internalization pathways reported. Active uptake processes mainly rely on endocytosis, which involves the formation of membrane invaginations (endosomal vesicles) that enable the entrapment of exogenous material and its subsequent transport and release inside the cell.[65] On the other hand, unassisted uptake mechanisms of engineered nanomaterials are proposed to involve either the enlargement

of existing pores or the formation of additional openings within the cell wall and membranes, both of which can enhance NC penetration. Independent of the uptake mechanism, these reports show that the extent to which NCs can penetrate plant tissue are strongly impacted by the size and shape, as well as the NCs' surface properties. Therefore, for a given NC, appropriate surface functionalization is crucial for optimizing NC delivery and subsequent subcellular targeting.

The functionalization of the NCs has been shown to significantly affect their internalization mechanism. One method to facilitate the cellular entry of NCs across the cell wall is through the formation of local nanopores in the cellulosic wall. Serag *et al.* showed that cup-stacked carbon nanotubes (CS-CNTs) functionalized with cellulase enzyme molecules can localize inside cells of *Arabidopsis thaliana*.[66] Cellulase enzymes are naturally capable of catalyzing cellulolysis, whereby cellulose is hydrolyzed into shorter chain saccharides. In their study, Serag *et al.* were able to induce local lesions in the plant walls, referred to as cellulase-induced nanoholes, through incubation with cellulase immobilized on CS-CNTs. The CS-CNTs subsequently permeated into the internal compartments of the cell following incubation. Compared to alternative methods of NC protoplast-based transformation, this strategy circumvents the need for complete cell wall removal. MWCNTs have also been used to penetrate plant cells by directly piercing the plant cell walls.[67] However, although MWCNTs were seen traversing the cell wall and entering the cellular cytoplasm (by up to 4 μm), complete internalization has not yet been achieved. Despite an increase in the number of MWCNTs piercing the cell wall over the course of the 28-day experiment, the authors observed no increase in the maximum depth of penetration. The inability for the MWCNT to completely internalize in the cell was partially attributed to the relatively large size of the MWCNTs.

Aside from direct penetration, active transport processes have also been reported for translocating NCs through outer cell barriers. For example, shortened carboxylated SWCNTs have demonstrated the capacity to traverse both the cell wall and subcellular membranes of *Chatharanthus roseus* and *tobacum* cells.[56,62,68,69] Liu *et al.* monitored SWCNT internalization in intact cells of *Nicotiana tobacu*[56] using nanotubes that were noncovalently labeled with FITC, and cell uptake over time was monitored with fluorescence microscopy.[56] This study showed a reduction in SWCNT uptake at low temperatures, indicative of active internalization mechanisms. When the cells were further pretreated with specific inhibitors of cellular endocytosis, the authors confirmed a significant decrease in localized fluorescence within the cell, confirming an uptake mechanism based on fluidic-phase endocytosis.

In another study, Serag *et al.* examined the uptake of SWCNTs functionalized with FITC (SWCNT-FITC) in *Catharanthus roseus* in the context of various subcellular phenomena, including carrier-mediated vacuolar transport (CMT), vesicle-mediated transport (VMT), and autophagy.[69] FITC is known to enter cells predominantly *via* passive diffusion and to rapidly transport across the vacuolar membrane *via* CMT. In the presence of probenecid, an

inhibitor of CMT, the authors observed an inhibition of cellular uptake of SWCNT-FITC. These observations imply an internalization mechanism based on FITC-controlled subcellular distribution of SWCNTs and accumulation in the cytoplasm. Moreover, probenecid-treated cells that were washed with probenecid-free cell medium resulted in the redistribution of SWCNT-FITC into cell vacuoles. These observations further support a SWCNT internalization mechanism based on FITC-based CMT. Serag *et al.* also discovered that SWCNT-FITC were expelled from the cell by increasing the washing medium pH (to pH = 7.2), leading them to propose a dual removal mechanism based on CMT followed by a VMT. According to this mechanism, the membrane vesicles traffic the SWCNTs between vacuoles and plasmalemma, releasing the nanotubes into the extracytoplasmic space. Once the SWCNTs are outside the cell, the anionic form of FITC on the surface hampers their reuptake, resulting in a progressive removal of SWCNT-FITC from the cell. In support of this mechanism, the authors similarly found that the initial uptake of SWCNT-FITC could also be inhibited by incubating the cells in slightly alkaline cell media (pH = 7.2). Furthermore, through raster scan image correlation spectroscopy (RICS), the authors were able to compare the distribution of diffusion values inside the cell vacuole to cytoplasmic diffusion in places in the vacuole close to the vacuolar membrane (tonoplast). The observed similarity in these values indicates that parts of the cytoplasm are penetrating into the vacuole through autophagy, with the passage of SWCNTs through the tonoplast occurring at interrupted and localized zones mediated by protein carriers. Though such studies exemplify the distinct challenges facing inter- and intra-cellular transport of intact cells, they highlight the overlapping dependency of both intact cells and their wall-less counterparts on NC surface functionalization.[68]

10.2.3 NC Biodistribution within Plant Tissue

In addition to organelles, protoplasts, and cells, multiple studies have also explored the effects of NCs on the whole seeds of different plant species. Plant seeds are surrounded by especially thick coatings that may inhibit NC penetration. Despite this thick barrier, seed coatings of various plant species have shown selective permeability to not only heavy metal ions,[70] but also certain nanomaterials.[71] Different NCs, including fluorescent carbon dots, fullerenes, carbon nano-horns, CNTs,[71–73] and GO nanoparticles, have been shown to penetrate the seeds of multiple crop species, such as tomato,[74,75] wheat,[76] rice,[77] and mung bean.[78] One of the earliest studies by Khodakovskaya *et al.* showed that MWCNTs could penetrate the thick seed coat and enhance seed germination and growth.[71] The internalization of the MWCNTs was verified using TEM and Raman microscopy, the latter of which was used to positively identify the CNT G-band inside seeds exposed to CNTs. Subsequent studies have since further explored MWCNT traversal through the thick seed coatings of additional crop species including tomato, tobacco, barley, corn, and soybean.[73,79–81] Complementary techniques, such as photothermal

or photoacoustic approaches, which are based on the non-irradiative conversion of absorbed laser energy into heat and acoustic phenomena, showed the uptake of MWCNTs from the soil by tomato plants and re-distribution of these NCs in different plant tissues, including fruits.[81] Similarly, Zhang *et al.* demonstrated that by partially breaking the husk, graphene nanoparticles could penetrate tomato plant seeds. Penetration was confirmed using Raman microscopy and TEM. Raman signals from the graphene D- and G-bands were detected inside graphene-treated seeds. Moreover, TEM images of root tip cells collected from the graphene-treated seedlings confirmed the presence of graphene sheets inside the cell wall and vacuoles, indicating that the graphene was also able to penetrate root tip cells during seedling growth.[75]

In spite of the consistency in the observed uptake of CNTs in plant seeds and seedlings, the research community lacks a complete understanding of the mechanism responsible for NC penetration and bio-distribution. Several investigations have aimed to shed some light on this aspect and to further characterize these possible internalization mechanisms for NCs, such as CDs and fullerenes. For example, work by Lin *et al.* suggested that C_{70} nanoparticles suspended with natural organic matter can access plant roots either through osmotic pressure, capillary force, diffusion through pores in the cell walls and the intercellular plasmodesmata, or through the highly regulated symplastic route.[77] Once localized in the plant roots and stems, C_{70} can be transported through the plant vascular system by transpiration. The surface properties of the fullerene particles greatly impact cellular penetration and the plant's cellular response. In support of this observation, Liu *et al.* showed that aggregates of carboxy-fullerenes preferentially adsorbed on the surface of *Nicotiana tobacum* cells, leading to profound changes in the cell wall integrity and chemical composition.[82] In an alternative study based on CD internalization, Li *et al.* hypothesized that CDs can penetrate intact seed coats of mung bean plants *via* the intercellular spaces in the parenchyma and subsequently move extracellularly from the plant roots to the stems and leaves through the apoplastic pathway of the vascular system.[77] In agreement with this mechanism, Liu *et al.* showed that small, fluorescent CDs on the order of ~5 nm were easily transported from the root to the stem and leaves of rice plants and that they could subsequently penetrate inside plant cells and subcellular compartments, including the cell nuclei.[83] In addition to uptake *via* seed penetration, leaf lamina infiltration has also been reported to offer an efficient and practical alternative for NC delivery directly into the leaves of living plants.[42,84–86]

10.3 Applications of Carbon Nanomaterials with Photosynthetic Organisms

The application of nanotechnology in the fields of plant science and photosynthesis research is still in its nascency. However, recent years have witnessed the development of incredibly promising technologies that have the potential to revolutionize many areas of study, from energy conversion to genetic engineering.[87] NCs hold the promise to enhance and even expand the

native capabilities of photosynthetic systems, enabling the development of cost-effective, "green" technologies that are based on abundant living organisms with improved performance.

However, the expanding plant applications of engineered NCs has also brought with it increasing concerns on the impact of NCs on plant and algal growth, structure, and function. The field remains faced with seemingly contradictory results from multiple studies that investigate the possible biohazards and adverse effects associated with the accumulation of synthetic NCs into plant and algal ecosystems.[87] These findings not only point to the complexity of these systems, but also motivate a systematic exploration of these systems under a wider range of controlled testing conditions. For this reason, unraveling the behavior and biocompatibility of NCs with a variety of different plants and organelles, especially focusing on their impact on growth and function, remains a crucial target of current research in the field.

The sections below present several recent NC applications with photosynthetic organisms that have shown minimal toxicity effects (Figure 10.1). Major applications have focused on:

(a) improving the native light-harvesting and photosynthetic efficiencies of photosynthetic systems;
(b) enhancing electricity generation inside photosynthetic bio-electrochemical devices;

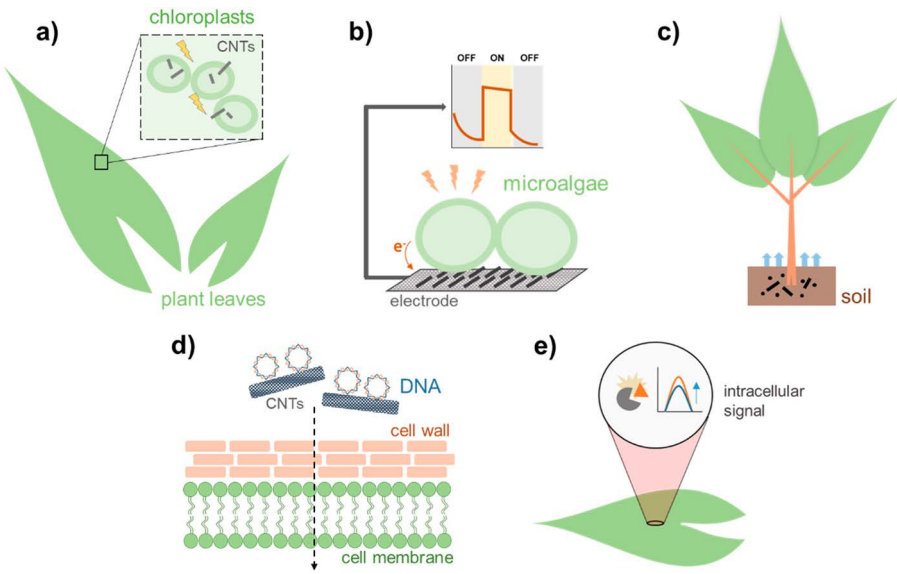

Figure 10.1 Schematic representation of the major applications based on the combination of synthetic NCs with photosynthetic organisms. (a) NC improvement of plant light-harvesting and photosynthetic efficiencies. (b) Enhancement of bio-electricity generation in photosynthetic electrochemical devices. (c) NC-mediated regulation of plant growth for enhanced plant productivity. (d) NC-mediated transport of genetic materials or biomolecules inside plant cells. (e) Monitoring of plant responses and sensing of target analytes.

(c) augmenting plant growth and productivity to allow for regulation of cellular metabolism;
(d) promoting effective transport of genetic materials or biomolecules inside the cell;
(e) imparting photosynthetic systems with sensing capabilities that allow for monitoring of cellular responses and analyte-detection.

These recent studies point to new promising directions for research within this growing field.

10.3.1 Light-harvesting and Energy Applications

Photosynthesis is the product of billions of years of optimization of light-harvesting for plant, algal, and bacterial survival.[88,89] Growing efforts over the last few years have focused on exploiting this biological light-harvesting capability for solar energy conversion and storage.[90] One approach has focused on the incorporation of naturally abundant photosynthetic complexes as photoactive components inside optoelectronic or electrochemical devices.[91,92] Although this approach benefits from direct interaction between photosynthetic apparatuses and electrodes, which facilitates charge transfer, it faces challenges with protein stability. Alternative approaches focus on integrating whole living cells of photosynthetic organisms to function as photoactive biomaterials in photovoltaic cells or bioreactors.[93–96] Despite advantages in prolonged lifetimes, robust environmental tolerance, and material abundance, whole-cell devices suffer from inefficient energy extraction to the electrode. In addition, they are limited by the relatively narrow fraction of light absorption cross-section inherent to most photosynthetic systems, which is limited to only half of the incident solar radiation.

Due to their unique optical and electronic properties, functional NCs represent viable options for improving the performance of natural photosynthetic systems.[12,44,97] NCs have the potential to enhance the native light-harvesting capabilities of photosynthetic systems through augmented photosynthesis and enhanced photo-protection by broadening the range of solar light absorption and scavenging reactive oxygen species (ROS), respectively. In addition to increased energy extraction, these photosynthetic enhancements can also contribute to increased crop productivity and improved adaptation to environmental changes.[98,99]

Several studies have demonstrated improvements in photosynthetic performance using NCs such as SWCNTs or CDs. Giraldo *et al.* demonstrated that the incorporation of semiconducting SWCNTs inside *Arabidopsis* leaves and in isolated chloroplasts contributed to an increase in photosynthetic electron transport rates.[42] The authors hypothesized that photo-generated excitons from the SWCNTs could be directly transferred to the electron transport chain, resulting in increased reduction of the electron acceptor dye, dichlorophenolindophenol (DCPIP), over six hours. Scholes *et al.* further highlighted the need for improved nanoparticle-chlorophyll systems to augment photosynthesis over a broader spectral bandwidth.[44]

Certain CDs have also been shown to improve photo-absorption in both extracted chloroplasts and intact leaves, while showing low toxicity and appreciable biocompatibility *in vivo*.[100] Most reported CDs show strong absorption in the UV,[83] and despite the diversity of their emitting states for luminescence, individual CDs typically only emit a single emission peak upon excitation. Studies by Zhou *et al.*[101] and Sun *et al.*[4] have shown that dual-emissive blue/yellow and blue/green CDs can be prepared through co-doping with nitrogen/sulfur and nitrogen/phosphorous, respectively. Similarly, Li *et al.* have created dual-emissive CDs using phellodendron chinense Schneid as the carbon source.[100] Such CDs absorb light in the UV region of the electromagnetic spectrum, where chloroplast absorption is at its minimum, and re-emit the absorbed energy as intense blue and red light that can be transferred to, and efficiently absorbed by, the photosynthetic apparatus. These studies represented the first instances of using CDs to enhance light-capture and augment electron-transfer efficiency within the photosystems through precise optical matching of the chloroplast absorption. Furthermore, these CDs have also been effective in promoting photosynthesis in the intact leaves of living plants.

Successful chloroplast electron transfer has also been achieved in the work of Chandra *et al.* describing the conjugation of amine-functionalized CDs to the surface of extracted chloroplasts from mung beans.[102] The increased energy transfer was hypothesized to promote photosynthesis by accelerating the conversion of light to electrical energy and ultimately to chemical energy. As a result, the nano-hybridized system leads to improved light energy conversion, enhanced oxygen evolution, and increased non-cyclic photophosphorylation and ATP synthesis. Amine-functionalized CDs were also employed in a study by Sai *et al.*, where the authors reported an 18% enhancement of photosynthesis in *Nicotiana tabacum* leaves upon UV irradiation.[103] Similarly, Wang *et al.* showed that CDs could penetrate the plant cells of mung bean sprouts and improve photosynthetic activity by accelerating the electron transport rate to photosystem I.[99] Moreover, CDs were found to increase the chlorophyll content and the activity of Rubisco, the enzyme responsible for catalyzing CO_2 fixation, by 14.8% and 31%, respectively. These observations suggested that CDs could improve carbohydrate production, and thereby positively impact plant growth and development. Beyond plant systems, Zhang *et al.* showed that pristine CDs could increase the growth rate of microalgae, like *Chlorella vulgaris*, by enhancing photosynthesis.[98] The CDs additionally acted as an antioxidant, protecting the cells against UV irradiation damage.

These enhancements suggest that similar combinations of NCs can be used to improve the electrical current extracted from photosynthetic microorganisms in biological photovoltaics (BPVs). Unicellular microalgae and photoautotrophic cyanobacteria have both been successfully employed for the development of bio-electrochemical cells that can operate in the absence of an added carbon feedstock.[104] Within a BPV device, the high-energy electrons generated either during the photosynthetic process (under illumination) or by oxidation of internally stocked carbon (in the dark) are transferred

from the cells to an external electrode. In cases where the electrode cannot directly access the internal regions of the insulating cells, their electrical and surface properties become critical for promoting extracellular electron transfer.

NCs offer concrete opportunities for optimizing device performance by improving electron transfer on the electrode surface. Because of their excellent conductivity and elevated electroactive surface area, CNTs are promising materials for current collectors in BPVs. In addition, they have demonstrated compatibility with the growth and electrochemical characterization of cyanobacteria.[105] By combining CNT anodes with a filamentous cyanobacterium, *Nostoc* sp. (NOS), Sekar *et al.* successfully produced BPVs with average power densities of 35 mW m^{-2} under light illumination using a laccase/CNT modified carbon paper as the cathode. They further increased the extracted power to 100 mW m^{-2} following the addition of 1,4-benzoquinone as a mediator.[105] The authors showed that chlorophyll-a was the major contributor to the light capture and resulting photocurrent generation. Further investigation revealed that the major pathway by which the light-induced electrons generated a photocurrent was predominantly *via* a route from photosystem II (PSII) to the CNT through the plastoquinone pool and quinol oxidase. More recent work by Sawa *et al.* fabricated thin-film, paper-based BPVs by printing a layer of cyanobacterial cells on top of substrates coated with a MWCNT-based conductive ink (Figure 10.2a,b).[94] In this study, the authors formed a uniform, solid layer of cells on the electrode surface using a "bio-ink" of bacterial cells. The cells remained viable after printing, retaining their photosynthetic activity. Currents were sustained for more than 100 hours of device operation.

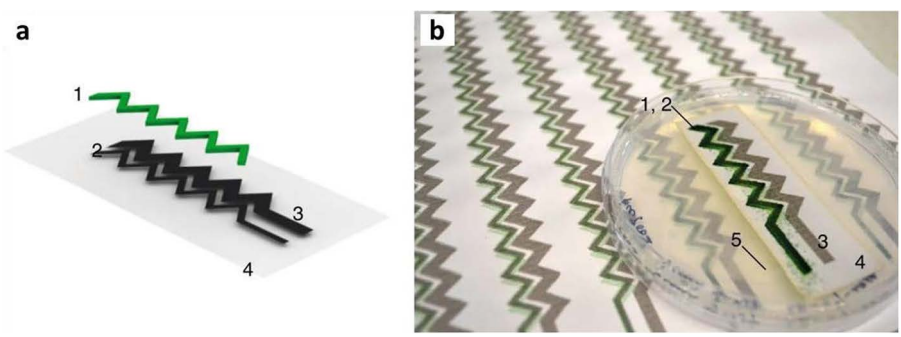

Figure 10.2 (a) Schematic representation (semi-exploded view) of the digitally printed bioelectrode module. 1: Printed photosynthetic organisms in green. 2: Printed CNT anode. 3: Printed CNT cathode. 4: Paper substrate. (b) Photograph of A4-size arrays with freshly printed cyanobacterial cells, compared to the incubated module grown on agar plate for 3 days. 1–4 are the same as in (a) and 5 is the solid agar. Reprinted from ref. 94, https://doi.org/10.1038/s41467-017-01084-4, under the terms of the CC-BY 4.0 license http://creativecommons.org/licenses/by/4.0/.

In addition to one-dimensional NCs, such as CNTs, planar two-dimensional NCs, including GO, have also been used to improve charge extraction from microbial BPVs. For example, sheets of reduced GO have been employed to fabricate highly porous electrodes that allowed for higher surface area and, hence, better attachment of a biofilm from *Chlorella* sp.[106] The presence of oxygen-containing functional groups on the surface of the reduced GO sheets was believed to positively impact the interaction of the microalgae with the electrode. In addition to the more intimate interaction, the GO could also promote more efficient electron transfer, leading to increased power densities compared to conventional setups based on indium-tin oxide (ITO) electrodes.

10.3.2 Enhancing Plant Growth and Cellular Metabolism

In the face of a growing global population, increased plant productivity and crop yields become crucial for agricultural and horticultural sustainability. NCs have recently emerged as crop regulatory tools that can improve agricultural yield.[14,107] A growing number of NCs have already been identified for their positive impact on plant growth regulation.[99,107,108] Structural characteristics such as length, diameter, shape, morphology, as well as the surface chemistry of nanomaterials, have all been shown to play a fundamental role not only for NC internalization, but also for the activation of specific plant cellular responses.

As discussed in the previous sections, several works have demonstrated the capacity of SWCNTs and MWCNTs, as well as graphene and CDs, to improve seed germination and stimulate plant growth, suggesting the possible use of NCs as soil fertilizers.[75,83,107–110] In fact, many NCs have been shown to positively affect the expression of multiple genes crucial for a diverse range of plant cellular functions. However, a deeper knowledge of the mechanism of this impact is needed to guide the engineering of these nanomaterials and expedite their incorporation in the development of "smart crops".

Seed germination represents the first step of plant development whereby water is absorbed by the plant seed's embryo, activating the metabolic functions responsible for triggering plant growth. This germination stage culminates in root elongation and the emergence of the plant's first shoots. Consequently, water constitutes one of the most critical factors for plant seed germination. As mature seeds are relatively dry, a substantial amount of water is needed in order to activate the cellular metabolism and promote plant root development and elongation. Many of the favorable effects observed for most NCs on plant germination have often been attributed to their role in promoting water uptake inside of seed embryos.[71,111,112]

Early studies by Khodakovskaya *et al.* that examined the impact of CNTs on seed germination and plant growth reported significantly faster germination rates for plants exposed to CNTs.[71] Having measured elevated moisture levels inside tomato seeds treated with SWCNTs, the authors attributed these increased rates to an activated water uptake inside the

seeds. Thermogravimetric analysis confirmed that seeds exposed to CNTs showed a significantly higher level of moisture compared to seeds that were not treated with CNTs. Whereas untreated seeds had only 38.9% of moisture, those that were exposed to CNTs accumulated about 57.6% of moisture over the course of the experiment. One hypothesis attributed this increase to new pores that are created by the CNTs in the seed coat, while another suggested that the CNTs impacted the existing water channels (aquaporins) in the coat of the plant seeds, thereby regulating their gating. Both pore formation and water gating can increase water penetration during the germination period, significantly accelerating the plant growth and leading to higher biomass production.

Subsequent studies have confirmed these findings on the enhancing effects of NCs on plant growth. Alternative investigations using poly-hydroxylated fullerenes, namely fullerenols, revealed a similar increase in the growth of bitter melon and wheat.[76,113] For the latter, ^{13}C-fullerenols were shown to also enhance chlorophyll content, although the authors observed no stimulating effects on plant biomass. Following studies showed that MWCNTs induced changes in the gene expression of the plants, specifically by up-regulating certain stress-related genes, including several gene families of aquaporins.[73,79–81] This finding supports the initial hypothesis of Khodakovskaya *et al.* that CNTs can regulate the activity of water channels in exposed plant organelles or cells.[81] Subsequent work by Villagarcia *et al.* further elucidated that the charge properties of MWCNTs strongly affected the regulation of these water channel proteins in tomato plants.[79]

In contrast to poorly dispersed or highly aggregated MWCNTs, negatively-charged, functionalized MWCNTs led to greater aquaporin expression, leading to even higher levels of plant growth and increased biomass. In a study by Lahiani *et al.*, seeds treated with MWCNTs showed significantly earlier germination compared to the control seeds, with 46% of the treated seeds germinating on the first day post-treatment (Figure 10.3a,b).[73] In addition, no negative developmental effects or symptoms of toxicity were reported for plants originating from treated seeds for any of the crop species tested.[73] Similarly, Wang *et al.* have attributed the improved activity of root dehydrogenase, which is responsible for water uptake and biomass production, to the enhanced water availability in MWCNT-treated wheat seedlings.[109] Carboxylated MWCNTs were also found to boost the growth of tobacco cell cultures between 55 and 64% compared to the control cells over a wide range of concentrations.[80] In this study, the augmented growth was attributed to the up-regulation of plant genes responsible for cell division and extension. More recent findings by Joshi *et al.* further supported previous observations of accelerated seedling growth for NC-treated bread wheat (*Triticum aestivum* L.) seeds, again largely attributing this growth to NC-mediated facilitation of the plant's water uptake.[114] The co-authors carefully examined the vascular bundles of the stems of MWCNT-treated plants, revealing that the MWCNT-plants show significantly increased cell sizes in both the water-conducting (xylem) and nutrient-conducting (phloem) tissues. They also noted that

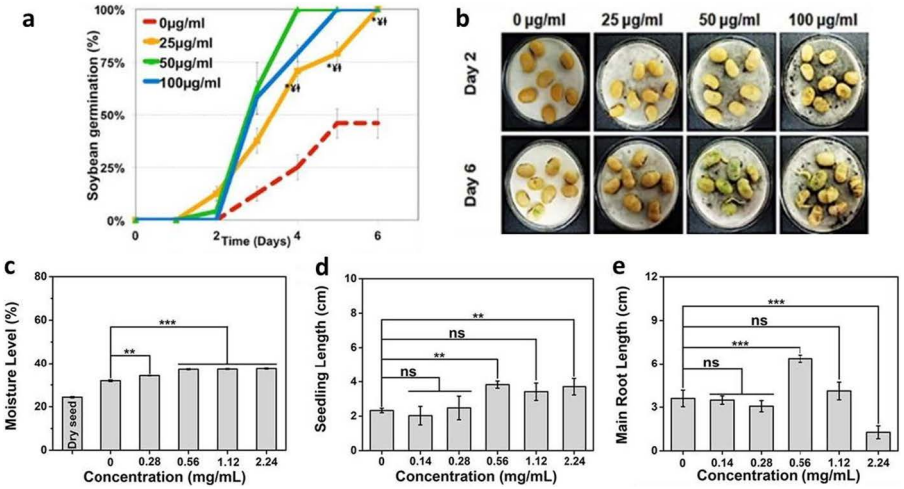

Figure 10.3 (a) MWCNTs (concentration: 0, 25, 50 and 100 μg mL^{-1}, respectively) affect the germination time and rate of soybean seeds. (b) Phenotype of control and MWCNT-coated seeds of soybean are presented on the second and sixth day after MWCNT treatment. (c) Mass loss of rice seeds incubated with CDs over 4 hours. (d) Seedling lengths of rice treated with different concentrations of CDs. (e) Main root lengths of rice treated with different concentrations of CDs. (a) and (b) Reprinted from ref. 73 with permission from American Chemical Society, Copyright 2013 and c–e Reproduced from ref. 83, https://pubs.acs.org/doi/10.1021/acsabm.8b00345, with permission from American Chemical Society, Copyright 2018. Please direct further permissions request to the ACS.

treated seeds had a significantly denser network of roots and root hair compared to the control seeds. These conclusions again supported the earlier findings that CNTs facilitated water uptake, resulting in increased nutrient transport that could consequently benefit plant germination and growth. Joshi *et al.* also applied similar methods to seeds pre-soaking in NC solutions (seed priming) in potted plants, where they demonstrated a significant growth stimulation for soil-grown *Triticum aestivum* L., highlighting the practical applicability of this approach to increase the yields of agricultural crops.

In addition to improving plant cell growth and division, MWCNTs have also been shown to inhibit the elongation and germination of important pathogenic fungal spores. Wang *et al.* found that the spore length of MWCNT-exposed fungi was one-fifth shorter, and that this length could be further reduced using nanotubes functionalized with either –COOH, –OH, or $-NH_2$ groups.[115] Owing to the superior antifungal activities and the low-cost facile production of the nanotubes, these NCs point towards promising applications for protecting plants from parasitic or competitive growth conditions.

Similar to CNTs, other NCs have also been shown to have profound effects on plant growth. CDs have been shown to accelerate plant growth and increase seedling and root lengths.[83] Li *et al.* studied the impact of various of CDs (of approximately 5 nm in size) with different oxygen contents on rice plants (Figure 10.3c–e).[83] They observed a NC concentration dependency for improving the water content of CD-treated rice seeds. The authors further observed that the oxygen content of the CDs can effectively promote rice-plant growth, reporting an optimum oxygen content of about 29%. The oxygen content is proportional to the number of hydrophilic groups (hydroxyl and carboxyl groups) on the CDs. As these groups are located on the CD surface, they are readily available to combine with water molecules to facilitate water uptake into the rice seeds. Lahiani *et al.* found that carbon nano-horns could also regulate the expression of multiple tomato genes involved either in the cellular, stress, or metabolic processes.[74] The authors observed elevated expression of expansin proteins, which have important roles in plant cell growth, fruit softening, and other developmental processes.

In contrast to the NCs mentioned above, graphene and active carbon are unable to penetrate plant tissue and as a result, have been shown not to significantly affect certain plants' growth, including tomatoes.[81] However, in spite of this lack of penetrability, He *et al.* have more recently shown that low doses of GO could significantly promote the germination and growth of spinach and chives.[116] The GO again led to increased water uptake, this time owing to the water transport properties of GO nanoparticles. This study indicates that NCs previously deemed unsuitable for improving crop growth could still be applied through appropriate dosing.

10.3.3 Gene and Biomolecule Delivery Applications

Various technologies are available today for delivering genetic material and biomolecules to different plant systems, most of which typically rely on either mechanical, chemical, or biological approaches. However, limited cargo loading capacity, narrow host specificity, poor efficiency, and possible adverse tissue damage represent important limitations of many conventional plant transformation techniques, motivating the search for alternative delivery approaches.[19] The potential of nanoparticles to overcome some of the drawbacks of standard biomolecular delivery techniques, such as gene-gun, microinjection, or Agrobacterium-mediated transformation, make them exceptional candidates for developing effective vehicles for plant genetic engineering.[19,117] The ability of NCs to interact with the multilayered cell wall that surrounds plant cells, together with their elevated surface areas and consequently increased biomolecule-carrying efficiency, are key properties needed for effective delivery. Additionally, as NCs offer great flexibility in nanoparticle design and functionalization, they can be easily targeted to specific cellular compartments in a manner that preserves cellular integrity and viability.

Different nanoparticle conjugation strategies have been developed to enable efficient biomolecule delivery into plant cells. Liu *et al.* were among the first to explore the delivery of DNA and small dye molecules into intact plant cells using SWCNTs.[118] In this study, DNA molecules were adsorbed on the hydrophobic outer surface of SWCNTs *via* the π-stacking interaction with the aromatic nucleobases. Their results indicated that more than 80% of the cells incubated with DNA-SWCNT complexes exhibited intracellular fluorescence as a result of efficient DNA internalization. More recently, Kwak *et al.* designed polycationic chitosan-conjugated SWCNTs, which were used to complex plasmid DNA molecules *via* electrostatic interactions.[119] The resulting complexes enabled selective delivery of functional genes to chloroplasts of different plant species, as well as to isolated *Arabidopsis thaliana* mesophyll protoplasts. Most recently, a remarkable study by Demirer *et al.* employed alternative DNA-CNT conjugates for biomolecule delivery to plants, which were prepared *via* electrostatic grafting.[120] In this method, carboxylated SWCNTs were first covalently functionalized with a cationic polymer, poly-ethylenimine (PEI). Next, negatively-charged double-stranded DNA vectors were electrostatically adsorbed on the surface of conjugated PEI-SWCNT particles. DNA-SWCNT conjugates were delivered into mature leaf cells by infiltration, enabling efficient transport of functional genes and strong protein expression without transgene integration in a variety of plant species. A similar approach allowed effective delivery of exogenous genes in the form of single-stranded RNA into plant cells, resulting in highly efficient gene silencing.[121,122] In addition to promoting high-efficiency, species-independent transport of genetic materials into plant cells, SWCNTs scaffolds have also been shown to protect polynucleotide cargos from plant-nuclease degradation. These pioneering studies on NC-mediated plant transformation offer an attractive and customizable alternative for future gene manipulation and biomolecule delivery methods.

10.3.4 Sensing Applications

The development of novel nanosensors has enabled the study of fundamental cellular processes including the spatiotemporal detection of biologically-relevant analytes and biomarkers, as well as the real-time monitoring of complex molecular dynamics. A rapid increase in the use of NCs in plant science and technology has been seen in recent years.[123] These NC-based sensors offer many opportunities to access vital information concerning plant regulation and plant responses against different environmental stimuli.[124]

One example is monitoring the dynamics of stomata, small pores found on the surfaces of plant leaves that are directly involved in the regulation of plant transpiration rates under different environmental conditions. The ability to monitor any changes in the dynamics of these stomata during drought conditions would allow agriculturists to infer crucial information surrounding plant health. With this information, the nanosensors would

allow agriculturists to mitigate the effects of water deficits on plant growth and development. Several NC-based sensors have already been immobilized on plant leaves to monitor plant moisture and stomatal behavior. Koman *et al.* utilized a NC-based conducting ink to print a highly stable, electrical conductometric sensor directly onto the leaves of wild-type peace lily plants, enabling real-time tracking of stomatal dynamics for persistent drought monitoring (Figure 10.4a–c).[125] Their results showed that the sensors, which could be actuated by the stomata pores themselves, operated repeatedly and reversibly for over one week, providing information on stomatal opening and closing latencies under different environmental states. In a recent study, Oren *et al.* installed tape-based graphene sensors onto maize leaves

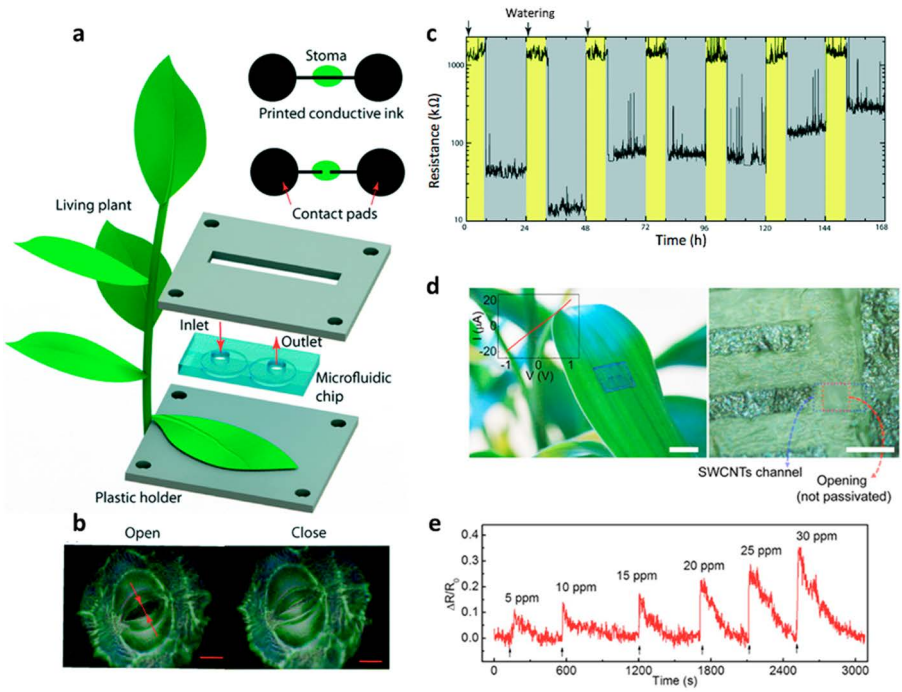

Figure 10.4 (a) Schematics of conductive circuits printing on the leaf surface. A microfluidic chip is placed on top of the leaf abaxial surface and clamped between two holders. (b) Microscopy picture of a plant stoma in the opened and closed states with the stomatal aperture indicated by red arrows. (c) Temporal resistance of stomatal pore size sensors on a specimen during days and nights (yellow and grey boxes, respectively). (d) A photograph, an optical microscope image, and characteristic I–V (inset) of SWCNT-graphite arrays transferred onto the surface of a live leaf. (e) Real-time sensing properties of a SWCNT-graphite array at different concentrations of DMMP. (a)–(c) Reproduced from ref. 125 with permission from the Royal Society of Chemistry and (d) and (e) Reproduced from Ref. 127 with permission from American Chemical Society, Copyright 2014.

to dynamically monitor relative humidity (RH) variations directly at the leaf surface. Changes in the electrical resistance of the graphene in response to different moisture environments were shown to enable real-time tracking of water loss. The authors were further able to use this information to estimate the time required for water movement within the plant from the roots to the lower and upper leaves.[126]

The incorporation of synthetic NC-sensors into different plant species can also enable plant-based chemical detection of target analytes that can be found in ambient soil or groundwater. For example, Wong *et al.* implanted fluorescent SWCNTs into the mesophyll leaves of living spinach plants to detect nitroaromatics.[85] The SWCNT sensors, which consisted of conjugated Bombolitin II peptides, were shown to modulate their near-infrared fluorescence emission at 1100 nm in response to nitroaromatics. The nitroaromatic targets were transported in solution up the roots and stem into the leaf tissues, accumulating in the mesophyll area in the vicinity of the embedded SWCNT sensors. The total response time of the sensor following the exposure of the plant roots was 5–15 minutes. Analogously, the incorporation of $(GT)_{15}$-wrapped-SWCNT has led to a plant-based technology for monitoring groundwater dopamine, which not only plays important roles in plant growth, development, and metabolism, but also presents an environmental concern for fish health.[85] Since this inaugural study, SWCNTs have been successfully incorporated into living plants to also facilitate the detection of nitric oxide (NO) and H_2O_2.[42,84] Lee *et al.* have also shown that toxic gases, such as dimethyl methylphosphonate (DMMP), can be sensed in real-time by integrating SWCNT-graphite arrays onto the surface of a live plant leaf (*Dracaena sanderiana cv. Virens*) (Figure 10.4d,e).[127]

10.4 Conclusions and Perspective

Nanomaterials offer a plethora of opportunities for enhancing the natural abilities of many living systems. Several examples of these augmented capabilities have been highlighted throughout this chapter, such as boosted photosynthetic activity or increased plant germination and crop productivity. However, a vast majority of applications remain to be investigated by the field. Most work has thus far focused on studying the fate of NCs in plants and other eukaryotic organisms, leading to a lack of knowledge regarding the impact of NCs on prokaryotic species. These species, which include bacteria such as cyanobacteria, are of particular interest to a number of green chemistry applications such as biophotovoltaics and biofuel production, as well as high-value microbial chemical synthesis. In addition, their incorporation into prokaryotes also present new sensing and imaging applications that are otherwise intractable using conventional approaches.

Continued development in the field therefore lies with NC design, application, and integration, with a focus on improving NC suitability for the diverse biological environments of both prokaryotic and eukaryotic species. Furthermore, future studies must also focus on the biocompatibility and

bioavailability of these materials. To date, the literature contains seemingly conflicting results on the possible side effects associated with nanoparticle uptake and distribution in plant and algal ecosystems. The variability in these findings indicates not only a species-dependent response to NCs, but also variability that may be strongly dependent on nanoparticle properties and functionalization, as well as exposure and incubation conditions. A clear delineation of exposure conditions, NC properties, and NC effects on the various species is therefore needed to promote and facilitate the implementation of NC-based technologies on the global scale. Large-scale NC implementation also requires an assessment of the long-term impact and wider environmental bioavailability and biodistribution of NCs into the ecosystem. Although similar assessments have already confirmed the benignity of commercially available nanoparticles found in the food and cosmetic industries, such rigorous assessments are lacking in the field of photosynthetic NC applications. Therefore, the potential benefits offered by NCs in photosynthetic applications can only be realized following the social and scientific acceptance of these nanoparticles in eukaryotic and prokaryotic organisms.

References

1. E. Roduner, *Chem. Soc. Rev.*, 2006, **35**, 583–592.
2. L. S. Li and X. Yan, *J. Phys. Chem. Lett.*, 2010, **1**, 2572–2576.
3. J. Peng, W. Gao, B. K. Gupta, Z. Liu, R. Romero-Aburto, L. Ge, L. Song, L. B. Alemany, X. Zhan, G. Gao, S. A. Vithayathil, B. A. Kaipparettu, A. a. Marti, T. Hayashi, J. J. Zhu and P. M. Ajayan, *Nano Lett.*, 2012, **12**, 844–849.
4. Y. P. Sun, B. Zhou, Y. Lin, W. Wang, K. A. S. Fernando, P. Pathak, M. J. Meziani, B. a. Harruff, X. Wang, H. Wang, P. G. Luo, H. Yang, M. E. Kose, B. Chen, L. M. Veca and S. Y. Xie, *J. Am. Chem. Soc.*, 2006, **128**, 7756–7757.
5. J. Wang, Y. Chen and W. J. Blau, *J. Mater. Chem.*, 2009, **19**, 7425–7443.
6. P. Avouris, M. Freitag and V. Perebeinos, *Nat. Photonics*, 2008, 341–350.
7. A. D. Franklin, *Nature*, 2013, **498**, 443–444.
8. R. J. Chen, S. Bangsaruntip, K. a. Drouvalakis, N. W. S. Kam, M. Shim, Y. Li, W. Kim, P. J. Utz and H. Dai, *Proc. Natl. Acad. Sci. U. S. A.*, 2003, **100**, 4984–4989.
9. Y. Li, F. Qian, J. Xiang and C. M. Lieber, *Mater. Today*, 2006, **9**, 18–27.
10. P. W. Barone, S. Baik, D. A. Heller and M. S. Strano, *Nat. Mater.*, 2005, **4**, 86–92.
11. D. A. Heller, H. Jin, B. M. Martinez, D. Patel, B. M. Miller, T.-K. Yeung, P. V. Jena, C. Höbartner, T. Ha, S. K. Silverman and M. S. Strano, *Nat. Nanotechnol.*, 2009, **4**, 114–120.
12. T. A. Swift, T. A. A. Oliver, M. C. Galan and H. M. Whitney, *Interface Focus*, 2018, **9**, 20180048.
13. D. S. Su and G. Centi, *J. Energy Chem.*, 2013, **22**, 151–173.

14. M. S. Mauter and M. Elimelech, *Am. Chem. Soc.*, 2008, 5843–5859.
15. S. Kruss, A. J. Hilmer, J. Zhang, N. F. Reuel, B. Mu and M. S. Strano, *Adv. Drug Deliv. Rev.*, 2013, **65**, 1933–1950.
16. S. F. Oliveira, G. Bisker, N. A. Bakh, S. L. Gibbs, M. P. Landry and M. S. Strano, *Carbon*, 2015, **95**, 767–779.
17. D. Maiti, X. Tong, X. Mou and K. Yang, *Front. Pharmacol.*, 2019, **9**, 1–16.
18. B. Lambert, A. J. Gillen, N. Schuergers, S. J. Wu and A. a. Boghossian, *Chem. Commun.*, 2019, **55**, 3239–3242.
19. F. J. Cunningham, N. S. Goh, G. S. Demirer, J. L. Matos and M. P. Landry, *Trends Biotechnol.*, 2018, **36**, 882–897.
20. K. Bates and K. Kostarelos, *Adv. Drug Deliv. Rev.*, 2013, **65**, 2023–2033.
21. P. D. Boyer, H. Shams, S. L. Baker, M. R. K. Mofrad, M. F. Islam and K. N. Dahl, *J. Mater. Chem. B*, 2016, **4**, 1324–1330.
22. G. Hong, S. Diao, A. L. Antaris and H. Dai, *Chem. Rev.*, 2015, **115**, 10816–10906.
23. L. Xie, G. Wang, H. Zhou, F. Zhang, Z. Guo, C. Liu, X. Zhang and L. Zhu, *Biomaterials*, 2016, **103**, 219–228.
24. K. Yang, S. Zhang, G. Zhang, X. Sun, S. T. Lee and Z. Liu, *Nano Lett.*, 2010, **10**, 3318–3323.
25. J. Qian, D. Wang, F.-H. Cai, W. Xi, L. Peng, Z.-F. Zhu, H. He, M.-L. Hu and S. He, *Angew. Chem., Int. Ed.*, 2012, **51**, 10570–10575.
26. Z. W. Ulissi, F. Sen, X. Gong, S. Sen, N. Iverson, A. a. Boghossian, L. C. Godoy, G. N. Wogan, D. Mukhopadhyay and M. S. Strano, *Nano Lett.*, 2014, **14**, 4887–4894.
27. R. M. Williams, C. Lee, T. V. Galassi, J. D. Harvey, R. Leicher, M. Sirenko, M. A. Dorso, J. Shah, N. Olvera, F. Dao, D. A. Levine and D. a. Heller, *Sci. Adv.*, 2018, **4**, 1090.
28. M. S. Strano, A. a. Boghossian, W.-J. Kim, P. W. Barone, E. S. Jeng, D. a. Heller, N. Nair, H. Jin, R. Sharma and C. Y. Lee, *MRS Bull.*, 2009, **34**, 950–961.
29. V. Zubkovs, A. Antonucci, N. Schuergers, B. Lambert, A. Latini, R. Ceccarelli, A. Santinelli, A. Rogov, D. Ciepielewski and A. A. Boghossian, *Sci. Rep.*, 2018, **8**, 1–10.
30. S. Kruss, D. P. Salem, L. Vuković, B. Lima, E. Vander Ende, E. S. Boyden and M. S. Strano, *Proc. Natl. Acad. Sci. U. S. A.*, 2017, **114**, 1789–1794.
31. L. Chio, J. T. Del Bonis-O'Donnell, M. P. Landry, G. F. Dorlhiac and I. R. McFarlane, *Nano Res.*, 2018, **11**, 5144–5172.
32. M. H. Wong, R. P. Misra, J. P. Giraldo, S. Y. Kwak, Y. Son, M. P. Landry, J. W. Swan, D. Blankschtein and M. S. Strano, *Nano Lett.*, 2016, **16**, 1161–1172.
33. V. Zubkovs, N. Schuergers, B. Lambert, E. Ahunbay and A. A. Boghossian, *Small*, 2017, **13**, 1–10.
34. A. J. Gillen, J. Kupis-Rozmyslowicz, C. Gigli, N. Schürgers and A. A. Boghossian, *J. Phys. Chem. Lett.*, 2018, 4336–4343.
35. A. Sciortino, A. Cannizzo and F. Messina, *J. Carbon Res.*, 2018, **4**, 67.

36. Y. Y. Hui, C. L. Cheng and H. C. Chang, *J. Phys. D: Appl. Phys.*, 2010, **43**, 37.
37. K. C. Neuman, *Biophys. J.*, 2017, **112**, 7a.
38. H. Wang, X. Wang, G. Qi, P. G. Luo, Y. Liu, S.-T. Yang, F. Lu, M. J. Meziani, Y.-P. Sun and L. Cao, *J. Am. Chem. Soc.*, 2009, **131**, 11308–11309.
39. Y. Wu and T. Weil, *Phys. Sci. Rev.*, 2017, **2**, 1–17.
40. J. Ge, Q. Jia, W. Liu, M. Lan, B. Zhou, L. Guo, H. Zhou, H. Zhang, Y. Wang, Y. Gu, X. Meng and P. Wang, *Adv. Healthcare Mater.*, 2016, **5**, 665–675.
41. J. Ge, Q. Jia, W. Liu, L. Guo, Q. Liu, M. Lan, H. Zhang, X. Meng and P. Wang, *Adv. Mater.*, 2015, **27**, 4169–4177.
42. J. P. Giraldo, M. P. Landry, S. M. Faltermeier, T. P. McNicholas, N. M. Iverson, A. A. Boghossian, N. F. Reuel, A. J. Hilmer, F. Sen, J. a. Brew and M. S. Strano, *Nat. Mater.*, 2014, **13**, 400–408.
43. Y. Gong and J. Zhao, *J. Agric. Food Chem.*, 2018, **66**, 9159–9161.
44. G. D. Scholes and E. H. Sargent, *Nat. Mater.*, 2014, **13**, 329–331.
45. Z. Liu, S. M. Tabakman, Z. Chen and H. Dai, *Nat. Protoc.*, 2009, **4**, 1372–1381.
46. D. Pantarotto, R. Singh, D. McCarthy, M. Erhardt, J. P. Briand, M. Prato, K. Kostarelos and A. Bianco, *Angew. Chem., Int. Ed.*, 2004, **43**, 5242–5246.
47. D. Pantarotto, J.-P. Briand, M. Prato and A. Bianco, *Chem. Commun.*, 2004, 16–17.
48. N. W. S. Kam, Z. Liu and H. Dai, *Angew. Chem., Int. Ed.*, 2006, **45**, 577–581.
49. Z. Liu, X. Sun, N. Nakayama-Ratchford and H. Dai, *ACS Nano*, 2007, **1**, 50–56.
50. L. Lacerda, H. Ali-Boucetta, M. A. Herrero, G. Pastorin, A. Bianco, M. Prato and K. Kostarelos, *Nanomedicine*, 2008, **3**, 149–161.
51. P. Wu, X. Chen, N. Hu, U. C. Tam, O. Blixt, A. Zettl and C. R. Bertozzi, *Angew. Chem., Int. Ed.*, 2008, **47**, 5022–5025.
52. G. Zuo, S. G. Kang, P. Xiu, Y. Zhao and R. Zhou, *Small*, 2013, **9**, 1546–1556.
53. N. Yanamala, V. E. Kagan and A. a. Shvedova, *Adv. Drug Deliv. Rev.*, 2013, **65**, 2070–2077.
54. X. Ma, J. Geiser-Lee, Y. Deng and A. Kolmakov, *Sci. Total Environ.*, 2010, **408**, 3053–3061.
55. A. Antonucci, J. Kupis-Rozmysłowicz and A. A. Boghossian, *ACS Appl. Mater. Interfaces*, 2017, **9**, 11321–11331.
56. Q. Liu, B. Chen, Q. Wang, X. Shi, Z. Xiao, J. Lin and X. Fang, *Nano Lett.*, 2009, **9**, 1007–1010.
57. J. Kupis-Rozmysłowicz, A. Antonucci and A. a. Boghossian, *ECS J. Solid State Sci. Technol.*, 2016, **5**, M3067–M3074.
58. S. J. Wu, N. Schuergers, K. H. Lin, A. J. Gillen, C. Corminboeuf and A. A. Boghossian, *ACS Appl. Mater. Interfaces*, 2018, **10**, 37386–37395.
59. A. J. Gillen and A. A. Boghossian, *Front. Chem.*, 2019, **7**, 612.
60. T. T. S. Lew, M. H. Wong, S. Y. Kwak, R. Sinclair, V. B. Koman and M. S. Strano, *Small*, 2018, **14**, 1–13.
61. M. F. Serag, N. Kaji, C. Gaillard, Y. Okamoto, K. Terasaka, M. Jabasini, M. Tokeshi, H. Mizukami, A. Bianco and Y. Baba, *ACS Nano*, 2011, **5**, 493–499.

62. M. F. Serag, N. Kaji, S. Habuchi, A. Bianco and Y. Baba, *RSC Adv.*, 2013, **3**, 4856.
63. S. Meiners, P. K. Gharyal and M. Schindler, *Planta*, 1991, **184**, 443–447.
64. H. I. Hussain, Z. Yi, J. E. Rookes, L. X. Kong and D. M. Cahill, *J. Nanopart. Res.*, 2013, **15**, 1–15.
65. L. Fan, R. Li, J. Pan, Z. Ding and J. Lin, *Trends Plant Sci.*, 2015, **20**, 388–397.
66. M. F. Serag, N. Kaji, M. Tokeshi and Y. Baba, *RSC Adv.*, 2012, **2**, 398–400.
67. E. Wild and K. C. Jones, *Environ. Sci. Technol.*, 2009, **43**, 5290–5294.
68. M. F. Serag, N. Kaji, E. Venturelli, Y. Okamoto, K. Terasaka, M. Tokeshi, H. Mizukami, K. Braeckmans, A. Bianco and Y. Baba, *ACS Nano*, 2011, **5**, 9264–9270.
69. M. F. Serag, K. Braeckmans, S. Habuchi, N. Kaji, A. Bianco and Y. Baba, *Nano Lett.*, 2012, **12**, 6145–6151.
70. M. Wierzbicka and J. Obidzinka, *Plant Sci.*, 1998, **137**, 155–171.
71. M. Khodakovskaya, E. Dervishi, M. Mahmood, Y. Xu, Z. Li, F. Watanabe and A. S. Biris, *ACS Nano*, 2009, **3**, 3221–3227.
72. A. Pourkhaloee, M. Haghigh, M. J. Saharkhiz, H. Jouzi and M. M. Doroodmand, *Seed Technol.*, 2011, **33**, 155–169.
73. M. H. Lahiani, E. Dervishi, J. Chen, Z. Nima, A. Gaume, A. S. Biris and M. V. Khodakovskaya, *ACS Appl. Mater. Interfaces*, 2013, **5**, 7965–7973.
74. M. H. Lahiani, J. Chen, F. Irin, A. a. Puretzky, M. J. Green and M. V. Khodakovskaya, *Carbon*, 2015, **81**, 607–619.
75. M. Zhang, B. Gao, J. Chen and Y. Li, *J. Nanopart. Res.*, 2015, 17, 78.
76. C. Wang, H. Zhang, L. Ruan, L. Chen, H. Li, X. L. Chang, X. Zhang and S. T. Yang, *Environ. Sci.: Nano*, 2016, **3**, 799–805.
77. S. Lin, J. Reppert, Q. Hu, J. S. Hudson, M. L. Reid, T. a. Ratnikova, A. M. Rao, H. Luo and P. C. Ke, *Small*, 2009, 1128–1132.
78. W. Li, Y. Zheng, H. Zhang, Z. Liu, W. Su, S. Chen, Y. Liu, J. Zhuang and B. Lei, *ACS Appl. Mater. Interfaces*, 2016, **8**, 19939–19945.
79. H. Villagarcia, E. Dervishi, K. De Silva, A. S. Biris and M. V. Khodakovskaya, *Small*, 2012, **8**, 2328–2334.
80. M. V. Khodakovskaya, K. De Silva, A. S. Biris, E. Dervishi and H. Villagarcia, *ACS Nano*, 2012, **6**, 2128–2135.
81. M. V. Khodakovskaya, K. de Silva, D. a. Nedosekin, E. Dervishi, a. S. Biris, E. V. Shashkov, E. I. Galanzha and V. P. Zharov, *Proc. Natl. Acad. Sci. U. S. A.*, 2010, **108**, 1028–1033.
82. Q. Liu, X. Zhang, Y. Zhao, J. Lin, C. Shu, C. Wang and X. Fang, *Environ. Sci. Technol.*, 2013, **47**, 7490–7498.
83. H. Li, J. Huang, F. Lu, Y. Liu, Y. Song, Y. Sun, J. Zhong, H. Huang, Y. Wang, S. Li, Y. Lifshitz, S.-T. Lee and Z. Kang, *ACS Appl. Bio Mater.*, 2018, **1**, 663–672.
84. J. P. Giraldo, M. P. Landry, S.-Y. Kwak, R. M. Jain, M. H. Wong, N. M. Iverson, M. Ben-Naim and M. S. Strano, *Small*, 2015, 3973–3984.
85. M. H. Wong, J. P. Giraldo, S.-Y. Kwak, V. B. Koman, R. Sinclair, T. T. S. Lew, G. Bisker, P. Liu and M. S. Strano, *Nat. Mater.*, 2016, **16**, 1–8.

86. G. S. Demirer, H. Zhang, J. L. Matos, N. S. Goh, F. J. Cunningham, Y. Sung, R. Chang, A. J. Aditham, L. Chio, M.-J. Cho, B. Staskawicz and M. P. Landry, *Nat. Nanotechnol.*, 2019, **14**, 456–464.
87. S. K. Verma, A. K. Das, S. Gantait, V. Kumar and E. Gurel, *Sci. Total Environ.*, 2019, **667**, 485–499.
88. J. Barber, *Chem. Soc. Rev.*, 2009, **38**, 185–196.
89. R. E. Blankenship, *Plant Physiol.*, 2010, **154**, 434–438.
90. J. Barber and P. D. Tran, *J. R. Soc., Interface*, 2013, **10**, 20120984.
91. F. Milano, A. Punzi, R. Ragni, M. Trotta and G. M. Farinola, *Adv. Funct. Mater.*, 2018, **1805521**, 1805521.
92. A. Operamolla, R. Ragni, F. Milano, R. Roberto Tangorra, A. Antonucci, A. Agostiano, M. Trotta and G. Farinola, *J. Mater. Chem. C*, 2015, **3**, 6471–6478.
93. T. Wenzel, D. Härtter, P. Bombelli, C. J. Howe and U. Steiner, *Nat. Commun.*, 2018, **9**, 1–9.
94. M. Sawa, A. Fantuzzi, P. Bombelli, C. J. Howe, K. Hellgardt and P. J. Nixon, *Nat. Commun.*, 2017, **8**, 1–9.
95. M. Mouhib, A. Antonucci, M. Reggente, A. Amirjani, A. J. Gillen and A. A. Boghossian, *Nano Res.*, 2019, 1–16.
96. J. M. Pisciotta, Y. Zou and I. V. Baskakov, *PLoS One*, 2010, **5**, e10821.
97. M. D. Lambreva, T. Lavecchia, E. Tyystjärvi, T. K. Antal, S. Orlanducci, A. Margonelli and G. Rea, *Photosynth. Res.*, 2015, **125**, 451–471.
98. Z. Kang, M. Zhang, Y. Liu, M. Shao, H. Li, H. Huang, Y. Song and H. Wang, *ACS Appl. Bio Mater.*, 2018, **1**, 894–902.
99. H. Wang, M. Zhang, Y. Song, H. Li, H. Huang, M. Shao, Y. Liu and Z. Kang, *Carbon*, 2018, **136**, 94–102.
100. W. Li, S. Wu, H. Zhang, X. Zhang, J. Zhuang, C. Hu, Y. Liu, B. Lei, L. Ma and X. Wang, *Adv. Funct. Mater.*, 2018, **1804004**, 1804004.
101. W. Zhou, J. Zhuang, W. Li, C. Hu, B. Lei and Y. Liu, *J. Mater. Chem. C*, 2017, **5**, 8014–8021.
102. S. Chandra, S. Pradhan, S. Mitra, P. Patra, A. Bhattacharya, P. Pramanik and A. Goswami, *Nanoscale*, 2014, **6**, 3647–3655.
103. L. Sai, S. Liu, X. Qian, Y. Yu and X. Xu, *Colloids Surf., B*, 2018, **169**, 422–428.
104. N. Schuergers, C. Werlang, C. M. Ajo-Franklin and A. A. Boghossian, *Energy Environ. Sci.*, 2017, **10**, 1102–1115.
105. N. Sekar, Y. Umasankar and R. P. Ramasamy, *Phys. Chem. Chem. Phys.*, 2014, **16**, 7862–7871.
106. F. L. Ng, M. M. Jaafar, S. M. Phang, Z. Chan, N. A. Salleh, S. Z. Azmi, K. Yunus, A. C. Fisher and V. Periasamy, *Sci. Rep.*, 2014, **4**, 2–8.
107. M. V. Khodakovskaya, B. S. Kim, J. N. Kim, M. Alimohammadi, E. Dervishi, T. Mustafa and C. E. Cernigla, *Small*, 2013, **9**, 115–123.
108. M. Haghighi and J. a. Teixeira Da Silva, *J. Crop Sci. Biotechnol.*, 2014, **17**, 201–208.
109. X. Wang, H. Han, X. Liu, X. Gu, K. Chen and D. Lu, *J. Nanopart.Res.*, 2012, **14**, 841.

110. N. Dasgupta-Schubert, D. K. Tiwari and L. M. Villaseñor Cendejas, *J. Nanobiotechnol.*, 2016, **14**, 1–10.
111. S. Tripathi, S. K. Sonkar and S. Sarkar, *Nanoscale*, 2011, **3**, 1176–1181.
112. M. Zhang, Y. Liu, Z. Kang, L. Hu, H. Li, H. Huang, H. Wang, M. Shao and Y. Song, *Nanoscale*, 2018, **10**, 12734–12742.
113. C. Kole, P. Kole, K. M. Randunu, P. Choudhary, R. Podila, P. C. Ke, A. M. Rao and R. K. Marcus, *BMC Biotechnol.*, 2013, 37.
114. A. Joshi, S. Kaur, K. Dharamvir, H. Nayyar and G. Verma, *J. Sci. Food Agric.*, 2018, **98**, 3148–3160.
115. X. Wang, Z. Zhou and F. Chen, *Materials*, 2017, **10**, 1375.
116. Y. He, R. Hu, Y. Zhong, X. Zhao, Q. Chen and H. Zhu, *Viruses*, 2017, **11**, 1–10.
117. P. Wang, F.-J. Zhao and P. M. Kopittke, *Trends Plant Sci.*, 2019, **24**, 1–4.
118. Q. Liu, B. Chen, Q. Wang, X. Shi, Z. Xiao, J. Lin and X. Fang, *Nano Lett.*, 2009, **9**, 1007–1010.
119. S.-Y. Kwak, T. T. S. Lew, C. J. Sweeney, V. B. Koman, M. H. Wong, K. Bohmert-Tatarev, K. D. Snell, J. S. Seo, N.-H. Chua and M. S. Strano, *Nat. Nanotechnol.*, 2019, **14**, 447–455.
120. G. S. Demirer, H. Zhang, J. L. Matos, N. S. Goh, F. J. Cunningham, Y. Sung, R. Chang, A. J. Aditham, L. Chio, M.-J. Cho, B. Staskawicz and M. P. Landry, *Nat. Nanotechnol.*, 2019, 1–31.
121. G. S. Demirer, H. Zhang, N. S. Goh, R. Chang and M. P. Landry, *bioRxiv*, 2019, 564427.
122. H. Zhang, G. S. Demirer, H. Zhang, T. Ye, N. S. Goh, A. J. Aditham, F. J. Cunningham, C. Fan and M. P. Landry, *Proc. Natl. Acad. Sci. U. S. A.*, 2019, **116**, 7543–7548.
123. J. P. Giraldo, H. Wu, G. M. Newkirk and S. Kruss, *Nat. Nanotechnol.*, 2019, **14**, 541–553.
124. S.-Y. Kwak, M. H. Wong, T. T. S. Lew, G. Bisker, M. A. Lee, A. Kaplan, J. Dong, A. T. Liu, V. B. Koman, R. Sinclair, C. Hamann and M. S. Strano, *Annu. Rev. Anal. Chem.*, 2017, **10**, 113–140.
125. V. B. Koman, T. T. S. Lew, M. H. Wong, S. Y. Kwak, J. P. Giraldo and M. S. Strano, *Lab Chip*, 2017, **17**, 4015–4024.
126. S. Oren, H. Ceylan, P. S. Schnable and L. Dong, *Adv. Mater. Technol.*, 2017, **2**, 1–14.
127. K. Lee, J. Park, M. S. Lee, J. Kim, B. G. Hyun, D. J. Kang, K. Na, C. Y. Lee, F. Bien and J. U. Park, *Nano Lett.*, 2014, **14**, 2647–2654.

Subject Index